# NMR Spectroscopic Mechanistic Investigations of Photocatalytic Transformations

## Dissertation

zur Erlangung des Doktorgrades der Naturwissenschaften

(Dr. rer. nat.)

der Fakultät für Chemie und Pharmazie

der Universität Regensburg

vorgelegt von

**Nele Berg**

aus Regensburg

**im Jahr 2020**

Die vorliegende Dissertation beruht auf Arbeiten, die zwischen Januar 2017 und Juni 2020 am Arbeitskreis von Frau Professor Dr. Ruth M. Gschwind am Institut für Organische Chemie der Universität Regensburg durchgeführt wurden.

Promotionsgesuch eingereicht am:     29. Juni 2020

Die Arbeit wurde angeleitet von:     Prof. Dr. Ruth M. Gschwind

Promotionsausschuss:

       Vorsitzender:     Prof. Dr. Oliver Tepner

       1. Gutachter:     Prof. Dr. Ruth M. Gschwind

       2. Gutachter:     Prof. Dr. Werner Kremer

       3. Prüfer/in:     Prof. Dr. Julia Rehbein

*Meinen Eltern*

O schwärme, schwärme, Lieber, ungezügelt,
nach jeder Erdenfreude lustbeflügelt!
Nur eins verliere nicht:
den roten Faden deiner tiefsten Pflicht.
Die aber ist:
Dich selber zu entdecken
und dann dich selber nach dir selbst zu strecken.

*Christian Morgenstern*

# NMR Spectroscopic Mechanistic Investigations of Photocatalytic Transformations

Nele Berg

# TABLE OF CONTENTS

## 3    Metal-free, Photocatalytic PCET-Induced Ring-Opening Remote Functionalization of Cyclo-Alkanols by Direct Intermolecular C-C-Coupling with Olefins – Beyond Simple $pK_a$-related Base Effects ...... 121

# 1 Introduction and Outline

## 1.1 Photochemistry and Photoredox Catalysis

### 1.1.1 General Concept

Visible light driven reactions are ubiquitous in nature and are responsible for the existence of most life on earth. Using photosynthesis, green plants are able to convert $CO_2$ and $H_2O$ into highly energetic organic molecules using sunlight as an energy source.[1] One of the pioneering scientists in the field of photochemistry, the Italian-born chemist Giacomo Ciamician, was inspired by the nature and published a paper outlining his seminal vision of using sunlight, which is available and accessible all over the earth, as energy source and thus set the cornerstone for the development of sustainable photochemical transformations being independent of finite fossil resources.[2] Imitating the concept of converting light into usable energy paved the way for the development of sustainable and forward-looking innovations such as solar cells, photovoltaics and molecular machines.[3][4] In the field of organic chemistry, the use of visible light driven reactions emerged as novel synthetic strategies. In general, a photochemical reaction is defined as any molecular transformation caused by the absorption of UV, IR or visible light.[5] A molecule is able to absorb light if the irradiation energy is sufficient to excite the molecule from the electronic ground state to the excited state.[6][7][8] The correlation between the frequency $\nu$ of the light and its resulting energy E is described by the Planck equation $E = h\nu$ (with h = Planck's constant). Typical classes of organic absorbers include conjugated alkenes, carbonyls and aromatic species with high electron density. The excited state is of high energy and thus has the power to enable reactions, which are endergonic in the ground state. The Jabłoński diagram in Figure 1 graphically illustrates the radiative excitation of an electron (blue arrow) and subsequent possible light dependent (corrugated lines) and light independent (solid lines) transitions. In the majority of the cases the absorbance leads to the excitation of an electron from the highest occupied orbital (HOMO) into the lowest unoccupied orbital (LUMO), which is mostly an antibonding $\pi^*$ orbital allowing new possibilities of chemical transformations. According to the Franck-Condon principle, the excitation can be described sufficiently by reorganization of electrons with nearly-static nuclei during its very short time frame ($\sim 10^{-15}$ s;[8] described by vertical lines in Figure 1). This results in a different geometry of the excited state, which is not at its energetic minimum. Moreover, the electron spin remains unchanged for this process, as inversion is quantum mechanically forbidden. Vibrational/thermal relaxation, which implies non-radiative transfer of thermal energy into the surrounding, quickly ($10^{-12}$-$10^{-10}$ s) brings the excited state to a new energy minimum. From this position on the potential energy

diagram, different processes are possible:[9] in general, the excited state can be deactivated by internal conversion ($10^{-11}$-$10^{-9}$ s). Furthermore, it can be transferred back to the ground state by emitting light, which is called fluorescence ($10^{-10}$-$10^{-7}$ s). The excited singlet state can further be transformed into a triplet state by intersystem crossing ($10^{-10}$-$10^{-8}$ s), which implies spin inversion. Via thermal relaxation, the energetic minimum is received again. The excited triplet state can then return to the ground state by emitting light, which is commonly referred to as phosphorescence ($10^{-6}$-10 s).
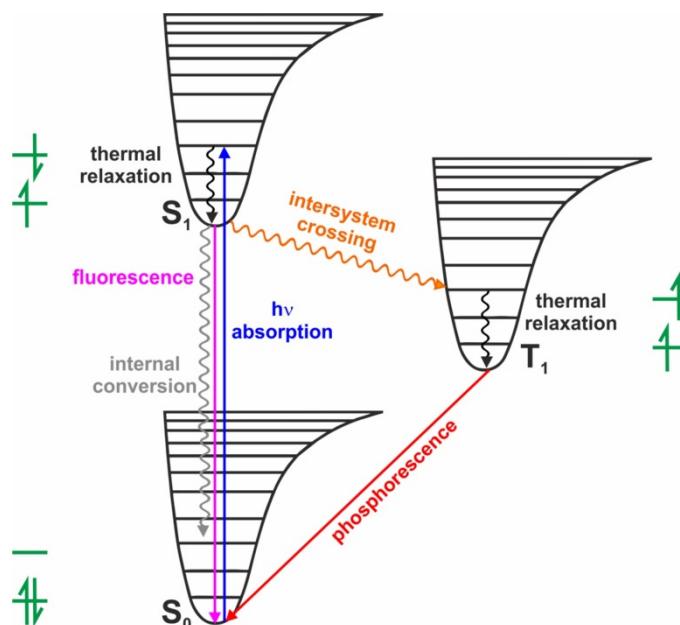


**Figure 1.1:** Jabłoński diagram of light induced excitation (blue) and possible radiative (strait lines) and non-radiative (corrugated lines) transitions including the corresponding spin orientations of the valence electrons (green); $S_0$: singlet ground state, $S_1$: first excited singlet state, $T_1$: first triplet state.

For a productive chemical reaction between two reactants, the energy needs to be transferred from one molecule the other. Depending on the characteristics of the species, this process mainly occurs via the triplet excited state of one compound and can be achieved by directly exciting the substrate or by using sensitizers/quenchers. For successful photosenzitation or quenching, several requirements have to be fulfilled: in order to prevent side reactions with other excitable species in the reaction mixture, the sensitizer or quencher as main absorber is required to have a faster intersystem crossing rate compared to the other compounds. Moreover, the triplet state of the sensitizer/quencher must be of higher energy than the triplet state of the species, which is produced after energy transfer with spin conversion. The efficiency of a photochemical reaction can be characterized by determining the quantum yield $\phi$, which describes the ratio of the converted molecules to the number of absorbed photons leading to the desired

reaction product. Usually the quantum yield is lower than 1 ($\phi$ = 1 means for every absorbed photon a product molecule is produced) but can also be higher for chain reactions.

One of the first photochemical reactions were developed by Norrish in 1932. In the so-called Norrish-Type-I reaction, the cleavage of C-C bonds vicinal to carbonyl groups of ketones and aldehydes was achieved using UV-light.[10] In a pursued protocol, protons in the γ-position of carbonyls could be abstracted (Norrish-Type-II).[11] The resulting radical species, however, can undergo multiple transformations lowering the selectivity of the overall reaction. Moreover, although quite a number of efficient photochemical transformations were developed, such systems are limited to light absorbing substrates. Using a sensitizer without regeneration, waste production also prevents an environmentally friendly strategy.
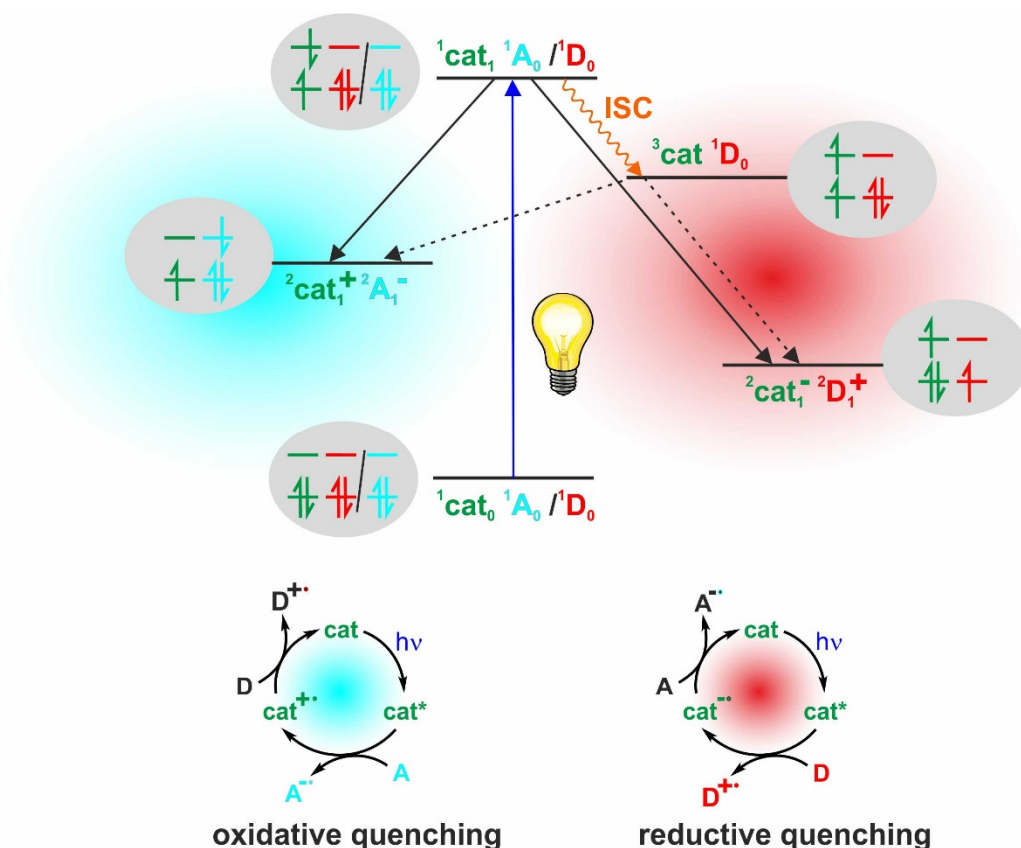


**Figure 1.2:** Jabłoński diagram of a photocatalyst/acceptor (blue) and photocatalyst/donor (red) system and the corresponding photocatalytic cycles of oxidative and reductive quenching; cat = photocatalyst, A = e- acceptor, D = e- donor; $^{1/2/3}X_{0/1}$ = singlet state ($^1$), charge transfer state ($^2$) and triplet state ($^3$) of species X in the ground state ($_0$) or excited state ($_1$).

Hence, the concept of photoredox catalysis paved the way for new synthetic strategies. On the one hand, the excitation step is separated from the actual reaction as the energy

is absorbed by the photocatalyst and transfered towards the substrate, which can be light-transparent. On the other hand, the photocatalyst is regenerated in a catalytic redox cycle and therefore contributes to a sustainable and atom-economic reaction design. For an effective photoredox catalysis the energy absorbed by the photocatalyst must be transferred to the reaction center without any molecular catalyst-substrate reaction. Therefore, the catalyst needs to be photo-stable and is required to produce a sufficient amount of excited state species ($S_1$ or $T_1$) with a lifetime long enough to transfer the energy to the substrate. The Jabłoński diagram in Figure 2 shows two possible photocatalytic pathways. The excited photocatalyst can interact with an acceptor (A) or a donor (D), which remain at their ground state during irradiation. Subsequently, either the energy is transferred from the singlet state catalyst to the acceptor (blue) or the donor donates an electron to the triplet state catalyst, which is formed by intersystem crossing (red). The corresponding photocatalytic cycles picture both general concepts of oxidative and reductive quenching.

$Ru(bpy)_3^{2+}$, which meanwhile has gained widespread applications, was used in one of the first photocatalytic reactions, the light-driven Pschorr reaction for the synthesis of phenanthrenes from aryldiazonium salts (Figure 3a).[12] In general, upon irradiation with light of 452 nm $Ru(bpy)_3^{2+}$ gets excited to $Ru(bpy)_3^{2+*}$, which implies the oxidation of the Ru(II) metal center via metal-to-ligand-charge-transfer (MLCT) and the accompanied reduction of the ligand via single-electron-reduction (SET; see Figure 3b).[13][14][15][16] After ISC the triplet state basically is both a better oxidizing and reducing agent than the ground state species which is clearly demonstrated by the respective redox potentials. In a reductive quenching cycle, an electron is transferred from a donor molecule (reductive quencher) towards the Ru-complex yielding $Ru(bpy)_3^+$ as strong reducing agent. Subsequently, the catalyst is regenerated by reducing an acceptor species. In the oxidative quenching process, an electron transfer from the catalyst towards an acceptor furnishs the strong oxidant $Ru(bpy)_3^{3+}$ which then is again reduced by a donor molecule. Typical reductive quenchers are tertiary amines, e.g. $Et_3N$, xanthates and ascorbates and for oxidative quenchers nitro compounds and $Fe^{3+}$ salts are commonly used.[14][17] Besides $Ru(bpy)_3Cl_2$ and $Ru(bpy)_3(BF_2)_2$, further polypyridine containing photocatalysts are well established including modified Ru(II) and Ir(II) species as well as metal free purely organic chromophores, such as *N*-alkylated 9-mesityl acridinium (Mes-Acr) salts (Figure 3c).[17][18][19]
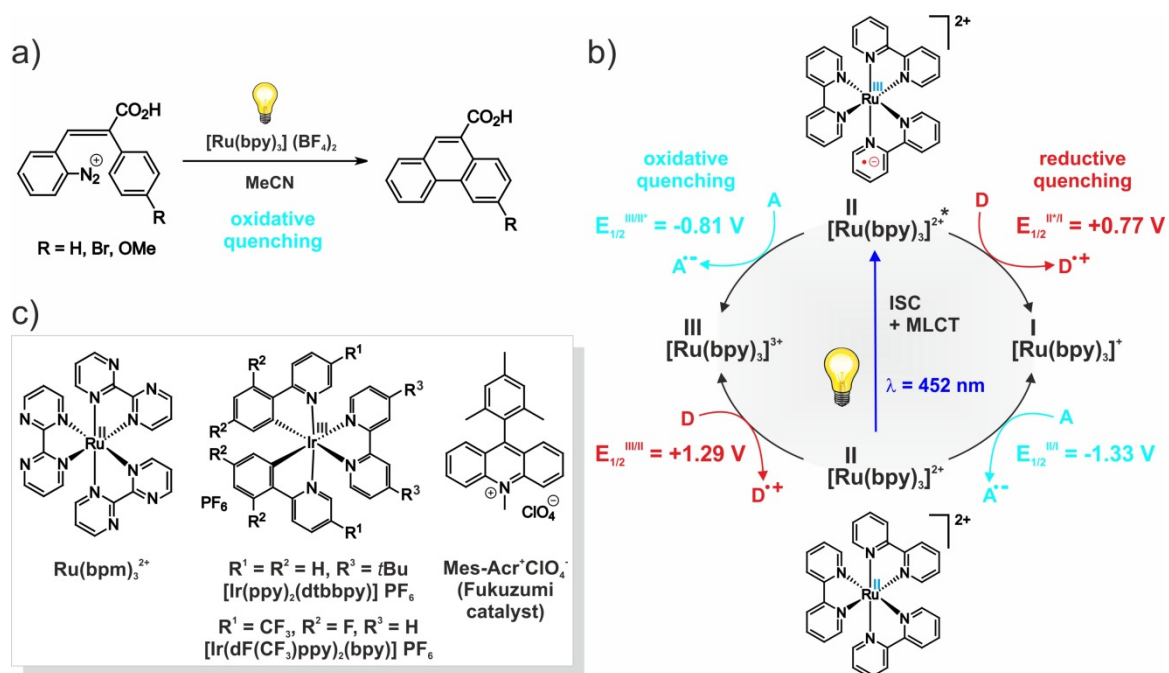
**Figure 1.3:** a) One of the first photocatalytic reactions: blue light-induced Pschorr reaction for the synthesis of phenanthrenes; b) general scheme for the oxidative and reductive quenching cycle of the Ru(bpy)$_3^{2+}$ photocatalyst; c) common classes of photocatalysts including Ru- and Ir-based and metal-free organic species.

Owing to its atom-economic, mild and operationally simple procedure, photocatalysis became one of the most important synthetic strategies for the development of new organic reaction protocols over the last decades. Cross-coupling reactions, cycloadditions, $\alpha$-amino C-H functionalization of amines, *anti*-Markovnikov additions to alkenes, arene functionalization, polymerizations and enantioselective transformations are only a few examples for the broad field.[17][20] Besides the environmental aspect, completely new strategies enabled even the activation of strong bonds, such as O-H, N-H and C-H, which is a very challenging tool using conventional synthetic tools (for a detailed explanation, see chapters 1.2.2 and 2). In general, for the development of new synthetic protocols a fundamental understanding of the reaction mechanism is vital.

## 1.1.2  NMR-Spectroscopy for Mechanistic Analysis of Photoreactions

The elucidation of chemical reaction mechanisms is indispensable for understanding the performance of molecules and their concrete interactions and thus is the key for the optimization of reaction conditions, yields, substrate scopes and the development of new synthetic strategies. In order to set the framework for a successful photocatalytic reaction, the reaction system including catalyst, reactants, solvent and wavelength of the light

needs to be optimized. UV/Vis absorption spectroscopy provides information about the absorbance of the photocatalyst and the substrates. Moreover, the photon absorption yield and the lifetime of an excited photocatalyst can be determined using UV absorptioin and/or fluorescence measurements.[7] For a successful photoinduced electron transfer (PET) the redox properties of both the donor and acceptor need to be suitable. In principle, standard redox potentials for commonly used photocatalysts and reagents can be gathered from literature.[15][21] For an experimental determination of redox potentials cyclic voltammetry (CV) is an established method. A successful energy transfer between excited photocatalyst and substrate and the suppression of unproductive back reactions are the basis for subsequent mechanistic events. Usually, a UV inactive reactive compound cannot be isolated due to its short lifetime or complex formation, which might involve a combination of more compounds whose composition cannot be preserved from the mixture during separation. Luminescence quenching analysis provides general information about the interaction between the excited state catalyst and other reaction species.[22] Furthermore, a combination of radical trapping experiments and structure determination methods, such as gas chromatography (GC) and mass spectrometry (MS), as well as electron paramagnetic resonance spectroscopy (EPR) reveal an existing radical based pathway and structural information about the compounds involved.[23][24] Beyond that, following the reaction with UV/Vis spectroscopy gives general insight into the absorption behavior of the reaction mixture over time and thus the generation of intermediates and reactive complexes can be uncovered.[25] Moreover, (ultrafast) transient absorption spectroscopy also known as laser flash photolysis (LFP) reveals the presence of even very short-lived intermediates (femto-second range) at specific wavelengths and their corresponding lifetimes.[26] But the described method often cannot be used to assign the concrete molecular structures of the involved species inside the mixture directly during the reaction.

Hence, despite low time resolution and sensitivity of conventional NMR methods, nuclear magnetic resonance (NMR) spectroscopy has unique possibilities to gain information about reaction kinetics, formation and nature of intermediates with lifetimes on the NMR time scale, product and by-product formation and at the same time, even about the formation of radical species and molecular aggregation. The analysis of photocatalytic reactions is often focused on the primary photo-excitation and energy transfer from catalyst to substrate. However, the elucidation of detailed downstream pathways including light-dependent and -independent reactivities, solvent effects and concrete intermolecular interactions are frequently neglected as basis for efficient molecular interactions.

In 2013, an *in-situ* illumination setup was developed in our group, which enables direct NMR analysis during the photocatalytic reaction and thus provides a flexible and simple

tool for mechanistic analyses.[27][28] The reaction mixture can directly be irradiated inside the NMR spectrometer using a glass fiber, which transfers the light into the sample inside the tube. The light-emitting diodes (LEDs) can be controlled by the NMR console, which offers continuous or pulsed irradiation and complete automation of the measurements. A few years later, this system, which was successfully adopted by other groups,[29][30][29] was further equipped with absorption spectroscopy. In an automated combination of *in-situ* illumination, NMR and UV/Vis spectroscopy, paramagnetic species, such as stable radicals, and diamagnetic species are detectable at the same time.[31] Hence, with these methods in hand, photocatalytic reactions as well as photoswitches and photo-induced isomerizations were monitored and combined with standard NMR measurements, crucial reactive transient species and downstream reaction pathways could be revealed.[32][33][34][35][36][37] By decreasing the temperature during or after illumination, reaction intermediates, which are inaccessible at room temperature, can be identified and assigned as well. In addition, light on-off experiments reveal light and dark reactions.[38][39] In order to guarantee sufficient stirring and direct irradiation, flow-NMR setups are of current interest.[40][41] Moreover, the meanwhile well-established concept of chemical induced dynamic nuclear polarization (photo-CIDNP) spectroscopy is an elegant tool for the indirect detection of transient radical and biradical species produced during a photocatalytic reaction, which are inaccessible by EPR.[33][42][43] Upon formation of unpaired electrons the spin coupling between electron and nuclei can be identified by changes of the $^1$H signal intensities. Furthermore, chemical exchange saturation transfer (CEST) was successfully applied for the identification of photocatalytic intermediates.[44] In principle, chemical exchange between two species on the ms time scale can be revealed when saturation transfer between the exchanging intermediate and an NMR detectable species occurs.[45] Due to enhanced sensitivity of CEST, it proofs to be a great method to detect low populated intermediates, which usually lay beyond the NMR detection limit. The identification of intermediates can further be accomplished by increasing the relaxation time. This can be achieved by reversible photoswitching between paramagnetic and diamagnetic species, applying photo-induced reversible acceleration of $T_1$-relaxation (PIRAT).[46] Here, the reversibility prevents from usual line broadening due to the presence of paramagnetic compounds. Moreover, the efficiency of the entire photocatalytic system can be analyzed using NMR actinometry-quantum yield determination.[32][47]

## 1.2 Hydrogen Bonds as Fundamental Concept for Chemical Transformations

### 1.2.1 Definition and Characteristics of Hydrogen Bonds

A hydrogen bond (H-bond) X-H···A is generally defined as interaction between a hydrogen bond donor X-H (X = O, N, etc.) and a hydrogen bond acceptor A exceeding pure van-der-Waals interactions (Figure 4a).[48][49][50] The H-bond formation is mediated by an interaction of the dipole of X-H and the lone pair of A. As H-bonds play an essential role in biological and biochemical transformations, such as receptor recognition of enzymes[51], protein folding,[52] and Watson-Crick base pairing in DNA,[53] as well as in organic and inorganic chemical molecular systems, they represent the most important non-covalent intermolecular interaction especially due to their unique directional properties.
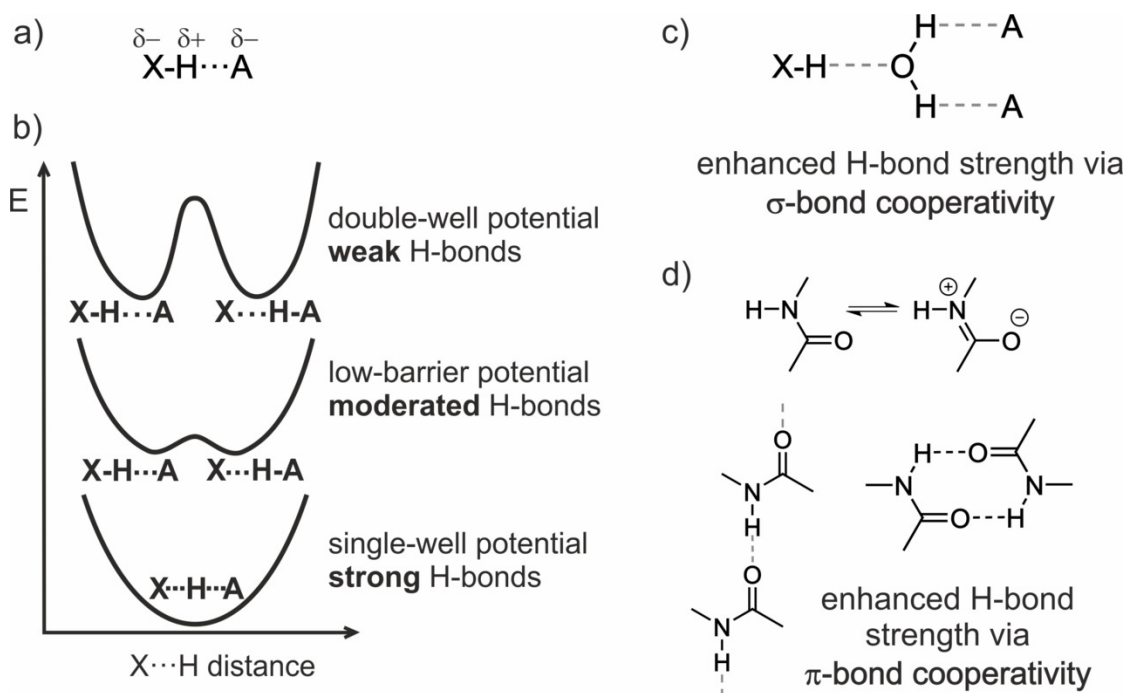


**Figure 1.4:** a) General definition of a hydrogen bond formed by non-covalent interaction between a donor X-H and an acceptor A; b) energy potential diagram and structural motifs of strong, moderate and weak symmetric H-bonds (X = A); c) example for a H-bond strengthening via σ-bond cooperativity furnished by a $H_2O$-mediated network; d) due to simultaneous acceptor and donor properties of amides, the zwitterionic structure is stabilized leading to strong intermolecular H-bonds enhanced via π-bond cooperativity.

In general, the H-bond can range from very weak to very strong non-covalent interactions with dissociation energies between 0.2 and 40 kcal/mol, which comprises of electrostatics, polarization, charge transfer or covalent bonding, dispersion and exchange repulsion (for

comparison: BDFE of covalent bonds lay between 50 and 100 kcal/mol).[48][54] The nature of the H-bond is influenced by the acidity/basicity of the interaction partners and the properties of the solvent. Besides simple X-H···A, bifurcated and trifurcated structures exist, in which two or three acceptors are attached to one donor. The geometry of the H-bond has also impact on the strength. In a strong H-bond (15-40 kcal/mol) the proton is localized approximately in the center between X and A with an angle around 180°, which is described by the corresponding "single-well" potential shown in Figure 4b (bottom).[54] For moderate ("low-barrier" potential) and weak (less than 4 kcal/mol) H-bonds the X···A distance is increased and the angle reduced.[55] The associated "double-well" potential shows two energetic minima at which the proton is either positioned on the donor or acceptor side (Figure 4b, top). The potentials are only symmetric in the case of identical X and A and varied functionalities show different energy minima. Examples for strong H-bonds are ionic structures, such as O-H···O⁻, ⁺N-H···N or F-H···F⁻ of acid/base pairs. Moderate H-bonds include the O-H···O motif in bulk water[48] and for weak H-bonds C-H···O[56] interactions are known, e.g. for intermolecular interactions between *N,N*-dimethylnitoamines.[57] The formation of this non-covalent interaction implies increased polarity of both donor and acceptor and thus, in an H-bond network, the individual interactions are even more strengthened via σ-bond cooperativity (Figure 4c). Structural motifs with simultaneous donor and acceptor abilities tend to form rings or larger aggregates. An amide, for example, which represents the main functionality inside proteins, potentially exists in two resonance forms and the resulting stabilized ionic structure leads to stronger intermolecular interactions to form rings and chains (Figure 4d). This effect is called π-bond cooperativity.

In order to predict and control the formation of a hydrogen bond between two species in a particular solvent the acceptor and donor abilities of different functional groups give first hints as investigated by Hunter.[58] Furthermore, concrete probabilities of the interaction between numerous organic pairs in the crystal structure help for assumption of reactivities in solution.[59][60][61]

## 1.2.2  Hydrogen Bonds in Photocatalysis

Hydrogen bonding is responsible for directed chemical transformations not only in biological systems but also in the field of catalytic synthesis in organic chemistry. Utilizing the dynamic nature of H-bonds the reaction path can be controlled by the generation of a geometrically defined pre-oriented substrate/catalyst, substrate/co-catalyst or intramolecular substrate complexation. One prominent scientific area is the asymmetric organocatalysis using H-bond donating chiral catalysts.[62][63][64][65][66][67] In this case, the H-

bond mediated activation of the substrate leads to a reduction of its electron density and therefore paves the way for nucleophilic attack. Besides, numerous effective organocatalytic transformations involving H-bonding were developed[68] including asymmetric Aldol reactions,[69] tetrahydropyranylation,[70] Michael-Michael cascade[71] and Diels-Alder reactions.[72][73][74][75] The concept of H-bonding is also known in the field of transition-metal catalysis and can be key to intrinsic substrate conversions.[76][77][78]

To this day, the successful energy transfer between substrate and photocatalyst was attributed mainly to matching redox potentials between the two compounds, whereas hydrogen bonding is still often neglected for the development of light-induced reactions in the area of photocatalysis. The formation of crucial preassemblies is the key to successful molecular interaction and thus has impact on electron and atom transfer events as well as on crucial downstream reactions. As such, a number of groups already adopted the concept of H-bonding for photocatalytic transformations. Charge transfer for example was shown to be enhanced for heterogeneous photocatalytic systems by using hydrogen bond assisted materials.[79] Moreover, in a recent paper the acceleration of $H_2O$ splitting and $H_2$ generation was published.[80] Due to the dynamic nature of hydrogen bonding the proton exchange could be accelerated in heterogeneous photocatalytic graphitic carbon nitride systems. Moreover, in the field of homogeneous photocatalysis, intramolecular H-bond formation of fluoro-arene substrates was found to improve selective C-F cleavage in hydrodefluorination reactions.[81] Furthermore, enabling an intermolecular linkage between a Ruthenium photosensitizer and a Rhenium catalyst the group of Kubiak could enhance the $CO_2$ reduction.[82]

But one of the most important applications of H-bonds in photocatalysis is the controlled synthesis of stereo-specific compounds. The use of chiral organic photocatalysts, which imbed the substrate in a guest-host complex, are well established, e.g. for inter- and intra-molecular photocylcoadditions, -dimerizations, Norrish-Yang and Diels-Alder reactions.[83][84][85][86] The group of Bach further developed chiral xanthone and thioxanthone photocatalysts to deracemize sulfoxides and allenes (Figure 5).[87][88] Moreover, the combination of H-bond mediated iminium and enamine catalysis with photocatalysis paved the way for efficient stereo-controlled activation of α,β-unsaturated carbonyl species.[89] In addition, photocatalytic proton-coupled electron transfer (PCET), which is one of the most promising methods for the cleavage of strong bonds in a mild and simple manner even in presence of weaker bonds, is based on the formation of H-bonds.[22][90] This concept, which was first known for biochemical systems, involves the excellent H-bond donor abilities of highly polarized functional groups, such as O-H and N-H, and was transferred to synthetic protocols.[91] As such, aryl-amines, -amides, -alcohols and even aliphatic C-H bonds could successfully be activated by forming H-bonds to an

acceptor co-catalyst.[22] An extensive review of this concept and a detailed mechanistic analysis of the PCET mediated hydroamidation of phenyl-amides developed by Knowles *et al.* is described in chapter 2 of this thesis. Such intermolecular specific co-catalyst/substrate interaction was also found to enable selective α-C-H functionalization of aliphatic alcohols.[92]
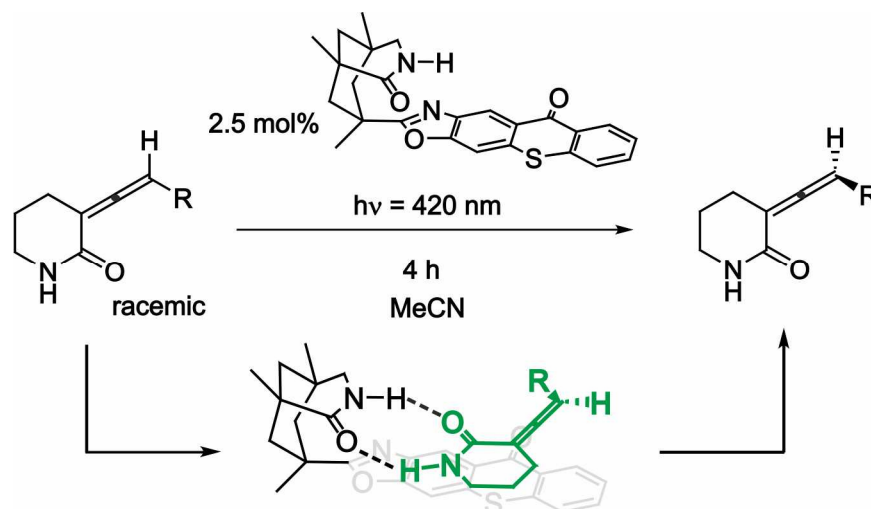


**Figure 1.5:** Photocatalytic H-bond mediated separation of allene-racemates developed by Bach *et al.*[88]

## 1.2.3 Investigation of Hydrogen Bonds by NMR

The formation of a hydrogen bond results in a change in the structural and electronic environment of the involved functional groups. The change of the stretching vibrational frequency of the hydrogen bond donor (X-H) and acceptor (A) groups according to non-covalent interaction can be determined by infrared (IR) spectroscopy.[93][48] Depending on the H-bond strength the X-H IR band gets red-shifted, broader and more intense. As such, this method easily indicates the existence of H-bonds. But mixtures containing several H-bonds result in an overlap of the corresponding IR bands and thus a detailed interpretation is compromised. NMR spectroscopy is another commonly used analytical method for H-bond investigation.[54][48] In the course of the formation of a X-H···A hydrogen bond the proton is shifted towards the center between X and A and thus the X-H distance is increased and the H···A as well as the X···A distances are reduced. This leads to deshielding of both acceptor and proton, which results in a low field shift of the corresponding NMR signals. In contrast, the donor is shielded and its signal is therefore shifted to high field. The position of the proton can further be determined by its coupling pattern depending on the spectroscopic accessibility of X and A. For example, X-H···A and X$^-$···H-A$^+$ motifs are potentially distinguishable by a visible X/H- or H/A-coupling,

respectively, depending on the NMR accessibility of the involved nuclei and the rate of the involved exchange equilibrium. The coupling constant gives additional information about the H-bond strength, as an enhanced X-H distance goes hand in hand with a diminished $^1J_{X-H}$ coupling. In biochemical and organic reactions proton, carbon, nitrogen and phosphorous containing molecules are common reagents. Especially, isotopes such as $^1H$, $^{15}N$ and $^{31}P$ are accessible via NMR due to their spin quantum number I = ½ and their high natural abundances.[94] In order to visualize H-bonds on the NMR time scale, a minimal chemical exchange rate of the proton is required which can be obtained by low temperature measurements. Hence, the solvent needs to fulfil two criteria – sufficient solubility at low temperatures and low tendency of proton exchange between solvent and substrate.

The correlation of NMR chemical shifts and concentration of the H-bond involved species can be achieved in a general and simple manner by titration experiments.[95][96] This method provides indirect information about the H-bond strength as well. In a similar fashion, the measurement of temperature dependent proton chemical shifts in combination with coupling constants for protein based H-bond networks provided a fundamental background for the stabilization mechanism essential to peptides.[97][98] Combining the $^1H$ NMR analysis with additional heteronuclei chemical shifts of the donor and/or acceptor moieties involved in H-bond an extended view on the nature of this non-covalent bond can be obtained. In this way, intra- and intermolecular O-H$\cdots$N hydrogen bonds in pyridoxal-5'-phosphate, which is an important cofactor for enzyme based reactions, and towards carboxylic acids were extensively studied by Limbach *et al*.[99][100][101] They developed a low temperature NMR correlation technique (Steiner-Limbach correlation) using $^1H$ and $^{15}N$ chemical shifts and applied coupling constant analysis in order to determine the position of the proton inside the hydrogen bond, which has major impact on the enzymatic reactivity. Figure 6 illustrates an ideally fitted Steiner-Limbach curve, which can be derived from NMR chemical shift analysis. In the publication, the data points of the intermolecular H-bond between pyridine and carboxylic acid (red), which were located on top of the graph, revealed a strong and quasi-symmetric interaction.[101] In contrast, the proton inside the intramolecular H-bond (blue) was identified to be located either on the nitrogen or on the oxygen side, which revealed two energetic minima and thus an equilibrium between two constellations. In our group, this strategy was further adopted for detailed analysis of H-bonds in Brønsted acid catalysis.[102]
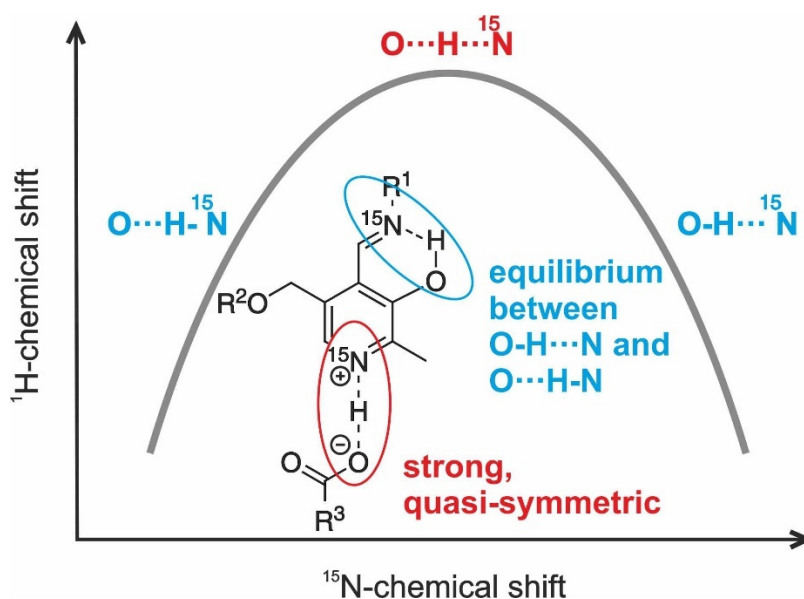
**Figure 1.6:** Steiner-Limbach correlation of ^{1}H and ^{15}N chemical shifts for the identification of the proton positions in intra- and intermolecular H-bonds of pyridoxal-5'-phosphates.[101]

Additional mechanistic information can be derived from hydrogen/deuterium isotope experiments. The chemical shift change between hydrogen and deuterium isotopes induced by differing chemical shielding reveals information about the H-bond strength.[103][104][105] In addition, Chemical Shift Anisotropy (CSA) is a sensitive tool for the detection of small conformational changes in protein structures.[106][107] Using 2D Nuclear/Heteronuclear Overhauser Spectroscopy (NOESY/HOESY) experiments, the H-bond can not only be identified through space,[108][109] but also the average distances between the involved moieties can be calculated.[110] Moreover, applying low temperature ^{1}H,^{15}N-HMQC and ^{1}H,^{31}P-HMBC experiments the nature of specific chiral phosphoric acid/imine complexes were revealed to exist as ion pairs.[102] Furthermore, for the resulting [N[+]-H$\cdots$O-P] H-bonds the related $^2J_{PN}$ and $^3J_{PN}$ scalar couplings could also be determined via 3D-HNPO experiments. The use of long-range, quantitative-$J_{NC}$-HNCO spectra further revealed $^3J_{NC}$ couplings in proteins.[111] In addition, 2D Transverse Relaxation-Optimized Spectroscopy (TROSY) enabled the measurement of [15]N-^{15}N and [1]H-^{15}N scalar couplings in Watson-Crick base pairs in the range of 2-7 Hz.[112] H-bond mediated interaction, however, is not attributed to the contact of only the strongest H-bond donor and acceptor, but other aggregates are often formed as well. Thus, the chemical shift and coupling of one signal of a specific species refers to average values for all molecules of the same species involving free and complexed structures in solution. As such, the analysis of the aggregation provides qualitative information about the relative H-bond strengths. The related reduced diffusion according to H-bond mediated complexation can be directly detected via Diffusion-Ordered Spectroscopy (DOSY).[113]

## 1.3 Outline

This thesis was engaged in the NMR spectroscopic investigation of photocatalytic transformations. Besides reaction monitoring, elucidation of reactive pathways and identification of intermediates, products and by-products, particular effort was made to analyze the impact of concrete intermolecular preaggregation, which is key to effective molecular transformations. The effect of hydrogen bonds in photocatalysis is still often disregarded as the focus is mainly set on crucial photon absorption of the photocatalyst and subsequent electron transfer. In this regard, the investigation of the nature and impact of these non-covalent interactions enabling efficient photocatalytic reactions was the main goal.

In chapter 2 the photocatalytic PCET mediated hydroamidation of phenyl-amides developed by Knowles *et al.* was analyzed. The literature known mechanism for oxidative PCET driven cleavage of the strong N-H bond (BDFE: 99 kcal/mol) involves the formation of a strong preformed H-bond between the amide substrate and the phosphate co-catalyst. But for the required hydrogen atom transfer (HAT) necessary to complete the photocatalytic cycle, common hydrogen atom donors, such as phenol, failed. Only thiophenol (PhSH), which contains a weaker S-H bond (BDFE: 79 kcal/mol), accelerated the reaction drastically without being converted itself. Thus, the strong enhancement of the reactivity upon addition of thiophenol, the selective activation of the amidyl N-H and the minor effect of phenol hint at an unexpected but decisive influence of thiophenol on the hydrogen bond situation of the amide-phosphate base complex in this PCET reaction. Earlier mechanistic investigations of the hydroamidation reaction were performed mainly focused on the radical properties. A combination of H-bond assemblies and kinetic properties was previously shown by the group of Knowles to be responsible for chemoselectivity factors of the selective cleavage of the stronger amide N-H bond in presence of thiols. However, the related Stern-Volmer Plots were produced in highly diluted mixtures hiding the actual aggregation and H-bond networks, which are ubiquitous for ion pairs and amides in apolar solvents. Moreover, a kinetic study of Nocera *et al.* revealed the importance of the overall efficiency of the PCET/back electron transfer (BET), which could be improved by adding disulfides as radical trap. As such, via an off-cycle equilibrium the key amidyl radical accumulates and the BET is reduced. However, both studies ignore the complex H-bond situation existent at synthetic conditions and its potential influence on the PCET, BET and corresponding back-proton transfer (BPT). As such, the central question is the role and effect of thiophenol on this H-bond network and the overall reaction rate.

Hence, initial rate kinetics of mixtures of thiophenol and diphenyldisulfide ($Ph_2S_2$) were performed in this work first, which revealed supportive cooperativity effects beyond the additivity expected for the mere radical effect and substantiate the importance of the H-bond networks. A complete NMR spectroscopic H-bond and aggregation analysis of the donor ($^{15}N$ labeled *N*-phenylpent-4-enamide) as well as the acceptor side (tetrabutylammonium di-*tert*-butylphosphate) was performed using low temperature $^1H$, $^{15}N$, $^{31}P$ chemical shift and $^1J_{NH}$ scalar coupling analysis. In combination with DOSY and additional molecular dynamics (MD) simulations complex aggregation and H-bond networks were observed, which affect the key properties of the reactivity. Besides its function as hydrogen atom donor, thiophenol partially protonates the phosphate base, which leads to the formation of phosphate-$H^+$-phosphate dimers. Based on this complex an extended H-bond network including amides provides a productive regeneration of the Iridium photocatalyst. The radical and acidic properties of PhSH were substituted by using $Ph_2S_2$ and phosphoric acid. Thus, the radical and ionic channels could be separated and the yields improved in up to one order of magnitude under synthetic conditions. Reaction profiles with different light intensities reveil photo-generated amidyl radical reservoirs lasting over minutes. This demonstrates the positive effect of the H-bond network prior to radical cyclization. In contrast, phenol, which is less acidic and therefore unable to generate the crucial base complex, is incorporated into the complex. As such, its competition with the substrate for H-bonding preventing an efficient PCET mediated amide activation is assumed to be one factor for the low reactivity. The results demonstrate an effective activation via H-bond networks and the reactivity improvement via the separation of ionic and radical channels, which we expect to be generally applicable in photoredox catalysis. In addition, this study shows that control of aggregates and ensembles will be a key to future photoredox catalysis.

The importance of distinctive H-bond mediated preassemblies in photocatalytic PCET transformations was also shown for the alcohol O-H activation in chapter 3. For the first time, cycloalkanols were functionalized under mild and operationally simple reaction conditions without prior preactivation of the strong alcohol O-H group. Using a combination of a mesityl-acridinium organic photocatalyst, a pyridine co-catalyst and blue light the alcohol substrate is transferred into an alkoxy radical in an oxidative PCET step. Subsequent ring-opening enables a late-stage remote functionalization of the carbon centered radical in a Giese type C-C bond generation in presence of electron poor Michael acceptors. For a successful PCET driven cleavage of strong bonds H-bond formation between substrate and base is required. Thus, owing to their literature known great H-bond acceptor ability, several pyridine bases were examined in the course of optimizing the reaction conditions. Interestingly, unsubstituted pyridine, which was assumed as best

performing base according to its high basicity, furnished the lowest product yields with 1-phenyl-cyclobutanol as starting material. In general, the reactivities of the different pyridines contradict their basicities described by the literature based $pK_a$ values. This indicates that the PCET is not accelerated by simply increasing the basicity, which should result in stronger alcohol-pyridine H-bonds. Furthermore, alkyl substituted cyclobutanols were transformed only in low amounts using these optimized conditions, which hints at a more complex interaction between substrate and base exceeding simple N⋯H-O H-bonding. As such, by elucidating the key interaction pattern between alcohol and base we hoped to further extend the substrate scope.

To gain knowledge about the crucial preassemblies and the nature of their interactions for successful PCET in cyclobutanols, low temperature NMR spectroscopic H-bond and aggregation investigations were performed. The N⋯H-O bond strengths were determined for three pyridine bases in presence of benzylic alcohol and ethanol, respectively, representing aryl- and alkyl-substituted test substrates as well as with 1-phenylcyclobutanol. In principle, from the $^1$H chemical shifts, the aryl-alcohols showed stronger interactions to the pyridines compared to ethanol. Moreover, all measurements revealed the same trend regarding the H-bond acceptor ability with 2-methoxypyridine as strongest acceptor, followed by 2-chloropyridine and 2,6-dimethoxypyridine. This trend is in line with the reaction yields. Unsubstituted pyridine was excluded from this study due to by-product formation. DOSY measurements disclosed an immense self-aggregation of phenyl-cyclobutanol and a reduction of complexation in presence of base with maximum deaggregation for the best performing 2-methoxypyridine. The low obtained diffusion coefficients for the pyridines suggesting a mainly monomeric existence confirm a specific substrate activating complex being masked by an alcohol bulk.

The success of 2-OMe-pyridine seemed to be attributed to a combination of optimal steric and electronic properties. A cooperation of aromatic, C-H-$\pi$, and H-bond interactions between the alcohol and the base revealed to be critical for an effective activation of alcohols. As such, the modulation of the base by applying an extended heteroaromatic halogen substituted system was the key to get access to the group of aliphatic cyclobutanols. The presented data emphasize, that H-bond mediatedpreassemblies, dispersion interactions and substrate specific activations are pivotal for planning photocatalytic PCET reactions exceeding mere $pK_a$ factors.

Additional findings revealed the formation of an intermediate during reaction. Moreover, the H-bonding situation in presence of unsubstituted pyridine and the related by-product formation are discussed. Complemental low temperature $^1$H chemical shift studies elucidate the impact of $H_2O$ and the trapping reagent on the entire H-bond situation.

In chapter 4, the crucial interaction between an activating boron containing Lewis acid/base pair and trifluoromethylarene substrates for the first successful photocatalytic single C(sp$^3$)—F bond cleavage was analyzed. The mono-defluorination, which is challenging due to the high bond dissociation energies of aryl-CF$_3$ groups and the problem of over-defluorination once the energy barrier is passed, was achieved in presence of HBpin and TMP using blue light and *fac*-Ir(ppy)$_3$ as photocatalyst. NMR mechanistic investigations of the photocatalytic transformation revealed that the borenium cationic species TMP-Bpin$^+$ is generated as key intermediate transferring the unreactive ArCF$_3$ radical anion, which is generated in the course of the photoredox catalytic cycle, into the defluorinated ArCF$_2$ radical. The free F$^-$ ions are scavenged by the Lewis acid/base pair producing F-Bpin and TMP. After trapping the ArCF$_2$ radical with methacrylamides, the highly valuable pharmaceutical aryldifluoromethyl compounds were obtained with good chemoselectivity and functional group tolerance.

In order to get deeper insight into the mono-defluorination step, the role of the *in-situ* generated TMP-Bpin$^+$ intermediate and its interaction towards the substrate anion radical as basis for efficient C-F bond cleavage, the reaction was analyzed by $^1$H, $^{11}$B, $^{19}$F and 2D NMR spectroscopy. As such, an H-bond between the 4-trifluoromethylbenzonitrile substrate and the separately synthesized borenium cation species was identified. However, instead of an interaction between the CF$_3$ groups and TMP-Bpin$^+$, the neutral substrate seems to be attached mainly via its nitrile functionality. But as the reduced substrate is supposed to have drastically higher hydrogen bond acceptor properties a stronger interaction was assumed promoting an efficient defluorination.

Additional findings present kinetic profiles of the photocatalytic *in-situ* and *ex-situ* illuminated reactions using trifluoromethylbenzonitrile, *N*-methyl-*N*-phenyl-methacrylamide, HBpin, TMP, *fac*-Ir(ppy)$_3$ and blue light. Moreover, the reactions were followed by $^1$H, $^{11}$B, $^{19}$F NMR, which revealed the formation of the borenium cationic species and additionally generated compounds, including F-Bpin, CNPhCF$_2$H, BF$_3$ and BF$_4^-$ were assigned.

## 1.4 References

[1]    L. N. M. Duysens, *Prog. Biophys. Mol. Biol.* **1964**, *14*, 1–104.

[2]    G. Ciamician, *Science (80-. ).* **1912**, *36*, 385–394.

[3]    A. L. Fahrenbruch, R. H. Bube, *Fundamentals of Solar Cells: Photovoltaic Solar Energy Conversion*, Academic Press, New York, **1983**.

[4]    J.-P. Sauvage, *Molecular Machines and Motors*, Springer, **2003**.

[5]  S. E. Braslavsky, K. N. Houk, *Pure Appl. Chem.* **1988**, *60*, 1055–1106.

[6]  F. A. Carey, R. J. Sundberg, *Advanced Organic Chemistry PART A, 5th Edition*, Springer, **2007**.

[7]  B. König, *Chemical Photocatalysis*, De Gruyter, **2013**.

[8]  B. Valeur, M. N. Berberan-Santos, *Molecular Fluorescence: Principles and Applications, Second Edition*, Wiley-VCH Verlag GmbH & Co. KGaA, **2012**.

[9]  A. P. Demchenko, J. Heldt, J. Waluk, P.-T. Chou, P. K. Sengupta, L. Brizhik, J. C. del Valle, *Angew. Chem. Int. Ed.* **2014**, *53*, 14316–14324.

[10]  R. G. W. Norrish, F. W. Kirkbride, *J. Chem. Soc.* **1932**, 1518–1530.

[11]  R. G. W. Norrish, C. H. Bamford, *Nature* **1937**, *140*, 195–196.

[12]  H. Cano-yelo, A. Deronzier, *J. Chem. Soc. Perkin Trans. 2* **1984**, 1093–1098.

[13]  A. Juris, V. Balzani, F. Barigelletti, S. Campagna, P. Belser, A. von Zelewsky, *Coord. Chem. Rev.* **1988**, *84*, 85–277.

[14]  J. M. R. Narayanam, C. R. J. Stephenson, *Chem. Soc. Rev.* **2011**, *40*, 102–113.

[15]  C. K. Prier, D. A. Rankic, D. W. C. Macmillan, *Chem. Soc. Rev.* **2013**, *113*, 5322–5363.

[16]  K. Zeitler, *Angew. Chem. Int. Ed.* **2009**, *48*, 9785–9789.

[17]  R. C. McAtee, E. J. McClain, C. R. J. Stephenson, *Trends Chem.* **2019**, *1*, 111–125.

[18]  A. G. Griesbeck, C. Miyeon, *Org. Lett.* **2007**, *9*, 611–613.

[19]  T. Koike, M. Akita, *Inorg. Chem. Front.* **2014**, *1*, 562–576.

[20]  C. R. J. Stephenson, T. P. Yoon, D. W. C. MacMillan, *Visible Light Photocatalysis in Organic Chemistry*, WILEY-VCH, **2018**.

[21]  H. G. Roth, N. A. Romero, D. A. Nicewicz, *Synlett* **2016**, *27*, 714–723.

[22]  D. C. Miller, K. T. Tarantino, R. R. Knowles, *Top. Curr. Chem.* **2016**, *374*, 1–59.

[23]  K. U. Ingold, D. A. Pratt, *Chem. Rev.* **2014**, *114*, 9022–9046.

[24]  J. C. Walton, *Analysis of Radicals by EPR*, John Wiley & Sons, Ltd., **2012**.

[25]  L. Buzzetti, G. E. M. Crisenza, P. Melchiorre, *Angew. Chem. Int. Ed.* **2019**, *58*, 3730–3747.

[26]  R. Berera, R. Van Grondelle, J. T. M. Kennis, *Photosynth. Res.* **2009**, *101*, 105–118.

[27]  C. Feldmeier, H. Bartling, E. Riedle, R. M. Gschwind, *J. Magn. Reson.* **2013**, *232*, 39–44.

[28]  P. Nitschke, N. Lokesh, R. M. Gschwind, *Prog. Nucl. Magn. Reson. Spectrosc.* **2019**, *114–115*, 86–134.

[29]  D. M. Schultz, F. Lévesque, D. A. DiRocco, M. Reibarkh, Y. Ji, L. A. Joyce, J. F. Dropinski, H. Sheng, B. D. Sherry, I. W. Davies, *Angew. Chem. Int. Ed.* **2017**, *56*, 15274–15278.

[30]  S. J. Wezenberg, B. L. Feringa, *Nat. Commun.* **2018**, *9*, 1–7.

[31]  A. Seegerer, P. Nitschke, R. M. Gschwind, *Angew. Chem. Int. Ed.* **2018**, *57*, 7493–7497.

[32]  Y. Ji, D. A. DiRocco, J. Kind, C. M. Thiele, R. M. Gschwind, M. Reibarkh, *ChemPhotoChem* **2019**, *3*, 984–992.

[33]  C. Feldmeier, H. Bartling, K. Magerl, R. M. Gschwind, *Angew. Chem. Int. Ed.* **2015**, *54*, 1347–1351.

[34]  D. Petzold, P. Nitschke, F. Brandl, V. Scheidler, B. Dick, R. M. Gschwind, B. König, *Chem. - A Eur. J.* **2019**, *25*, 361–366.

[35]  J. Kind, L. Kaltschnee, M. Leyendecker, C. M. Thiele, *Chem. Commun.* **2016**, *52*, 12506–12509.

[36]  L. Čechová, J. Kind, M. Dračínský, J. Filo, Z. Janeba, C. M. Thiele, M. Cigáň, E. Procházková, *J. Org. Chem.* **2018**, *83*, 5986–5998.

[37]  K. Rothermel, M. Melikian, J. Hioe, J. Greindl, J. Gramüller, M. Žabka, N. Sorgenfrei, T. Hausler, F. Morana, R. M. Gschwind, *Chem. Sci.* **2019**, *10*, 10025–10034.

[38]  H. Bartling, A. Eisenhofer, B. König, R. M. Gschwind, *J. Am. Chem. Soc.* **2016**, *138*, 11860–11871.

[39]  A. K. Schönbein, J. Kind, C. M. Thiele, J. J. Michels, *Macromolecules* **2018**, *51*, 4678–4687.

[40]  M. V. Gomez, A. De La Hoz, *Beilstein J. Org. Chem.* **2017**, *13*, 285–300.

[41]  P. Giraudeau, F. X. Felpin, *React. Chem. Eng.* **2018**, *3*, 399–413.

[42]  M. E. Halse, *Trends Anal. Chem.* **2016**, *83*, 76–83.

[43]  L. T. Kuhn, *Hyperpolarization Methods in NMR*, Springer, **2017**.

[44]  S. Wang, N. Lokesh, J. Hioe, R. M. Gschwind, B. König, *Chem. Sci.* **2019**, *10*, 4580–4587.

[45]  N. Lokesh, A. Seegerer, J. Hioe, R. M. Gschwind, *J. Am. Chem. Soc.* **2018**, *140*, 1855–1862.

[46]  E. Stadler, M. Dommaschk, P. Frühwirt, R. Herges, G. Gescheidt, *ChemPhysChem* **2018**, *19*, 571–574.

[47]  Y. Ji, D. A. DiRocco, C. M. Hong, M. K. Wismer, M. Reibarkh, *Org. Lett.* **2018**, *20*,

2156–2159.

[48]   T. Steiner, *Angew. Chem. Int. Ed.* **2002**, *41*, 48–76.

[49]   G. Gilli, P. Gilli, *The Nature of the Hydrogen Bond: Outline of a Comprehensive Hydrogen Bond Theory*, Oxford University Press, USA, **2009**.

[50]   P. A. Kollman, L. C. Allen, *Chem. Rev.* **1972**, 72, 283–303.

[51]   A. R. Fersht, *Trends Biochem. Sci.* **1987**, *12*, 301–304.

[52]   L. Pauling, R. B. Corey, H. R. Branson, *Proc. Natl. Acad. Sci. U. S. A.* **1951**, *37*, 205–211.

[53]   G. A. Jeffrey, W. Saenger, *Hydrogen Bonding in Biological Structures*, Springer, **1991**.

[54]   L. J. Prins, D. N. Reinhoudt, P. Timmerman, *Angew. Chem.* **2001**, *113*, 2446–2492.

[55]   G. A. Jeffrey, *An Introduction to Hydrogen Bonding*, Oxford University Press, Oxford, **1997**.

[56]   T. Steiner, *Chem. Commun.* **1997**, 727–734.

[57]   G. R. Desiraju, *Acc. Chem. Res.* **1996**, *29*, 441–449.

[58]   C. A. Hunter, *Angew. Chem. Int. Ed.* **2004**, *43*, 5310–5324.

[59]   F. H. Allen, W. D. S. Motherwell, P. R. Raithby, G. P. Shields, R. Taylor, *New J. Chem.* **1999**, *23*, 25–34.

[60]   C. Bilton, F. H. Allen, G. P. Shields, J. A. K. Howard, *Acta Crystallogr. Sect. B Struct. Sci.* **2000**, *56*, 849–856.

[61]   T. Steiner, *Acta Crystallogr. Sect. B Struct. Sci.* **2001**, *57*, 103–106.

[62]   M. S. Taylor, E. N. Jacobsen, *Angew. Chem. Int. Ed.* **2006**, *45*, 1520–1543.

[63]   X. Yu, W. Wang, *Chem. Asian J.* **2008**, *3*, 516–532.

[64]   H. Jiang, M. W. Paixão, D. Monge, K. A. Jørgensen, *J. Am. Chem. Soc.* **2010**, *132*, 2775–2783.

[65]   T. Inokuma, M. Furukawa, T. Uno, Y. Suzuki, K. Yoshida, Y. Yano, K. Matsuzaki, Y. Takemoto, *Chem. Eur. J.* **2011**, *17*, 10470–10477.

[66]   J. Seayad, B. List, *Org. Biomol. Chem.* **2005**, *3*, 719–724.

[67]   B. List, I. Čorič, O. O. Grygorenko, P. S. J. Kaib, I. Komarov, A. Lee, M. Leutzsch, S. Chandra Pan, A. V. Tymtsunik, M. Van Gemmeren, *Angew. Chem. Int. Ed.* **2014**, *53*, 282–285.

[68]   P. M. Pihko, *Hydrogen Bonding in Organic Synthesis*, WILEY-VCH, **2009**.

[69]   J. D. McGilvra, A. K. Unni, K. Modi, V. H. Rawal, *Angew. Chem. Int. Ed.* **2006**, *45*,

6130–6133.

[70]  M. Kotke, P. R. Schreiner, *Synthesis (Stuttg).* **2007**, 779–790.

[71]  J. Wang, H. Xie, H. Li, L. Zu, W. Wang, *Angew. Chem. Int. Ed.* **2008**, *47*, 4177–4179.

[72]  P. R. Schreiner, *Chem. Soc. Rev.* **2003**, *32*, 289–296.

[73]  S. Rajaram, M. S. Sigman, *Org. Lett.* **2005**, *7*, 5473–5475.

[74]  A. Wittkopp, P. R. Schreiner, *Chem. Eur. J.* **2003**, *9*, 407–414.

[75]  T. Schuster, M. Bauch, G. Dürner, M. W. Göbel, *Org. Lett.* **2000**, *2*, 179–181.

[76]  F. Burg, T. Bach, *J. Org. Chem.* **2019**, *84*, 8815–8836.

[77]  P. Fackler, C. Berthold, F. Voss, T. Bach, *J. Am. Chem. Soc.* **2010**, *132*, 15911–15913.

[78]  N. R. Mote, S. H. Chikkali, *Chem. Asian J.* **2018**, *13*, 3623–3646.

[79]  R. Jiang, G. Lu, Z. Yan, D. Wu, J. Liu, X. Zhang, *J. Colloid Interface Sci.* **2019**, *552*, 678–688.

[80]  C. Q. Xu, Y. H. Xiao, Y. X. Yu, W. De Zhang, *J. Mater. Sci.* **2018**, *53*, 409–422.

[81]  M. B. Khaled, R. K. El Mokadem, J. D. Weaver, *J. Am. Chem. Soc.* **2017**, *139*, 13092–13101.

[82]  P. L. Cheung, S. C. Kapper, T. Zeng, M. E. Thompson, C. P. Kubiak, *J. Am. Chem. Soc.* **2019**, *141*, 14961–14965.

[83]  D. F. Cauble, V. Lynch, M. J. Krische, *J. Org. Chem.* **2003**, *68*, 15–21.

[84]  C. Müller, T. Bach, *Aust. J. Chem.* **2008**, *61*, 557–564.

[85]  R. Brimioulle, D. Lenhart, M. M. Maturi, T. Bach, *Angew. Chem. Int. Ed.* **2015**, *54*, 3872–3890.

[86]  N. Vallavoju, J. Sivaguru, *Chem. Soc. Rev.* **2014**, *43*, 4084–4101.

[87]  L. Wimberger, T. Kratz, T. Bach, *Synthesis (Stuttg).* **2019**, *51*, 4417–4424.

[88]  A. Hölzl-Hobmeier, A. Bauer, A. V. Silva, S. M. Huber, C. Bannwarth, T. Bach, *Nature* **2018**, *564*, 240–243.

[89]  Y. Q. Zou, F. M. Hörmann, T. Bach, *Chem. Soc. Rev.* **2018**, *47*, 278–290.

[90]  S. Hammes-Schiffer, A. A. Stuchebrukhov, *Chem. Rev.* **2010**, *110*, 6939–6960.

[91]  S. Y. Reece, D. G. Nocera, *Annu. Rev. Biochem.* **2009**, *78*, 673–699.

[92]  J. L. Jeffrey, J. A. Terrett, D. W. C. MacMillant, *Science (80-. ).* **2015**, *349*, 1532–

1536.

[93]  A. N. Egorochkin, S. E. Skobeleva, *Russ. Chem. Rev.* **1979**, *48*, 1198–1211.

[94]  F. Cordier, L. Nisius, A. J. Dingley, S. Grzesiek, *Nat. Protoc.* **2008**, *3*, 235–241.

[95]  A. Bundi, K. Wüthrich, *Biopolymers* **1979**, *18*, 299–311.

[96]  J. D. Griffin, M. A. Zeller, D. A. Nicewicz, *J. Am. Chem. Soc.* **2015**, *137*, 11340–11348.

[97]  F. Cordier, S. Grzesiek, *J. Mol. Biol.* **2002**, *317*, 739–752.

[98]  S. H. Gellman, G. P. Dado, G. B. Liang, B. R. Adams, *J. Am. Chem. Soc.* **1991**, *113*, 1164–1173.

[99]  S. Sharif, E. Fogle, M. D. Toney, G. S. Denisov, I. G. Shenderovich, G. Buntkowsky, P. M. Tolstoy, M. C. Huot, H. H. Limbach, *J. Am. Chem. Soc.* **2007**, *129*, 9558–9559.

[100] H. H. Limbach, M. Chan-Huot, S. Sharif, P. M. Tolstoy, I. G. Shenderovich, G. S. Denisov, M. D. Toney, *Biochim. Biophys. Acta - Proteins Proteomics* **2011**, *1814*, 1426–1437.

[101] S. Sharif, G. S. Denisov, M. D. Toney, H.-H. Limbach, *J. Am. Chem. Soc.* **2007**, *129,* 6313–6327.

[102] N. Sorgenfrei, J. Hioe, J. Greindl, K. Rothermel, F. Morana, N. Lokesh, R. M. Gschwind, *J. Am. Chem. Soc.* **2016**, *138*, 16345–16354.

[103] A. Kohen, H.-H. Limbach, *Isotope Effects in Chemistry and Biology*, CRC Press, **2005**.

[104] I. G. Shenderovich, H. H. Limbach, S. N. Smirnov, P. M. Tolstoy, G. S. Denisov, N. S. Golubev, *Phys. Chem. Chem. Phys.* **2002**, *4*, 5488–5497.

[105] L. J. Altman, D. Laungani, G. Gunnarsson, H. W. S. Forsén32, *J. Am. Chem. Soc.* **1978**, *100*, 8264–8266.

[106] N. Tjandra, A. Bax, *J. Am. Chem. Soc.* **1997**, *119*, 8076–8082.

[107] D. Fushman, N. Tjandra, D. Cowburn, *J. Am. Chem. Soc.* **1998**, *120*, 10947–10952.

[108] H. B. Seba, B. Ancian, *J. Chem. Soc, Chem. Commun.* **1990**, 996–997.

[109] J. Greindl, J. Hioe, N. Sorgenfrei, F. Morana, R. M. Gschwind, *J. Am. Chem. Soc.* **2016**, *138*, 15965–15971.

[110] T. L. James, *Prog. NMR Spectrosc.* **1990**, *22*, 83–100.

[111] F. Cordier, S. Grzesiek, *J. Am. Chem. Soc.* **1999**, *121*, 1601–1602.

[112] K. Pervushin, A. Ono, C. Fernández, T. Szyperski, M. Kainosho, K. Wüthrich, *Proc. Natl. Acad. Sci. USA* **1998**, *95*, 14147–14151.

[113]  G. S. Kapur, E. J. Cabrita, S. Berger, *Tetrahedron Lett.* **2000**, *41*, 7181–7185.

[114]  G. R. Fulmer, A. J. M. Miller, N. H. Sherden, H. E. Gottlieb, A. Nudelman, B. M. Stoltz, J. E. Bercaw, K. I. Goldberg, *Organometallics* **2010**, *29*, 2176–2179.

[115]  D. C. Miller, G. J. Choi, H. S. Orbe, R. R. Knowles, *J. Am. Chem. Soc.* **2015**, *137*, 13492–13495.

# 2 Extended Hydrogen Bond Networks for Effective PCET Reactions: The Unexpected Role of Thiophenol and its Acidic Channel in Photocatalytic Hydroamidations
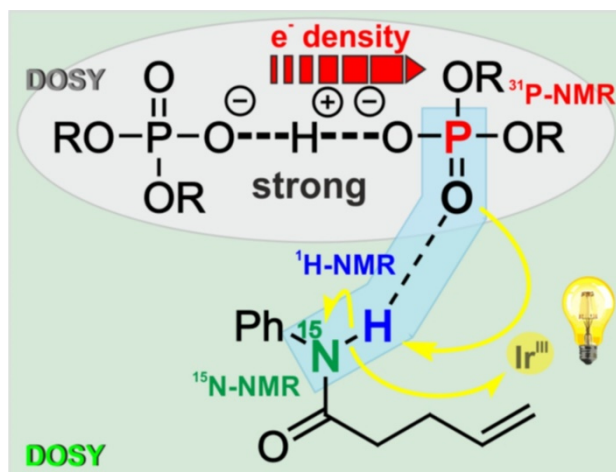
**Nele Berg**, Sebastian Bergwinkl, Patrick Nuernberger, Dominik Horinek, Ruth M. Gschwind

*under consideration*

The original manuscript was written by Nele Berg. The Figures, Schemes and the TOC graphic in the manuscript were designed by Nele Berg. The synthesis, the NMR and DOSY experiments and their evaluation were performed by Nele Berg and analyzed and discussed with Prof. Ruth M. Gschwind. The Supporting Information was written by Nele Berg except the passages about the MD simulations and Emission Spectroscopy (chapters 2.6.6 and 2.6.7). Prof. Dominik Horinek performed the MD simulations and prepared the corresponding experimental data and pictures (chapter 2.6.6). Sebastian Bergwinkl conducted the emission experiments and prepared the content in chapter 2.6.7 together with Prof. Patrick Nürnberger. Prof. Horinek, Sebastian Bergwinkl and Prof. Nürnberger strongly contributed to discussions and refining the text in the manuscript.

Text and Figures may differ from the original manuscript.

## 2.1 Abstract

Preorganization and aggregation in photoredox catalysis can significantly affect reactivities or selectivities but are often neglected in synthetic and mechanistic studies, since the averaging effect of flexible ensembles can effectively hide the key activation signatures. In addition, aggregation effects are often overlooked due to highly diluted samples used in many UV studies. One prominent example is Knowles's acceleration effect of thiophenol in proton-coupled electron transfer mediated hydroamidations, for which mainly radical properties were discussed. Here, cooperative reactivity enhancements of thiophenol/disulfide mixtures reveal the importance of H-bond networks. For the first time an in depths NMR spectroscopic aggregation and H-bond analysis of donor and acceptor combined with MD simulations was performed revealing that thiophenol acts also as acid. The formed phosphate-$H^+$-phosphate dimers provide an extended H-bond network with amides allowing a productive regeneration of the photocatalyst to become effective. The radical and acidic properties of PhSH were substituted by $Ph_2S_2$ and phosphoric acid. This provides a handle for optimization of radical and ionic channels and yields accelerations up to one order of magnitude under synthetic conditions. Reaction profiles with different light intensities unveil photo-generated amidyl radical reservoirs lasting over minutes, substantiating the positive effect of the H-bond network prior to radical cyclization. We expect the presented concept of effective activation via H-bond networks and the reactivity improvement via the separation of ionic and radical channels to be generally applicable in photoredox catalysis. In addition, this study shows that control of aggregates and ensembles will be a key to future photoredox catalysis.

## 2.2 Introduction

Light dependent as well as light independent proton-coupled electron transfer (PCET) reactions play an essential role in biological systems,[1–13] e.g. for the $O_2$ generation in the photosystem II.[14] Their potential was also successfully applied in electrochemistry, [2,15–24] transition metal chemistry[1,25–28] and photochemical transformations.[1,2,29–45] In synthetic organic chemistry the activation of strong covalent bonds, such as C-H, O-H, and N-H, is a very challenging task to access important synthetic building blocks. To overcome their high energy barriers in an atom economic and environmentally friendly manner, the combination of PCET and photocatalysis paved the way to an efficient reaction design. Especially, the photocatalytic concerted multisite PCET (MS-PCET) was found to be successful.[2,36,46] There, a decoupled proton and electron transfer event in one elementary

step omits highly energetic intermediates, which usually arise in conventional hydrogen atom transfer (HAT). In the oxidative MS-PCET, a proton and an electron originating from the same donor bond are transferred to a base and to a separate oxidant.[1,2,18] As a result, the proton and electron affinities of the two acceptor compounds can be fine-tuned independently allowing the activation of strong bonds which are not easily accessible via conventional redox processes.[36–38,47]
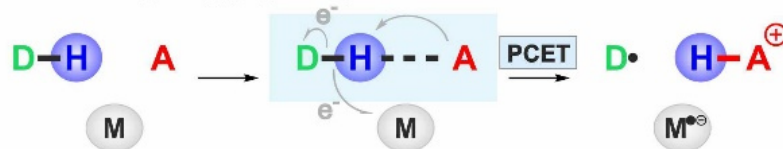
Thus, in the field of photocatalytic organic chemistry, using PCET, the group of Knowles transformed ketones into cyclic alcohols,[34,42,48] activated N-H bonds in extensive hydro-/carboamination and hydro-/carboamidation protocols, opened cyclic alcohols via PCET mediated alkoxy radical generation,[31,32,35,41,43,44,49] and succeeded even in the alkylation of remote C-H bonds via an amide PCET process.[33] More recently, they developed an aliphatic C-H bond activation[50] and a PCET driven $NH_3$ synthesis.[51] Even for the deracemization of ureas PCET is involved.[52] Further coupling reactions were recently designed including an aldehyde-olefin coupling via reductive ketyl radical formation,[29] the generation of pyridine based heterocycles,[53] and the copper-based photocatalytic coupling of ketones.[54] Moreover, the PCET concept was employed in visible light mediated selective C-C bond cleavage of lignines[55] and the C-H functionalization of cyclic ethers.[56]

In such light driven oxidative PCET reactions the formation of a D-H···A hydrogen bond (H-bond) between the D-H bond to be cleaved and the applied base A (Figure 2.1a) is stated to be responsible for lowering the reaction energy barrier.[1,2,37,36,47,51–58] Especially, the proton transfer requires an overlap of the vibronic states and thus a minimized donor-acceptor distance. Hence, the formation of strong donor-acceptor H-bonded preaggregates is proposed for the initiation of PCET.[1,2,46] Furthermore, the geometry and strength of the H-bond seem to be essential as shown for competing mechanisms, HAT versus PCET in benzyl/toluene pairs and phenoxy/phenol aggregates.[59,60] Internal H-bonds of the latter aggregate was shown to accelerate the coupled electron proton transfer rate in a pH independent manner.[61] The formation of a H-bond was even found to suppress a HAT mechanism due to steric reasons.[62] As expected, charge assisted H-bonds and solvents promoting strong H-bonds accelerate charge transfer events for an efficient PCET process.[63,64] Moreover, using IR spectroscopy, H-bond equilibrium constants were determined for a TEMPOH/pyridine complex.[65]

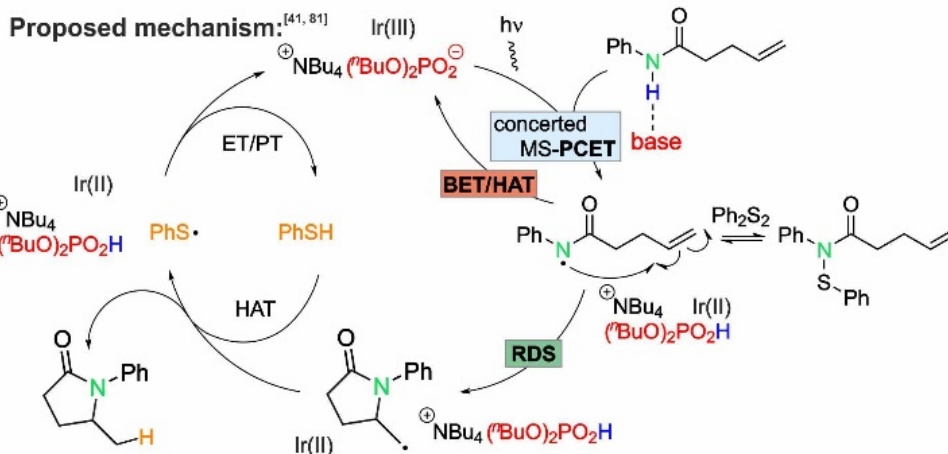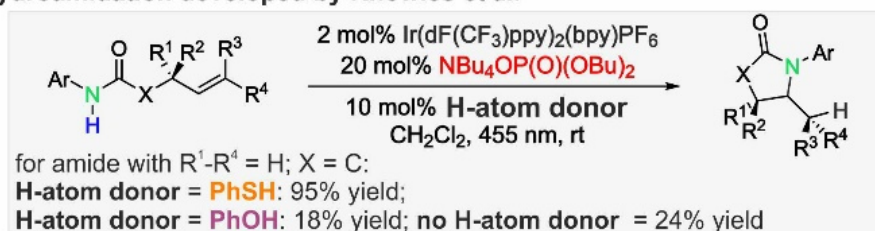Computational studies on model systems in biology, biochemistry, solution chemistry and electrochemistry corroborated the essential role of H-bond formation for PCET e.g. enhancing the vibronic donor-acceptor coupling.[3,12,17,18,66,67] For example, the PCET driven aerobic respiratory chain[3,17] and effects of antioxidants[68–70] were shown to occur via the formation of H-bond mediated aggregates.

In contrast, experimental studies are scarce in the field of photocatalytic PCET reactions. Via EPR spectroscopy, a strong H- bonded complex between histidine and a benzoquinone derivative (TolSQ) was detected.[71]
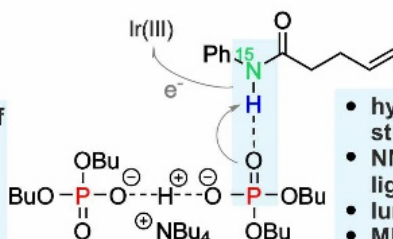


**Figure 2.1:** a) An H-bonded preaggregate is proposed as key interaction for an efficient selective cleavage of strong bonds via PCET in literature. b) The photocatalytic hydroamidation of phenylamides developed by Knowles and co-workers was chosen as model system for our investigations. The corresponding postulated light driven mechanism involves an excited state iridium catalyst and a phosphate base for the crucial PCET step, thiophenol as HAT donor and a highly effective unproductive BET. The N-H cleavage in presence of weaker S-H bonds is somewhat surprising concerning the BDFEs (see main text). c) Our studies reveal the potential to selectively access the radical and ionic properties of PhSH by the formation of extended H-bonded aggregates allowing for a productive back oxidation of Ir(II) prior to radical cyclization.

Furthermore, combined NMR, transient absorption and emission spectroscopic investigations demonstrated a correlation between H-bond strengths and charge transfer kinetics in model systems, using exclusively ^{1}H chemical shift changes for the H-bond analysis.[63,64] Later, applying a combination of ^{1}H NMR spectroscopy and cyclic voltammetry, this trend was further corroborated for an electrochemical reaction.[72] Via ^{1}H NMR titration experiments a phenol-pyridine interaction was identified.[73] Knowles and Alexanian even examined a non-covalent interaction between the iridium photocatalyst and a phosphate base to be responsible for successful C-H bond activation.[50]

One prominent example deviating from the general mechanistic concept of concerted MS-PCET is the accelerating effect of thiophenol in the oxidative photocatalytic hydroamidation of phenylamides developed by Knowles and co-workers (Figure 2.1b).[32] In the proposed mechanism, the excited state of the photocatalyst acts as electron acceptor and a phosphate base as proton acceptor for the activation of the amide substrate in a H-bonded amide/base preaggregate, followed by the intramolecular addition of the formed amidyl radical to the olefin. In a final HAT step involving thiophenol (PhSH) as hydrogen atom donor, the lactam product is furnished in up to 95% yield, however phenol (PhOH), which is a commonly known HAT transfer reagent, was unproductive.[32] PhSH as HAT donor was applied in other synthetic protocols[74–76] and other groups showed that the S-H bond can be directly activated via PCET reactions.[77–79] The chemoselectivity factors for the selective cleavage of the stronger amide N-H group was recently explained by Knowles and co-workers via a combination of H-bond networks and PCET kinetics.[80] However, the luminescence quenching experiments in these studies were conducted at highly diluted concentrations not addressing the complex aggregation and H-bond networks expected for ion pairs and amides in apolar organic solvents.[32,80] An in depth kinetic study of Nocera and co-workers revealed the importance of the overall performance of the PCET/ back-electron transfer (BET) equilibria for quantum efficiency in these hydroamidations.[81] By adding disulfides they allowed for an off-cycle equilibrium, could reduce the BET rate and increased the concentration of the key amidyl radical available for the downstream reaction. However, both studies neglect the complex H-bond situation present at synthetic conditions and its potential to influence the PCET, BET and corresponding back-proton transfer (BPT). Here, the central question is the role and effect of thiophenol on this H-bond network and the overall reaction rate.

Therefore, in this study first initial rate kinetics of mixtures of PhSH and diphenyldisulfide (Ph$_2$S$_2$) were performed. These showed cooperativity effects beyond the additivity expected for the mere radical effect and underpinned the importance of the H-bond network. Next, for the first time an in depths NMR spectroscopic analysis of donor and acceptor side of the H-bonds of this PCET driven hydroamidation reaction was performed

using low temperature $^1$H, $^{15}$N, $^{31}$P chemical shifts and $^1$J$_{NH}$ scalar couplings (Figure 2.1c). These and diffusion measurements reveal an unexpected modulation of the H-bonded aggregates by thiophenol. Furthermore, these special aggregates were corroborated by MD-simulations, which is to the best of our knowledge the first time of such a combined NMR/MD approach in chemical photoredox catalysis. Last but not least, PhSH was replaced by a combination of Ph$_2$S$_2$ and phosphoric acid, which allowed to dissect the ionic and the radical properties and optimize them separately. Luminescence quenching studies and reaction profiles with different light intensities were employed to dissect the various mechanistic steps and to reveal a productive regeneration pathway of Ir(II) to Ir(III) being affected by the extended H-bond network.

## 2.3  Results and Discussion

**Model system:** The employed PCET model system in this work is directly derived from the synthetic conditions of the hydroamidation protocol of Knowles and co-workers.[32] For the *in-situ* reaction kinetics 3,3-dimethyl-*N*-phenylpent-4-enamide was synthesized in order to exclude self-HAT. To get access to the H-bond donor side, a $^{15}$N labeled *N*-phenylpent-4-enamide was synthesized. As proton acceptor species, tetrabutylammonium di-*tert*-butylphosphate was used which showed excellent reactivity inside the photocatalytic reaction at room temperature (see SI chapter 2.6.3.1-2.6.3.4) and enables simplification of the spectra due to a reduced amount of NMR signals compared to the originally used *n*-butyl phosphate base. For the H-bond and aggregation studies 1:1 mixtures (50 mM) of amide, and phosphate as well as 1:1:1 mixtures of amide, phosphate and thiol or phenol were prepared in dichloromethane-d$_2$ (CD$_2$Cl$_2$) and measured at 300 and 180 K.[82] Due to chemical exchange reduction at low temperature, specific H-bonded aggregates are visible on the NMR time scale. Furthermore, dichloromethane was applied by the group of Knowles and is also suitable for our low temperature NMR studies.[31,32,83]

**Initial rate kinetics reveal importance of H-bonds**: For phenol and thiophenols as additives, huge reactivity differences[32] were observed previously, which can be attributed to their pronounced distinctions in radical and HAT properties, potential catalyst inhibition, side reactions of phenol or unproductive PCET activation of phenol. Our initial rate kinetics shown in Figure 2.2a (bottom) confirmed this reactivity difference. For phenol no catalyst inhibition by the product and only marginal by-product formation (see Figure 2.21) was found but significantly different H-bond networks (see below). Thus, both different radical properties and different H-bond networks may contribute to dissimilar reactivities of phenol and thiophenol. The radical/HAT properties of thiophenol and phenol are so different that

it is difficult to dissect the contributions of radical properties and H-bond network between these two. Therefore, we investigated $Ph_2S_2$, PhSH and mixtures of both. In agreement with Nocera's results, the system with 1 equiv. of disulfide shows a faster reaction rate than that with 1 equiv. of PhSH corroborating the importance of the off-cycle radical equilibrium for a reduced BET (Figure 2.2a; top). Most astonishing however are the data of the mixtures of $Ph_2S_2$ and PhSH (80:20 and 70:30). Considering mere radical effects reaction rates between those of pure $Ph_2S_2$ and PhSH are expected in terms of additivity. However, compared to pure $Ph_2S_2$, significantly higher reaction rates, i.e. non-linear effects, were detected. This indicates that aggregation may play a pivotal role in this reaction type, which is typical for complex H-bond networks and beyond mere radical properties of isolated molecules. We interpreted this special acceleration as a hint that H-bonds may really be important and may affect the PCET, the BPT back reaction or other parts of the mechanistic cycle. The principle importance of the H-bond binding constants for this reaction was already outlined by Qiu and Knowles in terms of chemoselectivity.[80] However, in their study highly diluted samples were used, which study the interactions between single molecules but not within the complex aggregates existing under synthetic conditions (see DOSY studies below).

**H-bond analysis by NMR:** Therefore, in depth H-bond studies were conducted next. In general, the formation of a H-bond influences the electronic environment of both, the H-bond donor and acceptor sites. The shift of the proton towards the acceptor leads to a change in electron density distribution by deshielding of donor and proton and shielding of the acceptor.[84–86] Thus, the strength of this non-covalent bond can be read out via NMR chemical shifts and scalar couplings.[83] Limbach and co-workers established a method for the determination of the H-bond strengths in a biological system using low temperature $^1$H and $^{15}$N chemical shift correlations.[83] This concept was already successfully applied in our group for the analysis of H-bonds in Brønsted acid catalysis.[87,88] Moreover, we recently investigated the importance of H-bond mediated interactions for the selective activation of strong single C-F bonds.[89]

**H-bond donor and reactivity profile:** First, the H-bond donor side was analyzed via $^1$H and $^{15}$N NMR chemical shifts and scalar coupling studies. An overview of the analyzed compounds is depicted in Figure 2.2b. The formation of an H-bond between amide and phosphate base is expected to go hand in hand with a low field shift for both the amidyl proton and nitrogen as well as a reduced $^{15}$N-H scalar coupling. In Figure 2.2c and 2.2d, the details of the $^1$H and $^{15}$N NMR spectra of pure $^{15}$N-phenylpent-4-enamide (bottom), the $^{15}$N-amide/base (middle) and the $^{15}$N-amide/base/thiophenol (top) mixtures are shown. For the applied concentration of 50 mM, the pure amide itself exists as oligomer (for detailed

studies see SI chapter 2.6.5.4) and the signals of the ^{15}N-H functionality at 8.45/134.49 ppm (89.9/91.3 Hz) refer therefore to the amide-amide H-bond (Figure 2.2c,d). In the presence of phosphate base both amide proton and nitrogen are drastically low field shifted and the coupling is reduced (12.34/138.65 ppm, 89.6/89.6 Hz) indicating a by far stronger H-bond of the amide to the phosphate in accordance to their H-bond donor and acceptor abilities (see SI chapter 2.6.4.4).[90] The addition of PhSH slightly weakens the ^{15}N-H⋯O-P H-bond, which was identified by the reduction of the chemical shifts and a small increase of the coupling constant (11.45/137.91 ppm, 89.9[91]/90.0 Hz). In contrast to the amide signals, the ^{1}H chemical shift changes of the thiol S-H proton with and without base and amide are quite small (3.73-4.07 ppm; see Figure 2.2c, orange signal), and hence denote minimal interaction with the phosphate base or the amide. Via ^{1}H,[1]H NOESY experiments, we further confirmed that the average amide-phosphate interaction is slightly reduced upon addition of thiophenol (see SI chapter 2.6.5.3).

Next, the situation with PhOH as HAT donor was investigated, which showed a drastically reduced reactivity compared to PhSH as additive (see Figure 2.2a, bottom). The phenolic O-H proton signal, which is located at 6.79 ppm for pure phenol, is significantly shifted to higher ppm values (12.26 ppm) in the presence of amide and base indicating that phenol is incorporated in a complex network of considerably strong H-bonds (Figure 2.2e). Simultaneously, the amidyl ^{15}N-H duplet shows in principal similar chemical shift and scalar coupling values (11.84/137.95 ppm, 89.7/90.6 Hz) compared to the amide/base/PhSH sample in both ^{1}H and ^{15}N spectra even with a trend to slightly stronger amide-phosphate H-bonds. As a result, the classical H-bond strength analysis using exclusively ^{1}H chemical shifts as sensor suggests a similar H-bond activation of the amide in presence of PhSH and PhOH and fails to explain the huge reactivity difference of these two HAT donors (see Figure 2.2a), which previously was mainly attributed to their different radical and HAT properties, potential catalyst inhibition or side reactions of phenol.[80] The only detectable difference is the inclusion of phenol into the H-bond network in contrast to mainly free thiophenol. However, this simplified donor only observation of H-bonds can also hide the full situation.
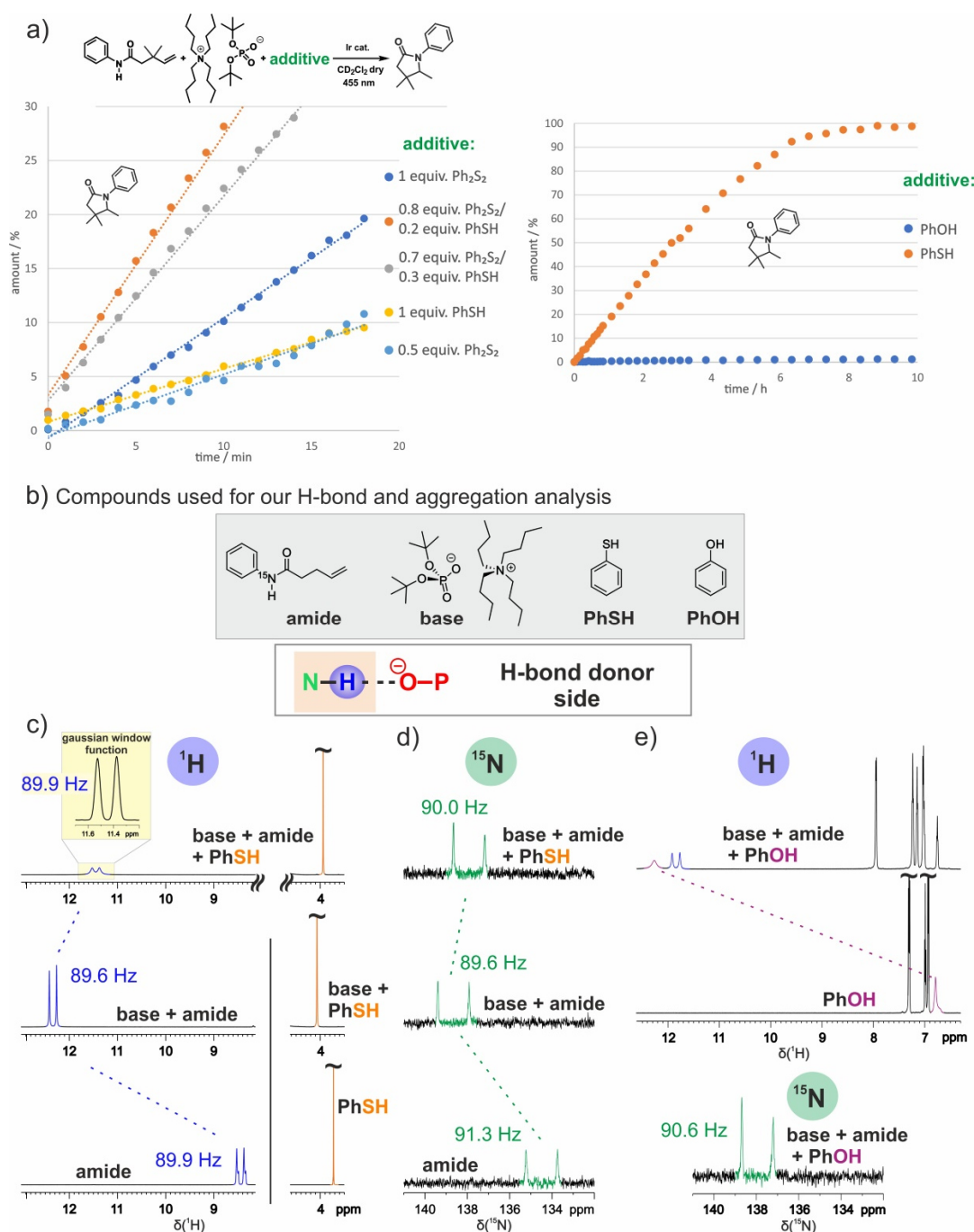
**Figure 2.2:** a) The *in-situ* NMR kinetics revealed a drastic acceleration of the overall PCET efficiency for mixtures of PhSh/$Ph_2S_2$ hinting at an H-bond effect in terms of cooperativity (left). The fast product formation (~100% after ~10 h) for the PhSH containing photocatalytic system and very low yields using PhOH (~1.2% after ~10 h) were confirmed by *in-situ* NMR kinetics, too (right). The trend of the H-bond donor chemical shifts deviates from the PCET reactivities: b) for the NMR based H-bond studies, ^{15}N-phenylpent-4-enamide (**amide**), tetrabutylammonium di-*tert*-butylphosphate (**base**), thiophenol (**PhSH**) and phenol (**PhOH**) were used. The H-bond donor side was studied via c) ^{1}H and d) ^{15}N NMR chemical shift and scalar coupling analysis in $CD_2Cl_2$ at 180 K and 1:1/1:1:1 mixtures were used for the multicomponent samples. The amidyl ^{15}N-H low field shift in both 1D spectra in presence of base confirmed the existence of an H-bond, which is weakened after adding PhSH. In contrast, PhSH is mainly free in solution as the δ-values are only barely affected; e) a significant ^{1}H low field shift of the phenol OH proton indicates its incorporation into the H-bonded complex, but the amide chemical shifts are similar to the PhSH containing samples.

**H-bond acceptor and phosphate dimer formation:** Therefore, next the H-bond acceptor side of these mixtures was analyzed by $^{31}$P NMR measurements. According to the trend demonstrated via $^{1}$H and $^{15}$N NMR, the movement of the proton towards the base predicts a shielding of the acceptor and therefore a high field shift of the $^{31}$P signal of the base. Furthermore, the diminished H-bond interaction after adding PhSH is expected to be reflected in a back shift to low field. As shown in Figure 2.3a, the $^{31}$P signal of the pure phosphate anion (-7.44 ppm; bottom) was shifted towards high field in presence of the amide (-8.19 ppm; above), which is in full accordance with the previous results. However, upon addition of PhSH to the pure base, the phosphate signal was even further high field shifted to -8.69 ppm, which is in strong contrast to the $^{1}$H spectra indicating only very weak H-bonds to PhSH in all thiol containing samples (*vide supra*). Thus, upon addition of PhSH another very strong H-bond has to be created independently of the thiol proton itself. This is also corroborated by the appearance of a $^{1}$H signal at 16.43 ppm (PhSH: 3.94 ppm) for all PhSH/base containing mixtures. Since in our group dimers of chiral phosphoric acids were found to produce H-bond signals with $^{1}$H chemical shifts around 16.00 ppm,[88] we suspected that a proton being H-bonded inside a phosphate dimer might cause this signal. Indeed, by adding high excess of $H_2O$ to the pure base in a control experiment, $^{1}$H and $^{31}$P signals at approximately equal positions appeared (16.54/-8.59 ppm; Figure 2.3a, top), albeit in small concentrations. In addition, in mixtures of PhSH and base the occurrence of thiophenolate species was identified by NMR spectroscopy (a detailed characterization is given in chapter 2.6.4.1, SI). Thus, the addition of PhSH creates a new species, the phosphate dimer **1**, with a strong intermolecular P-O···H···O-P H-bond and high electron density being located at the $^{31}$P nuclei identified by the high field shift. In the mixture of amide, base and PhSH the phosphate dimer **1** is present as well (see Figure 2.3a). In addition, the main and sharper $^{31}$P signal of the amide included complex is even further high field shifted (-9.05 ppm) indicating highest electron density located on the phosphate. This chemical shift reduction excludes a simple change in the concentration of the original amide-base complex and confirms a modulation of the overall aggregation. Therefore, the protonation of the phosphate by PhSH creates a classical network of phosphates H-bonded to both amide and phosphoric acid (N-H···A$^{-}$···H-A; with A being the phosphate). These structures could also be verified by MD simulations (*vide infra*). The higher electron density on the phosphates detected in these aggregates (see Figure 2.3a) indicates that a significant amount of phosphates is incorporated in extended H-bond networks with at least two H-bonds. The actual strengths of the N-H ···O-P H-bond is difficult to assess, since the DOSY experiments and the MD simulations discussed below show a release of the ammonium cations from the aggregate as well as a reduction of the overall amount of N-H moieties incorporated in H-bonds in the presence of phosphate dimers.
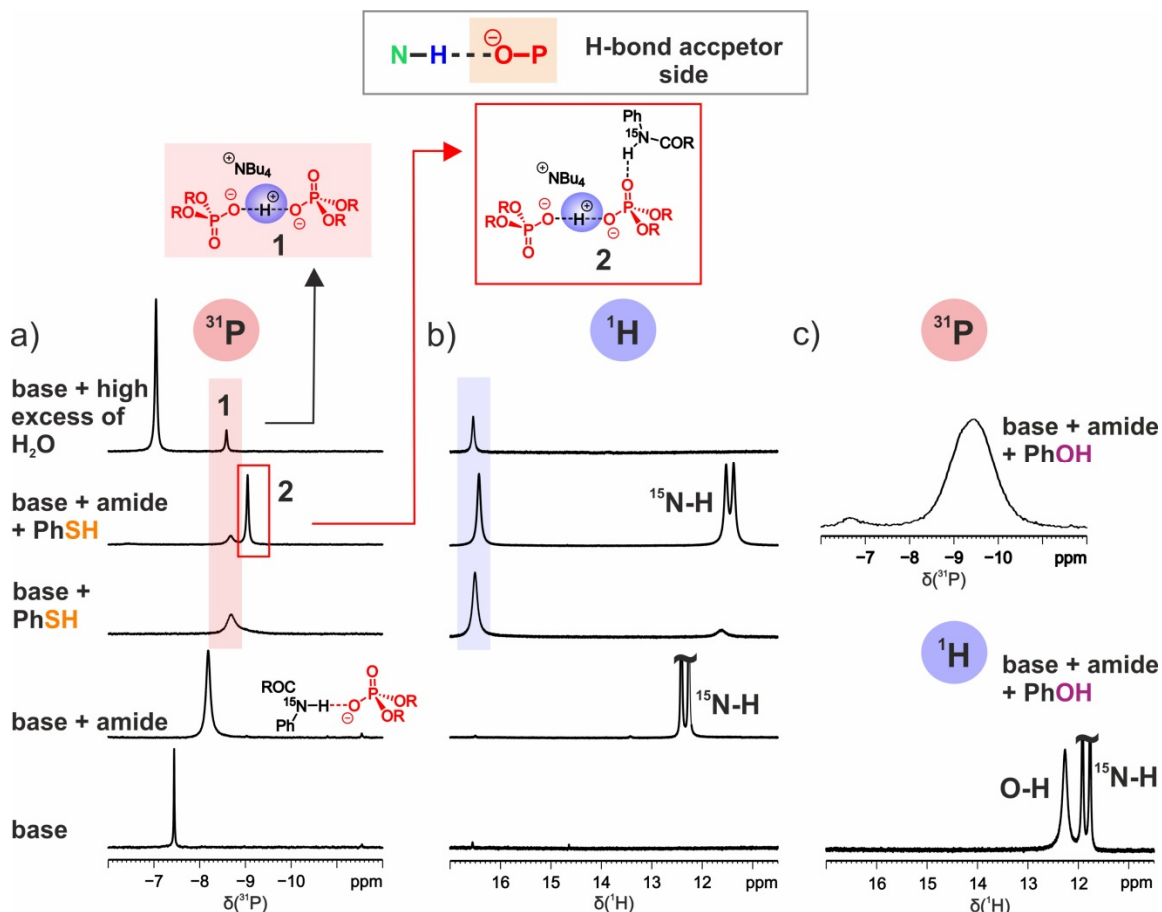
**Figure 2.3:** The phosphate dimer **1** possessing high electron density was identified as crucial complex enabling strong H-bonds to amide: a) the H-bond acceptor side was studied by $^{31}$P NMR chemical shift analysis in CD$_2$Cl$_2$ at 180 K and 1:1/1:1:1 mixtures were used for the multicomponent samples. For complete spectra, see SI. The high field shift of the phosphate after adding amide confirms the existence of an amide-base complex. Against the $^1$H/$^{15}$N chemical shift trend (Figure 2.2), the phosphate signal is further high field shifted in presence of PhSH (red box). We assume dimer **1** created by partial protonation of the base by PhSH (see chapter SI 2.6.4.1), which was also formed in a base/H$_2$O control experiment (top). The main signal (1:3 ratio) of the amide/base/PhSH mixture appeared at maximum high field position suggesting the strong H-bonded amide containing aggregate **2**; b) the low field $^1$H signal at ~16.5 ppm for PhSH containing as well as for the base/H$_2$O samples represents the hydrogen-bridged proton inside **1**; c) the broad $^{31}$P signal of the amide/base/PhOH sample corroborates a phenol containing large aggregate and the absence of dimer **1** is verified by $^1$H NMR.

In addition, an averaging of the chemical shifts with weaker bifurcated H-bond aggregates and/or a dynamic hopping of the amide from one phosphate to the other within dimer **1** may occur. Such proton exchange on the NMR time scale is corroborated by the line broadening of the N-H proton in the $^1$H NMR spectrum (Figure 2.2c, top). The bifurcation motif could directly be found in our MD derived snapshots (*vide infra*). Nevertheless, the interaction of the phosphate dimers with the amides and the resulting change of the overall aggregation is clearly visible form the $^{31}$P spectra.

In contrast, for the amide/base/phenol mixture only a very broad ^{31}P signal over a ppm region of -7.77 to -11.16 ppm was detected but no ^{1}H signal at around 16.50 ppm (see Figure 2.3c). This indicates no protonation of phosphate and in consequence no phosphate dimer formation with phenol in accordance with the relative $pK_a$ values of thiophenol and phenol ($pK_a$ (PhSH): 10; $pK_a$ (PhOH): 18; in DMSO).[92] The high field position of the base signal indicates high electron density also for this complex potentially induced by extended networks with phenol.

The presented data show that thiophenol is able to partially protonate the phosphate in an acid-base reaction and thus to form H-bond mediated P-O···H···O-P dimers in solution, while with phenol as additive no phosphate protonation occurs. However, the ^{1}H and ^{31}P chemical shifts as average parameters of the H-bond strengths are similar in both cases. This is an indication that beside H-bond strengths also the overall molecular arrangement has to be the second key to reactivity.

**Aggregation analysis by NMR:** Therefore, the nature of the different aggregates was analyzed in detail via diffusion ordered spectroscopy (DOSY) at 300 K and 180 K. From the obtained self-diffusion coefficients, which refer to averaged values for the species in the entire solution, the viscosity corrected volumes V (DOSY) were calculated (for details see SI chapter 2.6.5.2). In Figure 2.4, the volumes derived from DOSY for the amide/base, amide/base/PhSH and the amide/base/PhOH mixtures as well as the literature derived monomer volumes according to Bondi[93] are summarized.

At both temperatures large aggregates were detected as expected for ion pairs and molecules (amides), which can form H-bonds in apolar organic solvents. The modulation of aggregation between ambient and low temperature follows the expected trends. The amide tends to higher aggregates at 180 K, while the ion pair shows higher complexation at room temperature due to the reduced dielectric constant of the solvent (see Figure 2.4 and Table S1, SI).

However, at both temperatures the high amount of aggregation exemplifies that it is of utmost importance for the interpretation of H-bond networks in PCET reactions to check the aggregation situation at the concentrations used in catalysis and not in highly diluted samples usually used for UV luminescence quenching.

**Amide/base and amide/base/thiophenol:** In the following only the aggregation at low temperature is discussed as this can be analyzed in combination with the H-bond study and the MD simulations. For the amide/base sample, large volumes were obtained for both the amide (V(DOSY) = 1900 $\text{Å}^3$) and phosphate (V(DOSY) = 1681 $\text{Å}^3$) confirming the existence of an amide-base complex, proposed as aggregate **4** (Figure 2.4).[94] The low volume of NBu$_4^+$ indicates (V(DOSY) = 1389 $\text{Å}^3$) a partial dissociation from complex **4**. In

presence of PhSH, surprisingly, an immense reduction of the amide complexation was obtained ($\Delta V$(DOSY) = 591 Å$^3$). This suggests less self-aggregation and partial release of the substrate from the phosphate complex. This unexpected result also explains the reduction of the $^1$H and $^{15}$N chemical shifts after addition of PhSH. Due to the low time resolution of NMR spectroscopy the signals of the highly activated N-H moieties in H-bonds with the P-O···H···O-P dimers are averaged with non-activated N-H moieties of pure amides and the real activation is masked by the crowd of aggregates. Only in the non-averaged signal of the phosphate-amide interaction the extended H-bond network is reflected. In addition, the comparably small DOSY derived value of NBu$_4^+$ (V = 986 Å$^3$) indicates that upon addition of PhSH even a higher percentage of the cation is pushed away from the phosphate complex, which may support higher electron densities on phosphate as well. Of course, also the formation of thiolate-NBu$_4^+$ complexes may explain the small volumes to some extent. For the pure PhSH, the volume is within the range of the monomer, which is in full accordance with the poor H-bond donor ability.

**Amide/phosphate/phenol:** In contrast, the measurement of the amide/base/phenol sample yielded immense values for both the amide and phenol species (V(DOSY) = 2096 and 1966 Å$^3$). Thus, both compounds are incorporated in large aggregates (see aggregate **3** in Figure 2.4). As a result, the amide-phosphate and the phenol-phosphate H-bonds coexist competitively in large ensembles. The reduced activity using PhOH for the hydroamidation indicates that both H-bond competition and aggregation are potentially detrimental to reactivity as was shown for aggregation in flavin photocatalysis.[95]

These data show that PhSH generates a phosphate dimer with increased electron density and a H-bond network to amides within smaller aggregates, which partially release ammonium cations while phenol produces larger aggregates with H-bonds, which are competitive to those of the amide.
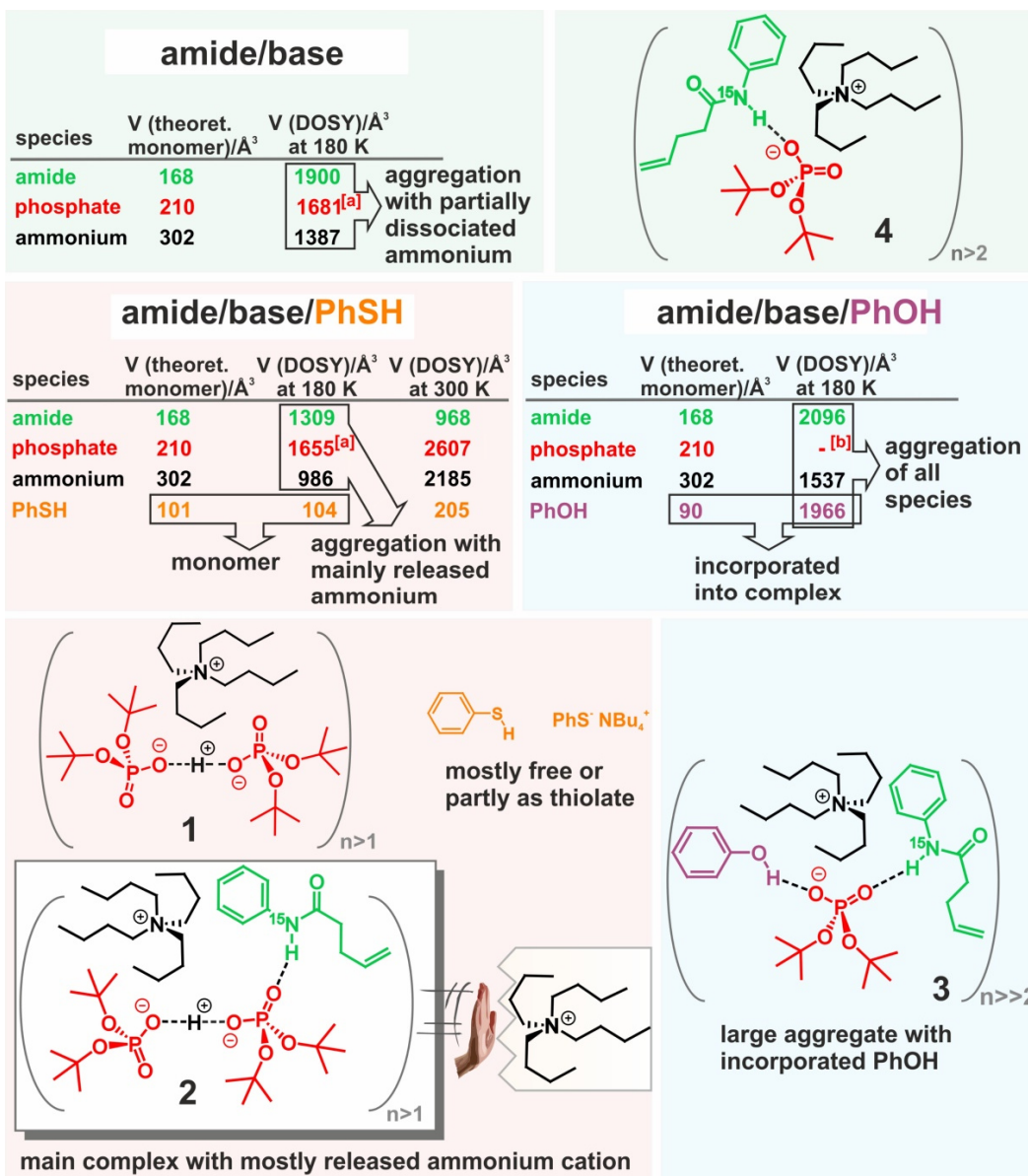
**Figure 2.4:** Reduced aggregation in presence of PhSH prevents from competing H-bonds to phosphate: An overview of the main aggregates identified by ^{1}H, ^{15}N, ^{31}P NMR, DOSY and MD simulations is given. The tables summarize the DOSY derived volumes and the estimated van-der-Waals monomer values according to Bondi.[93] Large amide-base aggregation (top) shown as complex **4** with partial release of the ammonium counterion was identified. In addition to dimer **1** the main amide containing aggregate **2** with mostly released counterion and an immense disaggregation was identified for the PhSH containing mixture. In contrast, for the amide/base/PhOH sample, the volumes verify the formation of a large PhOH containing aggregate **3**. [a] The value is assumed to be higher, as the phosphate signal is not completely baseline separated from the adjacent ammonium CH$_2$ groups. [b] Complete overlap of signals made the analysis of the phosphate diffusion impossible.

**Molecular-Dynamics (MD) simulations:** In order to obtain more details about the essential substrate activating aggregates MD simulations were performed. While the underlying classical force fields often require care for quantitative predictions of solution structures, they can give a qualitative account of the manifold of expected and unexpected aggregates that are present in complex mixed solutions. In Figure 2.5, selected PCET relevant snapshots of a simulation containing *N*-phenylpent-4-enamide, di-*tert*-butyl phosphate anion, tetrabutylammonium cation, thiophenolate, *tert*-butyl phosphoric acid, $H_2O$ and $H_3O^+$ are depicted. The acid was used in order to be able to mimic the phosphate-$H^+$ interaction. For detailed information about the simulations see chapter 2.6.6 in the SI. In general, the existence of phosphate dimer **1** was verified. The crucial complex **2**, which is formed via attachment of the amidyl N-H group to the phosphate dimer could also be directly found (Figure 2.5; top). In addition, hydrogen bridged to this complex by N-H···O=C a second amide was found to contribute to the extended H-bond network in a cooperative way. Also sterically demanding complexes with one amide attached to the phosphate and one on the phosphoric acid of dimer **1** could be detected, which showed geometrically distorted, i.e. weaker, H-bonds (see Figure 2.66). Furthermore, a significant reduction of the absolute number of H-bonds between amide and phosphate was calculated upon addition of PhSH.
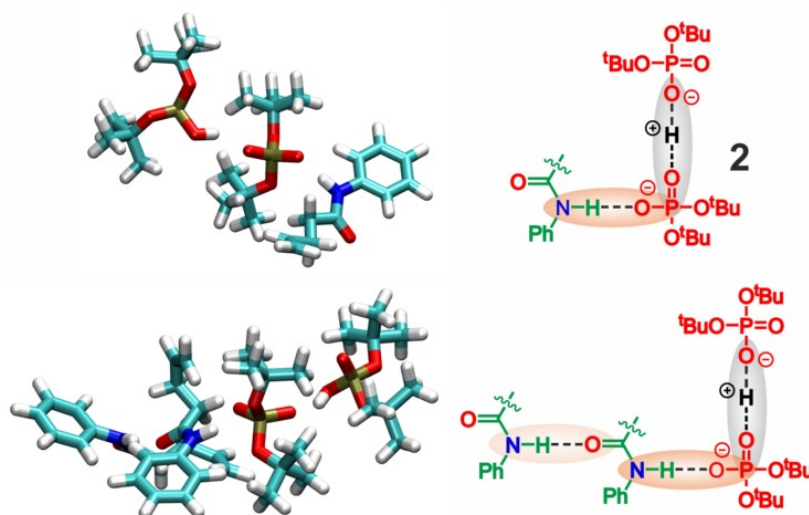


**Figure 2.5:** The PCET relevant amide containing aggregate **2** was verified by MD simulations: MD snapshots of a mixture containing *N*-phenylpent-4-enamide, di-*tert*-butyl phosphate anion, tetrabutylammonium cation, tert-butyl phosphoric acid, thiophenolate, $H_2O$ and $H_3O^+$ show the H-bond mediated amide-dimer complex **2** (top) and an additional H-bond cooperativity motif (bottom).

Considering the averaging function of the ensemble, these findings explain the overall reduction of the amide-phosphate H-bond strength in presence of PhSH indicated by the $^1$H/$^{15}$N high field shift of the $^{15}$N-H doublet representing all amide containing species inside the solution. Thus, also the MD simulations corroborate significant changes of the overall aggregates in presence of protons originating from the acidic channel of thiophenol.[96]

**Multisite effect of PhSH within the mechanism:** The mechanism of the photocatalyzed hydroamidation is extremely complex and the PhSH additive can act both as acid and as radical. Therefore, the presence of PhSH has impact on multiple rates at different stages of the reaction (see violet boxes for proton channels and grey boxes for radical channels of PhSH in Figure 2.6). The protonated phosphate dimers themselves and the resulting aggregates discussed above can influence the initial PCET step as well as the BPT via potential proton trapping and/or differences in their aggregate size. PhSH as radical may impact the radical off-cycle equilibrium as well as the two HAT steps. In addition, the amount of thiolate anions reduces the availability of PhSH for the radical channels thus radical and ionic channel intertwine. Therefore, PhSH and its derivatives were regarded as unfavorable additives to separate these effects and additives were selected which allow for separating the radical and the ionic pathways at least in the ground state.

**Acceleration effects substituting PhSH by diphenyldisulfide and phosphoric acid:** In case the radical and the ionic pathway influence the hydroamidation reaction independently from each other, it should be possible to replace the radical part of PhSH and the acidic part by two additives. Given the complex mechanism shown in Figure 2.6 it is key to the further understanding to avoid additional players in the cycle. Therefore, $Ph_2S_2$ was selected to represent the radical part of PhSH and phosphoric acid was chosen to replace the acidic part of PhSH. Both $Ph_2S_2$ and phosphoric acid were detected by NMR in the reaction mixtures with PhSH as exclusive additive. This separation of the properties of PhSH into two additives opens the unique opportunity to modulate the relative amount of acid and radicals by using different ratios.[97]

Indeed, the initial rate kinetics of amide, $Ph_2S_2$ and different mixtures of phosphate and phosphoric acid show that the addition of acid accelerates the photoredox catalytic reaction (Figure 2.7) up to three times, which is even higher than the acceleration effect of PhSH with its partially acidic function (see Figure 2.2a, top; di-*n*-butyl phosphoric acid was used because of instability of the *tert*-butyl acid).
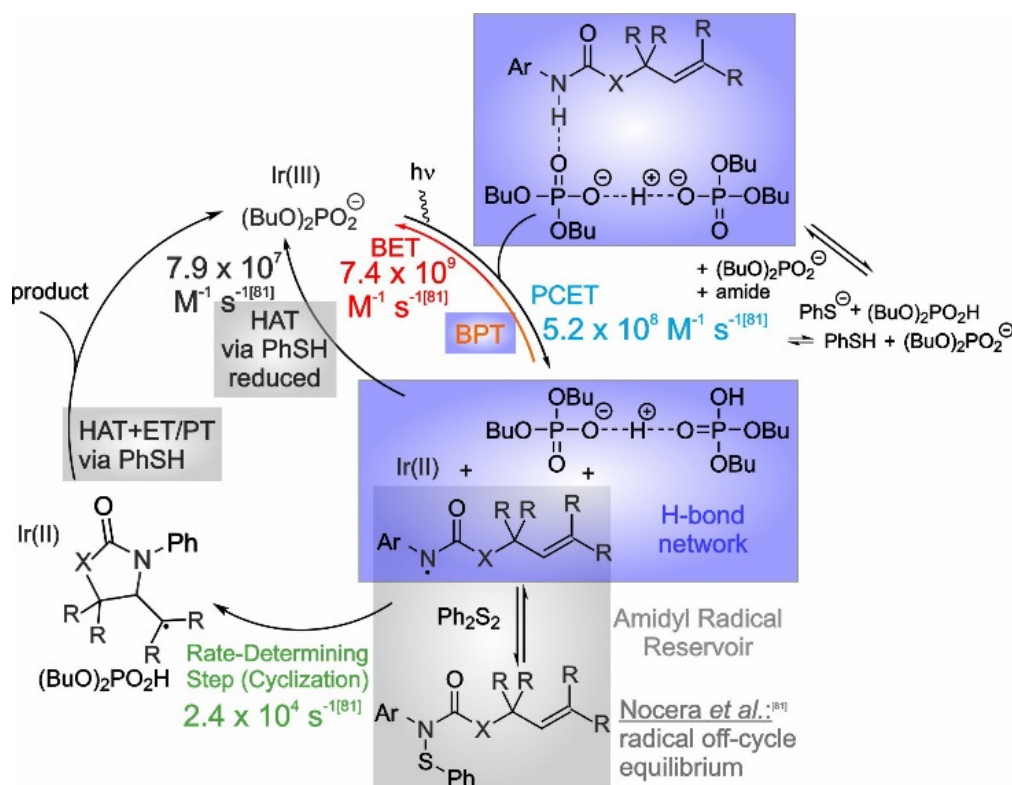
**Figure 2.6:** Multisite effects of PhSH on the mechanism in hydroamidation reactions. Mechanistic steps affected by the acidic properties of PhSH are highlighted with violet boxes, those affected by the radical properties with grey boxes. Ionic and radical channels are intertwined via the partial deprotonation of PhSH. The rates presented originate from previous studies by Nocera and co-workers.[81]

In addition, again the proton signature of the phosphate dimer was detected corroborating the assignment (see Figure 2.33). Under synthetic reaction conditions the acceleration effect is even more pronounced (see Figure 2.7b). Compared to the reaction with base and disulfide only the real reaction is accelerated up to a factor of ~4 (the values are derived from the comparison of the slopes; see chapter 2.6.3.6 and 2.6.3.7 in the SI). Compared to the initially published reaction conditions in presence of PhSH (see Figure 2.2a, bottom, and brown curve in Figure 2.7b) even a factor of ~10 is achieved.[32] As a result, these mechanistic investigations show that the radical and the acidic properties of PhSH can be successfully replaced by a combination of disulfide and acid. In addition, applying these two additives the radical and the acidic properties can be selectively modulated and optimized leading to a reactivity improvement of one order of magnitude. We expect that this will have a huge impact on the developments in synthetic chemistry.

**Effect of phosphoric acid on the mechanism:** Next, we investigated which steps in the mechanism contribute to the observed acceleration upon addition of phosphoric acid. First, the effect of the proton network on the photoreaction was tested via luminescence

quenching experiments at relevant synthetic concentrations (for details, see chapter 2.6.7, SI). Previous studies determined very fast and highly effective PCET rates close to the diffusion limit.[80,81] Indeed, the emission decays of the excited photocatalyst were fastest without acid as additive (see Figure 2.69). The luminescence decays show that addition of phosphoric acid significantly slows down the quenching of the photocatalyst's excited state, as expected for quenching species becoming bulkier with increasing amounts of acid. This is in agreement with DOSY measurements showing larger aggregates in presence of phosphoric acid (see Table S1) and excludes the photo-step effecting the acceleration of the overall reaction (for mechanistic scheme see Figure 2.8a). Since acid slows down the PCET step, the observed acceleration can be caused either by an acceleration of the productive radical cyclization or a reduction of the unproductive BET/BPT back reaction.

Therefore, next the availability of the photo-generated amidyl radical was tested, which is the key intermediate for the productive reaction. We achieved this by measuring NMR reaction profiles applying different light intensities during the reaction (see Figure 2.8b). The exclusive change of light intensity allows to dissect the different steps in the mechanism regarding the amount of amidyl radical. The PCET generation of the radical should be proportional to the light intensity. The rate constant of the cyclization step should be independent of the light intensity and constant at least within one reaction profile. As a result, the rate of the cyclization, which can be read out in the slope of the overall reaction profile is expected to be proportional to the amount of photogenerated amidyl radical available for the productive reaction.

The blue curve in Figure 2.8b shows the response of the overall reaction with disulfide and base. After reducing the light intensity to 50% or to 25%, a small persistence of the previous reaction rate is observed for about half a minute. An acceleration of the cyclization should reduce the amount of the photogenerated amidyl radical. In contrast the reduction of the BET/BPT should increase the amount of amidyl radical intermediate.

This is in contrast to our previous studies, in which direct responses to light reduction were detected (upon light reduction the systems relaxed below the NMR time resolution to the new photochemical equilibrium situation even in case of reaction intermediates).[98] This indicates the formation of an amidyl reservoir feeding the cyclization over a longer time span. Such an accumulation of the amidyl radical photo-generated at higher light intensity in presence of $Ph_2S_2$ is in agreement with the mechanistic proposal and the relative reaction rates previously proposed by Nocera and co-workers (see Figure 2.6), in which the amidyl radical is stored as the S-N intermediate shown in Figure 2.8.[81]
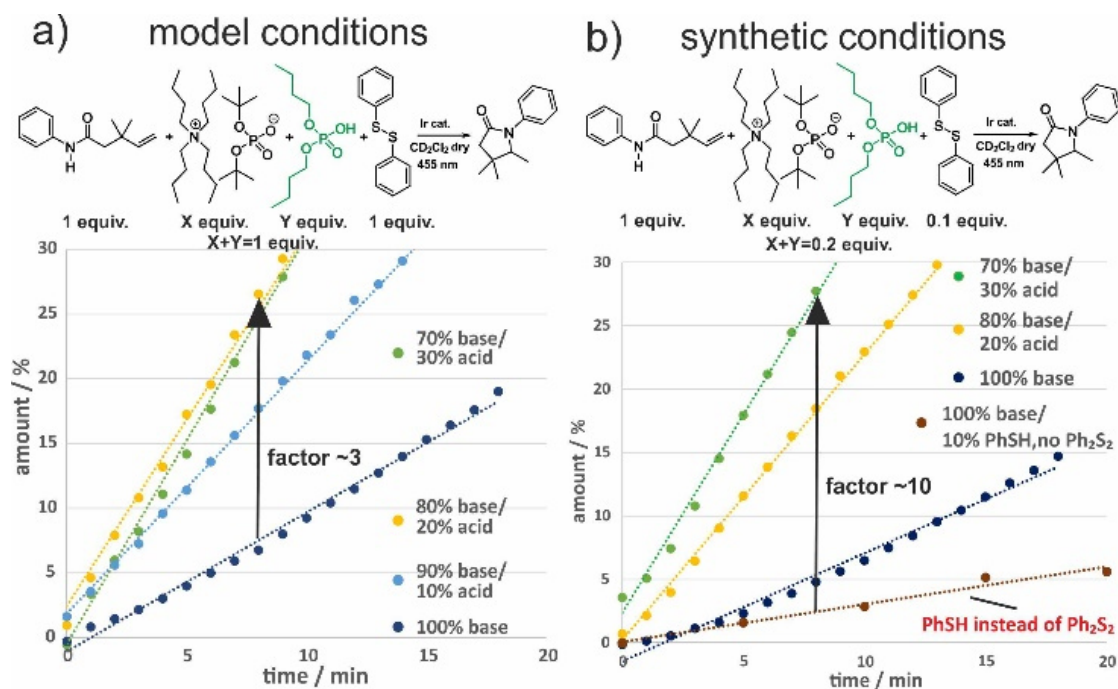
**Figure 2.7:** Acceleration effects substituting PhSH by phosphoric acid and $Ph_2S_2$ presented by initial rate kinetics of amide, $Ph_2S_2$ and different amounts of base and acid; a) in 1:1:1 mixtures of amide/ $Ph_2S_2$/acid+base acceleration effects up to 3 validate the effect of the proton network on the photoredox catalytic reaction; b) under synthetic conditions (1:0.1:0.2 of amide/$Ph_2S_2$/acid+base) the selective optimization of ionic and radical channels allows even an acceleration by one order of magnitude.

Thus, in the following the term amidyl radical reservoir describes both the amidyl radical itself and the amidyl radical stored in this S-N intermediate. The PCET step is very fast, while the amidyl cyclization is the rate determining step of the reaction. In case the BET/BPT back reaction can be slowed down, an excess formation of amidyl radical is expected. This was achieved by $Ph_2S_2$ as additive providing an off-cycle equilibrium to the S-N intermediate. This amidyl reservoir seems to be now visible in the persisting slope corresponding to the preceding light intensity (as well as in the slower initial buildup in the first minutes, see also Figure 2.7). In principle, different times for this persistence of the slope depending on the preceding light intensity are expected, however the slow time resolution of the NMR spectra (0.5 min per spectrum) is not sufficient in the case of $Ph_2S_2$ as exclusive additive.

Upon applying a 30:70 mixture of phosphoric acid and base, again a significant acceleration at 100% light was observed. After reducing the light to 50% intensity, a persistence of the initial reaction rate over 3 minutes can be observed (see green curve in Figure 2.8b). This directly shows that with acid as additive, a significantly larger amidyl reservoir is formed. In addition, this indirectly proves the presence of the S-N intermediate,

since pure amidyl radical would be consumed by far faster by the cyclisation reaction ($2.4 \times 10^4$ s$^{-1}$)[81]. Reducing the light intensity from 50 to 25%, this persistence of the previous rate is repeated but the length is shorter (2.5 min) as anticipated for lower light intensities. This pattern is corroborated by the third switching of the light intensity: Again, the previous slope continues, but for a shorter time. These data show that with acid such a huge excess of amidyl radical is formed (and stored in the S-N intermediate) and that even the slow time resolution of NMR spectroscopy is sufficient to resolve the additive-dependent offset between the photo-generated formation of an amidyl radical reservoir and its abreaction in the downstream dark reaction.

After reducing the light from 100 to 50% around 10% conversion is observed at the initial rate, which is significantly more than the 2% of Ir(III) catalyst available in this reaction (even in case the ongoing conversion at 50% is subtracted). This substantial size of the amidyl reservoir indicates that a productive regeneration pathway of Ir(II) to Ir(III) has to be present prior to the cyclization reaction. Initially this regeneration was proposed by Knowles and co-workers via a sequential ET/PT involving PhS· and phosphoric acid after the cyclization step (see Figure 2.1b). Considering the off-cycle equilibrium to the S-N intermediate creating PhS· and the presence of additional protons in close proximity within the phosphate dimers, we propose this additional Ir(III) regeneration pathway directly after the PCET step as shown in Figure 2.8a.

In principle, this shortcut should be also possible in presence of disulfide and without additional acid since phosphoric acid is generated in the PCET step and PhS· is available from the off-cycle equilibrium to the S-N intermediate. However, the reaction profiles only with disulfide in Figure 2.8b show only a very short persistence of the previous reaction rate upon light reduction. In contrast, with 30% acid a persistence up to three minutes is observed.

This shows clearly the importance of additional protons, which are in close proximity (phosphate dimers) to the reaction center being the key to an effective and productive regeneration of the reduced Ir(II) catalyst back to the initial Ir(III) state.

Overall, reaction profiles with variation of the light intensity are used to dissect the effect of acid on the different mechanistic steps within the catalytic cycle. In presence of acid persistence times of the reaction rate at higher light intensities were observed over minutes after attenuating the light indicating the formation of a large amidyl radical reservoir. This shows that additional protons in close proximity are able to open up a productive short cut for the photocatalyst regeneration prior to the slow cyclisation step.
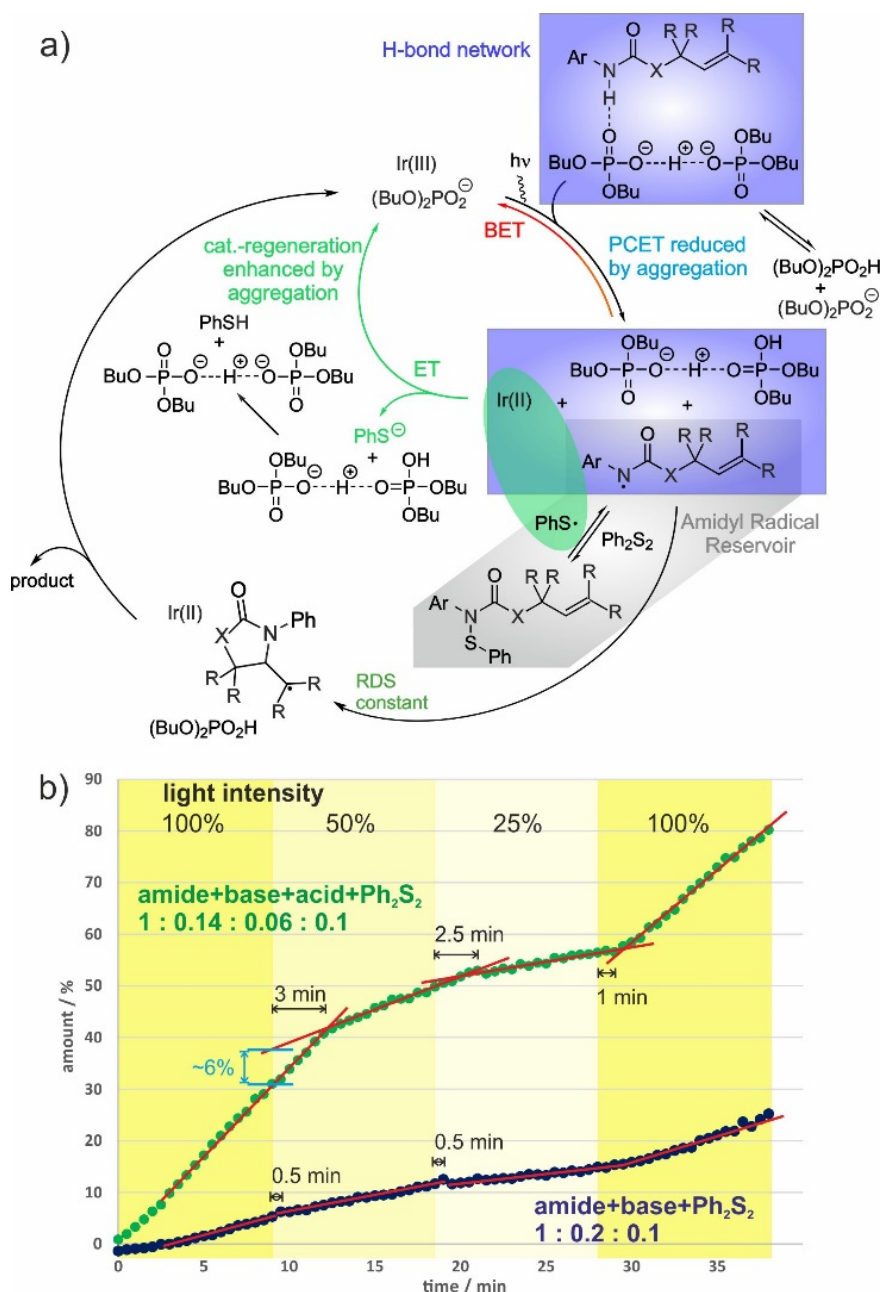
**Figure 2.8:** a) Mechanistic proposal using $Ph_2S_2$ and phosphoric acid instead of PhSH; b) light intensity dependent reaction profiles reflecting conditions of a mixture of amide/base/$Ph_2S_2$ (blue curve) and a mixture of amide, base+acid (70:30) and $Ph_2S_2$ (green curve). The observed persistence times after reducing the light intensity indicate a large amidyl radical reservoir in presence of acid. This as well as the light intensity dependent persistence times reveal a productive pathway of regenerating Ir(III). For details, see text.

## 2.4 Conclusion

In conclusion, this study shows that under synthetic condi-tions in photoredox catalysis, complex aggregation and H-bond networks are potentially present, which affect key properties in terms of reactivity. Due to highly diluted samples in many UV studies, these effects have been often overlooked so far. On the puzzling activation effect of thiophenol in PCET hydroami-dation reactions, it was shown that the interplay of sophisticated NMR studies, MD simulations, initial rate kinetics, and light-dependent reaction profiles allow the disclosure of activation patterns which are hidden by the average properties of the ensembles.

To our knowledge, the combination of techniques within this study reveals quite a number of aspects in photocatalysis for the first time: 1.) An extended H-bond network was directly detected as key element in photocatalysis, here allowing a pro-ductive shortcut for the regeneration of the reduced photocata-lyst to become effective. 2.) The broadly used PhSH additive in photocatalysis was shown to be replaceable by disulfide and acid, allowing for the first time an individual tuning of radical and ionic channel and yielding accelerations up to a factor of ~10 under synthetic conditions. 3.) Advanced NMR studies in combination with MD-simulations revealed activation modes of photoredox catalysis within a complex ensemble of H-bond assisted ion pairs. 4.) Light intensity dependent reaction profiles allowed to trace indirectly the accumulation of a photo-generated radical species and to correlate the overall reaction rate to individual mechanistic steps.

We expect that all aspects of this study, ensembles and ex-tended H-bond networks, proton transfer pathways and tuning of ionic and radical channels will play crucial roles in future photoredox catalysis.

## 2.5 References

[1]     Huynh, M. H. V.; Meyer, T. J. Proton-Coupled Electron Transfer. *Chem. Rev.* **2007**, *107* (11), 5004–5064.

[2]     Weinberg, D. R.; Gagliardi, C. J.; Hull, J. F.; Murphy, C. F.; Kent, C. A.; Westlake, B. C.; Paul, A.; Ess, D. H.; McCafferty, D. G.; Meyer, T. J. Proton-Coupled Electron Transfer. *Chem. Rev.* **2012**, *112* (7), 4016–4093.

[3]     Kaila, V. R. I.; Verkhovsky, M. I.; Wikström, M. Proton-Coupled Electron Transfer in Cytochrome Oxidase. *Chem. Rev.* **2010**, *110* (12), 7062–7081.

[4]     Reece, S. Y.; Nocera, D. G. Proton-Coupled Electron Transfer in Biology: Results from Synergistic Studies in Natural and Model Systems. *Annu. Rev. Biochem.* **2009**,

*78* (1), 673–699.

[5]     Migliore, A.; Polizzi, N. F.; Therien, M. J.; Beratan, D. N. Biochemistry and Theory of Proton-Coupled Electron Transfer. *Chem. Rev.* **2014**, *114* (7), 3381–3465.

[6]     Weinberg, D. R.; Gagliardi, C. J.; Hull, J. F.; Murphy, C. F.; Kent, C. A.; Westlake, B.C.; Paul, A.; Ess, D. H.; McCafferty, D. G.; Meyer, T. J. Proton-Coupled Electron Transfer. *Chem. Rev.* **20012**, *112*, 4016.

[7]     Meyer, T. J.; Huynh, M. H. V.; Thorp, H. H. The Possible Role of Proton-Coupled Electron Transfer (PCET) in Water Oxidation by Photosystem II. *Angew. Chemie - Int. Ed.* **2007**, *46* (28), 5284–5304.

[8]     Stubbe, J.; Nocera, D. G.; Yee, C. S.; Chang, M. C. Y. Radical Initiation in the Class I Ribonucleotide Reductase: Long-Range Proton-Coupled Electron Transfer? *Chem. Rev.* **2003**, *103* (6), 2167–2202.

[9]     Hatcher, E.; Soudackov, A. V.; Hammes-Schiffer, S. Proton-Coupled Electron Transfer in Soybean Lipoxygenase. *J. Am. Chem. Soc.* **2004**, *126* (18), 5763–5775.

[10]    Wang, Y.; Chen, H.; Makino, M.; Shiro, Y.; Nagano, S.; Asamizu, S.; Onaka, H.; Shaik, S. Theoretical and Experimental Studies of the Conversion of Chromopyrrolic Acid to an Antitumor Derivative by Cytochrome P450 StaP: The Catalytic Role of Water Molecules. *J. Am. Chem. Soc.* **2009**, *131* (19), 6748–6762.

[11]    Bonin, J.; Robert, M. Photoinduced Proton-Coupled Electron Transfers in Biorelevant Phenolic Systems. *Photochem. Photobiol.* **2011**, *87* (6), 1190–1203.

[12]    Kaila, V. R. I. Long-Range Proton-Coupled Electron Transfer in Biological Energy Conversion: Towards Mechanistic Understanding of Respiratory Complex I. *J. R. Soc. Interface* **2018**, *15* (141), 1–16.

[13]    Mora, S. J.; Odella, E.; Moore, G. F.; Gust, D.; Moore, T. A.; Moore, A. L. Proton-Coupled Electron Transfer in Artificial Photosynthetic Systems. *Acc. Chem. Res.* **2018**, *51* (2), 445–453.

[14]    Tommos, C.; Babcock, G. T. Oxygen Production in Nature: A Light-Driven Metalloradical Enzyme Process. *Acc. Chem. Res.* **1998**, *31* (1), 18–25.

[15]    Costentin, C.; Robert, M.; Savéant, J.-M. Electrochemical Approach to the Mechanistic Study of Proton-Coupled Electron Transfer. *Chem. Rev.* **2010**, *110* (12), 2145–2179.

[16]    Madhiri, N.; Finklea, H. O. Potential-, PH-, and Isotope-Dependence of Proton-Coupled Electron Transfer of an Osmium Aquo Complex Attached to an Electrode. *Langmuir* **2006**, *22* (25), 10643–10651.

[17]    Hammes-Schiffer, S.; Soudackov, A. V. Proton-Coupled Electron Transfer in Solution, Proteins, and Electrochemistry. *J. Phys. Chem. B* **2008**, *112* (45), 14108–14123.

[18]   Hammes-Schiffer, S. Proton-Coupled Electron Transfer: Moving Together and Charging Forward. *J. Am. Chem. Soc.* **2015**, *137* (28), 8860–8871.

[19]   Ghosh, S.; Soudackov, A. V.; Hammes-Schiffer, S. Electrochemical Electron Transfer and Proton-Coupled Electron Transfer: Effects of Double Layer and Ionic Environment on Solvent Reorganization Energies. *J. Chem. Theory Comput.* **2016**, *12* (6), 2917–2925.

[20]   Savéant, J. M. Electrochemical Approach to Proton-Coupled Electron Transfers: Recent Advances. *Energy Environ. Sci.* **2012**, *5* (7), 7718–7731.

[21]   Costentin, C.; Savéant, J. M. Theoretical and Mechanistic Aspects of Proton-Coupled Electron Transfer in Electrochemistry. *Curr. Opin. Electrochem.* **2017**, *1* (1), 104–109.

[22]   Savéant, J.-M. Concerted Proton-Electron Transfers: Fundamentals and Recent Developments. *Annu. Rev. Anal. Chem.* **2014**, *7* (1), 537–560.

[23]   Costentin, C.; Robert, M.; Savéant, J. M.; Tard, C. Breaking Bonds with Electrons and Protons. Models and Examples. *Acc. Chem. Res.* **2014**, *47* (1), 271–280.

[24]   Li, B.; Zhao, J.; Onda, K.; Jordan, K. D.; Yang, J.; Petek, H. Ultrafast Interfacial Proton-Coupled. *Science* **2006**, *311* (March), 1436–1440.

[25]   Symes, M. D.; Surendranath, Y.; Lutterman, D. A.; Nocera, D. G. Bidirectional and Unidirectional PCET in a Molecular Model of a Cobalt-Based Oxygen-Evolving Catalyst. *J. Am. Chem. Soc.* **2011**, *133* (14), 5174–5177.

[26]   Costentin, C.; Drouet, S.; Robert, M.; Saveant, J.-M. A Local Proton Source Enhances CO2 Electroreduction to CO by a Molecular Fe Catalyst. *Science* **2012**, *338* (6103), 90–94.

[27]   Markle, T. F.; Darcy, J. W.; Mayer, J. M. A New Strategy to Efficiently Cleave and Form C–H Bonds Using Proton-Coupled Electron Transfer. *Sci. Adv.* **2018**, *4* (7), 1–8.

[28]   Liu, T.; Guo, M.; Orthaber, A.; Lomoth, R.; Lundberg, M.; Ott, S.; Hammarström, L. Accelerating Proton-Coupled Electron Transfer of Metal Hydrides in Catalyst Model Reactions. *Nat. Chem.* **2018**, *10* (8), 881–887.

[29]   Fava, E.; Nakajima, M.; Nguyen, A. L. P.; Rueping, M. Photoredox-Catalyzed Ketyl-Olefin Coupling for the Synthesis of Substituted Chromanols. *J. Org. Chem.* **2016**, *81* (16), 6959–6964.

[30]   Lefebvre, Q.; Hoffmann, N.; Rueping, M. Photoorganocatalysed and Visible Light Photoredox Catalysed Trifluoromethylation of Olefins and (Hetero)Aromatics in Batch and Continuous Flow. *Chem. Commun.* **2016**, *52* (12), 2493–2496.

[31]   Choi, G. J.; Knowles, R. R. Catalytic Alkene Carboaminations Enabled by Oxidative Proton-Coupled Electron Transfer. *J. Am. Chem. Soc.* **2015**, *137* (29), 9226–9229.

[32]  Miller, D. C.; Choi, G. J.; Orbe, H. S.; Knowles, R. R. Catalytic Olefin Hydroamidation Enabled by Proton-Coupled Electron Transfer. *J. Am. Chem. Soc.* **2015**, *137* (42), 13492–13495.

[33]  Choi, G. J.; Zhu, Q.; Miller, D. C.; Gu, C. J.; Knowles, R. R. Catalytic Alkylation of Remote C–H Bonds Enabled by Proton-Coupled Electron Transfer. *Nature* **2016**, *539* (7628), 268–271.

[34]  Rono, L. J.; Yayla, H. G.; Wang, D. Y.; Armstrong, M. F.; Knowles, R. R. Enantioselective Photoredox Catalysis Enabled by Proton-Coupled Electron Transfer: Development of an Asymmetric Aza-Pinacol Cyclization. *J. Am. Chem. Soc.* **2013**, *135* (47), 17735–17738.

[35]  Yayla, H. G.; Wang, H.; Tarantino, K. T.; Orbe, H. S.; Knowles, R. R. Catalytic Ring-Opening of Cyclic Alcohols Enabled by PCET Activation of Strong O–H Bonds. *J. Am. Chem. Soc.* **2016**, *138* (34), 10794–10797.

[36]  Miller, D. C.; Tarantino, K. T.; Knowles, R. R. Proton-Coupled Electron Transfer in Organic Synthesis: Fundamentals, Applications and Opportunities. *Top. Curr. Chem.* **2016**, *374* (3), 1–59.

[37]  Gentry, E. C.; Knowles, R. R. Synthetic Applications of Proton-Coupled Electron Transfer. *Acc. Chem. Res.* **2016**, *49* (8), 1546–1556.

[38]  Yayla, H. G.; Knowles, R. R. Proton-Coupled Electron Transfer in Organic Synthesis: Novel Homolytic Bond Activations and Catalytic Asymmetric Reactions with Free Radicals. *Synlett* **2014**, *25* (21), 2819–2826.

[39]  Qiu, G.; Knowles, R. R. Rate–Driving Force Relationships in the Multisite Proton-Coupled Electron Transfer Activation of Ketones. *J. Am. Chem. Soc.* **2019**, *141* (6), 2721–2730.

[40]  Hoffmann, N. Proton-Coupled Electron Transfer in Photoredox Catalytic Reactions. *European J. Org. Chem.* **2017**, *2017* (15), 1982–1992.

[41]  Nguyen, L. Q.; Knowles, R. R. Catalytic C–N Bond-Forming Reactions Enabled by Proton-Coupled Electron Transfer Activation of Amide N–H Bonds. *ACS Catal.* **2016**, *6* (5), 2894–2903.

[42]  Tarantino, K. T.; Liu, P.; Knowles, R. R. Catalytic Ketyl-Olefin Cyclizations Enabled by Proton-Coupled Electron Transfer. *J. Am. Chem. Soc.* **2013**, *135* (27), 10022–10025.

[43]  Zhu, Q.; Graff, D. E.; Knowles, R. R. Intermolecular Anti-Markovnikov Hydroamination of Unactivated Alkenes with Sulfonamides Enabled by Proton-Coupled Electron Transfer. *J. Am. Chem. Soc* **2018**, *140*, 741–747.

[44]  Ota, E.; Wang, H.; Frye, N. L.; Knowles, R. R. A Redox Strategy for Light-Driven, Out-of-Equilibrium Isomerizations and Application to Catalytic C−C Bond Cleavage

Reactions. *J. Am. Chem. Soc* **2019**, *141*, 7.

[45] Wenger, O. S. Proton-Coupled Electron Transfer with Photoexcited Metal Complexes. *Acc. Chem. Res.* **2013**, *46* (7), 1517–1526.

[46] Hammes-Schiffer, S.; Stuchebrukhov, A. A. Theory of Coupled Electron and Proton Transfer Reactions. *Chem. Rev.* **2010**, *110* (12), 6939–6960.

[47] Mayer, J. M.; Rhile, I. J. Thermodynamics and Kinetics of Proton-Coupled Electron Transfer: Stepwise vs. Concerted Pathways. *Biochim. Biophys. Acta - Bioenerg.* **2004**, *1655* (1–3), 51–58.

[48] Zhao, K.; Yamashita, K.; Carpenter, J. E.; Sherwood, T. C.; Ewing, W. R.; Cheng, P. T. W.; Knowles, R. R. Catalytic Ring Expansions of Cyclic Alcohols Enabled by Proton-Coupled Electron Transfer. *J. Am. Chem. Soc.* **2019**, *141* (22), 8752–8757.

[49] Nguyen, S. T.; Zhu, Q.; Knowles, R. R. PCET-Enabled Olefin Hydroamidation Reactions with N-Alkyl Amides. *ACS Catal.* **2019**, *9* (5), 4502–4507.

[50] Morton, C. M.; Zhu, Q.; Ripberger, H.; Troian-Gautier, L.; Toa, Z. S. D.; Knowles, R. R.; Alexanian, E. J. C–H Alkylation via Multisite-Proton-Coupled Electron Transfer of an Aliphatic C–H Bond. *J. Am. Chem. Soc.* **2019**, *141* (33), 13253–13260.

[51] Wang, D.; Loose, F.; Chirik, P. J.; Knowles, R. R. N-H Bond Formation in a Manganese(V) Nitride Yields Ammonia by Light-Driven Proton-Coupled Electron Transfer. *J. Am. Chem. Soc.* **2019**, *141* (12), 4795–4799.

[52] Shin, N. Y.; Ryss, J. M.; Zhang, X.; Miller, S. J.; Knowles, R. R. Light-Driven Deracemization Enabled by Excited-State Electron Transfer. *Science* **2019**, *366*, 364–369.

[53] Bissonnette, N. B.; Ellis, J. M.; Hamann, L. G.; Romanov-Michailidis, F. Expedient Access to Saturated Nitrogen Heterocycles by Photoredox Cyclization of Imino-Tethered Dihydropyridines. *Chem. Sci.* **2019**, *10* (41), 9591–9596.

[54] Caron, A.; Morin, É.; Collins, S. K. Bifunctional Copper-Based Photocatalyst for Reductive Pinacol-Type Couplings. *ACS Catal.* **2019**, *9* (10), 9458–9464.

[55] Wang, Y.; Liu, Y.; He, J.; Zhang, Y. Redox-Neutral Photocatalytic Strategy for Selective C–C Bond Cleavage of Lignin and Lignin Models via PCET Process. *Sci. Bull.* **2019**, *64* (22), 1658–1666.

[56] Zhang, M.; Yang, L.; Yang, H.; An, G.; Li, G. Visible Light Mediated C(Sp3)-H Alkenylation of Cyclic Ethers Enabled by Aryl Ketone. *ChemCatChem* **2019**, *11* (6), 1606–1609.

[57] Hammes-Schiffer, S. Proton-Coupled Electron Transfer: Classification Scheme and Guide to Theoretical Methods. *Energy Environ. Sci.* **2012**, *5* (7), 7696–7703.

[58] Hammes-Schiffer, S. Theoretical Perspectives on Proton-Coupled Electron

Transfer Reactions. *Acc. Chem. Res.* **2001**, *34* (4), 273–281.

[59]   Mayer, J. M.; Hrovat, D. A.; Thomas, J. L.; Borden, W. T. Proton-Coupled Electron Transfer versus Hydrogen Atom Transfer in Benzyl/Toluene, Methoxyl/Methanol, and Phenoxyl/ Phenol Self-Exchange Reactions. *J. Am. Chem. Soc.* **2002**, *124*, 11142–11147.

[60]   Skone, J. H.; Soudackov, A. V.; Hammes-Schiffer, S. Calculation of Vibronic Couplings for Phenoxyl/Phenol and Benzyl/Toluene Self-Exchange Reactions: Implications for Proton-Coupled Electron Transfer Mechanisms. *J. Am. Chem. Soc.* **2006**, *128* (51), 16655–16663.

[61]   Sjödin, M.; Irebo, T.; Utas, J. E.; Lind, J.; Merényi, G.; Åkermark, B.; Hammarström, L. Kinetic Effects of Hydrogen Bonds on Proton-Coupled Electron Transfer from Phenols. *J. Am. Chem. Soc.* **2006**, *128* (40), 13076–13083.

[62]   Litwinienko, G.; Ingold, K. U. Solvent Effects on the Rates and Mechanisms of Reaction of Phenols with Free Radicals. *Acc. Chem. Res.* **2007**, *40* (3), 222–230.

[63]   Young, E. R.; Rosenthal, J.; Hodgkiss, J. M.; Nocera, D. G. Comparative PCET Study of a Donor−Acceptor Pair Linked by Ionized and Nonionized Asymmetric Hydrogen-Bonded Interfaces. *J. Am. Chem. Soc.* **2009**, *131* (22), 7678–7684.

[64]   Damrauer, N. H.; Hodgkiss, J. M.; Rosenthal, J.; Nocera, D. G. Observation of Proton-Coupled Electron Transfer by Transient Absorption Spectroscopy in a Hydrogen-Bonded, Porphyrin Donor-Acceptor Assembly. *J. Phys. Chem. B* **2004**, *108*, 6315–6321.

[65]   Morris, W. D.; Mayer, J. M. Separating Proton and Electron Transfer Effects in Three-Component Concerted Proton-Coupled Electron Transfer Reactions. *J. Am. Chem. Soc.* **2017**, *139* (30), 10312–10319.

[66]   Hammes-Schiffer, S.; Iordanova, N. Theoretical Studies of Proton-Coupled Electron Transfer Reactions. *Biochim. Biophys. Acta - Bioenerg.* **2004**, *1655*, 29–36.

[67]   Hammes-Schiffer, S.; Stuchebrukhov, A. A. Theory of Coupled Electron and Proton Transfer Reactions. *Chem. Rev.* **2010**, *110* (12), 6939–6960.

[68]   Meo, F. Di; Lemaur, V.; Lazzaroni, R.; Duroux, J.; Olivier, Y.; Trouillas, P. Free Radical Scavenging by Natural Polyphenols : Atom versus Electron Transfer. *J. Phys. Chem. A* **2013**, *117*, 2082–2092.

[69]   Hanthorn, J. J.; Valgimigli, L.; Pratt, D. A. Incorporation of Ring Nitrogens into Diphenylamine Antioxidants: Striking a Balance between Reactivity and Stability. *J. Am. Chem. Soc.* **2012**, *134* (20), 8306–8309.

[70]   DiLabio, G. A.; Johnson, E. R. Lone Pair-π and π-π Interactions Play an Important Role in Proton-Coupled Electron Transfer Reactions. *J. Am. Chem. Soc.* **2007**, *129*

(19), 6199–6203.

[71]    Yuasa, J.; Yamada, S.; Fukuzumi, S. One-Step versus Stepwise Mechanism in Protonated Amino Acid-Promoted Electron-Transfer Reduction of a Quinone by Electron Donors and Two-Electron Reduction by a Dihydronicotinamide Adenine Dinucleotide Analogue. Interplay between Electron Transfer and Hyd. *J. Am. Chem. Soc.* **2008**, *130* (17), 5808–5820.

[72]    Alligrant, T. M.; Alvarez, J. C. The Role of Intermolecular Hydrogen Bonding and Proton Transfer in Proton-Coupled Electron Transfer. *J. Phys. Chem. C* **2011**, *115* (21), 10797–10805.

[73]    Nomrowski, J.; Wenger, O. S. Photoinduced PCET in Ruthenium-Phenol Systems: Thermodynamic Equivalence of Uni- and Bidirectional Reactions. *Inorg. Chem.* **2015**, *54* (7), 3680–3687.

[74]    Nguyen, T. M.; Nicewicz, D. A. Anti-Markovnikov Hydroamination of Alkenes Catalyzed by an Organic Photoredox System. *J. Am. Chem. Soc.* **2013**, *135* (26), 9588–9591.

[75]    Margrey, K. A.; Nicewicz, D. A. A General Approach to Catalytic Alkene Anti-Markovnikov Hydrofunctionalization Reactions via Acridinium Photoredox Catalysis. *Acc. Chem. Res.* **2016**, *49* (9), 1997–2006.

[76]    Nguyen, T. M.; Manohar, N.; Nicewicz, D. A. Anti-Markovnikov Hydroamination of Alkenes Catalyzed by a Two-Component Organic Photoredox System: Direct Access to Phenethylamine Derivatives. *Angew. Chemie - Int. Ed.* **2014**, *53* (24), 6198–6201.

[77]    Gagliardi, C. J.; Murphy, C. F.; Binstead, R. A.; Thorp, H. H.; Meyer, T. J. Concerted Electron Proton Transfer (EPT) in the Oxidation of Cysteine. *J. Phys. Chem. C* **2015**, *119* (13), 7028–7038.

[78]    Kuss-Petermann, M.; Wenger, O. S. Mechanistic Diversity in Proton-Coupled Electron Transfer between Thiophenols and Photoexcited [Ru(2,2′-Bipyrazine)3]2+. *J. Phys. Chem. Lett.* **2013**, *4* (15), 2535–2539.

[79]    Gesmundo, N. J.; Grandjean, J. M. M.; Nicewicz, D. A. Amide and Amine Nucleophiles in Polar Radical Crossover Cycloadditions: Synthesis of γ-Lactams and Pyrrolidines. *Org. Lett.* **2015**, *17* (5), 1316–1319.

[80]    Qiu, G.; Knowles, R. R. Understanding Chemoselectivity in Proton-Coupled Electron Transfer: A Kinetic Study of Amide and Thiol Activation. *J. Am. Chem. Soc.* **2019**, *141*, 16574–16578.

[81]    Ruccolo, S.; Qin, Y.; Schnedermann, C.; Nocera, D. G. General Strategy for Improving the Quantum Efficiency of Photoredox Hydroamidation Catalysis. *J. Am. Chem. Soc.* **2018**, *140* (44), 14926–14937.

[82]    Gschwind, R. M.; Armbrüster, M.; Zubrzycki, I. Z. NMR Detection of Intermolecular NH⋯OP Hydrogen Bonds between Guanidinium Protons and Bisposphonate Moieties in an Artificial Arginine Receptor. *J. Am. Chem. Soc.* **2004**, *126* (33), 10228–10229.

[83]    Sharif, S.; Denisov, G. S.; Toney, M. D.; Limbach, H.-H. NMR Studies of Coupled Low-and High-Barrier Hydrogen Bonds in Pyridoxal-5'-Phosphate-Enzyme Model Systems in Polar Solution. *J. Am. Chem. Soc.* **2007**, *129* (11), 6313–6327.

[84]    Steiner, T. The Hydrogen Bond in the Solid State. *Angew. Chem. Int. Ed.* **2002**, *41* (1), 48–76.

[85]    Prins, L. J.; Reinhoudt, D. N.; Timmerman, P. Nichtkovalente Synthese Mit Wasserstoffbrücken. *Angew. Chem.* **2001**, *113* (13), 2446–2492.

[86]    Harris, T. K.; Zhao, Q.; Mildvan, A. S. NMR Studies of Strong Hydrogen Bonds in Enzymes and in a Model Compound. *J. Mol. Struct.* **2000**, *552* (1), 97–109.

[87]    Greindl, J.; Hioe, J.; Sorgenfrei, N.; Morana, F.; Gschwind, R. M. Brønsted Acid Catalysis - Structural Preferences and Mobility in Imine/Phosphoric Acid Complexes. *J. Am. Chem. Soc.* **2016**, *138*, 15965–15971.

[88]    Sorgenfrei, N.; Hioe, J.; Greindl, J.; Rothermel, K.; Morana, F.; Lokesh, N.; Gschwind, R. M. NMR Spectroscopic Characterization of Charge Assisted Strong Hydrogen Bonds in Brønsted Acid Catalysis. *J. Am. Chem. Soc.* **2016**, *138* (50), 16345–16354.

[89]    Chen, K.; Berg, N.; Gschwind, R.; König, B. Selective Single C(Sp3)-F Bond Cleavage in Trifluoromethylarenes: Merging Visible-Light Catalysis with Lewis Acid Activation. *J. Am. Chem. Soc* **2017**, *139*, 18444–18447.

[90]    Hunter, C. A. Quantifying Intermolecular Interactions: Guidelines for the Molecular Recognition Toolbox. *Angew. Chem. Int. Ed.* **2004**, *43* (40), 5310–5324.

[91]    The broad $^{15}$N-H signal was processed using a gaussian window function for better resolution (Figure 2.2b).

[92]    Bordwell, F. G.; McCallum, R. J.; Olmstead, W. N. Acidities and Hydrogen Bonding of Phenols in Dimethyl Sulfoxide. *J. Org. Chem.* **1984**, No. 49, 1424–1427.

[93]    Bondi, A. Van Der Waals Volumes and Radii. *J. Phys. Chem.* **1964**, *68* (3), 441–451.

[94]    Notably, the ammonium is partially separated from dimer **1** in the thiophenol/base mixture (for comparison of the DOSY values see SI).

[95]    Dadová, J.; Kümmel, S.; Feldmeier, C.; Cibulková, J.; Pažout, R.; Maixner, J.; Gschwind, R. M.; König, B.; Cibulka, R. Aggregation Effects in Visible-Light Flavin Photocatalysts: Synthesis, Structure, and Catalytic Activity of 10-Arylflavins. *Chem. - A Eur. J.* **2013**, *19* (3), 1066–1075.

[96]  The comparison of MD derived diffusion coefficients of the different species yielded additional information about the thiophenolate. As the values for the thiolate are significantly smaller than those of PhSH the complexation of the thiolate was verified.

[97]  Please be aware that $Ph_2S_2$ and acid can produce PhSH upon irradiation with blue light. That means that in photocatalysis acid, $Ph_2S_2$ and PhSH can interconvert into each other. Nevertheless, separation into acid and $Ph_2S_2$ allows for a selective tuning of the proton density and the H-bond networks in the ground state.

[98]  Bartling, H.; Eisenhofer, A.; Konig, B.; Gschwind, R. M. The Photocatalyzed Aza-Henry Reaction of N-Aryltetrahydroisoquinolines: Comprehensive Mechanism, H•- versus H+-Abstraction, and Background Reactions. *J. Am. Chem. Soc.* **2016**, *138* (36), 11860–11871.

## 2.6 Supporting Information

### 2.6.1 General Information

The standard NMR spectroscopic experiments, when not otherwise mentioned, were performed on a Bruker Avance III HD 400.13 MHz (400.13 MHz for ^{1}H) spectrometer with a 5 mm BBO BB-1H/D probe head with Z-gradients. Temperature was controlled by BVT 3000.

The advanced and low temperature NMR spectroscopic measurements were performed on a Bruker Avance III HD 600 (600.13 MHz) and a 5 mm TBI-F probe head with a z-gradient (53.5 Gauss/cm). The temperature of 180 K was controlled by a BVTE 3900.

If not otherwise noted, 5 mm NMR tubes were used and the spectra were referenced to the corresponding solvent.[1] The spectra were processed and evaluated using *TopSpin 3.2* (*Bruker*) and plotted with *TopSpin Plot Editor* and *Corel Draw 2017*. Molecular structures were pictured with *Chem Draw Professional 17.0*.

The solvents for NMR measurements, dichloromethane-$d_2$ ($CD_2Cl_2$) and chloroform-$d_1$ ($CDCl_3$), were purchased from Sigma Aldrich/Merck or Deutero. When water free samples were needed, $CD_2Cl_2$ was freshly dried over $CaH_2$ under Argon atmosphere. The $Ir(dF(CF_3)ppy)_2(bpy)PF_6$ photocatalyst, thiophenol, phenol and diphenyldisulfide were purchased from Sigma Aldrich/Merck, tetrabutylammonium di-*tert*-butylphosphate from Activate Scientific and the amides were synthesized. The solvents for synthesis were purchased from Sigma Aldrich/Merck and the substrates from Fisher Scientific (Acros) and Sigma Aldrich/Merck.

### 2.6.2 Synthesis of Amide Substrates

General Procedure for amide synthesis:
The amides were synthesized according to literature procedures.[2][3]

A round bottom flask was dried and purged with argon prior to use. Under inert conditions, (1-(3-dimethylaminopropyl)-3-ethylcarbodiimide hydrochloride (EDC·HCl; 1.3 equiv.) and DMAP (1.4 equiv.) were added and solved in DCM before the flask was cooled to 0 °C using an ice bath. Next, 4-pentenoic acid (1.0 equiv.) was added and the reaction mixture stirred for 5 minutes. After adding [15]*N*- or unlabeled aniline (1.2 equiv.) the mixture was then stirred at room temperature for at least 24 hours. Via TLC (PE/EE 1:1), the progress of the product formation was controlled and after full conversion, the mixture was quenched with HCl (1 M). The resulting organic and aqueous phases were separated and

the aqueous extracted with DCM. The combined organic layers were dried over $Na_2SO_4$ before the solvent was removed and the crude mixture was obtained. The crude product was recrystallized (PE/EE 4:1; 80-130 °C) and the product generated in up to 94% yield. The NMR spectroscopic data of the following amide species are in agreement with literature spectra.[2]
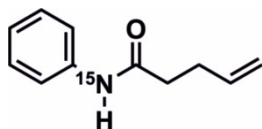


**$^{15}$N-Phenylpent-4-enamide**

The labeled amide was synthesized according to the general procedure using 4-pentenoic acid (8.8 mmol), $^{15}$N- aniline (10.6 mmol), EDC-HCl (11.5 mmol) and DMAP (12.4 mmol) in DCM (30 ml). After recrystallization of the white-orange crude product 1.02 g (65%) of white flakes were obtained.

$^1$H-NMR (400 MHz, CDCl$_3$): δ (ppm) = 7.50 (d, J = 7.6 Hz, 2 H), 7.32 (t, J = 7.8 Hz, 2 H), 7.14 (d, J = 88.7 Hz, 1H, $^{15}$N-H), 7.10 (t, J = 7.3 Hz, 1 H), 5.94-5.84 (m, 1 H), 5.13 (d, J = 16.8 Hz, 1 H), 5.06 (d, J = 10.2 Hz, 1 H), 2.53-2.44 (m, 4 H).
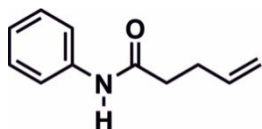


**$N$-Phenylpent-4-enamide**

The unlabeled amide was synthesized according to the general procedure using 4-pentenoic acid (20 mmol), aniline (24 mmol), EDC-HCl (26 mmol) and DMAP (28 mmol) in DCM (60 ml). After recrystallization of the white-orange crude solid, 3.28 g (94%) of white flakes were obtained.

$^1$H-NMR (400 MHz, CDCl$_3$): δ (ppm) = 7.50 (d, J = 7.9 Hz, 2 H), 7.32 (t, J = 7.9 Hz, 2 H), 7.10 (t, J = 7.4 Hz, 1 H), 5.99-5.84 (m, 1 H), 5.13 (d, J = 16.5 Hz, 1 H), 5.06 (d, J = 10.2 Hz, 1 H), 2.53-2.44 (m, 4 H).
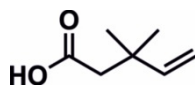
**3,3-Dimethylpent-4-enoic acid**

The synthesis was performed according to literature procedure.[4] To a solution of NaOH (15 g in 38 ml H$_2$O, 10 M), methyl-3,3-dimethylpent-4-enoate (10 ml, 64 mmol) was added and the mixture was stirred under reflux at 130 °C for 5.5 h. The reaction was quenched with HCl until acidic conditions were reached prior to extraction with methyl *tert*-butyl ether. The combined organic layers were washed with brine and dried over MgSO$_4$. The solvent was removed and 6.2 g (76%) of the liquid product were obtained.

$^1$H-NMR (400 MHz, CDCl$_3$): δ (ppm) = 5.91 (dd, J = 17.4 Hz, 10.7 Hz, 1 H), 5.89 (td, J = 17.2 Hz, 0.7 Hz, 2 H), 2.34 (s, 2 H), 1.7 (s, 6 H).
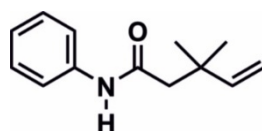


**3,3-Dimethyl-*N*-phenylpent-4-enamide**

The amide was synthesized according to the general procedure using the synthesized 3,3-dimethylpent-4-enoic acid (9 mmol), aniline (11 mmol), EDC-HCl (12 mmol) and DMAP (13 mmol) in DCM (20 ml). After recrystallization of the orange crude solid, 0.4 g (23%) of white product were obtained.

$^1$H-NMR (400 MHz, CD$_2$Cl$_2$): δ (ppm) = 7.46 (d, J = 8.0 Hz, 2 H), 7.30 (t, J = 7.8 Hz, 2 H), 7.22 (br s, 1 H, NH), 7.09 (t, J = 7.4 Hz, 1 H), 6.01 (dd, J = 17.4 Hz, 10.7 Hz, 1 H), 5.07-5.12 (m, J = 10.2 Hz, 2 H), 2.32 (s, 2 H), 1.18 (s, 6 H).

## 2.6.3  Reaction Monitoring

The photoredox catalytic hydroamidation reactions were followed by $^1$H NMR spectroscopy using *N*-phenylpent-4-enamide as well as 3,3-dimethyl-*N*-phenylpent-4-enamide. The dimethyl substrate was chosen in order to exclude self-HAT. *N*-phenylpent-4-enamide was chosen as representative amide for the low temperature hydrogen bonding and aggregation analysis (see chapter 2.6.5).

*In-situ* NMR illumination:

For the measurements of the $^1$H NMR spectra at room temperature a Bruker Avance III HD 600 MHz (600.13 MHz for $^1$H) with a 5 mm TBI-F probe head and Z-gradients and a Bruker Avance 600 MHz spectrometer with a Prodigy BBO probe head were used. The temperature was controlled by a BVT Unit or BCU II (298 or 300 K). The data were processed and plotted with Brukers Topspin 3.2, the graphs were generated with Excel (Office 2016) and pictured using Corel Draw 2017. The photoredox catalytic reaction mixtures were prepared in 5 mm amberized NMR tubes of Spintec. $CD_2Cl_2$ was used as solvent, which was freshly distilled over $CaH_2$ prior to use. For the *in-situ* illumination inside the NMR, the combined illumination setup described by Feldmeier at al. was applied.[5] As light source, a 450 nm Lumitronix Cree XT-E-1 (royalblue; 452 nm peak wavelength measured in our group) LED was used.

The amounts (in %) were obtained by integration of the corresponding amide and product signals. For accurate integration, the respective signal regions were baseline corrected. As no conversion was observed in the dark, the signal integral of the starting material was set to 100%. According to this reference, the progression of the photoredox catalytic reaction was determined after starting the illumination. Due to the hygroscopic properties of the phosphate base, residual $H_2O$ is observable in the NMR spectra.


General procedure of sample preparation:

The samples were prepared according to the procedure applied by Knowles *et al*.[2] For the corresponding proper amounts of reactants, see the detailed descriptions in the chapters 2.6.3.1-2.6.3.4.

A screw cap Schlenk tube was charged with amide starting material (1 equiv.), tetrabutylammonium di-*tert*-butylphosphate (0.2 equiv.) and Ir(dF(CF$_3$)ppy)$_2$(bpy)PF$_6$ (0.02 equiv., 2 mol%) and flushed with argon. Dry $CD_2Cl_2$ (sample concentration of 101 mM) was added followed by thiophenol (0.1 equiv.). The mixture was degassed using freeze-pump-thaw technique and subsequently transferred into an amberized NMR tube under inert conditions.

### 2.6.3.1 Photoredox Catalytic Hydroamidation of *N*-phenylpent-4-enamide with Thiophenol
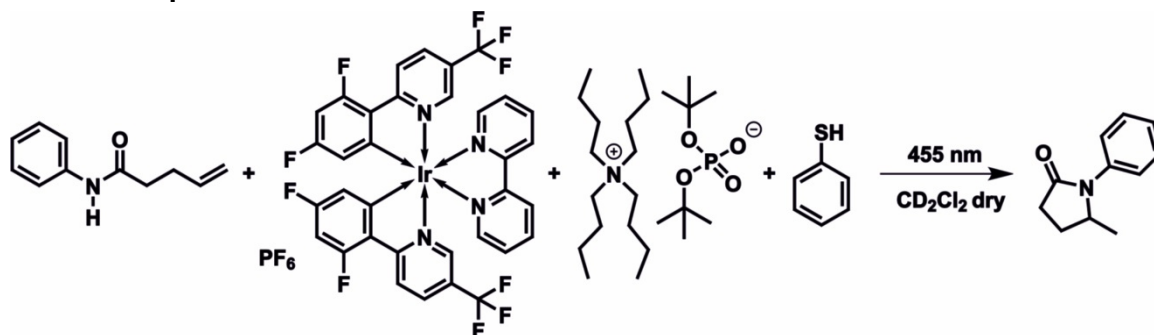


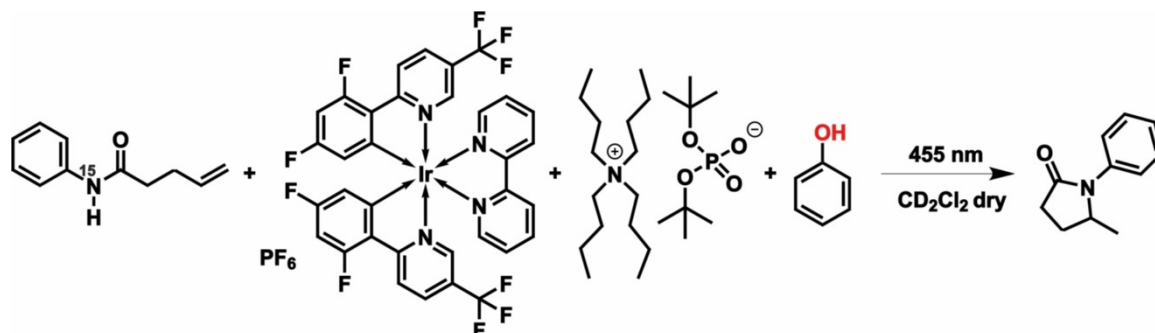**Figure 2.7:** Photoredox catalytic hydroamidation of *N*-phenylpent-4-enamide in presence of phosphate base, thiophenol and iridium photocatalyst with blue light.

The sample was prepared according to the general procedure (*vide supra*) using *N*-phenylpent-4-enamide (59 mg, 333 µmol), base (30 mg, 66.6 µmol), thiophenol (3.4 µl, 33.3 µmol) and Ir-photocatalyst (6.8 mg, 6.6 µmol) in $CD_2Cl_2$ (3.3 mL). The reaction was followed via *in-situ* illumination inside the NMR spectrometer. The corresponding amide degradation and product evolution curves are plotted in Figure 2.9.

For the determination of the amounts by integration, the amide signal at 5.85-5.92 ppm (m, 1 H) and the lactam signal at 4.29 ppm (s, 1 H) were used and the corresponding regions were baseline corrected prior to integration.
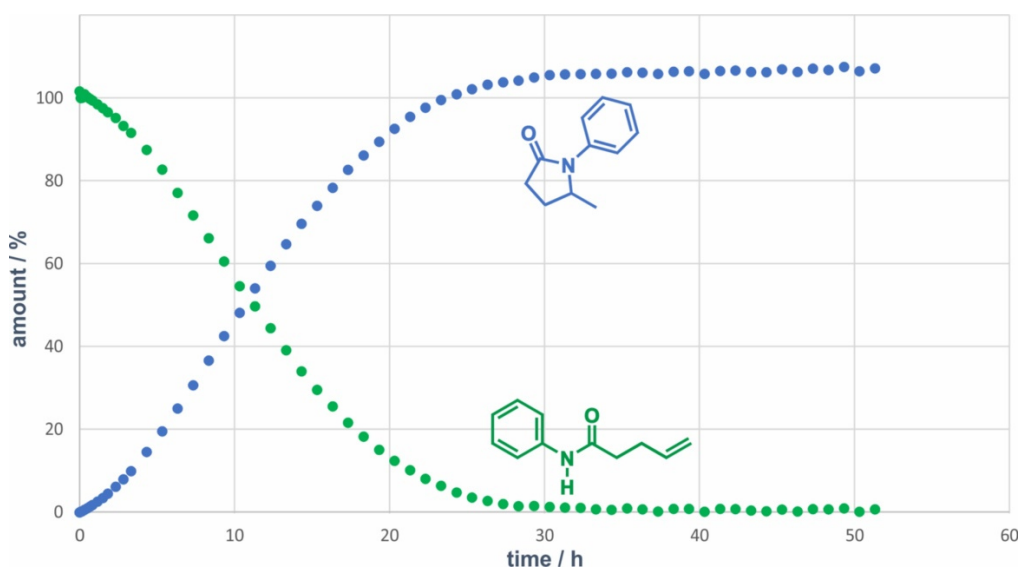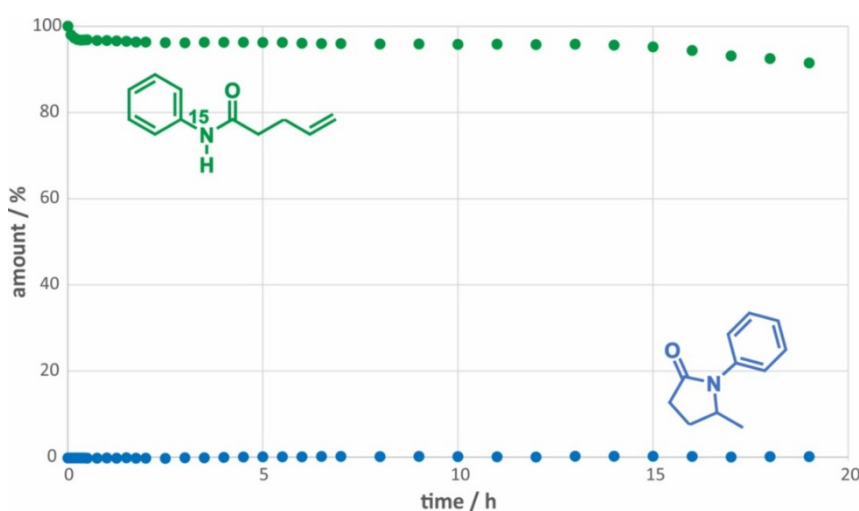


**Figure 2.9:** *In-situ* reaction profile for the hydroamidation of *N*-phenylpent-4-enamide using thiophenol as hydrogen atom donor followed by NMR.

After an initial linear conversion, the product formation was completed after around 30 hours. The comparison of the ^{1}H NMR spectra before illumination and after ≈51 hours in Figure 2.10 shows full conversion of the amide to the lactam product. The chemical shifts were referenced to $CD_2Cl_2$ (5.32 ppm[1]). Octamethylcyclotetrasiloxan (OMS) was added as internal NMR standard but was not included for the interpretation. The resulting product amount of above 100% is possibly a result of improper relaxation parameters or inaccuracy of integration. The complete spectra are shown at the end of the chapter (Figure 2.11).
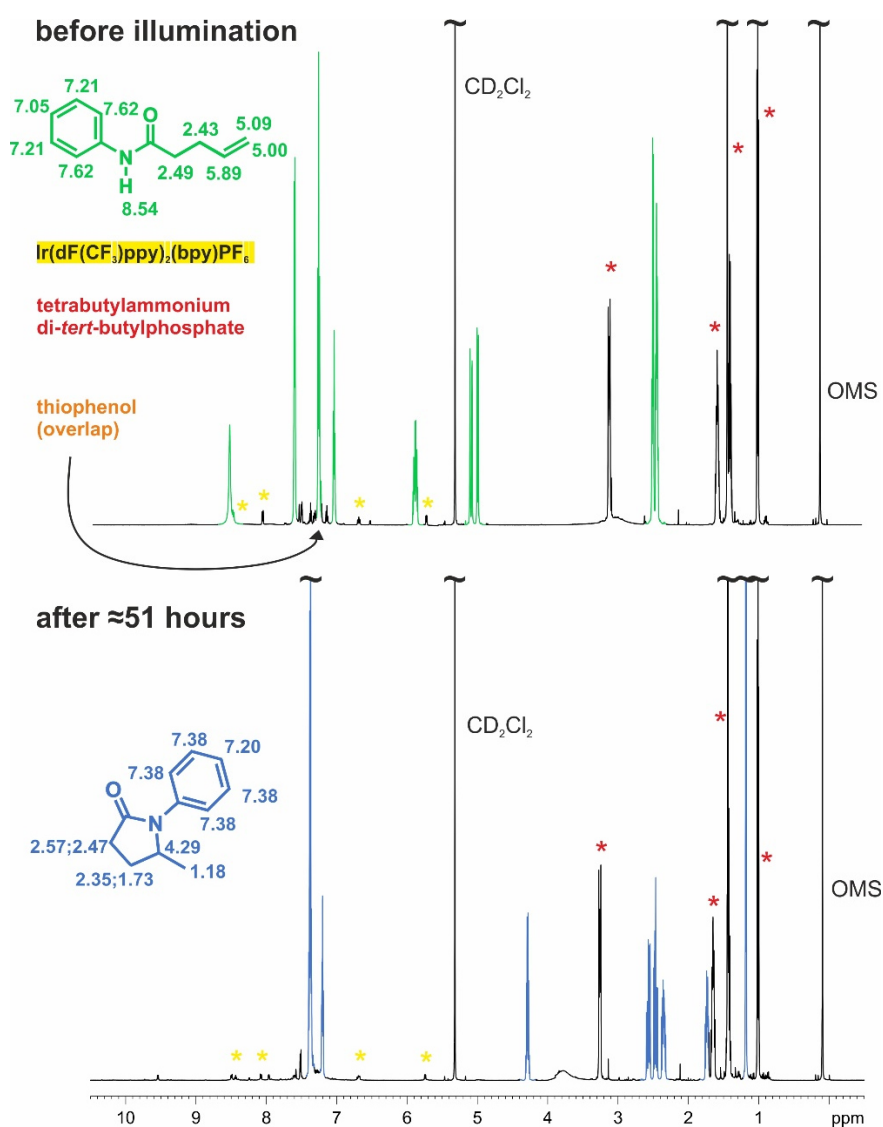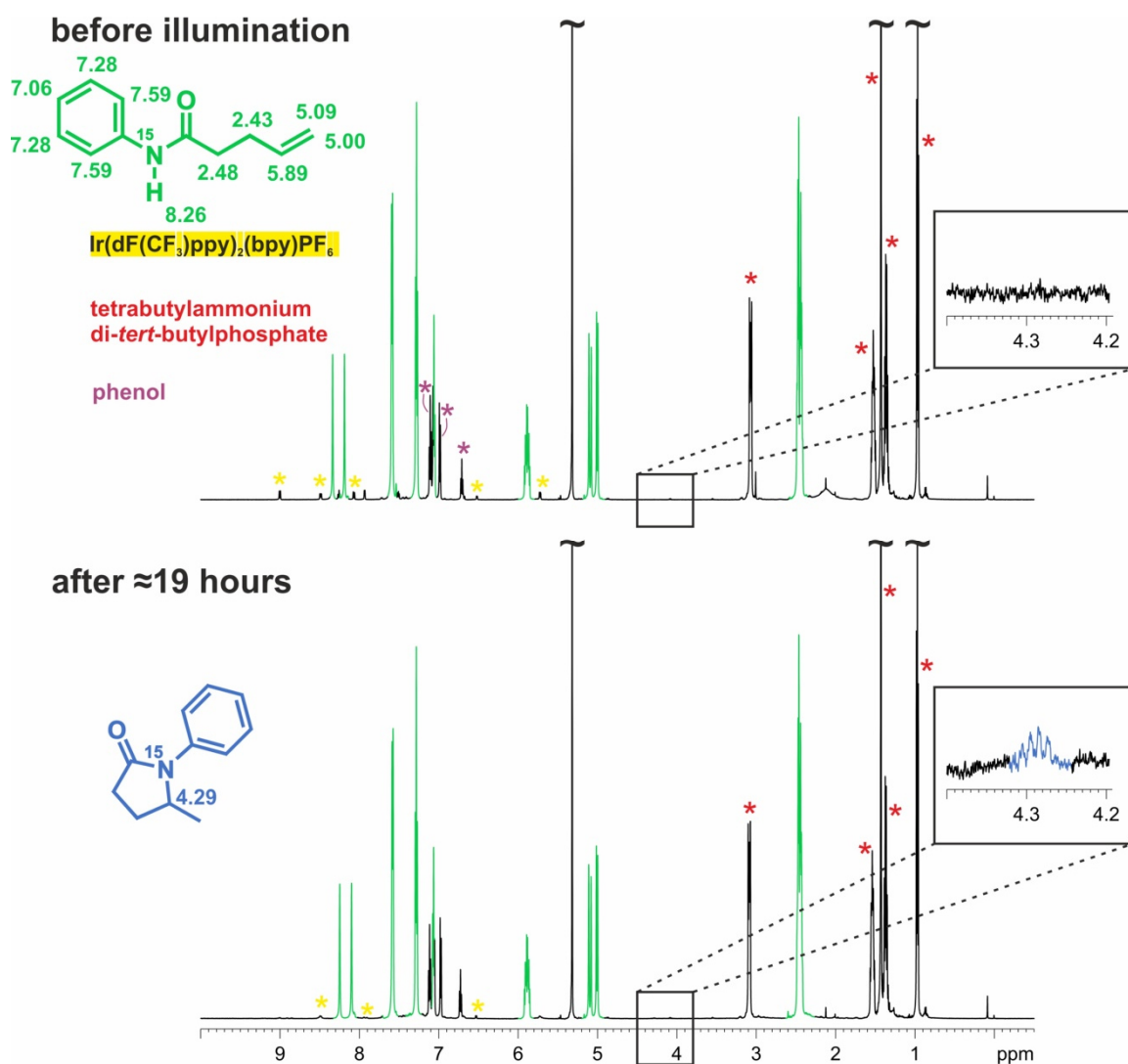


**Figure 2.10:** Excerpt of the ^{1}H NMR spectra before starting the illumination (top) and after around 51 hours of illumination (bottom). The *N*-phenylpent-4-enamide substrate signals are highlighted in green, the phosphate base signals in red, the photocatalyst signals in yellow and thiophenol is overlapped in the aromatic region. The product signals are marked in blue. The comparison of the spectra shows complete amide consumption, product formation and no formation of by-products.
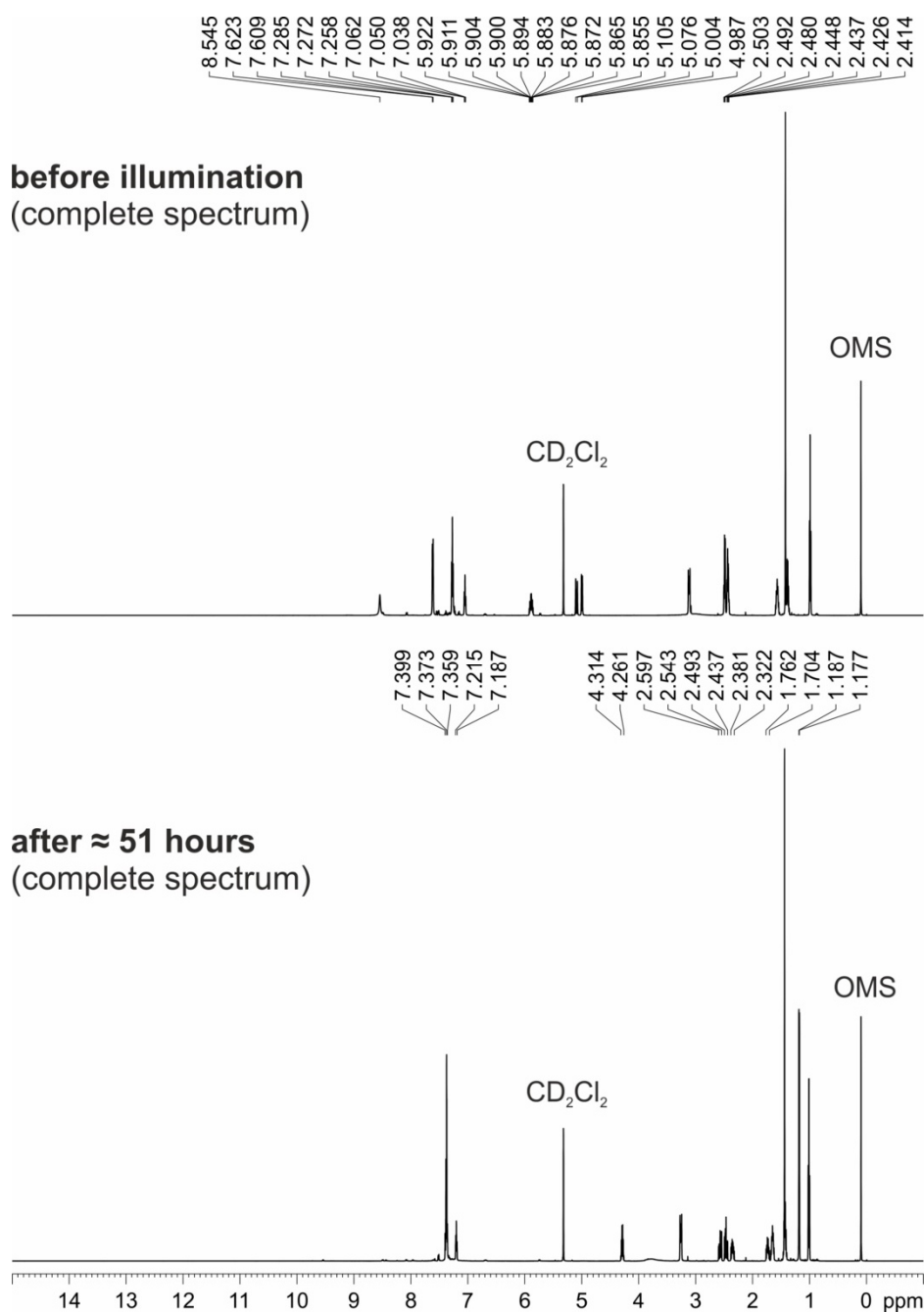
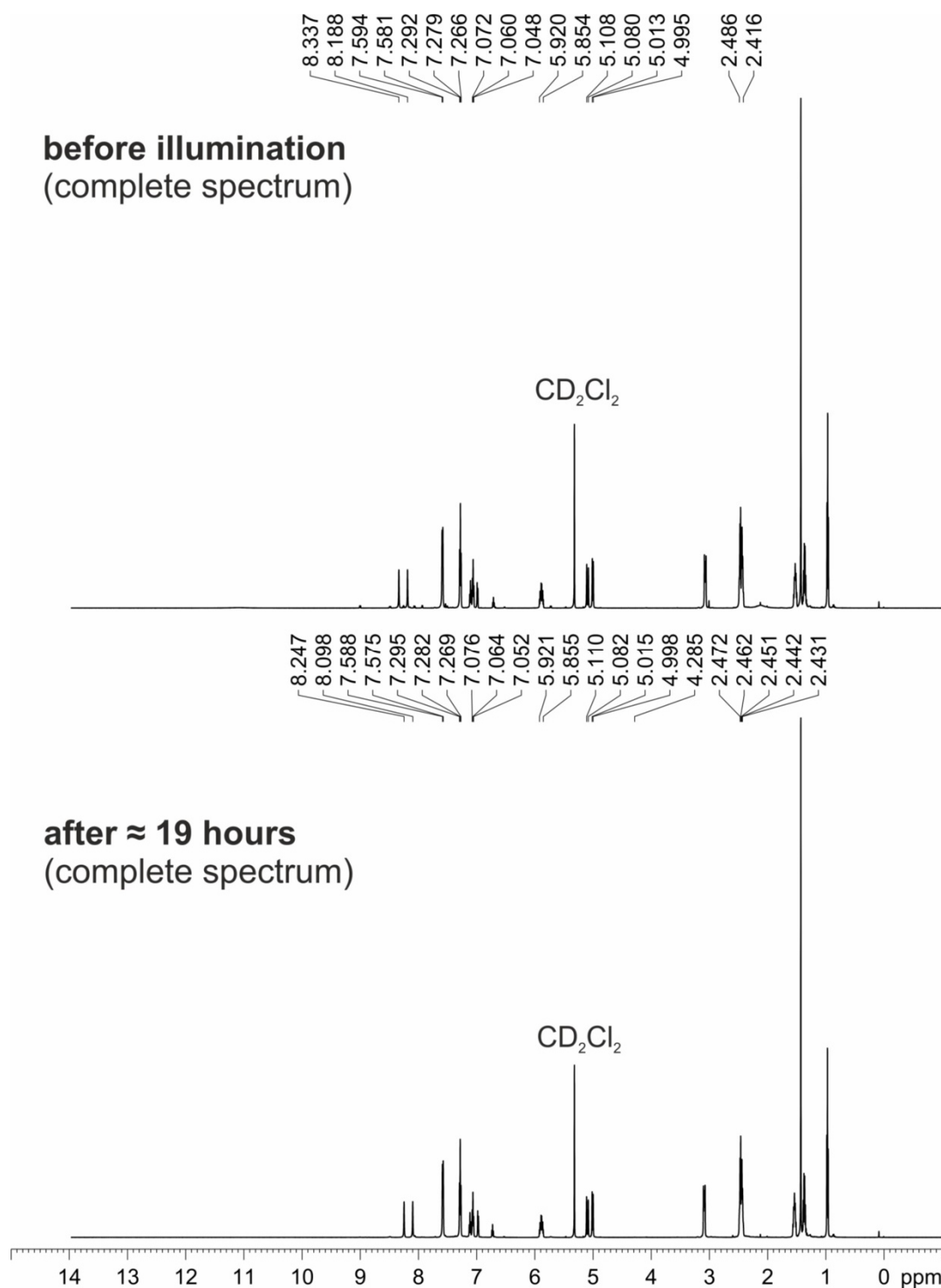**Figure 2.11:** Full $^1$H-NMR spectra of the photoredox catalytic hydroamidation reaction of *N*-phenylpent-4-enamide in presence of phosphate base, thiophenol and Ir-photocatalyst before illumination with blue light (top) and after around 51 hours (bottom); the peaks are labelled for substrate and product.
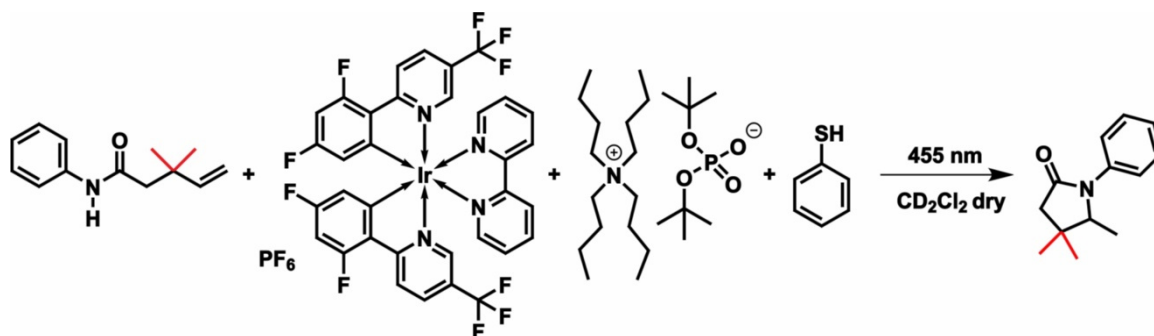
### 2.6.3.2 Photoredox Catalytic Hydroamidation of $^{15}N$-phenylpent-4-enamide with Phenol



**Figure 2.12:** Photoredox catalytic hydroamidation of $^{15}N$-phenylpent-4-enamide in presence of base and phenol with blue light.

The sample was prepared according to the general procedure (vide supra) using $^{15}N$-phenylpent-4-enamide (29 mg, 166.5 µmol), base (15 mg, 33.3 µmol), phenol (1.6 mg, 16.7 µmol) and Ir-photocatalyst (3.4 mg, 3.3 µmol) in CD$_2$Cl$_2$ (1.7 mL). The reaction was followed via *in-situ* illumination inside the NMR spectrometer. The corresponding amide degradation and product evolution curves are plotted in Figure 2.13.

For the determination of the amounts by integration, the amide signal at 5.85-5.92 ppm (m, 1 H) and the lactam signal at 4.29 ppm (q, 1 H) were used without baseline correction prior to integration. The chemical shifts were referenced to CD$_2$Cl$_2$ (5.32 ppm[1]).

The reaction profiles in Figure 2.13 show only marginal substrate conversion and product formation (0.1 % after 19 h). The corresponding $^1$H NMR spectra are shown in Figure 2.14 and the complete spectra at this end of the chapter (Figure 2.15).
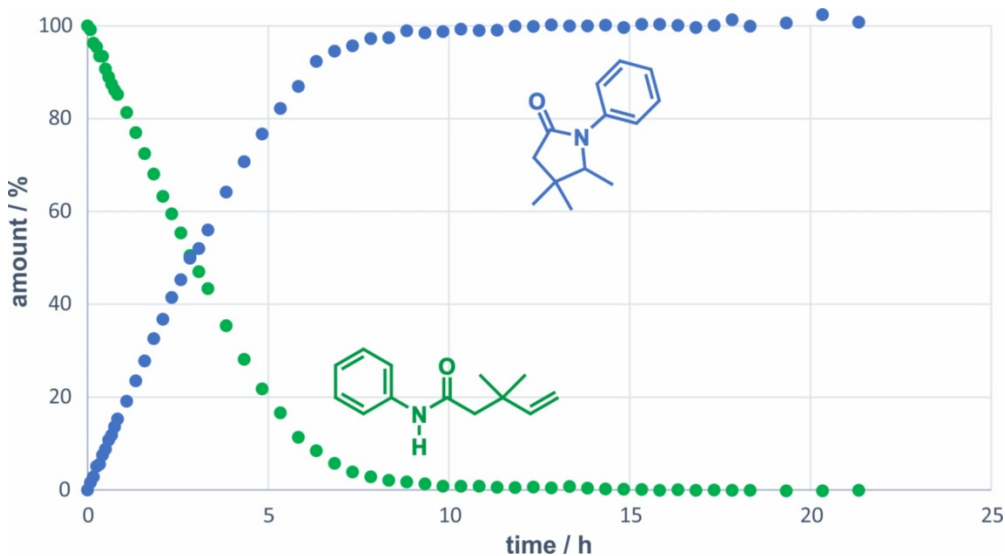


**Figure 2.13:** *In-situ* reaction profile for the hydroamidation of $^{15}N$-phenylpent-4-enamide using phenol as hydrogen atom donor followed by NMR.

**Figure 2.14:** Excerpt of the ^{1}H NMR spectra before starting the illumination (top) and after around 19 hours of illumination (bottom). The ^{15}N-phenylpent-4-enamide substrate signals are highlighted in green, the phosphate base signals in red, the photocatalyst signals in yellow and phenol in purple. The product signals are marked in blue. The comparison of the spectra shows bare amide consumption and bare product formation. The product signal is shown in the excerpt (right part).

**Figure 2.15:** Full $^1$H-NMR spectra of the photoredox catalytic hydroamidation reaction of $^{15}N$-phenylpent-4-enamide in presence of phosphate base, phenol and Ir-photocatalyst before illumination with blue light (top) and after around 19 hours (bottom); the peaks are labelled for substrate and for the only base line separated signal of the product (4.29 ppm).

### 2.6.3.3 Photoredox Catalytic Hydroamidation of 3,3-dimethyl-*N*-phenylpent-4-enamide with Thiophenol



**Figure 2.16:** Photoredox catalytic hydroamidation of 3,3-dimethyl-*N*-phenylpent-4-enamide in presence of base and thiophenol with blue light.

The sample was prepared according to the general procedure (vide supra) using 3,3-dimethyl-*N*-phenylpent-4-enamide (34 mg, 166.5 µmol), base (15 mg, 33.3 µmol), thiophenol (1.7 µl, 16.7 µmol) and Ir-photocatalyst (3.4 mg, 3.3 µmol), in $CD_2Cl_2$ (1.65 ml). The reaction was followed via *in-situ* illumination inside the NMR spectrometer.

The 3,3-dimethyl-*N*-phenylpent-4-enamide was used to exclude self-conversion of the amide starting material which is possible for *N*-phenylpent-4-enamide.[2] The corresponding amide degradation and product evolution curves are plotted in Figure 2.17. For the determination of the amounts by integration, the amide signal at 6.03 ppm (dd, 1 H) and the lactam signal at 3.86 ppm (q, 1 H) were used and the corresponding regions were baseline corrected prior to integration.



**Figure 2.17:** *In-situ* reaction profile for the hydroamidation of 3,3-dimethyl-*N*-phenylpent-4-enamide with thiophenol as hydrogen atom donor followed by NMR.

After an initial linear conversion, the product formation was completed after around 10 hours. The comparison of the ^{1}H NMR spectra before illumination and after ≈21 hours in Figure 2.18 shows full conversion of the amide to the lactam product. The chemical shifts were referenced to $CD_2Cl_2$ (5.32 ppm[1]). The complete spectra are shown at the end of the chapter (Figure 2.19).
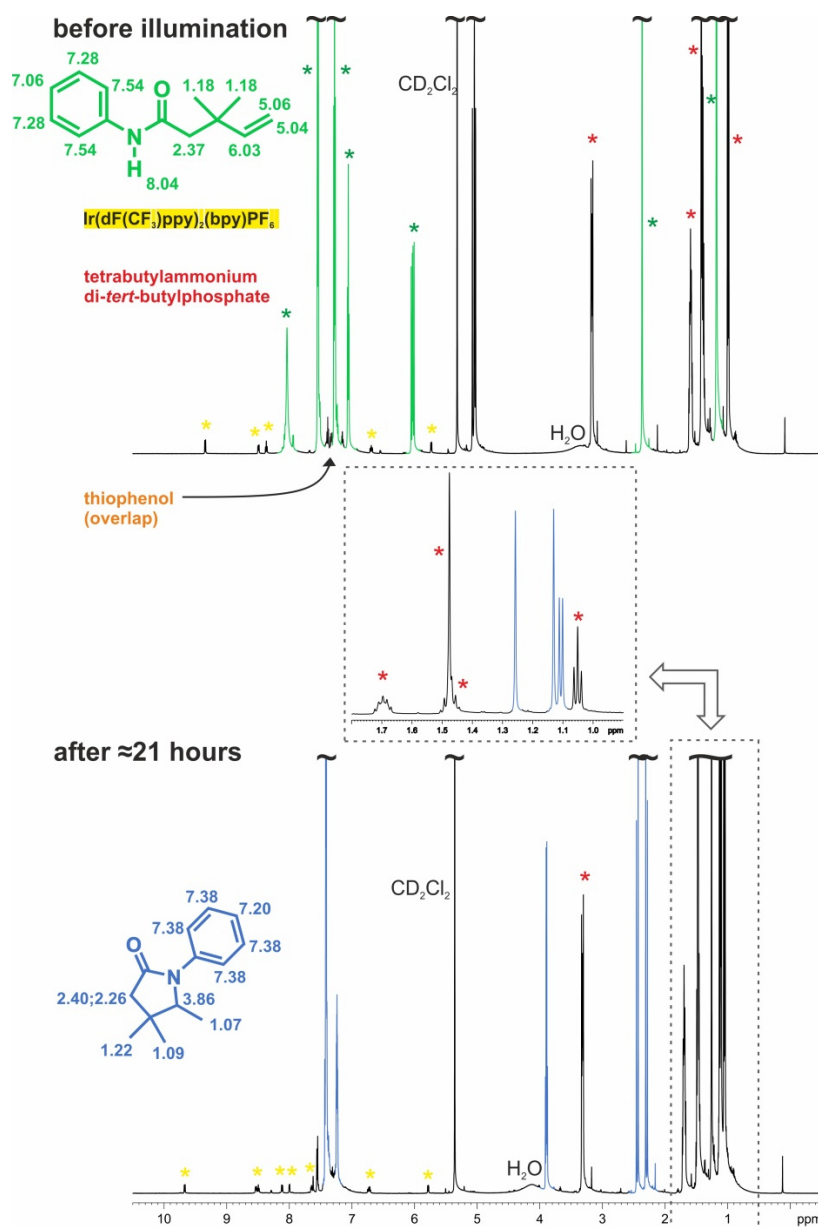


**Figure 2.18:** Excerpt of the ^{1}H NMR spectra before starting the illumination (top) and after around 21 hours of illumination (bottom). The 3,3-dimethyl-*N*-phenylpent-4-enamide substrate signals are highlighted in green, the phosphate base signals in red, the photocatalyst signals in yellow and thiophenol is overlapped in the aromatic region. The product signals are marked in blue. The crowded region in the dashed box is clarified with an inlet. The comparison of the spectra shows complete amide consumption, product formation and no formation of side products.
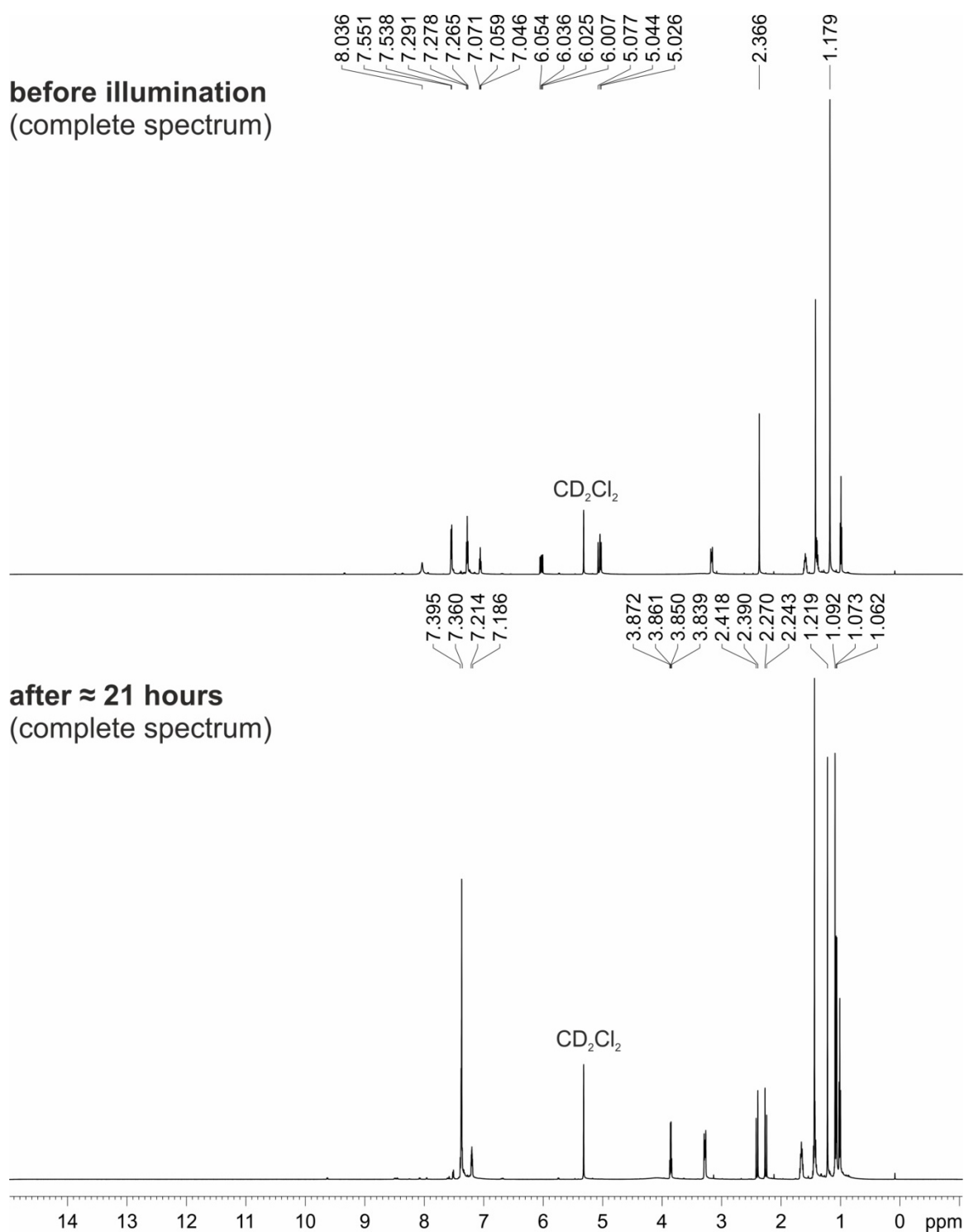
**Figure 2.19:** Full $^1$H-NMR spectra of the photoredox catalytic hydroamidation reaction of 3,3-dimethyl-*N*-phenylpent-4-enamide in presence of phosphate base, thiophenol and Ir-photocatalyst before illumination with blue light (top) and after around 21 hours (bottom).
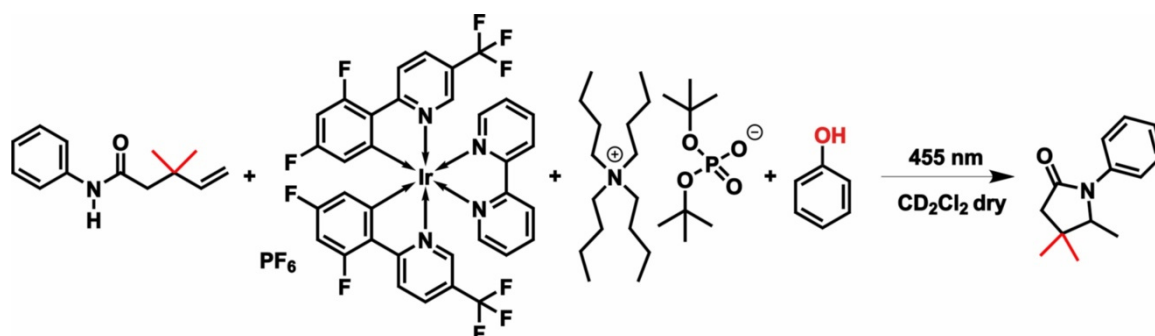
### 2.6.3.4 Photoredox Catalytic Hydroamidation of 3,3-dimethyl-*N*-phenylpent-4-enamide with Phenol



**Figure 2.20:** Photoredox catalytic hydroamidation of 3,3-dimethyl-*N*-phenylpent-4-enamide in presence of base and phenol with blue light.

The sample was prepared according to the general procedure (vide supra) using 3,3-dimethyl-*N*-phenylpent-4-enamide (34 mg, 167 µmol), base (15 mg, 33.3 µmol), phenol (1.6 mg, 16.7 µmol) and Ir-photocatalyst (3.4 mg, 3.3 µmol), in $CD_2Cl_2$ (1.65 ml). The reaction was followed via *in-situ* illumination inside the NMR spectrometer.

Again, the 3,3-dimethyl-*N*-phenylpent-4-enamide was used to exclude self-conversion of the amide starting material which is possible for *N*-phenylpent-4-enamide (chapter 2.6.3.3). The corresponding amide degradation and product evolution curves are plotted in Figure 2.21. For the determination of the amounts by integration, the amide signal at 6.03 ppm (dd, 1 H) and the lactam signal at 3.86 ppm (q, 1 H) were used and the corresponding regions were baseline corrected prior to integration. The chemical shifts were referenced to $CD_2Cl_2$ (5.32 ppm[1]).

The reaction profiles in Figure 2.21a show only marginal substrate conversion and product formation (1.7 % after 18.3 h). Regarding the amounts around 12% of by-product formation is probable. The excerpt of the product formation rate (first 3,3 hours) in Figure 2.21b indicates no inhibition of the photocatalyst. In the $^1$H spectra (Figure 2.22, bottom), an additional triplet at 4.46 ppm predict the formation of an amidyl by-product, which was not further identified. The complete spectra are shown at this end of the chapter (Figure 2.23).
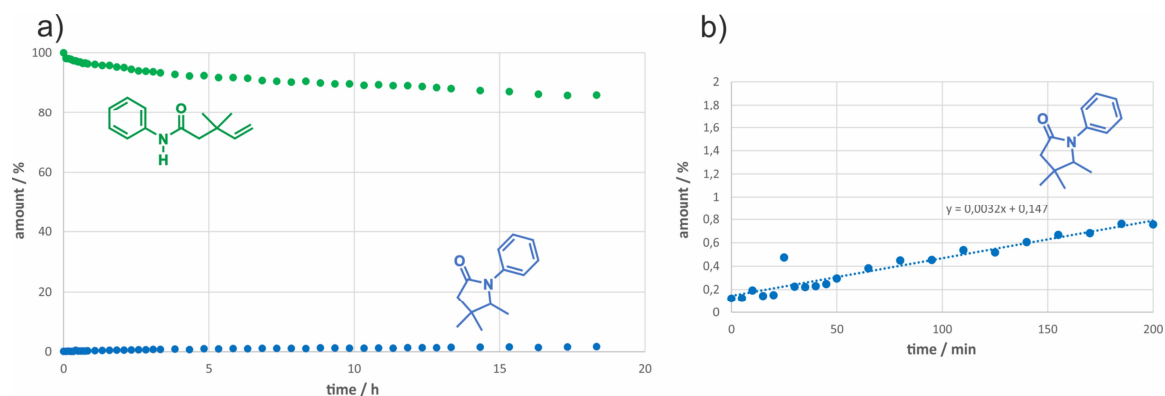
**Figure 2.21:** a) *In-situ* reaction profile for the hydroamidation of 3,3-dimethyl-*N*-phenylpent-4-enamide using phenol as hydrogen atom donor followed by NMR; b) excerpt of the product formation rate (first 3,3 hours) and corresponding linear equation of the trendline.
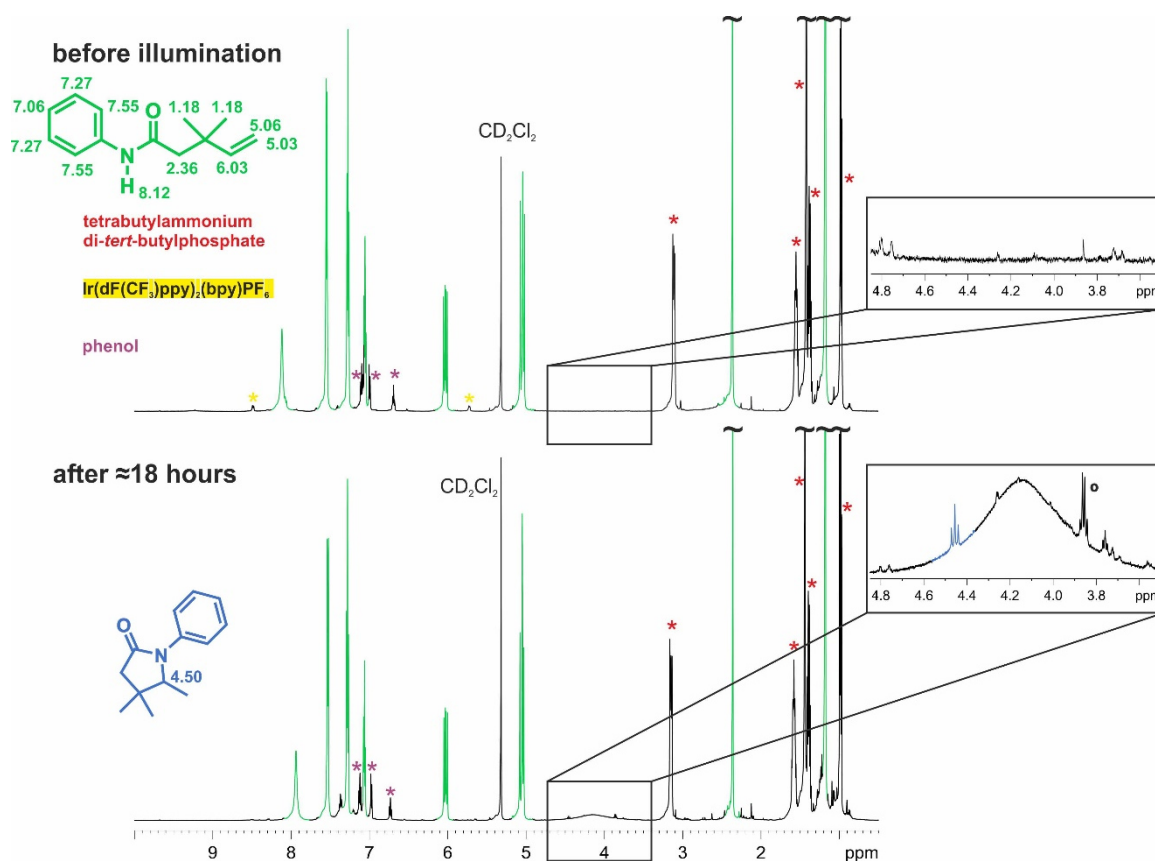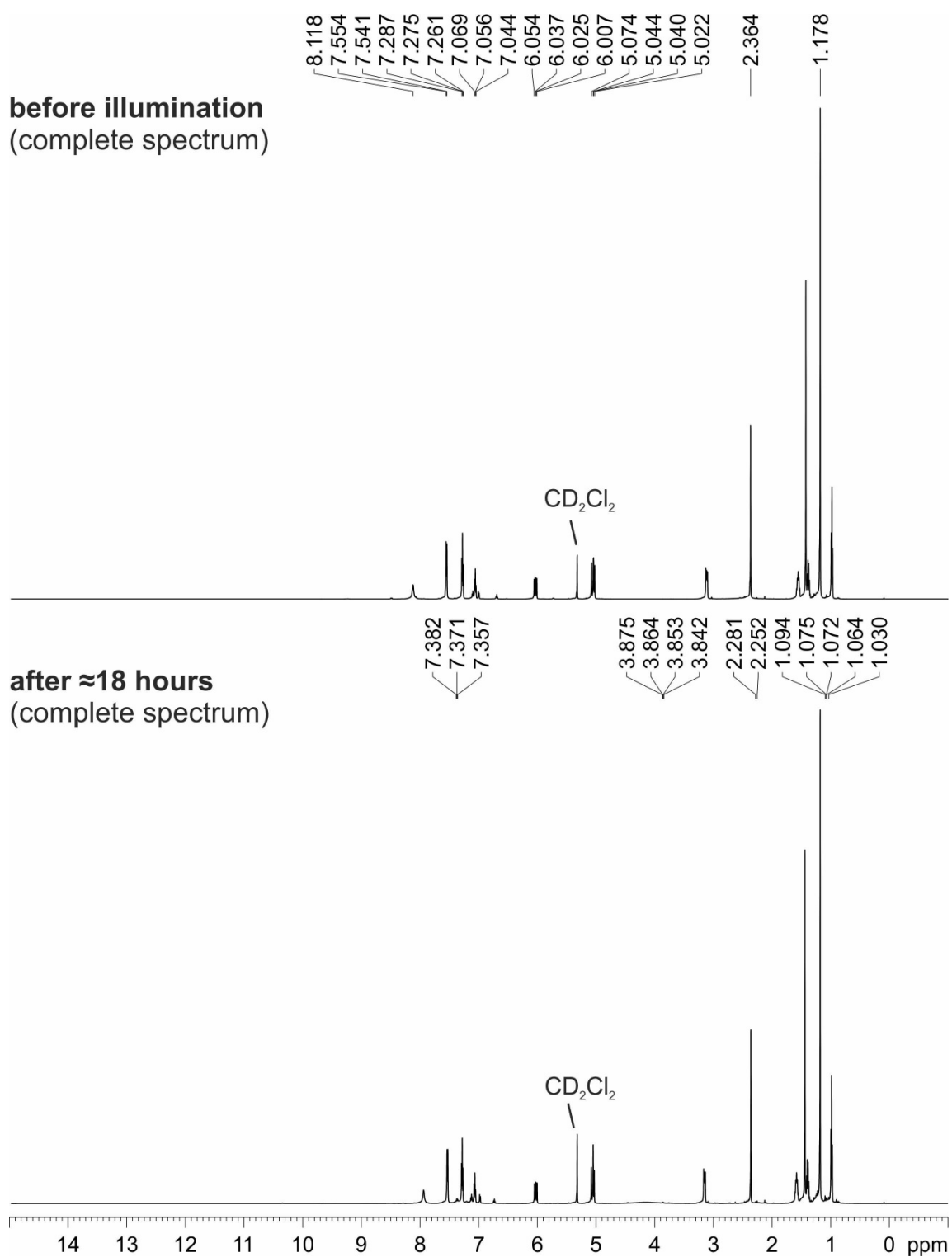


**Figure 2.22:** Excerpt of the ¹H NMR spectra before starting the illumination (top) and after around 18 hours of illumination (bottom). The 3,3-dimethyl-*N*-phenylpent-4-enamide substrate signals are highlighted in green, the phosphate base signals in red, the photocatalyst signals in yellow and the phenol signals in purple. The product signals are marked in blue. The comparison of the spectra shows only marginal product formation and the generation of a by-product (triplet marked with **º** in the inlet).

**before illumination**
(complete spectrum)

8.118
7.554
7.541
7.287
7.275
7.261
7.069
7.056
7.044
6.054
6.037
6.025
6.007
5.074
5.044
5.040
5.022
2.364
1.178

CD$_2$Cl$_2$

**after ≈18 hours**
(complete spectrum)

7.382
7.371
7.357
3.875
3.864
3.853
3.842
2.281
2.252
1.094
1.075
1.072
1.064
1.030

CD$_2$Cl$_2$

14  13  12  11  10  9  8  7  6  5  4  3  2  1  0 ppm

**Figure 2.23:** Full $^1$H-NMR spectra of the photoredox catalytic hydroamidation reaction of 3,3-dimethyl-*N*-phenylpent-4-enamide in presence of phosphate base, phenol and Ir-photocatalyst before illumination with blue light (top) and after around 18 hours (bottom).

**2.6.3.5 Initial Rate Kinetics Using PhSH, Ph$_2$S$_2$ and Mixtures Thereof**

Sample preparation:

The samples were prepared according to the procedure applied by Knowles *et al*.[2]

A screw cap Schlenk tube was charged with 3,3-dimethyl-*N*-phenylpent-4-enamide (1 equiv.; 0.1 mmol; 20.3 mg), tetrabutylammonium di-*tert*-butylphosphate (1 equiv.; 0.1 mmol; 45.2 mg) and Ir(dF(CF$_3$)ppy)$_2$(bpy)PF$_6$ (0.02 equiv., 2 mol%; 2 µmol; 2.0 mg). In case of using diphenyldisulfide (0.5 equiv., 1 equiv., 0.7 equiv. and 0.8 equiv., respectively) the solid was added as well. The mixture was flushed with argon. Dry CD$_2$Cl$_2$ (1 ml; sample concentration of 100 mM) was added followed by thiophenol if used (1 equiv., 0.3 equiv. and 0.2 equiv., respectively). The mixture was degassed using freeze-pump-thaw technique and subsequently transferred into an amberized NMR tube under inert conditions.

The reactions were followed via *in-situ* illumination inside the NMR spectrometer. For the determination of the amounts by integration, the amide signal at 5.85-5.92 ppm (m, 1 H) and the lactam signal at 3.86 ppm (q, 1 H) were used and the corresponding regions were baseline corrected prior to integration.

The corresponding amide degradation and product evolution curves of the first 18 min including the linear slopes and the corresponding equations are plotted in Figure 2.24. From the slopes the immense acceleration of the hydroamidations using mixtures of PhSH and Ph$_2$S$_2$ is visible.
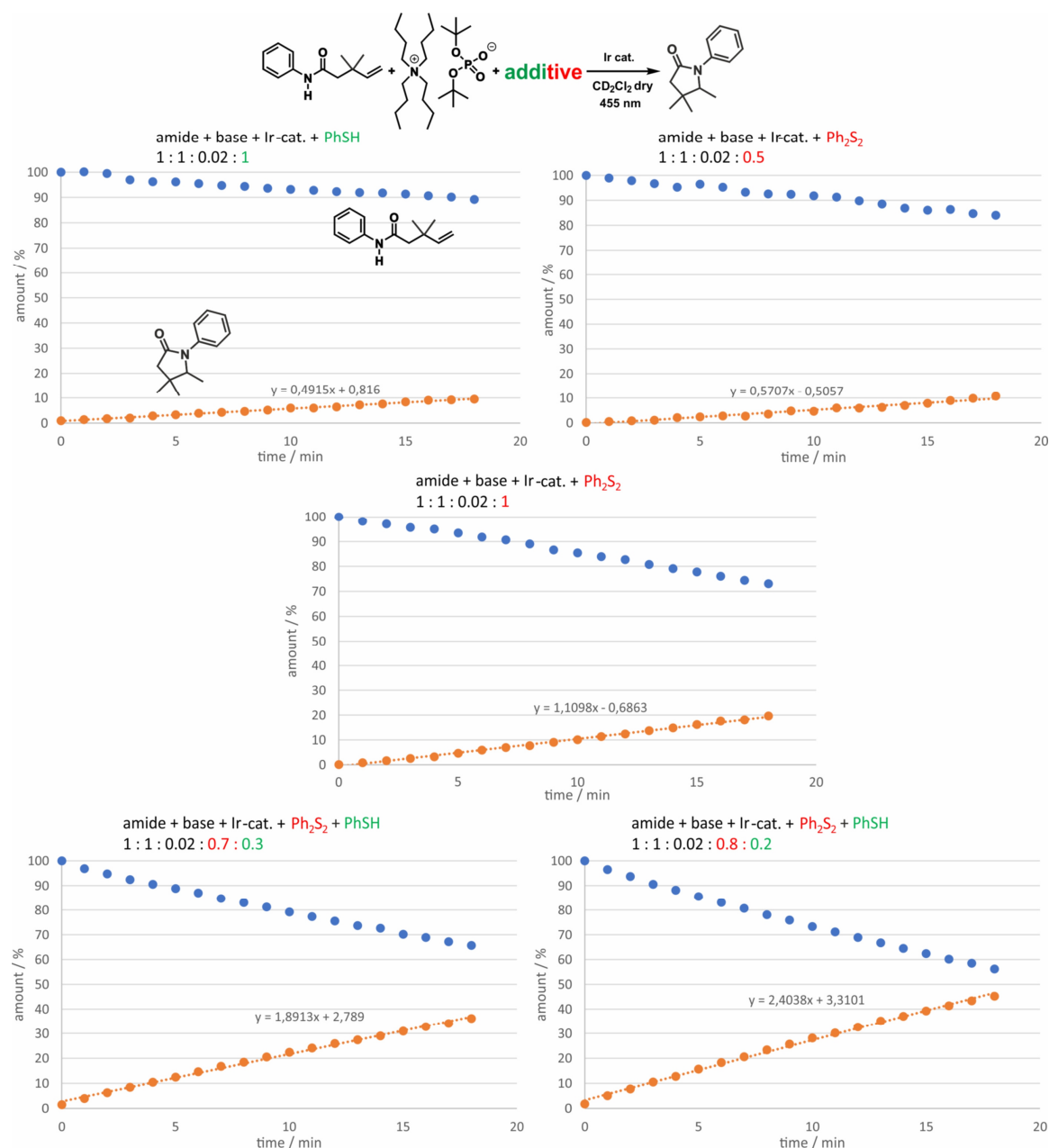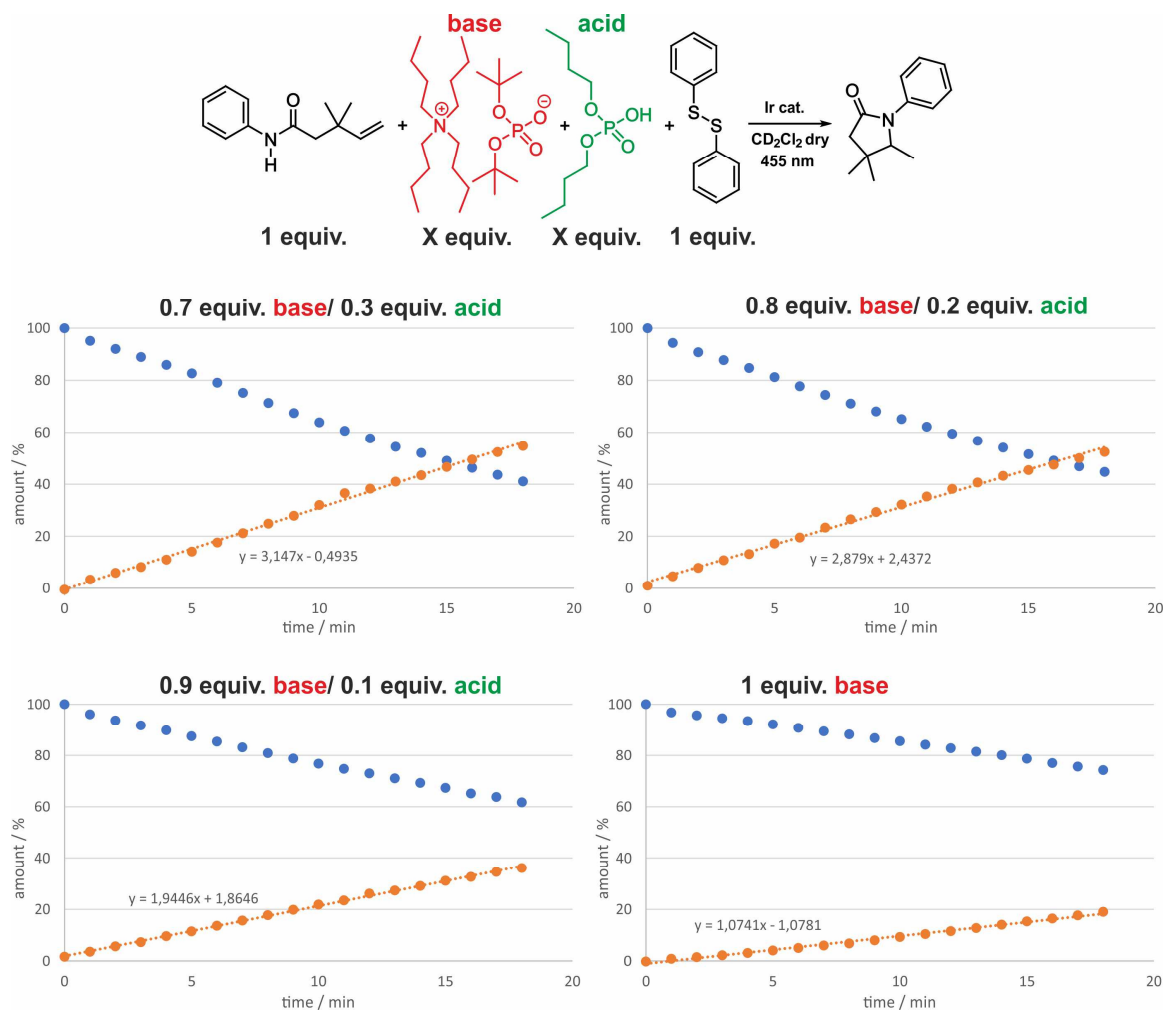
**Figure 2.24:** Comparison of the initial rate kinetics for the hydroamidation reactions of 3,3-dimethyl-*N*-phenylpent-4-enamide using PhSH and $Ph_2S_2$ as additives or a mixture thereof. The reactions were followed by *in-situ* $^1$H NMR and an immense acceleration of the photoredox catalysis was achieved by a combination of both thiol species; the dimethyl substrate was used in order to exclude self-HAT.

### 2.6.3.6 Initial Rate Kinetics Using Different Amounts of Base and Acid

Sample preparation:

In general, the samples were prepared as described in chapter 2.6.3.5.

A screw cap Schlenk tube was charged with 3,3-dimethyl-*N*-phenylpent-4-enamide (1 equiv.; 0.1 mmol; 20.3 mg), diphenyldisulfide (1 equiv.; 0.1 mmol; 21.8 mg) and

Ir(dF(CF$_3$)ppy)$_2$(bpy)PF$_6$ (0.02 equiv., 2 mol%; 2 µmol; 2.0 mg). Except for the reference mixture without acid, different mixtures of tetrabutylammonium di-*tert*-butylphosphate (0.7 equiv., 0.8 equiv., 0.9 equiv., respectively) and phosphoric acid dibutylester (0.3 equiv., 0.2 equiv., 0.1 equiv., respectively) were added as well. The mixture was flushed with argon. Dry CD$_2$Cl$_2$ (1 ml; sample concentration of 100 mM) was added. The mixture was degassed using freeze-pump-thaw technique and subsequently transferred into an amberized NMR tube under inert conditions.

The reactions were followed via *in-situ* illumination inside the NMR spectrometer and the spectra were evaluated as described in chapter 2.6.3.5.

The corresponding amide degradation and product evolution curves of the first 18 min including the linear slopes and the corresponding equations are plotted in Figure 2.25. From the slopes the immense acceleration of the hydroamidations by adding phosphoric acid dibutylester is visible.



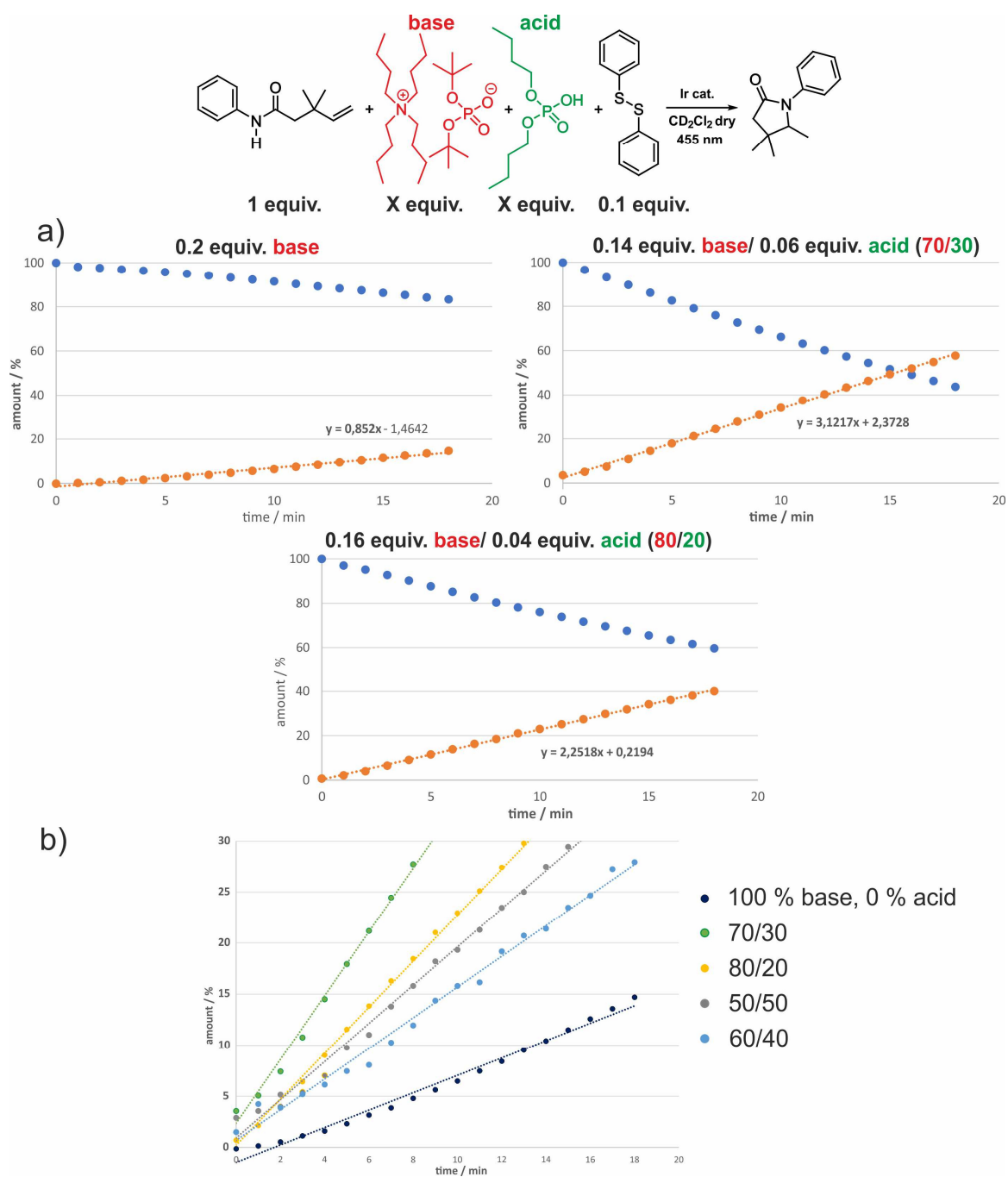**Figure 2.25:** Comparison of the initial rate kinetics for the hydroamidation reactions of 3,3-dimethyl-*N*-phenylpent-4-enamide using 1 equiv. of Ph$_2$S$_2$ and different mixtures of base and acid. The reactions were followed by *in-situ* $^1$H NMR and an immense acceleration of the photoredox catalysis was achieved by adding the acid; the dimethyl substrate was used in order to exclude self-HAT.

**2.6.3.7 Initial Rate Kinetics Using Different Amounts of Base and Acid in Equiv. Relevant for Synthesis**

Sample preparation:

In general, the samples were prepared as described in chapter 2.6.3.6 however using the synthetically relevant equivalents of the species.

A screw cap Schlenk tube was charged with 3,3-dimethyl-*N*-phenylpent-4-enamide (1 equiv.; 0.25 mmol; 50.8 mg), diphenyldisulfide (0.1 equiv.; 0.03 mmol; 5.5 mg) and Ir(dF(CF$_3$)ppy)$_2$(bpy)PF$_6$ (0.02 equiv., 2 mol%; 5 μmol; 5.0 mg). For the reference mixture without acid tetrabutylammonium di-*tert*-butylphosphate (0.2 equiv., 0.05 mmol, 22.6 mg) was added and for the mixtures containing base and acid 0.14 equiv. or 0.16 equiv. of base and 0.06 equiv. or 0.04 equiv. of phosphoric acid dibutylester were added. The mixture was flushed with argon. Dry CD$_2$Cl$_2$ (2.5 ml; sample concentration of 100 mM) was added. The mixture was degassed using freeze-pump-thaw technique and subsequently transferred into an amberized NMR tube under inert conditions.

The reactions were followed via *in-situ* illumination inside the NMR spectrometer and the spectra were evaluated as described in chapter 2.6.3.5.

The corresponding amide degradation and product evolution curves of the first 18 min including the linear slopes and the corresponding equations are plotted in Figure 2.26. From the slopes the immense acceleration of the hydroamidations by adding phosphoric acid dibutylester is visible.

**Figure 2.26:** a) Comparison of the initial rate kinetics for the hydroamidation reactions of 3,3-dimethyl-*N*-phenylpent-4-enamide using 0.1 equiv. of $Ph_2S_2$ and different mixtures of base and acid. The reactions were followed by *in-situ* ^{1}H NMR and an immense acceleration of the photoredox catalysis was achieved by adding the acid; the dimethyl substrate was used in order to exclude self-HAT: b) mixtures of 50/50 and 60/40 of base/acid added to Figure 2.7b show a maximum acceleration of the reaction for a 70/30 mixture.

**2.6.3.8 Light intensity dependent initial rate kinetics**

For the study of the impact of the light intensity on the reaction rates, a mixture containing amide/base/$Ph_2S_2$ and a mixture containing amide/base+acid (70:30)/$Ph_2S_2$ prepared exactly as written in chapter 2.6.3.7 were measured.

The results are presented in Figure 2.8b in the main text as well as in Figure 2.27. After 9 minutes of illumination at 0.5 A the light intensity was reduced to 50% (0.25 A). Again after 9 minutes the intensity was reduced to 25% by going down to 0.13 A. Lastly, it was switched back to 100% (0.5 A). In our illumination setup the different values for the applied current linearly correlate with the light intensity.[5] Therefore, the time slots shown in Figure 2.8b represent 100%, 50% and 25% light intensity.
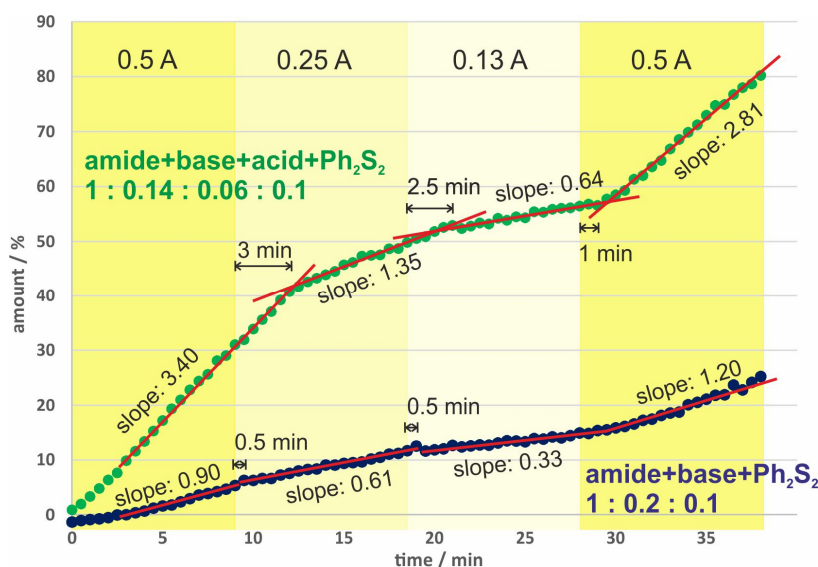


**Figure 2.27:** Light intensity dependent reaction profiles of a mixture of amide/base+acid (70:30)/$Ph_2S_2$ (green curve) and of a mixture of amide/base/$Ph_2S_2$ (blue curve). For details of sample preparation, see chapter 2.6.3.7. The red lines represent the different slopes of the linear parts and thus highlight the different time intervals for persisting reaction rates after reducing the light intensity (by reducing the applied current). The initial lower slope of the blue curve is in agreement with the mechanistic proposal of an off-cycle equilibrium with $Ph_2S_2$, which consumes in the beginning the photogenerated amidyl radical. At the moment this amidyl reservoir is filled the equilibrium between photogeneration, off-cycle equilibrium with $Ph_2S_2$, and abreaction via cyclisation creates a constant overall reaction rate (slope 0.90). This finds its repetition upon increasing the light intensity in the last part of the profile.

### 2.6.4  Low Temperature NMR Spectroscopic H-Bond Studies

General information:

The NMR spectroscopic measurements of the ^{1}H, ^{15}N and ^{31}P NMR spectra were performed in dry $CD_2Cl_2$ at 180 K on a Bruker Avance III HD 600 (600.13 MHz) and a 5 mm TBI-F probe head with a z-gradient (53.5 Gauss/cm). The temperature of 180 K was controlled by a BVTE 3900.

The ^{1}H NMR spectra were referenced on TMS (0 ppm).[1] The ^{15}N and ^{31}P spectra were referenced according to $v_{heteronucleus} = v_{TMS} \times \Xi_{reference} / 100\%$ published by Harris *et al.*[6] $v_{TMS}$ refers to the measured ^{1}H resonance of TMS. The corresponding frequency ratios $\Xi_{reference}$ were used: $\Xi$ (^{15}N) = 10.132912 % ($NH_3$ liquid), $\Xi$ (^{31}P) = 40.480742 % ($H_3PO_4$ 85%).[6] The data were processed and plotted with *Topspin 3.2* (Bruker). The Figures were generated using the *Topspin Plot Editor*, *Chem Draw Professional* and *Corel Draw 2017*. The two- and three-component samples were prepared as 1:1 and 1:1:1 mixtures (50 mM), respectively. Due to the hygroscopic properties of the phosphate base, residual $H_2O$ is observable in the ^{1}H NMR spectra.

In the following section, the complete spectra with information about the chemical shifts, integrals and the assignment of the different compounds are depicted.

### 2.6.4.1 Identification of Phosphate Dimer 1 and the Thiol Species

In every sample containing phosphate base and thiophenol the formation of new thiol species in the aromatic region of the ^{1}H NMR spectra is visible (chapter 2.6.4.5 and main text). In the following section, some of the generated thiol species are identified.

From a partial acid-base reaction between thiophenol and phosphate base, thiolate and phosphoric acid are generated (Figure 2.28). The phosphoric acid adds to a phosphate furnishing the phosphate dimer **1**, which is assumed to play the key role for the required aggregation for an efficient photoredox catalytic hydroamidation reaction (see main text). The broad ^{1}H signal at 16.43-16.51 ppm for every PhSH/base containing mixture indicates the formation of a strong hydrogen bond. Similar dimers were already identified in our group.[7][8]

For the identification of the generated thiol species selective 1D TOCSY experiments were conducted for the amide/base mixture. As depicted in Figure 2.29, the excitation of two different signals in the aromatic region yielded at least two new independent thiol species besides PhSH itself. The signals for species 1 overlap with species 2 and PhSH.
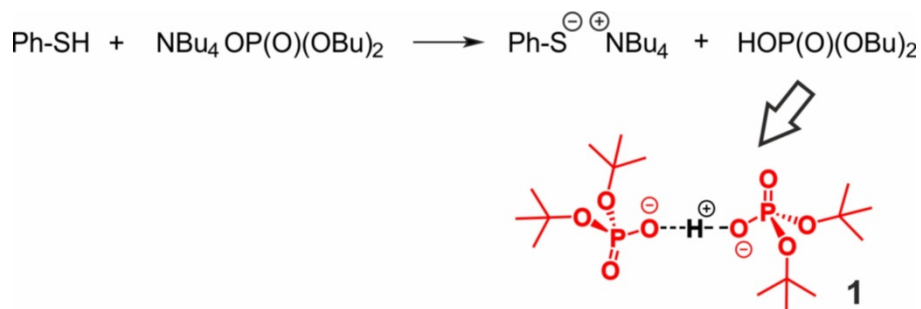
**Figure 2.28:** Via partial protonation of the phosphate base by thiophenol the crucial dimer **1** is generated.
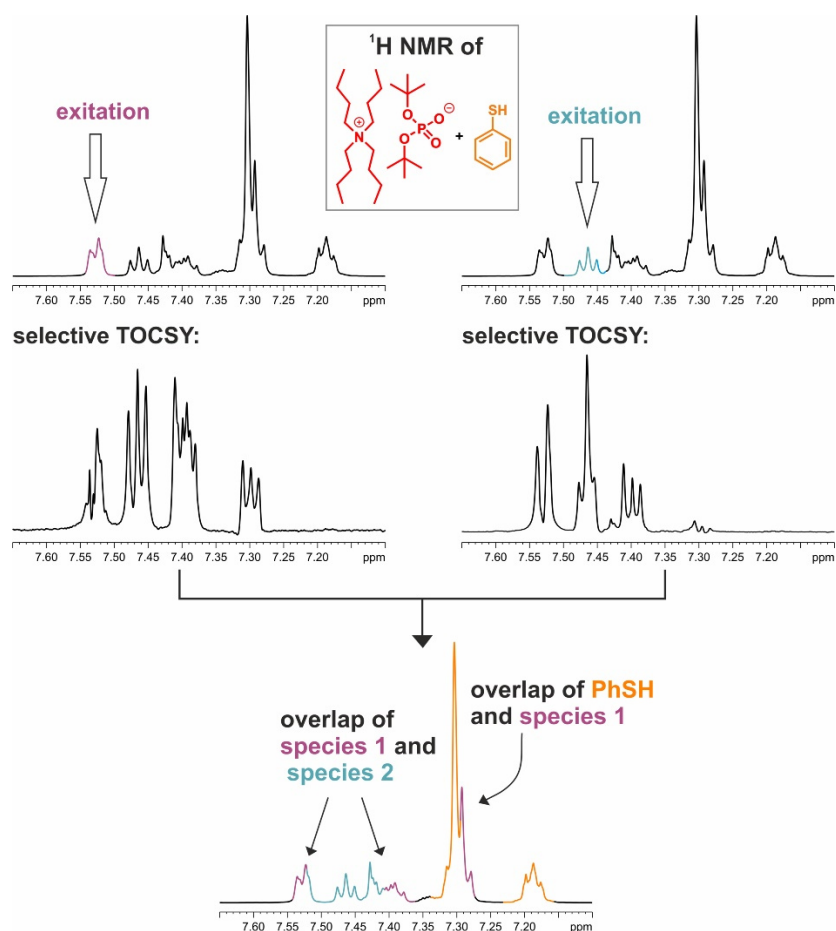


**Figure 2.29:** Via selective 1D TOCSY experiments, the existence of at least two new thiol species, apart from thiophenol itself, was identified for the amide/base mixture (1:1). From the excitation of the purple and blue signals (top), the overlap of at minimum two thiol species in the aromatic region was identified. The spectra were measured in $CD_2Cl_2$ at 180 K.

As the identification of the thiol species was complicated because of the overlap in the aromatic region, 4-methoxythiophenol was chosen for further NMR analysis due to better separation of the signals in the spectrum. In Figure 2.30, the spectrum of a 1:1 mixture of 4-methoxythiophenol and phosphate base is depicted (bottom). The formation of three new thiol species is clearly visible. After oxidizing 4-methoxypyridine by adding iodine, the signals for the pure substituted thiophenol completely disappeared and the signals of the disulfide increased. Thus, the blue marked duplet could be identified as the oxidation product.

The oxidation of thiophenol to its corresponding disulfide dimer in presence of a base and oxygen is well known in literature (Figure 2.31) and is triggered by residual oxygen in this case.[9][10] As the 4-methoxythiophenol/base sample was prepared under oxygen atmosphere the disulfide generation could be identified. But the photocatalytic mixture is prepared under argon atmosphere and such transformation is therefore unlikely.

By comparing the integrals of the residual thiol signals (Figure 2.30, purple signals) with the proton signal of the phosphate dimer **1**, the generation of the two thiol species corresponds to one phosphor dimer. Thus, we assume two different thiolate species with tetrabutylammonium thiolate as the main compound.

Furthermore, via Diffusion-ordered Spectroscopy (DOSY; see chapter 2.6.5.2) the volumes for the different thiol species were obtained. The higher value for the thiolate (declared as thiolate 1) in comparison to pure 4-methoxythiophenol can be described by the attachment of tetrabutylammonium as counterion, although the volume is smaller than expected for a combined aggregate (thiolate monomer value: $V = 125$ Å$^3$; ammonium monomer value: $V = 302$ Å$^3$; DOSY derived volume for the thiolate 1 species: $V = 192$ Å$^3$, see chapter 2.6.5.2, Table 2.1). Furthermore, the reduced ammonium volume ($V = 955$ Å$^3$) in comparison to the pure phosphate/ammonium mixture ($V_{ammonium} = 2399$ Å$^3$) hint at its release from the phosphate according to the generation of thiolate and phosphoric acid. Moreover, a second thiolate signal (thiolate 2) was identified, which we assume as thiophenolate being complexed by H-bond formation as the DOSY derived volume is larger than for thiolate 1 ($V = 539$ Å$^3$). For the disulfide a volume of 355 Å$^3$ was obtained, which follows the expected value of dimer generation.
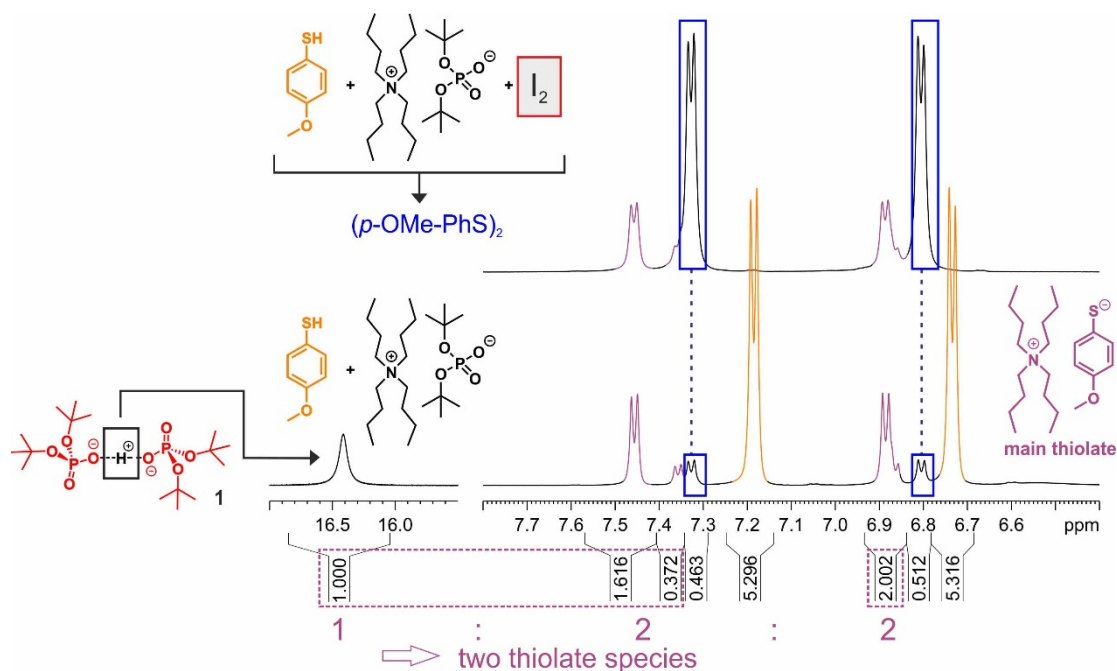
**Figure 2.30:** By the comparison of the $^1$H NMR spectra of a 4-methoxythiophenol/phosphate base mixture (bottom) and after addition of iodine (top) the oxidation product 4-methoxydiphenylsulfide (blue) was identified. Moreover, the signal at ~16.4 ppm was assigned as proton of dimer **1** generated by a partial acid/base reaction between thiol and base and two thiolate anion species (purple) were identified because the sum of the aromatic protons refers to one equivalent of dimer. As main thiolate we propose tetrabutylammonium thiolate.
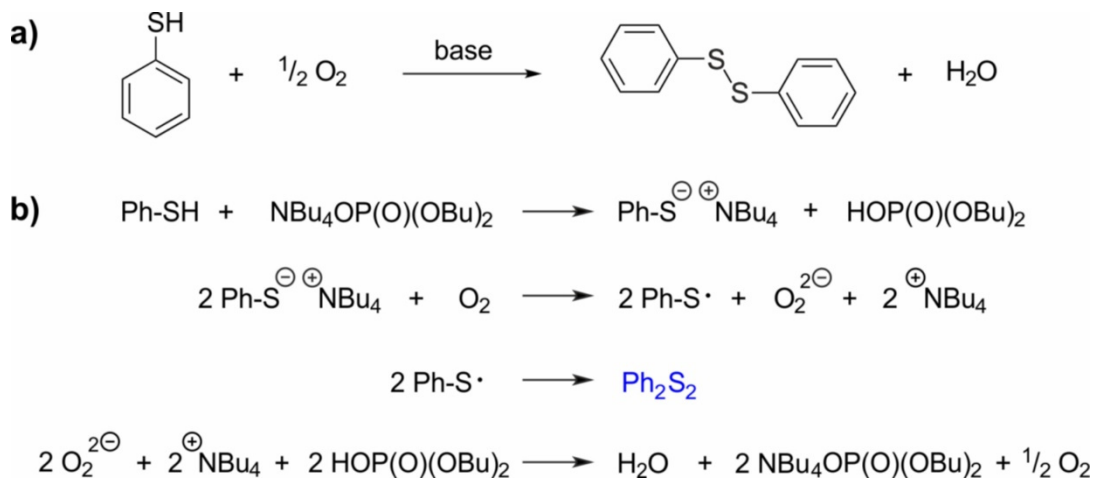


**Figure 2.31:** a) Literature known oxidation of thiophenol in presence of oxygen and base to the corresponding diphenyl disulfide and $H_2O$;[11] b) postulated oxidation process with phosphate bases.

Transferring these results to the sample containing unsubstituted thiophenol, we compared the chemical shifts of sodium thiolate with our PhSH/phosphate base mixture. In Figure 2.32a, the thiolate was verified for the PhSH/base mixture and assigned by the comparison of its low temperature $^1$H NMR spectrum with the spectrum of sodium thiolate (purple signals). Moreover, the thiolate was also identified in the amide/base/PhSH mixture. Therefore, species 1 of the selective TOCSY analysis (Figure 2.29) refers to tetrabutylammonium thiolate. The light blue marked signals of other generated thiol species were not further investigated.
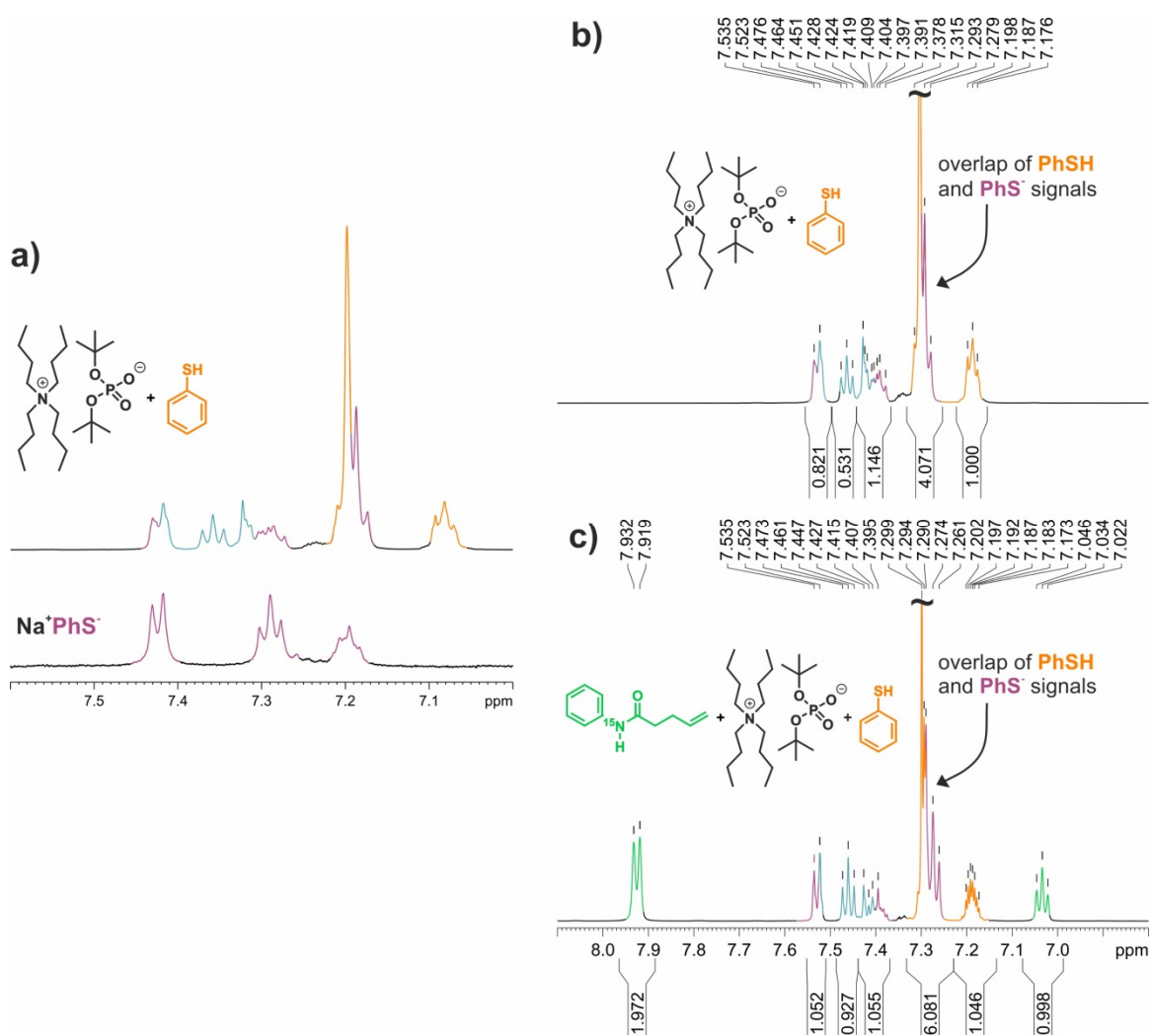


**Figure 2.32:** a) The comparison of the $^1$H NMR spectra of sodium thiolate and the PhSH/base mixture verifies the existence of a thiolate in the samples containing b) tetrabutylammonium di-*tert*-butylphosphate and PhSH and c) $^{15}$*N*-phenylpent-4-enamide, tetrabutylammonium di-*tert*-butylphosphate and PhSH; the spectra were measured in CD$_2$Cl$_2$ at 180 K.

**2.6.4.2 Identification of Phosphate Dimer 1 in the Photocatalytic Reaction Mixture**

Substituting thiophenol by phosphoric acid dibutylester and diphenyldisulfide in order to furnish the phosphate dimer **1** an immense acceleration of the photocatalytic hydroamidation reaction was obtained (see chapters 2.6.3.6 and 2.6.3.7). In addition, we identified the proton signal of the dimer in the photocatalytic reaction mixture ([15]*N*-phenylpent-4-enamide (1 equiv.), tetrabutylammonium di-*tert*-butylphosphate (0.2 equiv.), thiophenol (0.1 equiv.) and photocatalyt (0.02 equiv.); for details of sample preparation see chapter 2.6.3.1) by conducting low temperature ^{1}H NMR studies. In Figure 2.33, the related ^{1}H spectrum of the mixture at 180 K before starting the illumination is shown. The corresponding signal of the dimer was persitent during illumination, however, at this temperature no product formation was observed.
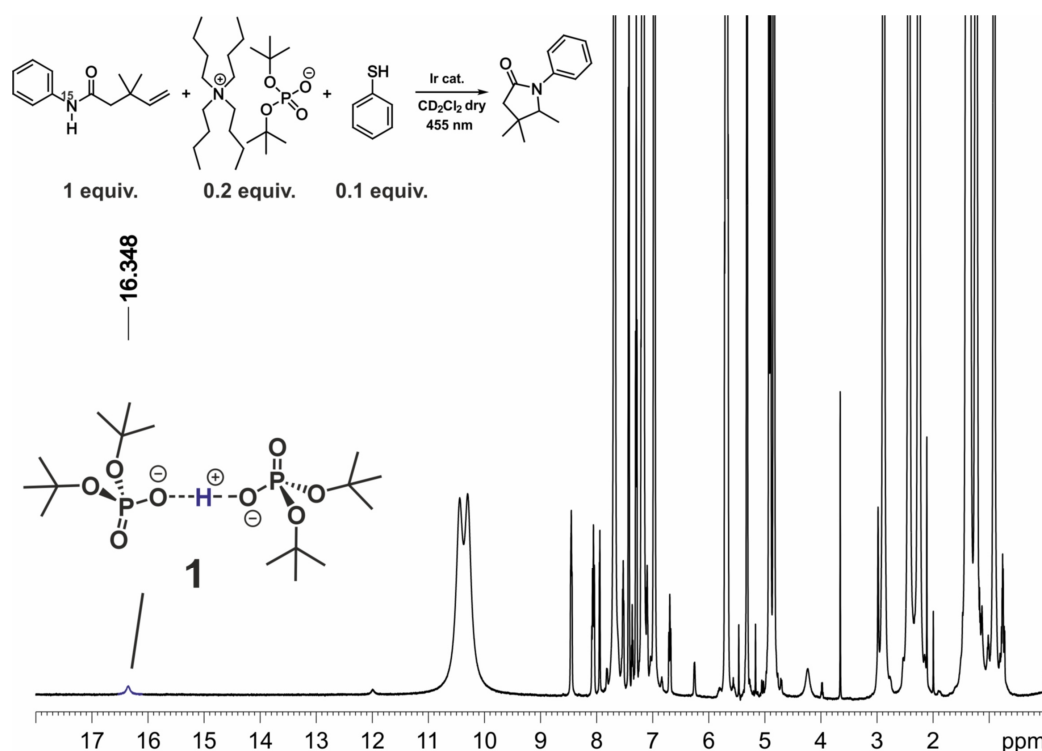


**Figure 2.33:** ^{1}H NMR spectrum of the photocatalytic reaction mixture at 180 K before starting the illumination reveals the existence of phosphate dimer **1**.

**2.6.4.3 Identification of Phosphate Dimer 1 in the Base/Acid Mixture**

In chapter 2.6.3.6 and 2.6.3.7, the immense acceleration of the photocatalytic hydroamidation reaction by directly adding phosphoric acid dibutylester instead of thiophenol was shown. As we identified the phosphate dimer **1** inside the thiophenol

containing reaction mixture and demonstrated its impact on the proton pathway of this photocatalytic transformation, we hoped to create this dimer directly by using a mixture of base and acid without thiophenol. In order to prove the existence of dimer **1** inside the amide/base/acid solution, low temperature $^1$H and $^{31}$P measurements were performed. In Figure 2.34, excerpts of the $^1$H (a) and $^{31}$P (b) spectra of the $^{15}$*N*-phenylpent-4-enamide/tetrabutylammonium di-*tert*-butylphosphate/phosphoric acid dibutylester mixture (1:1:1) are presented. A 1:1:1 mixture (50 mM) was preparred and the measurements were performed at 180 K in order to be able to compare the spectra with those in chapter 4.4.

As highlighted in Figure 2.34, the spectra show the corresponding signals of dimer **1** (for comparison, see Figure 2.3 in the main text and Figure 2.41 in chapter 2.6.4.5 and Figure 2.50,51 in chapter 2.6.4.7) and thus formation of the crucial H-bond mediated dimer was proven. Due to the 1:1 ratio of phosphate and phosphoric acid, a new $^1$H signal at 15.25 ppm and two new $^{31}$P signals at -2.1 and -2.4 ppm appeared. These are typical chemical shift combinations of phosphoric acids (most probably of the phosphoric acids, acid dimers or oligomers) and indicate as expected an equilibrium between tetrabutylammonium phosphates and phosphoric acids at these high concentrations of phosphoric acid. Therefore, reduced amounts of phosphoric acids (10%-30%) were used for the kinetic studies presented in Figure 2.25.
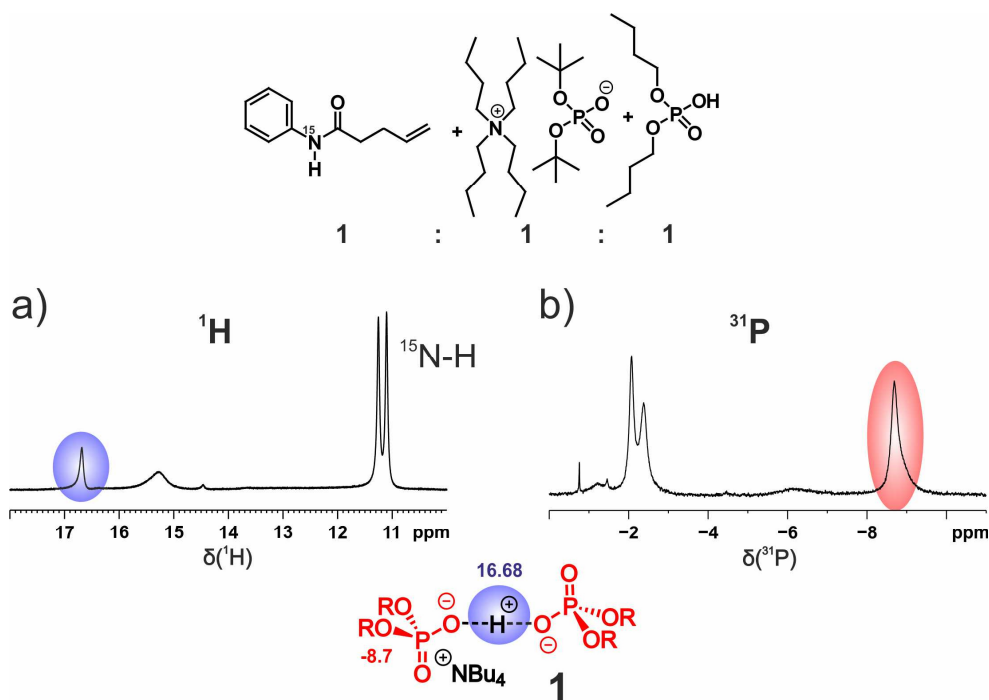


**Figure 2.34:** a) $^1$H and b) $^{31}$P NMR spectra of a mixture containing $^{15}$*N*-phenylpent-4-enamide, tetrabutylammonium di-*tert*-butylphosphate and phosphoric acid dibutylester (1:1:1) in CD$_2$Cl$_2$ at 180 K revealed the existence of dimer **1**. The additional signals in both spectra show the typical chemical shift combination of phosphoric acids (or their dimers or trimers). Therefore, reduced amounts of phosphoric acid were used for the kinetic studies shown in Figure 2.25.

**2.6.4.4 Hydrogen Bond Donor and Acceptor Abilities according to Hunter**

The hydrogen bond donor and acceptor abilities of the different species used for the hydrogen bonding and aggregation analysis are estimated from the publication of Hunter and summarized in Figure 2.35.[12] For dichloromethane (DCM), thiophenol and phenol, the values were directly taken from the tables on page 5316 in this publication. For the amide functionality, the values were read out of Figure 2.7c. The phosphonate diester value was chosen as approximation for the phosphate base. The graph in Figure 2.35b shows the resulting interactions for each species solved in dichloromethane. As such, phenyl-amides and phenol tend to aggregate in solution while thiophenol and the phosphonate diester should undergo solute-solvent interactions and are therefore predicted to exist as monomers.

These assumptions are in line with our hydrogen bond investigations, as *N*-phenylpent-4-enamide as well as phenol form aggregates in $CD_2Cl_2$.

a)

| | acceptor ability | donor ability |
|---|---|---|
| DCM | 1.1 | 1.9 |
| thiophenol | 2.2 | 1.8 |
| amide/phenyl-amide | 8.3 | 3.3[a] |
| phosphonate diester | 8.9 | ≈ 0 |
| phenol | 2.7 | 3.8 |
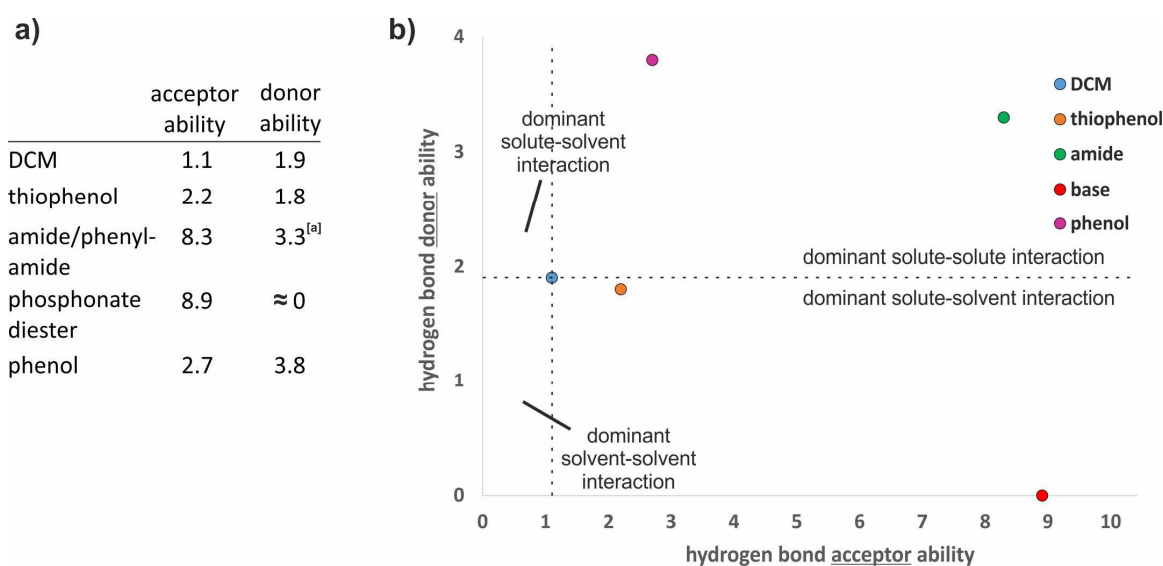


**Figure 2.35:** a) Hydrogen bond acceptor and donor abilities of the corresponding functionalities applied for our hydrogen bond and aggregation analysis according to Hunter;[12] b) the graphical presentation of the values suggests the formation of amide as well as phenol aggregates in DCM. In contrast, thiophenol and the phosponate diester as equivalent for the phosphate base are supposed to exist as monomers.

## 2.6.4.5 ¹H NMR Spectra

In the following sections, the complete NMR spectra of the different mixtures at 180 K are depicted and fully assigned.
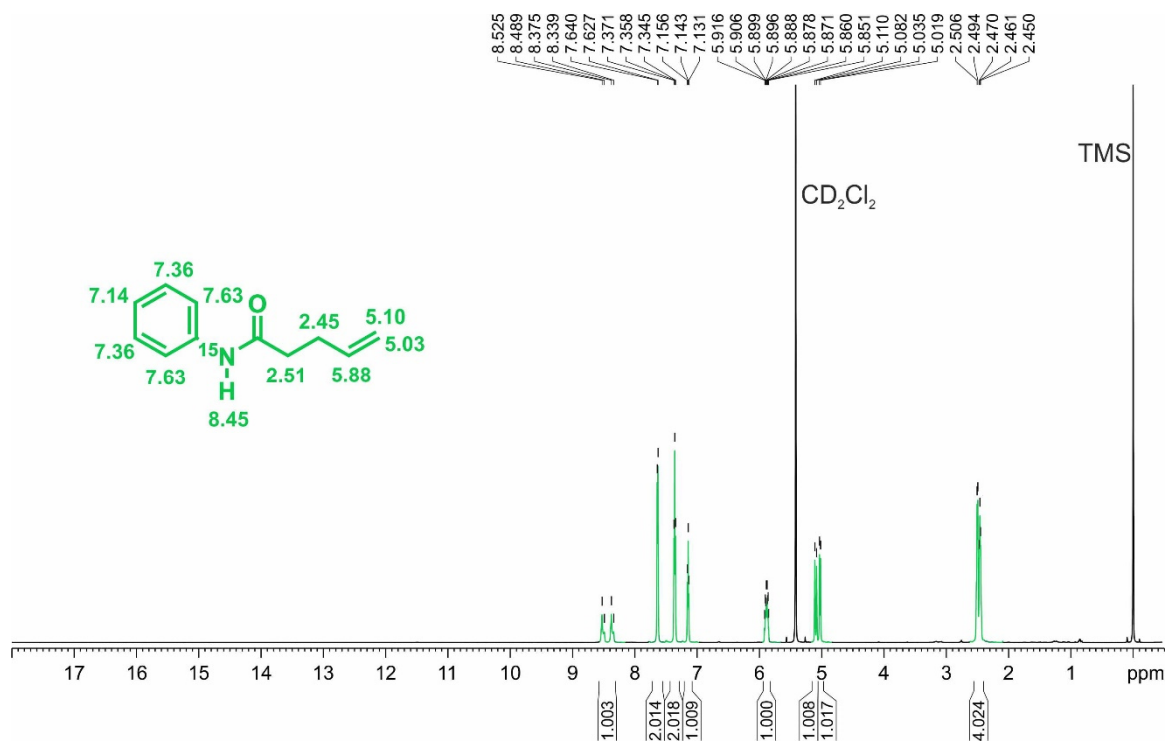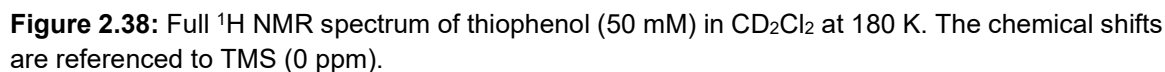


**Figure 2.36:** Full ¹H NMR spectrum of ¹⁵*N*-phenylpent-4-enamide (50 mM) in CD$_2$Cl$_2$ at 180 K. The chemical shifts are referenced to TMS (0 ppm).
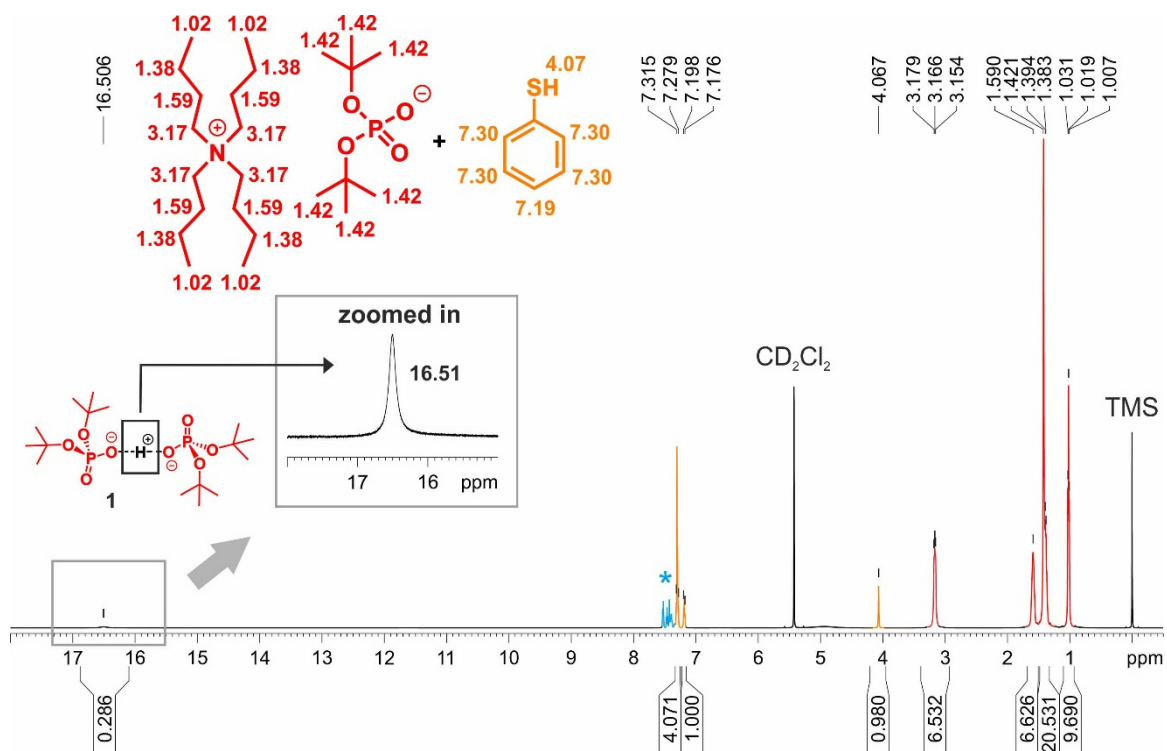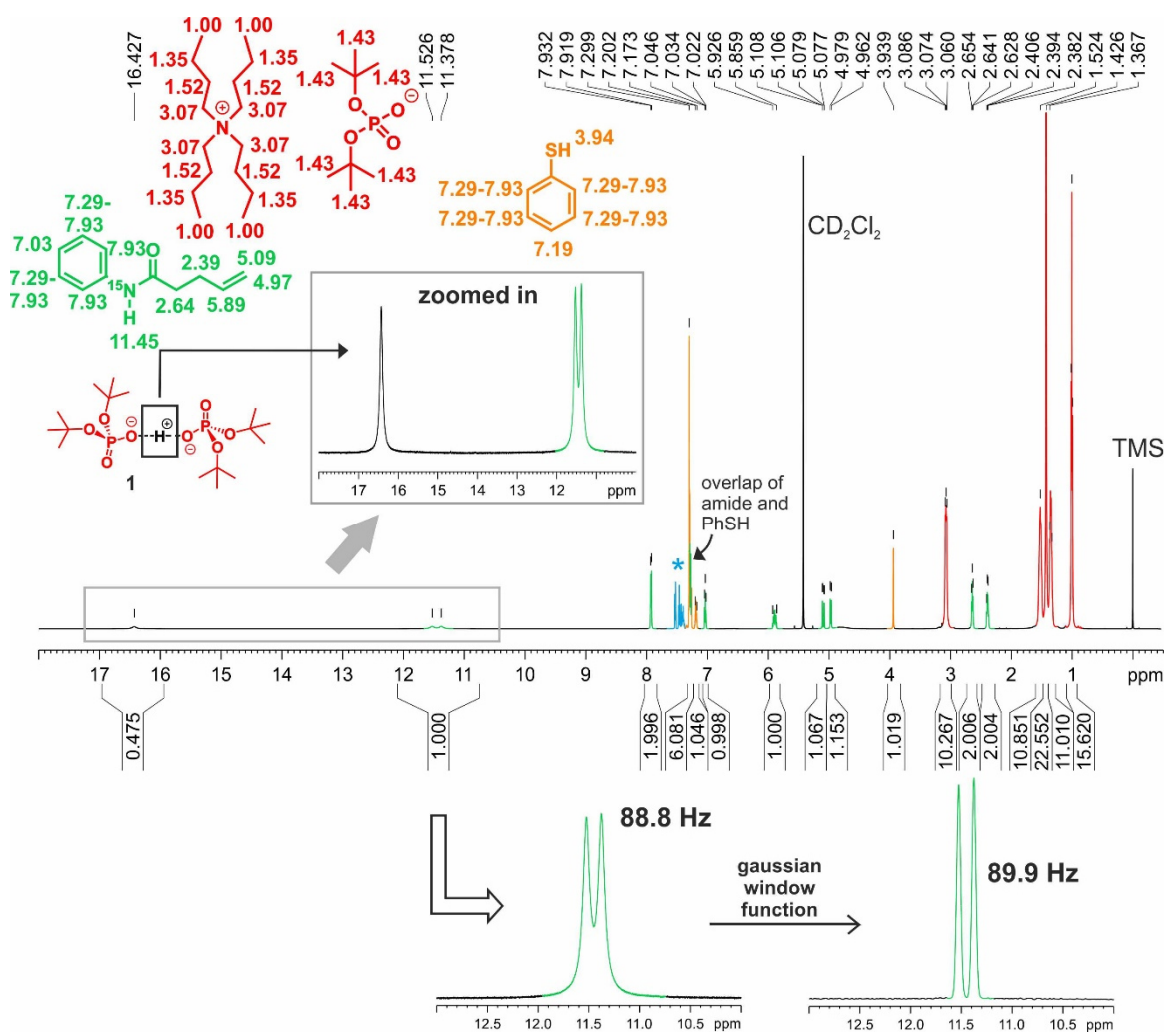
**Figure 2.37:** Full $^1$H NMR spectrum of the 1:1 mixture (50 mM) of $^{15}N$-phenylpent-4-enamide and tetrabutylammonium di-*tert*-butylphosphate in CD$_2$Cl$_2$ at 180 K. The chemical shifts are referenced to TMS (0 ppm).



**Figure 2.38:** Full $^1$H NMR spectrum of thiophenol (50 mM) in CD$_2$Cl$_2$ at 180 K. The chemical shifts are referenced to TMS (0 ppm).

**Figure 2.39:** Full $^1$H NMR spectrum of the 1:1 mixture (50 mM) of tetrabutylammonium di-*tert*-butylphosphate and PhSH in CD$_2$Cl$_2$ at 180 K. For better resolution, the excerpt shows the amplified the signal at 16.51 ppm. The chemical shifts are referenced to TMS (0 ppm). * Other thiol species formed whenever PhSH and base are present. They are discussed in chapter 2.6.4.1.
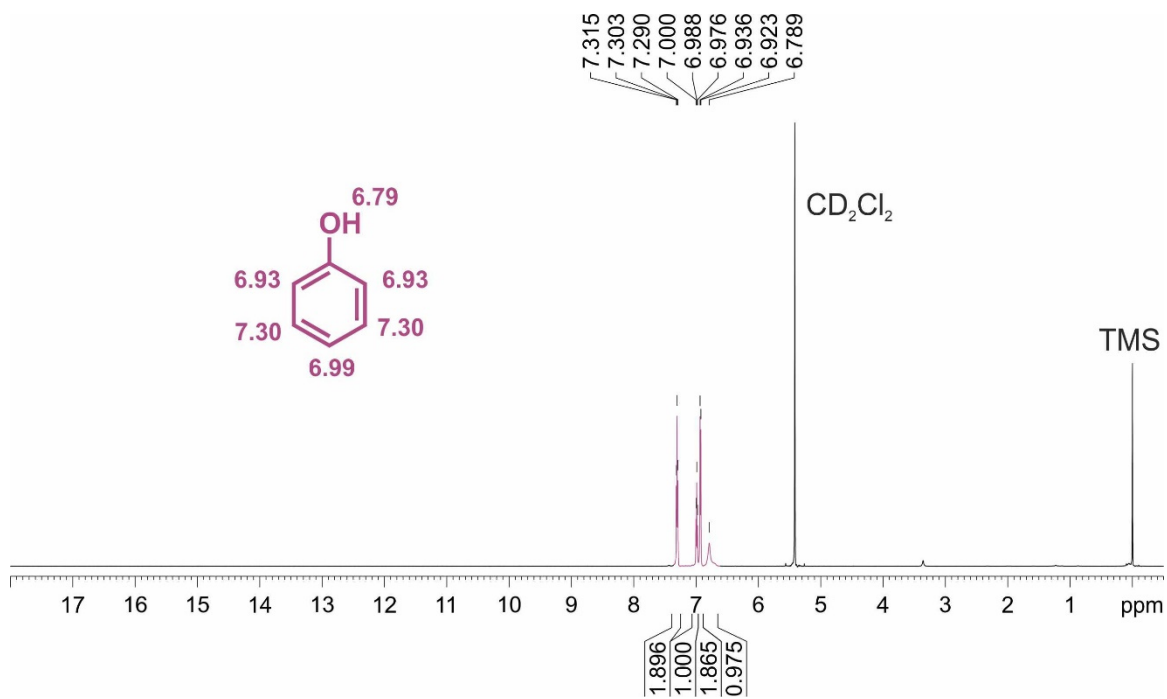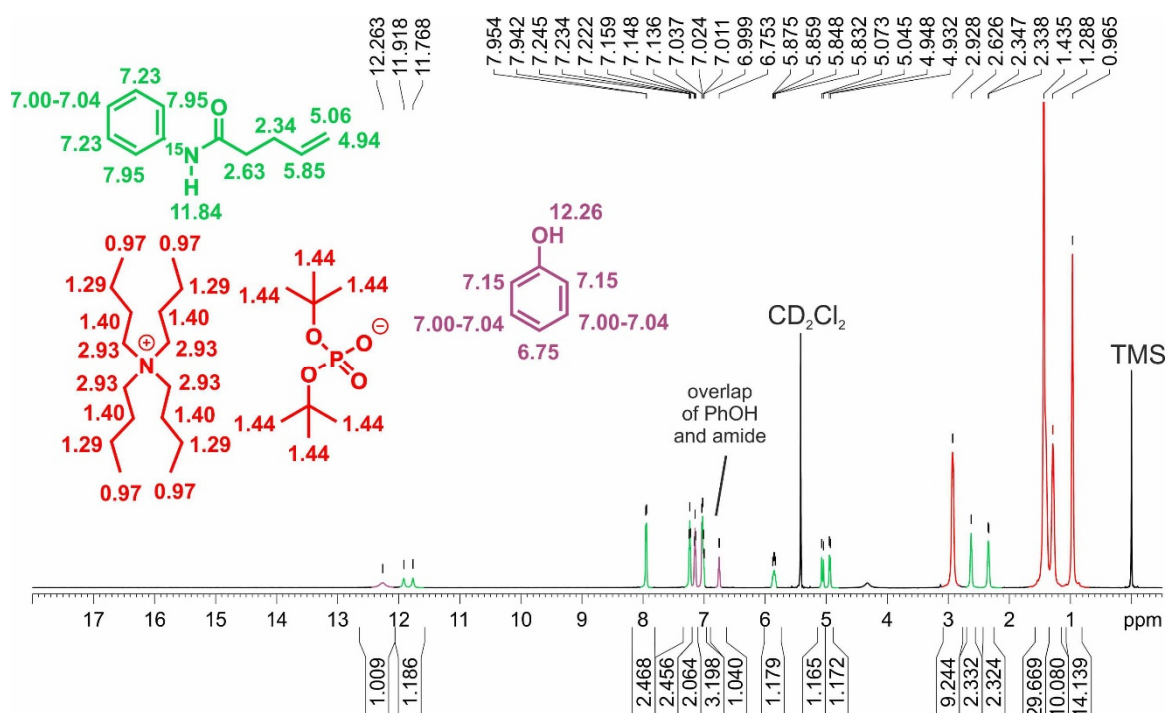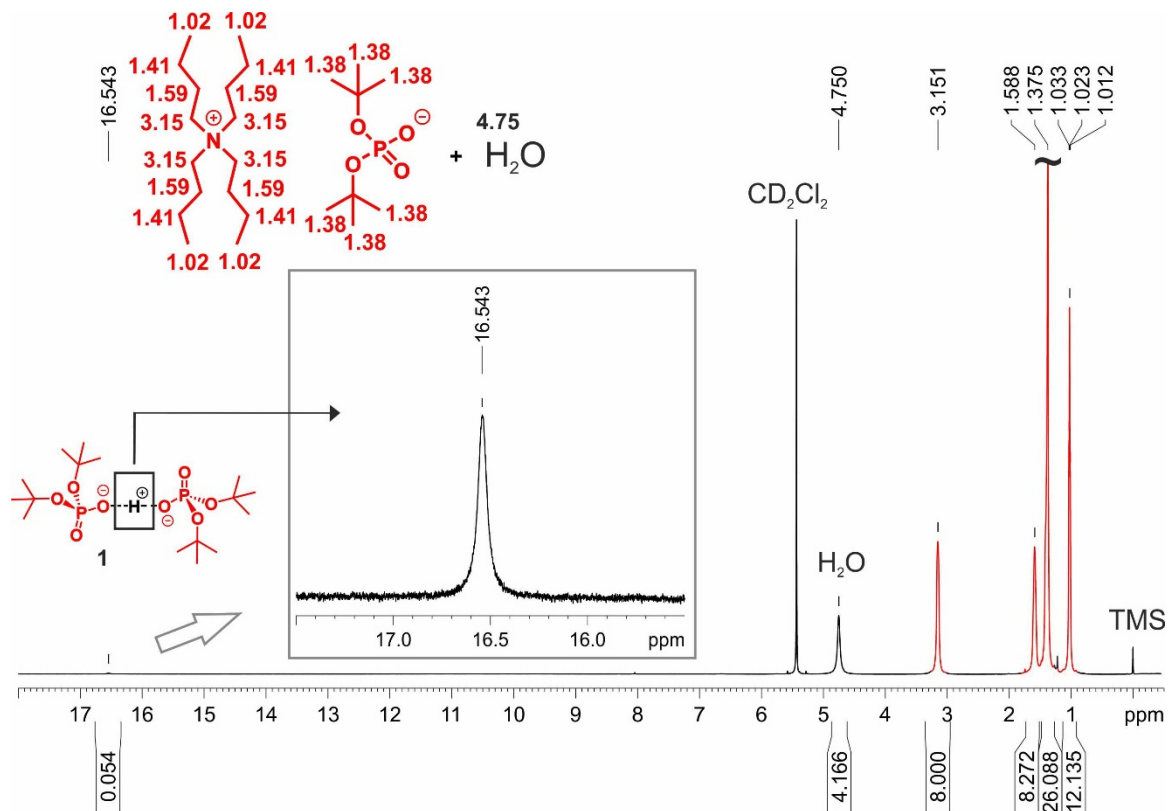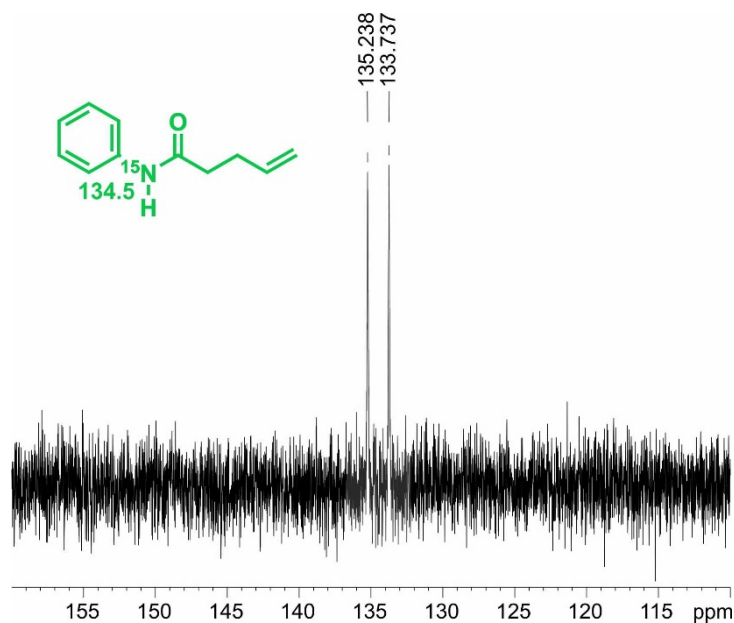


**Figure 2.40:** Full $^1$H NMR spectrum of phenol (50 mM) in CD$_2$Cl$_2$ at 180 K. The chemical shifts are referenced to TMS (0 ppm).

**Figure 2.41:** Full $^1$H NMR spectrum of the 1:1:1 mixture (50 mM) of $^{15}N$-phenylpent-4-enamide, tetrabutylammonium di-*tert*-butylphosphate and PhSH in CD$_2$Cl$_2$ at 180 K. For better resolution, the excerpt shows the amplified the signals at 16.43 ppm and 11.45 ppm. For baseline separation of the $^{15}$N-H doublet, a Gaussian window function was applied. The chemical shifts are referenced to TMS (0 ppm). * Other thiol species formed whenever PhSH and base are present. They are discussed in chapter 2.6.4.1.

**Figure 2.42:** Full $^1$H NMR spectrum of the 1:1:1 mixture (50 mM) of $^{15}N$-phenylpent-4-enamide, tetrabutylammonium di-*tert*-butylphosphate and PhOH in CD$_2$Cl$_2$ at 180 K. The chemical shifts are referenced to TMS (0 ppm).



**Figure 2.43:** Full $^1$H NMR spectrum of tetrabutylammonium di-*tert*-butylphosphate (50 mM) and H$_2$O (45 equiv.) in CD$_2$Cl$_2$ at 180 K. For better resolution, the excerpt shows the amplified the signal at 16.54 ppm. The chemical shifts are referenced to TMS (0 ppm).

**2.6.4.6 $^{15}$N NMR Spectra**



**Figure 2.44:** Full $^{15}$N NMR spectrum of $^{15}$N-phenylpent-4-enamide (50 mM) in CD$_2$Cl$_2$ at 180 K. The chemical shifts are referenced using the $^1$H resonance of TMS according to the method of Harris et *al.*[6]
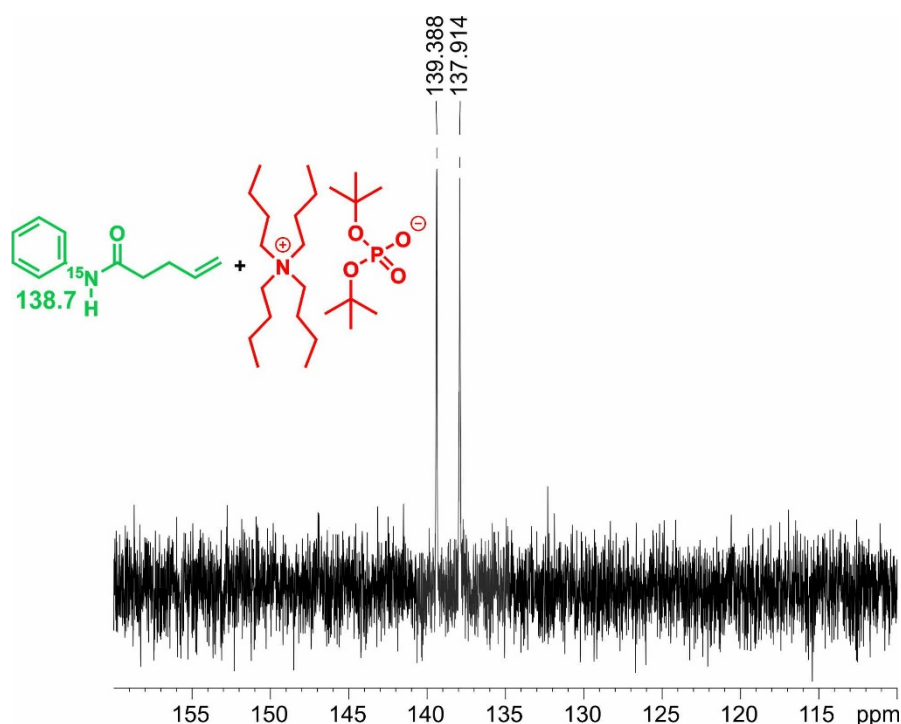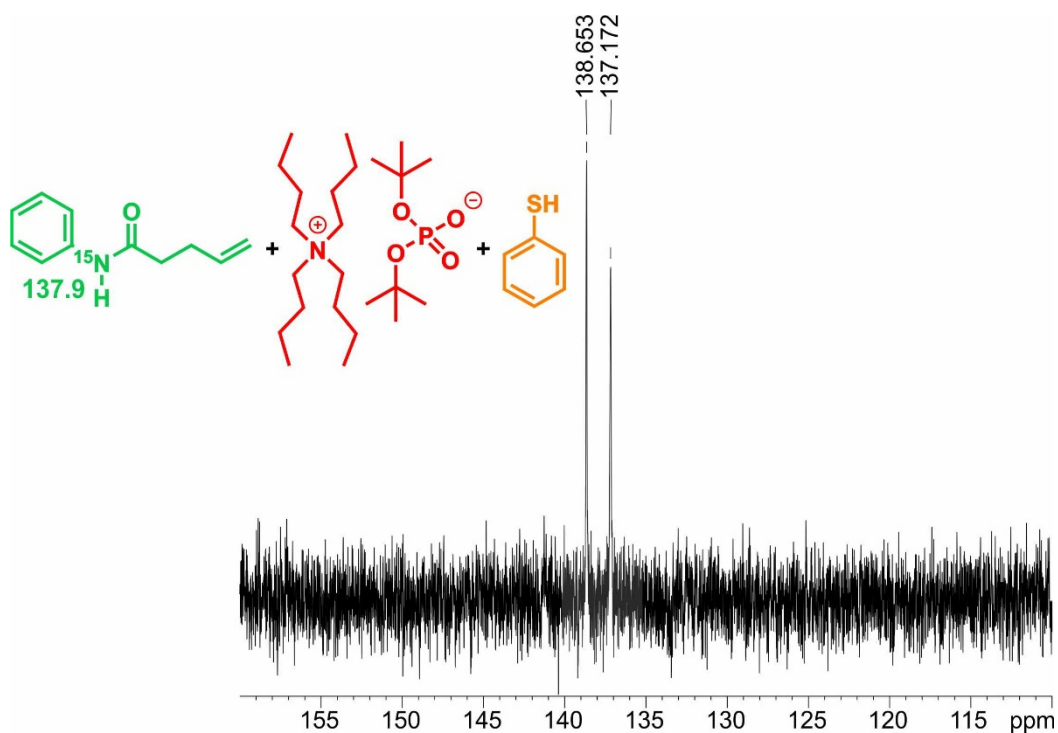


**Figure 2.45:** Full $^{15}$N NMR spectrum of the 1:1 mixture (50 mM) of $^{15}$N-phenylpent-4-enamide and tetrabutylammonium di-*tert*-butylphosphate in CD$_2$Cl$_2$ at 180 K. The chemical shifts are referenced using the $^1$H resonance of TMS according to the method of Harris et *al.*[6]
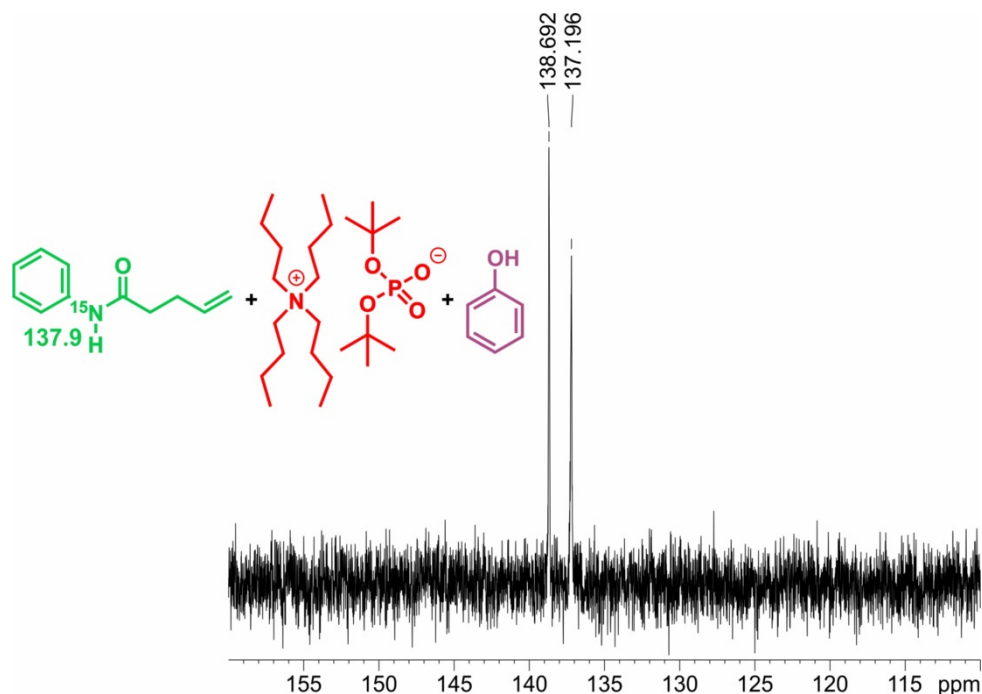
**Figure 2.46:** Full $^{15}$N NMR spectrum of the 1:1:1 mixture (50 mM) of $^{15}$N-phenylpent-4-enamide, tetrabutylammonium di-*tert*-butylphosphate and PhSH in CD$_2$Cl$_2$ at 180 K. The chemical shifts are referenced using the $^1$H resonance of TMS according to the method of Harris et *al*.[6]



**Figure 2.47:** Full $^{15}$N NMR spectrum of the 1:1:1 mixture (50 mM) of $^{15}$N-phenylpent-4-enamide, tetrabutylammonium di-*tert*-butylphosphate and PhOH in CD$_2$Cl$_2$ at 180 K. The chemical shifts are referenced using the $^1$H resonance of TMS according to the method of Harris et *al*.[6]
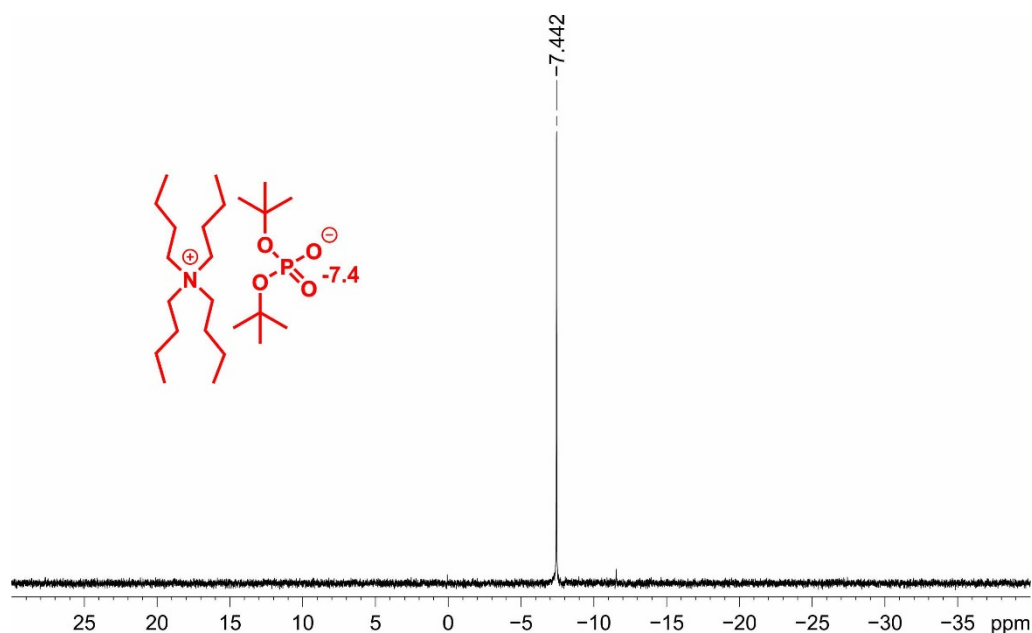
**2.6.4.7 $^{31}$P NMR Spectra**



**Figure 2.48:** Full $^{31}$P NMR spectrum of tetrabutylammonium di-*tert*-butylphosphate (50 mM) in CD$_2$Cl$_2$ at 180 K. The chemical shifts are referenced using the $^1$H resonance of TMS according to the method of Harris et *al*.[6]
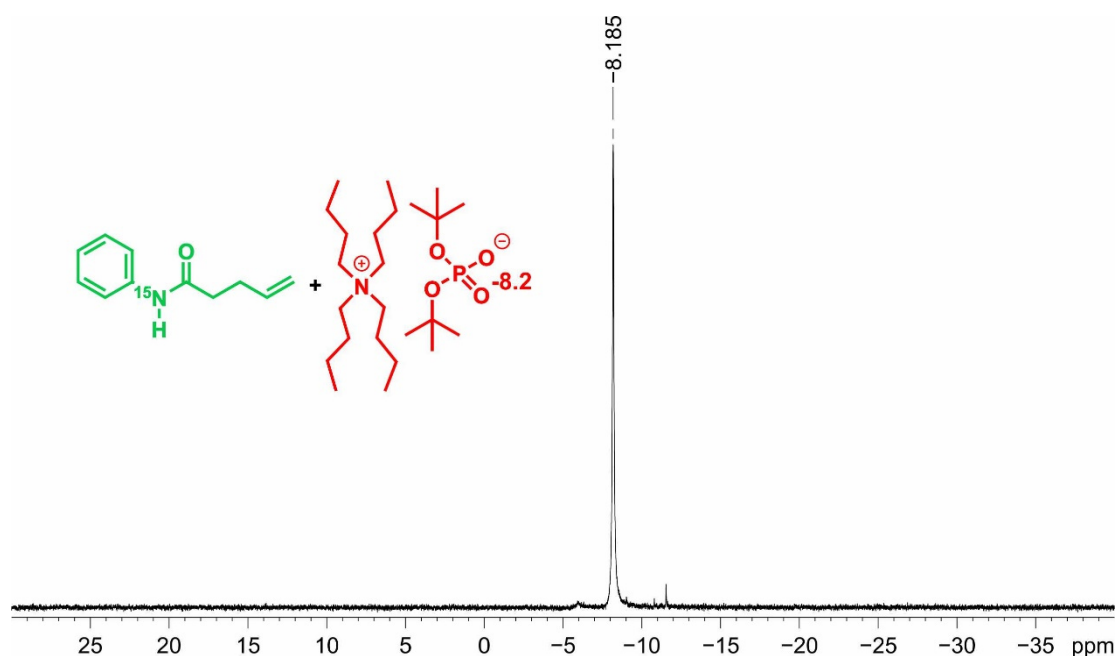


**Figure 2.49:** Full $^{31}$P NMR spectrum of the 1:1 mixture (50 mM) of $^{15}$N-phenylpent-4-enamide and tetrabutylammonium di-*tert*-butylphosphate in CD$_2$Cl$_2$ at 180 K. The chemical shifts are referenced using the $^1$H resonance of TMS according to the method of Harris et *al*.[6]
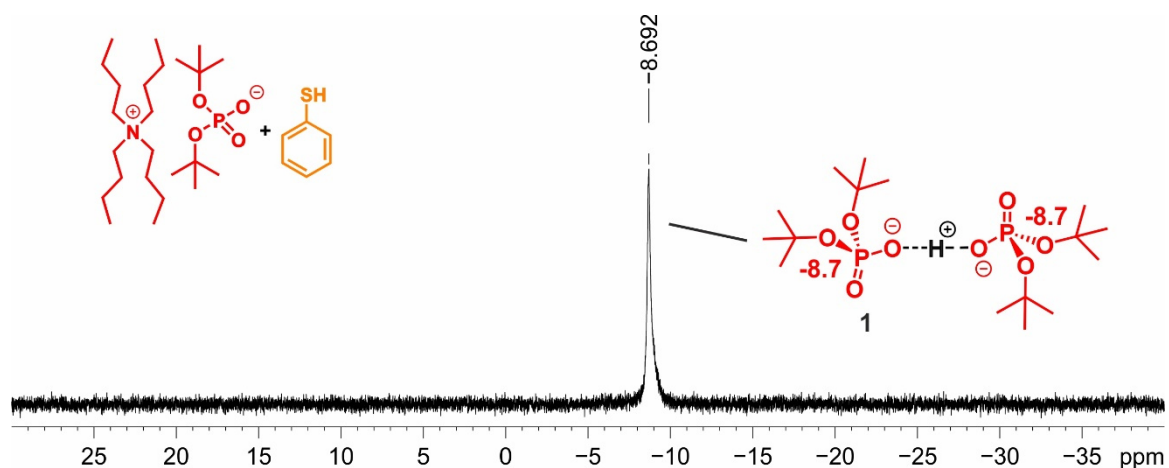
**Figure 2.50:** Full $^{31}$P NMR spectrum of the 1:1 mixture (50 mM) of tetrabutylammonium di-*tert*-butylphosphate and PhSH in CD$_2$Cl$_2$ at 180 K. The chemical shifts are referenced using the $^1$H resonance of TMS according to the method of Harris et *al.*[6]
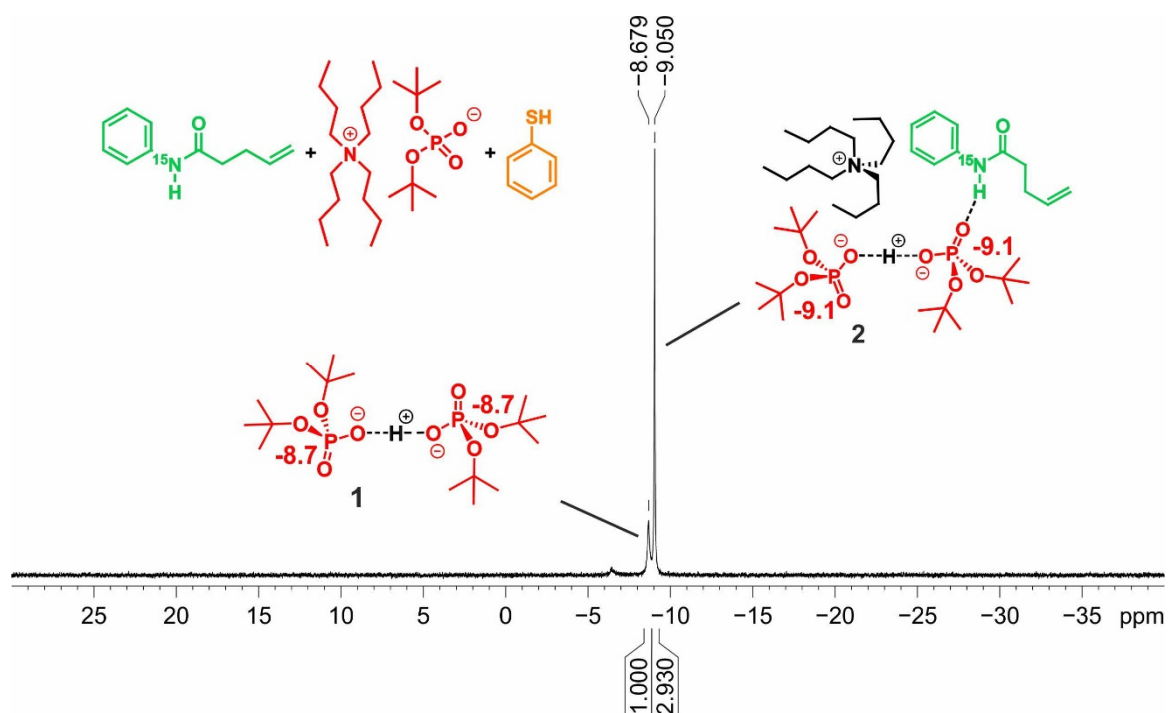


**Figure 2.51:** Full $^{31}$P NMR spectrum of the 1:1:1 mixture (50 mM) of $^{15}$N-phenylpent-4-enamide, tetrabutylammonium di-*tert*-butylphosphate and PhSH in CD$_2$Cl$_2$ at 180 K. The chemical shifts are referenced using the $^1$H resonance of TMS according to the method of Harris et *al.*[6]
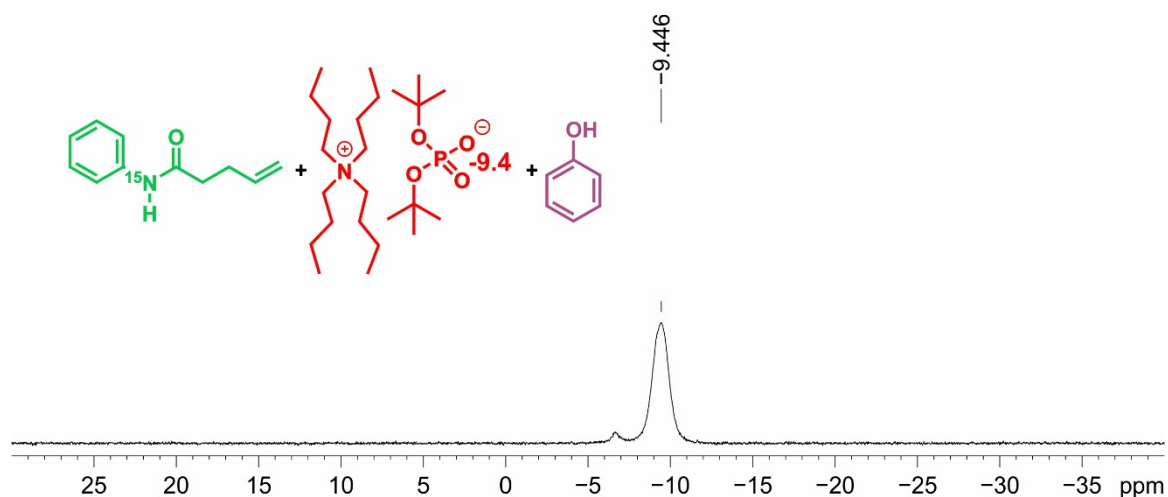
**Figure 2.52:** Full $^{31}$P NMR spectrum of the 1:1:1 mixture (50 mM) of $^{15}N$-phenylpent-4-enamide, tetrabutylammonium di-*tert*-butylphosphate and PhOH in CD$_2$Cl$_2$ at 180 K. The chemical shifts are referenced using the $^1$H resonance of TMS according to the method of Harris et *al.*[6] The broad signal hit at the formation of a large phenol involved aggregate.
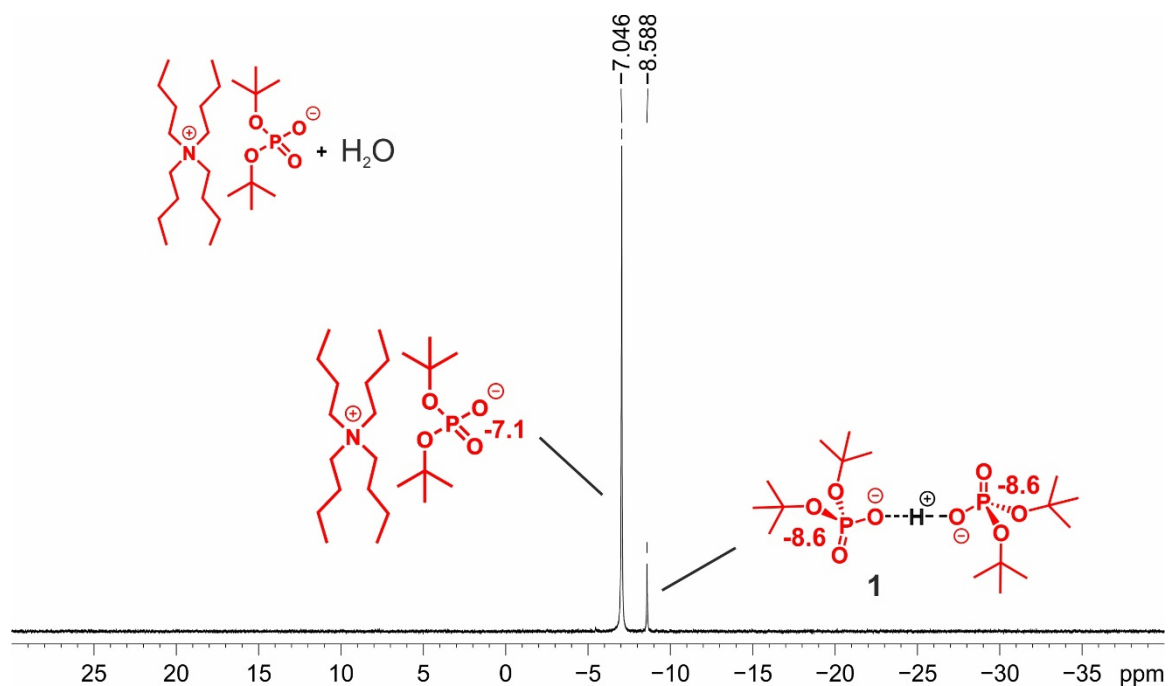


**Figure 2.53:** Full $^{31}$P NMR spectrum of tetrabutylammonium di-*tert*-butylphosphate (50 mM) and H$_2$O (45 equiv.) in CD$_2$Cl$_2$ at 180 K. The chemical shifts are referenced using the $^1$H resonance of TMS according to the method of Harris et *al.*[6]

## 2.6.5 Low Temperature NMR Spectroscopic Aggregation Analysis

### 2.6.5.1 Identification of the [1]H Exchange Signals

In order to identify the crucial aggregate being responsible for the effective PCET mediated hydroamidation, the complexation behavior of the reaction system containing amide, base and thiophenol is elucidated in detail in this chapter. The protonation of the phosphate base by thiophenol furnishing the phosphate dimer **1** was already described in chapter 2.6.4.1, but its generation as crucial requirement for an efficient photoredox catalytic reaction will be discussed in the following section.

Exchangeable protons inside hydrogen bonds can usually be detected as broad singlets in a ^{1}H spectrum and their chemical shifts are very sensitive to the corresponding surroundings. As these non-covalent interactions are the key to effective PCET, the analysis of these protons helps for the identification of the reactive aggregate.

In Figure 2.54, the ^{1}H spectra of the different phosphate containing samples are depicted and the signals referring to exchange protons are highlighted. For complete spectra, see chapter 2.6.4.5. As already mentioned in section 2.6.4.1, the proton inside phosphate dimer **1** (blue), which can also be formed after adding $H_2O$ to PhSH (Figure 2.3a/b, main text; and Figure 2.53), corresponds to the signal at 16.43-16.56 ppm. For the pure base containing sample and the amide/base mixture, this complex is already visible in very tiny amounts (compare proton at 16.56 ppm with ^{13}C satellites of $CD_2Cl_2$ in spectrum at the top in Figure 2.54). In presence of PhSH the signal is immensely increased, which argues for the dimer being a central compound in the reaction mixture. In addition, the strong low field position argues for a drastical electron reorganization in the complex having major impact on the reactivity. Importantly, this aggregation motif cannot be generated in presence of PhOH as hydrogen atom donor (see discussion in the main text). The influence of the chemical environment was also investigated for the chemical shift of residual $H_2O$ (orange), which is present in all base containing mixtures despite drying the phosphate salt and $CD_2Cl_2$ prior to use. Comparing the orange highlighted signals, $H_2O$ is shifted to 4.95 ppm at maximum indicating the formation of bulk water inside the samples (the solvent residual signal of $D_2O$ is 4.79 ppm[1]). Even the addition of amide has no further effect on the water chemical shift and thus this demonstrates no significant interaction with phosphate and therefore no influence on the main aggregation. Furthermore, a small amount of $H_2O$ seems to be attached to phosphate as a signal at 6.62-6.65 ppm is visible (green) for all samples except the pure base. But this signal is small even for the amide/base/PhSH mixture and its chemical shift is only barely changed indicating no influence on the crucial complex. For the PhSH/base sample, an additional

but small signal at 11.62 ppm is generated (yellow), which is either absent after adding the amide or overlaps with the ^{15}N-H doublet. As this signal is low field shifted in comparison to the $H_2O$ related singlets, we think a hydrogen bond between the generated thiophenolate and the phosphate is generated, which anyways has no influence on the amide-phosphate interaction and it is present in low concentration.

In total, from the chemical shifts and signal intensities, only the formation of phosphate dimer **1** has influence on the amide/base/PhSH mixture.
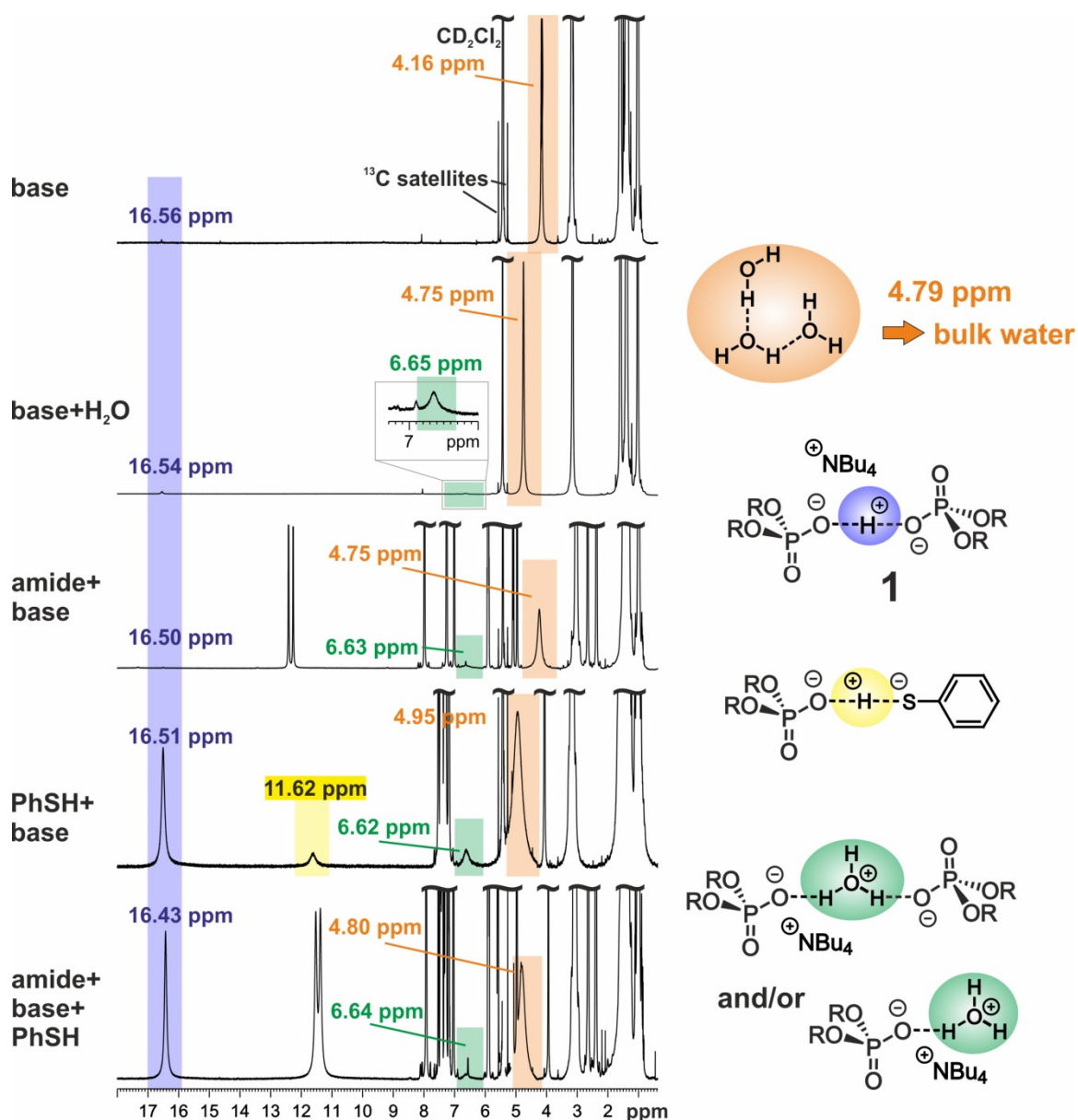


**Figure 2.54:** An excerpt of the ^{1}H spectra of pure base, base/$H_2O$, amide/base, PhSH/base and amide/base/PhSH samples is depicted and the exchange protons are highlighted and corresponding proposed complex structures are given.

**2.6.5.2 Diffusion-Ordered Spectroscopy (DOSY)**

Spectroscopic details:

The $^1$H-diffusion measurements were performed with the convection suppressing DSTE (double stimulated echo) pulse sequence, developed by Müller and Jerschow in a pseudo 2D mode.[13] Tetramethylsilane (TMS) was added as reference for the $^1$H chemical shifts and for temperature and viscosity corrections of the diffusion coefficients of the analytes.[14][15]

A set of 0 dummy scans/8 scans and 120 dummy scans/16 scans, respectively, were used with a relaxation delay of 2 s. Sinusoidal shapes were used for the gradient and a linear gradient ramp with 5 or 20 increments between 5 % and 95 % of the maximum gradient strength were applied. For the homospoil gradient strengths values of 100, -13.17, 20 and -17.13 % were used. An effective diffusion time of 45 ms was applied. For each compound in the sample, the gradient pulses were adjusted in order to obtain optimized diffusion times *Δ* and gradient lengths *δ* according to following correlation:

$$\Delta\,[ms] = D_{23} + \frac{\delta}{3}\;;\,P_{16}[ms] = \frac{\delta}{2}$$

The NMR spectra were processed with the Bruker program TopSpin 3.2 and the diffusion coefficients were determined according Müller and Jerschow.[13]

Size Estimation:

Via DOSY, the experimental translational self-diffusion coefficients *D* of the molecules in solution were determined according to the Stejskal-Tanner equation.[16][17][18] From the obtained diffusion coefficients, the hydrodynamic radii of the analytes $r_A$ were estimated following the Stokes-Einstein equation (1), with *k* = Boltzmann constant, *T* = temperature, *η* = viscosity of the sample, *c* = correcting factor, *F* = shape factor.[19]

$$D\,[m^2/s] = \frac{kT}{Fc\pi\eta r_A}\quad(1)$$

For spherical shape, *F* is equal to 1. The correction factor *c* of the Stokes-Einstein equation was calculated according to the semi-empirical modification according to Chen (2) using literature known values for the solvent ($r_{solv}$ = 2.46 Å for $CD_2Cl_2$ [20]).[21]

$$c_{Chen} = \frac{6F}{1 + 0.695\,(\frac{r_{solv}}{r_{ref}})^{2.234}}; \quad F = 1\ for\ spheres \quad (2)$$

The obtained diffusion coefficients *D* for the analytes were calibrated by viscosity calculation using the literature known radius of TMS ($r_{ref}$ = 2.96 Å, calculated from hard-sphere increments[22]) and the experimentally determined diffusion coefficient $D_{ref}$ of TMS for every sample (equation (3)).

$$\eta\,[kg/ms] = \frac{kT\,(1 + 0.695\,\left(\frac{r_{solv}}{r_{ref}}\right)^{2.234})}{6\pi D_{ref}\,r_{ref}} \quad (3)$$

Including all corrections and calibrations into the Stokes-Einstein equation (4), the hydrodynamic radii $r_A$ were calculated according to equation (5). For better imagination, the corresponding volumes $V_A$ were calculated assuming a spherical shape.

$$D = \frac{kT(1 + 0.695\,\left(\frac{r_{solv}}{r_{ref}}\right)^{2.234})}{6\pi\eta r_A} = \frac{kT(1 + 0.695\,r_{solv}^{2.234}\,r_{ref}^{-2.234})}{6\pi\eta r_A} \quad (4)$$

$$0 = D6\pi\eta r_A - kT\,0.695\,r_{solv}^{2.234}\,r_A^{-2.234} - kT \quad (5)$$

In Table 2.1 the experimental diffusion coefficients *D*, the corresponding calculated radii $r_A$, the resulting volumes $V_A$ (the calculations were performed assuming spherical molecular shapes) and the estimated monomer volumes $V_M$ for the corresponding species according to Bondi are depicted.[23] For each sample, the *D* values for every species and for TMS as reference are given. If not otherwise mentioned, the average *D* values of all baseline separated signals referring to the same species were used.

The interpretation of the DOSY derived data and further investigations of the aggregation situation including NOESY experiments from chapter 2.6.5.3 inside the different samples are given in chapter 2.6.5.4-2.6.5.6. The values for the 4-OMe-thiophenol/base mixture were already described in chapter 2.6.4.1.

**Table 2.1:** Information about the aggregation of the compounds in the different samples derived by diffusion ordered spectroscopy (DOSY) in $CD_2Cl_2$. The experiments were performed at 180 K if not otherwise stated.
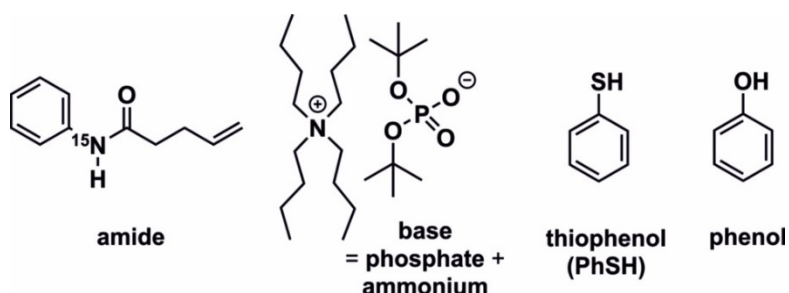


| sample | species inside sample | diffusion coefficient $D^{[a]}$ [m²/s] | hydrodynamic radius $r_A$ [Å] | volume $V_A$ [Å³] | monomer volume $V_M^{[c]}$ [Å³] |
|---|---|---|---|---|---|
| amide | amide | 1.05 x 10⁻¹⁰ | 5.19 | 587 | 168 |
| | TMS | 2.38 x 10⁻¹⁰ | - | - | |
| base | phosphate[b] | 6.81 x 10⁻¹¹ | 8.65 | 2715 | 210 |
| | ammonium | 7.13 x 10⁻¹¹ | 8.31 | 2399 | 302 |
| | TMS | 2.79 x 10⁻¹⁰ | - | - | |
| PhSH | PhSH | 2.69 x 10⁻¹⁰ | 3.06 | 120 | 101 |
| | TMS | 2.85 x 10⁻¹⁰ | - | - | |
| amide/base | amide | 6.48 x 10⁻¹¹ | 7.68 | 1900 | |
| | phosphate | 6.78 x 10⁻¹¹ | 7.38 | 1681 | |
| | ammonium | 7.29 x 10⁻¹¹ | 6.92 | 1387 | |
| | TMS | 2.33 x 10⁻¹⁰ | - | - | |
| PhSH /base | PhSH | 1.71 x 10⁻¹⁰ | 3.16 | 132 | |
| | phosphate[b] | 5.08 x 10⁻¹¹ | 8.01 | 2155 | |
| | ammonium | 6.12 x 10⁻¹¹ | 6.79 | 1310 | |
| | TMS | 1.91 x 10⁻¹⁰ | - | - | |
| amide/base/ PhSH | amide | 7.12 x 10⁻¹¹ | 6.79 | 1309 | |
| | phosphate | 6.52 x 10⁻¹¹ | 7.34 | 1655 | |
| | ammonium | 7.95 x 10⁻¹¹ | 6.18 | 986 | |
| | PhSH | 2.28 x 10⁻¹⁰ | 2.92 | 104 | |
| | TMS | 2.22 x 10⁻¹⁰ | - | - | |
| amide/base/ PhSH at 300 K | amide | 1.16 x 10⁻⁰⁹ | 6.14 | 968 | |
| | phosphate | 7.99 x 10⁻¹⁰ | 8.54 | 2607 | |
| | ammonium | 8.52 x 10⁻¹⁰ | 8.05 | 2185 | |
| | PhSH | 2.30 x 10⁻⁰⁹ | 3.66 | 205 | |
| | TMS | 3.22 x 10⁻⁰⁹ | - | - | |
| phenol | phenol | 1.76 x 10⁻¹⁰ | 3.70 | 212 | 89 |
| | TMS | 2.50 x 10⁻¹⁰ | - | - | |
| amide/base/phenol | amide | 5.64 x 10⁻¹¹ | 7.94 | 2096 | |
| | phosphate | - | - | - | |
| | ammonium | 6.33 x 10⁻¹¹ | 7.16 | 1537 | |
| | phenol | 5.78 x 10⁻¹¹ | 7.77 | 1966 | |
| | TMS | 2.10 x 10⁻¹⁰ | - | - | |

| 4-OMe-thiophenol/base | 4-OMe-PhSH | $1.53 \times 10^{-10}$ | 3.14 | 129 | 125 |
|---|---|---|---|---|---|
| | 4-OMe-PHS⁻ (thiolate 1) | $1.24 \times 10^{-10}$ | 3.58 | 192 | |
| | thiolate 2 | $7.73 \times 10^{-11}$ | 5.05 | 539 | |
| | (4-OMe-PhS)$_2$ | $9.29 \times 10^{-11}$ | 4.39 | 355 | |
| | phosphate[b]: | $5.20 \times 10^{-11}$ | 7.03 | 1454 | |
| | ammonium | $6.12 \times 10^{-11}$ | 6.11 | 955 | |
| | TMS | $1.69 \times 10^{-10}$ | - | - | |

[a] the diffusion coefficients D are average values of all base line separated signals; [b] the phosphate signal is not base line separated and overlapped with an ammonium signal and the diffusion coefficient refers therefore to an average value of both species; [c] estimated monomer values according to Bondi.[23]

### 2.6.5.3 ¹H,¹H NOESY

In order to obtain more information about the nature of the aggregates, 2D ¹H,¹H NOESY measurements were performed for the amide/base and amide/base/thiophenol samples at 180 K. Prior to the experiments, the mixing time (100 ms) was adjusted to achieve the best signal intensity without leaving the linear NOE buildup, which is necessary for the subsequent interproton distance calculation.

The distance calculations were performed by integrating the NOE crosspeaks.[24] The discrete interproton distances $r$ in nm were obtained according to equation 6. Importantly, the distance calculated between two integrals (protons) refers to the average value for all involved protons and for all possible conformations in the solution.

$$r = r_{ref} \left( a_{ref}/a \right)^{1/6} \quad (6)$$

For the amide/base sample, $r_{ref}$ refers to the distance between the amidyl aromatic protons in *ortho* and *meta* position, which was obtained using GaussView. The value of 2.5 nm, which is the average value for both *ortho-meta* distances in the aromatic ring, was applied as reference for the calculation of all intra- and intermolecular distances (Figure 2.55a). The integrals of the NOE crosspeaks $a_{ref}$ and $a$ were adapted according to their number of protons.

As the NOE cross peaks of the aromatic protons were not separated for the amide/base/PhSH sample, $r_{ref}$ refers to the distance between the *trans*-configured olefin protons also obtained by GaussView (3.1 nm; Figure 2.56a).

The ¹H,¹H NOESY spectrum of the amide/base mixture in Figure 2.55a shows intermolecular interactions between amide and phosphate (orange) and between amide

and the ammonium counterion of the base (yellow). As analyzed in the main text, the amide/phosphate interaction is based on a N-H···O-P hydrogen bond. The ammonium-amide interaction, however, is presumably attributed to a cation-π-interaction.[25] Distance calculations in Figure 2.55b visualize these interactions in more detail. The average distances show that the *tert*-butyl groups of the phosphate are in average closest to the amidyl N-H proton, which corroborates the amide/base hydrogen bond (top). Moreover, the shorter distances of the central $CH_2$ protons of the tetrabutylammonium towards the aromatic region of the amide verify the cation-π-interaction (bottom).
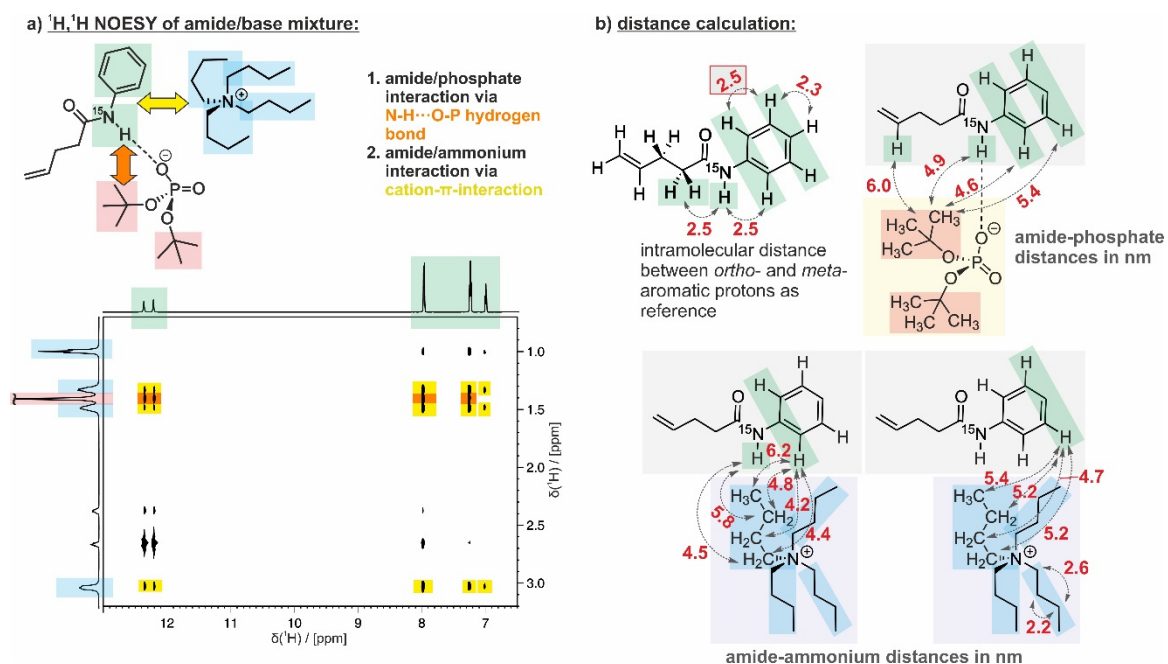


**Figure 2.55:** a) $^1H,^1H$ NOESY experiments of the amide/base mixture corroborate the existence of a hydrogen bond between amide and phosphate and suggest a cation-π-interaction between tetrabutylammonium and the phenyl group of the amide; b) these concepts are further supported by the calculation of the average intermolecular distances between the different species.

In Figure 2.56a, the $^1H,^1H$ NOESY spectrum of the amide/base/PhSH spectrum is depicted. As was obtained for the amide/base system, the existence of a N-H···O-P hydrogen bond is supported by a NOE crosspeak between the *tert*-butyl groups of the phosphate and the $^{15}$N-H proton. Furthermore, again, a cation- π--interaction between ammonium and the aromatic ring of the amide was identified. The distance calculations depicted in Figure 2.56b show the shortest average distance between the *tert*-butyl groups and the N-H proton albeit with increased values compared to the calculations of the amide/base mixture. This hints to a longer amide-phosphate distance, but as the reference distances are different for both samples, the values can only be accurately compared inside the same system. For the amide/base/PhSH sample, the central ammonium $CH_2$

protons are calculated to be closest to the aromatic region of the amide again, supporting the mentioned cation- π—interaction.



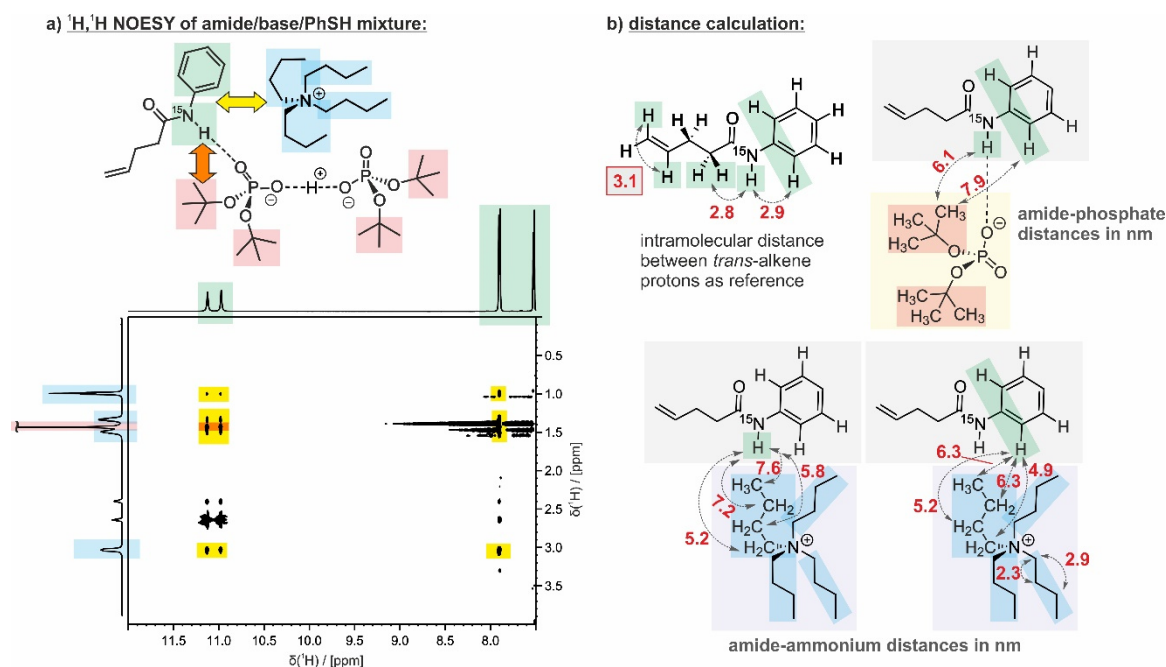**Figure 2.56:** a) $^1$H,$^1$H NOESY experiments of the amide/base/PhSH sample corroborate the existence of a hydrogen bond between amide and base and suggest a cation-π-interaction between tetrabutylammonium and the phenyl group of the amide as found for the amid/base mixture (Figure 2.55); b) these concepts are again further supported by the calculation of the average intermolecular distances between the different species.

### 2.6.5.4 Analysis of the Pure Compounds in CD$_2$Cl$_2$

Taking together the results of the $^1$H, $^{15}$N, $^{31}$P NMR hydrogen bond analysis, the DOSY and NOESY measurements and the MD simulations (for details about the MD simulations, see chapter 2.6.6), the nature of the aggregates inside the different mixtures can be described in detail. In the following sections, the aggregation situation is discussed for the pure compounds in CD$_2$Cl$_2$, the amide/base, base/thiophenol, amide/base/thiophenol and amide/base/phenol mixtures.

The description of the one- and two-compound systems provide basic and important information which help for the interpretation of the aggregation situation inside the three-compound mixtures being crucial for the overall PCET efficiency for a successful photoredox catalytic hydroamidation reaction.
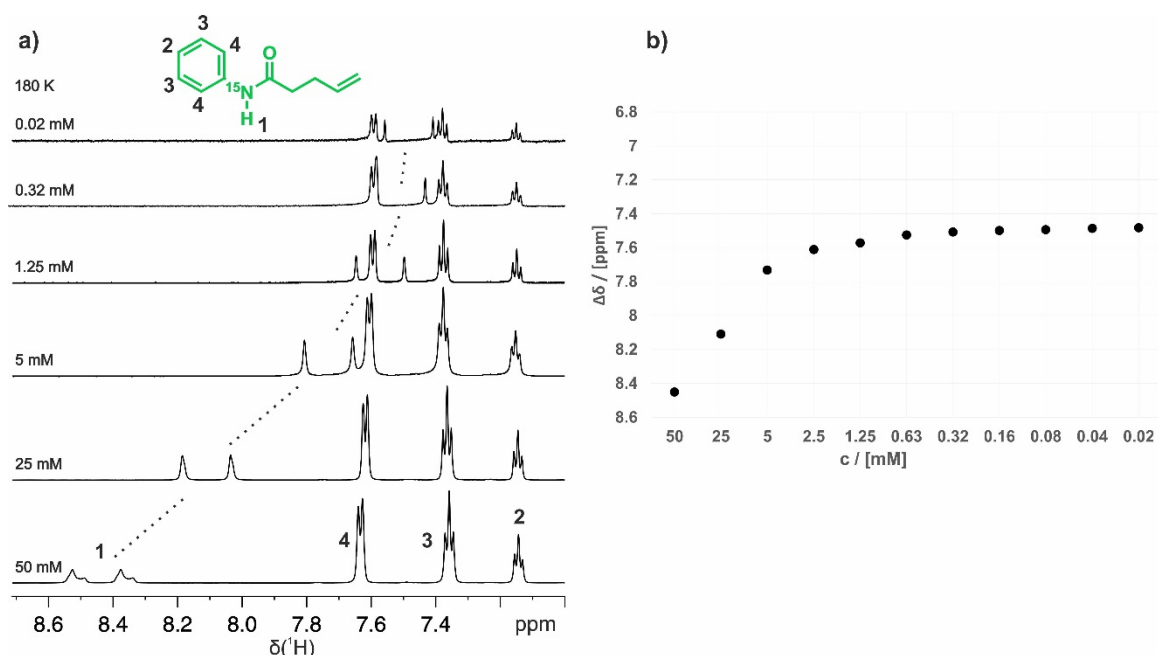
$^{15}N$-Phenylpent-4-enamide in $CD_2Cl_2$ at 180 K:



**Figure 2.57:** a) The $^1H$ low field shift of the N-H proton with higher concentrations (from 0.02 to 50 mM) indicates an increased hydrogen bond mediated amide/amide interaction by the formation of dimers or multimers; b) graphical representation of the correlation between concentration and shift of the N-H proton.

Via $^1H$ NMR titration experiments the behavior of the pure amide in $CD_2Cl_2$ was studied. In Figure 2.57a, an excerpt of the $^1H$ NMR spectra of the amide using different concentrations between 50 mM and 0.02 mM is depicted. The continuous shift of the $^{15}N$-H proton duplet towards low field with higher concentrations indicates an increase of the N···O-C hydrogen bond strength by forming dimers or multimers. Figure 2.57b shows the graphical correlation between the chemical shift dependence and the concentration including all measured dilutions. The graph illustrates that a molecular finite state is reached at 0.02 mM with a chemical shift of around 7.5 ppm, which could refer to the monomer or a dimer state. In general, via π-bond cooperativity of the amide functionality the hydrogen bond donor and acceptor ability is enhanced and dimer or multimer formation is favored (Figure 2.58a).[26] This solute-solute interaction is also supported by the investigations of Hunter (see chapter 2.6.4.4). Including the DOSY derived volume (587 $Å^3$) and comparing it to the estimated monomer value according to Bondi (168 $Å^3$, see Table 2.1 in chapter 2.6.5.2), an amide complex consisting of approximately two dimers or four monomers is assumed (Figure 2.58b).
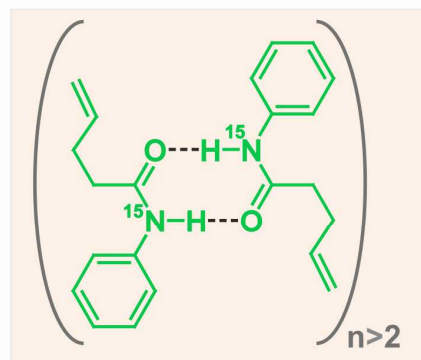
**a)** π-bond cooperativity:
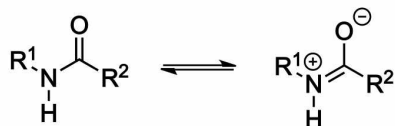


possible dimer formation:
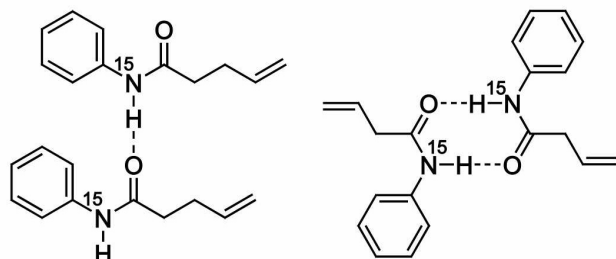


**b)** aggregation:



**volume of amide**
**estimated (Bondi):** **168 Å³**
**experiment (DOSY):** **609 Å³**

**Figure 2.58:** a) Literature known π-bond cooperativity leads to the formation of inter-amide dimer or oligomer formation;[26] b) the DOSY derived volumes for pure amide at 50 mM suggest the formation of an aggregate with in average at minimum 3 amides involved.

Tetrabutylammonium di-*tert*-butylphosphate in CD$_2$Cl$_2$ at 180 K:

The nature of the phosphate base was investigated via concentration dependent $^1$H NMR spectroscopy as well. The spectra the phosphate base including its tetrabutylammonium counterion at 50 and 25 mM show no chemical shift deviation of the corresponding signals (Figure 2.59a). Comparing the estimated monomer volumes with the values derived by DOSY, the base seems to be highly aggregated (Figure 2.59b). Interestingly, the value for the cation is decreased in comparison to the phosphate indicating a partial dissociation from the anion possibly caused by residual water inside the sample. As there is only one set of signals for each species in the spectrum and only one $^{31}$P signal for the phosphate (see Figure 2.48), the different complexes equilibrate on the NMR time scale.
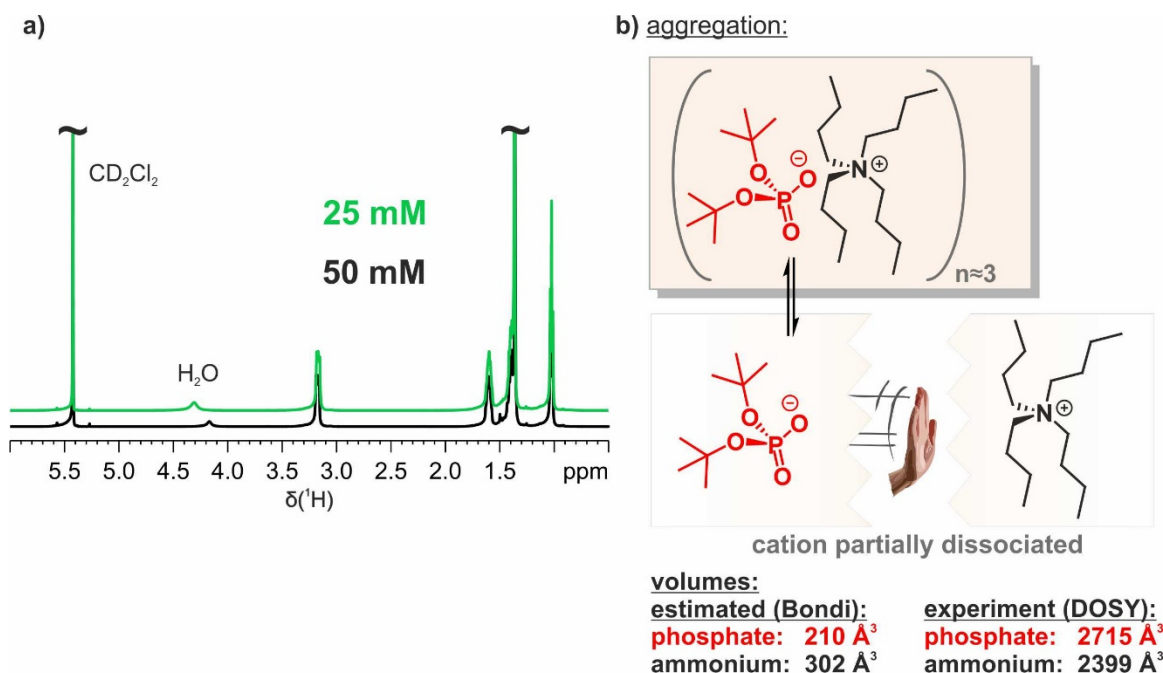
a)

b) aggregation:



volumes:
estimated (Bondi):
phosphate: 210 Å³
ammonium: 302 Å³

experiment (DOSY):
phosphate: 2715 Å³
ammonium: 2399 Å³

**Figure 2.59:** a) The $^1$H NMR spectra of the base at 180 K including phosphate anion and tetrabutylammonium cation show no chemical shift changes of the corresponding species using different concentrations (25 and 50 mM); b) the aggregation situation at 50 mM is proposed as phosphate/ammonium ion pair with the cation being partially released.

Thiophenol in $CD_2Cl_2$ at 180 K:

The concentration study and the DOSY derived volumes let suggest that thiophenol is present as a monomer in solution (Figure 2.60). According to Hunter, the S-H group is a poor hydrogen bond donor and acceptor (chapter 2.6.4.4), which confirm these results.
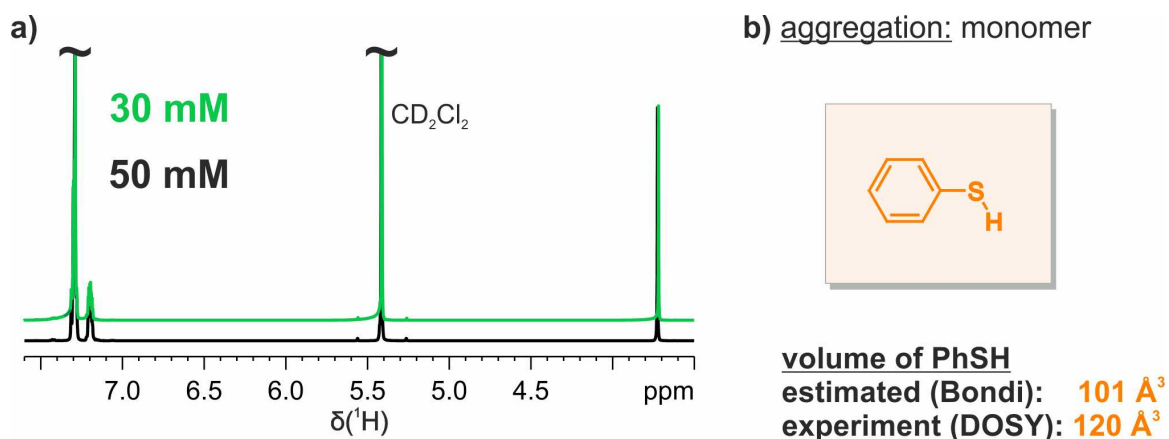
a)

b) aggregation: monomer



volume of PhSH
estimated (Bondi): 101 Å³
experiment (DOSY): 120 Å³

**Figure 2.60:** a) The $^1$H NMR spectra of thiophenol at 180 K show no chemical shift changes for 30 and 50 mM; b) including DOSY derived volumes the PhSH monomer is verified.

**2.6.5.5 Two-Component Mixtures**

$^{15}$*N*-Phenylpent-4-enamide + tetrabutylammonium di-*tert*-butylphosphate in CD$_2$Cl$_2$ at 180 K:

According to Hunter, a hydrogen bond mediated interaction between amide and phosphate is favored because of the high acceptor and donor abilities of the phosphate anion and the amide functionality (see chapter 2.6.4.4). The formation of a N-H···O-P hydrogen bond was already identified by low temperature $^1$H, $^{15}$N and $^{31}$P hydrogen bond analysis (see main text). The experimentally determined volumes assume an overall high complexation in solution (Figure 2.61). As only one $^{31}$P signal is present for this sample being high field shifted in comparison to the pure phosphate, a large hydrogen bonded amide-phosphate complex is assumed. The reduced volumes for phosphate compared to the amide suggests additional high complexation of amide molecules with each other (*vide supra*). As for the pure base, comparing the DOSY derived volumes, the ammonium cation is supposed to be partially dissociated from the phosphate, in general.
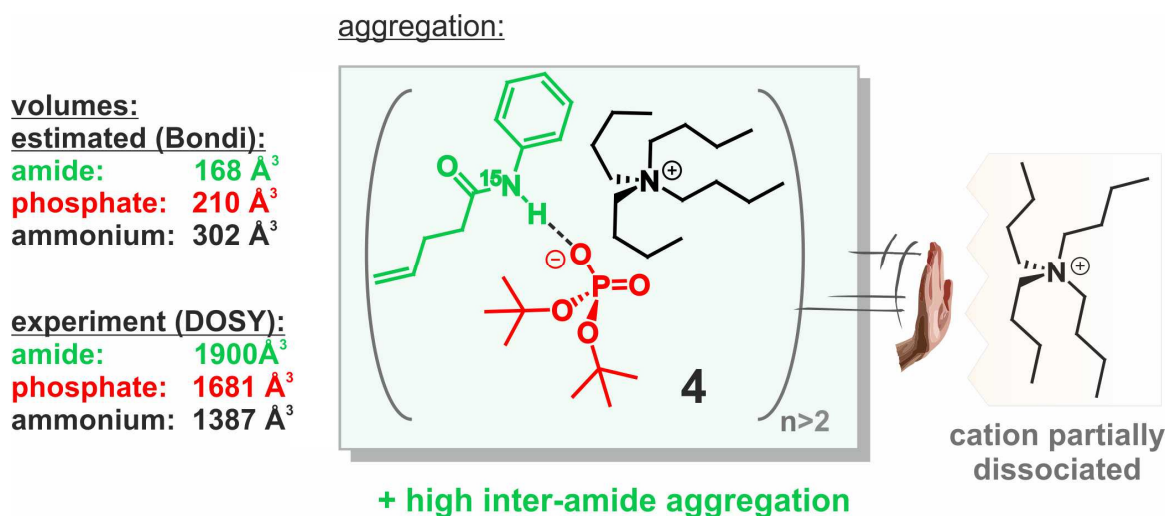


**volumes:**
**estimated (Bondi):**
amide:          168 Å$^3$
phosphate:   210 Å$^3$
ammonium:  302 Å$^3$

**experiment (DOSY):**
amide:          1900 Å$^3$
phosphate:   1681 Å$^3$
ammonium:  1387 Å$^3$

aggregation:

**4**

n>2

**+ high inter-amide aggregation**

cation partially dissociated

**Figure 2.61:**  Including all 1D NMR, NOESY and DOSY investigations a large hydrogen bond mediated complex with partial release of the ammonium counterion is proposed. In addition, high inter-amide complexation is observed via DOSY.

Thiophenol + tetrabutylammonium di-*tert*-butylphosphate in CD$_2$Cl$_2$ at 180 K:

As already investigated in chapter 2.6.4.1, an acid-base reaction takes place whenever thiophenol and di-*tert*-butylphosphate are present. The generated phosphoric acid leads to the formation of phosphate dimer **1** (see $^1$H, $^{15}$N and $^{31}$P NMR studies in the main text and chapter 2.6.4.1 of the SI). The further high field shift of the $^{31}$P signal in comparison to the amide/base system predicts high electron density being located on the phosphate (see main text and the spectra in chapter 2.6.4.7 of the SI). In the $^1$H NMR spectra of all PhSH and base containing mixtures the signal of the proton inside the strong P-O···H···O-P bond is located at 16.49-16.50 ppm (see main text and chapter 2.6.4.5 in the SI). Regarding the DOSY measurements, the volume for thiophenol verifies to be mainly free in solution with partial formation of thiolate according to the mentioned acid-base reaction (Figure 2.62). Furthermore, in comparison with the pure base, the volumes for phosphate and ammonium are in general reduced indicating a partial break of the phosphate-ammonium complex. But the ubiquitous size difference between both species was immensely increased corroborating the release of the cation because of the formation of dimer **1**. In comparison to the amide/base mixture, ammonium`s volumes remain similar, but the phosphate is drastically enlarged in presence of PhSH, which is attributed to the dimerization of the base.
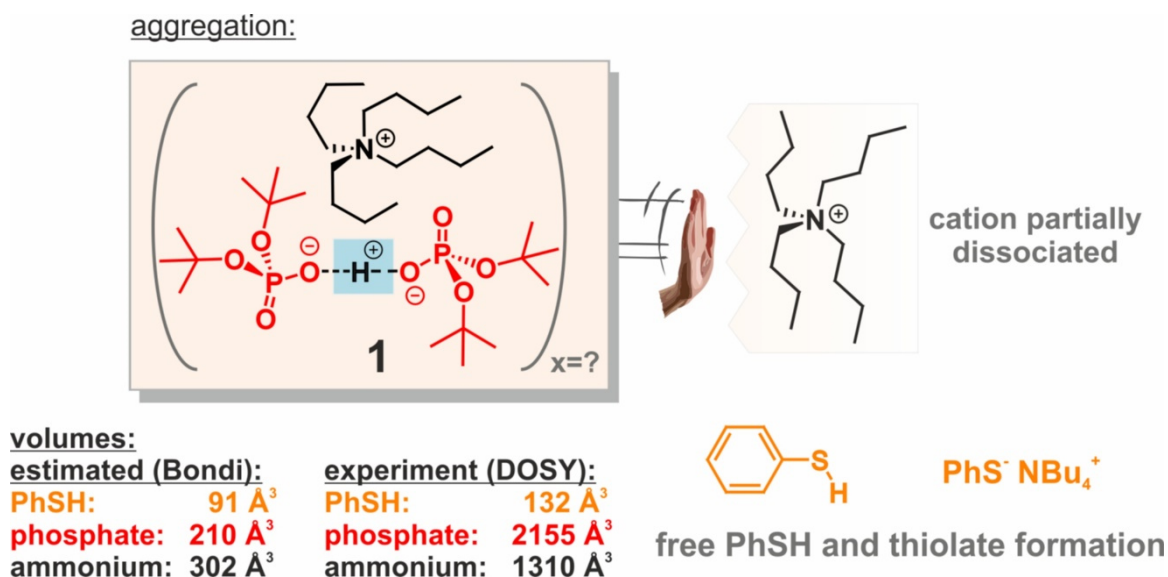


aggregation:

**1**  x=?

cation partially dissociated

**volumes:**

| estimated (Bondi): | | experiment (DOSY): | |
|---|---|---|---|
| PhSH: | 91 Å$^3$ | PhSH: | 132 Å$^3$ |
| phosphate: | 210 Å$^3$ | phosphate: | 2155 Å$^3$ |
| ammonium: | 302 Å$^3$ | ammonium: | 1310 Å$^3$ |

PhS$^-$ NBu$_4^+$

free PhSH and thiolate formation

**Figure 2.62:** Including all 1D NMR, NOESY and DOSY investigations a strong hydrogen bond mediated phosphate dimer **1** was identified with partial release of the ammonium counterion as found for other mixtures. In addition, DOSY corroborates a large phosphate complex and free thiophenol.

**2.6.5.6 Three-Component Mixtures**

$^{15}$N-Phenylpent-4-enamide + tetrabutylammonium di-*tert*-butylphosphate + thiophenol in CD$_2$Cl$_2$ at 180 K:

The partial protonation of the phosphate base by thiophenol as identified for the thiophenol/base mixture was also verified in presence of the amide. This was already shown in chapter 2.6.4.1. Taking together all 1D NMR, NOESY, DOSY investigations and MD simulations, the existence of dimer **1** and an amide containing aggregate **2** were identified (Figure 2.63).

Comparing the DOSY results for the amide, which is activated inside the photocatalytic mixture, of the amide/base and amide/base/PhSH sample, interestingly, a tremendous deaggregation of the substrate was obtained. This suggests very reduced self-aggregation and a dynamic nature in the whole system, which offers an extended amount of hydrogen bond acceptor sites due to dimer **1**. Moreover, the volume of the ammonium counterion is lowest for this mixture indicating its release from the phosphate because of the dimer formation as was found for the base/PhSH sample. But these small values imply that the formed thiophenolate is only barely attached to ammonium. The thiophenol value being similar to the monomer value again verifies its monomeric behavior.

The formed phosphate-H$^+$-phosphate dimers provide an extended H-bond network with amides allowing a productive regeneration of the photocatalyst (see discussion in the main text). Thus, complex **2**, with high electron density located on the phosphates is assumed to be the crucial aggregate for an effective PCET event.

All together, thiophenol acts not only as HAT reagent but helps to generate the phosphate dimer. Furthermore, its low hydrogen bond donor ability is neccessary as it is not incorporated into the reactive complex. We hope, this study reveals the importance of analyzing the aggregation of the reaction mixture and helps for the development of new PCET mediated photoredox catalytic protocols.

aggregation:

volumes:
| estimated (Bondi): | | experiment (DOSY): | |
|---|---|---|---|
| amide: | 168 Å³ | amide: | 1309 Å³ |
| PhSH: | 101 Å³ | PhSH: | 104 Å³ |
| phosphate: | 210 Å³ | phosphate: | 1655 Å³ |
| ammonium: | 302 Å³ | ammonium: | 986 Å³ |

free PhSH and thiolate formation

basic complex with mostly released
ammonium cation

further existing aggregates
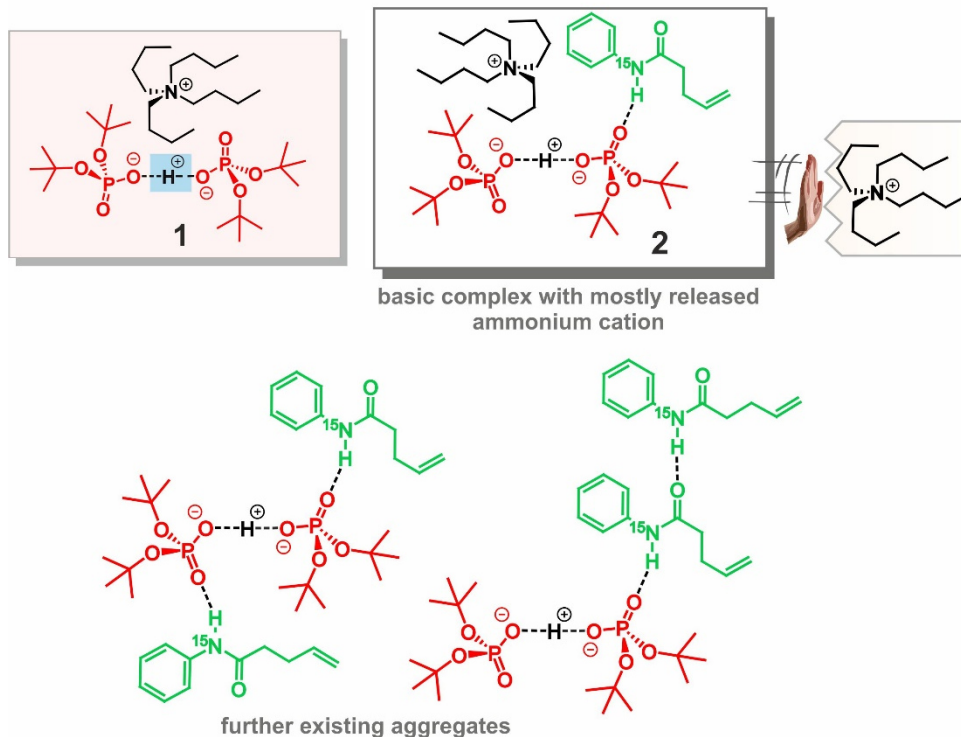
**Figure 2.63:** Including all results from 1D NMR, NOESY, DOSY investigations and MD simulations phosphate dimer **1** and the crucial amide containing complex **2** were identified with partial release of the ammonium counterion as found for other mixtures. Further aggregates including more than one amide corroborate an extended H-bond network. In addition, DOSY corroborates free thiophenol in solution.

[15]N-Phenylpent-4-enamide + tetrabutylammonium di-*tert*-butylphosphate + phenol in CD₂Cl₂ at 180 K:

In Figure 2.64, the DOSY derived volumes indicate high aggregation of amide, phenol and ammonium. Taking together all results from 1D NMR and DOSY analysis, phenol seems to be fully incorporated into the amide/base complex (see discussion in the main text). And, very importantly, no phosphate dimer is formed. Thus, the hydrogen bond donor ability and its incapability of modulating the electron density of the phosphate in an effective manner by generating the dimer is assumed to be one reason for being inefficient

for photoredox catalytic hydroamidation, besides its different radical and HAT properties compared to PhSH.
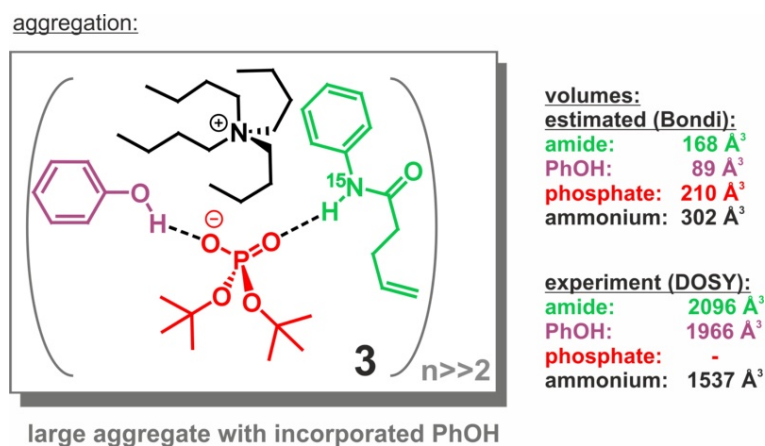


**Figure 2.64:** Including all 1D NMR and DOSY investigations the formation of complex **3** with phenol being incorporated into the amide/base complex is identified. The lack of phosphate dimer 1 and the hydrogen bond donor ability of phenol seem to be one reason for an ineffective PCET.

## 2.6.6 Molecular Dynamics Simulations

Methods:

All simulations were performed using Gromacs version 2018.[27] All molecular topologies were prepared with acpype[28] based on the General Amber Force Field (GAFF)[29]. Partial atomic charges were determined from HF/6-31G* wave functions with CHelpG[30] using the Orca 4.1.2 quantum chemical program[31]. The Lennard-Jones parameters for the Cl atom in the dichloromethane solvent were slightly adjusted (s = 0.33 nm, e = 1.2 kJ/mol) for reproducing the correct solvent density at 300 K. Van der Waals interactions were cut off above 1 nm and electrostatic interactions were determined with the smooth particle-mesh Ewald summation method. Simulations with different content of phenole, thiophenole, thiophenolate, *tert*-butyl phosphoric acid, hydronium, hydroxide, and water were performed. The phosphoric acid is presumably formed in an acid-base reaction between thiophenol and phosphate base. Table 2.2 gives a summary of the studied system compositions. All simulations were performed at 200 K temperature and 1 bar pressure using stochastic velocity rescaling[32] and a Parrinello-Rahman barostat[33]. All simulation times were 1 ms, configurations were saved every 50 ps. The first 200 ns were discarded for equilibration and the remaining 800 ns were used for analysis.

**Table 2.2:** System compositions (number of molecules) of the seven studied reaction mixtures (Sim = 1 - 7).  $H_3O^+$ = H3O, $OH^-$ = OH, phenol = PH, thiophenol = SPH, $H_2O$ = WAT, amide = AMD, $NBu_4^+$ = NB4, phosphoric acid = PHA, phosphate = PHO, thiophenolate = SPM, $CH_2Cl_2$ = DCM.

| Sim | H3O | OH | PH | SPM | WAT | AMD | NB4 | PHO | SPH | PHA | DCM |
|---|---|---|---|---|---|---|---|---|---|---|---|
| 1 | 0 | 0 | 27 | 0 | 0 | 27 | 27 | 27 | 0 | 0 | 6581 |
| 2 | 0 | 0 | 0 | 0 | 0 | 27 | 27 | 27 | 27 | 0 | 6581 |
| 3 | 0 | 0 | 0 | 0 | 27 | 27 | 27 | 27 | 27 | 0 | 6581 |
| 4 | 5 | 5 | 0 | 0 | 27 | 27 | 27 | 27 | 27 | 0 | 6581 |
| 5 | 5 | 0 | 0 | 5 | 27 | 27 | 27 | 27 | 22 | 0 | 6581 |
| 6 | 27 | 0 | 0 | 27 | 27 | 27 | 27 | 27 | 0 | 0 | 6581 |
| 7 | 13 | 0 | 0 | 27 | 27 | 27 | 27 | 13 | 0 | 14 | 6581 |

All diffusion constants were determined from the center of mass trajectories using the Einstein relation, $\langle r^2 \rangle = 6Dt$, with averaging over all present molecules of the given type and restarting the analysis every 10 ps. The slopes of the $\langle r^2 \rangle(t)$ data were determined for lag times up to 50 ns by linear regression. The diffusion constants were normalized by the $CH_2Cl_2$ diffusion constant obtained for the respective simulation, which is between $1.3143*10^{-9}$ $m^2$/s and $1.3615*10^{-9}$ $m^2$/s (which is approximately a factor of 2 to large compared to the experimental diffusion constant[34]).

Hydrogen bonds were determined following the Luzar-Chandler criterion for water-water hydrogen bonds[35]: donor-acceptor distance lower than 3.5 Å and donor-H-acceptor angle lower than 30°.

Results:

Aggregate structures in the reaction media comprise a huge variety of hydrogen-bonded (and furthermore also otherwise connected) pairs, triples, and larger aggregates. The chosen sampling approach is able to provide a look into the manifold of aggregate compositions in the solution.

The complete analysis of the aggregation in the seven different simulation systems is far too complex for a full analysis, and in the following we focus on observations that relate to the scope of this work – the existence of the aggregates observed by NMR and the weakening or strengthening of the amide-phosphate hydrogen bonds. Here, the simulations give an independent view that also allows to have a look at H-bonds involving thiophenolate as acceptor, which cannot be directly detected on the acceptor side by NMR

(see chapter 2.6.4.1). Figure 2.65 shows the average number of hydrogen bonds between amides and phosphates for the simulations 1-7. The most remarkable effect is seen when significant amounts of thiophenolate are present (simulation 6 and 7). In accordance with the disaggregation effect observed in the DOSY studies upon addition of thiophenol (see Figure 2.4, main text), the average number of amide-phosphate hydrogen bonds decreases when 27 thiophenolates are present (15.3 to 22.6 in the absence of thiophenolate compared to 8.8 in its presence for simulation 6).
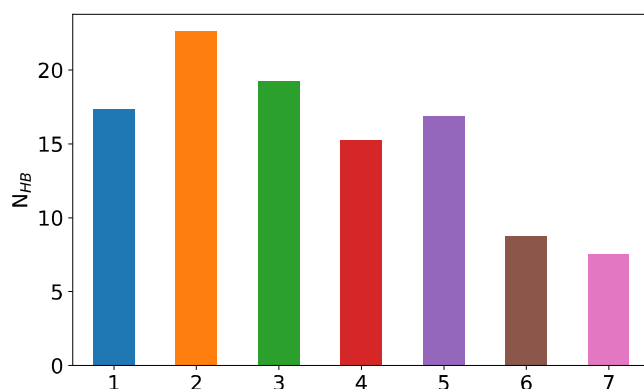


**Figure 2.65:** Average number of amide-phosphate hydrogen bonds ($N_{HB}$) in simulations 1-7. Note that in simulation 7 there are only 13 phosphate ions present compared to 27 in simulations 1-6.

Figure 2.66 shows a selection of PCET relevant aggregates observed for the mixture containing 14 *tert*-butyl phosphoric acid molecules. In general, phosphate dimer **1** could frequently be found in different frames of the snapshots derived by MD simulation. Figure 2.66a shows two randomly picked snapshots of our proposed crucial complex **2** containing the phosphate dimer and one amide attached. Those structures directly confirm our results obtained by NMR in a descriptive way. Moreover, aggregates including the dimer and two amides hydrogen bonded in a row were found and are depicted in Figure 2.66b. This structural motif corroborates further H-bond cooperativity leading to an enhanced hydrogen bond strength and thus to a facilitated activation of the amide. Furthermore, not only one amide can be attached to the phosphate dimer **1**. As there are multiple hydrogen bond acceptor positions, an extended network can be created. One possibility, which could be directly found by the MD simulations (Figure 2.66c), is the sterically demanding attachment of two amides on both sides of the dimer. We propose such network to be partially responsible for the overall reduction of the H-bond strength identified by ^{1}H and ^{15}N NMR (see discussion in the main text) as its geometrical nature leads to a lengthening of the N-H···O-P hydrogen bond. Furthermore, structures like depicted in Figure 2.67 were found for a system including $H_3O^+$. The attached amide points outward of the complex

regarding the N-H group. As residual water is present in the mixture these structures corroborate the reduction of the N-H chemical shift in the $^1$H and $^{15}$N spectra (see main text). But on the other hand, the amide cannot be activated via PCET and therefore these structural motifs do not account for enhanced reactivity. Moreover, as shown in chapter 2.6.5.1, the small signal of the postulated H$_3$O$^+$ involved structure is not affected in presence of PhSH.
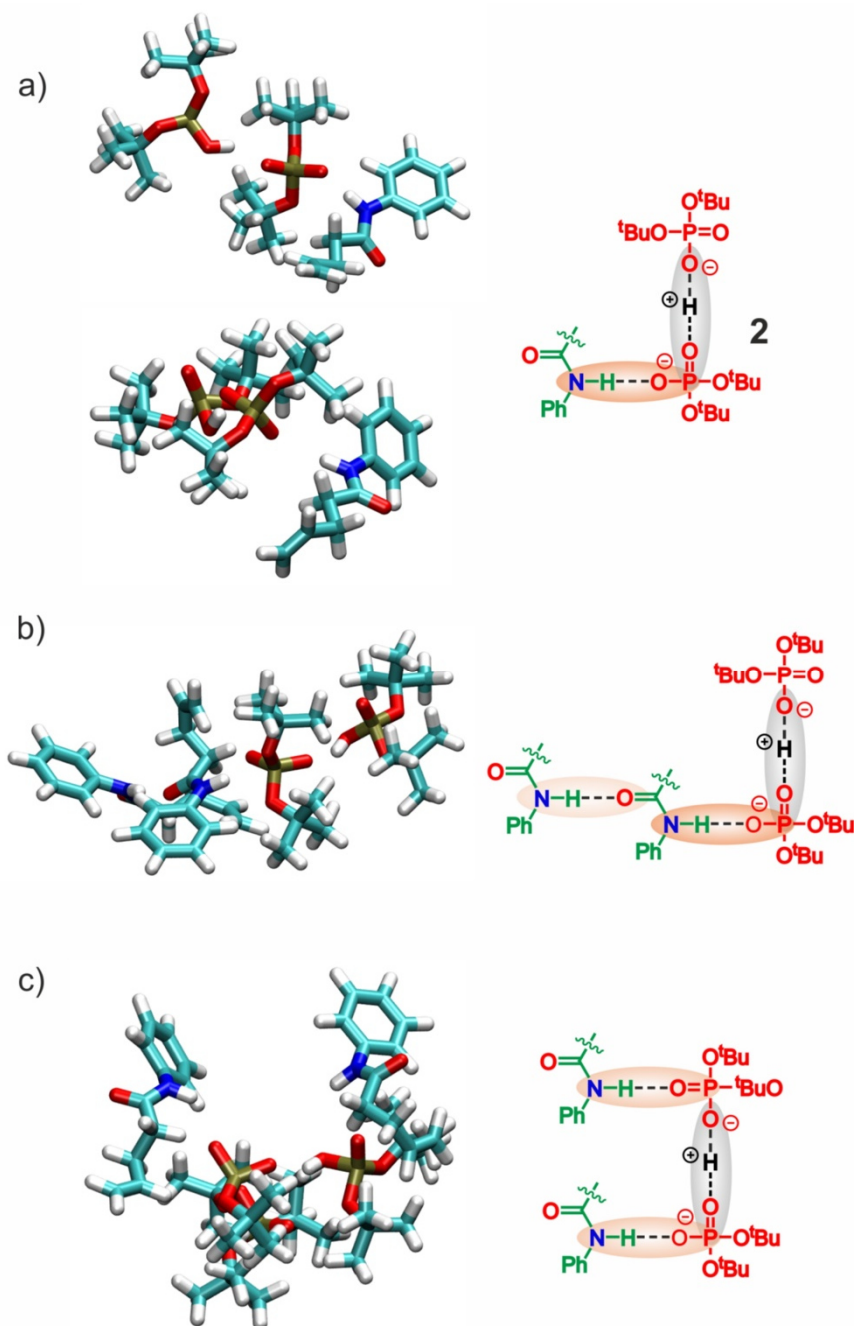


**Figure 2.66:** Selected PCET relevant aggregates a) - c) including phosphoric acid (PHA), amide (AMD) and phosphate (PHO) observed in the simulations. Shown are results from simulation 7.
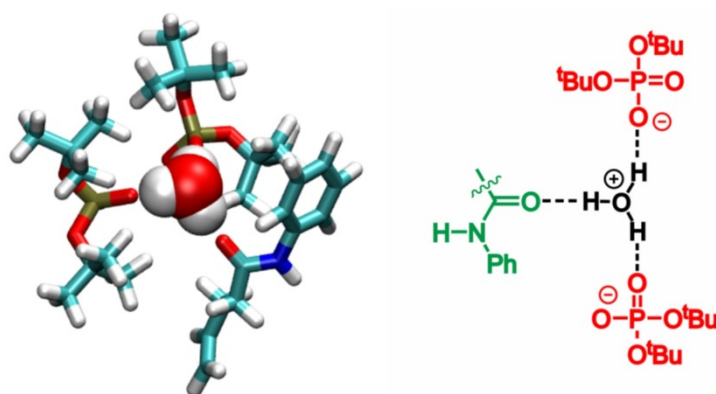
**Figure 2.67:** Aggregate including $H_3O^+$ (H3O), amide (AMD) and phosphate (PHO) observed in simulation 6.

In order to obtain more information about the role of thiophenolate inside the reaction mixture, the MD derived diffusion coefficients are opposed for the simulations 1-7 in Figure 2.68. The observed diffusion constants of thiophenolate are drastically smaller than the ones of thiophenol, which indicates its incorporation into a large complex because of its charged character.
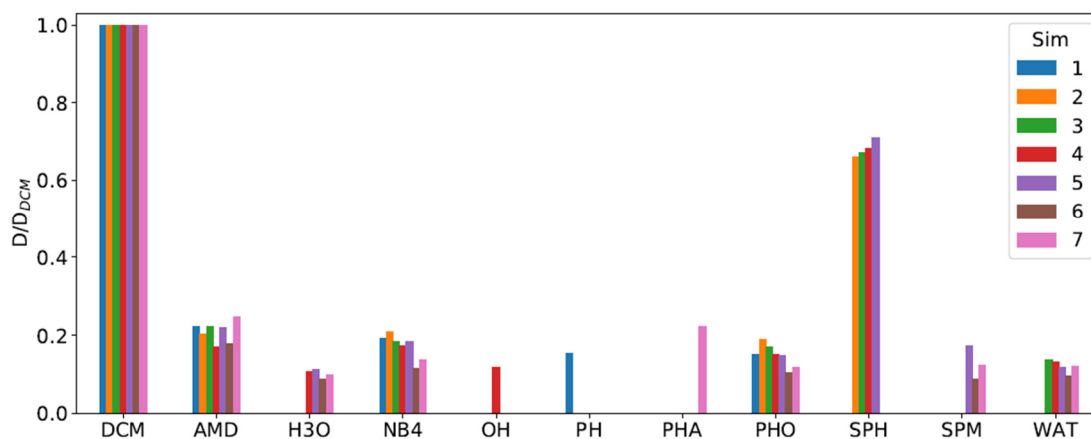


**Figure 2.68:** Diffusion constants normalized by the dichloromethane diffusion constants obtained from the respective simulation.

### 2.6.7 Emission Spectroscopy

Method:

A Fluorolog 3-22 spectrometer (Horiba Jobin Yvon) in combination with a multichannel scaler PCI card from FAST ComTec (time resolution 250 ps) and a pulsed diode laser (Picobrite PB-375L) with an excitation wavelength of $\lambda_{exc}$ = 378 nm (pulse width < 100 ps) was used to determine the emission decays. Because of the high optical densities of the sample, the experiments were performed in reflectance geometry, i.e. the detected emission direction was parallel to the cuvette window normal, whereas the excitation laser beam hit the same cuvette window under an angle of roughly 45° with regard to the window normal and thus the propagation direction of the emission detected.

A solution of 3,3-dimethyl-*N*-phenylpent-4-enamide (1 equiv.; 100 mM), diphenyldisulfide (1 equiv.; 100 mM), tetrabutylammonium di-*tert*-butylphosphate (1 equiv.; 100 mM) and $Ir(dF(CF_3)ppy)_2(bpy)PF_6$ (0.02 equiv., 2 mM) in $CH_2Cl_2$ was degassed in a cuvette using freeze-pump-thaw technique. After measuring the emission decay the cuvette was opened to add 0.3 equiv. of phosphoric acid dibutylester for the second decay curve and additional 0.6 equiv. for the third curve (Figure S69). The solution was again degassed for each emission decay curve.
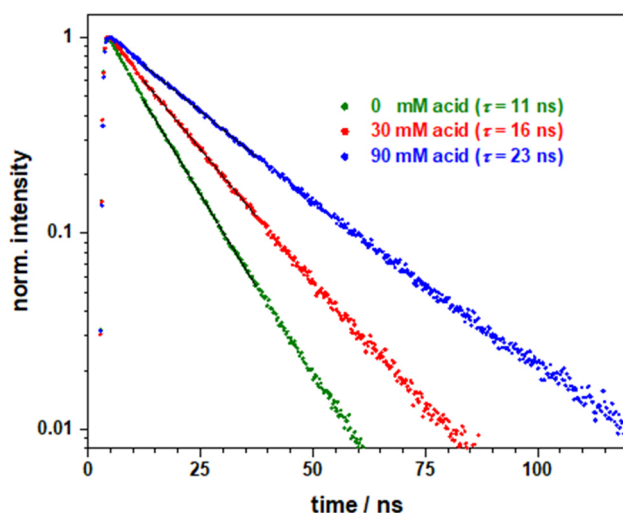


**Figure 2.69:** Emission decay curves and decay times of the iridium photocatalyst (*c* = 2 mM) at a detection wavelength of 500 nm in a degassed $CH_2Cl_2$ solution of substrate (1 equiv.; *c* = 100 mM), base (1 equiv.), diphenyldisulfide (1 equiv.) and the different amounts of acid as given in the figure legend.

## 2.6.8  References

[1]  G. R. Fulmer, A. J. M. Miller, N. H. Sherden, H. E. Gottlieb, A. Nudelman, B. M. Stoltz, J. E. Bercaw, K. I. Goldberg, *Organometallics* **2010**, *29*, 2176–2179.

[2]  D. C. Miller, G. J. Choi, H. S. Orbe, R. R. Knowles, *J. Am. Chem. Soc.* **2015**, *137*, 13492–13495.

[3]  M. R. Manzoni, T. P. Zabawa, D. Kasi, S. R. Chemler, *Organometallics* **2004**, *23*, 5618–5621.

[4]  G. Wang, Y. Zou, Z. Li, Q. Wang, A. Goeke, *J. Org. Chem.* **2011**, *76*, 5825–5831.

[5]  C. Feldmeier, H. Bartling, E. Riedle, R. M. Gschwind, *J. Magn. Reson.* **2013**, *232*, 39–44.

[6]  R. K. Harris, E. D. Becker, S. M. Cabral de Menezes, R. Goodfellow, P. Granger, *Pure Appl. Chem.* **2001**, *73*, 1795–1818.

[7]  N. Sorgenfrei, J. Hioe, J. Greindl, K. Rothermel, F. Morana, N. Lokesh, R. M. Gschwind, *J. Am. Chem. Soc.* **2016**, *138*, 16345–16354.

[8]  D. Jansen, J. Gramüller, H. Zhu, F. Niemeyer, T. Schaller, M. C. Letzel, S. Grimme, R. M. Gschwind, J. Niemeyer, *submitted.*

[9]  A. V. Joshi, S. Bhusare, M. Baidossi, N. Qafisheh, Y. Sasson, *Tetrahedron Lett.* **2005**, *46*, 3583–3585.

[10]  X. Qiu, X. Yang, Y. Zhang, S. Song, N. Jiao, *Org. Chem. Front.* **2019**, 1–5.

[11]  A. V. Joshi, S. Bhusare, M. Baidossi, N. Qafisheh, Y. Sasson, *Tetrahedron Lett.* **2005**, *46*, 3583–3585.

[12]  C. A. Hunter, *Angew. Chemie - Int. Ed.* **2004**, *43*, 5310–5324.

[13]  A. Jerschow, N. Müller, *J. Magn. Reson.* **1997**, *375*, 372–375.

[14]  E. J. Cabrita, S. Berger, *Magn. Reson. Chem.* **2002**, *39*, S142–S148.

[15]  T. D. W. Claridge, in *High-Resolution NMR Tech. Org. Chem.*, **2009**, pp. 303–334.

[16]  C. S. Johnson Jr., *Prog. Nucl. Magn. Reson. Spectrosc.* **1999**, *34*, 203–256.

[17]  W. S. Price, *Concepts Magn. Reson.* **1998**, *10*, 197–237.

[18]  E. O. Stejskal, J. E. Tanner, *J. Chem. Phys.* **1965**, *42*, 288–292.

[19]  A. Macchioni, G. Ciancaleoni, C. Zuccaccia, D. Zuccaccia, *Chem. Soc. Rev.* **2008**, *37*, 479–489.

[20]  D. Zuccaccia, A. Macchioni, *Organometallics* **2005**, *24*, 3476–3486.

[21]  H. C. Chen, S. H. Chen, *J. Phys. Chem.* **1984**, *88*, 5118–5121.

[22]  D. Ben-Amotz, K. G. Willis, *J. Phys. Chem.* **1993**, *97*, 7736–7742.

[23]  A. Bondi, *J. Phys. Chem.* **1964**, *68*, 441–451.

[24]  C. P. Butts, C. R. Jones, E. C. Towers, J. L. Flynn, L. Appleby, N. J. Barron, *Org. Biomol. Chem.* **2011**, *9*, 177–184.

[25]  E. A. Meyer, R. K. Castellano, F. Diederich, *Angew. Chemie Int. Ed.* **2003**, *42*, 1210–1250.

[26]  T. Steiner, *Angew. Chemie - Int. Ed.* **2002**, *41*, 48–76.

[27]  M. J. Abraham, T. Murtola, R. Schulz, S. Páll, J. C. Smith, B. Hess, E. Lindah, *SoftwareX* **2015**, *1–2*, 19–25.

[28]  A. W. Sousa da Silva, W. F. Vranken, *BMC Res. Notes* **2012**, *5*, 1–8.

[29]  J. Wang, R. M. Wolf, J. W. Caldwell, P. A. Kollman, D. A. Case, *J. Comput. Chem.* **2004**, *25*, 1157–1174.

[30]  C. M. Breneman, K. B. Wiberg, *J. Comput. Chem.* **1990**, *11*, 361–373.

[31]  F. Neese, *WIREs Comput. Mol. Sci.* **2012**, *2*, 73–78.

[32]  G. Bussi, D. Donadio, M. Parrinello, *J. Chem. Phys.* **2007**, *126*, 1–7.

[33]  M. Parrinello, A. Rahman, *J. Appl. Phys.* **1981**, *52*, 7182–7190.

[34]  F. X. Prielmeier, H. D. Ludemann, *Mol. Phys.* **1986**, *58*, 593–604.

[35]  A. Luzar, D. Chandler, *Phys. Rev. Lett.* **1996**, *76*, 928–931.

# 3 Metal-free, Photocatalytic PCET-Induced Ring-Opening Remote Functionalization of Cyclo-Alkanols by Direct Intermolecular C-C-Coupling with Olefins – Beyond Simple pKa-related Base Effects
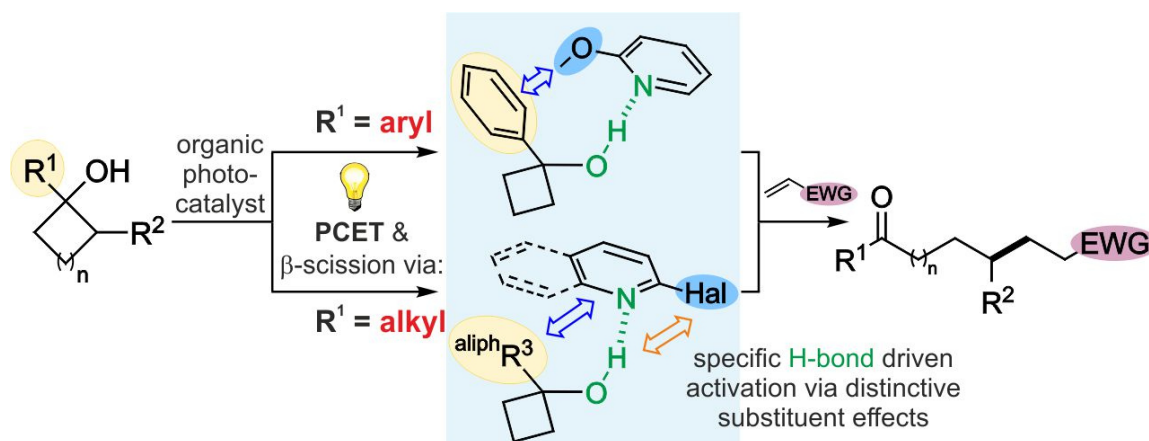


Michael Klimkait, **Nele Berg**, Ruth M. Gschwind, Kirsten Zeitler

*to be submitted*

The extended NMR mechanistic studies were conducted and evaluated by Nele Berg. Nele Berg performed the low temperature H-bond studies, DOSY experiments, the *in-situ* and *ex-situ* kinetics. The NMR based and mechanistic parts and of the manuscript and parts of the Conclusion were written by Nele Berg and Prof. Ruth Gschwind and discussed with Prof. Kirsten Zeitler. The related NMR based Figures in the manuscript and Supporting Information were designed by Nele Berg. The "Additional Findings" were written by Nele Berg. Introduction and the synthetic part of the manuscript were written by Prof. Kirsten Zeitler and Michael Klimkait. Michael Klimkait is responsible for the reaction design, the optimization of the conditions, the synthesis of the substrates and the substrate scope.

Text and Figures may differ from the original Manuscript.

## 3.1 Abstract

Herein, we report the redox-neutral photocatalytic cascade transformation of cyclic alcohols to terminally C(sp$^3$)-C(sp$^3$)-coupled, functionalized open-chain products. Initial key step of this operationally simple methodology is the base-promoted, oxidative proton-coupled electron transfer (PCET) activation of strong O-H bonds under metal-free photocatalytic conditions with visible light. The ring fission of the generated alkoxy radical yields a terminal nucleophilic ω-keto alkyl radical, which subsequently undergoes direct C-C coupling with electron-poor olefins furnishing distal alkylation products. Our approach allows for the selective activation of inert carbon-carbon bonds by cleavage of vicinal β-C-C bonds after *in-situ* generation of alkoxy radicals. Terminal radicals accessed by these ring-openings undergo the subsequent Giese-type addition to a great variety of electron-deficient alkenes in a polarity-matched process. NMR-based mechanistic studies have elucidated the crucial role of the base in this multisite MS-PCET, which exceeds typical p$K_a$-related and/or steric effects. Our gained insights into the key importance of additional weak interactions to promote a pivotal productive alcohol-base pre-organization could directly be put into practice to pioneer the successful transformation of formerly challenging alkyl-substituted cycloalkanols.

## 3.2 Introduction

Cyclic alcohol structural elements are ubiquitous in natural products and drugs. Hence, the ability to selectively target their O-H groups holds great potential for their unique late-stage functionalization and diversification.[1] The majority of typical known manipulation either involves their oxidation or the formation of novel C-O bonds. However, approaches using the O-H function as an ultimate handle for challenging scaffold reorganization or remote functionalization remain largely underexplored.

Selective homolysis of strong O-H bonds (~105 kcal/mol)[2] offers a powerful tool for generating highly reactive and synthetically valuable alkoxy radicals. Typical applications of these versatile intermediates include an unique approach for 1,5-hydrogen atom transfer (1,5-HAT) or the subsequent β-bond scission to selectively activate inert C-C bonds.[3] The cleavage of such β-C-C bonds of alkoxy radicals in cycloalkanols results in the concurrent formation of a carbonyl moiety and a corresponding carbon centered radical, which may be further transformed to afford a great variety of distally functionalized ketones.
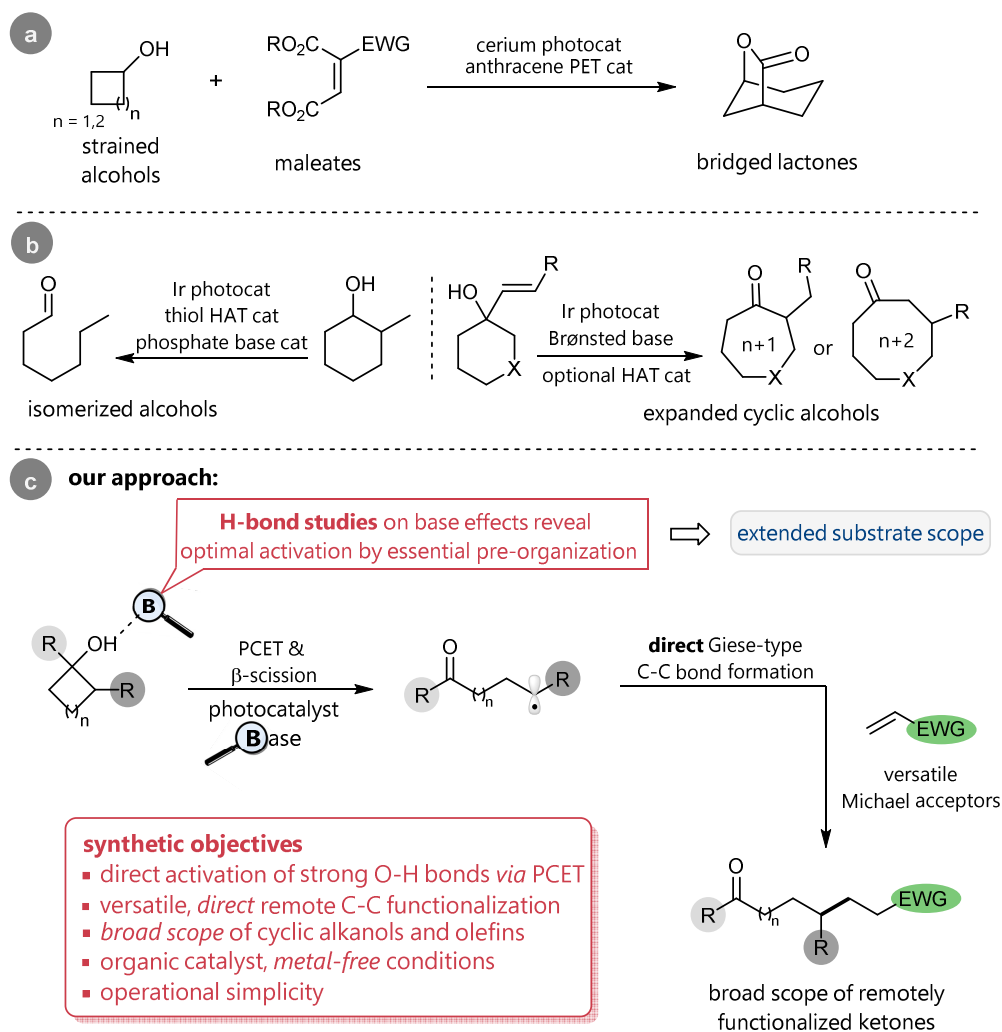
**Figure 3.1:** Ring opening of cyclic alcohols enabled by photoactivation of strong O-H bonds; a) Strained alcohols to bridged lactones;[9b] b) HAT-terminated ring-opening and expansion by Ir-catalyzed PCET;[12] c) our PCET initiated ring-opening with subsequent functionalization by terminal C-C coupling.

Despite this appealing synthetic utility and the enormous potential to broadly expand the breadth of possible bond disconnections, currently known routes to access high-energy alkoxy radicals typically either require pre-functionalized precursors,[4] harsh conditions and/or stoichiometric oxidants.[5,6]

Examples for the straightforward direct catalytic homolysis of free alcohols remain rather rare and hence limit the current practicability of this approach. In the last decade, visible light photoredox catalysis has proven to be a mild and powerful tool to access heteroatom-centered radicals via single-electron-transfer (SET).[7] Many examples for the generation of *N*-centered and carboxylic radicals are available. In contrast, only few methods for the direct activation of free alcohols have been disclosed due to their high bond dissociation energy (BDE).

Recently, Ce(III) has been used for photocatalytic activation of O-H bonds (Figure 3.1a).[8] The generation of the alkoxy radical and further ring expansion of strained cyclic alcohols (4- and 5-membered) was accomplished by a combination of LMCT (ligand-to-metal charge-transfer) and PET (photoinduced electron transfer) catalysis employing diphenylanthracene. Limited to activated maleates as coupling partners a series of bridged lactones could be obtained in a formal [5+2] cycloaddition (Figure 3.1b). An alternative, efficient approach to activate strong O-H bonds relies on the oxidative proton-coupled electron transfer (PCET) where a proton and an electron are transferred in a concerted elementary step by using a strongly oxidizing photocatalyst in combination with a Brønsted base. Knowles and co-workers could apply this concept to cyclic alcohols containing electron-rich arenes (not shown).[9] After the initial oxidation of the arene, an intramolecular PCET takes place followed by β-scission and simple trapping of the thereby formed radical by a hydrogen atom transfer (HAT).[10] More recently, they were able to extend this isomerization Figure 3.1b/left), respectively ring expansion to simple aliphatic cycloalkanols (Figure 3.1b/right).[11]

While these newer protocols cover a wide range of alcohol substrates, the requirement of an additional HAT-catalyst prevents the alkyl radical (obtained *in-situ* upon β-scission) to engage in further functionalization events, such as the synthetically important formation of new C-C bonds.[12] In addition to this current, incisive scope limitation, the employment of Ir-based photocatalysts is not only associated with elevated costs, but also may face restricted future availability. The strongly hygroscopic character of the typically used phosphate bases may pose additional challenges in handling. Consequently, a continuative catalytic method allowing for a broad scope, distal functionalization is highly desirable, best with a more facile protocol including an inexpensive and more sustainable photocatalyst. We therefore questioned whether oxidative PCET activation and subsequent selective β-scission of cyclic alcohols could be put into practice to develop a versatile method providing access to remotely functionalized ketones. In this context, especially the challenging participation of the *in-situ* generated alkyl radical in the formation of new C-C bonds caught our interest due to the potential great diversity of the corresponding products. Figure 3.1c summarizes our design plan for a versatile PCET-promoted ring-opening/remote C-C-bond forming functionalization that should additionally address practical synthetic issues, including an operationally simple protocol based on commercially available, metal-free reagents.

Initial experimentation results fueled our awareness, that identifying an appropriate combination of photocatalyst and Brønsted base would be crucial to realize this transformation and prompted us to engage in augmenting mechanistic studies. We were convinced that gaining deeper insight into the interaction of base and alcohol substrate

would improve our understanding of the key activation processes and hence would prove beneficial to find suitable reaction conditions.

Herein, we report an unprecedented, redox neutral and operationally simple protocol for the photocatalytic activation of strong O-H bonds by oxidative PCET induced, selective carbon-bond fission, and subsequent versatile, Giese type C-C bond formation.

In addition, our NMR-based H-bond studies elucidate an up-to-date rather neglected, but crucial, multifaceted role of bases in proton-coupled electron transfer processes beyond a simple p$K_a$ dependent substrate deprotonation. H-bond analysis of model bases revealed a combination of aromatic, C-H-π, and H-bond interactions as key for an effective substrate activation. This could be successfully transferred to activate challenging aliphatic substrates.

## 3.3 Results and Discussion

**General mechanistic considerations.** A prospective mechanistic proposal for our envisioned sequential transformation is outlined in Figure 3.2. Excitation of the organic photoredox catalyst **PC** by blue light should lead to the formation of a highly oxidizing excited state species.
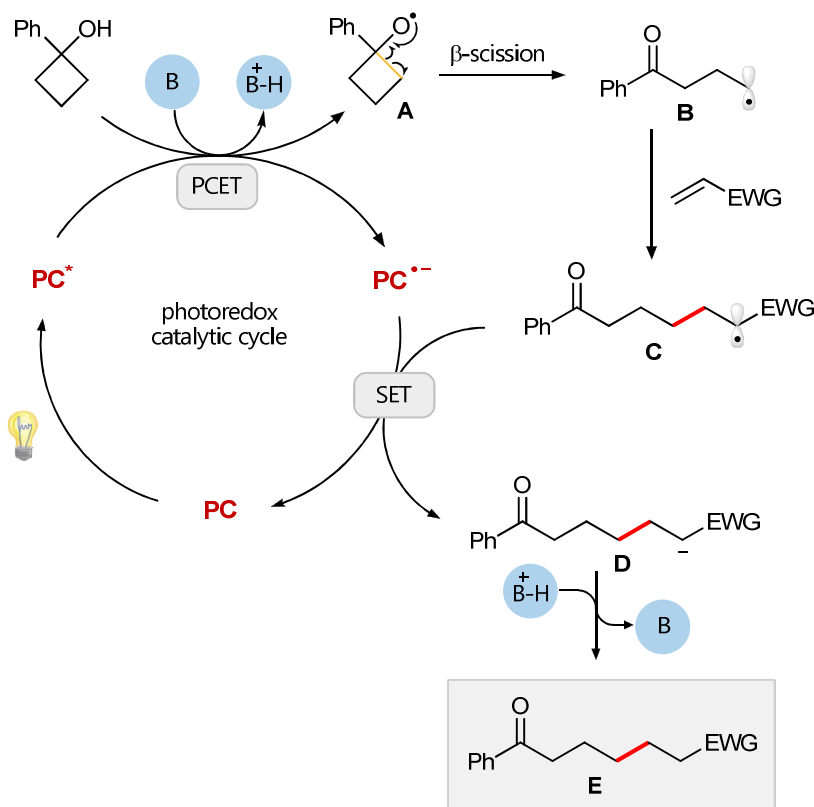


**Figure 3.2:** Proposed mechanistic course for the ring-opening/C-C-coupling sequence. PC: photocatalyst; B: base.

In combination with an appropriate base this strong oxidant **PC\*** would then generate the key alkoxy radical **A** in a PCET process, wherein oxidation and deprotonation may occur in a concerted elementary step. Upon C-C bond β-scission the nucleophilic, remote alkyl radical **B** could then further undergo conjugate addition onto an electron poor Michael acceptor in a Giese type C-C bond formation generating radical **C** in a polarity-matched process. Finally, SET reduction of the easily reducible radical **C** by the photocatalyst's reduced ground state **PC·⁻** should then yield the desired coupling product **E** after protonation and concurrently regenerate the photocatalyst **PC**.

**Basic reaction parameters and optimization.** We first examined the proposed ring opening and conjugate addition with 1-phenylcyclobutanol **1** as the radical precursor, and benzylidene malononitrile **2** as the Michael acceptor (Table 3.1). Following our synthetic objectives, we initially focused on highly oxidizing organic photocatalysts in combination with different commercially available pyridine bases. To effect this challenging direct activation of strong O-H bonds, we hoped to benefit from the already existing pool of comparable data for such pyridines, including p$K_a$ values in different solvents together with their well-studied H-bond interaction behavior,[13] contributing to an improved mechanistic insight for our target transformation.

Using a combination of the well-established organic photocatalyst **MesAcrClO₄** together with 2-methoxypyridine **5**, we were pleased to obtain the desired product in excellent yield (entry 2). Replacment of **MesAcrClO₄** against the more stable **Mes₂Acr$^t$Bu₂BF₄** as a photocatalyst[14] resulted in almost quantitative yield (entry 1). A survey of different bases revealed that 2-methoxypridine clearly outperformed any tested alternative pyridine base (entries 3-5).

Interestingly, the performance trends of the different pyridines are out of tune with their corresponding p$K_a$ values (for a comprehensive discussion, see section "NMR investigations"). Lowering the amount of water as a co-solvent resulted in a considerable decrease in efficiency (entries 6 and 7). Further control reactions showed product formation without base in the presence of water (entry 8), whereas without water and base no product was observed (entry 9). Importantly, this indicates a crucial role of water in this transformation. Water itself may serve as a proton transfer reagent and, in addition typically increases the rate constant for β-scission due to the higher solvent polarity and therefore the greater stabilization of the more polar transition state for β-scission by solvation.[4h] Final control experiments confirmed that no reaction occurred without photocatalyst or in the absence of visible light (entries 10 and 11).
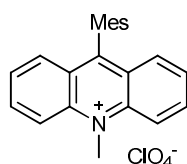
From a practical point of view it is important to note that our protocol does neither require the use of an inert atmosphere nor careful deoxygenation and thus provides great operational simplicity.

**Table 3.1:** Evaluation of reaction parameters and optimization.
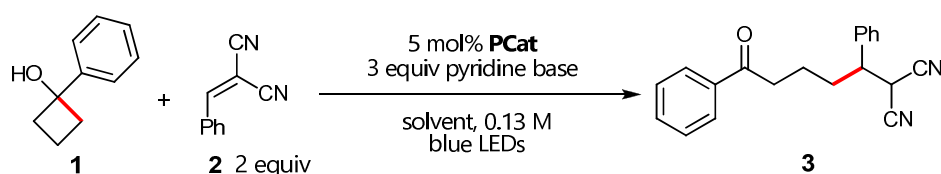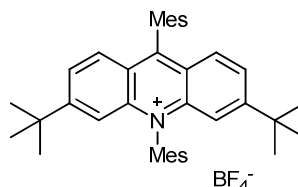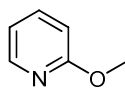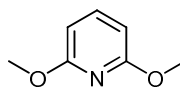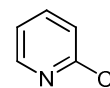


| pKₐ (in MeCN) | 12.5 | 9.9 | 7.6 | 6.8 |

| entry | conditions | yield[a] |
|---|---|---|
| 1 | **MesAcrClO₄**, 2-MeO-pyridine **5**, MeCN/H₂O 1:1 | 91%[b] |
| 2 | **Mes₂Acr^tBuBF₄**, 2-MeO-ypyridine **5**, MeCN/H₂O 1:1 | 99%[b] |
| | ***modification** from best condition/entry 2* | |
| 3 | pyridine **4** | 38% |
| 4 | 2,6-dimethoxypyridine **6** | 50% |
| 5 | 2-Cl-pyridine **7** | 65% |
| 6 | MeCN/H₂O 2:1 | 90% |
| 7 | MeCN | 40% |
| 8 | no base | 50% |
| 9 | no base and anhydrous MeCN | 0% |
| 10 | no light | 0% |
| 11 | no photocatalyst | traces |

[a] Reactions were performed on 0.1 mmol scale and a reaction time of 24 h. Yields determined by ¹H NMR using CH₂Br₂ as an internal standard. [b] Yields of isolated product on a 0.4 mmol scale after 3 h reaction time.

**Scope of electron deficient olefins.** With those optimized reaction conditions in hand, we next evaluated the scope of Michael acceptors for this remote ring opening/Giese-type C-C functionalization sequence (Table 3.2).

As depicted in Table 3.2, these mild conditions are compatible with a great variety of electron deficient alkenes. Double-activated Michael acceptors containing nitriles and esters including those bearing alkyl substitutions at the ß-position were also shown to be accommodated and reacted in good to quantitative yields (products **3**, **8**, **9**, **12**, 72-99% yield).

**Table 3.2:** Scope of electron deficient olefins.
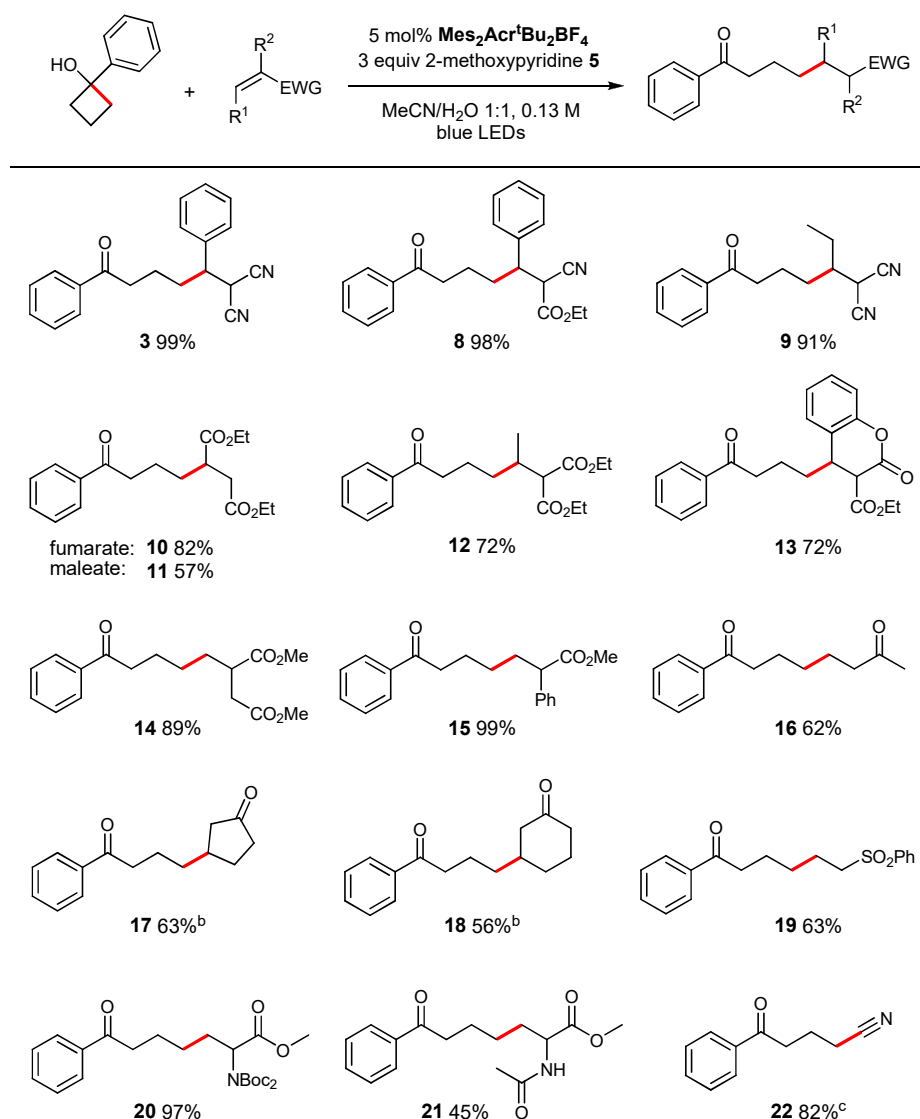


a General reaction conditions: alcohol substrate (0.4 mmol), alkene (0.8 mmol), 2-methoxypyridine (1.2 mmol), **Mes₂AcrᵗBu₂BF₄** (5 mol%) in 3 ml MeCN/H₂O 1:1, irradiated with blue LEDs. All yields are isolated yields. b 2 mmol alkene used. c TsCN (0.6 mmol) was used instead of alkene in 3 ml MeCN and 0.1 mmol H₂O.

Importantly, also only single-activated Michael acceptors such as ketones, esters and sulfones (products **14**-**19**) underwent the transformation in high yields (56-99%). A coumarin derivative was also found a suitable substrate to form **13** in good yield. Notably, dimethyl itaconate, which can be derived from itaconic acid, a sustainable biobased resource,[15] proceeded smoothly to give ketone **14** in 89%. Diethyl maleate gave 57% of the desired product whereas sterically less hindered diethyl fumarate proved to be a much more suitable acceptor olefin (82%). Tosyl cyanide as an alternative electrophilic coupling partner afforded the γ-cyanated ketone **22** in good yield.[16] Moreover, our versatile protocol could be further applied to dehydroalanine (Dha) substrates to furnish unnatural amino acids and hence offers a rich opportunity for the late stage functionalization of Dha peptides.[1] While the reaction with acetyl protected Dha resulted in 45% yield (**21**), Bis-Boc protected Dha underwent coupling in almost quantitative yield (**20**, 97%).

**Scope of cyclic alcohols.** Next, we investigated the scope of cyclic alcohols that can participate in this new protocol (Table 3.3). First we wanted to provide evidence that in the first step the reaction pathway does not require initial oxidation of the aryl substituent of cyclic alcohol by the excited state of the photocatalyst to form an arene radical cation.[10] We therefore replaced the phenyl group by an electron poor *para*-chloro substituted phenyl group without observing any loss in yield (**23**, 99%) despite an out-of-reach oxidation potential of the chloroarene part by our catalyst system. Next, we turned our attention to cyclic alcohols of varying ring sizes. A simple cylopentanol derivative could also be successfully cleaved and functionalized in good yield (product **24**). The introduction of additional methyl groups in the α-position to form a more stable alkyl radical significantly increased the yield of the desired product **25** to 98% yield. Expectedly, due to the intrinsic reversibility of the β-scission itself, the lacking ring strain of 6-membered rings and the low stability of the primary alkyl radical derived from 1-phenylcyclohexanol, only trace amounts of the desired product could be detected (product not shown). Indeed, the simple introduction of a phenyl group in the α-position to stabilize the carbon radical, formed upon selective ring scission, allows to overcoming this limitation and resulted in quantitative yield (**26**). In addition, further cyclohexanol derivatives were successfully opened and cross-coupled (products **27**-**29**). Our mild protocol could be even extended to seven and eight membered rings providing the corresponding products in very good to excellent yields (**30**, **31**). Underscoring the practicability of this protocol for the modification of more complex natural based molecules, camphor derived derivative **32** and the steroid related products **33** and **34** were obtained in good to excellent yields under our mild conditions (54-99%). These examples show the potential of this effective transformation for the selective (late-stage) functionalization and diversification of natural products and other biologically active compounds.

**Table 3.3:** Cyclic Alcohol Scope.



| starting material | product | starting material | product |
|---|---|---|---|
| | **23** 99% | | **24** 72% |
| | **25** 98% | | **26** 99% |
| | **27** 58% | | **28** 56% |
| | **29** 99% | | **30** 97% |
| | **31** 88% | | **32** 65% |
| | **33** 99%[b] | | **34** 54%[b] |
| | **35** 29%, 58%[c] | | **36** 40%[c] |
| | *via*    **37** 41%[c,d] | | |
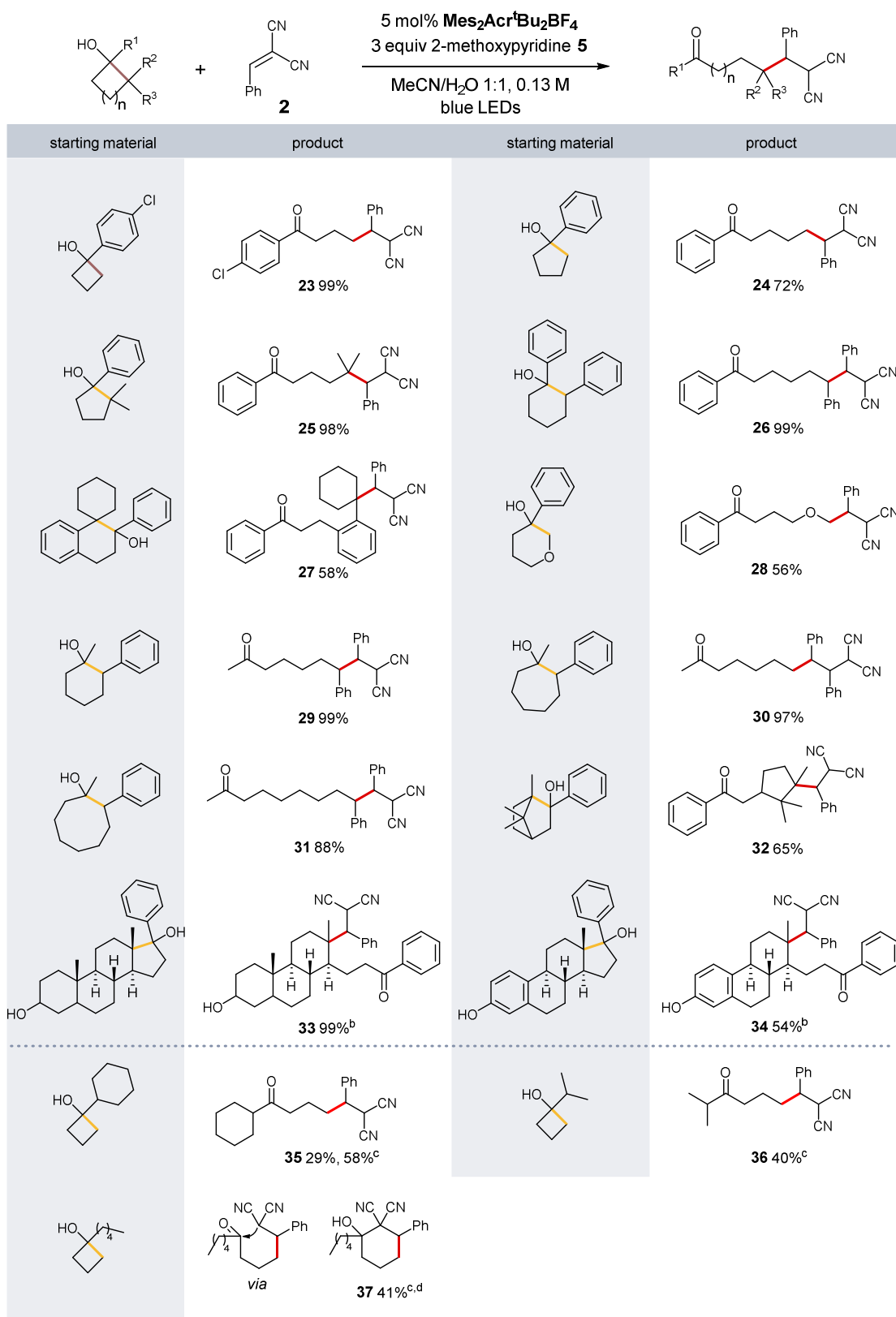
[a] General reaction conditions: alcohol substrate (0.4 mmol), alkene **2** (0.8 mmol), 2-methoxypyridine (1.2 mmol), **Mes₂Acr$^t$Bu₂BF₄** (5 mol%) in 3 ml MeCN/H₂O 1:1, irradiated with blue LEDs. All yields are isolated yields. [b] 5 mmol base used. [c] 2-chloroquinoline (0.4 mmol) was used instead of 2-methoxypyridine. [d] 1.2 mmol 2-chloroquinoline used.

However, surprisingly, alkyl substituted cyclobutanol underwent coupling to ketone **35** in only 29% yield by applying the optimized reaction conditions from Table 3.1. This result together with the gained insight that the reactivity trends of the pyridine bases **4**-**7** are not in line with their p$K_a$ values (see Table 3.1) prompted us to further investigate the base-induced alcohol activation in the context of hydrogen bond (H-bond) promoted preassemblies (as an essential part for the PCET key step) prior to our efforts to further extend the scope to alkyl substituted cycloalkanols.

**NMR investigations of the H-bond pre-assemblies.** In literature, the activation of strong bonds via PCET is postulated to occur upon formation of a strong H-bond between substrate and base.[17] In this context, the H-bond strength is often stated to go hand in hand with strong basicity of the corresponding base.[18]

However, as stated above the p$K_a$ values of our series of different pyridine bases deviate from their reacitvities and thus additional aspects have to be included for planning PCET involved activation of these strong bonds. In parallel investigations we could demonstrate that the success of the photocatalytic PCET mediated hydroamidation of *N*-phenylamides in presence of a phosphate base exceeds simple substrate-base H-bonds. The formation of a cooperative phosphate-H$^+$-phosphate based H-bond network within multiple aggregates was found to be one crucial aspect for successful transformation.[19] Hence, in order to understand the key features of activation and to apply these to potentially enlarge the substrate scope we performed a detailed NMR analysis of the H-bond situation and aggregation.

A reliable NMR analysis of individual H-bonds is only possible at very low temperatures in aprotic solvents but not in $CH_3CN/H_2O$ mixtures. Therefore, first the relative reactivity trends of the pyridines under optimal synthetic conditions in $CH_3CN/H_2O$ were proven to be consistent with those in $CH_2Cl_2$ (for details, see Supporting Information in chapter 3.6). As next step, the interactions found to be key for the reactivity in our test systems were proven to be active under synthetic conditions (see below). Therefore, the measurements of the corresponding alcohols and pyridines could be performed in dichloromethane-d$_2$ ($CH_2Cl_2$) at 180 K using 1:1 mixtures (50 mM) to reveal the key interactions based on chemical shift pattern and diffusion measurements.[20]

**Low temperature $^1$H chemical shift H-bond analysis.** First, we performed $^1$H NMR chemical shift analysis to elucidate the substituent effects of the bases for successful substrate activation and to reveal the differences between aryl- and alkyl-substituted alcohols.  Based on our experience with H-bond investigations[21] benzyl alcohol and ethanol were employed as simplified model substrates in combination with the three best performing pyridine bases **5**-**7**. In Figure 3.3a, the comparison of the resulting alcohol O-

H ^{1}H signals of both model alcohols in presence of the different bases is shown. For ethanol, the chemical shift changes of the O-H are very small. In contrast, the benzylic alcohol O-H shows a significant spreading with different bases, but follow the same trend (Figure 3.3a). In general, the H-bonds to 2-methoxypyridine are the strongest (BnOH: 5.46 ppm; EtOH: 4.76 ppm), followed by the 2-chloropyridine/alcohol (BnOH: 5.27 ppm; EtOH: 4.76 ppm) and 2,6-dimethoxy-pyridine/alcohol (BnOH: 4.83 ppm; EtOH: 4.70 ppm) mixtures.

The detected intrinsic H-bond strengths of the individual pyridines differ from the literature known basicity trends for 2-Cl-pyridine and 2,6-di-OMe-pyridine suggesting a supportive function of chlorine.[22] Moreover, the aryl-alcohol forms stronger H-bonds to pyridine than the aliphatic alcohol, which is in line with lower synthetic yields of aliphatic substrates. In addition, a high field shift of the methoxy-group in presence of aryl-alcohols suggests a distinctive interaction between the aromatic ring and the methoxy-group of the best performing 2-OMe-pyridine (see Supporting Information in chapter 3.6).

Having these fundamentals in hand, the study was extended to the synthetic substrate **1**, which showed H-bond trends and strengths similar to the benzylic alcohol test system (MeO-pyridine: 4.88 ppm; Cl-pyridine: 4.82 ppm; di-MeO-pyridine: 4.65 ppm). These trends explicitly map the relative reactivities of alcohol **1** (see Table 3.1). The pyridines are mainly free in solution (see DOSY measurements below), i.e. the discussed chemical shift changes are caused by a small amount of alcohol-pyridine complexes averaged with the whole ensemble. Hence, for the concrete O-H···N complexes we would expect by far more pronounced chemical shift changes.

The presented data show that the specific intrinsic basicities of preassemblies deviate from standard basicities and is a superior measure for substrate activation in PCET steps. The impact of substrate specific activations has recently be shown for light independent chiral ion pair catalysis,[23] but the importance of H-bond preassemblies has been neglected in photocatalysis so far.

**Analysis of the aggregates by diffusion-ordered spectroscopy (DOSY).** The chemical shifts discussed above are average values of the corresponding species in the entire ensemble, which is reflected by the existence of only one O-H proton signal in the ^{1}H spectrum even at 180 K.[24,25] Therefore, to get further insight into the composition of these preassemblies and the overall aggregation states before illumination diffusion-ordered spectroscopy (DOSY) was applied.
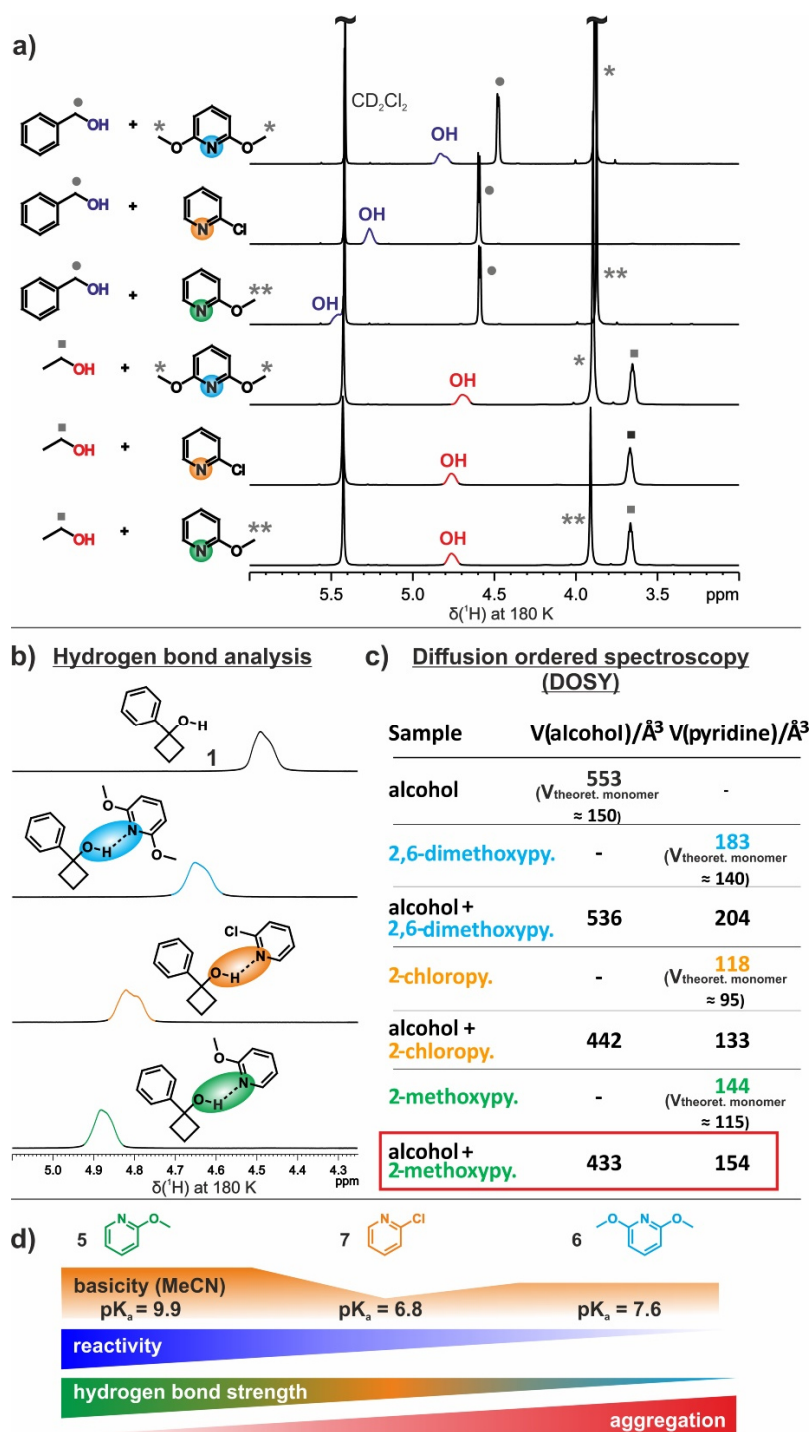
**Figure 3.3:** a) The ^{1}H chemical shift H-bond analysis of the test system including benzylic alcohol and ethanol in presence of different pyridines reveal stronger interactions for aryl-alcohols being congruent to the synthetic yields (see Table 3.1). Moreover, 2-OMe-pyridine furnished the strongest H-bonds to alcohol, followed by 2-Cl-pyridine and 2,6-di-OMe-pyridine, which contradicts the literature based $pK_a$ values. The ^{1}H NMR measurements were performed in $CD_2Cl_2$ at 180 K using 1:1 mixtures; b) the H-bond analysis of the different 1-phenylbutanol/pyridine mixtures shows an equal trend of H-bond strengths; c) the diffusion-ordered spectroscopy (DOSY) derived volumes indicate highest disaggregation of the alcohol in the OMe-pyridine mixture and only bare incorporation of the bases into the complex; d) the overview of the results for the pyridine bases includes strongest basicity, highest reactivity, strongest hydrogen bond formation and lowest aggregation of the alcohol/2-methoxypyridine mixture being crucial for successful PCET mediated alcohol activation.

Thus, DOSY was measured for alcohol **1** and the three pyridine bases **5-7** at 180 K to be able to directly compare the aggregation results with those of the H-bonds. The corresponding volumes were calculated from the experimental self-diffusion coefficients for each sample (for details of experimental setup and interpretation see Supporting Information in chapter 3.6). The results and the estimated monomer values for every species according to Bondi[26] are given in Figure 3.3c.

The alcohol **1** itself forms significant aggregates (cf. 553 Å$^3$ compared to 150 Å$^3$ of the monomer) in CD$_2$Cl$_2$. In presence of the pyridine bases this alcohol aggregate is significantly reduced. The best performing 2-methoxypyridine **5** reduces the alcohol aggregate to the greatest extent, followed by 2-chloropyridine and 2,6,-dimethoxypyridine. That and the small values of the pyridines reveal that the bases interact only partially with the alcohol via disaggregation. In acetonitrile or acetonitrile/water mixtures by far less self-aggregation of the alcohol is expected in general. However, the DOSY derived volumes suggest that the base activates not only the O-H bond but improves also the accessibility of the alcohol by the photocatalyst via disaggregation.

Altogether, the reduction of alcohol aggregation in presence of the different pyridines goes hand in hand with the alcohol/pyridine H-bond strengths and clearly follows the observed reactivities of the different bases within the synthetic transformation (Figure 3.3d and Table 3.1). The positive effect of disaggregation was already found for the acceleration of Flavin photocatalysis.[27] The pronounced alcohol self-aggregation and the mainly free pyridines in solution underline our hypothesis of an averaged O-H signal, which masks the specific substrate activating complex. Thus, the H-bond strength of our best performing BnOH/2-MeO-pyridine system (see H-bond analysis) is underestimated and the immense acceleration of the photocatalytic reaction can effectively be rationalized by intrinsic H-bond analysis.

**Implication of base effects for alkyl substrates.** The H-bond analysis revealed that beyond stronger bases aromatic moieties, C-H-π-interactions and chlorine substituents have a special effect in this transformation of cycloalkanols (for interaction pattern see Figure 3.4). Therefore, we tried as next step to benefit from this knowledge and to enlarge the substrate scope to alkyl-alcohols.

Consequently, we introduced extended aromatic motifs and halogens on the pyridine side. This should furnish the activating C-H-π and halogen interactions between the alkyl substituent of the alcohol and the aromatic base. We selected 1-cyclohexyl cyclobutanol **38** as test substrate to enlarge the potential CH-π/dispersion interface to the base.[28] A screening of ten pyridine bases with different substituents at position 2 (see Supporting Information in chapter 3.6 for details) was performed. Alkyl substituents are not effective. For the more basic alkoxy substituents enthalpic and entropic effects have to be balanced

and isopropoxy-pyridine gain a moderate yield of 31%. Halogens, CF$_3$ and CN substituents also worked up to 40% for 2-Cl-pyridine. Again these results corroborate that pure basicity is not the key factor for reactivity. The relative reactivities of the 2-substituted bases discussed give a hint for the key interactions to be a combination of basicity, a second H-bond to the substituent in 2-position and dispersion interactions. Alkoxy substituents seem to provide basicity but less favorable H-bond geometries. In contrast to that, halogens and CF$_3$ groups reduce basicity but provide superior H-bond geometry since halogens are known to form H-bonds perpendicular to the covalent bond. The reactivity analysis show that chlorine provides the best combination.
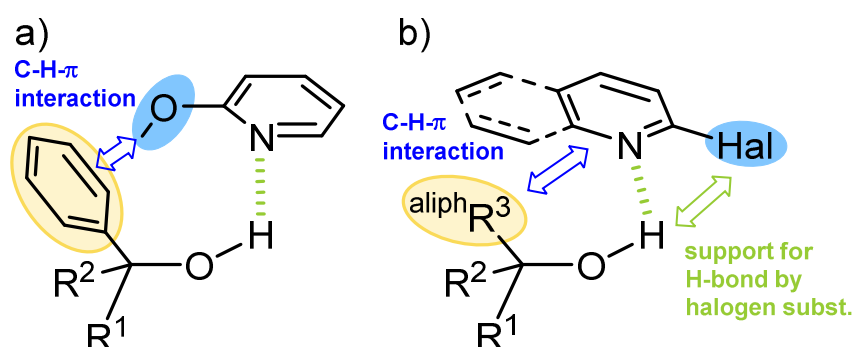


**Figure 3.4:** Substrate-base interaction pattern a) based on chemical shift changes, b) assumed on reactivity enhancements of a screening of bases (for data see Supporting Information in chapter 3.6).

To enhance the attractive dispersion interactions with enlarged aromatic systems even further and to test our interaction hypothesis, we examined nine "benzannellated pyridine derivatives". Bases without H-bond acceptor or with a fixed oxygen geometry in 2-position showed 0% yield. In contrast, for quinolines with halogens, OH or CF$_3$ groups in 2-position improved yields could be gained. Indeed, by using 2-chloroquinoline **39** instead of 2-OMe-pyridine **5** we were able to adjust our former reaction conditions to double the product formation (up to 58% yield) for the challenging, alkyl-substituted cycloalkanols (see Figure 3.5). Also Br and CF$_3$ in 2-position revealed to be effective while electron withdrawing substituents in position 8 seem to reduce the attractive dispersion interactions.

As such, the attractiv part of the extended dispersion interaction interfaces or direct stabilization effects on the H-bond by substituents can effectively overwrite p$K_a$ values as key factor for the evaluation of PCET feasibility.
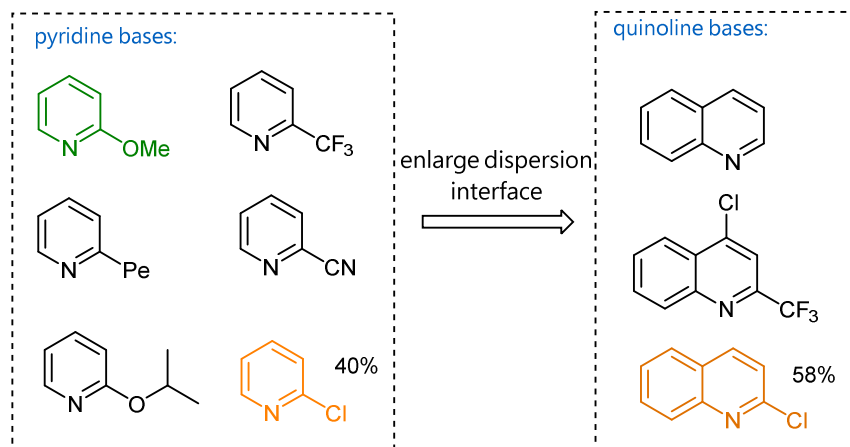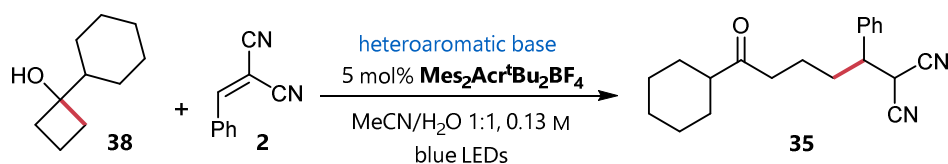
**Figure 3.5:** Compared reaction performance of pyridine and quinoline bases for transformation of 1-cyclohexyl cyclobutanol.

To demonstrate the general applicability we also successfully employed our alternative condition set to further substrates. *Iso*-propyl substituted cyclobutanol was transformed into the expected, remotely functionalized *iso*propyl ketone **36.** The C-C coupling of the less sterically encumbered *n*-pentyl substituted cyclobutanol derivative with alkene **2** was followed by a base promoted aldol-type cyclization onto the carbonyl moiety to yield cyclic product **37**.

## 3.4  Conclusion

In conclusion, we have developed a visible light induced, redox neutral oxidative PCET activation of strong O-H bonds with subsequent Giese-type addition onto a great variety of electron deficient olefins. Free cycloalkanols are photocatalytically activated under mild, metal-free and operationally simple conditions. Furthermore, the synthetic value of this protocol could be demonstrated by the late stage modification of two steroid derivatives. NMR-based H-bond and aggregation investigations revealed H-bond activations deviating from $pK_a$ values. In contrast, aromatic moieties, C-H-π-interactions and halogen substituents provide special activations in this reaction outperforming mere $pK_a$ values. Extended versions of these key interactions were used to successfully activate aliphatic

substrates. This study reveals the importance of preassemblies, dispersion interactions and substrate specific activations in photocatalysis.

## 3.5   References

[1]   Henkel, T.; Brunne, R. M.; Müller, H.; Reichel, F. *Angew. Chem. Int. Ed.* **1999**, *38*, 643.

[2]   Blanksby, S. J.; Ellison, G. B. *Acc. Chem. Res*. **2003**, *36*, 255.

[3]   (a) Gray, P.; Williams, A. *Chem. Rev.* **1959**, *59*, 239. (b) Kochi, J. K. *J. Am. Chem. Soc*. **1962**, *84*, 1193. (c) Bacha, J. D.; Kochi, J. K. *J. Org. Chem*. **1965**, *30*, 3272. (d) Walling, C.; Padwa, A. *J. Am. Chem. Soc*. **1963**, *85*, 1593 (e) Walling, C.; Wagner, P. J. *J. Am. Chem. Soc*. **1964**, *86*, 3368. (f) Avila, D. V.; Brown, C. E.; Ingold, K. U.; Lusztyk, J. *J. Am. Chem. Soc*. **1993**, *115*, 466. (g) Weber, M.; Fischer, H. *J. Am. Chem. Soc*. **1999**, *121*, 7381. (h) Salamone, M.; Bietti, M. *Synlett* **2014**, *25*, 1803.

[4]   (a) Zhang J.; Li Y.; Zhang F.; Hu C.; Chen Y. *Angew. Chem., Int. Ed*. **2016**, *55*, 1872. (b) Wang C.; Harms K.; Meggers E. *Angew. Chem. Int. Ed*. **2016**, *55*, 13495. (c) Zhang J.; Li Y.; Xu R.; Chen Y. *Angew. Chem. Int. Ed*. **2017**, *56*, 12619.

[5]   (a) Cekovic Z. *Tetrahedron*, **2003**, *59*, 8073. (b) Hartung J.; Gottwald T.; Špehar K. *Synthesis* **2002**, *11*, 1469.

[6]   (a) Chiba, S.; Cao, Z.; El Bialy, S. A. A.; Narasaka, K. *Chem. Lett.* **2006**, *35*, 18. (b) Zhao, H.; Fan, X.; Yu, J.; Zhu, C. *J. Am. Chem. Soc*. **2015**, *137*, 3490. (c) Ren, R.; Wu, Z.; Xu, Y.; Zhu, C. *Angew. Chem., Int. Ed*. **2016**, *55*, 2866. (d) Guo, J.-J.; Hu, A.; Chen, Y.; Sun, J.; Tang, H.; Zuo, Z. *Angew. Chem., Int. Ed*. **2016**, *55*, 15319. (e) Jia, K.; Zhang, F.; Huang, H.; Chen, Y. *J. Am. Chem. Soc*. **2016**, *138,* 1514. (f) Wu, X.; Wang, M.; Huan, L.; Wang, D.; Wang, J.; Zhu, C. *Angew. Chem., Int. Ed*. **2018**, *57*, 1640. (g) Wang, D.; Mao, J.; Zhu, C. *Chem. Sci*. **2018**, *9*, 5805.

[7]   a) Zuo Z., Ahneman D. T., Chu L., Terrett J. A., Doyle A. G., MacMillan D. W.C. *Science* **2014**, *345*, 437. (b) Jeffrey J. L., Terrett J. A., MacMillan D. W. C. *Science* **2015**, *349*, 1532. (c) Choi G. J.; Zhu Q. L.; Miller D. C.; Gu C. J.; Knowles R. R. *Nature* **2016**, *539*, 268. (d) Chu J. C. K.; Rovis T. *Nature* **2016**, *539*, 272.

[8]   (a) Hu, A.; Guo, J. J.; Pan, H.; Tang, H.; Gao, Z.; Zuo, Z. *J. Am. Chem. Soc*. **2018**, *140*, 1612. (b) Hu, A.; Chen, Y.; Guo, J. J.; Yu, N.; An, Q.; Zuo, Z. *J. Am. Chem. Soc*. **2018**, *140*, 13580.

[9]   Yayla, H. G.; Wang, H.; Tarantino, K. T., Orbe, H. S.; Knowles, R. R. *J. Am. Chem. Soc*. **2016**, *138*, 10794.

[10]   During the finalization of this manuscript Huang and Rueping just disclosed a consecutive radical trapping with Ni catalysts to engage cross-coupling arylation with electron-poor aryl halides: Huang, L.; Ji, T.; Rueping, M. *J. Am. Chem. Soc*. **2020**, *142*, 3532.

[11]    (a) Ota E.; Wang, H.; Frye, N. L.; Knowles, R. R. *J. Am. Chem. Soc.* **2019**, *141*, 1457. (b) Zhao, K.; Yamashita, K.; Carpenter, J. E.; Sherwood, T. C.; Ewing, W. R.; Cheng, P. T. W.;  Knowles, R. R. *J. Am. Chem. Soc.* **2019**, *141*, 8752–8757.

[12]    Due to the requirement of the aforementioned intramolecular PCET promoted by an initial arene oxidation, current protocols (ref. **Fehler! Textmarke nicht definiert.,Fehler! Textmarke nicht definiert.**) are limited to the use of   (electron-rich) 1-aryl-substituted cycloalkanols.

[13]    (a) Szatyłowicz, H. *J. Phys. Org. Chem.* **2008**, *21*, 897–914. (b) Shishkin, O. V.; Konovalova, I. S.; Gorb, L.; Leszcynski, J. *Struct. Chem.* **2009**, *20*, 37. (c) Tessensohn, M. E.; Koh, Y. R.; Lim, S.; Hirao, H.; Webster, R. D. *Chem. Phys. Chem.* **2017**, *18*, 2250–2257.

[14]    (a) Fukuzumi, S.; Kotani, H.; Ohkubo, K.; Ogo, S.; Tkachenko, N. V.; Lemmetyinen, H. *J. Am. Chem. Soc.* **2004**, *126*, 1600. (b) Romero,    N.    A.; Margrey, K. A.; Tay, N. E.; Nicewicz, D. A. *Science* **2015**, *349*, 1326. (c) Joshi-Pangu, A.; Lévesque, F.; Roth, H. G.; Oliver, F. S.; Campeau, L.-C.; Nicewicz, D.; DiRocco, D. A. *J. Org. Chem.* **2016**, *81*, 7244. (d) Pitzer, L.; Sandfort, F.; Strieth-Kalthoff, F.; Glorius, F. *Angew. Chem. Int. Ed.* **2018**, *57*, 16219.

[15]    One of the top 12 potential bio-based platform chemicals by the U.S. Department of Energy:  Werpy, T.; Petersen, G. Top Value Added Chemicals from Biomass. Vol. I Results of Screening for Potential Candidates from Sugars and Synthesis Gas; DOE/GO-102004-1992; U.S. Department of Energy: **2004**.

[16]    Only 0.1 mmol $H_2O$ were used due to the water sensitivity of TsCN.

[17]    (a) Miller, D.C., Tarantino, K. T.; Knowles, R.R. *Top. Curr. Chem.* **2016**, *374*, 1–59. (b) Weinberg, D. R.; Gagliardi, C. J.; Hull, J. F.; Murphy, C. F.; Kent, C. A.; Westlake, B. C.; . Paul, A.; Ess, D. H.; McCafferty, D. G.; Meyer, T. J.; *Chem. Rev.* **2012**, *112*, 4016–93.

[18]    Gilli, P.; Pretto, L.; Bertolasi, V.; Gilli, G. *Acc. Chem. Res.* 2009, *42*, 33– 44.

[19]    N. Berg, D. Horinek, R. M. Gschwind, *manuscript under consideration.*

[20]    Pyridine itself was excluded to this study due to significant (non PCET-related) side-reactions:

[21]    (a) Greindl, J.; Hioe, J.; Sorgenfrei, N.; Morana, F.; Gschwind, R. M. *J. Am. Chem. Soc.* **2016**, *138*, 15965–15971. (b) Sorgenfrei, N.; Hioe, J.; Greindl, J.; Rothermel, K.; Morana, F.; Lokesh, N.; Gschwind, R. M. *J. Am. Chem. Soc.* **2016**, *138*, 16345–16354.

[22]    chlorine

[23]    Rothermel, K.; Melikian, M.; Hioe, J.; Greindl, J.; Gramüller, J.; Žabka, M.; Sorgenfrei, N.; Hausler, T.; Morana, F.; Gschwind, R. M. *Chem. Sci.* **2019**, *10*, 10025-10034.

[24]    It is clearly visible that the broad O-H signal includes a shoulder (see Figure 3.3b), which hints at a second species being separated on the NMR time scale, but with very similar chemical shifts. This shoulder is also obtained for pure alcohol and thus is not caused by the presence of pyridine.

[25] Furthermore, the low average ppm-value for an O-H···N H-bond hints at a masking of the crucial alcohol-pyridine complex by the self-aggregated alcohol bulk (see DOSY experiments). In addition, the potential of the specific pyridine bases to break the alcohol self-aggregation may also contribute to the reactivity profile of this reaction.

[26] Bondi, A. *J. Phys. Chem.* **1964**, *68*, 441.

[27] Dadová, J.; Kümmel, S.; Feldmeier, C.; Cibulková, C.; Pažout, R.; Maixner, J.; Gschwind, R. M.; König, B.; Cibulka, R. *Chem. - A Eur. J.* **2013**, *19*, 1066–1075.

[28] (a) Ran, J.; Wogn, M. W. *J. Phys. Chem. A* **2006**, *110*, 9702. (b) Kumari, M.; Balaji, P. V.; Sunoj, R. B. *Phys. Chem. Phys.* **2011**, *13*, 6517. (c) Bloom, J. W. G.; Raju, R. K.; Wheeler, S. E. *J. Chem. Theory Comput.* **2012**, *8*, 3167. (d) Wheeler, S. E.; Bloom, J. W. G. *Phys. Chem. A* **2014**, *118*, 6133. (e) Ninkovic, D. B.; Vojislavljevic-Vasilev, D. Z.; Medakovic, V. B.; Hall, M. B.; Brothers, E. N.; Zaric, S. D. *Phys. Chem. Phys.* **2016**, *18*, 25791. (f) Ninkovic, D. B.; Malenov, D. P.; Petrovic, P. V.; Brothers, E. N.; Niu, S.; Hall, M. B.; Belic, M. R.; Zaric, S. D. *Chem. Eur. J.* **2017**, *23*, 11046.

## 3.6 Supporting Information

### 3.6.1 General Methods

Unless otherwise noted, all commercially available compounds were used as received without further purification.

NMR spectra were recorded on a Varian Mercury plus 300 (300.08 MHz) and Varian Mercury plus 400 (400.00 MHz) using the solvent peak as internal reference (CDCl$_3$: δ H 7.26; δ C 77.16 and (CD$_3$)$_2$CO: δ H 2.05; δ C 29.84). Multiplicities are indicated, s (singlet), d (doublet), t (triplet), q (quartet), quint (quintet), sept (septet), m (multiplet); coupling constants (*J*) are in Hertz (Hz). Asterisks (*) indicate signal doubling due to diastereomer formation.

For the mechanistic NMR measurements at room temperature and 180 K a Bruker Avance III HD 600 MHz (600.13 MHz for 1H) with a 5 mm TBI-F probe head and Z-gradients was used. For experiments at room temperature a BVT Unit or a BCU II controlled the temperature, for low temperature measurements at 180 K a BVTE 3900 was used. The spectra were processed and plotted with Bruker's Topspin 3.2, the graphs of the kinetic measurements were generated with Excel (Office 2016) and pictured using Corel Draw 2017. The Figures were designed using the Topspin Plot Editor, Chem Draw Professional and Corel Draw 2017.

ESI-MS spectra were recorded on a Bruker Daltonics Esquire 3000 Plus ESI-Ion Trap mass spectrometer or Bruker Daltonics Impact II ESI-TOF mass spectrometer. Ionization modes are specified in the descriptions of the corresponding experiments.

All reactions were monitored by thin-layer chromatography using Merck silica gel plates 60 F$_{254}$; visualization was accomplished with UV light and/or staining with vanillin stain. Flash chromatography was performed on a Biotage Isolera One using 50 g, 25 g or 10 g SNAP cartridge KP-Sil columns filled with MACHEREY NAGEL silica gel 60 (size 40−63 µm).

Irradiation was performed with twelve Osram Oslon SSL royal blue (455 nm) attached to an aluminum heat sink. The LEDs were operated at approx. 700 mA per LED.

Stern-Volmer experiments were done with a Shimadzu RF-6000 Spectro Fluorophotometer in 1 cm quartz cuvettes.

### 3.6.2  Synthesis of Starting Materials

#### 3.6.2.1 Synthesis of Olefins

**Benzylidenemalononitrile (2)**
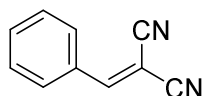


A solution of benzaldehyde (4.9 ml, 5.1 g, 48 mmol, 1.2 equiv.) in ethanol (40 ml) was treated with piperidine (0.40 ml, 0.34 g, 4 mmol, 0.1 equiv.) and malononitrile (2.6 g, 40 mmol, 1.0 equiv.). After stirring at room temperature over night, the reaction mixture was concentrated in vacuum, diluted with $H_2O$ and extracted three times with EtOAc. The combined organic layers were dried over anhydrous $Na_2SO_4$, filtered and evaporated. Purification by column chromatography (100 g silica gel, hexanes/ethyl acetate 2-14%) gave **2** (4.4 g, 28.5 mmol, 71%) as a white solid. ^{1}H NMR (400 MHz, CDCl$_3$): δ 7.91 (d, *J* = 7.7 Hz, 2H), 7.78 (s, 1H), 7.64 (t, *J* = 7.4 Hz, 1H), 7.55 (t, *J* = 7.7 Hz, 2H). Data in accordance with the literature.[1]

**Ethyl 2-cyano-3-phenylacrylate (S8)**
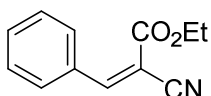


A solution of Benzaldehyde (1,01 ml, 1.06 g, 10 mmol, 1 equiv.) in toluene (50 ml) was treated with piperidine (0.05 ml, 0.04 g, 0.5 mmol, 0.05 equiv.) and ethyl cyanoacetate (1.19 g, 10.5 mmol, 1.05 equiv.). After stirring at 115°C over night, the reaction mixture was concentrated in vacuum, diluted with $H_2O$ and extracted three times with EtOAc. The combined organic layers were dried over anhydrous $Na_2SO_4$, filtered and evaporated. Purification by column chromatography (hexanes/ethyl acetate 10%) gave **S8** (1.96 g, 9.8 mmol, 98%) as a colorless solid. ^{1}H NMR (400 MHz, CDCl$_3$): δ 8.25 (s, 1H), 8.06 – 7.95 (m, 2H), 7.61 – 7.45 (m, 3H), 4.38 (q, *J* = 7.1 Hz, 2H), 1.40 (t, *J* = 7.2 Hz, 3H). ^{13}C NMR (101 MHz, CDCl$_3$) δ 162.6, 155.1, 133.4, 131.6, 131.2, 129.4, 115.6, 103.2, 62.8, 14.3. Data in accordance with the literature.[2]

**2-Propylidenemalononitrile (S9)**
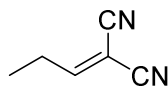


A solution of malonitrile (1.3 g, 20 mmol, 1 equiv.) in chloroform (15 ml) was treated with propionaldehyde (2.9 ml, 40 mmol, 2 equiv.) and $Al_2O_3$ (activated basic) (2.9 g, 28 mmol, 1.4 equiv.). After stirring at room temperature for 1 h, the aluminium oxide was filtered off and filtrate was concentrated in vacuum. Purification by column chromatography (100 g silica gel, hexanes/ethyl acetate 2-20%) gave **S9** (1.5 g, 14 mmol, 71%) as a colourless oil. ^{1}H NMR (400 MHz, CDCl_3): δ 7.32 (t, *J* = 7.9 Hz, 1H), 2.62 (p, *J* = 7.6 Hz, 2H), 1.20 (t, *J* = 7.5 Hz, 3H). 13C NMR (101 MHz, CDCl_3) δ 170.6, 112.0, 110.4, 89.6, 26.3, 12.0. Data in accordance with the literature.[3]

**Ethyl 2-oxo-2*H*-chromene-3-carboxylate (S13)**
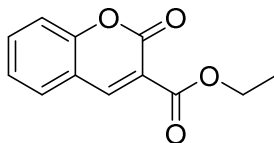


A solution of 2-hydroxy-benzaldehyde (3.2 ml, 3.7 g, 30 mmol, 1 equiv.) and diethyl malonate (7.3 ml, 7.7 g, 48 mmol, 1.6 equiv.) in ethanol (40 ml) was treated with piperidine (0.613 ml, 613 mg, 7.2 mmol, 0.24 equiv.) and acetic acid (0.878 ml, 757 mg, 12.5 mmol, 0.42 equiv.). The mixture was heated to reflux overnight and cooled to room temperature. After pouring into cold water, the resulting precipitate was collected via filtration, washed with cold water and dried under vacuum to give **S13** as a white solid. ^{1}H NMR (400 MHz, CDCl_3) δ 8.55 (s, 1H), 7.72 – 7.60 (m, 2H), 7.43 – 7.32 (m, 2H), 4.44 (q, *J* = 7.1 Hz, 2H), 1.44 (t, *J* = 7.1 Hz, 3H). Data in accordance with the literature.[4]

**Methyl 2-phenylacrylate (S15)**
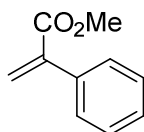


To a solution of methyl phenylacetate (2.1 ml, 2.3 g, 15 mmol, 1 equiv.) in toluene (30 ml) was added paraformaldehyde (2.5 ml, 2.2 g, 45 mmol, 3 equivl), $K_2CO_3$ (6.2 g, 45 mmol, 3 equiv.) and tetrabutylammonium bromide (242 mg, 0.750 mmol, 0.05 equiv.). The

mixture was heated to 60 °C overnight and cooled to room temperature. Water was added and the aqueous layer was extracted with $Et_2O$ (3x). The combined organic layers were dried over anhydrous $Na_2SO_4$, filtered and evaporated. Purification by column chromatography (100 g silica gel, hexanes/ethyl acetate 1-4%) gave **S15** (888 mg, 5.48 mmol, 37%) as a colourless oil. ^{1}H NMR (400 MHz, $CDCl_3$) δ 7.46 – 7.30 (m, 5H), 6.37 (s, 1H), 5.90 (s, 1H), 3.83 (s, 3H). Data in accordance with the literature.[5]

**Methyl 2-[di(*tert*-butoxycarbonyl)amino]acrylate (S20)**
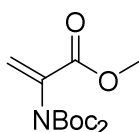


A suspension of serine methyl ester hydrochloride (4.4 g, 28 mmol, 1 equiv.) in DCM (20 ml) at 0°C was treated with trimethylamine (8.6 ml, 6.2 g, 62 mmol, 2.2 equiv.) followed by a solution of $Boc_2O$ (6.7 g, 31 mmol, 1.1 equiv) in DCM (20 ml). The mixture was stirred at room temperature overnight. The solvents were removed under vacuum, the crude oily product was taken up in ethyl acetate (25 ml) and washed successively with $KHSO_4$ 1 N (2 × 20 ml), $NaHCO_3$ 1 N (20 ml) and brine (20 ml). The organic layer was dried over anhydrous $Na_2SO_4$, filtered and evaporated to afford Boc-Ser-OMe (5.98 g, 27 mmol, 97%) as a colourless oil, which was used without further purification.

A solution of Boc-Ser-OMe (5.9 g, 27 mmol, 1 equiv.) in acetonitrile (25 ml) at 0 °C was treated with DMAP (0.66 g, 5.4 mmol, 0.2 equiv.) followed by $Boc_2O$ portionwise (12 g, 54 mmol, 2 equiv.). The mixture was stirred at room temperature for 15 minutes and was then heated to 60 °C until starting material was consumed (TLC monitoring). The solvents were removed under vacuum, the crude oily product was taken up in ethyl acetate (25 ml) and washed successively with $KHSO_4$ 1 N (2 x 20 ml), $NaHCO_3$ 1 N (20 ml) and brine (20 ml). The organic layer was dried over anhydrous $Na_2SO_4$, filtered and evaporated to afford **S20** (6.9 g, 23 mmol, 85%) as an off white solid. ^{1}H NMR (400 MHz, $CDCl_3$) δ 6.34 (s, 1H), 5.64 (s, 1H), 3.79 (s, 3H), 1.46 (s, 18H). Data in accordance with the literature.[6]

### 3.6.2.2 Synthesis of Cyclic Alcohols

General procedure A:

A dry Schlenk flask under argon was charged with cyclic ketone (1 equiv.) in $Et_2O$ (1.2 M) and commercial available Grignard solution (1.2 equiv.) was syringed dropwise into the solution at 0 °C. The mixture was stirred at room temperature overnight and then quenched by slow addition of saturated ammonium chloride. The aqueous layer was extracted with $Et_2O$ (3x). The combined organic layers were dried over anhydrous $Na_2SO_4$, filtered and evaporated. The crude was purificated by column chromatography on silica gel.

General procedure B:

A dry Schlenk flask was charged with cerium chloride (1.5 equiv.) and heated in an oil bath to 130 °C with evacuation. After 1 h the cerium chloride was further dried by stirring for an additional hour. While the flask was still hot, argon gas was introduced and the flask was cooled under argon to 0 °C. Freshly distilled THF (0.25 M) was added and the resulting suspension was stirred at room temperature overnight. The reaction mixture was again cooled to 0 °C, commercial available phenyl magnesium bromide solution (1.5 equiv., 3 M $Et_2O$ solution) was added. After stirring the suspension for 1.5 h at 0 °C the cyclic ketone (1 equiv.) was added and the stirring was continued for 30 minutes. The reaction was quenched by slow addition 10% aqueous acetic acid. The aqueous layer was extracted with $Et_2O$ (3x). The combined organic layers were washed with $NaHCO_3$, brine, dried over anhydrous $Na_2SO_4$, filtered and evaporated. The crude was purified by column chromatography on silica gel.

### 1-Phenylcyclobutan-1-ol (1)
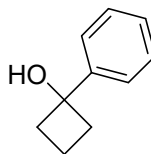


Prepared according to general procedure A using cyclobutanone (1.07 ml, 1.0 g, 14.3 mmol, 1 equiv.) and phenylmagnesium chloride solution (2 M in THF) to afford **1** (1.71 g, 11.5 mmol, 81%) as a colorless solid. ^{1}H NMR (400 MHz, $CDCl_3$) δ 7.56 – 7.48 (m, 2H), 7.43 – 7.35 (m, 2H), 7.33 – 7.27 (m, 1H), 2.65 – 2.53 (m, 2H), 2.38 (tdd, *J* = 9.5, 7.4, 2.9 Hz, 2H), 2.12 – 1.97 (m, 2H), 1.70 (dtt, *J* = 11.2, 8.8, 7.5 Hz, 1H). Data in accordance with the literature.[7]

**1-(4-Chlorophenyl)cyclobutan-1-ol (S23)**
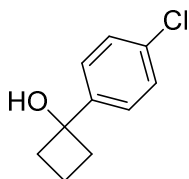


Prepared according to general procedure A using cyclobutanone (1.1 ml, 1.0 g, 14 mmol, 1 equiv.) and 4-chlorophenylmagnesium bromide solution (1 M in 2-Me-THF) to afford **S23** (1.9 g, 10 mmol, 72%) as a colorless oil. ^{1}H NMR (400 MHz, CDCl$_3$) δ 7.44 (d, *J* = 8.5 Hz, 2H), 7.34 (d, *J* = 8.5 Hz, 2H), 2.58 – 2.48 (m, 2H), 2.42 – 2.32 (m, 2H), 2.10 – 1.99 (m, 1H), 1.97 (bs, 1H), 1.76 – 1.64 (m, 1H). Data in accordance with the literature.[7]

**1-Phenylcyclopentan-1-ol (S24)**
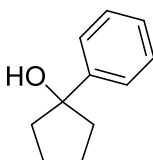


Prepared according to general procedure A using cyclopentanone (1.26 ml, 1.2 g, 14.3 mmol, 1 equiv.) and phenylmagnesium chloride solution (2 M in THF) to afford **S24** (1.48 g, 9.1 mmol, 64%) as a colorless oil. ^{1}H NMR (400 MHz, CDCl$_3$) δ 7.54 – 7.48 (m, 2H), 7.35 (td, J = 7.0, 1.7 Hz, 2H), 7.28 – 7.23 (m, 1H), 2.11 – 1.93 (m, 6H), 1.92 – 1.79 (m, 2H), 1.54 (s, 1H). Data in accordance with the literature.[7]

**2,2-Dimethyl-1-phenylcyclopentan-1-ol (S25)**
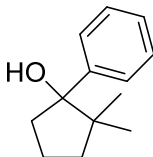


Prepared according to general procedure B using 2,2-dimethylcyclopentanone (502 µl, 449 mg, 4 mmol, 1 equiv.) to afford **S25** (657 mg, 3.45 mmol, 86%) as a colorless oil. ^{1}H NMR (400 MHz, CDCl$_3$) δ 7.56 – 7.44 (m, 2H), 7.34 (td, *J* = 7.1, 6.2, 1.3 Hz, 2H), 7.30 – 7.22 (m, 1H), 2.82 – 2.69 (m, 1H), 2.03 – 1.74 (m, 4H), 1.68 – 1.56 (m, 1H), 1.52 (s, 1H), 1.01 (s, 3H), 0.64 (s, 3H). ^{13}C NMR (75 MHz, CDCl$_3$) δ 143.5, 127.5, 126.7, 126.6, 85.8, 46.0, 38.9, 37.8, 26.5, 21.1, 19.1. HRMS (EI) m/z: [M]: Calcd. for C$_{13}$H$_{18}$O 190.1358; Found: 190.1351.

**1,2-Diphenylcyclohexan-1-ol (S26)**
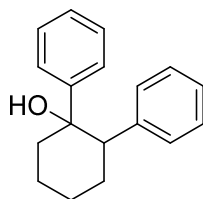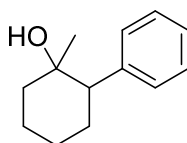


Prepared according to general procedure B using 2-phenylcyclohexanone (523 mg, 3 mmol, 1 equiv.) to afford **S26** (521 mg, 2.06 mmol, 69%) as a colorless oil. ^{1}H NMR (400 MHz, CDCl$_3$) δ 7.26 – 7.16 (m, 4H), 7.16 – 7.01 (m, 4H), 6.90 (dd, *J* = 6.8, 3.0 Hz, 2H), 3.06 (dd, *J* = 12.8, 3.7 Hz, 1H), 2.25 (qd, *J* = 13.0, 3.5 Hz, 1H), 2.16 – 2.02 (m, 1H), 2.02 – 1.94 (m, 1H), 1.94 – 1.82 (m, 2H), 1.82 – 1.69 (m, 3H), 1.61 – 1.50 (m, 1H). ^{13}C NMR (101 MHz, CDCl$_3$) δ 147.9, 141.7, 129.0, 127.8, 127.8, 126.4, 126.3, 124.8, 75.9, 53.0, 40.5, 28.5, 26.6, 22.1. Data in accordance with the literature.[8]

**2'-Phenyl-3',4'-dihydro-2'*H-spiro*[cyclohexane-1,1'-naphthalen]-2'-ol (S27)**
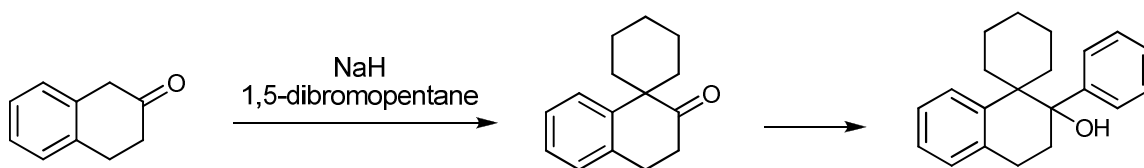


3',4'-dihydro-2'*H-spiro*[cyclohexane-1,1'-naphthalen]-2'-one ("*spiro*-cyclohexyl-2-tetralone") was prepared following literature procedure. Spectra are consistent with reported literature values.

Prepared according to general procedure B using *spiro*-cyclohexyl-2-tetralone (643 mg, 3 mmol, 1 equiv.) to afford **S27** (481 mg, 1.65 mmol, 55%) as a colorless oil. ^{1}H NMR (400 MHz, CDCl$_3$) δ 7.58 – 7.53 (m, 1H), 7.46 – 7.40 (m, 2H), 7.28 – 7.12 (m, 6H), 3.17 – 3.02 (m, 2H), 2.68 (ddd, *J* = 14.2, 9.2, 6.4 Hz, 1H), 2.09 (ddd, *J* = 14.3, 9.2, 5.0 Hz, 1H), 2.03 – 1.96 (m, 1H), 1.80 – 1.70 (m, 3H), 1.67 – 1.49 (m, 5H), 1.39 – 1.28 (m, 1H), 1.05 – 0.93 (m, 1H). ^{13}C NMR (101 MHz, CDCl$_3$) δ 145.3, 143.7, 136.7, 129.4, 129.1, 127.9, 127.3, 126.7, 126.2, 125.5, 79.9, 46.6, 33.3, 31.7, 30.2, 26.7, 25.5, 23.8, 22.9. HRMS (ESI) m/z: [M + Na]$^+$: Calcd. for C$_{21}$H$_{24}$ONa 315.1719; Found: 315.1727.

**3-Phenyltetrahydro-2*H*-pyran-3-ol (S28)**
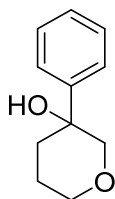


Prepared according to general procedure B using 2H-Pyran-3(4H)-one (501 mg, 5 mmol, 1 equiv.) to afford **S28** (500 mg, 2.81 mmol, 62%) as a white solid. $^1$H NMR (400 MHz, CDCl$_3$) δ 7.53 (dd, J = 7.4, 1.7 Hz, 2H), 7.43 – 7.33 (m, 2H), 7.32 – 7.26 (m, 1H), 4.08 – 3.98 (m, 1H), 3.72 – 3.58 (m, 2H), 3.51 (tt, J = 11.5, 2.9 Hz, 1H), 2.69 (s, 1H), 2.18 – 2.00 (m, 2H), 2.00 – 1.88 (m, 1H), 1.71 – 1.59 (m, 1H). $^{13}$C NMR (101 MHz, CDCl$_3$) δ 144.1, 128.4, 127.5, 125.2, 77.0, 71.1, 68.2, 35.3, 22.3. HRMS (ESI) m/z: [M + Na]$^+$: Calcd. for C$_{11}$H$_{14}$O$_2$Na 201.0886; Found: 201.0892.

**1-Methyl-2-phenylcyclohexan-1-ol (S29)**



Prepared according to general procedure A using 2-phenylcyclohexanone (871 mg, 5 mmol, 1 equiv.) to afford **S29** (614 mg, 3.23 mmol, 65%) as a colorless oil. $^1$H NMR (400 MHz, CDCl$_3$) δ 7.34 – 7.20 (m, 5H), 2.50 (dd, *J* = 12.9, 3.5 Hz, 1H), 2.05 (qd, *J* = 13.1, 3.6 Hz, 1H), 1.92 – 1.67 (m, 3H), 1.67 – 1.56 (m, 2H), 1.56 – 1.45 (m, 1H), 1.45 – 1.30 (m, 1H), 1.20 (d, 1H), 0.98 (s, 3H). $^{13}$C NMR (75 MHz, CDCl$_3$) δ 142.9, 129.0, 128.1, 126.4, 70.6, 53.2, 40.1, 30.1, 28.4, 26.5, 21.9. HRMS (ESI) m/z: [M + Na]$^+$: Calcd. for C$_{13}$H$_{18}$ONa 213.1250; Found: 213.1251.

**1-Methyl-2-phenylcycloheptan-1-ol (S30)**
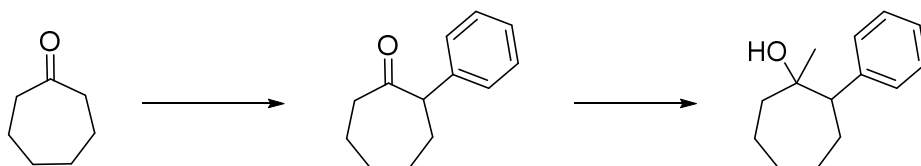


A dry Schlenk tube was charged with Pd(OAc)$_2$ (7.9 mg, 0.035 mmol, 0.01 equiv.), Johnphos (23 mg, 0.077 mmol, 0.022 equiv.), K$_3$PO$_4$ (1.71 g, 8.05 mmol, 2.3 equiv.) and was evacuated and backfilled with argon three times. THF (3.5 ml), brombenzol (0.44 ml, 0.66 g, 4.2 mmol, 1.2 equiv.) and cycloheptanone (0.41 ml, 0.39 mg, 3.5 mmol, 1 equiv.)

were added and the mixture was stirred 17 h at 80 °C. The mixture was diluted with EtOAc, filtered and the solvents were evaporated. The crude was purificated by column chromatography (50 g, hexanes/ethyl acetate 4%) to obtain the arylated ketone (211 mg, 1.12 mmol, 32%) as a colorless oil. $^1$H NMR (400 MHz, CDCl$_3$) δ 7.38 – 7.31 (m, 2H), 7.30 – 7.23 (m, 3H), 3.75 (dd, *J* = 11.4, 4.2 Hz, 1H), 2.79 – 2.67 (m, 1H), 2.63 – 2.50 (m, 1H), 2.24 – 2.13 (m, 1H), 2.13 – 1.94 (m, 4H), 1.76 – 1.60 (m, 1H), 1.57 – 1.42 (m, 2H). $^{13}$C NMR (101 MHz, CDCl$_3$) δ 213.4, 140.4, 128.5, 127.8, 126.9, 58.8, 42.7, 32.0, 30.0, 28.6, 25.3.

Following general procedure A using 2-phenylcycloheptanone (215 mg, 1.12 mmol, 1 equiv.) and methylmagnesium bromide solution (3 M in Et$_2$O) **S30** (174 mg, 0.852 mmol, 76%) was obtained as a colorless oil. $^1$H NMR (400 MHz, CDCl$_3$) δ 7.35 – 7.27 (m, 2H), 7.25 – 7.18 (m, 3H), 2.60 (d, *J* = 10.6 Hz, 1H), 2.29 – 2.12 (m, 1H), 1.93 – 1.79 (m, 4H), 1.69 – 1.59 (m, 1H), 1.56 – 1.38 (m, 3H), 1.22 (s, 1H), 1.08 (s, 3H), 0.97 – 0.86 (m, 1H). $^{13}$C NMR (101 MHz, CDCl$_3$) δ 144.8, 129.5, 128.5, 128.1, 126.2, 73.6, 56.0, 42.2, 30.6, 30.1, 29.5, 29.4, 22.1. HRMS (ESI) m/z: [M + Na]$^+$: Calcd. for C$_{14}$H$_{20}$ONa 227.1406; Found: 227.1405.

### 1-Methyl-2-phenylcyclooctan-1-ol (S31)
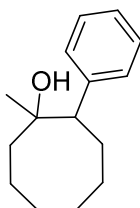


A dry Schlenk tube was charged with Pd(OAc)$_2$ (7.9 mg, 0.035 mmol, 0.01 equiv.), Johnphos (23 mg, 0.077 mmol, 0.022 equiv.), K$_3$PO$_4$ (1.71 g, 8.05 mmol, 2.3 equiv.) and was evacuated and backfilled with argon three times. THF (3.5 ml), brombenzol (0.44 ml, 0.66 g, 4.2 mmol, 1.2 equiv.) and cyclooctanone (0.46 ml, 0.44 mg, 3.5 mmol, 1 equiv.) were added and the mixture was stirred 17 h at 80 °C. The mixture was diluted with EtOAc, filtered and the solvents were evaporated. The crude was purificated by column chromatography to obtain the arylated ketone (322 mg) as a crude product.

Following general procedure A using crude 2-phenylcyclooctanone (322 mg, 1.56 mmol) and methylmagnesium bromide solution (3 M in Et$_2$O) **S31** (95 mg) was obtained as a colorless oil. $^1$H NMR (400 MHz, CDCl$_3$) δ 7.33 – 7.28 (m, 2H), 7.25 – 7.19 (m, 3H), 2.80 (dd, *J* = 7.6, 1.7 Hz, 1H), 2.39 – 2.27 (m, 1H), 2.19 – 2.05 (m, 1H), 1.77 – 1.61 (m, 7H), 1.60 – 1.48 (m, 3H), 1.33 – 1.25 (m, 1H), 0.99 (s, 3H). $^{13}$C NMR (101 MHz, CDCl$_3$) δ 145.9, 129.7, 128.2, 126.3, 74.1, 52.0, 37.6, 30.9, 29.5, 28.7, 27.3, 25.5, 23.2. HRMS (ESI) m/z: [M + Na]$^+$: Calcd. for C$_{15}$H$_{22}$ONa 241.1563; Found:241.1558.

### 1,7,7-Trimethyl-2-phenylbicyclo[2.2.1]heptan-2-ol (S32)
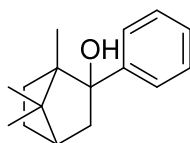
Prepared according to general procedure B using (+)-camphor (304 mg, 2 mmol, 1 equiv.) to afford **S32** (448 mg, 1.94 mmol, 97%) as a colorless oil. ^{1}H NMR (400 MHz, CDCl$_3$, diastereomers) δ 7.57 – 7.51 (m, 2H), 7.39 – 7.20 (m, 3H), 2.34 (2 × s, 1H), 2.24 – 2.16 (m, 1H), 1.91 (t, *J* = 4.3 Hz, 1H), 1.82 – 1.68 (m, 2H), 1.28 (s, 3H), 1.26 – 1.15 (m, 2H), 0.92 (s, 6H), 0.88 – 0.82 (m, 1H). ^{13}C NMR (75 MHz, CDCl$_3$) δ 146.3, 131.9*, 128.2*, 127.7, 126.9, 126.9, 126.8*, 126.5*, 83.7, 57.2*, 55.1*, 53.6, 51.8*, 50.6, 45.8, 45.6, 32.1*, 31.4, 26.7, 25.8*, 21.8, 21.8, 19.9*, 19.8*, 12.8*, 12.8*, 10.0. Data in accordance with the literature.[9]

## (8*R*,9*S*,10*S*,13*S*,14*S*)-10,13-Dimethyl-17-phenylhexadecahydro-1*H*-cyclopenta[*a*]phen-anthrene-3,17-diol (S33)
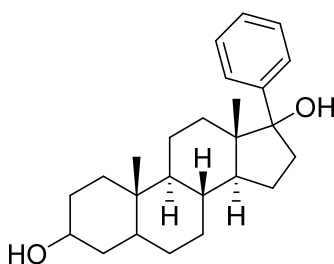


Prepared according to general procedure B using *epi*-androsterone (508 mg, 1.75 mmol, 1 equiv.) to afford **S33** (420 mg, 1.14 mmol, 65%) as a white solid. ^{1}H NMR (400 MHz, CDCl$_3$) δ 7.39 – 7.30 (m, 4H), 7.28 – 7.24 (m, 1H), 3.58 – 3.46 (m, 1H), 2.38 (ddd, *J* = 14.7, 9.8, 5.1 Hz, 1H), 2.14 – 2.04 (m, 1H), 1.87 – 1.69 (m, 4H), 1.61 – 1.13 (m, 15H), 1.05 (s, 3H), 1.03 – 0.96 (m, 1H), 0.90 – 0.80 (m, 2H), 0.79 (s, 3H). ^{13}C NMR (101 MHz, CDCl$_3$) δ 146.1, 127.3, 127.2, 126.7, 86.0, 71.2, 53.7, 49.0, 46.7, 44.8, 38.6, 38.1, 36.8, 36.2, 35.4, 33.6, 31.7, 31.4, 28.6, 24.4, 20.8, 14.9, 12.3. HRMS (ESI) m/z: [M + Na]$^+$: Calcd. for C$_{25}$H$_{36}$O$_2$Na 391.2608; Found: 391.2601

**(8*R*,9*S*,13*S*,14*S*)-13-Methyl-17-phenyl-7,8,9,11,12,13,14,15,16,17-decahydro-6*H*-cyclopenta[*a*]phenanthrene-3,17-diol (S34)**
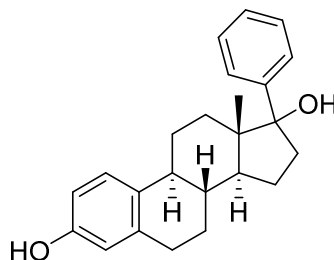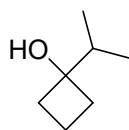


Prepared according to general procedure B using estrone (2.03 g, 7.5 mmol, 1 equiv.) to afford **S34** (1.53 g, 4.39 mmol, 59%) as a white solid. $^1$H NMR (400 MHz, (CD$_3$)$_2$CO) δ 7.86 (s, 1H), 7.49 – 7.42 (m, 2H), 7.30 (ddd, *J* = 8.0, 7.0, 0.8 Hz, 2H), 7.26 – 7.18 (m, 1H), 7.02 – 6.95 (m, 1H), 6.58 – 6.48 (m, 2H), 4.00 (s, 1H), 2.84 – 2.68 (m, 2H), 2.42 – 2.32 (m, 1H), 2.24 – 2.11 (m, 2H), 2.00 – 1.90 (m, 2H), 1.81 – 1.71 (m, 1H), 1.70 – 1.54 (m, 2H), 1.49 – 1.15 (m, 5H), 1.10 (d, J = 0.8 Hz, 3H). $^{13}$C NMR (101 MHz, (CD$_3$)$_2$CO) δ 155.9, 148.2, 138.4, 132.0, 128.5, 127.7, 127.1, 126.9, 115.9, 113.5, 85.9, 49.0, 47.8, 44.5, 40.7, 39.0, 34.6, 30.3, 28.4, 27.2, 24.9, 15.4. HRMS (ESI) m/z: [M - H]$^-$: Calcd. for C$_{24}$H$_{27}$O$_2$ 347.2017; Found: 347.2005.

**1-Cyclohexylcyclobutan-1-ol (S35)**
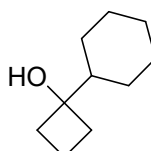


Prepared according to general procedure A using cyclobutanone (715 mg, 10 mmol, 1 equiv.) and cyclohexylmagnesium chloride solution (1 M in THF) to afford **S35** (924 mg, 5.99 mmol, 60%) as a colorless oil. $^1$H NMR (400 MHz, CDCl$_3$) δ 2.20 – 2.09 (m, 2H), 1.97 – 1.65 (m, 8H), 1.59 – 1.45 (m, 2H), 1.37 (tt, *J* = 11.9, 3.1 Hz, 1H), 1.29 – 1.10 (m, 3H), 1.09 – 0.98 (m, 2H). $^{13}$C NMR (101 MHz, CDCl$_3$) δ 78.2, 45.7, 34.0, 26.6, 26.6, 25.8, 12.5. Data in accordance with the literature.[7]

**1-Isopropylcyclobutan-1-ol (S36)**



Prepared according to general procedure A using cyclobutanone (1.07 g, 15 mmol, 1 equiv.) and isopropylmagnesium chloride solution (2 M in THF) to afford **S36** (805 mg, 7.05 mmol, 47%) as a colorless liquid. $^1$H NMR (400 MHz, CDCl$_3$) δ 2.20 – 2.06 (m, 2H), 2.01 – 1.89 (m, 2H), 1.89 – 1.71 (m, 2H), 1.62 – 1.43 (m, 2H), 0.90 (d, $J$ = 6.8 Hz, 6H).. $^{13}$C NMR (101 MHz, CDCl$_3$) δ 78.6, 35.2, 34.2, 15.7, 12.1. HRMS (EI) m/z: [M]: Calcd. for C$_7$H$_{14}$O 114.1045; Found: 114.1036.

**1-Pentylcyclobutan-1-ol (S37)**
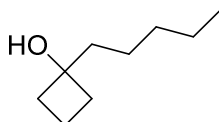


Prepared according to general procedure A using cyclobutanone (715 mg, 10 mmol, 1 equiv.) and pentylmagnesium chloride solution (1.3 M in THF) to afford **S37** (1.33 g, 9.35 mmol, 94%) as a colorless liquid. $^1$H NMR (400 MHz, CDCl$_3$) δ 2.13 – 1.83 (m, 4H), 1.80 – 1.66 (m, 1H), 1.64 – 1.44 (m, 3H), 1.43 – 1.22 (m, 6H), 0.96 – 0.82 (m, 4H). $^{13}$C NMR (101 MHz, CDCl$_3$) δ 75.6, 39.7, 36.1, 32.4, 23.2, 22.8, 14.2, 12.3. Data in accordance with the literature.[7]

### 3.6.3 Reaction Optimization for Aliphatic Alcohols

#### 3.6.3.1 Survey of Optimal Base Equivalents

**Table 3.4:** Survey of optimal base equivalents.
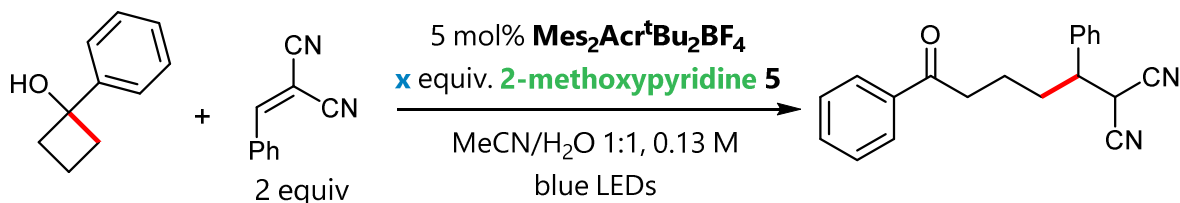


| entry | base equivalents | yield[a] |
|---|---|---|
| 1 | 1 equiv 2-methoxypyridine | 60% |
| 2 | 2 equiv 2-methoxypyridine | 90% |
| **3** | **3 equiv 2-methoxypyridine** | **99%** |

#### 3.6.3.2 Reaction Optimization for Aliphatic Alcohols

**Table 3.5:** Survey of different heteroaromatic bases for the ring-opening C-C cross coupling with alkyl-substituted cycloalkanols.
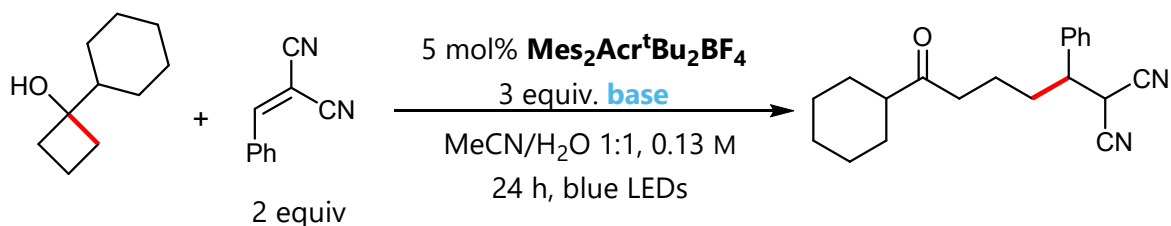


| entry | base | yield[a] |
|---|---|---|
| 1 | 3 equiv 2-methoxypyridine | 26% |
| 2 | 3 equiv 2-isopropoxypyridine | 31% |
| 3 | 3 equiv 2-ethoxypyridine | 23% |
| 4 | 3 equiv 2-F-pyridine | 28% |
| 5 | 3 equiv 2-Cl-pyridine | 40% |

| 6 | 3 equiv 2-Br-pyridine | 20% |
| 7 | 3 equiv 2-CN-pyridine | 26% |
| 8 | 3 equiv 2-$CF_3$-pyridine | 21% |
| 9 | 3 equiv lutidine | 0% |
| 10 | 3 euqiv 2-pentylpyridine | 0% |
| 11 | 3 equiv 2-isobutylpyridine | 0% |
| 12 | 3 equiv tetrahydroquinoline | 0% |
| 13 | 3 equiv quinoline | 0% |
| 14 | 3 equiv isoquinoline | 0% |
| 15 | 3 equiv 2,8-Cl-quinoline | 49% |
| 16 | 3 equiv 4-Cl-2-$CF_3$-quinoline | 57% |
| 17 | 3 equiv 8-Cl-2-OH-quinoline | 28% |
| 18 | 1 equiv 2-Cl-quinoline | 58% |
| 19 | 1 equiv 2-Br-quinoline | 56% |
| 20 | 3 equiv Yu Ligand | 0% |
| 21 | 3 equiv acridine | 0% |

[a] Reactions were performed on 0.1 mmol scale. Yields determined by GC-FID using mesitylene as an internal standard.

### 3.6.4  Reaction Products

General procedure C:

A screw cap culture tube (16 × 100 mm) was charged with **Mes₂AcrᵗBu₂BF₄** (5 mol%), 1-phenylcyclobutanol (0.4 mmol, 59.3 mg, 1 equiv.) and the relevant electron deficient olefin (0.8 mmol, 2 equiv.; liquid alkenes were instead added after the solvent). Then, MeCN/$H_2O$ (1:1, 3 ml) and 2-methoxypyridine (1.2 mmol, 126 µl, 3 equiv.) were added. The reaction mixture was subsequently irradiated with blue LEDs for the time indicated. The mixture was dilute with water and EtOAc. The layers were separated and the aqueous layer was extracted with EtOAc (3x). The combined organic layers were dried over $Na_2SO_4$, filtered an evaporated. The residue was purified by column chromatography on silica gel.
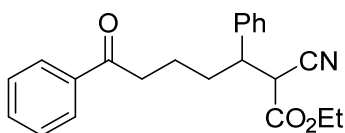
General procedure D:

A screw cap culture tube (16 × 100 mm) was charged with **Mes₂AcrᵗBu₂BF₄** (5 mol%), the relevant alcohol (0.4 mmol, 1 equiv.; liquid alcohols were instead added after the solvent) and benzylidene malononitrile (0.8 mmol, 123 mg, 2 equiv.). Then, MeCN/$H_2O$ (1:1, 3 ml)

and the appropriate base (1-3 equiv.) were added. The reaction mixture was subsequently irradiated with blue LEDs for the time indicated. The mixture was dilute with water and EtOAc. The layers were separated and the aqueous layer was extracted with EtOAc (3x). The combined organic layers were dried over $Na_2SO_4$, filtered an evaporated. The residue was purified by column chromatography on silica gel.

### 3.6.4.1 Olefine Scope

**2-(5-Oxo-1,5-diphenylpentyl)malononitrile (3)**
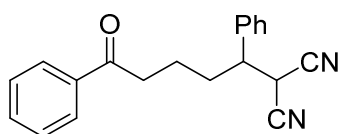


Prepared according to general procedure C using benzylidene malononitrile (123 mg, 0.8 mmol, 2 equiv.) and an irradiation time of 3 h. Yield after column chromatography (25 g silica gel, hexanes/ethyl acetate 15%): 120 mg (0.397 mmol, 99%), colorless resin. ^{1}H NMR (300 MHz, CDCl_3) δ 7.98 – 7.84 (m, 2H), 7.63 – 7.52 (m, 1H), 7.49 – 7.33 (m, 7H), 3.94 (d, J = 6.2 Hz, 1H), 3.27 (dt, *J* = 9.2, 6.3 Hz, 1H), 3.01 (td, *J* = 7.0, 5.3 Hz, 2H), 2.20 – 2.03 (m, 2H), 1.78 – 1.64 (m, 2H). ^{13}C NMR (101 MHz, CDCl_3) δ 199.2, 136.8, 136.4, 133.4, 129.5, 129.2, 128.8, 128.1, 128.0, 111.9, 46.8, 37.8, 31.7, 30.4, 21.6. HRMS (ESI) m/z: [M + Na][+]: Calcd. for $C_{20}H_{18}N_2ONa$ 325.1311; Found: 325.1317.

**Ethyl 2-cyano-7-oxo-3,7-diphenylheptanoate (8)**



Prepared according to general procedure C using ethyl-2-cyano-3-phenylacrylate **S8** (161 mg, 0.8 mmol, 2 equiv.) and an irradiation time of 16 h. Yield after column chromatography (25 g silica gel, hexanes/ethyl acetate 3-24%): 137 mg (0.39 mmol, 98%), pale yellow oil. ^{1}H NMR (400 MHz, CDCl_3) δ 7.99 – 7.85 (m, 2H), 7.61 – 7.52 (m, 1H), 7.52 – 7.41 (m, 2H), 7.39 – 7.27 (m, 5H), 4.21 – 4.04 (m, 2H), 3.74 (2 d, *J* = 6.5 Hz, Σ 1H), 3.45 – 3.32 (m, 1H), 3.06 – 2.87 (m, 2H), 2.13 – 1.88 (m, 2H), 1.81 – 1.59 (m, 2H), 1.14 (2 t, *J* = 7.2 Hz, Σ 3H). ^{13}C NMR (101 MHz, CDCl_3) δ 199.5, 165.4*, 165.4, 138.9*, 138.2, 137.0*, 137.0, 133.2, 133.1*, 129.1*, 129.0, 128.8, 128.7*, 128.3, 128.3*, 128.2*,

128.1, 128.1, 128.0*, 115.9*, 115.5, 62.9*, 62.8, 46.2*, 45.9, 45.3*, 44.8, 38.2*, 38.0, 33.1, 31.9*, 22.0, 21.9*, 14.0*, 13.9. HRMS (ESI) m/z: [M + Na]$^+$: Calcd. for $C_{22}H_{23}NO_3Na$ 372.1570; Found: 372.1578.

### Ethyl 2-cyano-7-oxo-3,7-diphenylheptanoate (9)
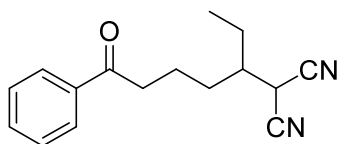


Prepared according to general procedure C using 2-Propylidenemalononitrile (**S3**) (84.9 mg, 0.8 mmol, 2 equiv.) and an irradiation time of 20 h. Yield after column chromatography (25 g silica gel, hexanes/ethyl acetate 14%): 93 mg (0.37 mmol, 91%), pale yellow oil. $^1$H NMR (400 MHz, CDCl$_3$) δ 8.02 – 7.91 (m, 2H), 7.63 – 7.54 (m, 1H), 7.51 – 7.44 (m, 2H), 3.90 (d, *J* = 4.9 Hz, 1H), 3.05 (td, *J* = 6.9, 3.0 Hz, 2H), 2.03 – 1.94 (m, 1H), 1.91 – 1.77 (m, 2H), 1.76 – 1.63 (m, 4H), 1.03 (t, *J* = 7.4 Hz, 3H). $^{13}$C NMR (101 MHz, CDCl$_3$) δ 199.3, 136.8, 133.4, 128.8, 128.1, 112.3, 42.1, 38.1, 30.8, 27.0, 24.3, 20.9, 11.0. HRMS (ESI) m/z: [M + Na]$^+$: Calcd. for $C_{16}H_{18}N_2ONa$ 277.1311; Found: 277.1326.

### Diethyl 2-(4-oxo-4-phenylbutyl)succinate (10/11)
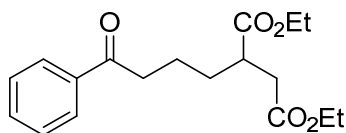


### Starting with maleate (→10)

Prepared according to general procedure C using diethyl maleate (138 mg, 0.8 mmol, 2 equiv.) and an irradiation time of 16 h. Yield after column chromatography (25 g silica gel, hexanes/ethyl acetate 13%): 73.2 mg (0.23 mmol, 57%), pale yellow liquid.
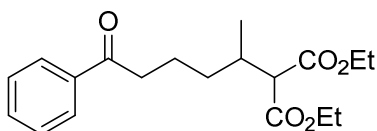
### Starting with fumarate (→11)

Prepared according to general procedure C using diethyl fumarate (138 mg, 0.8 mmol, 2 equiv.) and an irradiation time of 16 h. Yield after column chromatography (25 g silica gel, hexanes/ethyl acetate 13%): 107 mg (0.33 mmol, 82%), pale yellow liquid.

$^1$H NMR (400 MHz, CDCl$_3$) δ 8.01 – 7.91 (m, 2H), 7.61 – 7.52 (m, 1H), 7.52 – 7.42 (m, 2H), 4.24 – 4.06 (m, 4H), 3.07 – 2.94 (m, 2H), 2.93 – 2.83 (m, 1H), 2.73 (dd, *J* = 16.3, 9.1

Hz, 1H), 2.46 (dd, *J* = 16.3, 5.2 Hz, 1H), 1.86 – 1.71 (m, 3H), 1.69 – 1.59 (m, 1H), 1.25 (td, *J* = 7.1, 2.7 Hz, 6H). $^{13}$C NMR (101 MHz, CDCl$_3$) δ 199.7, 174.8, 172.0, 137.0, 133.2, 128.7, 128.1, 60.8, 60.8, 41.3, 38.2, 36.2, 31.6, 21.7, 14.3, 14.3. HRMS (ESI) m/z: [M + Na]$^+$: Calcd. for C$_{18}$H$_{24}$O$_5$Na 343.1516; Found: 343.1522.

### Diethyl 2-(6-oxo-6-phenylhexan-2-yl)malonate (12)



Prepared according to general procedure C using diethyl ethylidenemalonate (149 mg, 0.8 mmol, 2 equiv.) and an irradiation time of 16 h. Yield after column chromatography (25 g silica gel, hexanes/ethyl acetate 1-13%): 96 mg (0.29 mmol, 72%), pale yellow oil. $^1$H NMR (400 MHz, CDCl$_3$) δ 8.03 – 7.88 (m, 2H), 7.59 – 7.42 (m, 3H), 4.19 (qd, *J* = 7.1, 1.6 Hz, 4H), 3.26 (d, *J* = 8.0 Hz, 1H), 3.07 – 2.89 (m, 2H), 2.38 – 2.21 (m, 1H), 1.94 – 1.78 (m, 1H), 1.76 – 1.63 (m, 1H), 1.57 – 1.46 (m, 1H), 1.38 – 1.30 (m, 1H), 1.26 (td, *J* = 7.1, 2.3 Hz, 6H), 1.03 (d, *J* = 6.8 Hz, 3H). $^{13}$C NMR (101 MHz, CDCl$_3$) δ 200.1, 169.1, 137.1, 133.1, 128.7, 128.2, 61.3, 61.3, 57.8, 38.6, 34.1, 33.4, 21.6, 17.0, 14.3, 14.3. HRMS (ESI) m/z: [M + Na]$^+$: Calcd. for C$_{19}$H$_{26}$O$_5$Na 357.1672; Found: 357.1677.

### Ethyl 2-oxo-4-(4-oxo-4-phenylbutyl)chromane-3-carboxylate (13)
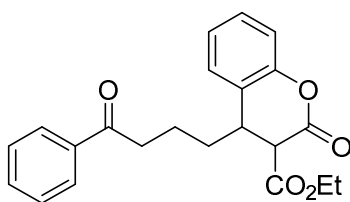


Prepared according to general procedure C using ethyl 2-oxo-2H-chromene-3-carboxylate (**S13**) (175 mg, 0.8 mmol, 2 equiv.) and an irradiation time of 42 h. Yield after column chromatography (25 g silica gel, hexanes/ethyl acetate 12%): 106 mg (0.29 mmol, 72%), pale yellow oil. $^1$H NMR (400 MHz, CDCl$_3$) δ 7.98 – 7.88 (m, 2H), 7.60 – 7.52 (m, 1H), 7.52 – 7.42 (m, 2H), 7.30 – 7.17 (m, 2H), 7.14 – 7.03 (m, 2H), 4.15 – 3.97 (m, 2H), 3.80 (d, *J* = 2.6 Hz, 1H), 3.48 – 3.38 (m, 1H), 3.10 – 2.89 (m, 2H), 1.94 – 1.60 (m, 4H), 1.03 (t, *J* = 7.1 Hz, 3H). $^{13}$C NMR (101 MHz, CDCl$_3$) δ 199.4, 167.1, 164.6, 150.8, 136.9, 133.3, 129.0, 128.9, 128.8, 128.1, 124.9, 124.0, 117.2, 62.3, 52.3, 40.0, 38.0, 34.0, 21.3, 13.9. HRMS (ESI) m/z: [M + Na]$^+$: Calcd. for C$_{22}$H$_{22}$O$_5$Na 389.1359; Found: 389.1370.

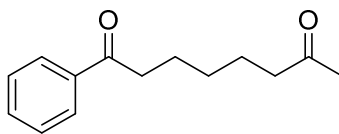**Dimethyl 2-(5-oxo-5-phenylpentyl)succinate (14)**
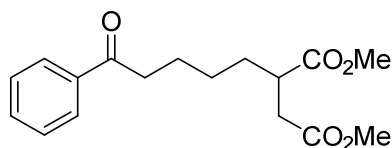


Prepared according to general procedure C using dimethyl itaconate (127 mg, 0.8 mmol, 2 equiv.) and an irradiation time of 24 h. Yield after column chromatography (25 g silica gel, hexanes/ethyl acetate 2-20%): 109 mg (0.36 mmol, 89%), pale yellow resin. $^1$H NMR (400 MHz, CDCl$_3$) δ 7.99 – 7.90 (m, 2H), 7.56 (t, $J$ = 7.3 Hz, 1H), 7.46 (t, $J$ = 7.6 Hz, 2H), 3.68 (d, $J$ = 9.7 Hz, 6H), 2.97 (t, $J$ = 7.3 Hz, 2H), 2.93 – 2.83 (m, 1H), 2.78 – 2.69 (m, 1H), 2.45 (dd, $J$ = 16.5, 5.2 Hz, 1H), 1.82 – 1.66 (m, 3H), 1.62 – 1.54 (m, 1H), 1.40 (p, $J$ = 7.8 Hz, 2H). $^{13}$C NMR (101 MHz, CDCl$_3$) δ 200.1, 175.4, 172.5, 137.1, 133.1, 128.7, 128.1, 52.0, 51.9, 41.2, 38.3, 36.0, 31.9, 26.8, 24.1. HRMS (ESI) m/z: [M + Na]$^+$: Calcd. for C$_{17}$H$_{22}$O$_5$Na 329.1359; Found: 329.1369.
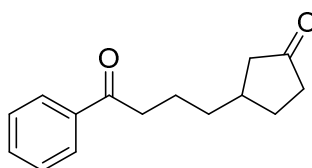
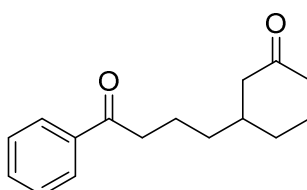**Methyl 7-oxo-2,7-diphenylheptanoate (15)**
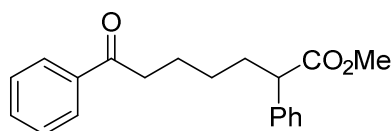


Prepared according to general procedure C using methyl 2-phenylacrylate (**S15**) (130 mg, 0.8 mmol, 2 equiv.) and an irradiation time of 24 h. Yield after column chromatography (25 g silica gel, hexanes/ethyl acetate 1-8%): 123 mg (0.39 mmol, 99%), pale yellow solid. $^1$H NMR (400 MHz, CDCl$_3$) δ 7.95 – 7.91 (m, 2H), 7.58 – 7.52 (m, 1H), 7.48 – 7.42 (m, 2H), 7.33 – 7.23 (m, 5H), 3.65 (s, 3H), 3.56 (t, $J$ = 7.7 Hz, 1H), 2.99 – 2.90 (m, 2H), 2.20 – 2.08 (m, 1H), 1.89 – 1.72 (m, 3H), 1.41 – 1.31 (m, 2H). $^{13}$C NMR (75 MHz, CDCl$_3$) δ 200.2, 174.6, 139.2, 137.1, 133.1, 128.8, 128.7, 128.1, 128.0, 127.4, 52.1, 51.6, 38.4, 33.5, 27.4, 24.0. HRMS (ESI) m/z: [M + Na]$^+$: Calcd. for C$_{20}$H$_{22}$O$_3$Na 333.1461; Found: 33.1488.

**1-Phenyloctane-1,7-dione (16)**



Prepared according to general procedure C using methyl 3-buten-2-one (56 mg, 0.8 mmol, 2 equiv.) and an irradiation time of 24 h. Yield after column chromatography (25 g silica gel, hexanes/ethyl acetate 2-20%): 54.1 mg (0.25 mmol, 62%), pale yellow liquid. $^{1}$H NMR (400 MHz, CDCl$_3$) δ 7.99 – 7.91 (m, 2H), 7.59 – 7.52 (m, 1H), 7.45 (t, *J* = 7.7 Hz, 2H), 2.97 (t, *J* = 7.3 Hz, 2H), 2.45 (t, *J* = 7.4 Hz, 2H), 2.13 (s, 3H), 1.75 (p, *J* = 7.4 Hz, 2H), 1.63 (p, *J* = 7.4 Hz, 2H), 1.44 – 1.33 (m, 2H). $^{13}$C NMR (75 MHz, CDCl$_3$) δ 209.2, 200.4, 137.2, 133.1, 128.7, 128.2, 43.6, 38.4, 30.0, 28.9, 24.1, 23.7. HRMS (ESI) m/z: [M + Na]$^{+}$: Calcd. for C$_{14}$H$_{18}$O$_2$Na 241.1199; Found: 241.1198.

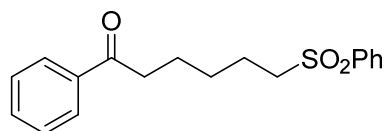**3-(4-Oxo-4-phenylbutyl)cyclopentan-1-one (17)**



Prepared according to general procedure C using methyl 2-cyclopentenone (168 mg, 2 mmol, 5 equiv.) and an irradiation time of 24 h. Yield after column chromatography (25 g silica gel, hexanes/ethyl acetate 2-20%): 58 mg (0.25 mmol, 63%), pale yellow liquid. $^{1}$H NMR (400 MHz, CDCl$_3$) δ 7.99 – 7.93 (m, 2H), 7.56 (t, *J* = 7.4 Hz, 1H), 7.47 (t, *J* = 7.6 Hz, 2H), 3.00 (t, *J* = 7.2 Hz, 2H), 2.45 – 2.13 (m, 5H), 1.89 – 1.73 (m, 3H), 1.60 – 1.48 (m, 3H). $^{13}$C NMR (101 MHz, CDCl$_3$) δ 219.7, 200.1, 137.1, 133.2, 128.8, 128.1, 45.3, 38.6, 38.6, 37.3, 35.5, 29.6, 22.6. HRMS (ESI) m/z: [M + Na]$^{+}$: Calcd. for C$_{15}$H$_{18}$O$_2$Na 253.1199; Found: 253.1197.

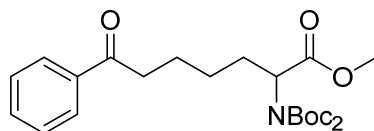**3-(4-Oxo-4-phenylbutyl)cyclohexan-1-one (18)**

Prepared according to general procedure C using methyl 2-cyclohexenone (192 mg, 2 mmol, 5 equiv.) and an irradiation time of 24 h. Yield after column chromatography (25 g silica gel, hexanes/ethyl acetate 2-20%): 54.2 mg (0.22 mmol, 56%), pale yellow liquid. $^1$H NMR (400 MHz, CDCl$_3$) δ 7.98 – 7.91 (m, 2H), 7.60 – 7.52 (m, 1H), 7.50 – 7.42 (m, 2H), 2.97 (t, $J$ = 7.2 Hz, 2H), 2.50 – 2.20 (m, 3H), 2.11 – 1.99 (m, 2H), 1.99 – 1.90 (m, 1H), 1.86 – 1.71 (m, 3H), 1.68 – 1.60 (m, 1H), 1.48 – 1.31 (m, 3H). $^{13}$C NMR (101 MHz, CDCl$_3$) δ 211.9, 200.1, 137.1, 133.1, 128.7, 128.1, 48.2, 41.6, 39.1, 38.5, 36.3, 31.2, 25.3, 21.4. HRMS (ESI) m/z: [M + Na]$^+$: Calcd. for C$_{16}$H$_{20}$O$_2$Na 267.1356; Found: 267.1366.

**1-Phenyl-6-(phenylsulfonyl)hexan-1-one (19)**



Prepared according to general procedure C using methyl phenyl vinylsulfone (135 mg, 0.8 mmol, 2 equiv.) and an irradiation time of 24 h. Yield after column chromatography (25 g silica gel, hexanes/ethyl acetate 2-30%): 79.2 mg (0.25 mmol, 63%), pale yellow solid. $^1$H NMR (400 MHz, CDCl$_3$) δ 7.98 – 7.85 (m, 4H), 7.70 – 7.62 (m, 1H), 7.61 – 7.52 (m, 3H), 7.50 – 7.42 (m, 2H), 3.16 – 3.07 (m, 2H), 2.95 (t, $J$ = 7.1 Hz, 2H), 1.85 – 1.67 (m, 4H), 1.54 – 1.41 (m, 2H). $^{13}$C NMR (101 MHz, CDCl$_3$) δ 199.8, 139.3, 137.0, 133.8, 133.2, 129.4, 128.7, 128.2, 128.1, 56.2, 38.0, 28.0, 23.6, 22.7. HRMS (ESI) m/z: [M + Na]$^+$: Calcd. for C$_{18}$H$_{20}$O$_3$Na 339.1025; Found: 339.1037.

**Methyl 2-(bis(*tert*-butoxycarbonyl)amino)--7-oxo-7-phenylheptanoate (20)**



Prepared according to general procedure C using Dha(Boc)$_2$ (**S20**) (246 mg, 0.8 mmol, 2 equiv.) and an irradiation time of 24 h. Yield after column chromatography (25 g silica gel, hexanes/ethyl acetate 2-16%): 174 mg (0.39 mmol, 97%), pale yellow resin. $^1$H NMR (400 MHz, CDCl$_3$) δ 8.01 – 7.88 (m, 2H), 7.62 – 7.50 (m, 1H), 7.50 – 7.41 (m, 2H), 4.87 (dd, $J$ = 9.4, 5.2 Hz, 1H), 3.71 (s, 3H), 2.97 (t, $J$ = 7.4 Hz, 2H), 2.27 – 2.12 (m, 1H), 2.02 – 1.89 (m, 1H), 1.79 (dt, $J$ = 14.8, 7.1 Hz, 2H), 1.49 (s, 18H), 1.46 – 1.43 (m, 2H). $^{13}$C NMR (101 MHz, CDCl$_3$) δ 200.2, 171.5, 152.3, 137.2, 133.1, 128.7, 128.2, 83.2, 58.1, 52.3,

38.5, 29.9, 28.1, 26.2, 24.1. HRMS (ESI) m/z: [M + Na]$^+$: Calcd. for $C_{24}H_{35}NO_7Na$ 472.2306; Found: 472.2304.

### Methyl 2-acetamido-7-oxo-7-phenylheptanoate (21)
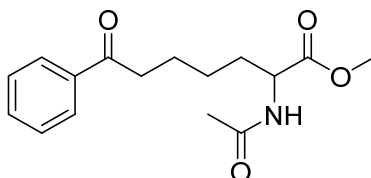


Prepared according to general procedure C using methyl 2-acetamidoacrylate (115 mg, 0.8 mmol, 2 equiv.) and an irradiation time of 24 h. Yield after column chromatography (25 g silica gel, hexanes/ethyl acetate 1-10%): 52 mg (0.18 mmol, 45%), pale yellow resin. $^1$H NMR (400 MHz, CDCl$_3$) δ 8.04 – 7.88 (m, 2H), 7.62 – 7.53 (m, 1H), 7.52 – 7.40 (m, 2H), 6.02 (2 d, *J* = 8.0 Hz, Σ 1H), 4.64 (td, *J* = 7.6, 5.3 Hz, 1H), 3.75 (2 s, Σ 3H), 3.06 – 2.90 (m, 2H), 2.03 (s, 3H), 1.96 – 1.85 (m, 1H), 1.84 – 1.68 (m, 3H), 1.50 – 1.32 (m, 2H). $^{13}$C NMR (101 MHz, CDCl$_3$) δ 200.0, 173.2, 169.9, 137.1, 133.2, 128.7, 128.2, 52.5, 52.2, 38.3, 32.6, 25.1, 23.8, 23.4. HRMS (ESI) m/z: [M + Na]$^+$: Calcd. for $C_{16}H_{21}NO_4Na$ 314.1363; Found: 314.1371.

### 5-Oxo-5-phenylpentanenitrile (22)
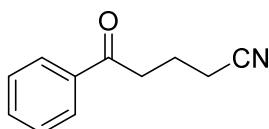


A srew cap test tube was charged with **Mes$_2$Acr$^t$Bu$_2$BF$_4$** (12.3 mg, 5 mol%), 1-phenylcyclobutanol (0.4 mmol, 59.3 mg, 1 equiv.) and *p*-toluensulfonyl cyanide (109 mg, 0.6 mmol, 1.5 equiv.). Then, MeCN (3 ml), water (1.8 µl, 0.1 mmol, 0.25 equiv.) and 2-methoxypyridine (126 µl, 1.2 mmol, 3 equiv.) were added. The reaction mixture was subsequently irradiated with blue LEDs for 24 h. The mixture was dilute with water and EtOAc. The layers were separated and the aqueous layer was extracted with EtOAc (3x). The combined organic layers were dried over Na$_2$SO$_4$, filtered an evaporated. Yield after column chromatography (25 g silica gel, hexanes/ethyl acetate 14%): 57 mg (0.33 mmol, 83%), colorless oil. $^1$H NMR (400 MHz, CDCl$_3$) δ 8.03 – 7.91 (m, 2H), 7.61 – 7.55 (m, 1H), 7.51 – 7.44 (m, 2H), 3.17 (t, *J* = 6.8 Hz, 2H), 2.52 (t, *J* = 7.0 Hz, 2H), 2.11 (p, *J* = 6.9 Hz,

2H). ^{13}C NMR (101 MHz, CDCl$_3$) δ 198.2, 136.6, 133.6, 128.8, 128.1, 119.5, 36.4, 19.8, 16.8. Data in accordance with the literature.[10]

### 3.6.4.2 Cyclic Alcohol Scope

**2-(5-(4-Chlorophenyl)-5-oxo-1-phenylpentyl)malononitrile (23)**
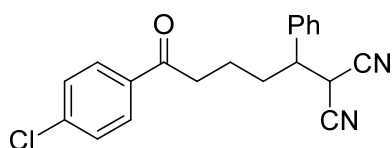


Prepared according to general procedure D using 1-(4-chlorophenyl)cyclobutan-1-ol (**S23**) (73.1 mg, 0.4 mmol, 1 equiv.), 2-methoxypyridin (126 µl, 131 mg, 1.2 mmol, 3 equiv.) and an irradiation time of 24 h. Yield after column chromatography (25 g silica gel, hexanes/ethyl acetate 2-20%): 134 mg (0.398 mmol, 99%), pale yellow resin. ^{1}H NMR (400 MHz, CDCl$_3$) δ 7.91 – 7.76 (m, 2H), 7.49 – 7.34 (m, 7H), 3.94 (d, *J* = 6.2 Hz, 1H), 3.27 (dt, *J* = 9.6, 6.1 Hz, 1H), 3.09 – 2.88 (m, 2H), 2.23 – 2.03 (m, 2H), 1.76 – 1.60 (m, 2H). ^{13}C NMR (101 MHz, CDCl$_3$) δ 197.9, 139.8, 136.4, 135.1, 129.6, 129.5, 129.2, 129.1, 128.0, 111.9, 111.9, 46.8, 37.8, 31.6, 30.4, 21.5. HRMS (ESI) m/z: [M + Na][+]: Calcd. for C$_{20}$H$_{17}$ClN$_2$ONa 359.0922; Found: 359.0930.
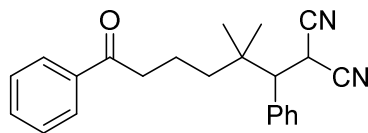
**2-(6-Oxo-1,6-diphenylhexyl)malononitrile (24)**
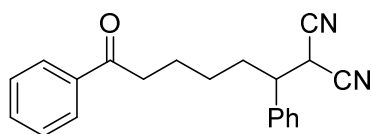


Prepared according to general procedure D using 1-phenylcyclopentanol (**S24**) (64.9 mg, 0.4 mmol, 1 equiv.), 2-methoxypyridin (126 µl, 131 mg, 1.2 mmol, 3 equiv.) and an irradiation time of 72 h. Yield after column chromatography (25 g silica gel, hexanes/ethyl acetate 3-20%): 91 mg (0.288 mmol, 72%), pale yellow resin. ^{1}H NMR (400 MHz, CDCl$_3$) δ 7.96 – 7.88 (m, 2H), 7.61 – 7.52 (m, 1H), 7.49 – 7.36 (m, 5H), 7.35 – 7.29 (m, 2H), 3.92 (d, J = 6.2 Hz, 1H), 3.24 (dt, *J* = 9.3, 6.3 Hz, 1H), 2.93 (t, *J* = 7.2 Hz, 2H), 2.12 – 2.00 (m, 2H), 1.87 – 1.68 (m, 2H), 1.41 – 1.27 (m, 2H). ^{13}C NMR (101 MHz, CDCl$_3$) δ 199.8, 137.0,

136.7, 133.2, 129.5, 129.1, 128.8, 128.1, 128.0, 112.0, 46.5, 38.1, 32.1, 30.3, 26.7, 23.6. HRMS (ESI) m/z: [M + Na]$^+$: Calcd. for C$_{21}$H$_{20}$N$_2$ONa 339.1468; Found: 339.1473.

**2-(2,2-Dimethyl-6-oxo-1,6-diphenylhexyl)malononitrile (25)**



Prepared according to general procedure D using 2,2-dimethyl-1-phenylcyclopentan-1-ol (**S25**) (76.1 mg, 0.4 mmol, 1 equiv.), 2-methoxypyridin (126 µl, 131 mg, 1.2 mmol, 3 equiv.) and an irradiation time of 24 h. Yield after column chromatography (25 g silica gel, hexanes/ethyl acetate 3-20%): 134 mg (0.39 mmol, 98%), pale yellow resin. $^1$H NMR (400 MHz, CDCl$_3$) δ 8.03 – 7.91 (m, 2H), 7.62 – 7.54 (m, 1H), 7.51 – 7.35 (m, 7H), 4.63 (d, $J$ = 5.2 Hz, 1H), 3.16 (d, $J$ = 5.2 Hz, 1H), 2.99 (td, $J$ = 6.7, 1.8 Hz, 2H), 1.85 – 1.68 (m, 2H), 1.61 – 1.46 (m, 1H), 1.46 – 1.34 (m, 1H), 1.19 (s, 3H), 1.01 (s, 3H). $^{13}$C NMR (101 MHz, CDCl$_3$) δ 199.9, 137.0, 136.1, 133.4, 129.8, 128.9, 128.8, 128.8, 128.1, 113.7, 113.3, 54.7, 40.8, 38.3, 37.6, 26.1, 25.2, 24.8, 18.2. HRMS (ESI) m/z: [M + Na]$^+$: Calcd. for C$_{23}$H$_{24}$N$_2$ONa 367.1781; Found:367.1792.

**2-(7-Oxo-1,2,7-triphenylheptyl)malononitrile (26)**
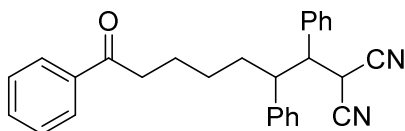


Prepared according to general procedure D using 1,2-diphenylcyclohexan-1-ol (**S26**) (101 mg, 0.4 mmol, 1 equiv.), 2-methoxypyridin (126 µl, 131 mg, 1.2 mmol, 3 equiv.) and an irradiation time of 24 h. Yield after column chromatography (25 g silica gel, hexanes/ethyl acetate 3-20%): 161 mg (0.39 mmol, 99%), pale yellow resin. $^1$H NMR (400 MHz, CDCl$_3$, diastereomers 1:1) δ 7.98 – 7.79 (m, 2H), 7.60 – 7.31 (m, 8H), 7.26 – 7.17 (m, 3H), 6.96 – 6.82 (m, 2H), 4.02 (d, $J$ = 8.9 Hz, 0.5H), 3.59 – 3.49 (m, 0.5H*, 0.5H*), 3.41 – 3.28 (m, 0.5H), 3.28 – 3.20 (m, 1H), 2.89 (t, $J$ = 7.3 Hz, 1H), 2.73 (td, $J$ = 7.3, 2.3 Hz, 1H), 1.87 – 1.41 (m, 4H), 1.40 – 1.21 (m, 1H), 1.16 – 0.99 (m, 1H). $^{13}$C NMR (101 MHz, CDCl$_3$) δ 200.0*, 200.0, 140.5*, 138.2, 137.1*, 137.1, 135.8*, 134.8, 133.1, 133.0*, 129.9*, 129.5, 129.3*, 129.2*, 129.0, 128.8, 128.7*, 128.7, 128.6, 128.6*, 128.3*, 128.1, 128.1*, 127.7, 112.7, 112.3, 112.1*, 111.6*, 53.0, 51.8*, 47.8, 47.5*, 38.4, 38.3*, 33.9,

33.6, 28.9*, 27.5, 27.2, 27.2*, 24.2, 23.9*. HRMS (ESI) m/z: [M + Na]$^+$: Calcd. for C$_{28}$H$_{26}$N$_2$ONa 429.1937; Found: 429.1942.

**2-((1-(2-(3-Oxo-3-phenylpropyl)phenyl)cyclohexyl)(phenyl)methyl)malononitrile (27)**
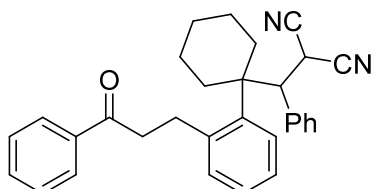


Prepared according to general procedure D using 2'-phenyl-3',4'-dihydro-2'*H*-*spiro*[cyclohexane-1,1'-naphthalen]-2'-ol (**S27**) (117 mg, 0.4 mmol, 1 equiv.), 2-methoxypyridin (126 µl, 131 mg, 1.2 mmol, 3 equiv.) and an irradiation time of 24 h. Yield after column chromatography (25 g silica gel, hexanes/ethyl acetate 1-12%): 103 mg (0.23 mmol, 58%), pale yellow resin. $^1$H NMR (400 MHz, CDCl$_3$) δ 7.40 – 7.28 (m, 5H), 7.25 – 7.18 (m, 3H), 7.18 – 7.03 (m, 5H), 7.03 – 6.93 (m, 1H), 4.54 (td, *J* = 10.1, 5.3 Hz, 1H), 4.37 (d, *J* = 4.6 Hz, 1H), 3.82 (dd, *J* = 10.4, 4.6 Hz, 1H), 3.19 (qd, *J* = 13.1, 7.7 Hz, 2H), 2.86 – 2.74 (m, 1H), 1.91 – 1.75 (m, 4H), 1.65 – 1.44 (m, 4H), 1.43 – 1.25 (m, 2H). $^{13}$C NMR (101 MHz, CDCl$_3$) δ 201.5, 145.9, 137.6, 135.7, 133.4, 133.1, 130.7, 129.2, 128.6, 128.3, 127.8, 127.8, 126.6, 126.1, 112.1, 111.7, 49.7, 48.7, 39.8, 35.0, 34.9, 34.3, 27.6, 27.0, 26.9, 26.4. HRMS (ESI) m/z: [M + Na]$^+$: Calcd. for C$_{31}$H$_{30}$N$_2$ONa 469.2250; Found: 469.2264.

**2-(2-(4-Oxo-4-phenylbutoxy)-1-phenylethyl)malononitrile (28)**
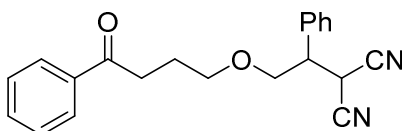


Prepared according to general procedure D using 3-phenyltetrahydro-2H-pyran-3-ol (**S28**) (71.3 mg, 0.4 mmol, 1 equiv.), 2-methoxypyridin (126 µl, 131 mg, 1.2 mmol, 3 equiv.) and an irradiation time of 64 h. Yield after column chromatography (25 g silica gel, hexanes/ethyl acetate 3-20%): 74 mg (0.223 mmol, 56%), pale yellow oil. $^1$H NMR (400 MHz, CDCl$_3$) δ 8.04 – 7.93 (m, 2H), 7.61 – 7.56 (m, 1H), 7.54 – 7.47 (m, 2H), 7.42 – 7.33 (m, 5H), 4.31 (d, *J* = 6.0 Hz, 1H), 3.83 (qd, *J* = 9.9, 6.6 Hz, 2H), 3.67 – 3.61 (m, 2H), 3.44 – 3.36 (m, 1H), 3.10 (t, *J* = 7.0 Hz, 2H), 2.11 (q, *J* = 6.4 Hz, 2H). $^{13}$C NMR (101 MHz,

CDCl$_3$) δ 199.7, 137.0, 134.7, 133.3, 129.4, 128.9, 128.2, 128.2, 125.2, 112.2, 111.9, 71.1, 70.1, 46.5, 35.1, 26.4, 24.3. HRMS (ESI) m/z: [M + Na]$^+$: Calcd. for C$_{21}$H$_{20}$N$_2$O$_2$Na 355.1417; Found: 355.1425.

## 2-(7-Oxo-1,2-diphenyloctyl)malononitrile (29)
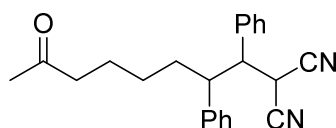


Prepared according to general procedure D using 1-methyl-2-phenylcyclohexan-1-ol (**S29**) (76.1 mg, 0.4 mmol, 1 equiv.), 2-methoxypyridin (126 µl, 131 mg, 1.2 mmol, 3 equiv.) and an irradiation time of 24 h. Yield after column chromatography (25 g silica gel, hexanes/ethyl acetate 5-40%): 137 mg (0.398 mmol, 99%), pale green resin. $^1$H NMR (400 MHz, CDCl$_3$, diastereomers 1:1) δ 7.53 – 7.41 (m, 4H), 7.39 – 7.28 (m, 2H), 7.25 – 7.18 (m, 2H), 6.92 – 6.85 (m, 2H), 4.01 (d, *J* = 8.9 Hz, 0.5H), 3.57 – 3.47 (m, 1H), 3.35 – 3.27 (m, 0.5H), 3.27 – 3.16 (m, 1H), 2.34 (t, *J* = 7.3 Hz, 1H), 2.19 (ddd, *J* = 8.8, 7.0, 2.2 Hz, 1H), 2.08 (s, 1.5H), 2.00 (s, 1.5H), 1.85 – 1.65 (m, 1H), 1.63 – 1.50 (m, 1H), 1.47 – 1.41 (m, 1H), 1.34 – 1.06 (m, 2H), 1.03 – 0.89 (m, 1H). $^{13}$C NMR (101 MHz, CDCl$_3$) δ 208.6, 140.4, 138.2*, 135.8, 134.8*, 129.9*, 129.5, 129.3*, 129.1*, 129.0, 128.8, 128.6, 128.6*, 128.4, 127.7*, 112.7, 112.2, 112.1*, 111.5*, 53.0, 51.8*, 47.8, 47.4*, 43.5, 43.4*, 33.8*, 33.5, 29.9, 29.9*, 28.9*, 27.5, 27.0, 27.0*, 23.6, 23.4*. HRMS (ESI) m/z: [M + Na]$^+$: Calcd. for C$_{23}$H$_{24}$N$_2$O$_2$Na 367.1781; Found: 367.1792.
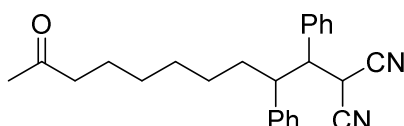
## 2-(8-Oxo-1,2-diphenylnonyl)malononitrile (30)
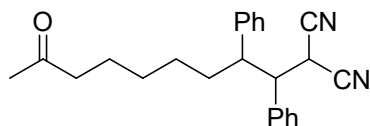


Prepared according to general procedure D using 1-methyl-2-phenylcycloheptan-1-ol (**S30**) (81.7 mg, 0.4 mmol, 1 equiv.), 2-methoxypyridin (126 µl, 131 mg, 1.2 mmol, 3 equiv.) and an irradiation time of 24 h. Yield after column chromatography (25 g silica gel, hexanes/ethyl acetate 5-35%): 139 mg (0.388 mmol, 97%), pale green resin. $^1$H NMR (400 MHz, CDCl$_3$, diastereomers 1:1) δ 7.52 – 7.40 (m, 4H), 7.39 – 7.30 (m, 2H), 7.24 – 7.18 (m, 2H), 6.93 – 6.86 (m, 2H), 4.03 (d, *J* = 8.7 Hz, 0.5H), 3.60 – 3.47 (m, 1H), 3.35 – 3.25 (m, 0.5H), 3.25 – 3.17 (m, 1H), 2.35 (t, *J* = 7.3 Hz, 1H), 2.24 (t, *J* = 7.4 Hz, 1H), 2.09 (s, 1.5H), 2.04 (s, 1.5H), 1.71 – 1.60 (m, 1H), 1.53 – 1.40 (m, 2H), 1.37 – 1.23 (m, 2H),

1.16 – 1.08 (m, 1H), 1.06 – 0.97 (m, 1H), 0.97 – 0.87 (m, 1H). $^{13}$C NMR (101 MHz, CDCl$_3$) δ 209.1*, 209.0, 140.5, 138.3*, 135.8, 134.8*, 129.8*, 129.5, 129.3*, 129.1*, 129.0, 128.8, 128.6, 128.5*, 128.3, 127.6*, 112.7, 112.3, 112.1*, 111.6*, 52.9, 51.8*, 47.8*, 47.4, 43.6, 43.5*, 33.8*, 33.4, 30.0*, 30.0, 29.0, 28.9*, 28.7, 27.5*, 27.2*, 27.2, 23.6*, 23.5. HRMS (ESI) m/z: [M + Na]$^+$: Calcd. for C$_{24}$H$_{26}$N$_2$O$_2$Na 381.1937; Found: 381.1945.

### 2-(9-Oxo-1,2-diphenyldecyl)malononitrile (31)



Prepared according to general procedure D using 1-methyl-2-phenylcyclooctan-1-ol (**S31**) (65.5 mg, 0.3 mmol, 1 equiv.), 2-methoxypyridin (95 µl, 98 mg, 0.9 mmol, 3 equiv.) and an irradiation time of 24 h. Yield after column chromatography (25 g silica gel, hexanes/ethyl acetate 5-35%): 98 mg (0.263 mmol, 88%), pale green resin. $^1$H NMR (400 MHz, CDCl$_3$, diastereomers 1:1) δ 7.57 – 7.40 (m, 4H), 7.38 – 7.27 (m, 2H), 7.25 – 7.17 (m, 2H), 6.96 – 6.85 (m, 2H), 4.05 (d, *J* = 8.6 Hz, 0.5H), 3.55 (d, *J* = 3.6 Hz, 0.5H), 3.50 (dd, *J* = 8.6, 7.1 Hz, 0.5H), 3.33 – 3.26 (m, 0.5H), 3.26 – 3.15 (m, 1H), 2.37 (t, *J* = 7.4 Hz, 1H), 2.29 (t, *J* = 7.4 Hz, 1H), 2.10 (s, 1.5H), 2.07 (s, 1.5H), 1.85 – 1.74 (m, 0.5H), 1.71 – 1.60 (m, 0.5H), 1.55 – 1.47 (m, 1H), 1.47 – 1.37 (m, 2H), 1.35 – 1.15 (m, 3H), 1.14 – 0.90 (m, 3H). $^{13}$C NMR (101 MHz, CDCl$_3$) δ 209.3*, 209.2, 140.6, 138.4*, 135.9, 134.9*, 129.8*, 129.5, 129.3*, 129.1*, 129.0, 128.7, 128.6, 128.5*, 128.3, 127.5*, 112.7, 112.3, 112.1*, 111.6*, 52.9*, 51.7, 47.8*, 47.5, 43.7, 43.7*, 33.9*, 33.5, 30.0, 30.0*, 29.2*, 29.0*, 29.0, 28.9, 27.5, 27.3*, 27.2, 23.7, 23.7*. HRMS (ESI) m/z: [M + Na]$^+$: Calcd. for C$_{25}$H$_{28}$N$_2$O$_2$Na 395.2094; Found: 395.2093.
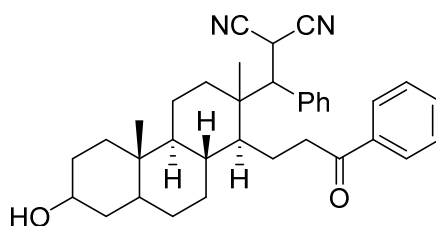
### 2-(Phenyl(1,2,2-trimethyl-3-(2-oxo-2-phenylethyl)cyclopentyl)methyl)malononitrile (32)
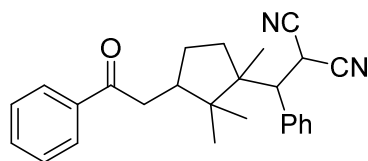


Prepared according to general procedure D using 1,7,7-trimethyl-2-phenylbicyclo[2.2.1]heptan-2-ol (**S32**) (92.1 mg, 0.4 mmol, 1 equiv.), 2-methoxypyridin (126 µl, 131 mg, 1.2 mmol, 3 equiv.) and an irradiation time of 24 h. Yield after column

chromatography (25 g silica gel, hexanes/ethyl acetate 2-22%): 99.5 mg (0.26 mmol, 65%), pale green resin. $^1$H NMR (300 MHz, CDCl$_3$, diastereomers 2:1) δ 7.96 – 7.89 (m, 2H), 7.59 – 7.37 (m, 8H), 4.23 (dd, $J$ = 28.9, 3.6 Hz, 1H), 3.37 – 3.32 (m, 1H), 3.20 – 3.02 (m, 1H), 2.90 – 2.77 (m, 1H), 2.57 – 2.42 (m, 1H), 1.94 – 1.43 (m, 2.5H), 1.37 (2 s, 3H), 1.34 – 1.23 (m, 1H), 1.14 (s, 2H), 1.09 (s, 1H), 0.97 (s, 2H), 0.95 – 0.84 (m, 0.5H), 0.48 (s, 1H). $^{13}$C NMR (75 MHz, CDCl$_3$) δ 199.9*, 199.8, 137.2*, 137.2, 137.2, 136.4*, 133.3, 133.2*, 130.6*, 130.6*, 129.8, 129.1, 128.9*, 128.9, 128.8, 128.8*, 128.1, 128.1*, 113.5, 113.1*, 113.1, 111.4*, 53.0*, 51.6, 51.1*, 51.0, 47.3, 47.2*, 45.6*, 43.8*, 43.5, 41.4, 38.1*, 36.3, 29.1*, 28.8*, 28.2*, 28.1, 27.3, 24.6, 21.3, 20.8*, 19.3, 19.0*. HRMS (ESI) m/z: [M + Na]$^+$: Calcd. for C$_{26}$H$_{28}$N$_2$ONa 407.2094; Found: 407.2100.

## 2-(((1*S*,4a*S*,4b*S*,10a*R*)-7-Hydroxy-2,4*b*-dimethyl-1-(3-oxo-3-phenylpropyl)tetradecahydro-phenanthren-2-yl)(phenyl)methyl)malononitrile (33)
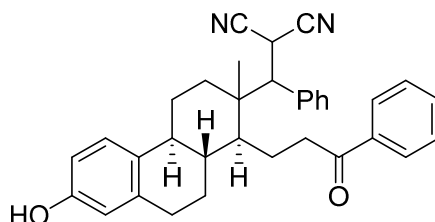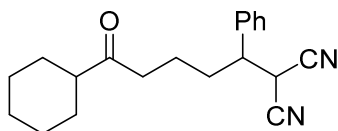


Prepared according to general procedure D using 1,7,7-trimethyl-2-phenylbicyclo[2.2.1]heptan-2-ol (**S33**) (147 mg, 0.4 mmol, 1 equiv.), 2-methoxypyridin (210 µl, 218 mg, 1.2 mmol, 5 equiv.) and an irradiation time of 62 h. Yield after column chromatography (25 g silica gel, hexanes/acetone 7-60%): 207 mg (0.396 mmol, 99%), brown-beige solid. $^1$H NMR (400 MHz, CDCl$_3$, diastereomers 3:2) δ 8.03 – 7.99 (m, 1.2H), 7.76 – 7.71 (m, 0.8H), 7.62 – 7.27 (m, 8H), 4.30 (d, $J$ = 5.6 Hz, 0.6H), 4.16 – 4.09 (m, 0.4H), 3.66 (d, $J$ = 5.7 Hz, 0.6H), 3.64 – 3.53 (m, 1H), 3.40 (d, $J$ = 3.9 Hz, 0.4H), 3.30 – 3.07 (m, 1H), 2.79 – 2.62 (m, 0.4H), 2.15 – 2.06 (m, 0.6H), 2.01 – 1.23 (m, 17H), 1.21 (s, 1.2H), 1.19 – 0.88 (m, 4H), 0.78 (2 × s, 3H), 0.66 (s, 1.8H). $^{13}$C NMR (101 MHz, CDCl$_3$) δ 200.0, 199.8*, 137.0*, 136.8, 136.3, 135.5*, 133.6, 133.2*, 130.8*, 130.1, 129.1, 129.0*, 128.9, 128.9*, 128.6, 128.3, 127.9*, 114.0, 113.6, 113.4*, 113.2*, 71.3*, 71.2, 60.5*, 56.6*, 53.0, 52.8, 48.3, 47.9*, 44.2, 42.4*, 41.8, 40.5, 39.7*, 39.7, 39.6*, 38.0, 36.9, 36.9*, 35.7, 35.7*, 34.2*, 33.5, 33.0, 32.3*, 31.5, 28.9, 28.7*, 26.1*, 24.8, 24.0, 22.9*, 20.9*, 20.2, 19.8, 12.5, 12.4*. HRMS (ESI) m/z: [M + Na]$^+$: Calcd. for C$_{35}$H$_{42}$N$_2$O$_2$Na 545.3138; Found: 545.3135.

**2-(((1S,4aS,10aS)-7-Hydroxy-2-methyl-1-(3-oxo-3-phenylpropyl)-1,2,3,4,4a,9,10,10a-octahydrophenanthren-2-yl)(phenyl)methyl)malononitrile (34)**
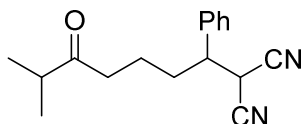


Prepared according to general procedure D using (8R,9S,13S,14S)-13-methyl-17-phenyl-7,8,9,11,12,13,14,15,16,17-decahydro-6H-cyclopenta[a]phenanthrene-3,17-diol (**S34**) (139 mg, 0.4 mmol, 1 equiv.), 2-methoxypyridine (210 µl, 218 mg, 1.2 mmol, 5 equiv.) and an irradiation time of 62 h. Yield after column chromatography (25 g silica gel, hexanes/acetone 5-35%): 108 mg (0.215 mmol, 54%), pale yellow oil. $^1$H NMR (300 MHz, (CD$_3$)$_2$CO, diastereomers 7:3) δ 8.12 – 8.05 (m, 1.4H), 7.96 (2 × s, 1H), 7.89 – 7.81 (m, 0.6H), 7.75 – 7.60 (m, 3H), 7.57 – 7.53 (m, 1H), 7.53 – 7.48 (m, 1H), 7.47 – 7.37 (m, 3H), 7.14 (d, J = 8.5 Hz, 1H), 6.61 (dd, J = 8.4, 2.7 Hz, 1H), 6.51 (dd, J = 12.0, 2.6 Hz, 1H), 5.09 (2 × d, J = 5.0 Hz, 1H), 3.94 (d, J = 5.6 Hz, 0.7H), 3.75 (d, J = 4.2 Hz, 0.3H), 3.47 – 3.35 (m, 1.5H), 2.83 – 2.70 (m, 2H), 2.45 – 2.30 (m, 2H), 2.28 – 2.12 (m, 2.5H), 2.01 – 1.70 (m, 3H), 1.63 – 1.42 (m, 2H), 1.38 (s, 1H), 1.35 – 1.16 (m, 2H), 0.80 (s, 2H). $^{13}$C NMR (75 MHz, (CD$_3$)$_2$CO) δ 200.1, 199.8*, 156.1, 156.1*, 138.3, 138.2*, 138.2, 138.1, 137.5*, 133.8, 133.6*, 131.5, 131.3*, 131.2, 130.8, 130.4*, 130.1, 130.0, 129.5*, 129.5, 129.4, 129.3*, 129.3, 129.0, 128.9, 128.6, 127.5*, 127.5, 127.4*, 115.7, 115.6*, 115.2, 113.9*, 56.0*, 53.0, 52.9*, 47.4*, 47.3, 44.4, 43.8, 43.7*, 43.2*, 42.5, 40.1, 39.9*, 34.9*, 34.2, 34.2*, 31.1, 31.0*, 28.6, 28.0*, 28.0*, 27.3, 26.8*, 25.5, 23.4, 22.9*, 20.3, 20.0*. HRMS (ESI) m/z: [M + Na]$^+$: Calcd. for C$_{34}$H$_{34}$N$_2$O$_2$Na 525.2512; Found: 525.2503.

**2-(5-Cyclohexyl-5-oxo-1-phenylpentyl)malononitrile (35)**



Prepared according to general procedure D using 1-cyclohexylcyclobutan-1-ol (**S35**) (61.7 mg, 0.4 mmol, 1 equiv.), 2-Cl-quinoline (65.4 mg, 0.4 mmol, 1 equiv.) and an irradiation time of 62 h. Yield after column chromatography (25 g silica gel, hexanes/ethyl acetate 3-20%): 71 mg (0.23 mmol, 58%), pale yellow resin. $^1$H NMR (400 MHz, (CDCl$_3$) δ 7.44 – 7.29 (m, 5H), 3.91 (d, J = 6.2 Hz, 1H), 3.20 (dt, J = 9.7, 5.9 Hz, 1H), 2.46 (q, J = 6.9 Hz, 2H), 2.35 – 2.23 (m, 1H), 2.05 – 1.91 (m, 2H), 1.86 – 1.72 (m, 4H), 1.71 – 1.62 (m, 1H), 1.50 (dt, J = 8.4, 7.0 Hz, 2H), 1.35 – 1.19 (m, 5H). $^{13}$C NMR (101 MHz, CDCl$_3$) δ 213.2, 136.5, 129.5, 129.2, 128.0, 111.9, 111.9, 51.0, 46.8, 39.7, 31.7, 30.4, 28.6, 28.6,

25.9, 25.8, 21.1. HRMS (ESI) m/z: [M + Na]$^+$: Calcd. for $C_{20}H_{24}N_2ONa$ 331.1781; Found: 331.1787.

**2-(6-Methyl-5-oxo-1-phenylheptyl)malononitrile (36)**



Prepared according to general procedure D using 1-isopropylcyclobutan-1-ol (**S36**) (45.7 mg, 0.4 mmol, 1 equiv.), 2-Cl-quinoline (65.4 mg, 0.4 mmol, 1 equiv.) and an irradiation time of 62 h. Yield after column chromatography (25 g silica gel, hexanes/ethyl acetate 3-20%): 43 mg (0.16 mmol, 40%), pale yellow resin. $^1$H NMR (400 MHz, (CDCl$_3$) δ 7.43 – 7.30 (m, 5H), 3.91 (d, $J$ = 6.1 Hz, 1H), 3.20 (dt, $J$ = 9.8, 5.9 Hz, 1H), 2.60 – 2.40 (m, 3H), 2.06 – 1.92 (m, 2H), 1.57 – 1.45 (m, 2H), 1.07 (d, $J$ = 6.9 Hz, 6H). $^{13}$C NMR (101 MHz, CDCl$_3$) δ 213.8, 136.5, 129.5, 129.2, 128.0, 112.0, 111.9, 46.8, 41.0, 39.4, 31.7, 30.4, 21.2, 18.4, 18.4. HRMS (ESI) m/z: [M + Na]$^+$: Calcd. for $C_{17}H_{20}N_2ONa$ 291.1468; Found: 291.1473.

**2-Hydroxy-2-pentyl-6-phenylcyclohexane-1,1-dicarbonitrile (37)**
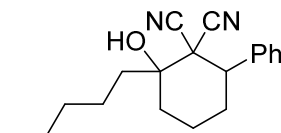


Prepared according to general procedure D using 1-pentylcyclobutan-1-ol (**S37**) (56.9 mg, 0.4 mmol, 1 equiv.), 2-Cl-quinoline (196 mg, 1.2 mmol, 3 equiv.) and an irradiation time of 62 h. Yield after column chromatography (25 g silica gel, hexanes/ethyl acetate 6%): 48.2 mg (0.163 mmol, 41%), pale yellow resin. $^1$H NMR (400 MHz, (CDCl$_3$) δ 7.46 – 7.37 (m, 5H), 3.52 (dd, $J$ = 12.9, 3.3 Hz, 1H), 2.17 – 2.13 (m, 1H), 2.10 – 1.90 (m, 5H), 1.86 – 1.76 (m, 2H), 1.73 – 1.61 (m, 1H), 1.53 – 1.45 (m, 2H), 1.40 – 1.32 (m, 4H), 0.95 – 0.89 (m, 3H). $^{13}$C NMR (101 MHz, CDCl$_3$) δ 138.2, 128.9, 128.8, 114.7, 114.2, 76.4, 52.8, 45.8, 40.2, 32.0, 30.7, 27.5, 22.7, 22.5, 20.1, 14.1. HRMS (ESI) m/z: [M + Na]$^+$: Calcd. for $C_{19}H_{24}N_2ONa$ 319.1781; Found: 319.1788.

### 3.6.5 *In-situ* NMR Kinetics

For the sample preparation a 5 mm amberized NMR tube of Spintec was charged with 1-phenylcyclobutan-1-ol (1 equiv.), p-toluenesulfonyl cyanide (1.5 equiv.), 9-mesityl-10-methylacridinium perchlorate photocatalyst (0.02 equiv., 2 mol%), pyridine base (3 equiv.) and $H_2O$ (0.25 equiv.). Dry $CD_3CN$ (100 mM, 0.6 ml) was added, which was freshly distilled over $CaH_2$ prior to use.
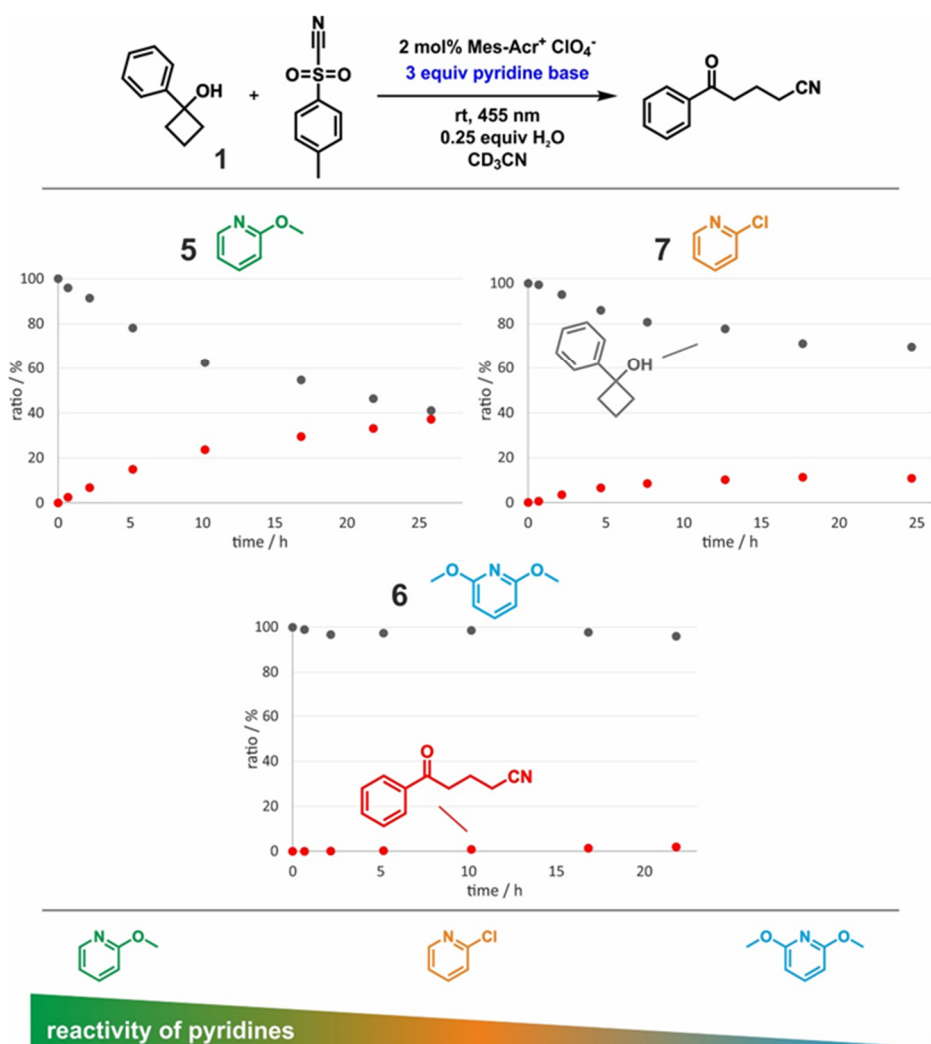


**Figure 3.6:** *In-situ* kinetic followed by $^1$H NMR: In presence of 2-methoxypyridine ~40% product (red curve) was achieved after ~25 h, with 2-chloropyridine the product formation was drastically reduced (~11% after 25 h) and using 2,6-dimethoxypyridine the reaction was ineffective (2% after ~22 h).

For the *in-situ* illumination inside the NMR, the combined illumination setup described by Feldmeier et al. was applied.[11] As light source, a 450 nm Lumitronix Cree XT-E-1 (royalblue; 452 nm peak wavelength measured in our group) LED was used.

The amounts (%) were obtained by integration of the corresponding alcohol and product signals. For accurate integration, the respective signal regions were baseline corrected. As no conversion was observed in the dark, the signal integral of the starting material was set to 100%. According to this reference, the progression of the photocatalytic reaction was determined after starting the illumination.

### 3.6.6 Hydrogen Bond Investigations by NMR

The reactivity of the different pyridines was also confirmed using $CH_2Cl_2$ as solvent.

**Table 3.6:** Base performance for ring-opening cyanation with TsCN.
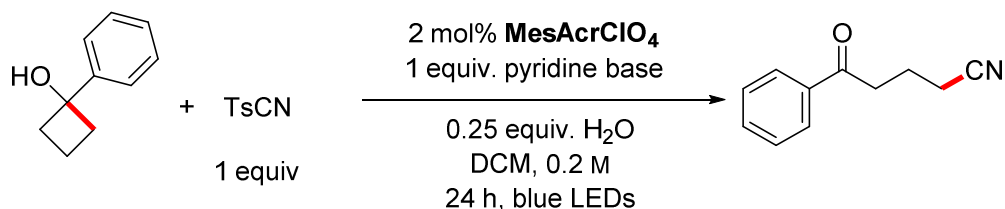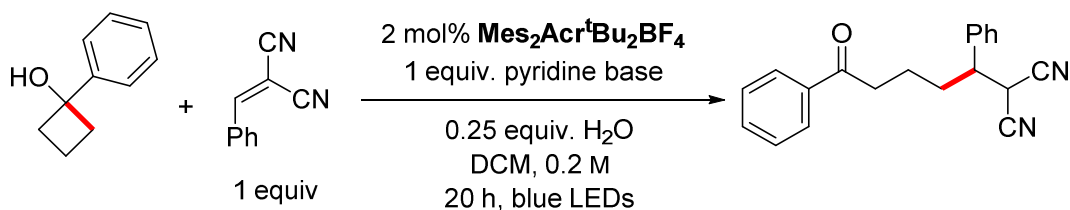


| base | yield |
|---|---|
| 2-methoxypyridine (**5**) | 29% |
| 2-chloropyridine (**7**) | 18% |
| 2,6-dimethoxypyridine (**6**) | 12% |

Reactions were performed on 0.2 mmol scale. Yields of isolated product.

**Table 3.7:** Base performance for ring-opening/Giese-type addition in dichloromethane.



| base | conversion alcohol | yield |
|---|---|---|
| 2-methoxypyridine (**5**) | 100% | 45% |
| 2-chloropyridine (**7**) | 100% | 15% |
| 2,6-dimethoxypyridine (**6**) | 38% | 25% |

Reactions were performed on 0.1 mmol scale. Yields and conversion determined by $^1$H NMR using $CH_2Br_2$ as an internal standard.

Thus, $CD_2Cl_2$ was used for the following low temperature hydrogen bond investigations by NMR spectroscopy. Due to chemical exchange reduction at low temperature, specific hydrogen bonded aggregates are potentially visible on the NMR time scale.[12,13]

The two-component samples were prepared as 1:1 mixtures of the corresponding alcohols and pyridines (50 mM) using stock solutions. The $^1$H NMR spectra were referenced on TMS (0 ppm).[14]

In the following section, the complete spectra with information about the chemical shifts, integrals and the assignment of the different compounds are depicted.

**3.6.6.1 Spectra with Benzylic Alcohol**

**Figure 3.7:** Full $^1$H NMR spectrum of benzyl alcohol (50 mM) in $CD_2Cl_2$ at 180 K. The chemical shifts are referenced to TMS (0 ppm).



**Figure 3.8:** Full $^1$H NMR spectrum of the 1:1 mixture (50 mM) of benzyl alcohol and 2,6-dimethoxypyridine in $CD_2Cl_2$ at 180 K. The chemical shifts are referenced to TMS (0 ppm).

**Figure 3.9:** Full $^1$H NMR spectrum of the 1:1 mixture (50 mM) of benzyl alcohol and 2-chloroypyridine in CD$_2$Cl$_2$ at 180 K. The chemical shifts are referenced to TMS (0 ppm).



**Figure 3.10:** Full $^1$H NMR spectrum of the 1:1 mixture (50 mM) of benzyl alcohol and 2-methoxyypyridine in CD$_2$Cl$_2$ at 180 K. The chemical shifts are referenced to TMS (0 ppm).
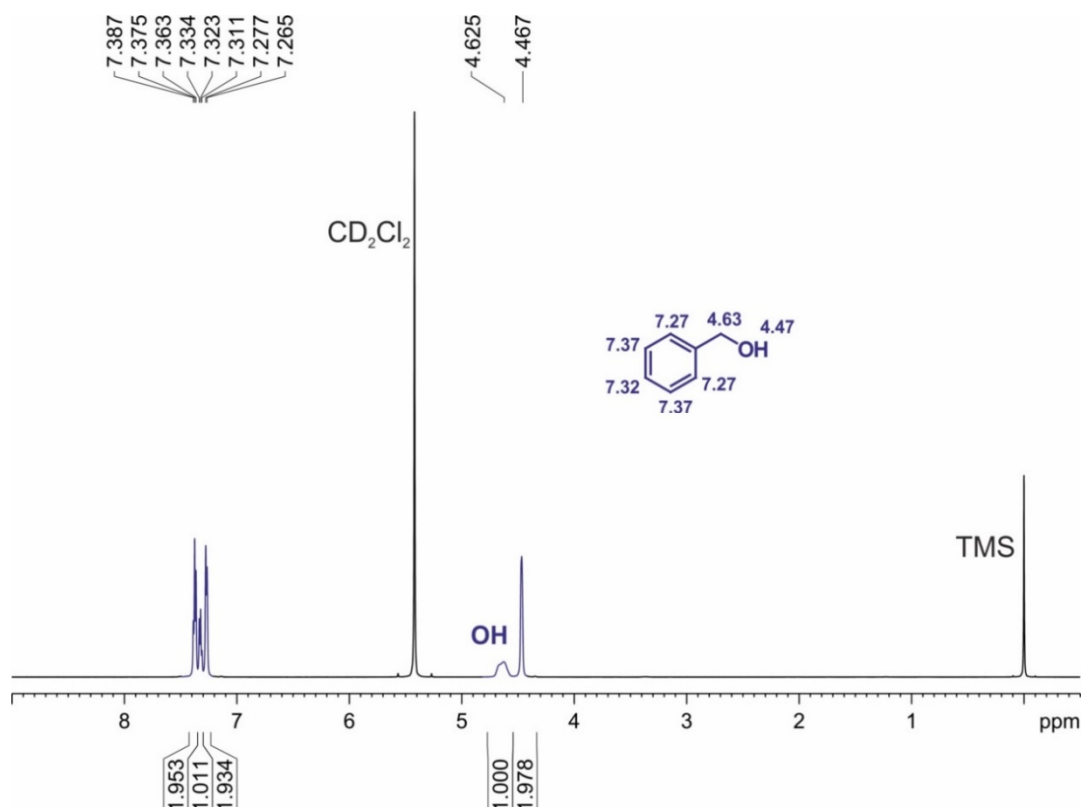
### 3.6.6.2 Spectra with Ethanol
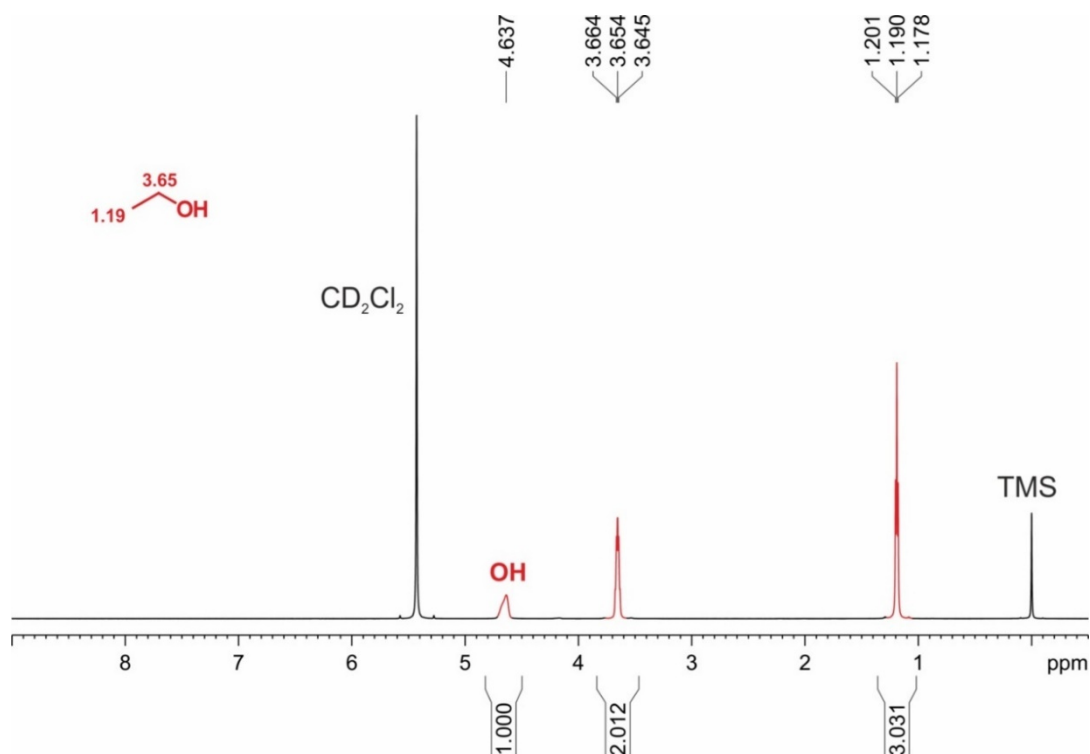
**Figure 3.11:** Full $^1$H NMR spectrum of ethanol (50 mM) in $CD_2Cl_2$ at 180 K. The chemical shifts are referenced to TMS (0 ppm).



**Figure 3.12:** Full $^1$H NMR spectrum of the 1:1 mixture (50 mM) of ethanol and 2,6-dimethoxypyridine in $CD_2Cl_2$ at 180 K. The chemical shifts are referenced to TMS (0 ppm).
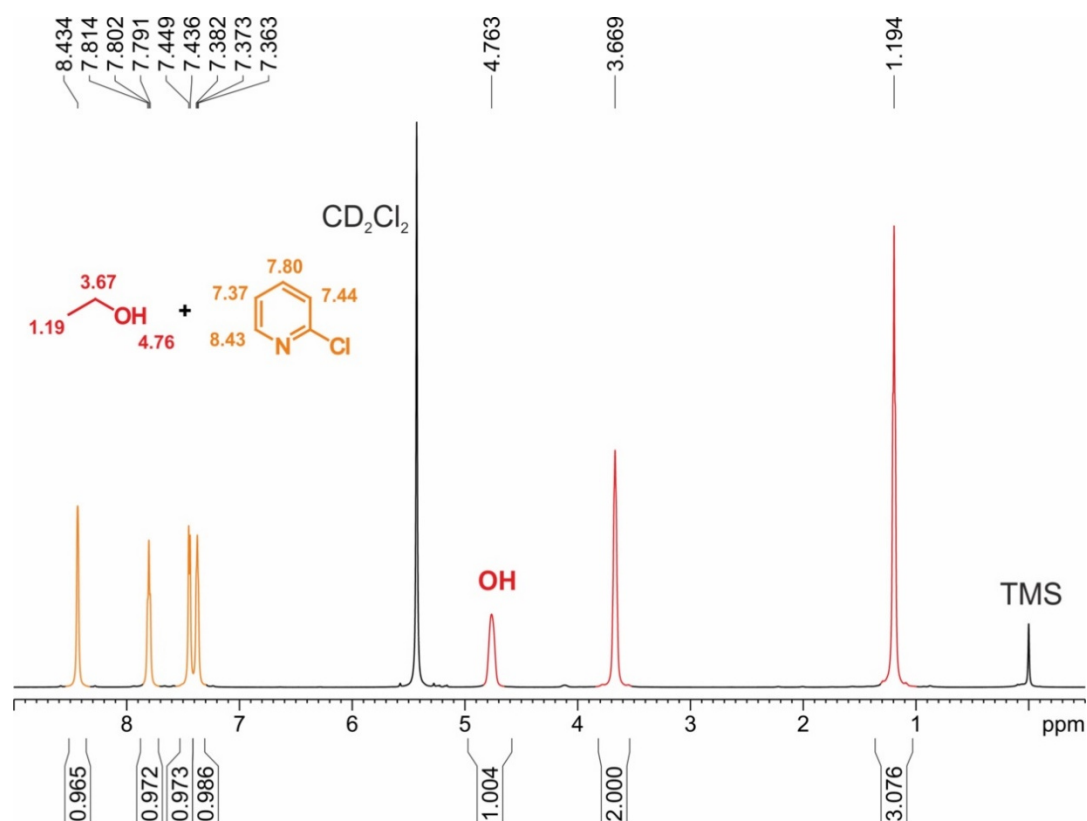
**Figure 3.13:** Full $^1$H NMR spectrum of the 1:1 mixture (50 mM) of ethanol and 2-chloropyridine in CD$_2$Cl$_2$ at 180 K. The chemical shifts are referenced to TMS (0 ppm).
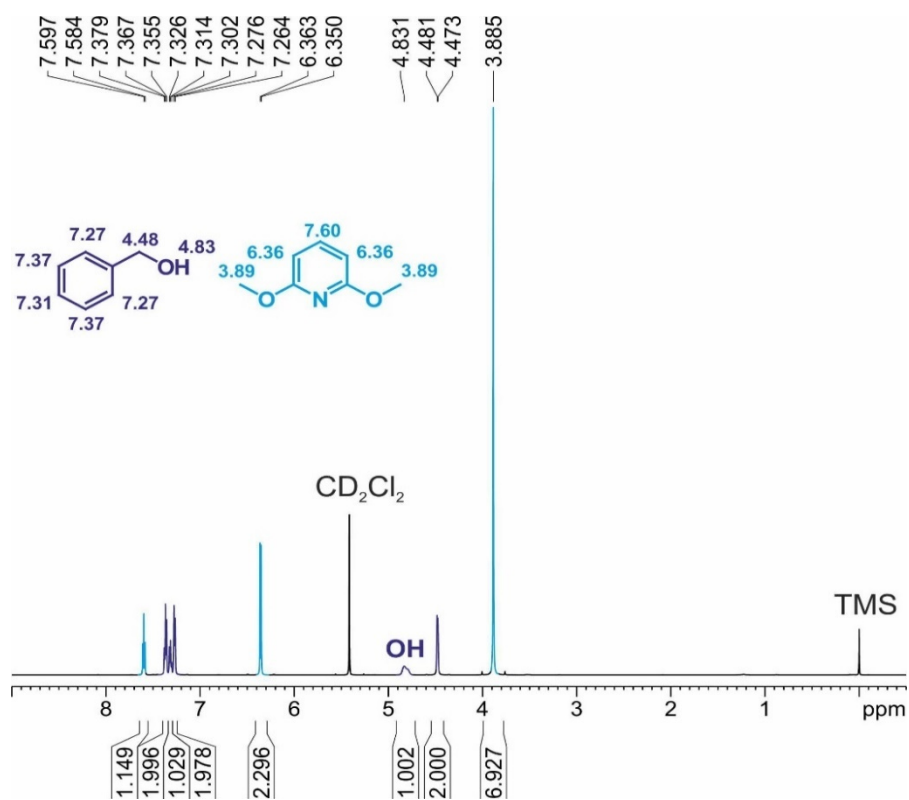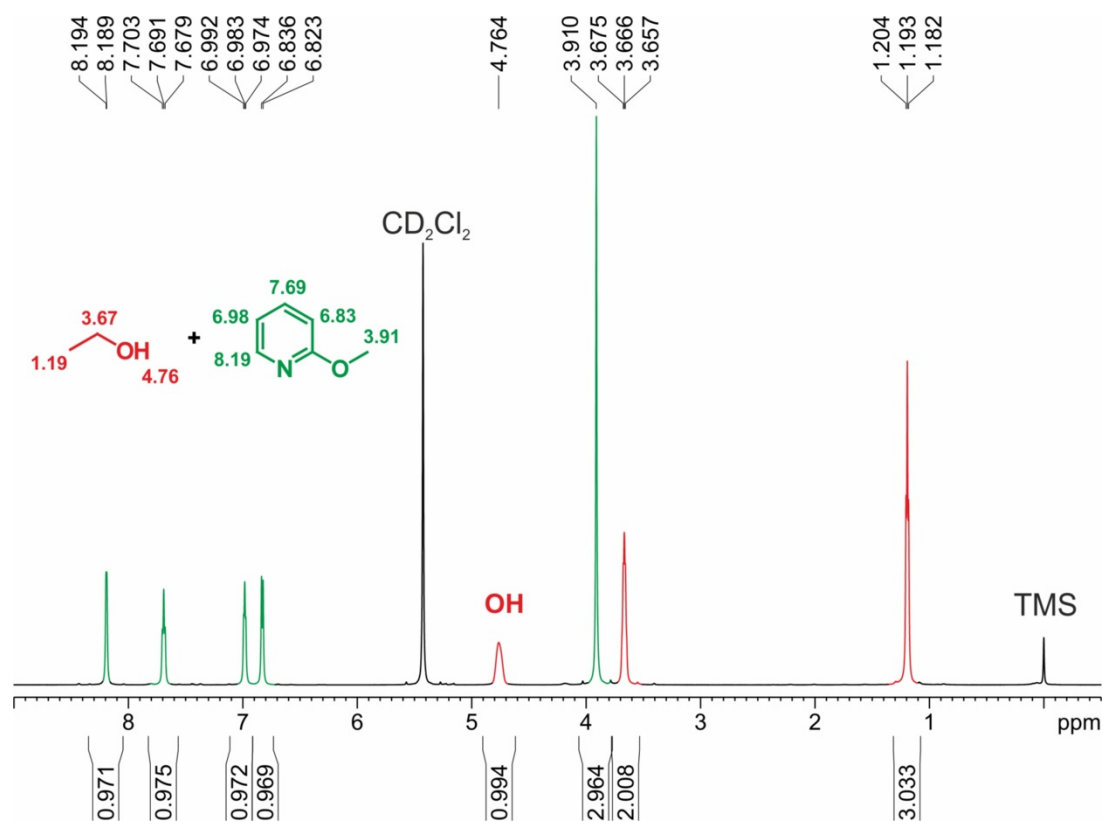


**Figure 3.14:** Full $^1$H NMR spectrum of the 1:1 mixture (50 mM) of ethanol and 2-methoxypyridine in CD$_2$Cl$_2$ at 180 K. The chemical shifts are referenced to TMS (0 ppm).

### 3.6.6.3 Spectra with 1-Phenyl-cyclobutan-1-ol
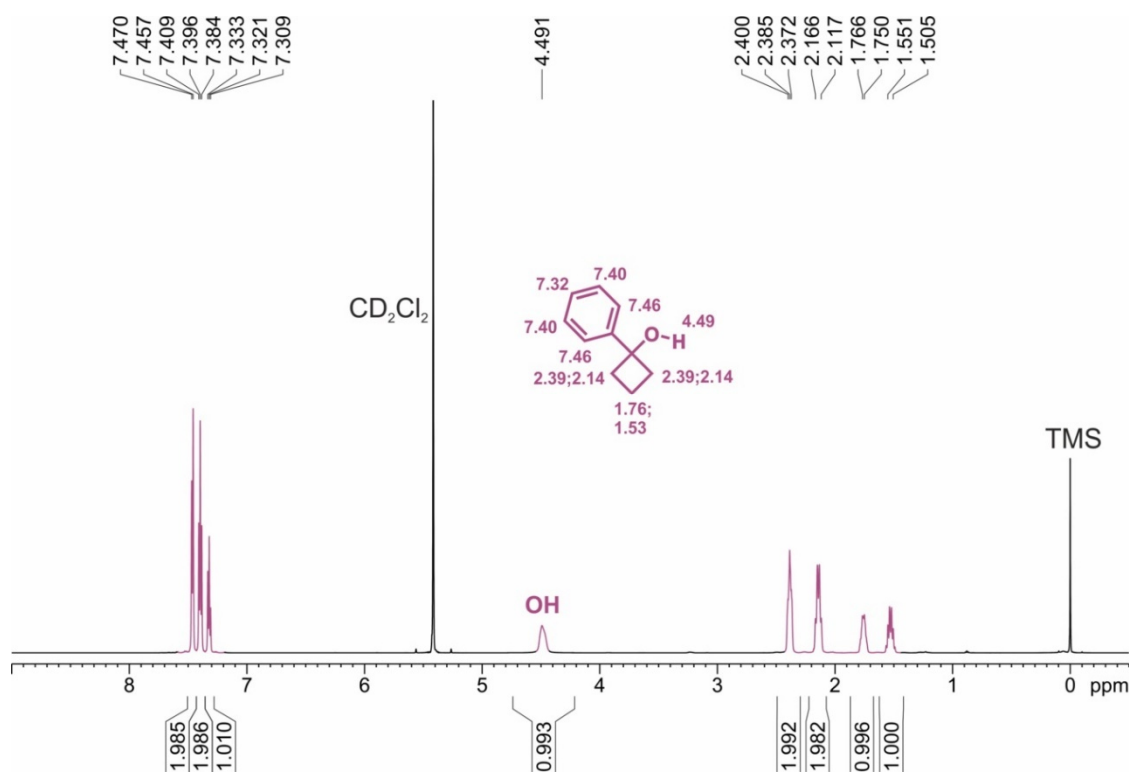


**Figure 3.15:** Full $^1$H NMR spectrum of 1-phenylcyclobutanol (50 mM) in CD$_2$Cl$_2$ at 180 K. The chemical shifts are referenced to TMS (0 ppm).
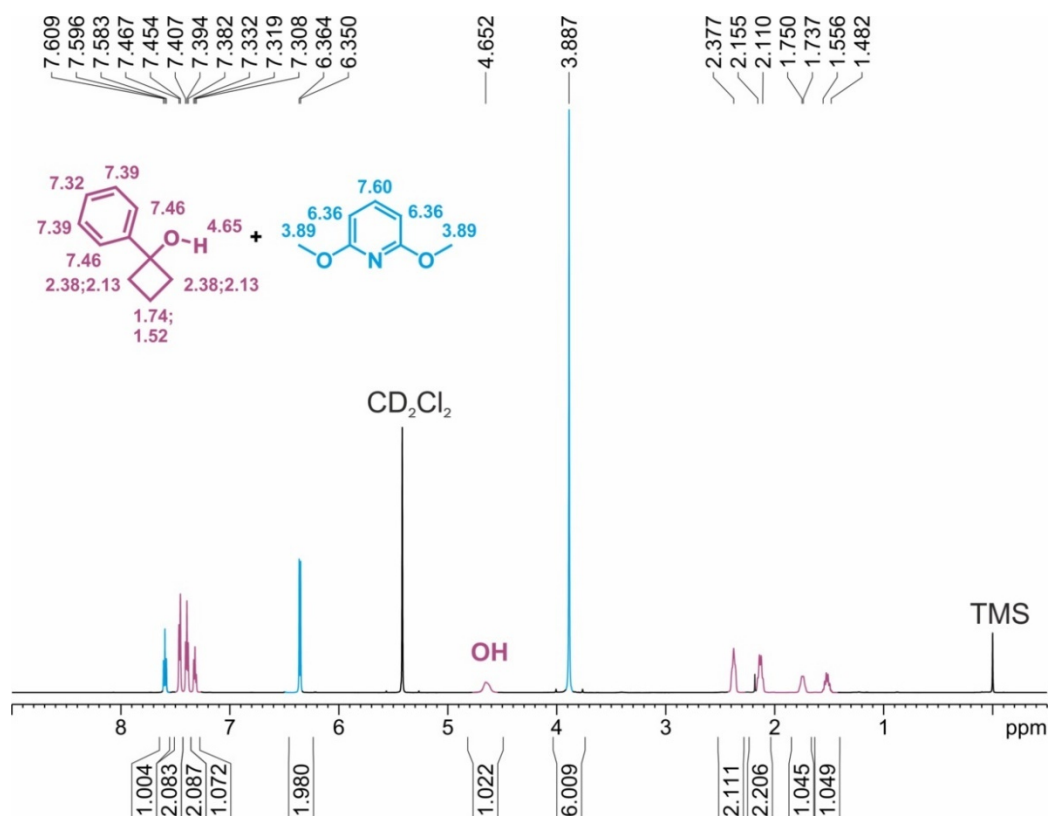


**Figure 3.16:** Full $^1$H NMR spectrum of the 1:1 mixture (50 mM) of 1-phenylcyclobutanol and 2,6-dimethoxypyridine in CD$_2$Cl$_2$ at 180 K. The chemical shifts are referenced to TMS (0 ppm).
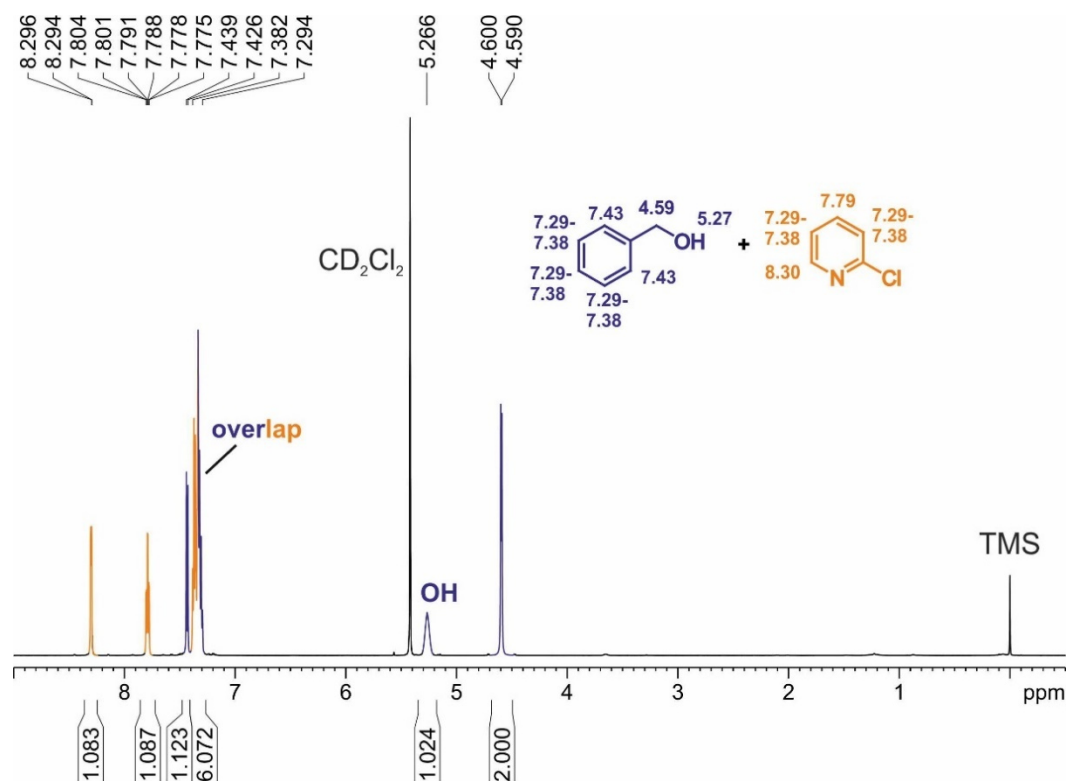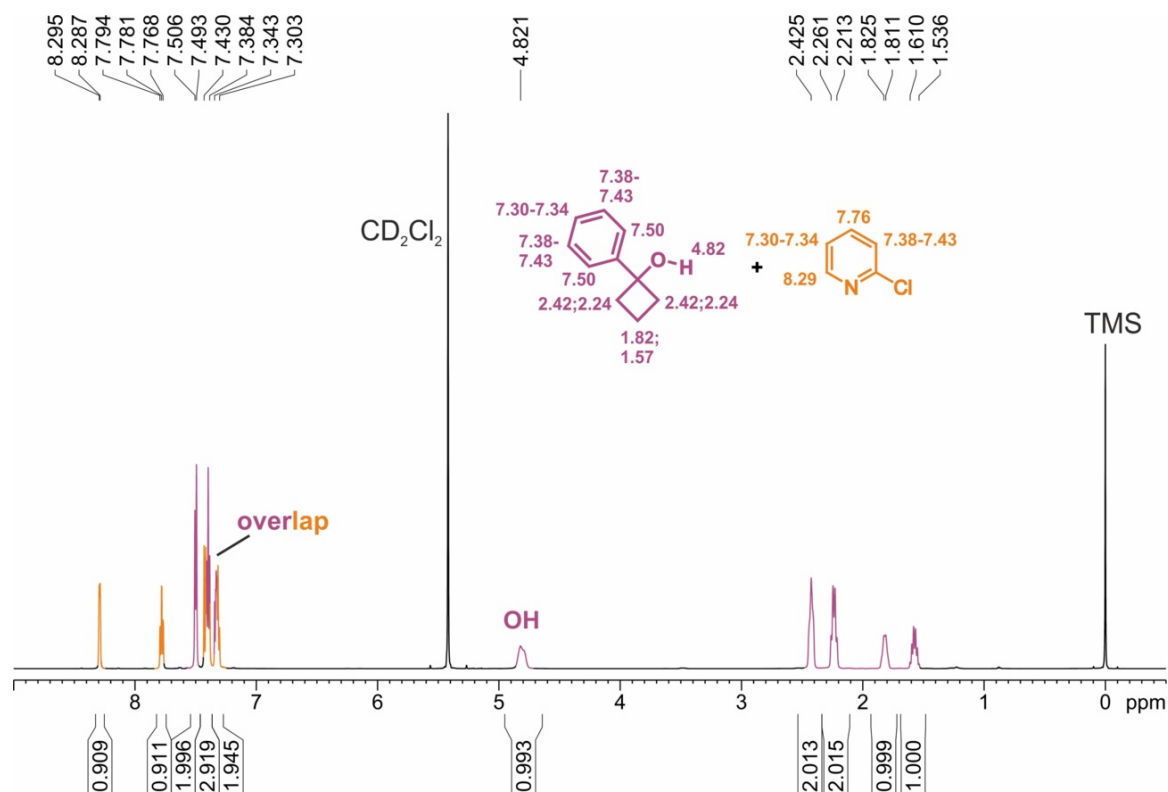
**Figure 3.17:** Full $^1$H NMR spectrum of the 1:1 mixture (50 mM) of 1-phenylcyclobutanol and 2-chloropyridine in CD$_2$Cl$_2$ at 180 K. T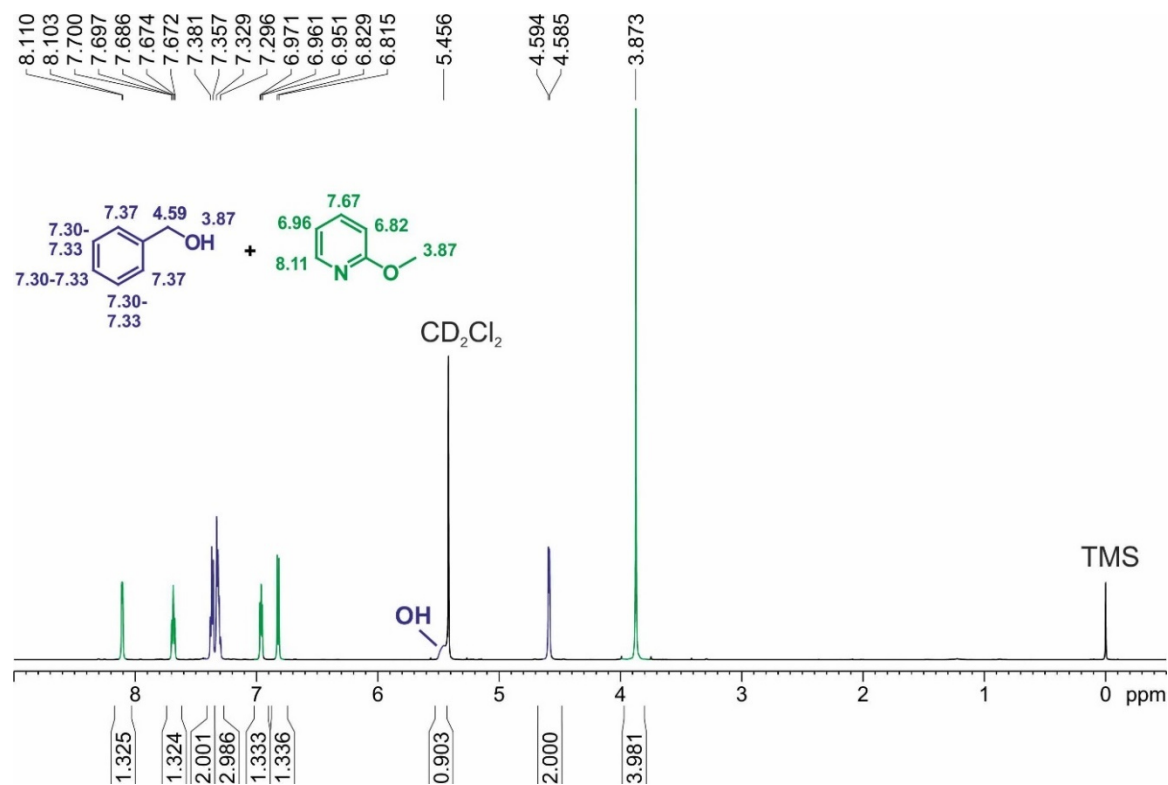he chemical shifts are referenced to TMS (0 ppm). For signal assignment see Figure 3.19 ($^1$H,$^1$H NOESY; aromatic region).
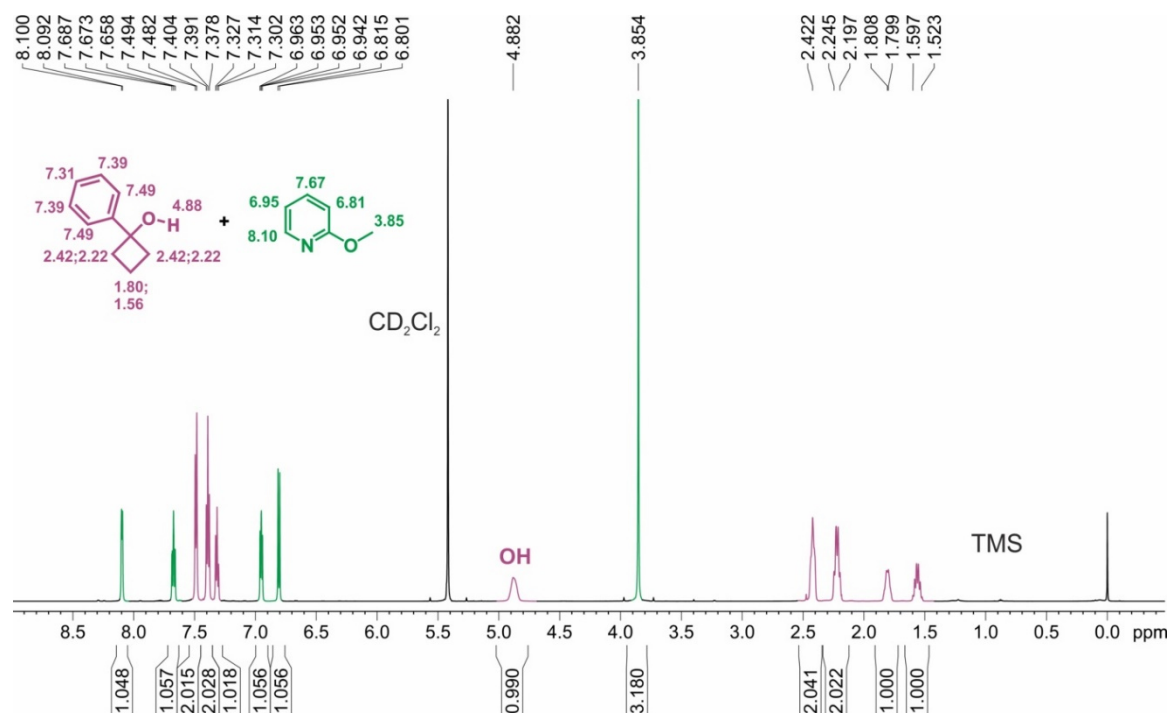


**Figure 3.18:** Full $^1$H NMR spectrum of the 1:1 mixture (50 mM) of 1-phenylcyclobutanol and 2-methoxypyridine in CD$_2$Cl$_2$ at 180 K. The chemical shifts are referenced to TMS (0 ppm).
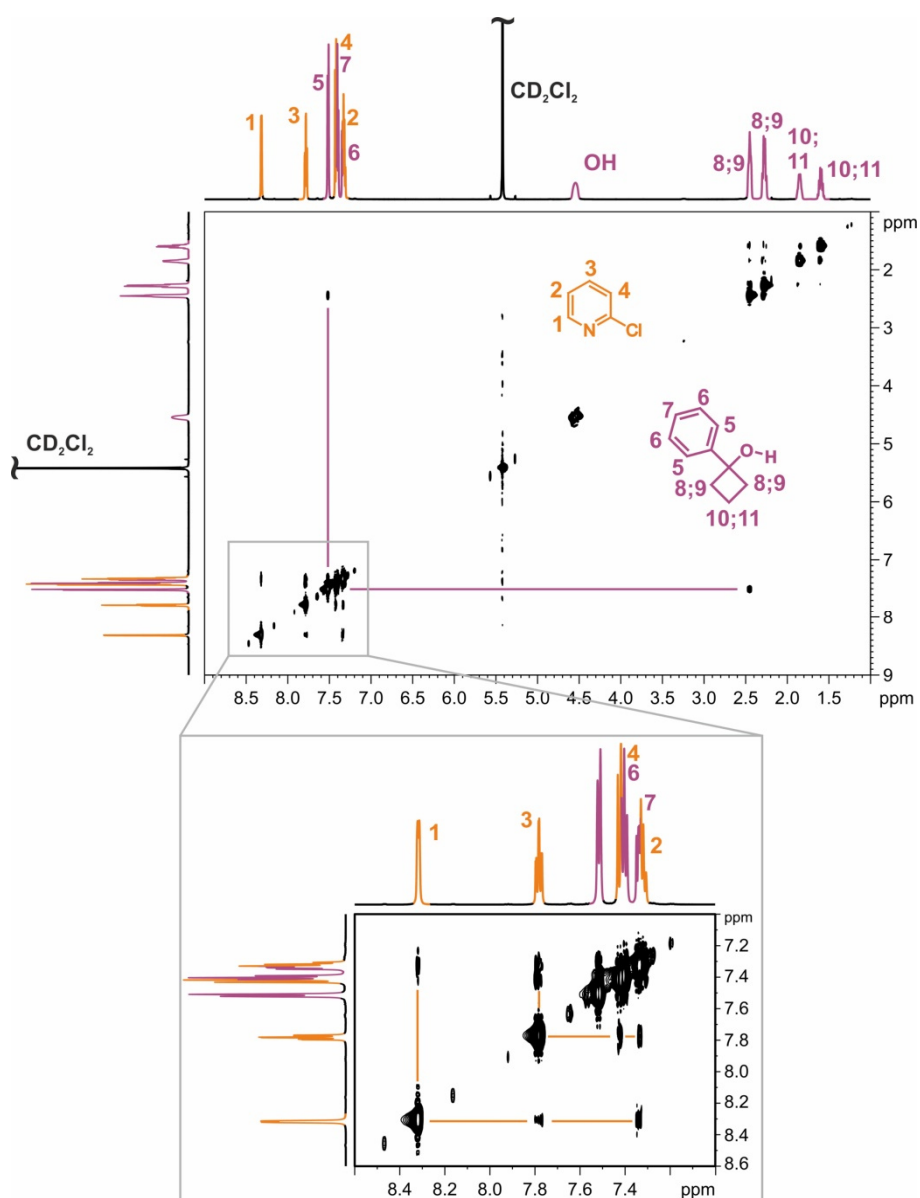
**Figure 3.19:** $^1$H,$^1$H NOESY spectrum of the mixture depicted in Figure 3.17 for assignment of the corresponding signals in the aromatic region. The chemical shifts are referenced to TMS (0 ppm).

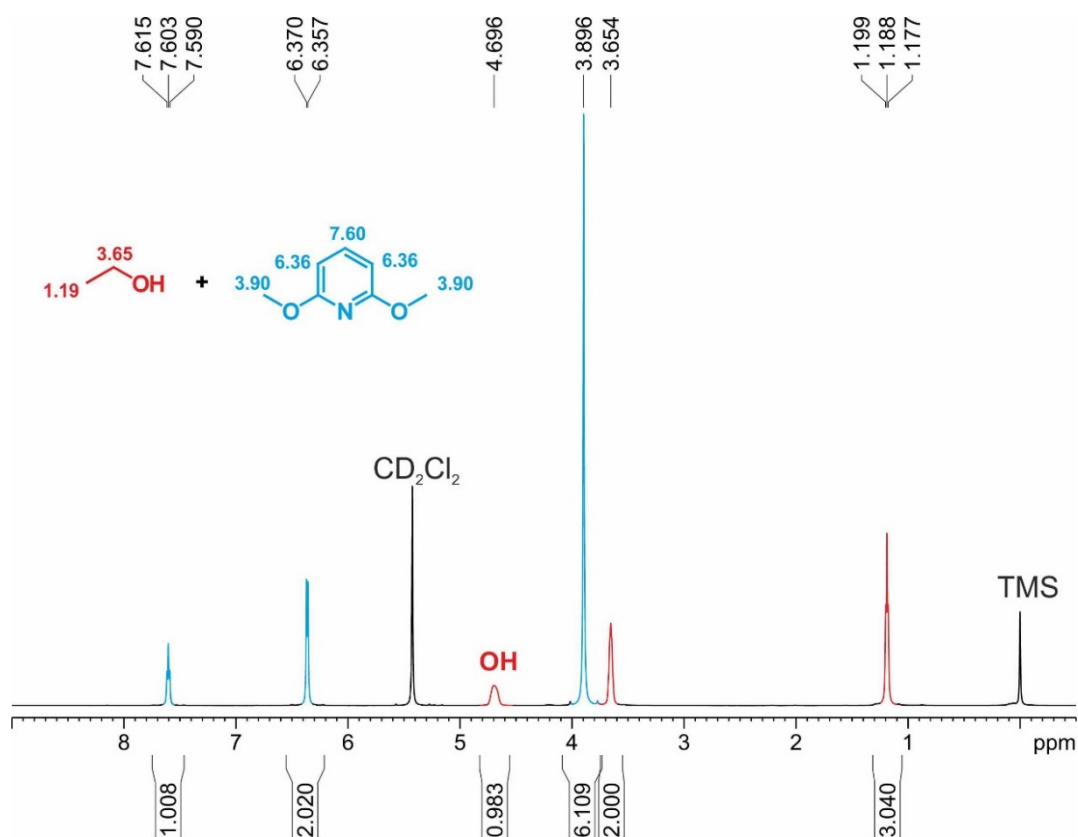### 3.6.6.4 Spectra with Different Pyridine Derivatives
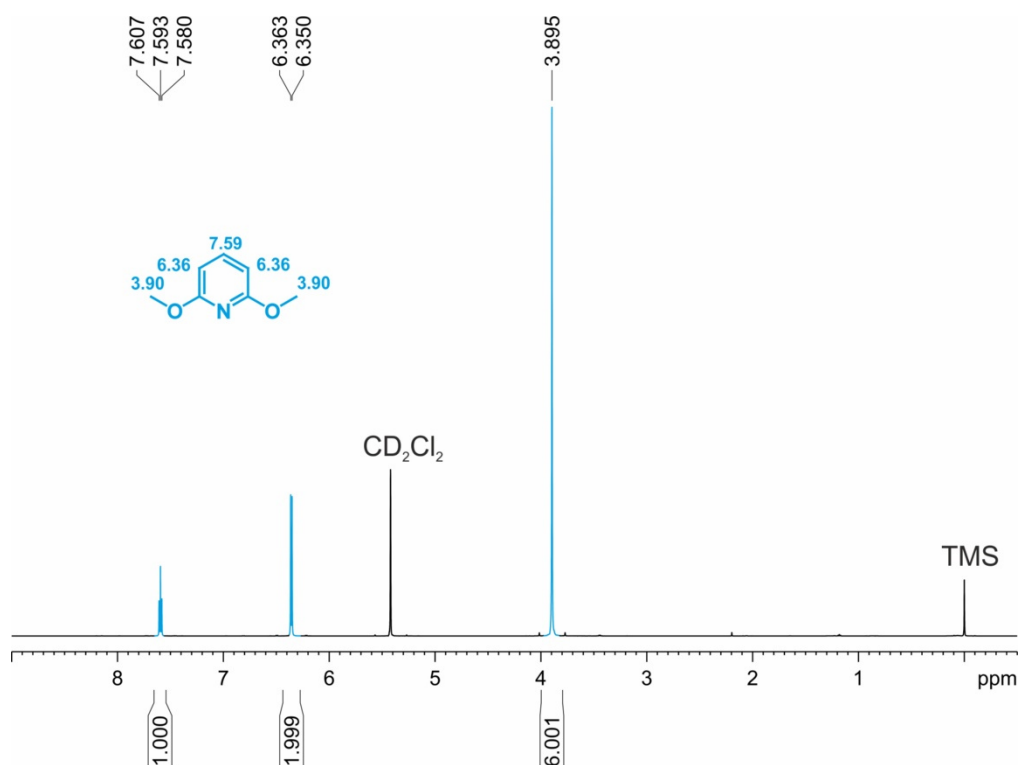


**Figure 3.20:** Full $^1$H NMR spectrum of 2,6-dimethoxypyridine (50 mM) in CD$_2$Cl$_2$ at 180 K. The chemical shifts are referenced to TMS (0 ppm).
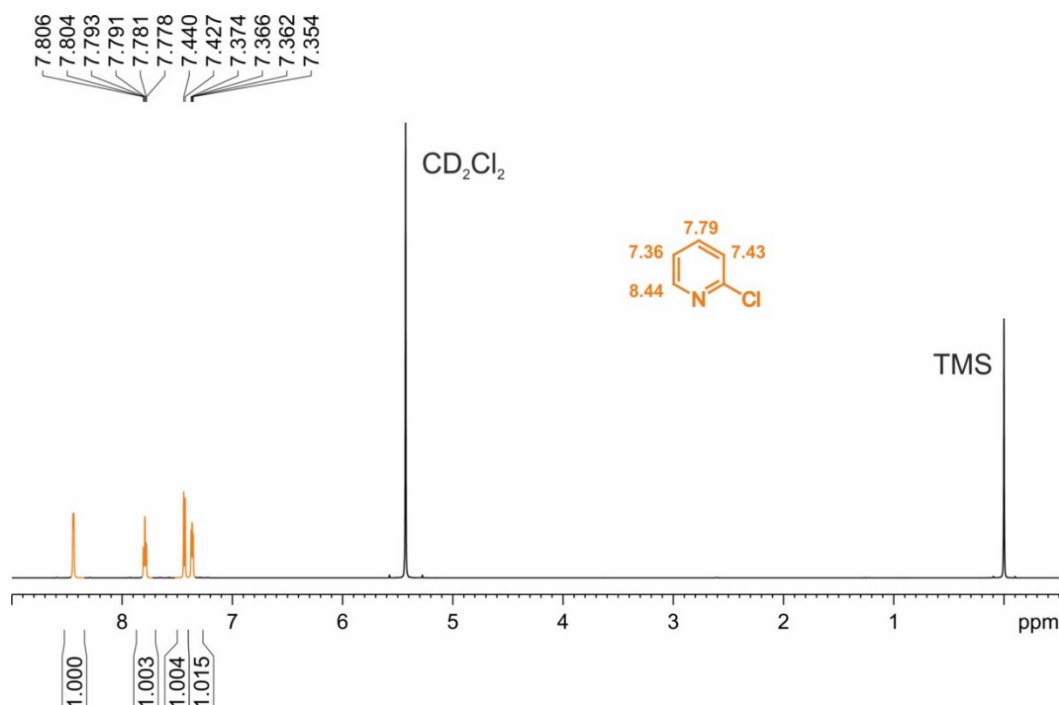


**Figure 3.21:** Full $^1$H NMR spectrum of 2-chloropyridine (50 mM) in CD$_2$Cl$_2$ at 180 K. The chemical shifts are referenced to TMS (0 ppm).
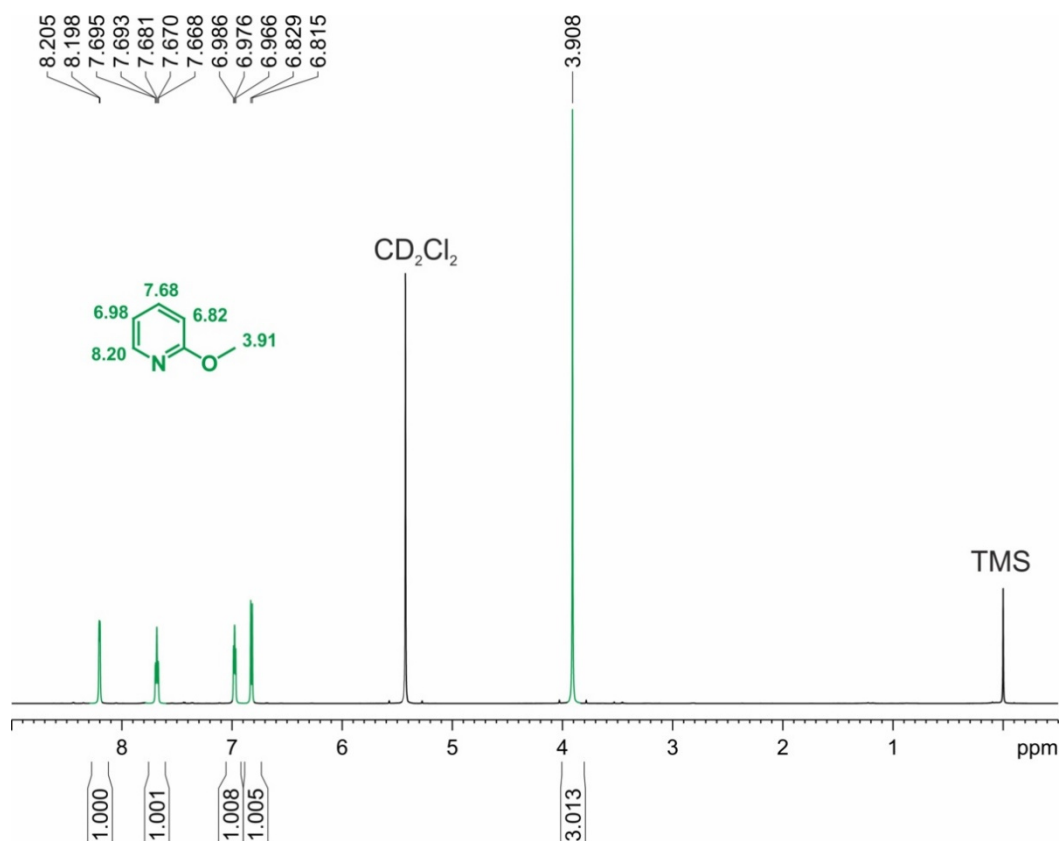
**Figure 3.22:** Full $^1$H NMR spectrum of 2-methoxypyridine (50 mM) in $CD_2Cl_2$ at 180 K. The chemical shifts are referenced to TMS (0 ppm).

### 3.6.6.5 Comparison of Chemical Shifts of the Hydroxy Group in BnOH and EtOH Test Systems
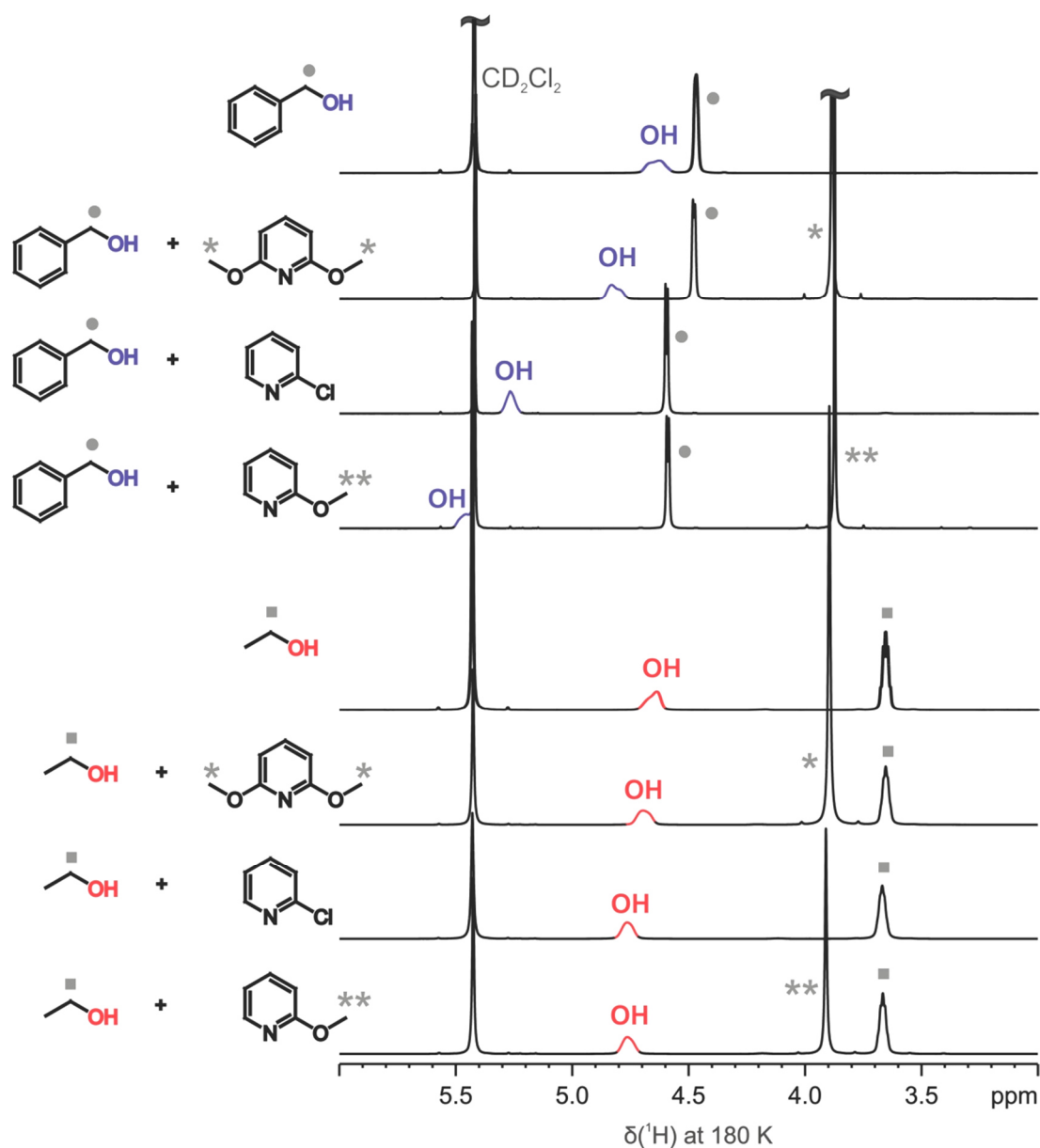


**Figure 3.23:** Comparison of O-H $^1$H chemical shifts of the benzylic alcohol and ethanol test systems including free alcohols and alcohols in presence of 2,6-dimethoxypyridine, 2-chloropyridine and 2-methoxypyridine in CD$_2$Cl$_2$ at 180 K. The chemical shifts are referenced to TMS (0 ppm); for complete spectra see Figures 3.7-3.14.

### 3.6.6.6 Comparison of [1]H Chemical Shifts of Pyridines in Presence of Different Alcohols
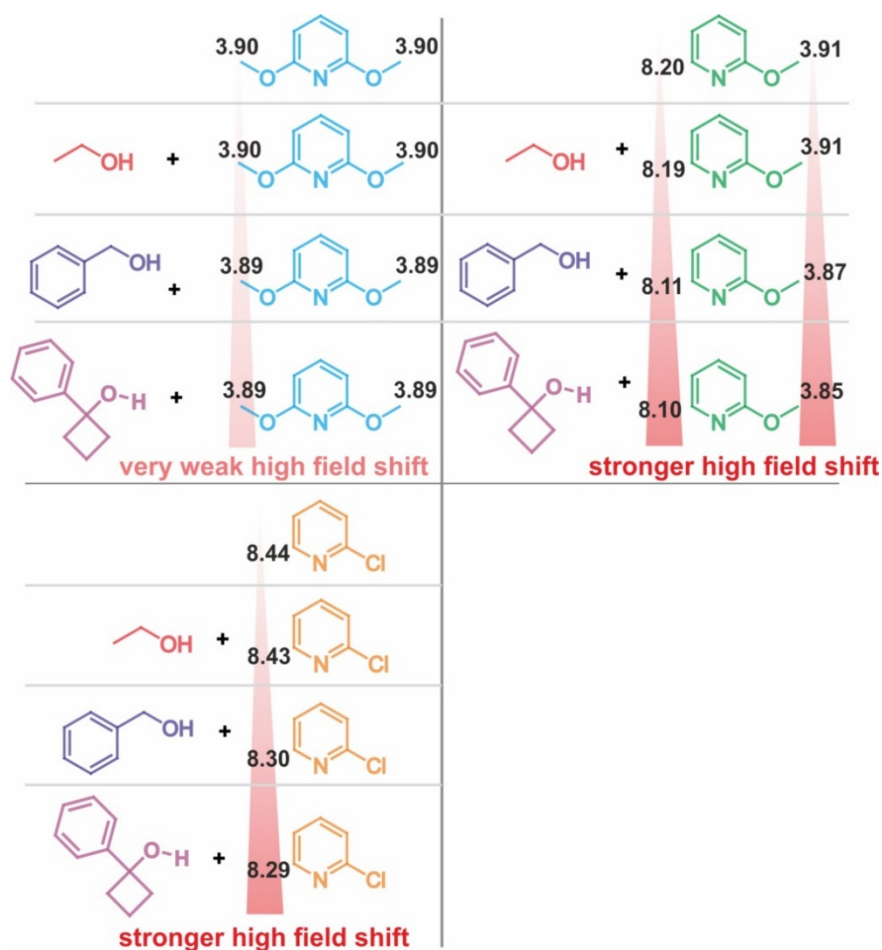


**Figure 3.24:** Comparison of the ^{1}H chemical shifts of the methoxy group protons (methoxy- and dimethoxypyridine) and the protons (C6-H) in *ortho*-position of the pyridine's nitrogen (chloropyridine) of the pure pyridines and in mixtures containing after adding either ethanol, benzylic alcohol, or 1-phenylcyclobutan-1-ol. For complete spectra see Figures 3.15-3.18 and 3.20-3.22.

### 3.6.7 Diffusion Ordered Spectroscopy (DOSY)

Spectroscopic details:

For the [1]H-diffusion measurements, the convection suppressing DSTE (double stimulated echo) pulse sequence, developed by Müller and Jerschow in a pseudo 2D mode, was applied.[15] As reference for the ^{1}H chemical shifts and for temperature and viscosity corrections of the diffusion coefficients of the analytes, Tetramethylsilane (TMS) was added.[16,17]

A set of 0 dummy scans/8 scans and 120 dummy scans/16 scans, respectively, were used with a relaxation delay of 2 s. Sinusoidal shapes were used for the gradient and a linear gradient ramp with 5 or 20 increments between 5% and 95% of the maximum gradient strength were applied. For the homospoil gradient strengths values of 100, -13.17, 20 and -17.13% were used. An effective diffusion time $D_{23}$ of 45 ms was applied. For each compound in the sample, the gradient pulses *P16* were adjusted in order to obtain optimized diffusion times Δ and gradient lengths δ according to following correlation:

$$\Delta\ [ms] = D_{23} + \frac{\delta}{3}\ ; P_{16}[ms] = \frac{\delta}{2}$$

The NMR spectra were processed with the Bruker program TopSpin 3.2 and the diffusion coefficients were determined with the Bruker software *T1/T2* relaxation module.

Size Estimation:

Via DOSY, the experimental translational self-diffusion coefficients *D* of the molecules in solution were determined according to the Stejskal-Tanner equation.[18-20] From the obtained diffusion coefficients, the hydrodynamic radii of the analytes $r_A$ can be estimated following the Stokes-Einstein equation (1), with *k* = Boltzmann constant, *T* = temperature, *η* = viscosity of the sample, *c* = correcting factor, *F* = shape factor.[21]

$$D\ [m^2/s] = \frac{kT}{Fc\pi\eta r_A} \quad (1)$$

For spherical shape, *F* is equal to 1. The correction factor *c* of the Stokes-Einstein equation was calculated according to the semi-empirical modification according to Chen (2) using literature known values for the solvent ($r_{solv}$ = 2.46 Å for $CD_2Cl_2$ [22]).[23]

$$c_{Chen} = \frac{6F}{1 + 0.695\ (\frac{r_{solv}}{r_{ref}})^{2.234}};\ \ F = 1\ for\ spheres\ \ (2)$$

The obtained diffusion coefficients *D* for the analytes were calibrated by viscosity calculation using the literature known radius of TMS (2.96 Å, calculated from hard-sphere increments[24]) and the experimentally determined diffusion coefficient $D_{ref}$ of TMS for every sample (equation (3)).

$$\eta\ [kg/ms] = \frac{kT\ (1 + 0.695\ \left(\frac{r_{solv}}{r_{ref}}\right)^{2.234})}{6\pi D_{ref}\ r_{ref}} \quad (3)$$

Including all corrections and calibrations into the Stokes-Einstein equation (4), the hydrodynamic radii $r_A$ were calculated according to equation (5). For better imagination, the corresponding volumes $V_A$ were calculated assuming a spherical shape ($V = 4/3 \, \pi \, r^3$).

$$D = \frac{kT(1 + 0.695 \left(\frac{r_{solv}}{r_{ref}}\right)^{2.234})}{6\pi\eta r_A} = \frac{kT(1 + 0.695 \, r_{solv}{}^{2.234} \, r_{ref}{}^{-2.234})}{6\pi\eta r_A} \quad (4)$$

$$0 = D6\pi\eta r_A - kT \, 0.695 \, r_{solv}{}^{2.234} \, r_A{}^{-2.234} - kT \quad (5)$$

The experimental diffusion coefficients $D$, the corresponding calculated radii $r_A$, the resulting volumes $V_A$ and the estimated monomer volumes $V_M$ for the corresponding species according to Bondi are depicted in Table 3.8.[25] For each sample, the $D$ values for every species and for TMS as reference are given. If not otherwise mentioned, the average $D$ values of all baseline separated signals referring to the same species were used.

**Table 3.8:** From DOSY experiments obtained diffusion coefficients at 180 K in $CD_2Cl_2$, the calculated hydrodynamic radii and volumes for the corresponding species of each sample; the monomer values of the pure species according to Bondi[25] are given for comparison.
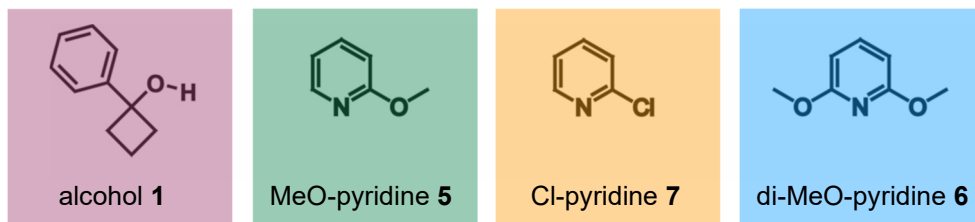
| alcohol 1 | MeO-pyridine 5 | Cl-pyridine 7 | di-MeO-pyridine 6 |
|---|---|---|---|

| sample | species inside sample | diffusion coefficient $D^{[a]}$ [m$^2$/s] | hydrodynamic radius $r_A$ [Å] | volume $V_A$ [Å$^3$] | monomer volume $V_M^{[b]}$ [Å$^3$] |
|---|---|---|---|---|---|
| alcohol | alcohol: | 1.09 x 10$^{-10}$ | 5.09 | 553 | 150 |
| | TMS: | 2.40 x 10$^{-10}$ | - | - | |
| MeO-pyridine 5 | MeO-pyridine 5: | 2.00 x 10$^{-10}$ | 3.25 | 144 | 115 |
| | TMS: | 2.33 x 10$^{-10}$ | - | - | |
| alcohol + MeO-pyridine 5 | alcohol: | 9.56 x 10$^{-11}$ | 4.69 | 433 | |
| | MeO-pyridine 5: | 1.57 x 10$^{-10}$ | 3.33 | 154 | |
| | TMS: | 1.90 x 10$^{-10}$ | - | - | |
| di-MeO-pyridine 6 | 2,6-di-MeO-pyridine 6: | 1.68 x 10$^{-10}$ | 3.53 | 183 | 140 |
| | TMS: | 2.22 x 10$^{-10}$ | - | - | |
| alcohol + di-MeO-pyridine 6 | alcohol: | 9.06 x 10$^{-11}$ | 5.04 | 536 | |
| | 2,6-di-MeO-pyridine 6 | 1.41 x 10$^{-10}$ | 3.65 | 204 | |
| | TMS: | 1.98 x 10$^{-10}$ | - | - | |
| Cl-pyridine 7 | Cl-pyridine 7: | 2.06 x 10$^{-10}$ | 3.04 | 118 | 95 |
| | TMS: | 2.16 x 10$^{-10}$ | - | - | |
| alcohol + Cl-pyridine 7 | alcohol: | 1.06 x 10$^{-10}$ | 4.73 | 442 | |
| | Cl-pyridine 7: | 1.89 x 10$^{-10}$ | 3.17 | 133 | |
| | TMS: | 2.12 x 10$^{-10}$ | - | - | |

[a] The diffusion coefficients D are average values of all base line separated signals; [b] Estimated monomer values according to Bondi.[25]

### 3.6.8 Stern-Volmer Experiments

All fluorescence measurements were performed in a quartz cuvette (d = 1 cm) with an excitation wavelength of 420 nm and a slit width of 5 nm.
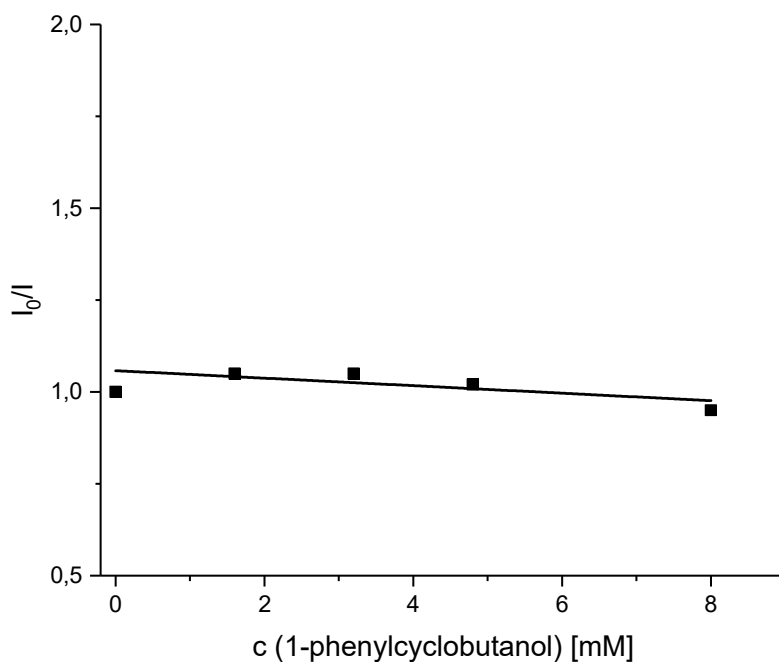


**Figure 3.25:** Stern-Volmer plot of **Mes$_2$Acr$^t$Bu$_2$BF$_4$** (25 µM) with varied concentration of 1-phenyl-cyclobutanol (**1**) (0-8 mM) in MeCN/H$_2$O 1:1.

**Table 3.9:** Results from Stern-Volmer experiments with of **Mes$_2$Acr$^t$Bu$_2$BF$_4$** (25 µM) with varied concentration of 1-phenylcyclobutanol (**1**) (0-8 mM) in MeCN/H$_2$O 1:1.

| **1** (mM) | scan 1 (493 nm) | scan 2 (493 nm) | scan 3 (493 nm) | average | I$_0$/I |
|---|---|---|---|---|---|
| 0 | 21904 | 21630 | 22174 | 21903 | 1.00 |
| 1.6 | 20899 | 21225 | 20514 | 20879 | 1.05 |
| 3.2 | 20330 | 21591 | 20933 | 20951 | 1.05 |
| 4.8 | 21186 | 21154 | 21803 | 21381 | 1.02 |
| 8.0 | 22699 | 24234 | 22475 | 23136 | 0.95 |
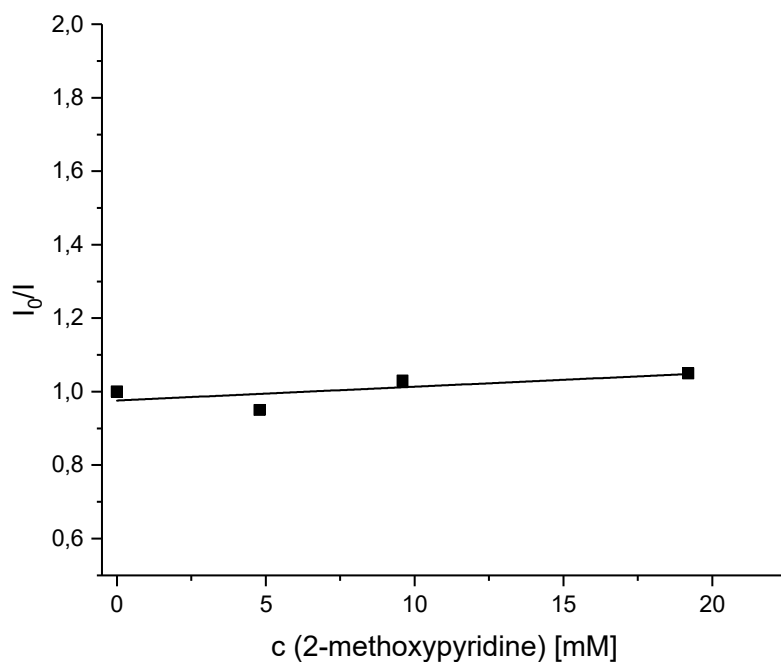
**Figure 3.26:** Stern-Volmer plot of **Mes₂AcrᵗBu₂BF₄** (25 µM) with varied concentration of 2-methoxypyridine (**5**) (0-19.2 mM) in MeCN/H₂O 1:1.

**Table 3.10:** Results from Stern-Volmer experiments with of **Mes₂AcrᵗBu₂BF₄** (25 µM) with varied concentration of 2-methoxypyridine (**5**) (0-19.2 mM) in MeCN/H₂O 1:1.

| **1** (mM) | scan 1 (493 nm) | scan 2 (493 nm) | scan 3 (493 nm) | average | $I_0/I$ |
|---|---|---|---|---|---|
| 0 | 21904 | 21630 | 22174 | 21903 | 1.00 |
| 4.8 | 20893 | 24934 | 23034 | 22954 | 0.95 |
| 9.6 | 20118 | 21598 | 21848 | 21188 | 1.03 |
| 19.2 | 20969 | 22506 | 18812 | 20762 | 1.05 |

## 3.6.9  p$K_a$ Values of Heteroaromatic Bases

**Table 3.11:** p$K_a$ values in $H_2O$ and MeCN of different pyridine and quinoline bases.

| base | p$K_a$ in MeCN | p$K_a$ in $H_2O$ |
|:---:|:---:|:---:|
| pyridine | 12.5[26] | 5.2[26] |
| 2-methoxypyridine | 9.9[26] | 3.1[27] |
| 2,6-dimethoxypyridine | 7.6[26] | 1.6[27] |
| 2-chloropyridine | 6.8[26] | 0.5[27] |
| quinoline | 12[26] | 4.9[26] |
| 2-chloroquinoline | - | 0.4±0.4 (predicted) |

## 3.6.10 NMR Spectra
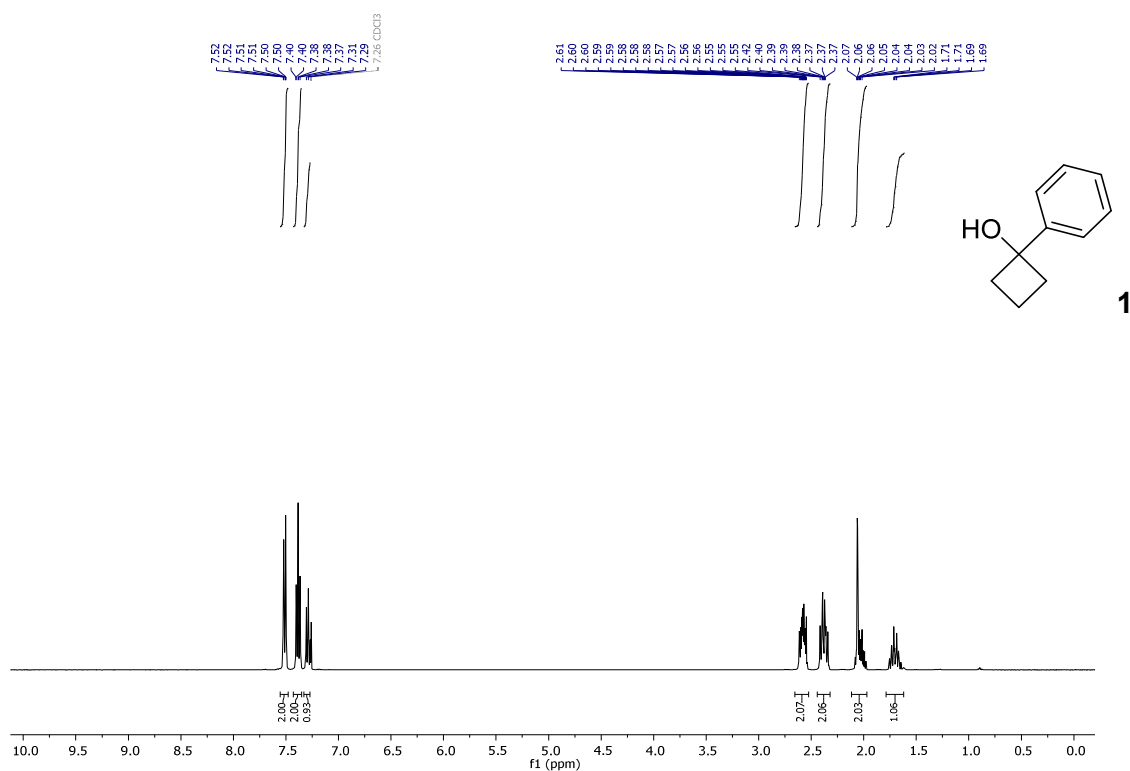


**Figure 3.27:** $^1$H NMR of **1** (400 MHz, CDCl$_3$).
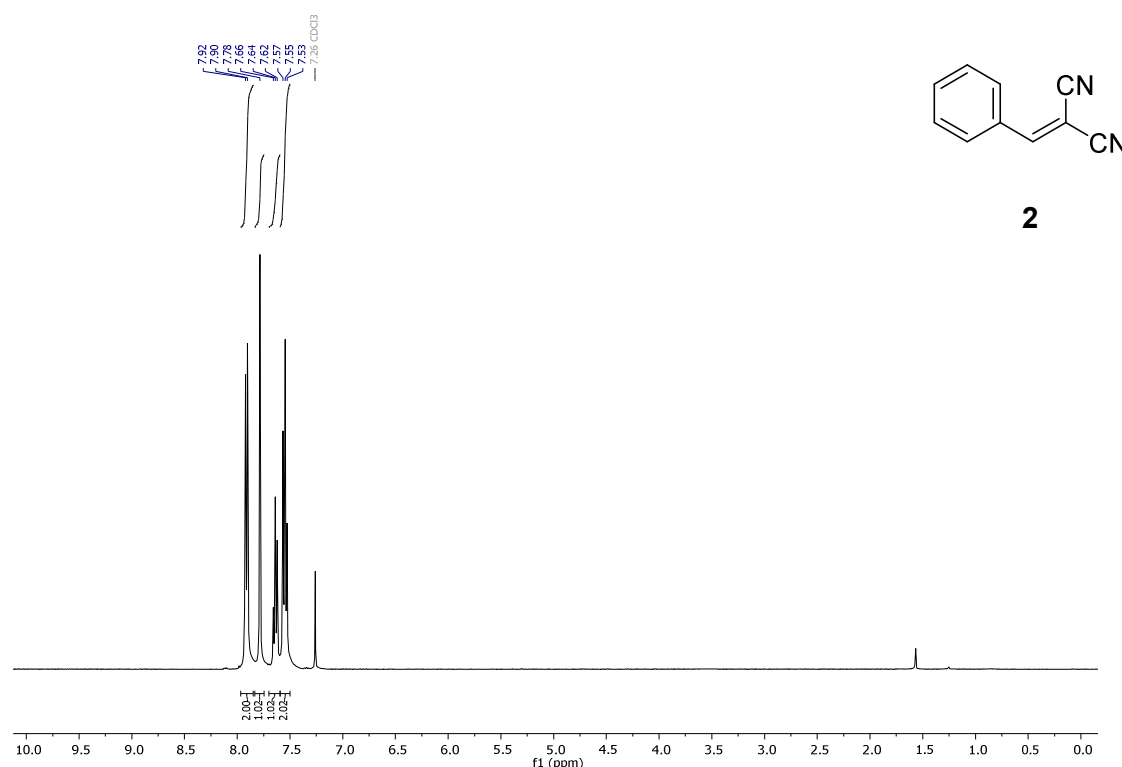
**Figure 3.28:** $^{1}$H NMR of **2** (400 MHz, CDCl$_3$).

For further NMR spectra see original Supporting Information of the manuscript (pages S54-S101).

### 3.6.11 References

[1]     Yamashita, K.; Tanaka T.; Hayashi, M. *Tetrahedron* **2005**, *61*, 7981.

[2]     Li, G.; Xiao, J.; Zhang W. *Green Chem*., **2011**, *13*, 1828.

[3]     Longstreet, A. R.; Campbell, B. S.; Gupton, B. F.; McQuade D. T. *Org. Lett.* **2013**, *15*, 5298.

[4]     Alvim Jr., J.; Dias, R. L. A.; Castillho, M. S.; Oliva, G.; Corrêa, A. G. *J. Braz. Chem. Soc*. **2005**, *16*, 763.

[5]     Peng, C.; Wang, Y.; Wang, J. *J. Am. Chem. Soc*. **2008**, *130*, 1566.

[6]     Adams, L. A.; Aggarwal, V. K.; Bonnert, R. V.; Bressel, B.; Cox, R. J.; Shepherd, J.; de Vicente, J.; Walter, M.; Whittingham, W. G.; and Winn, C. L. *J. Org. Chem*. **2003**, *68*, 9433.

[7]     Xu, B.; Wang, D.; Hu, Y.; Shen, Q. *Org. Chem. Front*. **2018**, *5*, 1462.

[8]     Su, Y.; Sun, X.; Wu, G.; Jiao, N. *Angew. Chem. Int. Ed.* **2013**, *52*, 9808.

[9]     Rüedi, G.; Hansen, H. J. *Helv. Chim. Acta* **2004**, *87*, 1968.

[10]    Kamijo, S.; Amaoka, Y.; Inoue, M. *Synthesis* **2010**, *14*, 2475.

[11]    Feldmeier, C; Bartling, H.; Riedle, E.; Gschwind, R. M. *J. Magn. Reson*. **2013**, *232*, 39.

[12]    Gschwind, R. M.; Armbrüster, M.; Zubrzycki, I. Z. *J. Am. Chem. Soc.* **2004**, *126*, 10228.

[13]    Sharif, S.; Denisov, G. S.; Toney, M. D.; Limbach, H.-H. *J. Am. Chem. Soc.* **2007**, *129*, 6313.

[14]    Fulmer, G. R.; Miller, A. J. M.; Sherden, N. H.; Gottlieb, H. E.; Nudelman, A.; Stoltz, B. M.; Bercaw, J. E.; Goldberg, K. I. *Organometallics* **2010**, *29*, 2176.

[15]    Jerschow, A.; Müller*,* N. *J. Magn. Reson.* **1997**, *375*, 372.

[16]    Cabrita, E. J.; Berger, S. *Magn. Reson. Chem*. **2002**, *39*, 142.

[17]    Claridge, T. D. W. *High-Resolution NMR Tech. Org. Chem*., **2009**, 303.

[18]    Johnson Jr., C. S. *Prog. Nucl. Magn. Reson. Spectrosc*. **1999**, *34*, 203.

[19]    Price, W. S. *Concepts Magn. Reson*. **1998**, *10*, 197.

[20]    Stejskal, E. O.; Tanner, J. E. *J. Chem. Phys*. **1965**, *42*, 288.

[21]    Macchioni, A.; Ciancaleoni, G.; Zuccaccia, C.; Zuccaccia, D. *Chem. Soc. Rev*. **2008**, *37*, 479.

[22]    Zuccaccia, D.; Macchioni, A. *Organometallics* **2005**, *24*, 3476.

[23]    Chen, H. C.; Chen, S. H. *J. Phys. Chem*. **1984**, *88*, 5118.

[24]    Ben-Amotz, D.; Willis, K. G. *J. Phys. Chem.* **1993**, *97*, 7736.

[25]    Bondi, A. *J. Phys. Chem*. **1964**, *68*, 441.

[26]    Lõkov, M.; Tshepelevitsh, S.; Heering, A.; Plieger, P. G.; Vianello, R.; Leito, I. *Eur. J. Org.  Chem*. **2017**, 4475.

[27]    Kaljurand, I.; Kütt, A.; Sooväli, L.; Rodima, T.; Mäemets, V.; Leito, I.; Koppel, I. A. *J. Org. Chem.* **2005**, *70*, 1019.

## 3.7 Additional Findings

### 3.7.1 General Information

The *in-situ* illumination and low temperature H-bond experiments were performed on a Bruker Avance III HD 600 (600.13 MHz) and a 5 mm TBI-F probe head with a z-gradient (53.5 Gauss/cm). The temperature was controlled either by a BCU II (300 K) or a BVTE 3900 (180 K). *Ex-situ* measurements were conducted on a Bruker Avance III HD 400 MHz (400.13 MHz for $^{1}$H) spectrometer with a 5 mm BBO BB-1H/D probe head with Z-gradients. The temperature of 298 K was controlled by BVT 3000. 5 mm NMR tubes were used.

The spectra were referenced to the corresponding solvent,[1] processed and evaluated using TopSpin 3.2 (Bruker) and plotted with TopSpin Plot Editor and Corel Draw 2017.

The solvents for NMR measurements, dichloromethane-$d_2$ ($CD_2Cl_2$) and acetonitrile-$d_3$ ($CD_3CN$) were purchased from Sigma Aldrich/Merck or Deutero. When water free samples were needed, the solvent was freshly dried over $CaH_2$ under Argon atmosphere. $^{15}$N-pyridine was obtained from Eurisotop, 2-methoxypyridine, 2-chloropyridine and 2,6-dimethoxypyridine from Sigma Aldrich/Merck.

Mass spectra were recorded on a ThermoQuest Finnigan TSQ 7000 spectrometer (Electrospray Ionization Mass Spectrometry (ESI-MS)).

*In-situ* NMR illumination:

The photocatalytic reaction mixtures were prepared in 5 mm amberized NMR tubes of Spintec. For the *in-situ* illumination inside the NMR, the combined illumination setup described by Feldmeier *et al.* was applied.[2] As light source, a 450 nm Lumitronix Cree XT-E-1 (royalblue; 500 mW, 452 nm peak wavelength measured in our group) LED was used.

The amounts (%) were obtained by integration of the corresponding signals. For accurate integration, the respective signal regions were baseline corrected. As no conversion was observed in the dark, the signal integral of the starting material was set to 100%. According to this reference, the progression of the photocatalytic reaction was determined after starting the illumination.

The samples were prepared according to the following procedure: An NMR tube was charged with 1-phenylcyclobutanol (1 equiv., 0.05 mmol, 7.4 mg), tosyl cyanide (1.5 equiv., 0.075 mmol, 13.6 mg), *$^{15}$N*-pyridine (0.5/2 equiv., 0.025/0.1 mmol, 2.0 µl/8.1 µl), 9-mesityl-10-methylacridinium perchlorate (Fukuzumi catalyst; 0.02 equiv., 0.001 mmol, 0.4 mg) and solvent (0.5 ml, 95 mM).

*Ex-situ* illumination:

General procedure: A crimp cap vial was charged with alcohol (1 equiv.), tosyl cyanide (1.5 equiv.) and Fukuzumi photocatalyst (0.02 equiv.). Substituted pyridine (3 equiv.), $H_2O$ (0.25 equiv.), if used, and dry $CD_3CN$ (2 ml) were added. The vial was sealed and placed about 1 cm above a 455 nm LED (Osram Oson SSL80, 500 mW) inside a cooling block, which was connected to a JULABO cyclic water cooling system, and the mixture was irradiated at room temperature under stirring. For NMR-measurements at specific times 0.05 ml of the reaction mixture were transferred into an NMR tube and 0.40 ml of solvent and 0.05 ml of a 50 mM octamethylcyclotetrasiloxan (OMS) solution (0.85 ppm in the $^1H$ spectrum) were added.

The amounts (%) were obtained by integration of the corresponding signals and referenced according to OMS as internal standard.

Photoreaction in presence of 2-methoxypyridine:

1-phenylcyclobutanol (0.3 mmol, 39.4 mg), tosylcyanide (0.4 mmol, 72.3 mg), 2-methoxypyridine (0.8 mmol, 0.08 ml), 9-mesityl-10-methylacridinium perchlorate (0.005 mmol, 2.1 mg) and $H_2O$ (0.07 mmol, 0.001 ml) were used.

Photoreaction in presence of 2,6-dimethoxypyridine:

1-phenylcyclobutanol (0.2 mmol, 29.6 mg), tosylcyanide (0.3 mmol, 54.4 mg), 2,6-dimethoxypyridine (0.6 mmol, 0.08 ml), 9-mesityl-10-methylacridinium perchlorate (0.004 mmol, 1.7 mg) were used.

Low temperature H-bond analysis:

For the measurements at 180 K, dry $CD_2Cl_2$ was used as solvent and tetramethylsilane (TMS) as internal standard (0 ppm). For the 1:1 mixtures (50 mM) presented in the Figures 3.32-3.34 an NMR tube was charged with 1-phenylcyclobutanol (0.05 mmol), solvent and the respective pyridines (0.05 mmol) were added. For the 1:1 and 1:1:1 mixtures of alcohol/pyridine and alcohol/pyridine/TsCN, respectively, as well as for the 1:1:1:0.25 mixtures of alcohol/pyridine/TsCN/$H_2O$ shown in Figure 3.38, stock solutions were generated for all compounds prior to sample preparation (50 mM).

### 3.7.2  NMR-Based Analysis of the Photocatalytic System Using $^{15}$N-Pyridine

The development of our photocatalytic PCET-driven functionalization of cycloalcohols was initially started on the basis of the literature-postulated requirement of creating the strongest possible H-bond between a Brønsted base and our alcohol substrates. Thus, we hoped to benefit from the H-bonding experiences and known basicities of pyridines. In Table 3.1 in chapter 3.3, the pKₐ values of different pyridines are shown clearly indicating the unsubstituted pyridine as the most basic species. Therefore, a strong H-bond to the alcohol is supposed. However, using unsubstituted pyridine resulted in a reduction of the reactivity of the photocatalytic system. Therefore, we initially focused our mechanistic study on the elucidation of the influence of the pyridine structure on the reaction.

The photocatalytic reaction was followed by *in-situ* illumination (450 nm) inside the NMR device including the 1-phenylcyclobutanol substrate (1 equiv.), the tosyl cyanide (TsCN) trapping reagent (1.5 equiv.), $^{15}$N-pyridine as base/H-bond acceptor and the Fukuzumi photocatalyst (2 mol%). The samples were prepared according to the procedure described in the chapter "General Information" (chapter 3.7.1). The reactions were performed at room temperature in different solvent mixtures and with different amounts of pyridine. $CD_3CN$ was used as acetonitrile was the best performing solvent for the light-induced reaction. In order to get information about the reaction system in $CD_2Cl_2$, which is the required solvent for low temperature H-bond investigations, mixtures of 15% $CD_3CN$ and 85 % $CD_2Cl_2$ were applied as well. $^{15}$N-labeled pyridine was applied in order to provide access to the H-bond acceptor side for further NMR-based H-bond analysis. In Figure 3.29, the reaction profiles are depicted. Neither acetonitrile nor acetonitrile/dichloromethane mixtures yielded more than 13% reaction product (red curves). Instead, a by-product was generated (brownish curve), which was assigned as the light-independent substitution product between the cyclo-alcohol and rearranged TsCN (*vide infra*). Moreover, increasing the amount of base to 2 equivalents furnished an immensely enhanced by-product formation (up to 68%).
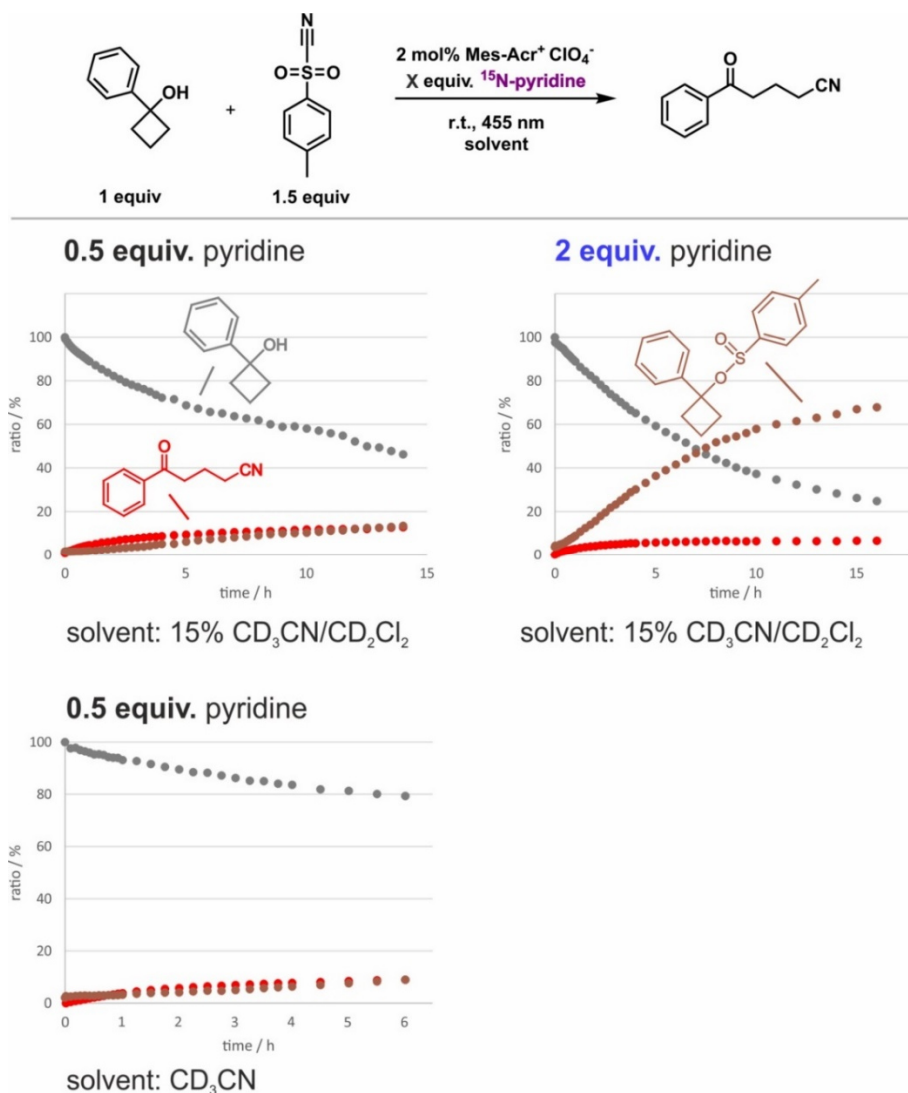
**Figure 3.29:** The *in-situ* NMR-based reaction profiles of the photocatalytic PCET-mediated ring-opening of 1-phenylcyclobutanol using different equivalents of ^{15}N-pyridine base/H-bond acceptor (0.5/2 equiv.) and different solvent mixtures revealed the formation of a by-product (for assignment, see next section of this chapter).

In order to identify the origin for the by-product formation, control reactions were performed. In Table 3.12, an overview of the different mixtures is shown including any combination of the reaction partners. Interestingly, the by-product was already generated in the absence of light and photocatalyst, but only for the triple combination of 1-phenylbutanol, TsCN and pyridine.

**Table 3.12:** Control reactions without irradiation and photocatalyst reveal a light- and catalyst-independent by-product.
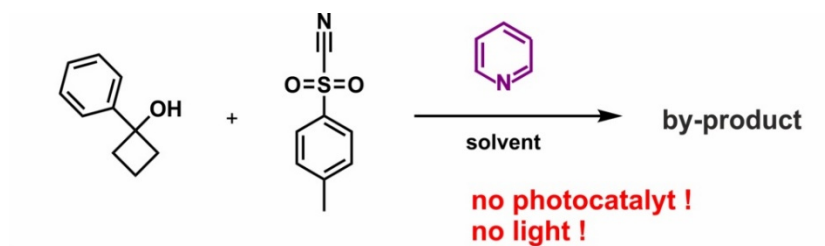


| | | | by-product |
|:---:|:---:|:---:|:---:|
| yes | yes | – | – |
| yes | – | yes | – |
| yes | yes | yes | yes |

The composition of the by-product was assigned by NMR and mass spectrometry (MS). Comparing the ^{1}H spectra of the *in-situ* illumination after 16 hours and the control experiment, the pattern and chemical shifts of the by-product signals are similar to the cyclic $CH_2$ groups of the alcohol starting material (Figure 3.30). This hints at a substitution reaction of the O-H group without ring opening. The pyridine mediated rearrangement of tosyl cyanide is literature known and the resulting sulfinyl moiety can act as a nucleophile furnishing the 1-phenylcyclobutyl 4-methylbenzenesulfinate (Figure 3.31).[3] ES-MS measurements confirm the postulated formation of the by-product.

$t_R$ = 3.213 min (ES): m/z = 287 [MH[+]], 131, 157.

It follows that due to by-product formation, the starting materials are consumed to the disadvantage of the photocatalytic transformation. The reactivity of pyridine seems to be caused by its high nucleophilicity, which in this case is represented by the large $pK_a$ value. As such, the side reaction in the dark is in accordance with the low photocatalytic product yields. This demonstrates that the application of simple basicity trends is insufficient for establishing a successful PCET driven reaction.
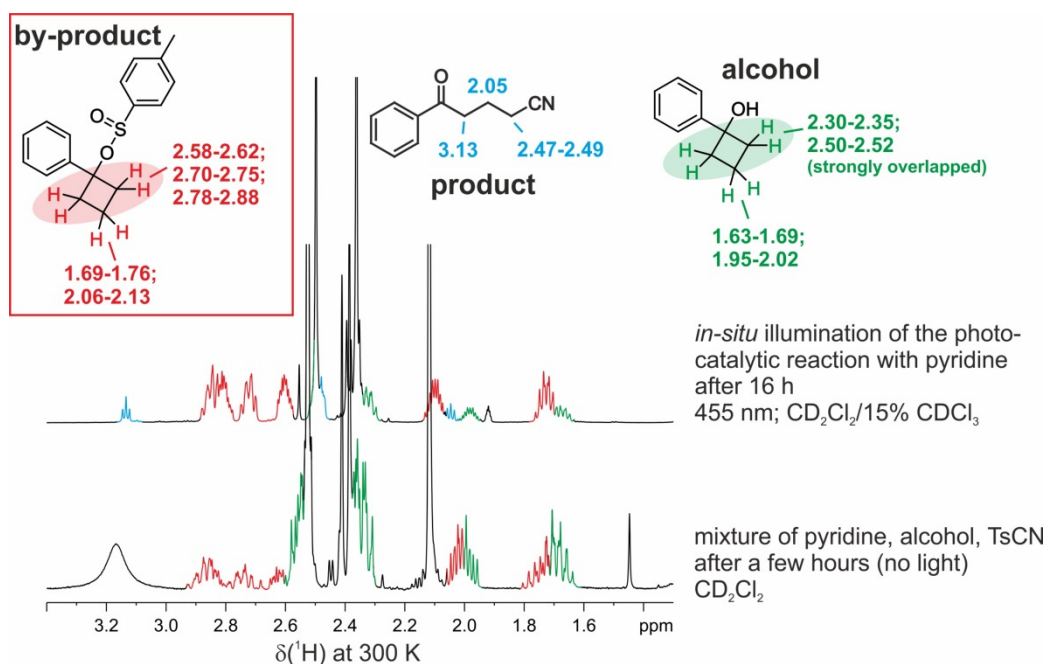
**Figure 3.30:** The comparison of the ^{1}H chemical shifts and patterns of the by-product signals (red), which were obtained for the *in-situ* illuminated reaction mixture after 16 hours as well as for the light-independent control experiment suggesting a substituted cyclobutanol species.
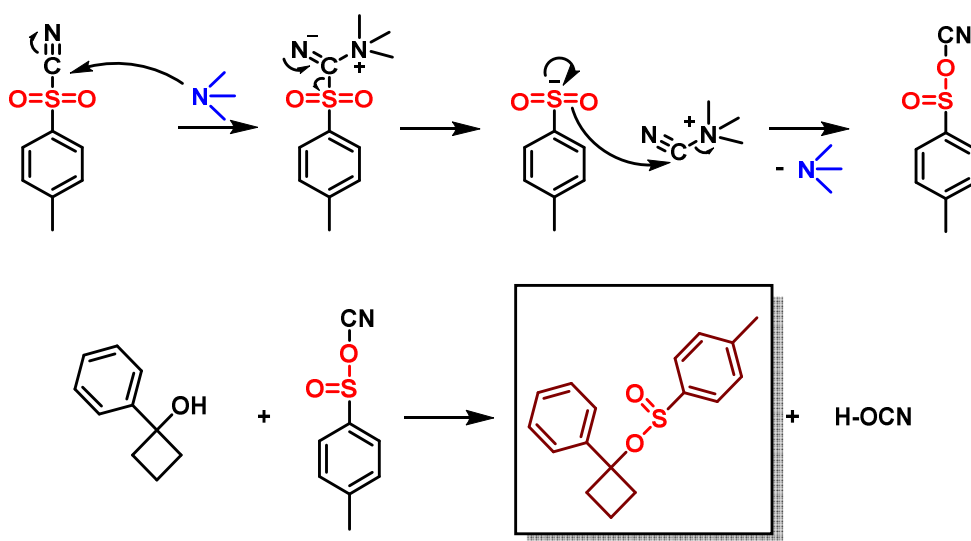


**Figure 3.31:** Literature-known rearrangement of tosyl cyanide in presence of pyridine (top) and subsequently the postulated substitution reaction of the alcohol generating 1-phenylcyclobutyl 4-methylbenzenesulfinate (bottom).

In order to get a general overview of the entire H-bonding situation not only for the three best performing bases, 2-methoxypyridine, 2-chloropyridine and 2,6-dimethoxypyridine, but also for unsubstituted pyridine, NMR spectroscopic low temperature experiments were

performed. A 1:1 mixture of $^{15}$N-pyridine and 1-phenylcyclobutanol was measured in CD$_2$Cl$_2$ at 180 K and the O-H chemical shift was compared to those of pure alcohol, and OMe-pyridine/alcohol (1:1) and Cl-pyridine/alcohol (1:1) mixtures. In Figure 3.32, an excerpt of the resulting spectra is depicted. Notably, the alcohol O-H proton is drastically low field shifted in presence of $^{15}$N-pyridine (purple; 6.48 ppm). In contrast, the ppm-values of OMe-pyridine/alcohol (4.75 ppm) and Cl-pyridine/alcohol (4.60 ppm) are only slightly shifted to low field and generally lie within the range of the pure alcohol (4.32 ppm). These results indicate the formation of an immensely stronger H-bond between unsubstituted pyridine and the alcohol, which is in accordance with its high basicity. As already stated in chapter 3.3, the broad O-H signal mostly includes a shoulder even for the pure cyclobutanol indicating a second alcohol-related species on the NMR-time scale with a very similar ppm-value.
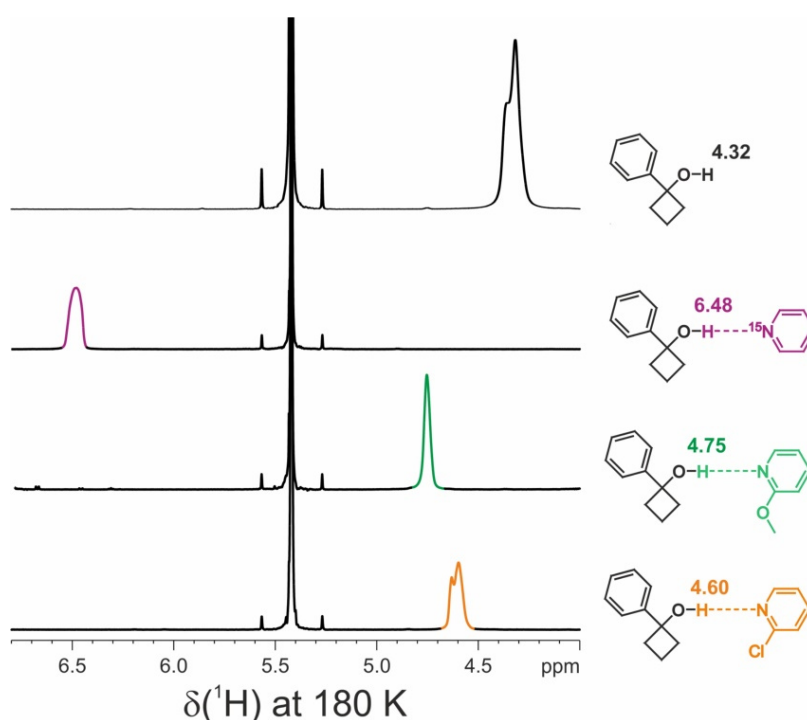


**Figure 3.32:** Excerpt of the $^1$H NMR spectra of pure 1-phenylalcohol and 1:1 mixtures of $^{15}$N-pyridine/alcohol, 2-methoxypyridine/alcohol and 2-chloropyridine/alcohol mixtures in CD$_2$Cl$_2$ at 180 K. The spectra are referenced to TMS as internal standard (0 ppm).

Moreover, the H-bond acceptor side was analyzed via low temperature $^{15}$N NMR measurements of the $^{15}$N-pyridine/1-phenylalcohol mixture. The comparison of the chemical shift of pure pyridine (312.1 ppm) and in presence of the alcohol (304.5 ppm) in Figure 3.33 shows a distinctive shift of the $^{15}$N signal to high field, which is in accordance with a shielding of the nitrogen due to H-bond formation.
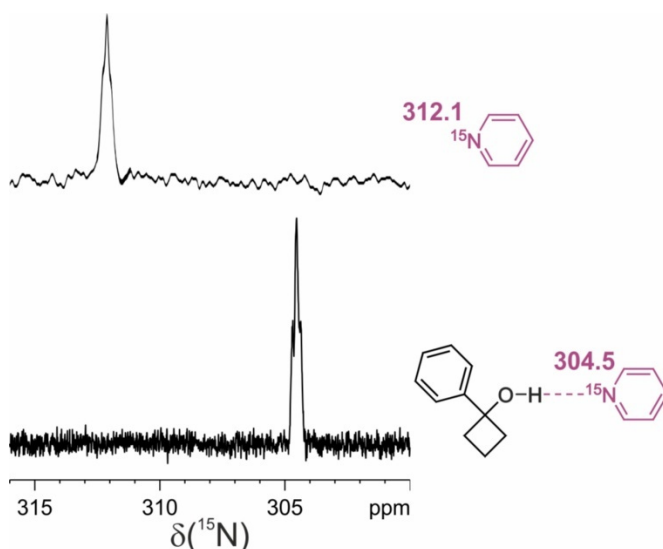
**Figure 3.33:** Comparison of the $^{15}$N NMR spectra of pure $^{15}$N-pyridine and a 1:1 mixture of $^{15}$N-pyridine and 1-phenylbutanol in $CD_2Cl_2$ at 180 K.

Additionally, the nature of the H-bond could further be elucidated by 2D $^1$H,$^1$H NOESY. The spectrum was measured for the $^{15}$N-pyridine/alcohol mixture at 180 K. As such, a NOE between the alcohol O-H proton and the ortho-substituted protons of pyridine confirmed the existence of an H-bond (Figure 3.34). Moreover, spatial proximity was detected between one pair of C-H groups of the chair conformation of cyclobutanol and the ortho-protons of pyridine.
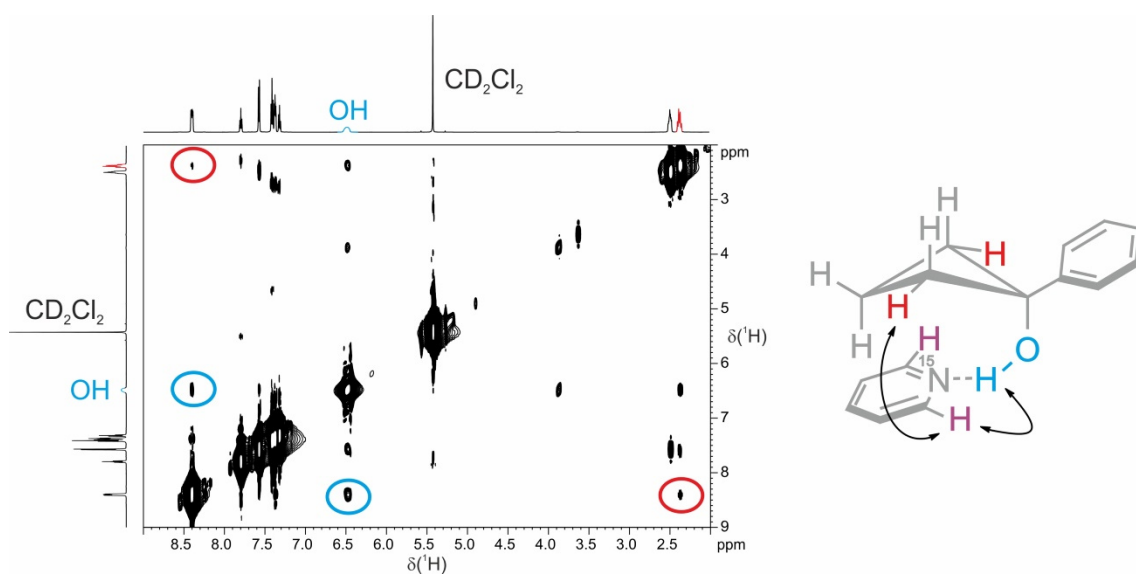


**Figure 3.34:** $^1$H,$^1$H NOESY of the 1:1 mixture including 1-phenylcyclobutanol and $^{15}$N-pyridine in $CD_2Cl_2$ at 180 K and the corresponding suggested interaction scheme (right).

### 3.7.3 *Ex-situ* Illumination with 2-Methoxypyridine and 2,6-Dimethoxypyridine

In order to provide more information about the immense reactivity gap between monosubstituted OMe-pyridine and disubstituted 2,6-dimethoxypyridine for the photocatalytic ring-opening of cyclobutanol, the reactions were tested for efficient conversion of the starting material, product formation and side reactions. Therefore, the batch reactions were irradiated *ex-situ* and the progress was followed by NMR. In presence of 2-methoxypyridine, 71% of starting material was consumed after 70 hours and 51% product was formed (Figure 3.35a). Within the first two hours the formation of up to 4% of a transient species and its subsequent consumption is visible (Figure 3.35a, excerpt). Moreover, the formation of a by-product was detected (8% after 70 hours).
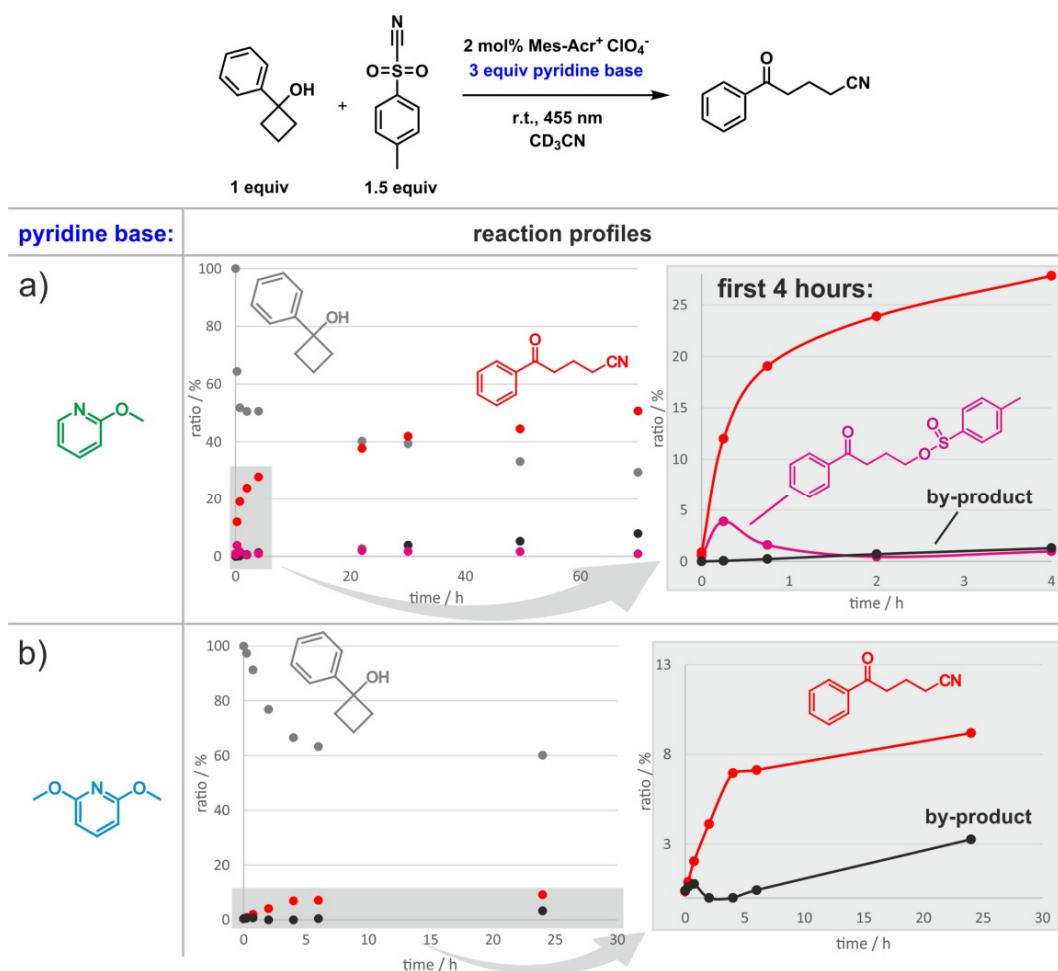


**Figure 3.35:** NMR-based reaction profiles of the *ex-situ* illuminated photocatalytic reactions using different pyridine bases; a) with 2-methoxypyridine, after 70 hours 71% of starting material was consumed and 51% of product formed. The excerpt of the first four hours show the formation up to 4%) and consumption of an intermediate and by-product formation (8% after 70 hours); b) in presence of 2,6-dimethoxypyridine the efficiency of the reaction is immensely reduced (after 24 hours 40% of starting material is consumed and 9% of product generated. Moreover, the same by-product as for OMe-pyridine was identified (3% after 24 hours).

In contrast, in presence of 2,6-dimethoxypyridine, the phototcatalysis was less effective furnishing only 9% of product after 24 hours (Figure 3.35b, bottom). However, up to 40% of the alcohol substrate were consumed. Furthermore, the same by-product as found for OMe-pyridine was generated (same signals in the $^1$H spectra) in low amounts (3% after 24 hours).

In total, the use of monosubstituted OMe-pyridine seems to efficiently act as H-bond acceptor although producing small amounts of by-product. As the product formation is not accelerated after consumption of the intermediate, we think that its generation has only minor impact on the phototcatalytic transformation. Using di-OMe-pyridine instead, which was proven as an inefficient H-bond acceptor (see chapter 3.3), a certain amount of the alcohol could be activated by the excited photocatalyst, but the downstream reaction was ineffective for successful product formation. Moreover, as the same by-product was generated for both reactions and only in small amounts, its formation is unlikely the reason for the large difference in base reactivity. The by-product was not further investigated.

The nature of the intermediate was identified by 2D NMR and mass spectrometry. A $^1$H,$^1$H COSY experiment was performed for the reaction mixture after 15 min. In comparison to the product signals (blue signals in Figure 3.36), the signal patterns of the intermediate (pink signals) were found to be similar, which let assume an open ring structure. The extreme low field shift of the remote $CH_2$ group suggest a deshielding by an oxygen-bridged tosyl moiety. 4-oxo-4-phenylbutyl benzenesulfinate was also confirmed by ES-MS.

$t_R$ = 2.682 min (ESI EIC): m/z = 303 [MH$^+$].

Thus, a reaction between the carbon-centered radical of the carbonyl and the tosyl radical inside the photocatalytic cycle is proposed. In Figure 3.37, the proposed catalytic cycle of the specific visible light mediated phototcatalytic transformation of phenylcyclobutanol in presence of tosyl cyanide as electron deficient trapping reagent, pyridine base and Fukuzumi catalyst is depicted including the off-cycle equilibrium for the generation of the intermediate. The concrete mechanism for the cleavage of the intermediate, which is again supplied into the catalytic cycle, was not further analyzed. However, a light and photocatalyst dependend conversion as was found for specific intermediate formation during the cross-dehydrogenative coupling of N-aryltetrahydroisoquinolines cannot be excluded.[4]
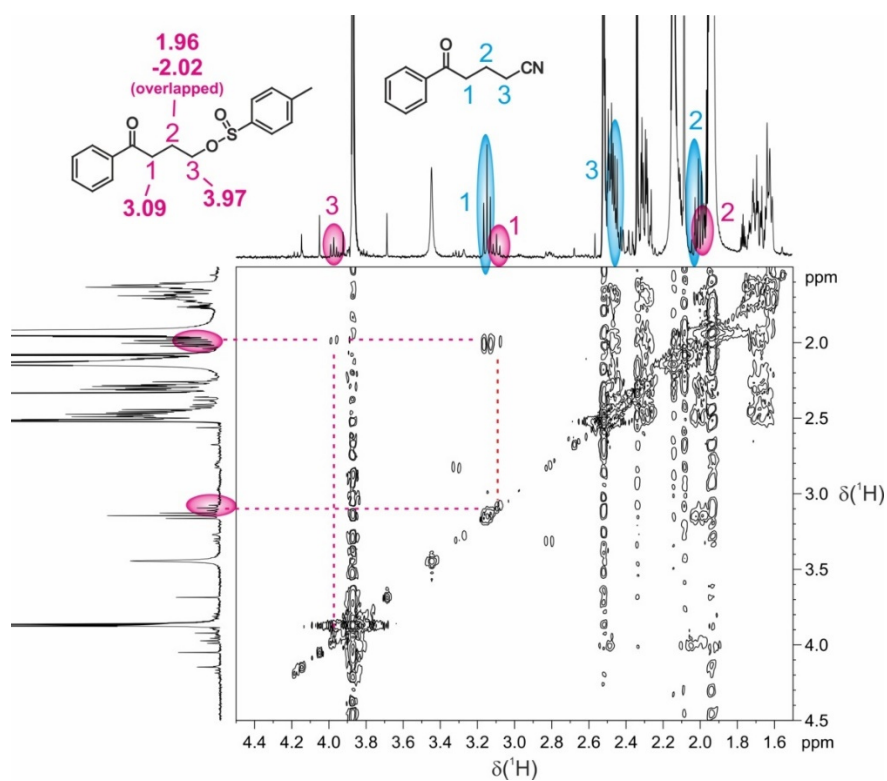
**Figure 3.36:** $^1$H,$^1$H COSY spectrum of the *ex-situ* photocatalytic reaction after 15 min with 2-methoxypyridine (see previous Figure 3.35a) in CD$_3$CN at room temperature. The blue signals refer to the product and the pink signals to the intermediate.
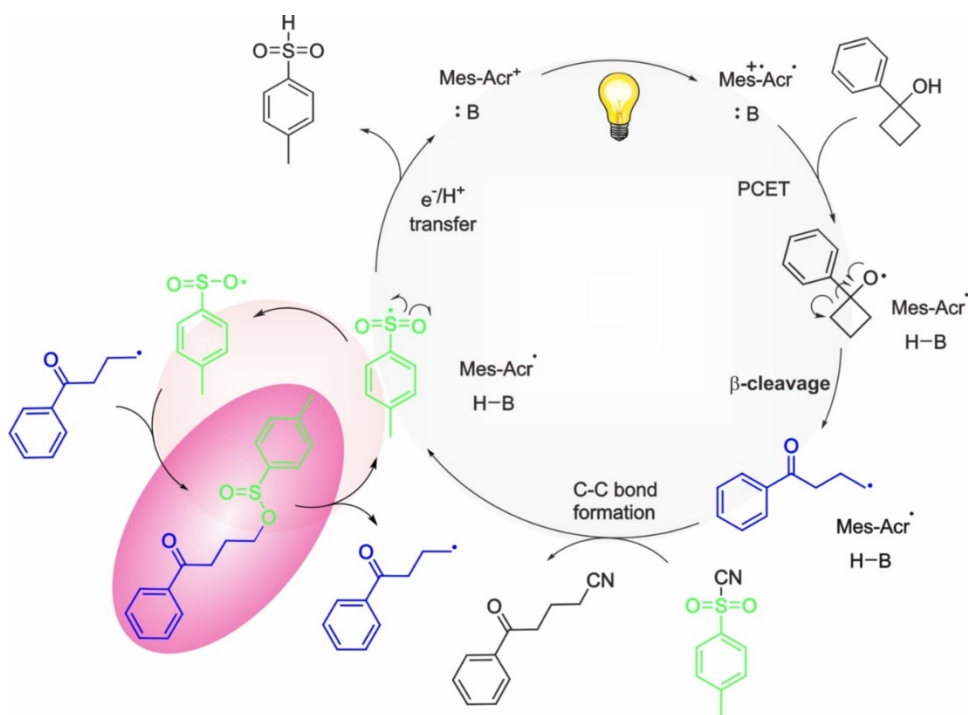


**Figure 3.37**: Proposed photocatalytic cycle for the functionalization of 1-phenylcyclobutanol with tosyl cyanide using blue light (455 nm) including off-cycle generation of an intermediate.

### 3.7.4  Extended NMR-Based H-bond and Aggregation Analysis

The formation of aggregates inside a solution is in general very dynamic and dependent on the entire molecular composition. Besides the expected and confirmed H-bond formation between cyclobutanol and the pyridine bases (see chapter 3.3), a more complex overall aggregation is assumed in presence of the tosyl cyanide trapping reagent and water. Especially the function of $H_2O$ on the reaction system was investigated. It plays a detrimental role for the acceleration of our photocatalytic transformation and is a good H-bond donor as well as acceptor. Therefore, in order to obtain an overview of the influence of TsCN and water as additive, a complete low temperature H-bond analysis was performed. In Figure 3.38, an excerpt of the ^{1}H spectra showing the O-H signals of alcohol **1** (bottom), the **1**/substituted pyridine mixtures, the **1**/substituted pyridine/TsCN mixtures and the same samples in presence of $H_2O$ is depicted. The samples were measured in $CD_2Cl_2$ at 180 K and 1:1/1:1:1-mixtures were used except for the $H_2O$ containing samples (1:1:1:0.25). The alcohol/pyridine mixtures and the corresponding spectra are identical to those shown in Figure 3.3 (chapter 3.3) and are added for comparability. As was already described in chapter 3.3, 2-methoxypyridine in general forms the strongest H-bond to the alcohol, followed by 2-chloropyridine and 2,6-dimethoxypyridine. Interestingly, the O-H signals are high field shifted after adding TsCN and $H_2O$, which indicates a weakening of the H-bond. In principle, the shift is most prominent for di-OMe-pyridine. Its O-H signal is located even at higher field than pure alcohol **1**, but notably, the alcohol sample is water free. As such, in presence of $H_2O$ we expect the alcohol proton to be located at lower ppm-values. Furthermore, the shoulder of the broad O-H signal indicates the existence of a second complex visible on the NMR time scale but with similar chemical shifts. As we think, that the actual pyridine-alcohol H-bond is masked by the alcohol self-aggregation, an average signal is postulated for the $H_2O$ containing mixtures, which in total produces weaker H-bonds in solution.
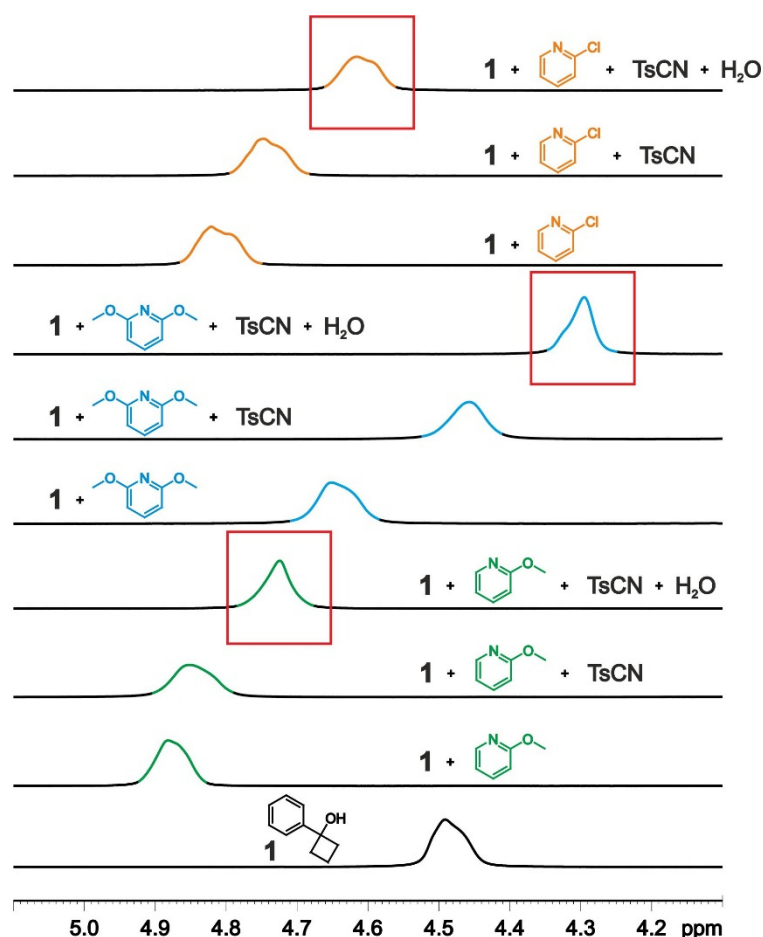
**Figure 3.38:** Overview of the O-H $^1$H chemical shifts of alcohol **1** (bottom) and for **1**/pyridine, **1**/pyridine/TsCN and **1**/pyridine/TsCN/H$_2$O mixtures in CD$_2$Cl$_2$ at 180 K. 1:1/1:1:1 ratios were used for the different samples except for mixtures containing H$_2$O (0.25 equiv.). The chemical shifts are referenced to TMS as internal standard.

### 3.7.5 Conclusion

Regarding the high basicity of unsubstituted pyridine in acetonitrile, which is the relevant solvent for the photocatalytic activation of cycloalkanols, a strong H-bond between the base and the substrate O-H functionality was expected. However, already in chapter 3.3 pyridine was shown to be inefficient. Therefore, the reason for its poor reactivity in the PCET step was elucidated by NMR in detail. Following the reaction directly inside the NMR spectrometer using different amounts of pyridine and varied solvent compositions the formation of a by-product could be revealed. Further studies suggested a light-independent rearrangement of the TsCN trapping reagent in presence of pyridine and subsequent substitution between cyclobutanol and the converted TsCN furnishing 1-phenylcyclobutyl 4-methylbenzenesulfinate. Thus, the side reaction of pyridine according to its high nucleophilicity seems to prevent an efficient PCET.

Low temperature ^{1}H and ^{15}N NMR chemical shift analysis revealed a drastically enhanced interaction between 1-phenylcyclobutanol and ^{15}N-pyridine in contrast to using the best performing 2-methoxypyridine, in general. As such, the unsubstituted base would be predestinated for an efficient PCET. However, due to the light-independent side reaction, the photocatalytic transformation cannot take advantage of the strong acceptor ability of pyridine. Via NOESY spectroscopy, spatial proximity between the ortho-positioned protons of pyridine and one side of the cyclobutanol ring was identified, which gives general information about the nature of the complex.

*Ex-situ* kinetics using 2-OMe-pyridine and 2,6-dimethoxypyridine revealed the entirely different impact of both bases onto the photocatalytic reaction. For the best performing mono-substituted pyridine 4-oxo-4-phenylbutyl benzenesulfinate was identified as off-cycle intermediate in a ^{1}H,^{1}H COSY experiment. Moreover, small amounts of by-product were found for both reactions, which was not further assigned.

Lastly, the H-bond situation of different mixtures including 1-phenylcyclobutanol **1**, **1**/substituted pyridine, **1**/ substituted pyridine/TsCN and **1**/ substituted pyridine/TsCN/$H_2O$ using 2-OMe-, 2-Cl- and 2,6-di-OMe-pyridine was discussed in detail using ^{1}H chemical shift analysis. As water was found to accelerate the photocatalytic reaction acting as H-bond acceptor as well, its influence on the complexation was of major interest. In general, the addition of both the trapping reagent and water weakened the overall interaction between alcohol and pyridine. However, for the best performing OMe-pyridine, the H-bond strength was less reduced. Furthermore, the chemical shift of the O-H signal is supposed to represent mainly the strength of the alcohol self-aggregation, which masks the actual H-bond to pyridine. This is supported by a shoulder of the O-H signal indicating the existence of at least two different alcohol involved aggregates with similar chemical shifts on the NMR time scale.

### 3.7.6  References

[1]    G. R. Fulmer, A. J. M. Miller, N. H. Sherden, H. E. Gottlieb, A. Nudelman, B. M. Stoltz, J. E. Bercaw, K. I. Goldberg *Organometallics* **2010**, *29*, 2176–2179.

21]    C. Feldmeier, H. Bartling, E. Riedle, R. M. Gschwind *J. Magn. Reson.* **2013**, *232*, 39–44.

[3]    D. H. R. Barton, J. C. Jaszberenyi, E. A. Theodorakis *Tetrahedron Lett.* **1991**, *47*, 9167–9178.

[4]    H. Bartling, A. Eisenhofer, B. König, R. M. Gschwind *J. Am. Chem. Soc.* **2016**, *138*, 36, 11860-11871.

# 4 Selective Single C(sp³)-F Bond Cleavage in Trifluoromethylarenes: Merging Visible-Light Catalysis with Lewis Acid Activation
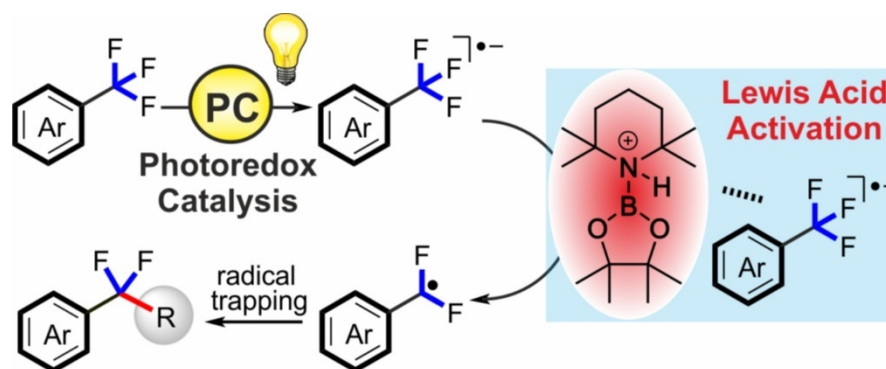


Kang Chen, **Nele Berg**, Ruth Gschwind, and Burkhard König

*J. Am. Chem. Soc.* **2017**, *139*, 51, 18444-18447

The extended NMR mechanistic studies were conducted and evaluated by Nele Berg. Nele Berg performed the ${}^1$H, ${}^{11}$B and ${}^{19}$F NMR experiments for the *in-situ* and *ex-situ* illuminated samples, the H-bond studies and the 2D spectra. The mechanistic parts of the manuscript and Supporting Information were prepared by Nele Berg. Nele Berg performed the measurements in "Addidional Findings" and wrote the entire chapter. Dr. Kang Chen is responsible for the reaction design, the optimization of the conditions, the synthesis of the substrates and the substrate scope. He performed the CV measurements and radical trapping experiments. A basic reaction profile by following the batch reaction by ${}^{19}$F NMR was generated by him and he prepared the NMR samples as well as the main part of the manuscript and SI.

Text and Figures may differ from the original publication.

## 4.1  Abstract

The conversion of easily available trifluoromethylarenes into aryldifluoromethyl compounds, which are valuable motifs in pharmaceutical chemistry, is highly atom- and step-economic. However, the single $C(sp^3)-F$ bond cleavage of $ArCF_3$ is a great challenge because of the chemical inertness of the $C(sp^3)-F$ bond and the difficult selectivity control of monodefluorination. We report here the first example of single $C(sp^3)-F$ functionalization of trifluoromethylarenes via visible-light catalysis merged with Lew-is acid activation. The method allows good chemoselectivity control and shows good functional group tolerance. Mechanistic studies suggest an *in-situ* generated borenium cationic species as the key intermediate for $C(sp^3)-F$ bond cleavage in this reaction.

## 4.2  Introduction

Organofluorine compounds are important in pharmaceutical chemistry and agrochemistry because of their special chemical and biological properties.[1] As the demand for novel organofluorine compounds has grown, organofluorine chemistry has developed rapidly in recent years.[2] Conventional strategies for the synthesis of organofluorine compounds mainly focus on new $C-F$ (or F-containing moiety) bond formation.[3] Alternatively, selective $C-F$ bond cleavage of multifluorinated compounds can also provide facile access to complex fluorinated molecules, which has recently drawn increasing attention.[4]

Aryldifluoromethyl derivatives ($ArCF_2R$) are important building blocks in many bioactive compounds (Figure 4.1a).[5] It is an appealing goal to achieve the straightforward synthesis of valuable $ArCF_2R$ derivatives from easily available trifluoromethylarenes ($ArCF_3$) via selective single $C(sp^3)-F$ bond cleavage. Since no preactivation of the starting material is required and only the $F^-$ anion is released as a byproduct, this transformation is highly atom- and step-economical. However, single $C(sp^3)-F$ bond cleavage of $ArCF_3$ is a challenging problem in organic synthesis, as the high bond dissociation energy[6] makes $C(sp^3)-F$ bonds usually quite inert under various reaction conditions. Furthermore, the dissociation energy of the remaining $C(sp^3)-F$ bonds decreases after one $C(sp^3)-F$ bond in the trifluoromethyl group is cleaved. Thus, avoiding multiple defluorinations is rather difficult.[6-8] In several previous reports, all three $C(sp^3)-F$ bonds in $ArCF_3$ were cleaved without selectivity[9] and only very few methods for single $C(sp^3)-F$ bond cleavage of $ArCF_3$ have been developed. The very recent work by Hosoya used *o*-silyl cation activation,[10] while Lalic employed transition metal catalysis to realize the

monohydrodefluorination of ArCF₃.[11] Other reports mainly relied on the single electron transfer (SET) strategy via active metal reduction (usually Mg), electrochemistry, or UV irradiation (Figure 4.1b).[12-14]

**a) Selected Bioactive Aryldifluoromethyl Compounds**



HIV-1 reverse transcriptase inhibitor

FKBP12 rotamase activity inhibitor

thrombin inhibitor

**b) Selective Single C(sp³)-F Cleavage in Trifluoromethylarenes (Ref. 10-14)**



**c) Our Design (This Work)**
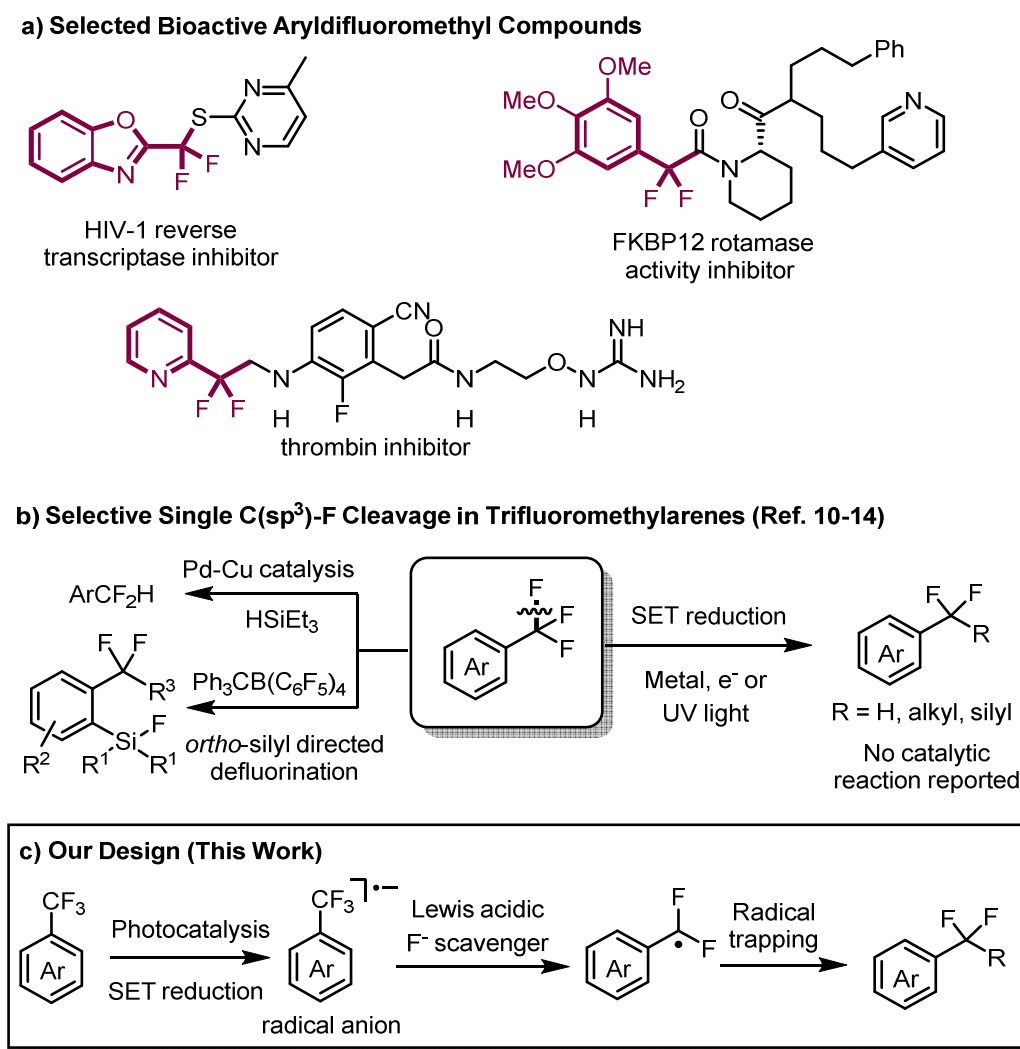


**Figure 4.1:** a) Relevant bioactive aryldifluorinated species; b) literature known synthetic strategies for selective single C-F bond cleavage; c) our design of photocatalytic selective single C(sp³)−F bond cleavage of Trifluoromethylarenes.

These reactions still suffer from the use of a large excess of reductants, limited substrate scope, and sometimes low selectivity of monodefluorination. Moreover, no catalytic SET reaction system has been established to date. Visible-light-induced photoredox catalysis may facilitate the SET process under mild conditions.[15] Elegant examples of visible-light-induced C−F bond cleavage have been reported. Weaver realized selective aromatic C−F bond functionalization of multifluoroarenes.[16] Hashmi developed radical-radical cross

coupling between amines and F-containing compounds.[17] Zhou and Molander managed to prepare *gem*-difluoroalkenes from α-trifluoromethyl olefins via a radical-polar crossover process.[18,19] Despite the above achievements, single $C(sp^3)-F$ bond cleavage of $ArCF_3$ driven by visible-light catalysis has remained a challenge. Herein we report the first monodefluorination of $ArCF_3$ via visible-light catalysis merged with Lewis acid activation.

## 4.3 Results and Discussion

### 4.3.1 Reaction Design and Optimization

In our design, stepwise activation of the inert $ArCF_3$ molecule is envisaged. First, $ArCF_3$ is converted into the corresponding radical anion via photocatalytic SET reduction in the presence of a suitable photocatalyst and electron donor. This radical anion would be able to release $F^-$ to form the aryldifluoromethyl radical ($ArCF_2^{\bullet}$), albeit at a very low rate because of the poor leaving group ability of $F^-$.[8] Since the radical anion is not reactive enough, we speculated that the use of a proper Lewis acidic fluoride scavenger[20,21] could further accelerate the radical generation and suppress the electron transfer.[22] An appropriate interaction between the Lewis acid (fluoride scavenger) and base (electron donor) would be the key to a successful reaction. Finally, the aryldifluoromethyl radical could be captured by a trapping reagent to give the corresponding $ArCF_2R$ product (Figure 4.1c). We hypothesized that the combination of electronic control of the photocatalyst and steric control of the Lewis pair might offer more opportunities to realize monodefluorination selectivity than a sole activation system.

With this design in mind, we chose *fac*-Ir(ppy)$_3$ as the photocatalyst (for Ir(III)/Ir(II), $E_{red}$ = -2.19 V vs. SCE),[23] *N*-methyl-*N*-phenyl-methacrylamide (**2a**) as the trapping reagent to initiate the optimization of a selective single $C(sp^3)-F$ cleavage of 4-trifluoromethylbenzonitrile (**1a**) in 1,2-dichloroethane (DCE) solution under blue-light irradiation (455 nm). To our delight, the combination of pinacolborane (HBpin) with the sterically hindered, *α*-H atom-free amine 2,2,6,6-tetramethyl-piperidine (TMP) remarkably improved the reaction efficiency, while in the absence of HBpin (Table 4.3, entry 3, SI) or TMP (Table 4.3, entry 4, SI), the reaction did not afford the desired product. The inferior results with other amine-boron or silicon reagent combinations indicated that the chemical properties of both additives were critical for this reaction (Tables 4.3 and 4.4, SI). Control experiments showed that the Ir catalyst (Table 4.5, entry 5) and blue-light irradiation (Table 4.5, entry 6, SI) were essential for this reaction. After an extensive screening of photocatalysts, solvents, reaction times, and equivalents of components (Tables 4.5 – 4.7, SI), we found the optimal conditions to be 1.0 mol% Ir catalyst, 2.0 equiv. of TMP and **2a**,

and 3.0 equiv. of HBpin in 1.0 ml of DCE under blue-light irradiation (455 nm) for 24 h (Table 4.7, entry 6). Good selectivity for single $C(sp^3)-F$ cleavage was achieved under these conditions, and a less than 5% of didefluorinated product was detected in the crude reaction mixture.

**Table 4.1:** Substrate Scope of Methacrylamides[a].
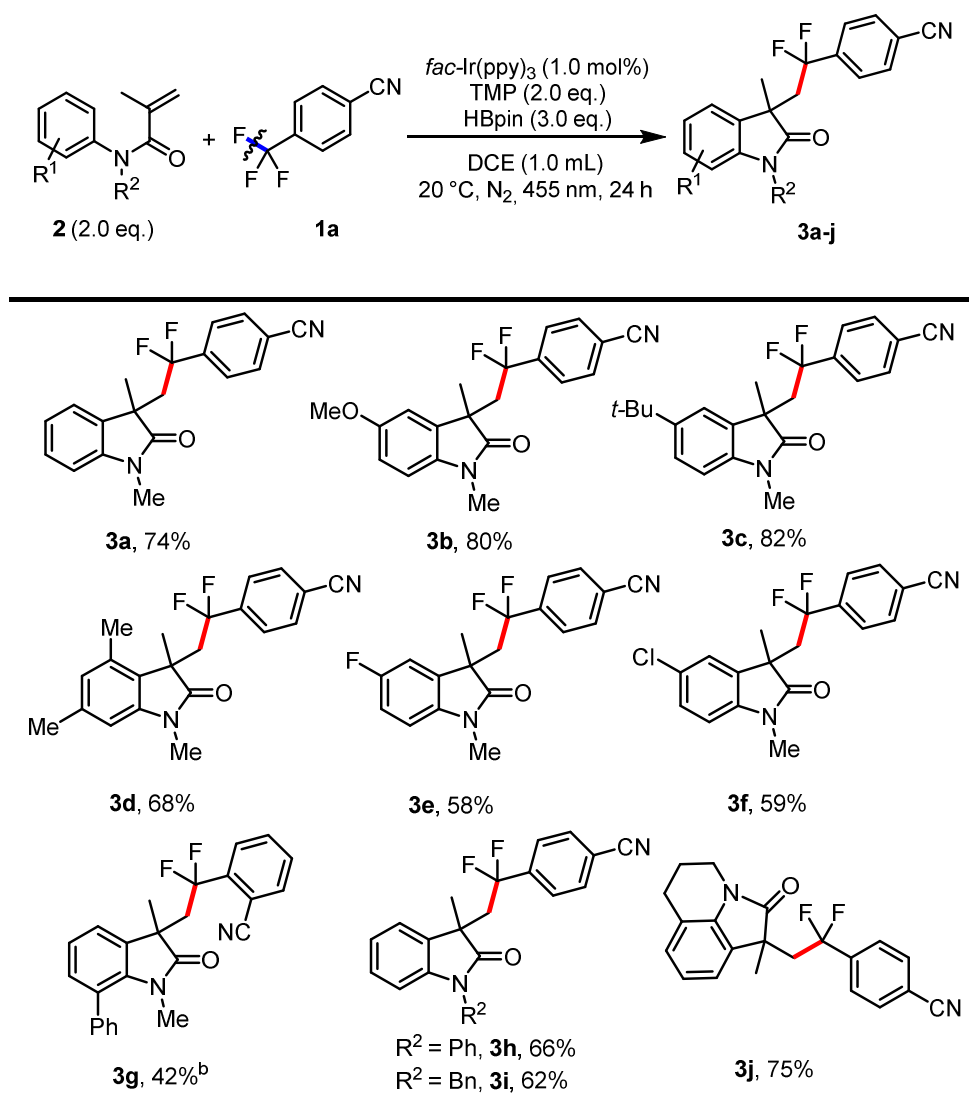
[a] Reactions were performed on a 0.1 mmol scale, and isolated yields are shown. [b] 2-CF₃-benzonitrile was used; the reaction time was 36 h.
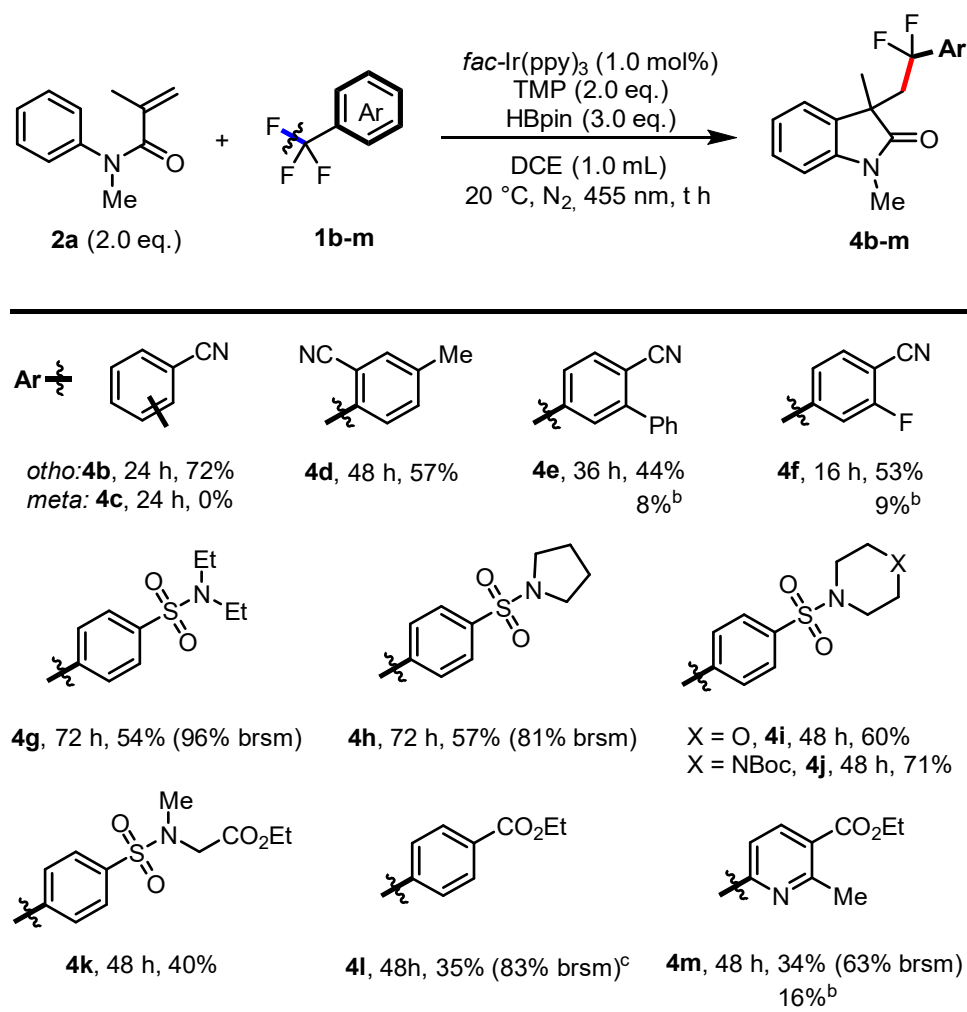
With the optimized conditions in hand, we tested the scope of methacrylamides **2** as trapping reagents (Table 4.1). The reaction between **1a** and amide **2a** gave product **3a** in good isolated yield under the standard conditions. Generally, electron-rich methacrylamides facilitated the capture of the electron-deficient aryldifluoromethyl radical

and the following cyclization step, which resulted in better yields of **3b** and **3c** compared with their electron-deficient analogues **3e** and **3f**. Steric hindrance of the substrate affected the cyclization step, resulting in a slightly lower yield of **3d**. Notably, even the presence of a $C(sp^2)-Cl$ bond was tolerated under these conditions, which illustrates the good chemoselectivity of the specific $C(sp^3)-F$ bond (**3f**). The biphenyl derivative **2g** gave the lowest product yield (**3g**). Methacrylamides bearing different N-protecting groups gave the corresponding products in good yields (**3h-3j**).

Next, we further investigated the scope of $ArCF_3$ compounds (Table 4.2). Compared with the para-cyano-substituted benzotrifluoride, the ortho isomer showed similar reactivity (**4b**), while the meta-cyano-substituted benzotrifluoride did not yield any product (**4c**). Even methyl group substitution significantly slowed the reaction (**4d**), and biphenyl substrates showed lower reactivity than phenyl derivatives (**4e**). Though bearing two strong electron-withdrawing groups (-$CF_3$ and -CN) on the aromatic ring, the aryl $C(sp^2)-F$ bond in **1f** still remained untouched, and the $C(sp^3)-F$ bond cleavage product was obtained instead (**4f**). A 4-trifluoromethylbenzenesulfonyl-protected acyclic secondary amine, synthetically useful heterocycles (pyrrolidine, morpholine, *N*-Boc-piperazine), and a glycine derivative gave the corresponding products (**4g-4k**) in moderate to good yields, albeit with longer reaction times (48-72 h). However, aromatic carboxylic esters do not convert well in this transformation. The ethyl ester **1l** was less than 50% converted even after 48 h of reaction time. Poor monodefluorination selectivity was observed in the case of the nicotinic ester derivative **1m**.

**Table 4.2:** Substrate Scope of Trifluoromethylarenes[a].



Reaction scheme: 2a (2.0 eq.) + 1b-m, with *fac*-Ir(ppy)$_3$ (1.0 mol%), TMP (2.0 eq.), HBpin (3.0 eq.), DCE (1.0 mL), 20 °C, N$_2$, 455 nm, t h, giving 4b-m.



Ar = 

*otho:* **4b**, 24 h, 72%
*meta:* **4c**, 24 h, 0%

**4d**, 48 h, 57%

**4e**, 36 h, 44%
8%[b]

**4f**, 16 h, 53%
9%[b]

**4g**, 72 h, 54% (96% brsm)

**4h**, 72 h, 57% (81% brsm)

X = O, **4i**, 48 h, 60%
X = NBoc, **4j**, 48 h, 71%

**4k**, 48 h, 40%

**4l**, 48h, 35% (83% brsm)[c]

**4m**, 48 h, 34% (63% brsm)
16%[b]

[a] Reactions were performed on a 0.1 mmol scale and, isolated yields are shown. Yields in parenthesis are based on the recovered starting materials. [b] $^{19}$F NMR yield of the di-defluorinated product. [c] $^{19}$F NMR yield of the desired product.

### 4.3.2 Investigation of the Mechanism

With a series of experiments, we investigated the reaction mechanism. 2,2,6,6-tetramethylpiperidin-1-oxyl (TEMPO) and 1,1-diphenylethylene were used as radical scavengers, and the corresponding trapping adducts were detected (Figures 4.10 and 4.11, SI), which indicated that the aryldifluoromethyl radical was involved in this reaction. From the reaction profile, we observed a relatively low reaction rate in the first hour with an induction period of about 0.5 h (Figure 4.9, SI). This may indicate the generation and accumulation of an active species for the C(sp$^3$)—F bond cleavage at the early stage of the reaction. During *in-situ* illumination inside the NMR spectrometer, the formation of a

new boron species ($^{11}$B NMR, δ = 25.0 ppm in CD$_2$Cl$_2$) was detected at low concentration (Figure 4.2A).The observed species had the same $^{11}$B chemical shift as the borenium cationic species **5**, which could be prepared independently from TMP, HBpin and [Ph$_3$C]$^+$[B(C$_6$F$_5$)$_4$]$^-$ following a reported procedure (Figure 4.2B).[24]
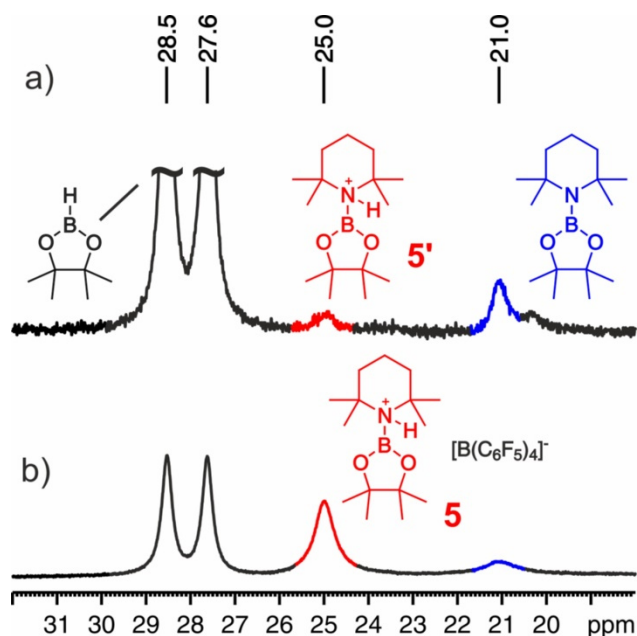


**Figure 4.2:** $^{11}$B NMR studies of the reaction intermediate; a) *in-situ* irradiation of the single C(sp$^3$)−F bond cleavage reaction of **1a** (450 nm, 22 h) in CD$_2$Cl$_2$ (0.1 M) inside the NMR spectrometer showed the generation of **5′**; b) generation of borenium cationic species **5** in a mixture containing [Ph$_3$C]$^+$[B(C$_6$F$_5$)$_4$]$^-$ (0.1 M), HBpin (0.11 M), and TMP (0.1 M) in CD$_2$Cl$_2$.

Upon addition of **1a** to a sample of **5**, a low-field shift of the N−H proton in **5** was observed, while its $^{11}$B spectrum was not affected at all and its $^{19}$F signal shifted only by 0.1 ppm (Figures 4.21-4.23, SI). Further investigations via $^{1}$H-$^{19}$F HOESY showed no interaction between **5** and the trifluoro-methyl group of **1a**, and $^{1}$H-$^{1}$H NOESY corroborated a preferred interaction with the CN group of **1a** (Figures 4.25 and 4.26, SI) according to its better H-bond acceptor properties.[25] These observations contradict a direct C(sp$^3$)−F bond activation in the noncharged molecule **1a** by the borenium cationic species **5**. Interestingly, when the photoreduction system and *in-situ* generated **5** were combined, **1a** underwent the desired monodefluorination reaction to afford **3a** (Figure 4.3, Eq. 1), which suggests that **5** prefers to abstract a fluoride anion from the radical anion of **1a**. On the basis of the above results, the borenium cation **5'** observed in our reaction could act as a fluoride scavenger. Furthermore, we suggest that **5'** is generated *in-situ* from the reaction of TMP, HBpin and a proton. Notably, the methacrylamide has a dual role as a trapping

reagent and proton source. It releases one proton in every catalytic cycle during the radical trapping/-intramolecular cyclization/rearomatization cascade, which continuously provides the driving force for the generation of **5'** and the $C(sp^3)-F$ bond cleavage. This proposal was supported by another control experiment without **2a**. Most of the starting material was recovered, and the $C(sp^3)-F$ bond cleavage hardly proceeded even after irradiation for 24 h (Figure 4.14, SI).

Finally, we explored the origin of the chemoselectivity in this reaction. Although the reduction potential of **3a** ($E_{red}$ = -1.91 V vs. SCE) was even slightly more positive than that of the starting material **1a** ($E_{red}$ = -1.94 V vs. SCE),[26] **3a** remained stable under the reaction conditions. Only ca. 2% yield of **7** was detected in the crude mixture, and most of the **3a** was recovered (Figure 4.3, Eq. 2). Compared with **1a**, the steric hindrance of **3a** was significantly increased, which likely inhibited further defluorination caused by the steric bulky borenium cation **5'**. Other substrates such as **1e** ($E_{red}$ = -1.86 V vs. SCE), **1f** ($E_{red}$ = -1.82 V vs. SCE), and **1m** ($E_{red}$ = -1.82 V vs. SCE) were more susceptible to SET reduction, which decreased their selectivity of monodefluorination. We therefore propose that the synergy of steric and electronic factors controls the chemoselectivity of the single $C(sp^3)-F$ bond cleavage.[27]
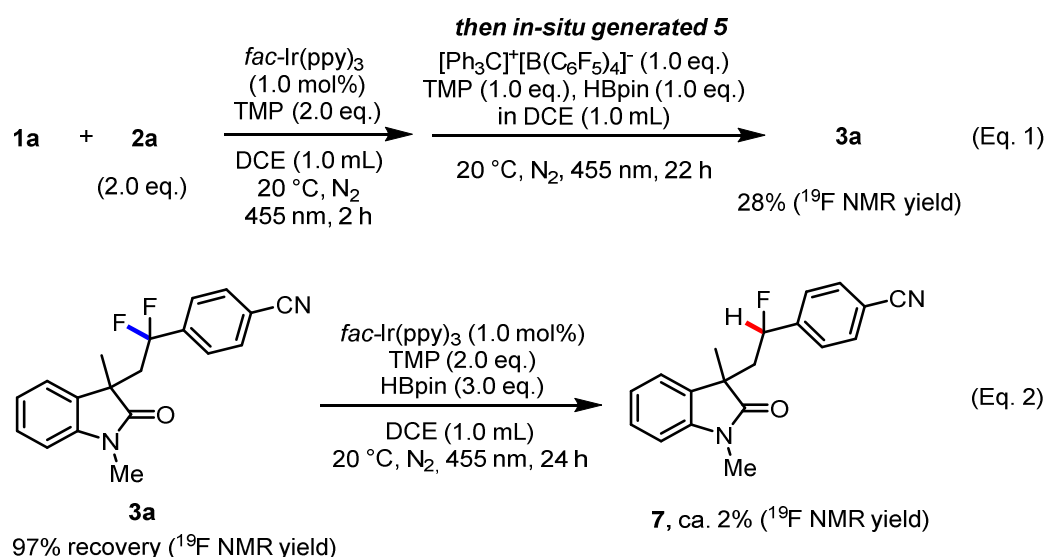


**Figure 4.3:** Mechanistic studies of the photoreduction system: the addition of *in-situ* generated **5** to the reaction mixture furnished the desired monodefluorination product **3a** (Eq. 1). Stability of **3a** under the reaction conditions was proven. Most of 3a was recovered and ~2% yield of **7** were formed (Eq. 2).

On the basis of the experimental observations, we propose a plausible reaction mechanism (Figure 4.4). Initially, the blue-light-excited *fac*-Ir(ppy)$_3$ is reductively quenched by TMP, affording an Ir(II) species and TMP radical cation A.[28] The Ir(II) species reduces **1a** to its corresponding radical anion B. The reaction between the protonated TMP species C and HBpin should produce the Lewis acidic borenium cation **5'**,[29] which abstracts F- from B to give the aryldifluoromethyl radical D. Finally, **2a** captures D, and subsequent cyclization and oxidative rearomatization give product **3a**. The proton released during the rearomatization step regenerates C, which is essential for the continuous aryldifluoro-methyl radical generation.



**Figure 4.4:** Proposed mechanism.

## 4.4 Conclusion

In summary, single C(sp$^3$)−F bond activation in trifluoromethylarenes has been achieved by merging Ir photoredox catalysis with Lewis acid activation. This reaction provides a highly atom- and step-economical approach to construct aryldifluoromethyl moieties, which are valuable in pharmaceutical chemistry. The reaction shows good chemoselectivity control and functional group tolerance. Mechanistic studies reveal that the synergy of steric and electronic factors contro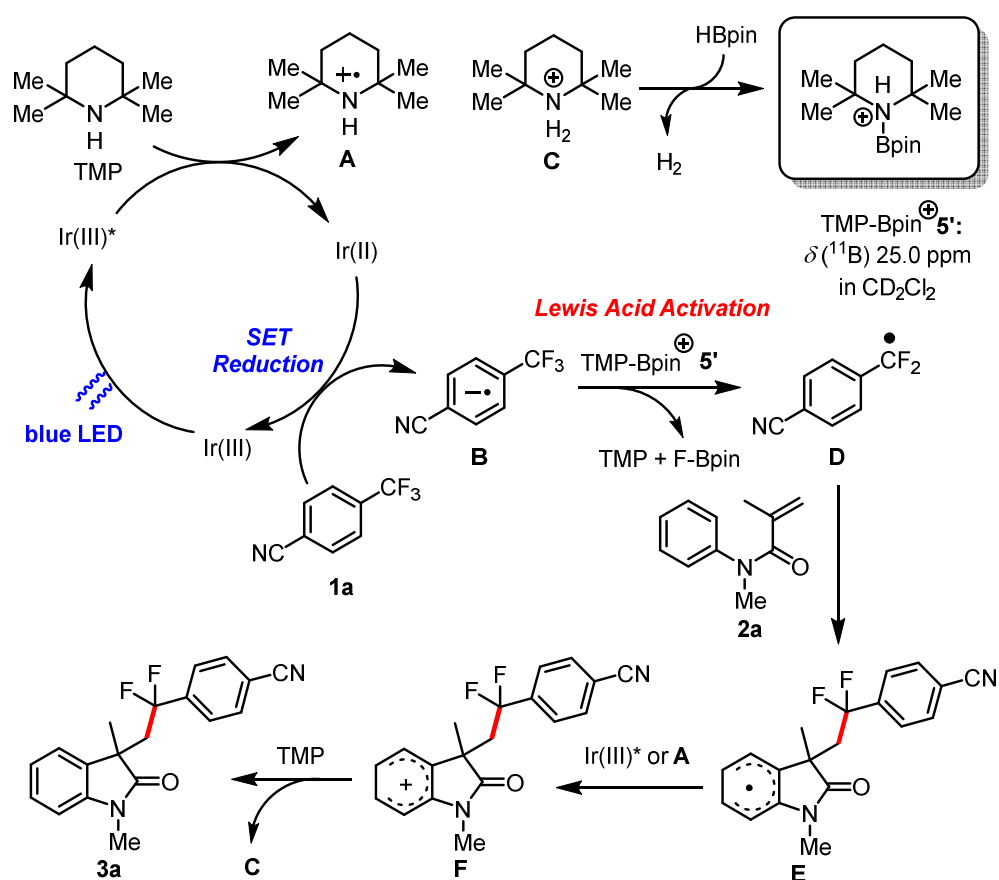ls the chemoselectivity of single C(sp$^3$)−F bond cleavage. An *in-situ* generated borenium cationic species is suggested as the key intermediate for the C(sp$^3$)−F bond cleavage step. The trapping reagent methacrylamide, which also acts as a proton source, provides the pace for the defluorination process.

## 4.5 References

[1]     (a) Müller, K., Faeh, C., Diederich, F. *Science* **2007**, *317,* 1881–1886. (b) Hagmann, W. K. *J. Med. Chem.* **2008**, *51,* 4359–4369. (c) Gillis, E. P., Eastman, K. J., Hill, M. D.; Donnelly, D. J., Meanwell, N. A. *J. Med. Chem.* **2015**, *58,* 8315–8359.

[2]     Modern Fluoroorganic Chemistry: Synthesis, Reactivity, Applications; Kirsch, P., Ed., Wiley-VCH: Weinheim, **2004**.

[3]     (a) Furuya, T., Kamlet, A. S., Ritter, T.*Nature* **2011***, 473,* 470–477. (b) Campbell, M. G., Ritter, T. *Chem. Rev.* **2015**, *115,* 612−633. (c) Ni, C., Hu, M., Hu, J. *Chem. Rev.* **2015**, *115,* 765–825. (d) Yang, X., Wu, T., Phipps, R. J., Toste. F. D. *Chem. Rev.* **2015**, *115,* 826–870.

[4]     (a) Amii, H., Uneyama, K. *Chem. Rev.* **2009**, *109,* 2119–2183. (b) Stahl, T., Klare, H. F. T., Oestreich, M. *ACS Catal.* **2013**, *3,* 1578–1587. (c) Ahrens, T., Kohlmann, J., Ahrens, M., Braun, T. *Chem. Rev.* **2015**, *115,* 931–972.

[5]     (a) N. A. Meanwell, *J. Med. Chem.* **2011**, *54,* 2529–2591. (b) Boyer, J., Arnoult, E., Médebielle, M., Guillemont, J., Unge, J., Jochmans, D. *J. Med. Chem.* **2011**, *54,* 7974−7985.

[6]     Burdeniuc, J., Jedlicka, B., Crabtree, R. H. *Chem. Ber.* **1997**, *130,* 145–154.

[7]     (a) Wiberg, K. B. Rablen, P. R. *J. Am. Chem. Soc.* **1993**, *115,* 614–625. (b) O'Hagan, D. *Chem. Soc. Rev.* **2008**, *37,* 308–319.

[8]     Andrieux, C. P., Combellas, C., Kanoufi, F., Savéant, J.-M., Thiébault, A. *J. Am. Chem. Soc.* **1997**, *119,* 9527–9540.

[9]     (a) Scott, V. J., Çelenligil-Çetin, R., Ozerov, O. V. *J. Am. Chem. Soc.* **2005**, *127,*

2852–2853. (b) Fuchibe, K., Akiyama, T. *J. Am. Chem. Soc.* **2006**, *128,* 1434–1435. (c) Douvris, C., Ozerov, O. V. *Science* **2008**, *321,* 1188–1190. (d) Terao, J., Nakamura, M., Kambe, N. *Chem. Commun.* **2009**, 6011–6013. (e) Stahl, T., Klare, H. F. T., Oestreich, M. *J. Am. Chem. Soc.* **2013**, *135,* 1248–1251. (f) Zhu, J., Pérez, M., Caputo, C. B., Stephan, D. W. *Angew. Chem. Int. Ed.* **2016**, *55,* 1417–1421.

[10]   Yoshida, S., Shimomori, K., Kim, Y., Hosoya, T. *Angew. Chem. Int. Ed.* **2016**, *55,* 10406–10409.

[11]   Dang, H., Whittaker, A. M., Lalic, G. *Chem. Sci.* **2016**, 7, 505–509.

[12]   (a) Amii, H., Hatamoto, Y., Seo, M., Uneyama, K. *J. Org. Chem.* **2001**, *66,* 7216–7218. (b) S. Utsumi, T. Katagiri, K. Uneyama, *Tetrahedron* **2012**, *68*, 1085–1091. (c) Munoz, S. B., Ni, C., Zhang, Z., Wang, F., Shao, N., Mathew, T., Olah, G. A., Prakash, G. K. S. *Eur. J. Org. Chem.* **2017**, 2322–2326.

[13]   Clavel, P., Lessene, G., Biran, C., Bordeau, M., Roques, N., Trévin, S. Montauzon, D. D. *J. Fluorine Chem.* **2001**, *107,* 301–310.

[14]   (a) Mattay, J., Runsink, J., Gersdorf, J., Rumbach, T., Ly, C. *J. Am. Chem. Soc.* **1985**, *107,* 2557–2558. (b) Kako, M., Morita, T., Torihara, T., Nakadaira. Y *J. Chem. Soc. Chem. Commun.* **1993**, 678–680.

[15]   (a) Yoon, T. P., Ischay, M. A., Du, J. *Nat. Chem.* **2010**, *2*, 527–532. (b) Narayanam, J. M. R., Stephenson, C. R. J. *Chem. Soc. Rev.* **2011**, *40*, 102–113. (c) Prier, C. K., Rankic, D. A., MacMillan, D. W. C. *Chem. Rev.* **2013**, *113*, 5322–5363. (d) Romero, N. A., Nicewicz, D. A. *Chem. Rev.* **2016**, *116 ,*10075–10166.

[16]   (a) Senaweera, S. M., Singh, A., Weaver, J. D. *J. Am. Chem. Soc.* **2014**, *136,* 3002–3005. (b) Singh, A., Kubik, J. J., Weaver, J. D. *Chem. Sci.* **2015**, *6, * 7206–7212. (c) Senaweera, S., Weaver, J. D. *J. Am. Chem. Soc.* **2016**, *138,* 2520–2523. (d) Singh, A., Fennell, C. J., Weaver, J. D. *Chem. Sci.* **2016**, *7,* 6796–6802. (e) Khaled, M. B., Mokadem, R. K. E., Weaver, J. D. *J. Am. Chem. Soc.* **2017**, *139,* 13092–13101. For a recent review, see: (f) Senaweera, S., Weaver, J. D. *Aldrichimica Acta* **2016**, *49,* 45–54.

[17]   (a) Xie, J., Yu, J., Rudolph, M., Rominger, F., Hashmi, A. S. K. *Angew. Chem. Int. Ed.* **2016**, *55,* 9416–9421. (b) Xie, J., Rudolph, M., Rominger, F., Hashmi, A. S. K. *Angew. Chem. Int. Ed.* **2017**, *56,* 7266–7270.

[18]   (a) Xiao, T., Li, L., Zhou, L. *J. Org. Chem.* **2016**, *81,* 7908–7916. (b) Li, L., Xiao, T., Chen, H., Zhou, L. *Chem. Eur. J.* **2017**, *23,* 2249–2254.

[19]   Lang, S. B., Wiles, R. J., Kelly, C. B., Molander, G. A. *Angew. Chem. Int. Ed.* **2017**, *56,* 15073–15077.

[20]   For a review involving photoredox and Lewis acid dual catalysis, see: Skubi, K. L., Blum, T. R., Yoon, T. P. *Chem. Rev.* **2016**, *116,* 10035−10074, and references therein.

[21]   Lewis acids as F$^-$ scavenger for complete C–F bonds cleavage in ArCF$_3$, also see Ref. **4b** and **9**; controlled single C–F bond cleavage in –CF$_3$ group, see Ref. [10]

and Fuchibe, K., Hatta, H., Oh, K., Oki, R., Ichikawa. J. *Angew. Chem. Int. Ed.* **2017**, *56,* 5890-5893.

[22]   (a) Pac, C., Ihama, M., Yasuda, M., Miyauchi, Y., Sakurai, H. *J. Am. Chem. Soc.* **1981**, *103,* 6495−6497. (b) Mizuno, K., Nakanishi, K., Otsuji, Y. *Chem. Lett.* **1988**, *17,* 1833−1836.

[23]   Flamigni, L., Barbieri, A., Sabatini, C., Ventura, B., Barigelletti, F. *Top Curr. Chem.* **2007**, *281,* 143–203.

[24]   Eisenberger, P., Bailey, A. M., Crudden, C. M. *J. Am. Chem. Soc.* **2012**, *134*, 17384−17387.

[25]   Hunter, C. A. *Angew. Chem. Int. Ed.* **2004**, *43,* 5310–5324. For a more detailed discussion of this issue, see Supporting Information.

[26]   See Supporting Information for more detailed results.

[27]   See Supporting Information for a detailed discussion of the possible pathways of over-defluorination and the influence of steric and electronic factors on the chemo-selectivity.

[28]   Emission decay experiments indicated that *fac*-Ir(ppy)$_3$ preferred reductive quenching by TMP other than oxidative quenching by 4-trifluoromethylbenzonitrile **1a**. See Supporting Information for details.

[29]   We hypothesized that at the initial generation of protons might be due to the trapping of a 2-chloroethyl radical by **2a**, which was generated from the SET reduction of DCE. The trapping adduct was detected by mass spectrometry. See Supporting Information for details.

## 4.6 Supporting Information

### 4.6.1 General Information

The photocatalyst *fac*-Ir(ppy)$_3$ was synthesized according to literature procedure.[1]  Other iridium, ruthenium, rhodamine photocatalysts, 2,2,6,6-tetramethylpiperidine (TMP) and pinacolborane were purchased from Sigma-Aldrich and used without further purification. Other chemicals were purchased from Alfa Aesar, Merck or abcr GmbH and directly used without further purification. Solvents were dried with 3 Å molecular sieves according to the reported procedure.[2] CD$_2$Cl$_2$ for NMR mechanistic study was distilled over CaH$_2$ and stored in glove box.

Photocatalytic reactions were carried out by using Eaglerise ELP8X3LS 3W blue LEDs (λ = 455 nm), which was connected to HAAKE-FK cyclic water cooling system. Analytical TLC was performed on silica gel coated alumina plates (MN TLC sheets ALUGRAM® Xtra SIL G/UV254). Visualization was done by UV light (254 or 366 nm). Flash column chromatography for photocatalytic reactions was performed on a Biotage® Isolera™ Spektra system and silica gel of particle size 25 µm was used.
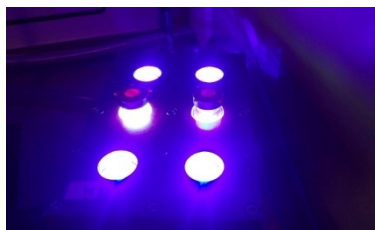


NMR measurements:

$^1$H, $^{11}$B, $^{13}$C, and $^{19}$F NMR spectra were measured on Bruker Advance 300 or 600 spectrometers (300 MHz or 600 MHz) in CDCl$_3$ or CD$_2$Cl$_2$. Chemical shifts are reported in parts per million (ppm) and relative to the solvent residual peaks as the internal standard.[3] Data were reported as follows: chemical shift, multiplicity, coupling constant J (Hz) and integration. Abbreviations used for signal multiplicity: b = broad, s = singlet, d = doublet, t = triplet, q = quartet, and m = multiplet; High resolution mass spectra (HRMS) were obtained from the central analytic mass spectrometry facilities of the Faculty of Chemistry and Pharmacy, Regensburg University. GC/MS measurements were performed on a 7890A GC system from Agilent Technologies with an Agilent 5975 MSD Detector. Data acquisition and evaluation were done with MSD ChemStation E.02.02.1431. A capillary column HP-5MS/30 m x 0.25 mm/0.25 µM film and helium as carrier gas (flow rate of 1 mL/min) were used.

### 4.6.2 Optimization of Reaction Conditions

**Table 4.3:** Screening of Amines
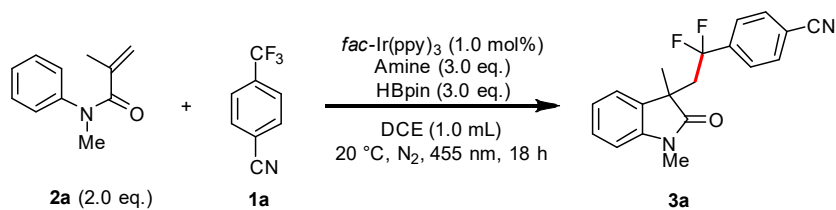


| Entry[a] | Amine | Conversion[b] | Yield[b] |
|---|---|---|---|
| 1[c] | DIPEA | 65% | 10% |
| 2[c] | N(*n*-Bu)$_3$ | 57% | 16% |
| 3[c] | TMP | --- | n.d. |
| 4 | --- | --- | n.d. |
| 5 | DIPEA | 100% | 17% |
| 6 | N(*n*-Bu)$_3$ | 68% | 18% |
| 7[d] | TMP | 76% | 63% |
| 8 | quinuclidine | 28% | 13% |
| 9 | piperidine | 27% | 5% |

[a] Reactions were run in 0.1 mmol scale. [b] $^{19}$F NMR yield of crude mixture, with (trifluoromethoxy)-benzene as the internal standard. [c] Without HBpin. [d] The combination of TMP and HBpin improves both reaction efficiency and mass balance, detailed analysis shown as follows:
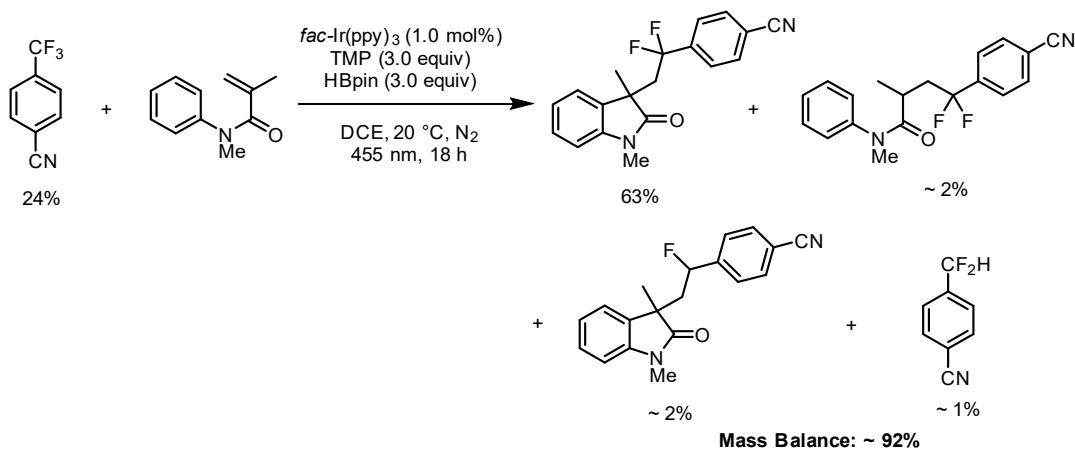


**Mass Balance: ~ 92%**

**Table 4.4:** Screening of F⁻ Scavengers
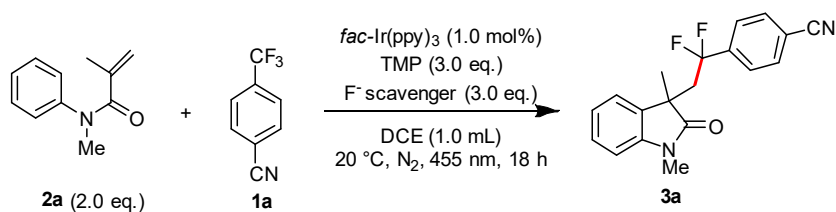


| Entry[a] | F⁻ scavenger | Yield |
|---|---|---|
| 1[b] | $B_2pin_2$ | n.d. |
| 2 | $HSiEt_3$ | n.d. |
| 3 | $B(OMe)_3$ | n.d. |
| 4 | $BF_3 \cdot Et_2O$ | n.d. |
| 5 | --- | n.d. |

[a] Reactions were run in 0.1 mmol scale. [b] 1.5 eq. $B_2Pin_2$

**Table 4.5:** Screening of Photocatalysts
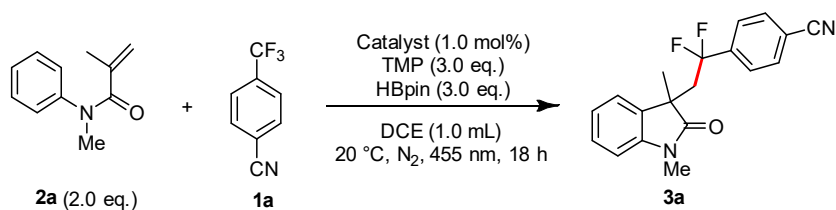


| Entry[a] | Catalyst | Yield |
|---|---|---|
| 1 | $Ru(bpy)Cl_2 \cdot 6H_2O$ | n.d. |
| 2 | $Ir(dF\text{-}CF_3ppy)(dtbpy)PF_6$ | n.d. |
| 3 | Rhodamine 6G | n.d. |
| 4 | Rhodamine B | n.d. |
| 5 | --- | n.d. |
| 6[b] | *fac*-Ir(ppy)$_3$ | n.d. |

[a] Reactions were run in 0.1 mmol scale. [b] Without irradiation.

**Table 4.6:** Screening of Solvents and Reaction Time
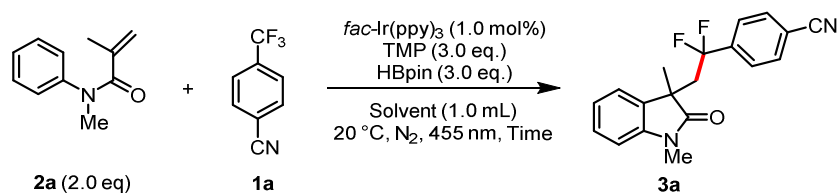


| Entry[a] | Solvent | Time (h) | Conversion[b] | Yield[b] |
|---|---|---|---|---|
| 1 | DCE | 18 | 76% | 63% |
| 2 | DCM | 18 | 80% | 61% |
| 3 | MeCN | 18 | 81% | 49% |
| 4 | DCE/THF(9:1) | 18 | 76% | 61% |
| 5 | DCE/DMF(9:1) | 18 | 92% | 60% |
| 6 | DCE/MeCN(9:1) | 18 | 88% | 65% |
| 7 | DCE/MeCN(8:2) | 18 | 92% | 65% |
| 8 | DCE/MeCN(9:1) | 24 | 94% | 68% |
| 9 | DCE | 24 | 86% | 73% |
| 10 | DCE | 30 | 92% | 72% |

[a] Reactions were run in 0.1 mmol scale. [b] $^{19}$F NMR yield of crude mixture, with (trifluoromethoxy)-benzene as the internal standard.

**Table 4.7**: Screening of Equivalents of Components
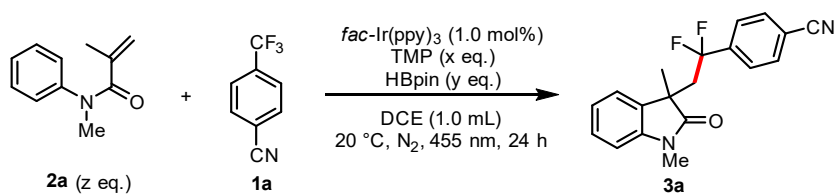


| Entry[a] | x | y | z | Conversion[b] | Yield[b] |
|---|---|---|---|---|---|
| 1 | 3 | 3 | 2 | 86% | 73% |
| 2[c] | 3 | 3 | 2 | 88% | 67% |
| 3[d] | 3 | 3 | 2 | 94% | 73% |
| 4 | 3 | 3 | 1.5 | 84% | 66% |
| 5 | 3 | 4 | 2 | 88% | 68% |
| **6** | **2** | **3** | **2** | **91%** | **79%** |
| 7 | 1.5 | 3 | 2 | 72% | 59% |
| 8 | 1 | 2 | 2 | 44% | 26% |

[a] Reactions were run in 0.1 mmol scale. [b] $^{19}$F NMR yield of crude mixture, with (trifluoromethoxy)benzene as the internal standard. [c] 1.5 mol% Ir catalyst. [d] In 0.5 mL DCE solution.

### 4.6.3  Synthesis of the Substrates

Methacrylamide **2a-j** and compound **1m** were synthesized according to a previous reported procedure.[4,5]

<u>Synthesis of biphenyl derivative **1e**.</u>[6]

A mixture of 2-chloro-4-(trifluoromethyl)benzonitrile (2.0 mmol, 0.41 g), phenyl boronic acid (2.4 mmol, 0.29 g) were dissolved in toluene/dioxane/2 N Na$_2$CO$_3$ (aq) (2:1:1) solution (12 mL) in a Schlenk flask. Pd(PPh$_3$)$_4$ (0.2 mmol, 0.23 g) and dppf (0.2 mmol, 0.22 g) was added to the mixture. The solution was degassed by N$_2$ bubbling for 10 min. Then it was refluxed under N$_2$ atmosphere for 12 h. After cooled down to ambient temperature, the reaction mixture was filtered over celite and extracted with EtOAc (15 mL*3). The combined organic extracts were dried over anhydrous Na$_2$SO$_4$, and concentrated in vacuo. The residue was purified by flash column chromatography (eluent PE/EtOAc = 10:1) to obtain product **1e**.
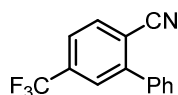
**5-(Trifluoromethyl)-[1,1'-biphenyl]-2-carbonitrile (1e)**

White solid, 0.34 g, 68% yield. $^1$H NMR (300 MHz, CDCl$^3$) δ 7.91 (d, J = 8.1Hz, 1H), 7.79 (s, 1H), 7.71 (dd, J = 8.1, 1.1 Hz, 1H), 7.57-7.52 (m, 5H); $^{13}$C NMR (75 MHz, CDCl3) δ 146.4, 136.7, 134.6 (q, J = 33.0 Hz), 134.3, 129.5, 129.0, 128.7, 127.0 (q, J = 3.7 Hz), 124.3 (q, J = 3.6 Hz), 123.0 (q, J = 273.2 Hz), 117.4, 114.7; $^{19}$F NMR (282 MHz, CDCl$_3$) δ -63.9 (s, 3F) . HRMS (EI) calculated for C$_{14}$H$_8$NF$_3$ [M$^+$H]$^+$: 247.0609, found 247.0605.

General Procedure for the synthesis of sulfonylamides **1g-j**.[7]

To a solution of secondary amines (3.0 mmol) in DCM (25 mL) was added DIPEA (6.0 mmol). Then a solution of 4-(trifluoromethyl)benzenesulfonyl chloride (3.3 mmol) in DCM (5 mL) was added slowly. The reaction mixture was stirred for 1.5 h at room temperature and then quenched with H$_2$O. The separated organic layer was washed by H$_2$O (20 mL*2) and brine (20 mL), dried over anhydrous Na$_2$SO$_4$, and then concentrated under reduced pressure. The residue was further purified by flash column chromatography to obtain the corresponding products.

Synthesis of N-protected glycine derivative **1k**.

Ethyl sarcosinate hydrochloride (3.0 mmol, 0.46 g) was slowly added to a solution of DIPEA (7.5 mmol, 0.97 g, 1.3 mL) in DCM (25 mL) at 0°C. The mixture was stirred at the same temperature for 15 min. Then a solution of 4-(trifluoromethyl)benzenesulfonyl chloride (3.3 mol, 0.81 g) in DCM (5 mL) was slowly added to the above mixture. The reaction mixture was stirred for 2 h at room temperature and then quenched with H$_2$O. The separated organic layer was washed by H$_2$O (20 mL*2) and brine (20 mL), dried over anhydrous Na$_2$SO$_4$, and then concentrated under reduced pressure. The residue was further purified by flash column chromatography (eluent PE/EtOAc = 3:1) to obtain the desired product **1k**.

For detailed information about the eluents for column chromatography, the yields and NMR spectroscopic data of **1g-k**, see Supporting Information pages S-7 – S9 of our original publication: Kang Chen, Nele Berg, Ruth Gschwind, and Burkhard König *J. Am. Chem. Soc.* **2017**, *139*, 51, 18444-18447.

### 4.6.4 General Procedure for Visible Light Induced Single C(sp³)-F Bond Cleavage of Trifluoromethylarenes

ArCF$_3$ **1** (0.1 mmol, 1.0 equiv), methacrylamide **2** (0.2 mmol, 2.0 equiv) and fac-Ir(ppy)$_3$ (0.001 mmol, 0.7 mg, 1.0 mol%) were added into a 5 mL snap vial equipped with a stirring bar. The vial was purged with N$_2$ for three times via a syringe needle. Then TMP (0.2 mmol, 28.2 mg, 34 µl, 2.0 equiv), dry DCE (1.0 ml) and HBpin (0.3 mmol, 38.4 mg, 44 µl, 3.0 equiv) were added sequentially by syringes. After degassing by freeze-pump-thaw process for three cycles, the reaction mixture was irradiated through the bottom side of the vial by blue LED at 20 °C. After the reaction was stopped, the mixture was transferred into a separating funnel and diluted by DCM (30 ml). The organic layer was washed by H$_2$O (10 ml*2) and brine (10 ml), dried over anhydrous Na$_2$SO$_4$, and then concentrated under reduced pressure. The resulting residue was purified by flash column chromatography to obtain the desired product.

Small amounts of pinacol may still contaminate products **4g-k** after the flash column. These products were dissolved in DCM (30 ml), washed again with H$_2$O (10 ml*3), dried over anhydrous Na$_2$SO$_4$ and concentrated in vacuo. This removes the pinacol impurity and analytically pure products were obtained.
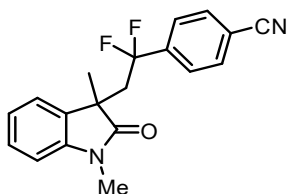


**4-(2-(1,3-Dimethyl-2-oxoindolin-3-yl)-1,1-difluoroethyl)benzonitrile (3a)**

The compound was prepared by following the general procedure for 24 h irradiation and purified by flash column chromatography (gradient eluent PE/EtOAc = 4 : 1 to 3 : 1). White solid, 24.0 mg, 74% yield. ^{1}H NMR (300 MHz, CDCl3) δ 7.53 (d, J = 8.6 Hz, 2H), 7.26 (td, J = 7.6, 1.3 Hz, 1H), 7.13 (t, J = 7.9 Hz, 3H), 6.99 (td, J = 7.5, 0.9 Hz, 1H), 6.75 (d, J = 7.8 Hz, 1H), 3.07-2.90 (m, 1H), 2.97 (s, 3H), 2.73 (ddd, J = 17.4, 15.1, 11.5 Hz, 1H), 1.34 (s, 3H); ^{13}C NMR (75 MHz, CDCl3) δ 178.6, 142.7, 140.0 (t, J = 26.8 Hz), 131.6, 131.1, 128.2, 126.0 (t, J = 6.4 Hz), 123.9, 122.4, 120.6 (t, J = 246.0, 244.8 Hz), 117.9, 113.6, 108.0, 45.2 (t, J = 27.0 Hz), 44.9 (dd, J = 4.2, 2.3 Hz), 26.3, 26.1; ^{19}F NMR (282 MHz, CDCl3) δ -90.0 (ddd, J = 250.9, 17.6, 11.5 Hz, 1F), -93.3 (dt, J = 250.9, 17.2 Hz, 1F). HRMS (ESI) calculated for C$_{19}$H$_{17}$N$_2$OF$_2$ [M+H]$^+$ : 327.1309, found 327.1307.

For detailed information about the eluents for column chromatography, the yields and NMR spectroscopic data of **3b-j** and **4b-m**, see Supporting Information pages S-10 – S21 of our original publication: Kang Chen, Nele Berg, Ruth Gschwind, and Burkhard König *J. Am. Chem. Soc.* **2017**, *139*, 51, 18444-18447.

### 4.6.5  Cyclic Voltammetry Measurements

CV measurements were performed with the three-electrode potentiostat galvanostat PGSTAT302N from Metrohm Autolab by using a glassy carbon working electrode, a platinum wire counter electrode, a silver wire as a reference electrode. The voltammograms were taken in a degassed MeCN solution ([*n*-Bu$_4$NBF$_4$] = 0.1 M, [substrate] = 1 mM, referenced by ferrocene) under Ar atmosphere. The scan rate was 0.1 V/s. Potentials vs. SCE were reported according to $E_{SCE} = E_{Fc/Fc^+} + 0.38$ V.[8]



**Index Peak position**

| Index | Peak position |
|---|---|
| 1 | $E_p$ = -1.6969 V |
| 2 | $E_p$ = 0.5891 V |
| 3 | $E_p$ = 0.6647 V |

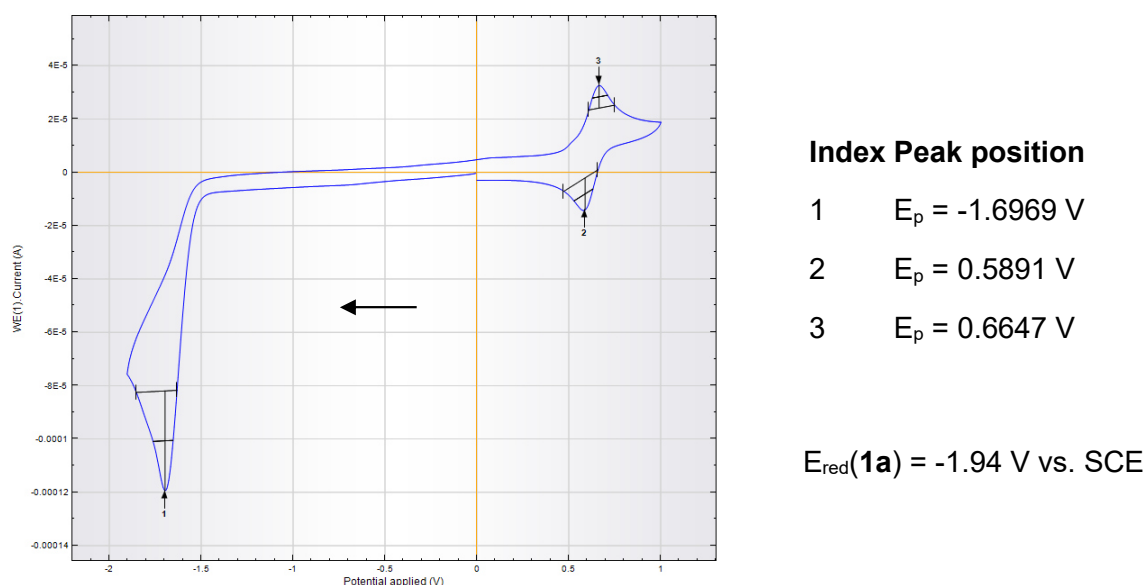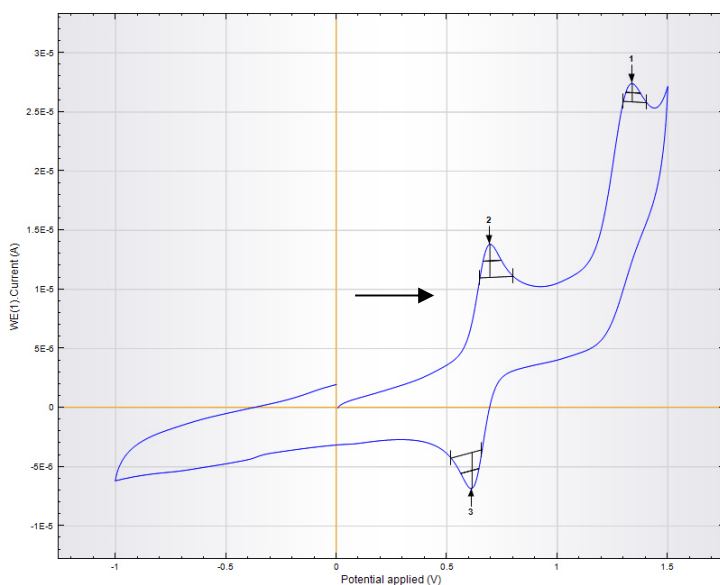$E_{red}$(**1a**) = -1.94 V vs. SCE

**Figure 4.5:** Cyclic Voltammogram of **1a** in MeCN.

For the cyclic voltammograms of **1b-m** see Supporting Information pages S-24 – S-29 of our original publication: Kang Chen, Nele Berg, Ruth Gschwind, and Burkhard König *J. Am. Chem. Soc.* **2017**, *139*, 51, 18444-18447.

**Index Peak position**

1     $E_p$ = 1.3394 V

2     $E_p$ = 0.6949 V

3     $E_p$ = 0.6143 V

$E_{ox}$(TMP) = 1.06 V vs. SCE

**Figure 4.6:** Cyclic Voltammogram of TMP in MeCN.
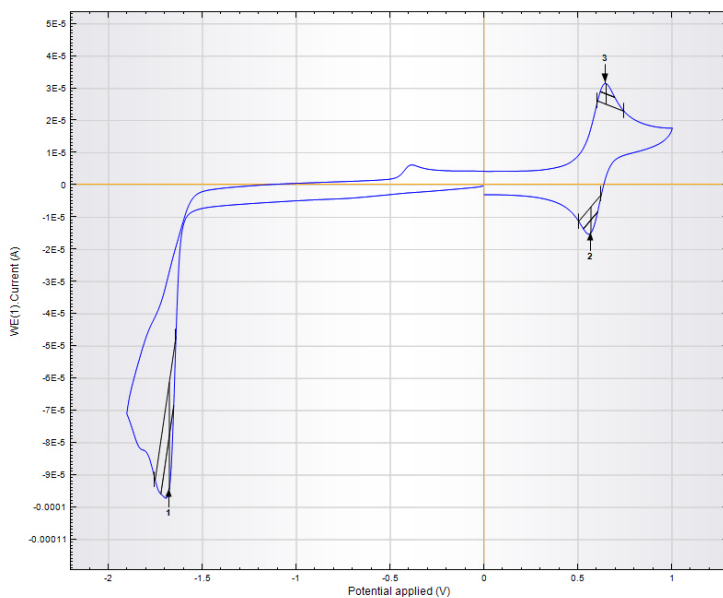


**Index Peak position**

1     $E_p$ = -1.6768 V

2     $E_p$ = 0.5690 V

3     $E_p$ = 0.6496 V

$E_{red}$(**3a**) = -1.91 V vs. SCE

**Figure 4.7:** Cyclic Voltammogram of **3a** in MeCN.

| Index | Peak position |
|-------|---------------|
| 1 | $E_p = -2.2055$ V |
| 2 | $E_p = 0.5841$ V |
| 3 | $E_p = 0.6647$ V |
| 4 | $E_p = 2.0041$ V |

$E_{ox}(\textbf{2a}) = 1.76$ V vs. SCE
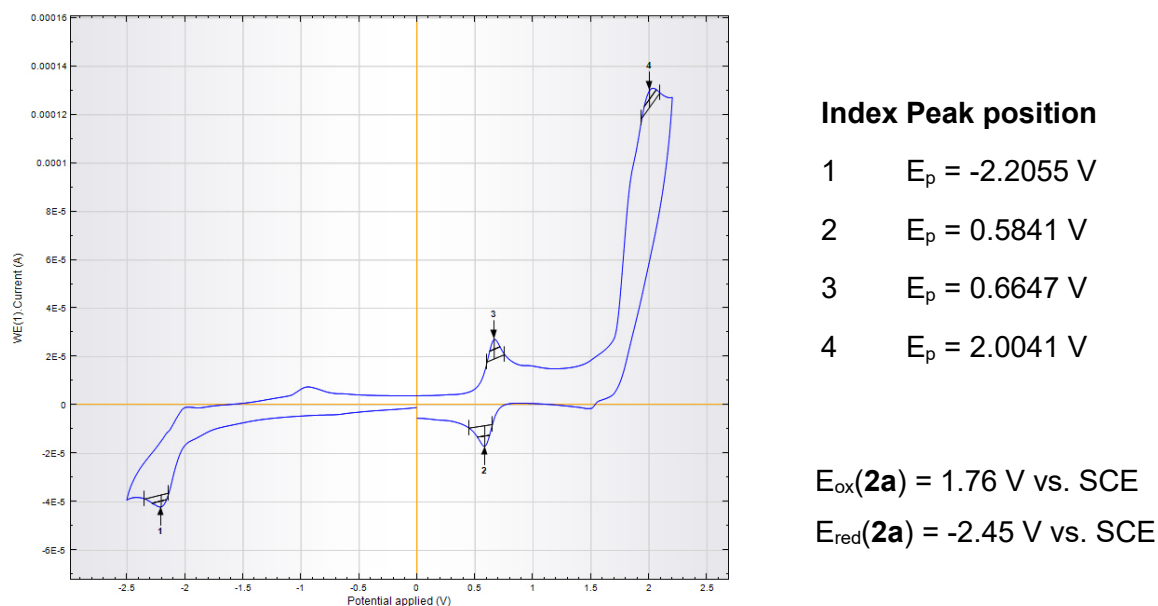
$E_{red}(\textbf{2a}) = -2.45$ V vs. SCE

**Figure 4.8:** Cyclic Voltammogram of **2a** in MeCN.

### 4.6.6  Mechanistic Studies

### 4.6.6.1 Reaction Profile

4-(Trifluoromethyl)benzonitrile **1a** (0.1 mmol, 17.1 mg 1.0 equiv), *N*-methyl-*N*-phenylmethacrylamide **2a** (0.2 mmol, 35.0 mg, 2.0 equiv) and *fac*-Ir(ppy)$_3$ (0.001 mmol, 0.7 mg, 1.0 mol%) were added into a 5 mL snap vial equipped with a stirring bar. The vial was purged with N$_2$ for three times via a syringe needle. Then TMP (0.2 mmol, 28.2 mg, 34 µL, 2.0 equiv), dry DCE (1.0 mL) and HBpin (0.3 mmol, 38.4 mg, 44 µL, 3.0 equiv) were added sequentially by syringes. After degassing by freeze-pump-thaw process for three cycles, the reaction mixture was irradiated through the bottom side of the vial by blue LED at 20 °C. Parallel Reactions were carried out for various reaction times. The conversion of **1a** and yield of **3a** were determined by $^{19}$F NMR analysis with PhOCF$_3$ as the internal standard.
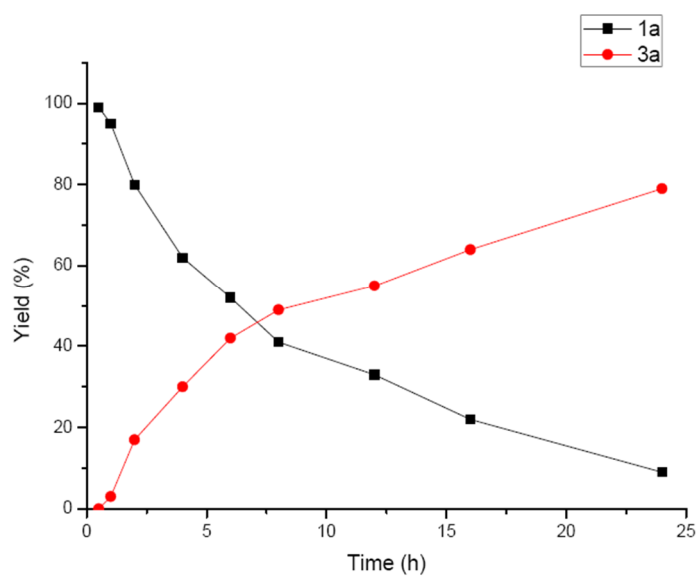
**Figure 4.9:** Reaction Profile Plot.

**Table 4.8:** Time Studies of the Visible-light Induced Single $C(sp^3)-F$ Cleavage of **1a**.

| Time (h) | Remaining **1a** | Yield of **3a** | Time (h) | Remaining **1a** | Yield of **3a** |
|----------|------------------|-----------------|----------|------------------|-----------------|
| 0.5 | 99% | 0% | 8 | 41% | 49% |
| 1 | 95% | 3% | 12 | 33% | 55% |
| 2 | 80% | 17% | 16 | 22% | 64% |
| 4 | 62% | 30% | 24 | 9% | 79% |
| 6 | 52% | 42% | --- | --- | --- |

**4.6.6.2 Radical Trapping Experiments**



**Figure 4.10:** Radical Trapping by TEMPO.

4-(Trifluoromethyl)benzonitrile **1a** (0.1 mmol, 17.1 mg 1.0 equiv), *N*-methyl-*N*-phenylmethacrylamide **2a** (0.2 mmol, 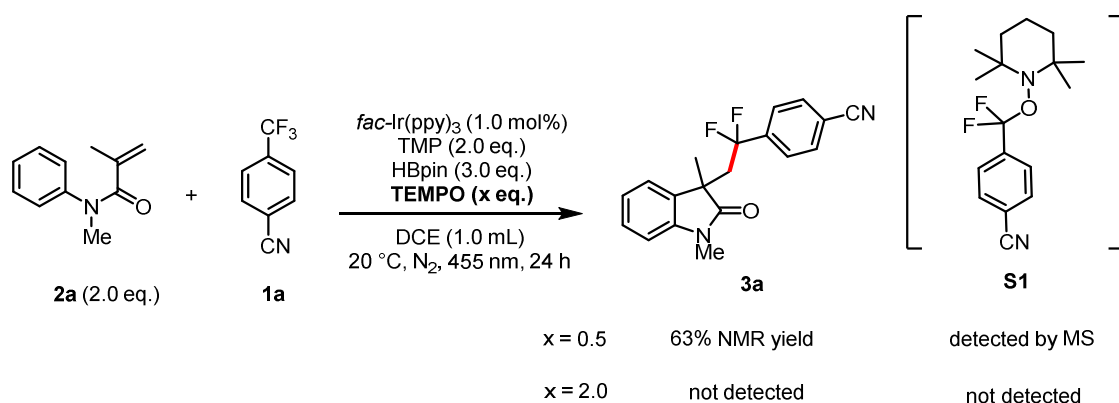35.0 mg, 2.0 equiv), TEMPO ( x equiv, x = 0.5, 7.8 mg; x = 2.0, 31.2 mg) and *fac*-Ir(ppy)$_3$ (0.001 mmol, 0.7 mg, 1.0 mol%) were added into 5 mL snap vials equipped with stirring bars. The vials were purged with N$_2$ for three times via syringe needles. Then TMP (0.2 mmol, 28.2 mg, 34 µL, 2.0 equiv), dry DCE (1.0 mL) and HBpin (0.3 mmol, 38.4 mg, 44 µL, 3.0 equiv) were added sequentially by syringes. After degassing by freeze-pump-thaw process for three cycles, the reactions were irradiated through the bottom side of the vials by blue LED at 20 °C for 24 h. Then the reactions were concentrated under reduced pressure. The crude residues were analyzed by ^{19}F NMR, GC-MS and HRMS. When deficient amount of TEMPO were added into the reaction mixture (0.5 equiv), the ^{19}F NMR yield of **3a** were reduced to 63%, and TEMPO trapped aryldifluoromethyl radical **S1** was detected by GC-MS. MS (EI) m/z: 308, HRMS (ESI) m/z [m+H]$^+$: 309.1781. When excess amount of TEMPO was added (2.0 equiv), the reaction was totally inhibited and neither product **3a** nor TEMPO-trapped radical was detected.

For the MS-EI spectra see Supporting Information page S33 of our original publication: Kang Chen, Nele Berg, Ruth Gschwind, and Burkhard König *J. Am. Chem. Soc.* **2017**, *139*, 51, 18444-18447.
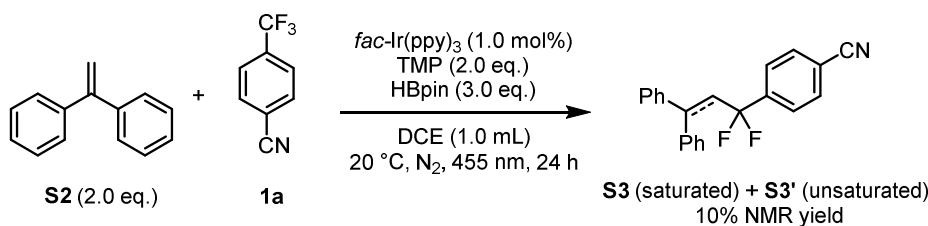
**Figure 4.11:** Radical Trapping by 1,1-Diphenylethylene.

4-(Trifluoromethyl)benzonitrile **1a** (0.1 mmol, 17.1 mg 1.0 equiv), 1,1-diphenyl-ethene **S2** (0.2 mmol, 36.0 mg, 2.0 equiv), and *fac*-Ir(ppy)$_3$ (0.001 mmol, 0.7 mg, 1.0 mol%) were added into a 5 mL snap vial equipped with a stirring bar. The vial was purged with N$_2$ for three times via a syringe needle. Then TMP (0.2 mmol, 28.2 mg, 34 µL, 2.0 equiv), dry DCE (1.0 mL) and HBpin (0.3 mmol, 38.4 mg, 44 µL, 3.0 equiv) were added sequentially by syringes. After degassing by freeze-pump-thaw process for three cycles, the reaction mixture was irradiated through the bottom side of the vial by blue LED at 20 °C for 24 h. Then the reaction mixture was concentrated under reduced pressure. The crude residue was analyzed by $^{19}$F NMR (17.1 mg of PhOCF$_3$ as internal standard) and HRMS (ESI). The conversion of **1a** was 27%. A mixture of saturated and unsaturated trapping products **S3** and **S3'** were obtained in 10% yield. $^{19}$F NMR (282 MHz, CDCl$_3$) δ -82.0 (d, J = 11.4 Hz) (unsaturated), -94.8 (t, J = 15.7 Hz) (saturated). HRMS (EI) m/z: 331.1173 (unsaturated); 333.1326 (saturated).
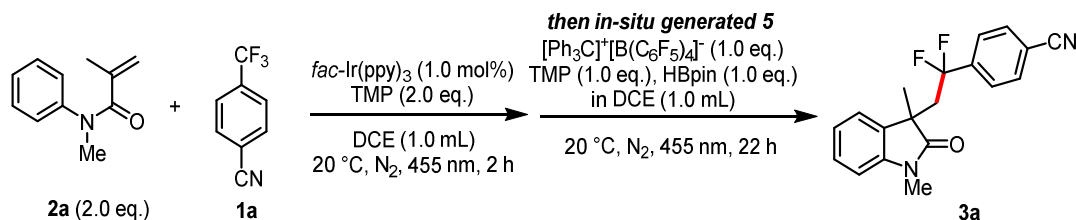
### 4.6.6.3 Control Experiments



**Figure 4.12:** *In-situ* Generated Borenium Cationic Species **5** as Fluoride Scavenger.

4-(Trifluoromethyl)benzonitrile **1a** (0.1 mmol, 17.1 mg 1.0 equiv), *N*-methyl-*N*-phenylmethacrylamide **2a** (0.2 mmol, 35.0 mg, 2.0 equiv) and *fac*-Ir(ppy)$_3$ (0.001 mmol, 0.7 mg, 1.0 mol%) were added into a 5 mL snap vial equipped with a stirring bar. The vial

was purged with N$_2$ for three times via a syringe needle. Then TMP (0.2 mmol, 28.2 mg, 34 μL, 2.0 equiv), dry DCE (1.0 mL) were added sequentially by syringes. After degassing by freeze-pump-thaw process for three cycles, the reaction mixture was irradiated through the bottom side of the vial by blue LED at 20 °C for 2 h. Then, a 1.0 mL DCE solution of [Ph$_3$C]+[B(C$_6$F$_5$)$_4$]$^-$ (0.1 mmol, 92.2 mg, 1.0 equiv), TMP (0.1 mmol, 14.1 mg, 17 μL, 1.0 equiv) and HBpin (0.1 mmol, 12.8 mg, 15 μL, 1.0 equiv) (*in-situ* generation of borenium cation species)[9] was transferred into the original reaction vial by syringe under N$_2$ atmosphere. The resulting mixture was irradiated under the same condition for 22 h. The crude mixture was analyzed by $^{19}$F NMR with PhOCF3 as the internal standard. The conversion of **1a** was 51% and the yield of **3a** was 28%.
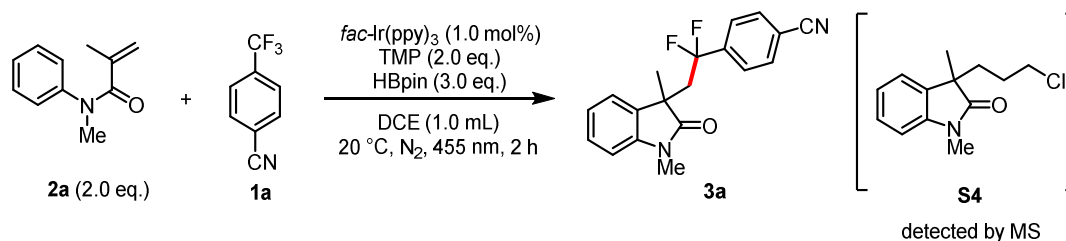


**Figure 4.13:** Plausible Proton Source at the Initial Stage of Reaction.

4-(Trifluoromethyl)benzonitrile **1a** (0.1 mmol, 17.1 mg 1.0 equiv), *N*-methyl-*N*-phenylmethacrylamide **2a** (0.2 mmol, 35.0 mg, 2.0 equiv) and *fac*-Ir(ppy)$_3$ (0.001 mmol, 0.7 mg, 1.0 mol%) were added into a 5 mL snap vial equipped with a stirring bar. The vial was purged with N$_2$ for three times via a syringe needle. Then TMP (0.2 mmol, 28.2 mg, 34 μL, 2.0 equiv), dry DCE (1.0 mL) and HBpin (0.3 mmol, 38.4 mg, 44 μL, 3.0 equiv) were added sequentially by syringes. After degassing by freeze-pump-thaw process for three cycles, the reaction mixture was irradiated through the bottom side of the vial by blue LED at 20 °C for 2 h. Then the reaction mixture was analyzed by GC-MS and HRMS. Compound **S4**, which was generated from the radical caused by SET reduction of DCE, was detected by GC-MS. MS(EI) m/z: 237. HRMS (ESI) m/z [m+H]$^+$: 238.0990.

The formation of compound **S4** can provide protons at the early phase of the reaction, which initiates the generation of the borenium cation species as fluoride scavenger. Once ArCF2• is formed, the subsequent radical trapping process releases one proton in every catalytic cycle maintaining the defluorination step.

During the optimization of reaction conditions, we also found that the desired product **3a** could be obtained in a Cl-free solvent MeCN (Table S4, Entry 3). Similarly, compound **S5**, a trapping product of the cyanomethyl radical by acrylamide **2a** was also detected by GC-

MS (m/z: 214) after 2 h reaction. We suggest **S5** is generated by the oxidized TMP radical cation abstracting a hydrogen atom from the solvent MeCN (secondary amine radical cation, calculated N−H BDE: ~ 420 kJ/mol, C−H BDE of MeCN: 406 kJ/mol).[10] The protonated TMP is formed at the same time initiating the generation of the borenium cation species. The observations suggest that the proton, instead of a chloride anion, is necessary during the initiation of the defluorination reaction.

For the MS-EI spectra see Supporting Information pages S36 – S37 of our original publication: Kang Chen, Nele Berg, Ruth Gschwind, and Burkhard König *J. Am. Chem. Soc.* **2017**, *139*, 51, 18444-18447.
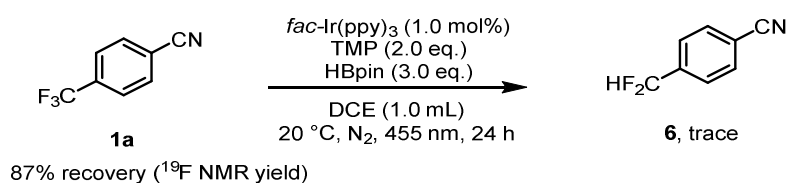


**Figure 4.14:** Reaction without Trapping Reagent **2a.**

4-(Trifluoromethyl)benzonitrile **1a** (0.1 mmol, 17.1 mg 1.0 equiv) and *fac*-Ir(ppy)₃ (0.001 mmol, 0.7 mg, 1.0 mol%) were added into a 5 mL snap vial equipped with a stirring bar. The vial was purged with $N_2$ for three times via a syringe needle. Then TMP (0.2 mmol, 28.2 mg, 34 µL, 2.0 equiv), dry DCE (1.0 mL) and HBpin (0.3 mmol, 38.4 mg, 44 µL, 3.0 equiv) were added sequentially by syringes. After degassing by a freeze-pump-thaw process for three cycles, the reaction mixture was irradiated through the bottom side of the vial by blue LED at 20 °C for 24 h. Then the reaction mixture was concentrated under reduced pressure. The crude residue was analyzed by ¹⁹F NMR (16.2 mg of $PhOCF_3$ as internal standard) and GC-MS. 87% of **1a** was recovered. Trace amount of reduced product **6** was detected by GC-MS. MS(EI) m/z: 153 and 152 (m-1).

For the MS-EI spectra see Supporting Information page S38 of our original publication: Kang Chen, Nele Berg, Ruth Gschwind, and Burkhard König *J. Am. Chem. Soc.* **2017**, *139*, 51, 18444-18447.
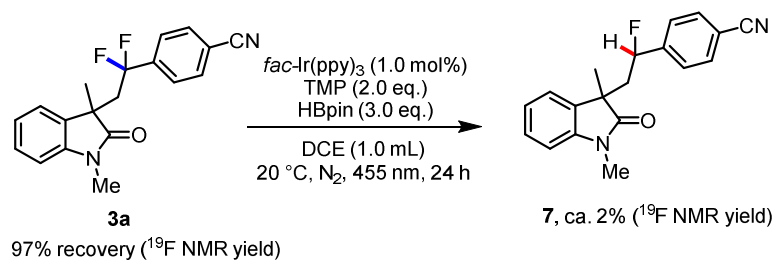
**Figure 4.15:** The Stability of Product **3a** under Standard Conditions.

Compound **3a** (0.1 mmol, 32.6 mg 1.0 equiv) and fac-Ir(ppy)$_3$ (0.001 mmol, 0.7 mg, 1.0 mol%) were added into a 5 mL snap vial equipped with a stirring bar. The vial was purged with N$_2$ for three times via a syringe needle. Then TMP (0.2 mmol, 28.2 mg, 34 µL, 2.0 equiv), dry DCE (1.0 mL) and HBpin (0.3 mmol, 38.4 mg, 44 µL, 3.0 equiv) were added sequentially by syringes. After degassing by freeze-pump-thaw process for three cycles, the reaction mixture was irradiated through the bottom side of the vial by blue LED at 20 °C for 24 h. Then the reaction mixture was concentrated under reduced pressure. The crude residue was analyzed by $^{19}$F NMR (16.8 mg of PhOCF$_3$ as internal standard) and HRMS (ESI). 97% of **3a** was recovered and ca. 2% di-defluorinated product **7** was observed. $^{19}$F NMR δ -174.7－-175.0 (m), -180.1－-180.5 (m). HRMS (ESI) m/z [m+H]+: 309.1348.

### 4.6.6.4 Discussion of Over-Defluorination Pathways and the Mono-defluorination Selectivity Control
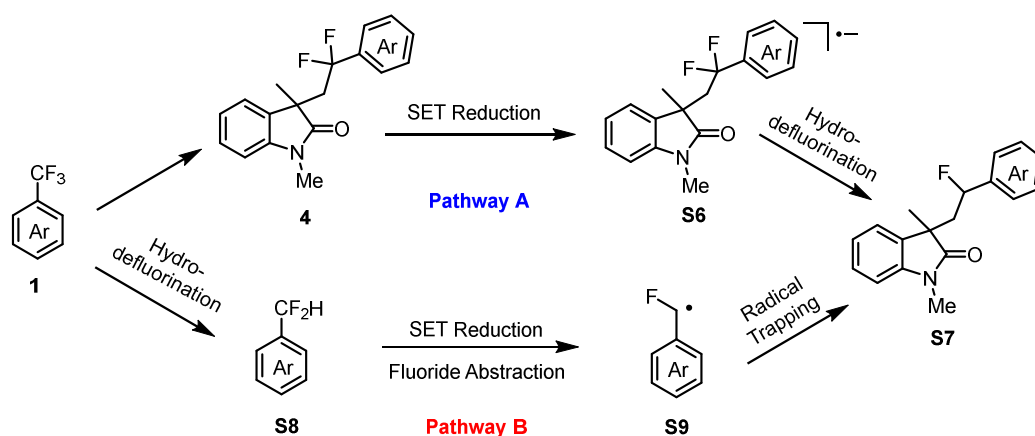


**Figure 4.16:** Possible Over-Defluorination Pathways.

In some cases of the trifluoromethylarenes scope study, considerable amounts of di-defluorination products could be observed. We propose two possible over-defluorination pathways to explain the generation of these byproducts (Figure 4.16). Pathway A describes that the product **4** of this reaction can be further reduced to its corresponding radical anion **S6** (since **4** has similar reduction potential to the starting material **1**). Then the radical anion S6 undergoes hydrodefluorination to afford the over-defluorinated byproduct **S7**. Pathway B suggests that the hydro-defluorination of trifluoromethylarenes **1** can lead to the corresponding difluoromethylarene **S8**, which can be detected in the crude mixture. **S8** is further converted into the arylmonofluoromethyl radical **S9**, which is finally trapped to give **S7**.

As shown in Figure 4.3, Eq. 2 in the main text, pathway A can be significantly inhibited, because the increased steric hindrance of the product disfavors further fluoride abstraction from **S6** by the sterically demanding borenium cation. The mono-defluorination selectivity has its origin in part in the steric control.

However, the steric control would not be successful in pathway B since **S8** is even less steric hindered than the starting material. So the extent of over-defluorination depends on the efficiency of further SET reduction of **S8**. Considering that the reduction potential of difluoromethylarene **S8** is only ca. 0.1 V more negative than the trifluoromethyl starting material ($E_{red}$ ($ArCF_3$)),[11] difluoromethylarenes derived from substrates with more positive reduction potential, such as **1e**, **1f** and **1m** ($E_{red}$ ($ArCF_3$) > -1.9 V vs. SCE) are more thermodynamically favored to undergo further reduction by Ir(II) and finally afford byproduct **S7**. On the contrary, the further reduction of difluoromethylarenes derived from substrates such as **1g** and **1h** ($E_{red}$ ($ArCF_3$) < -2.1 V vs. SCE) by Ir(II) could even be endothermic. This shows the importance of the electronic factor of the substrates for the mono-defluorination selectivity. Based on the above arguments, we propose that the synergy of steric and electronic factors control the chemo-selectivity of the single $C(sp^3)$ －F bond cleavage.

### 4.6.6.5 Emission Decay of *fac*-Ir(ppy)₃

Emission decay of *fac*-Ir(ppy)₃ solution was measured with HORIBA Jobin Yvon Fluorolog 3 spectrometer. Samples in degassed DCE were excited by a 30 mW PicoQuant LDH-P-C-375 pulsed laser instrument ($\lambda_{exc}$ = 372 nm, pulse width = 100 ps) and data of emission intensity at 510 nm were collected.
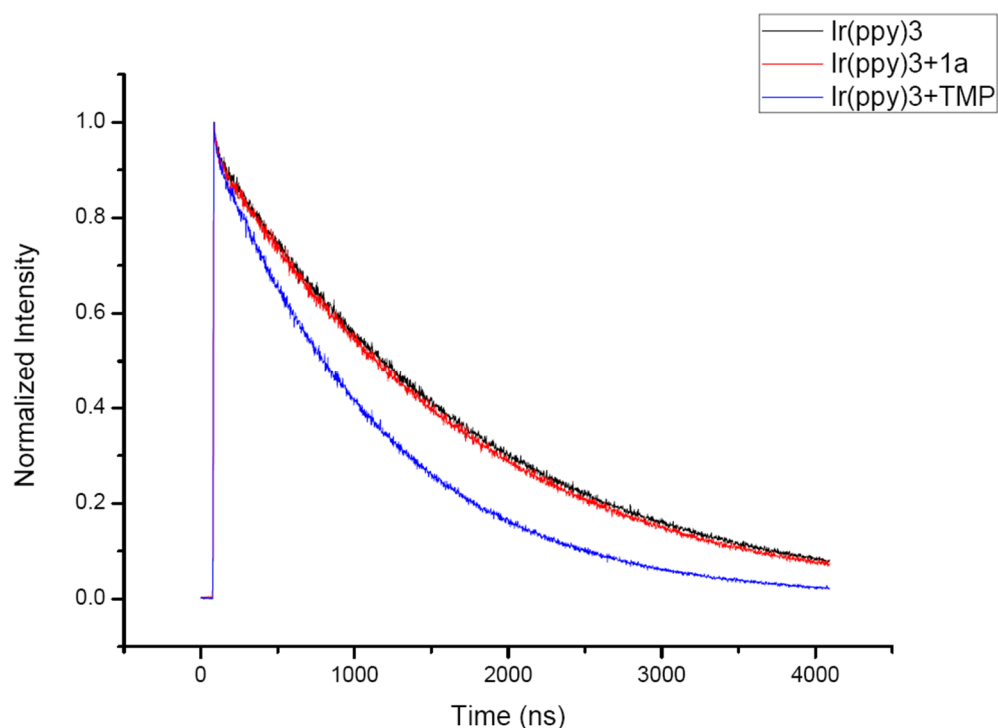
**Figure 4.17:** Time-resolved Phosphorescence Decays of *fac*-Ir(ppy)$_3$ in Deaerated DCE at 510 nm. (a) 3×10-5 M *fac*-Ir(ppy)$_3$ (black), τ = 1.7 µs; (b) 3×10-5 M *fac*-Ir(ppy)$_3$ + 0.3 M **1a** (red), τ = 1.6 µs; (c) 3×10-5 M *fac*-Ir(ppy)$_3$ + 0.3 M TMP (blue), τ = 1.0 µs.

**4.6.6.6 NMR Mechanistic Studies**

General Information:

The NMR measurements were recorded on a Bruker Avance III HD 600 MHz spectrometer with a 5 mm TBI-F probe and a Bruker Avance III 600 MHz with a Prodigy BBO-probe. The temperature was controlled by a BCU II unit (300 K).

The solvent residual peak (CD$_2$Cl$_2$ (300 K): $^1$H δ = 5.32 ppm) was used as reference. For the heteronuclei $^{11}$B and $^{19}$F the spectra were referenced according to ν(heteronucleus) = ν(CD$_2$Cl$_2$) x Ξ(reference) / 100% published by Harris *et al.*[12] ν(CD$_2$Cl$_2$) refers to the measured $^1$H resonance of CD$_2$Cl$_2$. The corresponding frequency ratios Ξ(reference) were used: Ξ ($^{11}$B) = 32.083974 (BF$_3$·Et$_2$O), Ξ ($^{19}$F) = 94.094011 (CCl$_3$F). The data were processed and plotted with Brukers Topspin 3.2.

<u>*In-situ* NMR illumination:</u>

For the illumination the LED based device described by Feldmeier *et al.* was applied.[13] The sample was prepared in 5 mm amberized NMR tubes of spintec which were used together with an insert for the optical fibre and a transistor circuit operated by the spectrometer to switch the LED automatically. The temperature (300 K) was kept constant by the BCU II unit of the spectrometer. As light source a Lumitronix Cree XT-E (royalblue) with a peak wavelength of 450 nm and 500 mW optical output was used. Starting with a $^1$H NMR spectrum of the not illuminated mixture a series of $^1$H, $^{19}$F and $^{11}$B NMR spectra were recorded with the light being switched on and off between each experiment in order to obtain the exact illumination time.
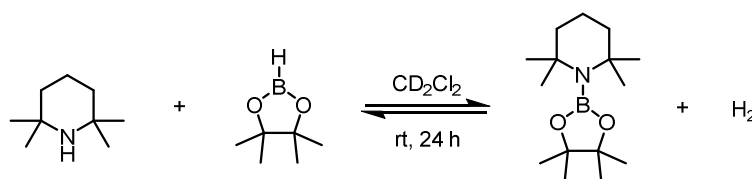


In a glove box, TMP (42.4 mg, 50 µl, 0.3 mmol) was dissolved into $CD_2Cl_2$ (1.0 ml) in an oven-dried 5 ml snap vial equipped with a stirring bar. Then HBpin (38.4 mg, 44 µl, 0.3 mmol) was added to the above solution. The mixture was stirred for 24 h and analyzed by $^{11}$B NMR (Figure 4.18).
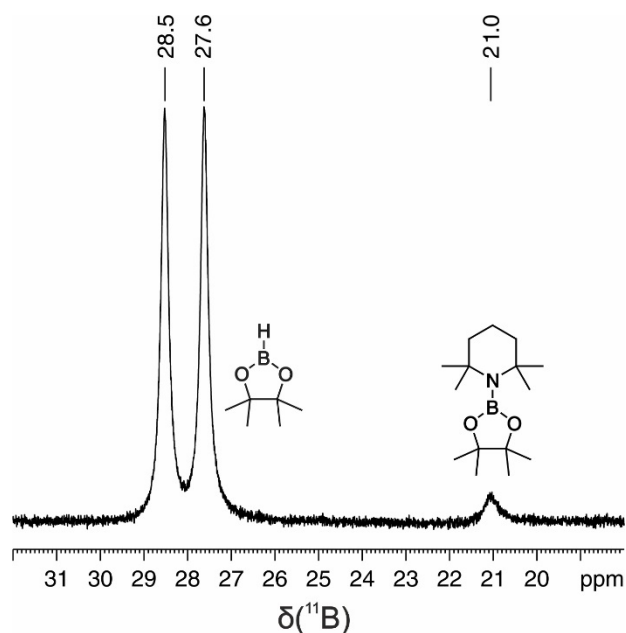


**Figure 4.18:** $^{11}$B NMR of the reaction between TMP (0.3 mmol) and HBpin (0.3 mmol) in $CD_2Cl_2$ (1.0 mL) for 24 h under Ar atmosphere.

The signal at 21.0 ppm in the $^{11}$B NMR spectrum (Figure 4.18) represents the neutral amino-borane species and appears whenever TMP and HBpin are present. The free TMP and HBpin reach an equilibrium with the amino-borane adduct. However, most of the free TMP and HBpin still remain even after a long reaction time (24 h) and only a small amount of amino-borane adduct can be detected.

Although an excess of HBpin is used in our reaction system for the C(sp$^3$) – F cleavage, free TMP can still be detected in the crude mixture after 24 h reaction (Figure 4.19).
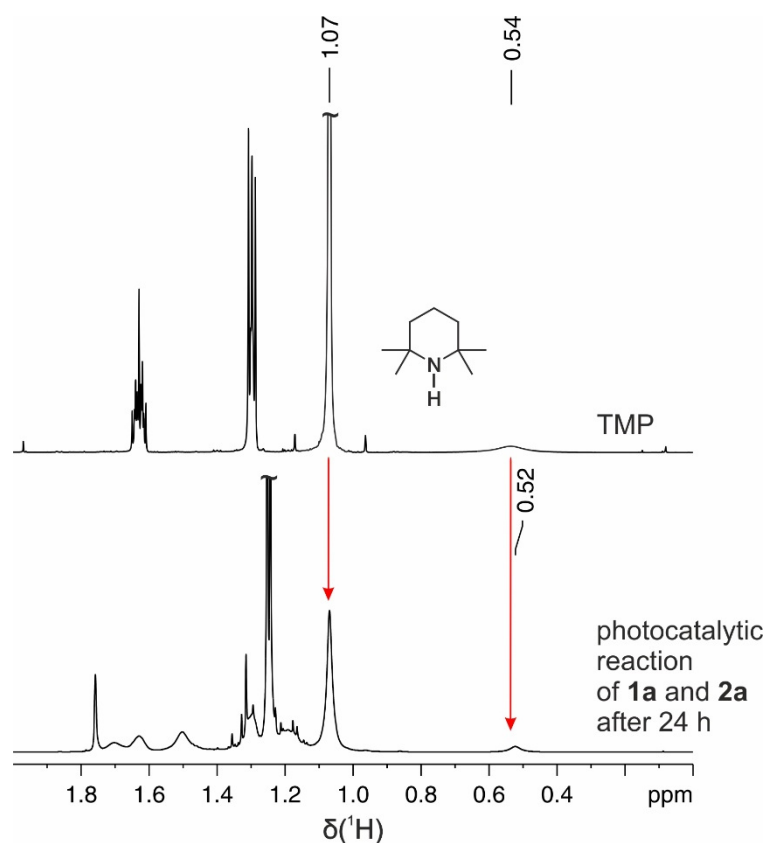


**Figure 4.19**: Detection of free TMP in the crude reaction mixture.
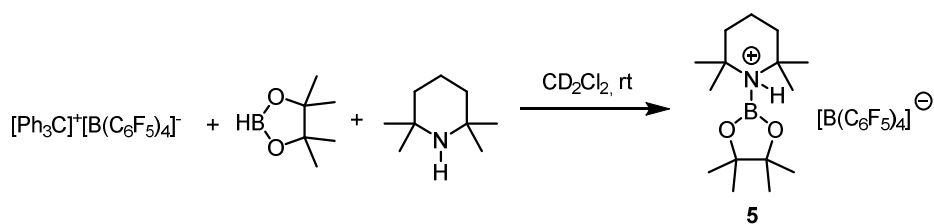


**Figure 4.20**: Preparation of the Borenium cationic species **5**.

The borenium cationic species **5** was prepared according to a literature reported procedure.[9] In a glove box, to a solution of trityltetra-(penta-fluorophenyl)borate (92.2 mg, 0.1 mmol) in $CD_2Cl_2$ (1.0 ml) was added HBpin (16 µl, 0.11 mmol) followed by TMP (14.1 mg, 17 µl, 0.1 mmol). The reaction mixture was then transferred into a dried NMR tube for analysis (Figure 4.21a). ^{11}B NMR ($CD_2Cl_2$, 192 MHz): δ (ppm) = 25.0 (TMP-Bpin+), -16.7 (B($C_6F_5$)$_4$-). In presence of 4-trifluoromethylbenzonitrile **1a** (Figure 4.21b), the [11]B chemical shift of **5** remained unchanged.
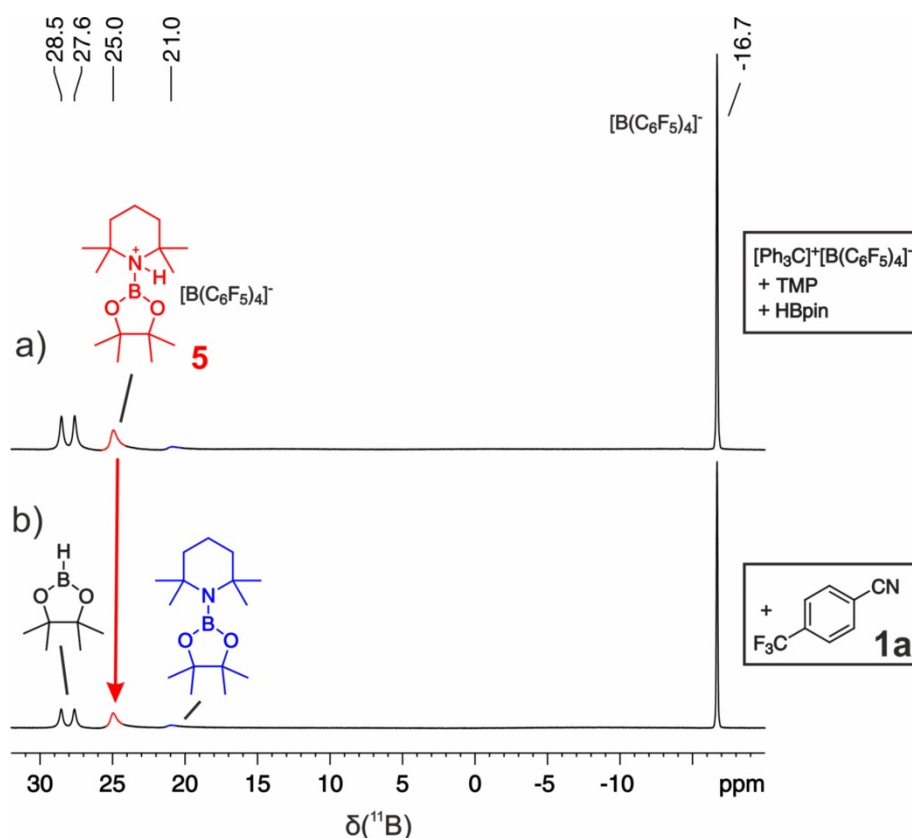


**Figure 4.21**: ^{11}B NMR chemical shift of **5** a) *in-situ* generation of **5** from a mixture of [Ph$_3$C]+[B($C_6F_5$)$_4$]- (0.1 mmol), HBpin (0.11 mmol) and TMP (0.1 mmol) in 1.0 mL of $CD_2Cl_2$; b) **1a** (0.1 mmol) was added to the above mixture.
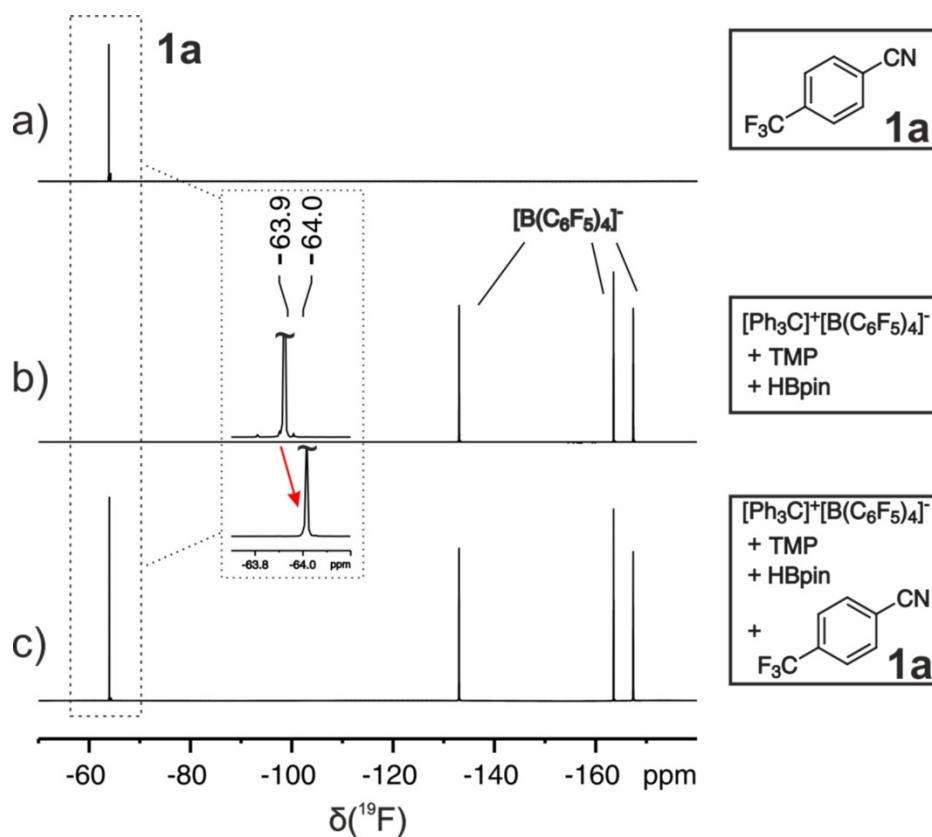
**Figure 4.22**: $^{19}F$ NMR spectra at 300 K of a) **1a**; b) *in-situ* generated **5**; c) the mixture of **5** and **1a**.

In addition, the $^{19}F$ chemical shift of 4-trifluoromethylbenzonitrile **1a** was only slightly shifted to high field by 0.1 ppm after **1a** and **5** were mixed together, while the anion $[B(C_6F_5)_4]^-$ remained unchanged (Figure 4.22).

While there was no chemical shift change in the $^{11}B$ spectrum, the proton signal of the N-H bond in **5** was low field shifted in the $^1H$ spectrum from 4.86 ppm (Figure 4.23a) to 5.36 ppm (Figure 4.23b) indicating the existence of a hydrogen bond interaction between **5** and **1a**.

$^1H$-$^1H$ NOESY and $^1H$-$^{19}F$ HOESY spectra of the reaction mixture containing **5** and **1a** are shown in Figure 4.24-24.6. Inside the borenium cation, NOEs were observed between the N-H proton (5.36 ppm) and the methyl groups (1.50 ppm) as well as the neighboring $CH_2$ groups (1.74 ppm; Figure 4.24).
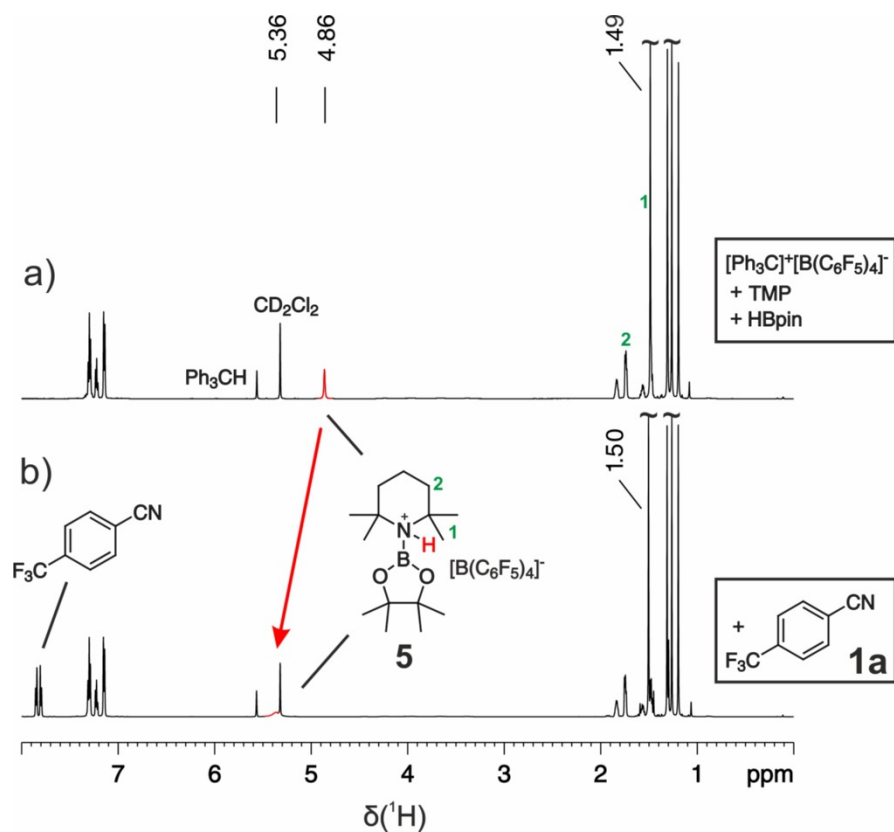
**Figure 4.23:** ^{1}H NMR spectra of a) *in-situ* generated **5**; b) the mixture of **5** and **1a**.
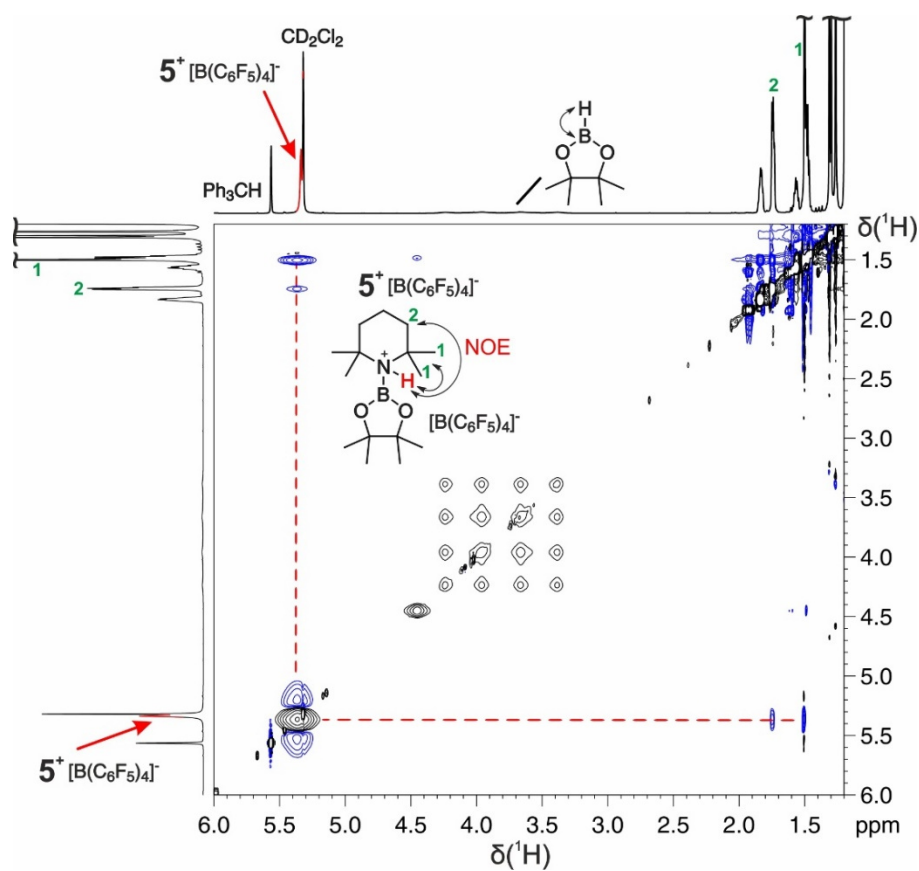


**Figure 4.24:** [1]H-^{1}H NOESY spectrum of the mixture of **5** and **1a** (NOEs inside the borenium cation).

$^1$H-$^1$H NOESY and $^1$H-$^{19}$F HOESY spectroscopy indicated that there was no intermolecular interaction between the N−H bond in **5** and the trifluoromethyl group in **1a** (Figure 4.25, S26; no signal inside the dashed circle). However, an NOE between the methyl groups of **5** and the aromatic protons next to the nitrile group corroborated a preferred interaction between these functionalities due to the better hydrogen bond acceptor property of the nitrile group (Figure 4.25; green dashed line).[14] These observations contradict the direct C(sp$^3$)−F activation in the non-charged **1a** molecule by borenium cationic species **5**.
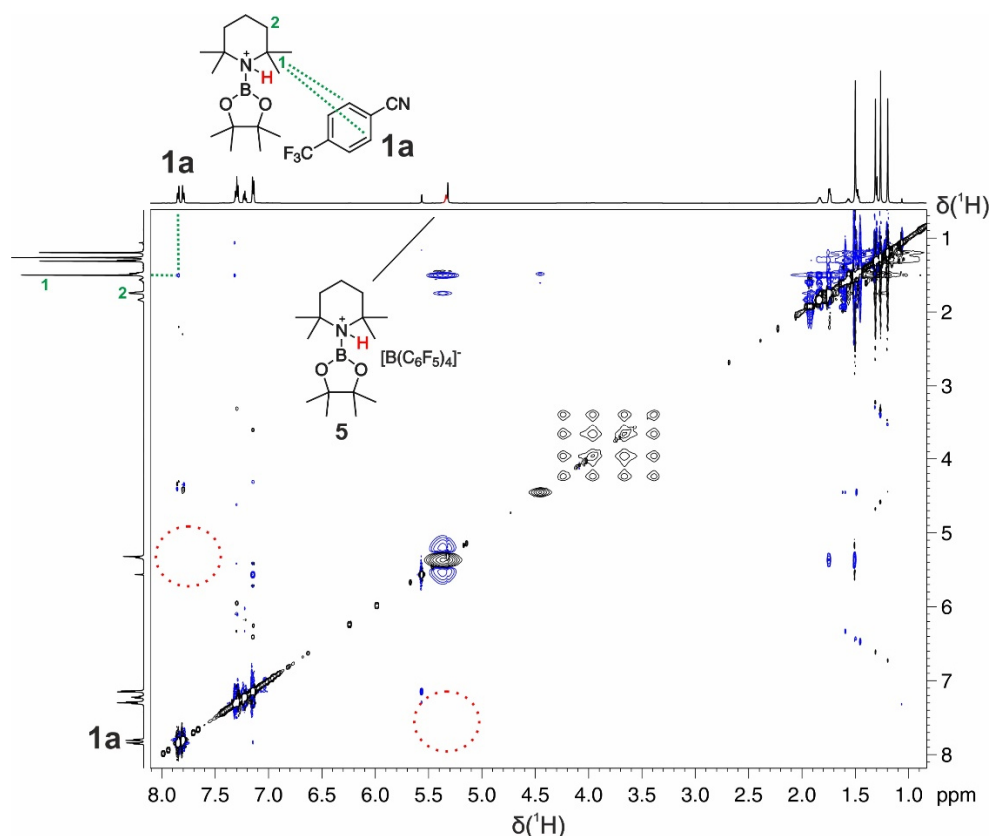


**Figure 4.25**: $^1$H-$^1$H NOESY spectrum of the mixture of **5** and **1a**.
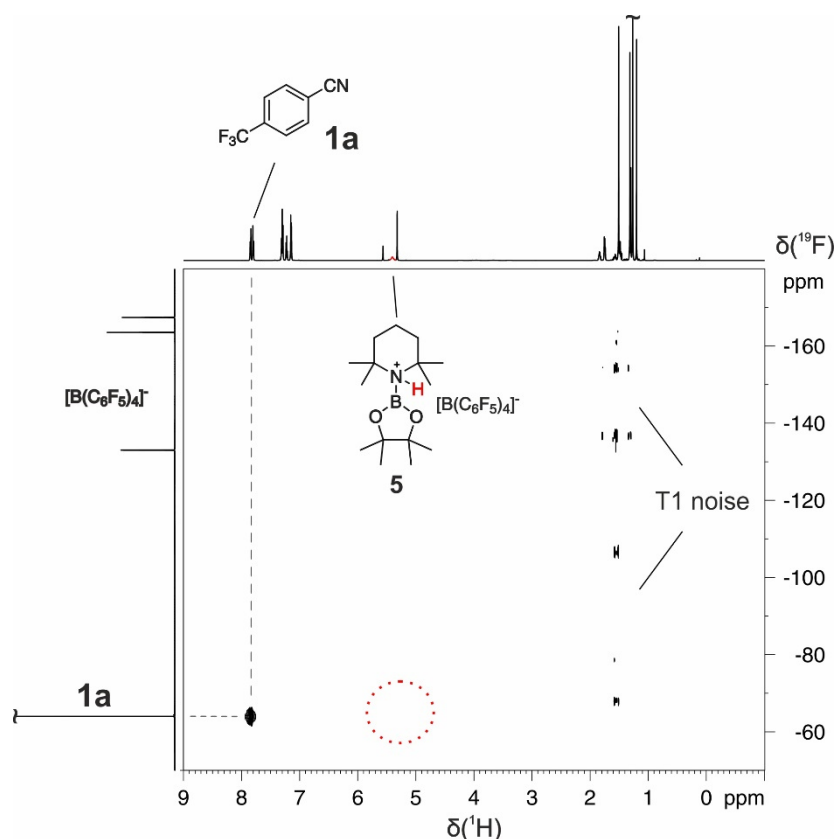
**Figure 4.26**: $^1$H-$^{19}$F HOESY spectrum of the mixture of **5** and **1a**.

### 4.6.6.7 Discussion

In the actual system we can observe a hydrogen bond interaction between the –CN group of the substrate as a hydrogen bond acceptor towards the borenium cation (Figure 4.23-4.26). Notably, more components are involved in our reaction mixture than in the sample used for NMR study. The excess amount of acrylamide and TMP would interrupt the hydrogen bonding interaction between **1a** and borenium cation since amides and amines are better hydrogen bond acceptors than the cyano group.[14] Additionally, the hydrogen bond acceptor (-CN group) in **1a** (4-CF$_3$benzonitrile) and **1b** (2-CF$_3$-benzonitrile) are at different positions to the -CF$_3$ group, so the corresponding distances from the fluoride scavenger borenium cation to the reaction site -CF$_3$ group are also different. However, the reactivity of **1a** and **1b** are quite similar (74% in 24 h reaction vs. 72% in 24 h reaction) (Table 1 and 2). Based on the above two points, it seems that the hydrogen bonding between the non-charged substrate and the borenium cation does not contribute significantly to the reactivity.

However, it is important to notice that in our reaction system the substrates are reduced to their corresponding radical anions, which have drastically different properties compared to the non-charged substrate. Given the detection of the –CN group to borenium cation interaction discussed above, an interaction between the borenium cation and the radical anion species is more probable due to the higher hydrogen bond acceptor property of the radical anion and may have influence on the defluorination process.
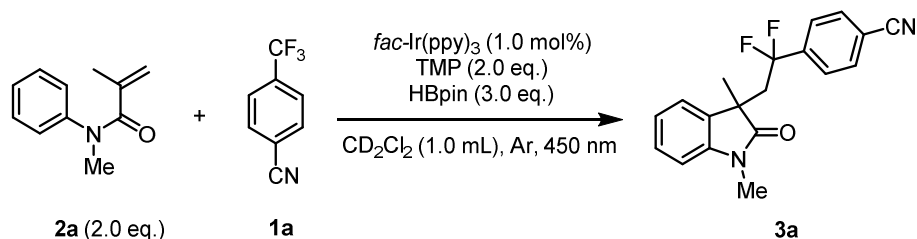


**Figure 4.27:** *In-situ* NMR illumination of the single C(sp$^3$)—F Bond cleavage reaction of 4-trifluoromethylbenzonitrile **1a**.

4-(Trifluoromethyl)benzonitrile **1a** (17.1 mg, 0.1 mmol), *N*-methyl-*N*-phenylmethacrylamide **2a** (35.0 mg, 0.2 mmol) and *fac*-Ir(ppy)$_3$ (0.7 mg, 0.001 mmol) were added into a 5 mL dried Schlenk tube. Then the tube was transferred into a glove box and TMP (28.2 mg, 0.2 mmol, 34 µl), dry CH$_2$Cl$_2$ (1.0 ml) and HBpin (38.4 mg, 0.3 mmol, 44 µL) were further added sequentially. About 0.5 ml of the solution was transferred into a dried 5 mm amberized NMR tube. Under Ar atmosphere, an optical fibre was inserted inside the NMR tube containing the reaction mixture. The sample was irradiated inside the NMR spectrometer and spectra were collected (Figure 4.27).

At early stage of the reaction, Cl$^-$ is expected to be the counter ion of **5'**, which is generated due to the SET reduction of Cl-containing solvent (DCE or CD$_2$Cl$_2$). When higher conversion of starting material is achieved, we observe the formation of BF$_4^-$, which can also act as the counter ion. Given these possibilities, the counter ion is omitted for the sake of clarity.
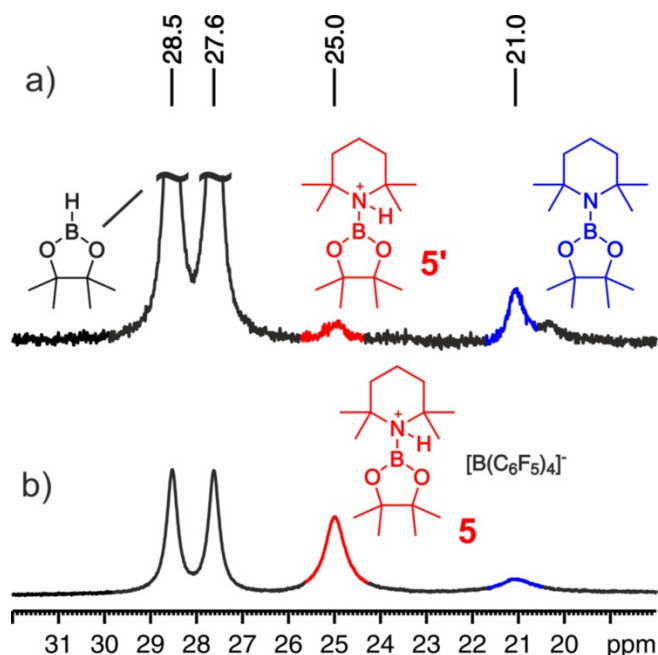
**Figure 4.28:** $^{11}$B NMR studies of the reaction intermediate: a) *in-situ* illumination of the single C(sp$^3$) $-$F cleavage reaction of **1a** (450 nm, 22 h) in CD$_2$Cl$_2$ (0.1 M) inside the NMR spectrometer; b) generation of borenium cationic species **5** in a mixture containing [Ph$_3$C]$^+$[B(C$_6$F$_5$)$_4$]$^-$ (0.1 M), HBpin (0.11 M) and TMP (0.1 M) in CD$_2$Cl$_2$.

### 4.6.7  References

[1]      a) Sprouse, S., King, K. A., Spellane, P. J., Watts, R. J. *J. Am. Chem. Soc.* **1984**, *106,* 6647–6653. b) Sun, J., Wu, W., Zhao, J. *Chem. Eur. J.* **2012**, *18*, 8100–8112.

[2]      Bradley, D., Williams, G., Lawton, M. *J. Org. Chem.* **2010**, *75,* 8351–8354.

[3]      Gottlieb, H. E., Kotlyar, V., Nudelman, A. *J. Org. Chem.* **1997**, *62,* 7512–7515.

[4]      a) Pinto, A., Jia, Y., Neuville, L., Zhu, J. *Chem. Eur. J.* **2007**, *13*, 961–967;.b) Mu, X., Wu, T., Wang, H.-Y., Guo, Y.-L., Liu, G.-S. *J. Am. Chem. Soc.* **2012**, *134,* 878–881. c) Zheng, L., Huang, H., Yang, C., Xia, W. *Org. Lett.* **2015**, *17,* 1034–1037.

[5]      Pajouhesh, H., Holland, R., Zhou, Y., Zhu, Y., Grimwood, M. E., Chahal, N. WO 2012061926.

[6]      Ann, J., Jung, A., Kim, M.-Y., Kim, H.-M., Ryu, H., Kim, S., Kang, D. W., Hong, S., Cui, M., Choi, S., Blumberg, P. M., Frank-Foltyn, R., Bahrenberg, G., Stockhausen, H., Christoph, T., Lee. J. *Bioorg. Med. Chem.* **2015**, *23,* 6844–6854.

[7]      Beswick, P. J., Campbell, A., Cridland, A. P., Gleave, R. J., Heer, J. P., Nicholson, N. H., Page, L. W., Vile, S. WO 2010007072.

[8]      Pavlishchuk, V. V., Addison, A. W. *Inorg. Chim. Acta.* **2000**, *298,* 97–102.

[9]     Eisenberger, P., Bailey, A. M., Crudden, C. M. *J. Am. Chem. Soc.* **2012**, *134*, 17384−17387.

[10]    Šakić, D., Zipse, H. *Adv. Synth. Catal.* **2016**, *358,* 3983–3991.

[11]    Andrieux, C. P., Combellas, C., Kanoufi, F., Savéant, J.-M., Thiébault, A. *J. Am. Chem. Soc.* **1997**, *119,* 9527–9540.

[12]    Harris, R. K., Becker, E. D., Cabral de Menezes, S. M., Goodfellow, R., Granger, P. *Pure Appl. Chem.* **2001**, *73*, 1795–1818.

[13]    Feldmeier, C., Bartling, H., Riedle, E., Gschwind, R. M. *J. Magn. Reson.* **2013**, *232*, 39–44.

[14]    Hunter, C. A. *Angew. Chem. Int. Ed.* **2004**, *43*, 5310–5324.

## 4.7   Additional Findings

### 4.7.1   General Information

The NMR measurements were recorded on a Bruker Avance III HD 600 (600.13 MHz) spectrometer with a 5 mm TBI-F probe head with a z-gradient (53.5 Gauss/cm). The temperature was controlled either by a BCU II (300 K) or a BVTE 3900 (180 K).

The compounds used were obtained as described in chapter 4.6.1 "General Information". Dichloromethane-$d_2$ ($CD_2Cl_2$) was purchased from Sigma Aldrich/Merck or Deutero and freshly dried over $CaH_2$ under Argon atmosphere prior to use.

The solvent residual peak ($CD_2Cl_2$ (300 K): $^1H$ δ = 5.32 ppm) was used as chemical shift reference for the NMR spectra. For the heteronuclei $^{11}B$ and $^{19}F$ the spectra were referenced according to ν(heteronucleus) = ν($CD_2Cl_2$) x Ξreference / 100% published by Harris *et al.*[1] ν($CD_2Cl_2$) refers to the measured $^1H$ resonance of $CD_2Cl_2$. The corresponding frequency ratios Ξreference were used: Ξ ($^{11}B$) = 32.083974 (BF$_3$·Et$_2$O), Ξ ($^{19}F$) = 94.094011 (CCl$_3$F). The data were processed and plotted with Brukers Topspin 3.2.

<u>*In-situ* NMR illumination:</u>

The *in-situ* illumination was performed just as described in chapter 4.6.6.6 "NMR Mechanistic Studies". The sample was prepared according to the description in chapter 4.6.6.7 "Discussion" (see also Figure 4.27). The reaction was followed by $^1H$, $^{11}B$ and $^{19}F$ NMR.

The amounts (%) were obtained by $^1H$ integration of the corresponding signals. As no conversion was observed in the dark, the signal integral of the starting material was set to 100%.

<u>*Ex-situ* illumination:</u>

The *ex-situ* photocatalytic reactions were carried out by using a 455 nm LED (Osram Oson SSL80, 500 mW), which was connected to a JULABO cyclic water-cooling system.

ArCF$_3$ **1** (0.1 mmol, 1.0 equiv), methacrylamide **2** (0.2 mmol, 2.0 equiv) and fac-Ir(ppy)$_3$ (0.001 mmol, 0.7 mg, 1.0 mol%) were added into a 5 mL snap vial equipped with a stirring bar. The vial was purged with N$_2$ for three times via a syringe needle. Then TMP (0.2 mmol, 28.2 mg, 34 µl, 2.0 equiv), dry $CD_2Cl_2$ (1.0 ml) and HBpin (0.3 mmol, 38.4 mg, 44 µl, 3.0 equiv) were added sequentially by syringes. After degassing by freeze-pump-

thaw process for three cycles, the reaction mixture was irradiated through the bottom side of the vial by blue LED at 20 °C.

For the assignment of the involved compounds, NMR spectra of the mixture were measured after 21.5 hours (chapter 4.7.2). For following the progression of the photocatalytic reaction, NMR samples were taken before starting the illumination (0 hours) and after 0.5, 2, 4, 6. 12, 16, and 24 hours (chapter 4.7.4).

The amounts (%) were obtained by $^1H$ integration of the corresponding signals. As no conversion was observed in the dark, the signal integral of the starting material was set to 100%.

## 4.7.2  Assignment of the Species in the Reaction Mixture

The composition of the photocatalytic reaction mixture was elucidated in detail in order to obtain information about intermediates and/or by-products generated via different reaction pathways and downstream transformations. First, the photocatalytic single C-F bond cleavage was performed *ex-situ* with blue light and $^1H$, $^{19}F$ and $^{11}B$ NMR spectra were recorded after 24 hours of irradiation. Trifluoromethylbenzonitrile (1 equiv.) and *N*-methyl-*N*-phenylmethacrylamide (2 equiv.) were converted to 4-(2-(1,3-dimethyl-2-oxoindolin-3-yl)-1,1-difluoroethyl)benzonitrile in presence of TMP (2 equiv.), HBpin (3 equiv.) and *fac*-Ir(ppy)$_3$. The mixtures were prepared according to the procedure described in "General Information" (chapter 4.7.1). After 24 hours, ~50% of product were furnished and besides the photocatalyst all compounds used were assigned in the $^1H$ NMR spectrum (see Figure 4.29). The production of H$_2$ was detected as well (4.60 ppm).

As already shown in chapter 4.6.6.6, free TMP is still present after hours of reaction. Additionally, comparing the proton chemical shifts of pure TMP and pure HBpin with a mixture of both, the ppm-values for TMP remained unchanged and no additional signals appeared although 27% of amino-borane (TMP-Bpin) containing TMP were generated (Figure 4.30). In contrast, a second singlet for the borane methyl groups was formed, which was slightly shifted to low field. The formation of TMP-Bpin could also be identified in the $^{11}B$ spectrum (21.0 ppm in comparison to 28.1 ppm for pure HBpin; see Figure 4.18 in chapter 4.6.6.6) and thus, the significant influence on the $^{11}B$ environment was confirmed. The borenium cationic species **5'** produced during the photocatalysis could not be assigned via $^1H$ NMR.
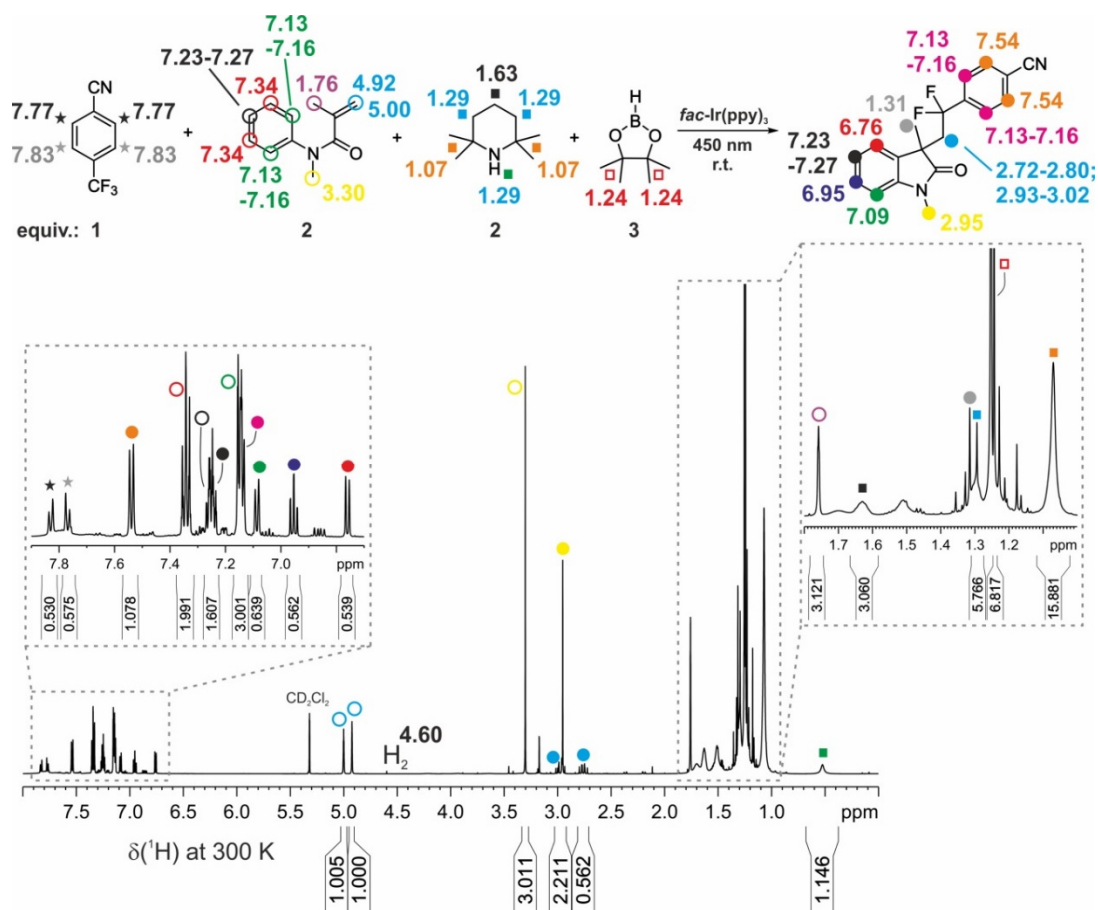
**Figure 4.29:** ^{1}H NMR spectrum of the *ex-situ* illuminated (blue light) photocatalytic reaction in dry CD$_2$Cl$_2$ at 300 K. ~50% of product were obtained after 24 hours. The starting materials as well as the Lewis acid/base additives, the product and H$_2$ as by-product were assigned.

To get deeper insight into the formation of the fluorine- and boron-containing species, ^{19}F and ^{11}B NMR spectra were measured for the same *ex-situ* reaction mixture after 24 hours in CD$_2$Cl$_2$. In Figure 4.31, the ^{19}F spectrum is depicted including the corresponding identified molecular structures. The product signals (marked in turquoise; -90.3, -91.7 ppm) were assigned according to the ^{19}F NMR chemical shifts already presented in chapter 4.6.4 and the non-converted starting material (marked in green; -60.9 ppm) according to literature (-63.7 ppm in CDCl$_3$).[2] For the red marked doublet with a chemical shift of -113.4 ppm 4-difluoromethyl-benzonitrile (CNPhCF$_2$H) was proposed, which was already identified as by-product by mass spectrometry in chapter 4.6.2. A similar ^{19}F peak of this species (-113.2 ppm) in CDCl$_3$ can be found in literature.[3]
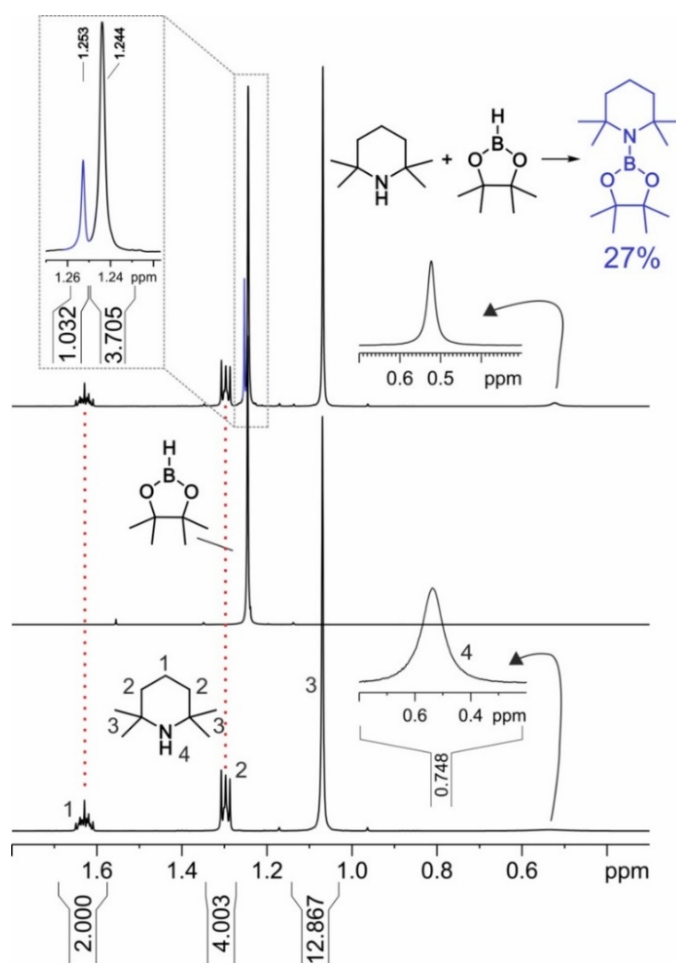
**Figure 4.30:** Comparison of the $^1$H NMR spectra of TMP (bottom), HBpin and a mixture of TMP and HBpin (top), which leads to the formation of the neutral amino-borane (TMP-Bpin). The spectra were recorded in dry CD$_2$Cl$_2$ at 300 K.

Moreover, regarding the high field chemical shifts of the orange and blue marked signals, we assume the existence of both BF$_3$ and BF$_4^-$ compounds. For the generation of trifluoroborane the conversion of F-Bpin, which was already stated as by-product of the photocatalysis (Figure 4.4), to pinacol and BF$_3$ in presence of fluorine anions derived by the C-F bond cleavage is supposed. In literature, a chemical shift of -158.2 ppm is known for piperidine·BF$_3$ in CDCl$_3$.[4] Thus, TMP·BF$_3$ would be feasible, as the additional *ortho*-positioned methyl groups are sterically demanding and are therefore supposed to lead to a deshielding of the BF$_3$ group resulting in a signal position at higher field (-134.9 ppm; Figure 4.31). Further conversion to BF$_4^-$ is proposed to result in an ion pair with **5′** as counterion. The initially suggested TMP$^+$BF$_4^-$, which was separately measured at 300 K ($\delta(^{19}$F$) = $-146.0 ppm; Figure 4.32a) and 180 K ($\delta(^{19}$F$) = $-145.1 ppm; Figure 4.32b), was excluded via a 2D test experiment. As demonstrated in Figure 4.32, the species showed distinctive NOE patterns between the fluorine atoms of BF$_4^-$ and the $^+$NH$_2$ protons and the

methyl groups of TMP⁺ at both temperatures. This was not observed in the $^{1}H,^{19}F$ HOESY spectrum of our reaction mixture (*vide infra*; blue signal in Figure 4.33). In general, two separated N-H proton signals exist in the 2D spectrum at low temperature (5.91 ppm; 6.34 ppm), whereas only one shows NOE contact to BF₄⁻ (Figure 4.32b).

In addition, according to literature, F-Bpin was suggested for the broad signal at - 151.7 ppm.[5] Due to NOE contact to TMP an aggregate of F-Bpin and TMP is assumed (Figure 4.33).
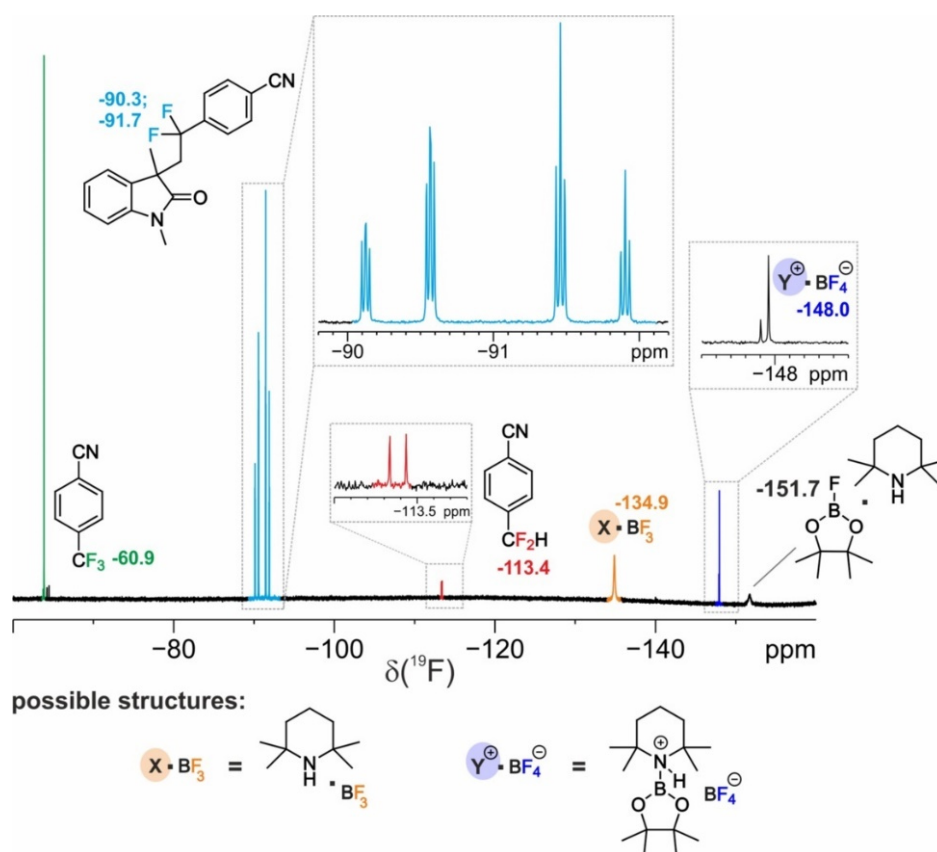


**Figure 4.31**: $^{19}F$ spectrum of the *ex-situ* illuminated photocatalytic single C-F bond cleavage in trifluoromethylbenzonitrile in CD₂Cl₂ at 300 K after 24 hours including the assignment of starting material (green), product (turquoise) and by-products.
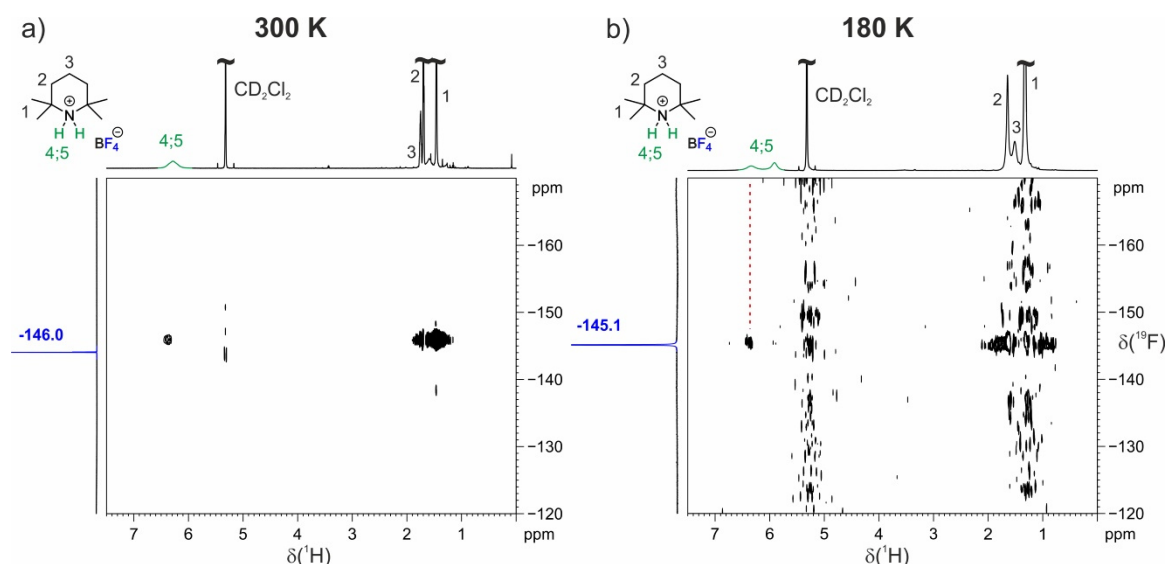
**Figure 4.32**: $^1H,^{19}F$ HOESY spectra of TMP$^+$BF$_4^-$ in CD$_2$Cl$_2$ at a) 300 K and b) 180 K.

The $^1H,^{19}F$ HOESY spectrum of the corresponding reaction mixture after 24 hours is depicted in Figure 4.33. The highlighted $^1H$ region between 7.7 – 7.9 ppm demonstrates the presence of a broad signal overlapping with the CF$_3$-benzonitrile aromatic protons. The broad shape and the 2D cross signal to the N-H proton of the free TMP (green) suggest an exchange between both species and thus a structure incorporating exchangeable protons, such as TMP$^+$X$^-$, is proposed. Its chemical shift is drastically low field shifted in comparison to TMP$^+$BF$_4^-$ (cf. Figure 4.32), which indicates a high hydrogen bond donor ability. As already demonstrated, BF$_4^-$ was excluded as counterion. X$^-$ could not be identified.

Notably, 2D cross signals were detected between free TMP and the postulated BF$_3$ (orange) and F-Bpin (black) species as well as between TMP$^+$ and the same fluorine species. As the TMP/fluorine NOEs are more intense, we assume the cross signals of TMP$^+$/fluorine to be derived via transferred TMP/TMP$^+$ exchange.

On the other hand, no NOE is visible for BF$_4^-$, which would reveal a potential counterion. At this point, we suggest a complex consisting of BF$_4^-$ and **5´**, whose generation was detected by $^{11}B$ NMR (see following section).
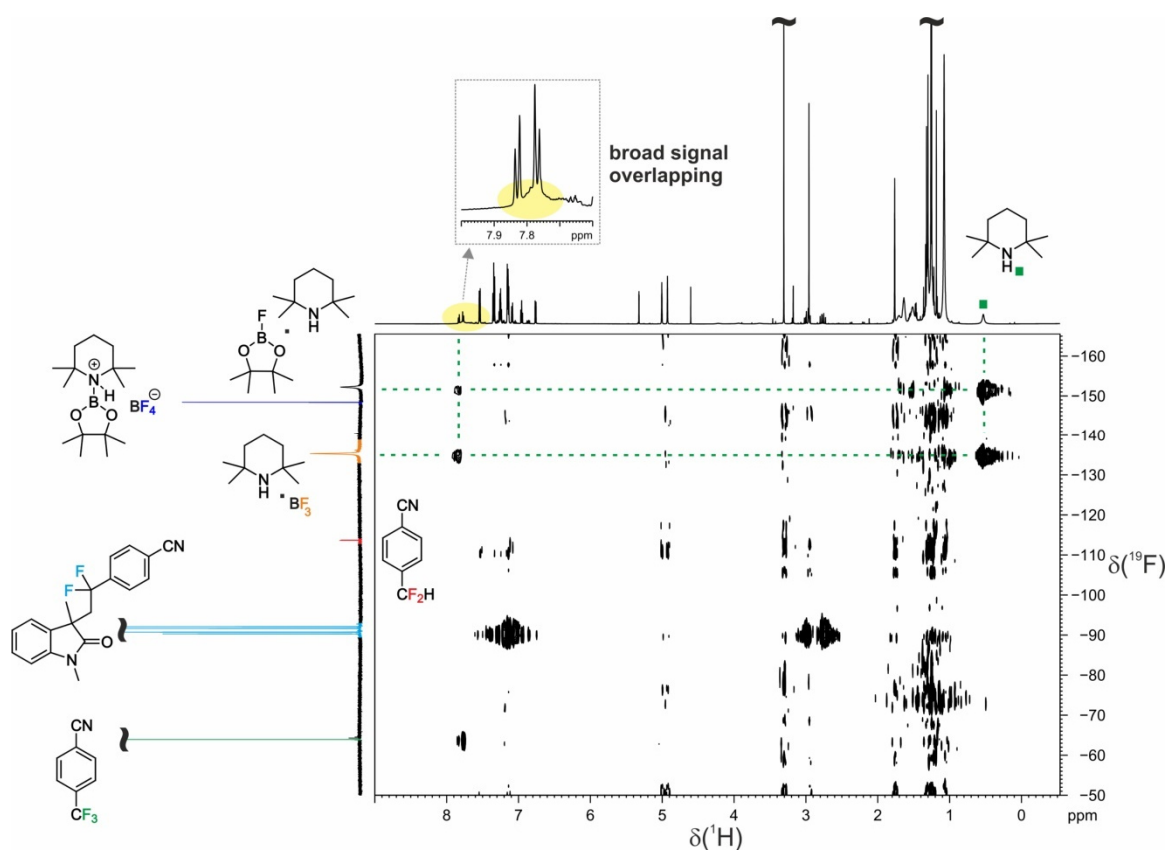
**Figure 4.33:** $^1$H,$^{19}$F HOESY spectrum of the photocatalytic reaction mixture after 24 hours in CD$_2$Cl$_2$ at 300 K.

The *ex-situ* batch reaction after 24 h was further analyzed by $^{11}$B NMR. In Figure 4.34, the $^{11}$B spectrum is depicted including the assigned species. HBpin, the borenium cationic species **5'** and the neutral amino-borane TMP-Bpin, which is formed spontaneously without light, were already identified in chapter 4.6.6.6 (Figure 4.18). As described in the same chapter, the $^{11}$B chemical shifts of **5'** and separately synthesized **5** were not affected despite their different counter ions. Therefore, we assume that a BF$_4^-$ counterion would result in an equal ppm-value of **5'** as well.

For the signal at 23.7 ppm, we suggest HO-Bpin as an oxidation product of the air and moisture sensitive HBpin.[6][7] Its formation could be the result of introducing traces of O$_2$ during the transfer of the reaction mixture into the NMR tube. Moreover, the F-Bpin signal seems to be overlapped with TMP-Bpin (19.0-22.0 ppm). From literature, $^{11}$B chemical shifts of ~20.0 ppm (in CD$_2$Cl$_2$) and 23.0 ppm (in CDCl$_3$) are known.[5][6] Additionally, the boron chemical shift is influenced by the attachment of TMP to F-Bpin, which was identified by 2D NMR. The BF$_3$ and BF$_4^-$ species were assigned according to their similar signal shapes comparing to those found in the $^{19}$F spectrum and according to the simultaneous generation in both $^{11}$B and $^{19}$F spectra during reaction (see chapter 4.7.4). $^{11}$B,$^{19}$F-

HOESYs and other boron related 2D NMR experiments were unsuccessful probably due to very short relaxation time of [11]B species.
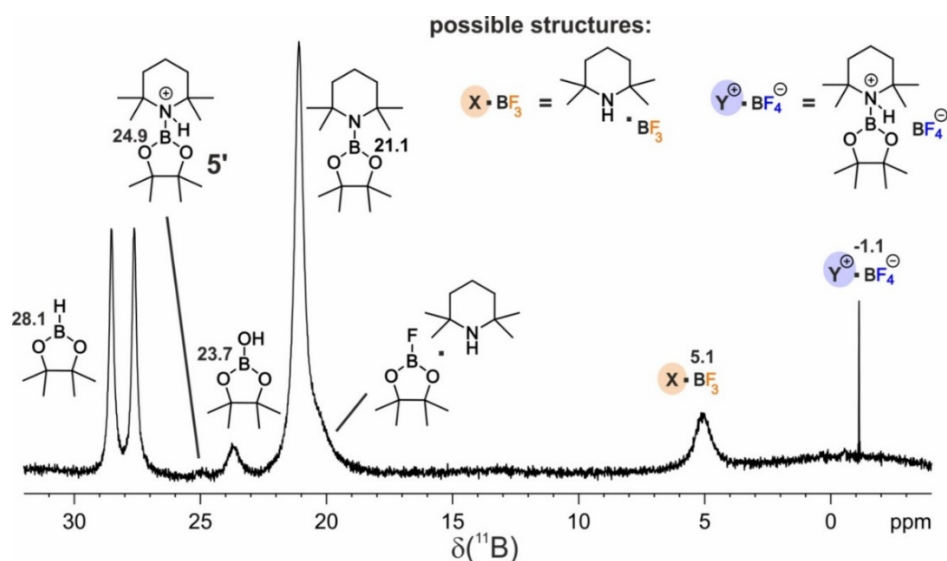


**Figure 4.34:** [11]B spectrum of the *ex-situ* illuminated phototcatalytic reaction in $CD_2Cl_2$ at 300 K after 24 hours.

### 4.7.3   Reaction Monitoring via *In-Situ* Illumination Inside the NMR

The photocatalytic single C-F bond cleavage in trifluoromethylbenzonitrile in presence of TMP and HBpin was followed by *in-situ* illumination inside the NMR device and ^{1}H, [11]B and ^{19}F spectra were recorded consecutively during reaction. The reaction mixture was prepared according to the procedure described in chapter 4.7.1. The reaction kinetic depicted in Figure 4.35a shows a product formation of 26% after 21.5 hours. We hoped to take advantage of the slow reaction rate for detecting potential intermediates. In Figure 4.35b, the [11]B spectra of the mixture before illumination and after 21.5 hours reveal the formation of **5'** and F-Bpin in low and barely detectable amounts. Both species were formed constantly (not shown) and are therefore by-products or very long-lived intermediates. Additionally, besides HBpin, the neutral TMP-Bpin was still present after this reaction time. Besides visible emergence of the 4-(2-(1,3-Dimethyl-2-oxoindolin-3-yl)-1,1-difluoroethyl)benzonitrile product signals, the ^{19}F spectra confirm the formation of F-Bpin over time with low signal intensity. The by-products identified in chapter 4.7.2 including $BF_3$, $BF_4^-$ and $CNPhCF_2H$ species were not formed at least not in NMR required amounts.
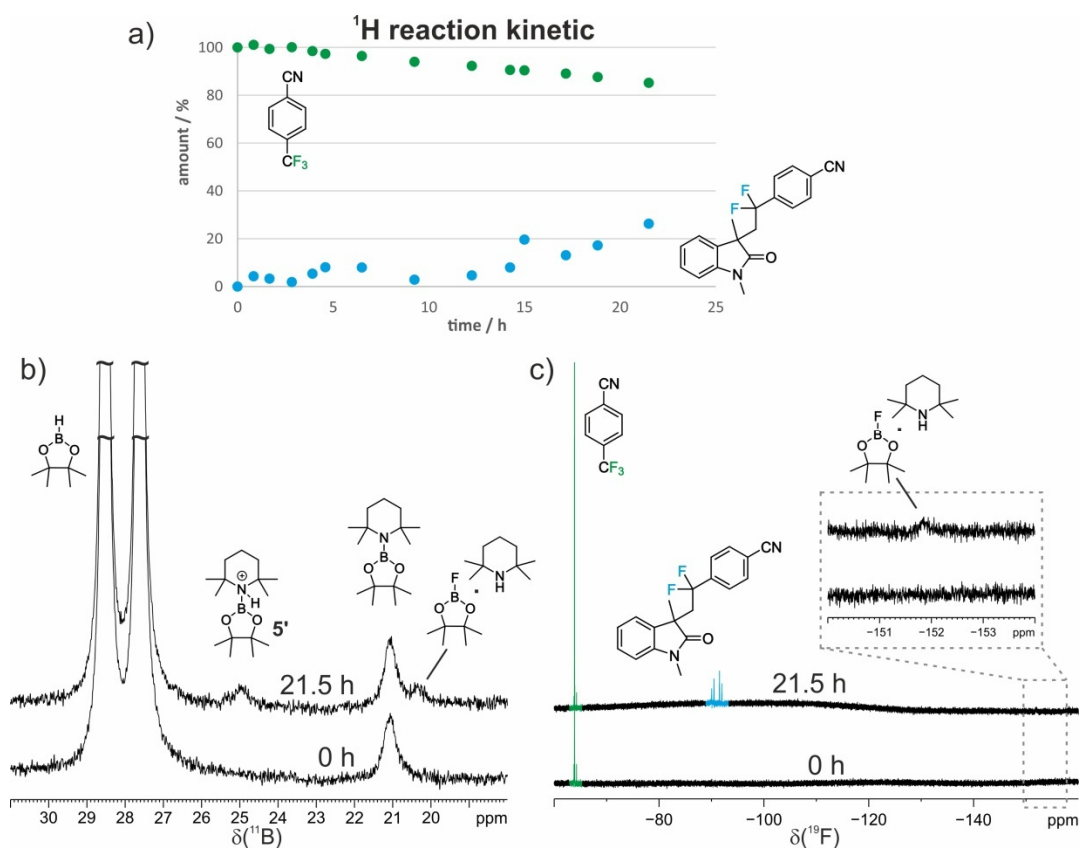
**Figure 4.35:** a) *In-situ* reaction kinetic of the photocatalytic mono-defluorination based on $^1$H integration of the corresponding signals; b) excerpt of the $^{11}$B NMR spectra before illumination (0 hours) and after 24 hours in dry and degassed CD$_2$Cl$_2$ at 300 K; c) excerpt of the corresponding $^{19}$F spectra.

## 4.7.4 Reaction Monitoring via *Ex-Situ* Illumination Inside the NMR

In order to obtain more information about the reaction mechanism and the formation of the by-products we tried to improve the reaction outcome by performing the photocatalysis outside the NMR spectrometer using the optimized conditions. The batch reaction was followed by NMR of the corresponding extracted samples. The photocatalytic mixture and NMR samples were prepared according to the method described in chapter 4.7.1. The excerpt of $^{19}$F spectra in Figure 4.36a clearly demonstrates the consumption of the trifluoromethylbenzonitrile starting material and the evolution of the product signals over time (0 – 24 hours). Via $^1$H integration the reaction progression was monitored (Figure 4.36b). 78% product yield were achieved after 24 hours and 83% of substrate were consumed. An additional excerpt of the $^{19}$F spectra in Figure 4.36c shows constant emergence of BF$_3$ and F-Bpin over time, which was already detected after 0.5 hours. The simultaneous generation of both signals confirms the proposed BF$_3$ generation coming

from F-Bpin (*vide supra*). In contrast, the formation of $BF_4^-$ seems to be a downstream reaction as its signal first appeared in the 2-hours-sample. In addition, $CNPhCF_2H$ (red marked) was already present in the sample after 0.5 hours and thus is assumed as unproductive by-product formed subsequently to the C-F bond cleavage of the trifluoromethyl-substrate. Interestingly, the spectrum representing the reaction after 16 hours shows a reduced $BF_3$ and an enhanced F-Bpin signal, which can potentially be a result of inconsistent sample preparation. However, this demonstrates a clear relation of both species.
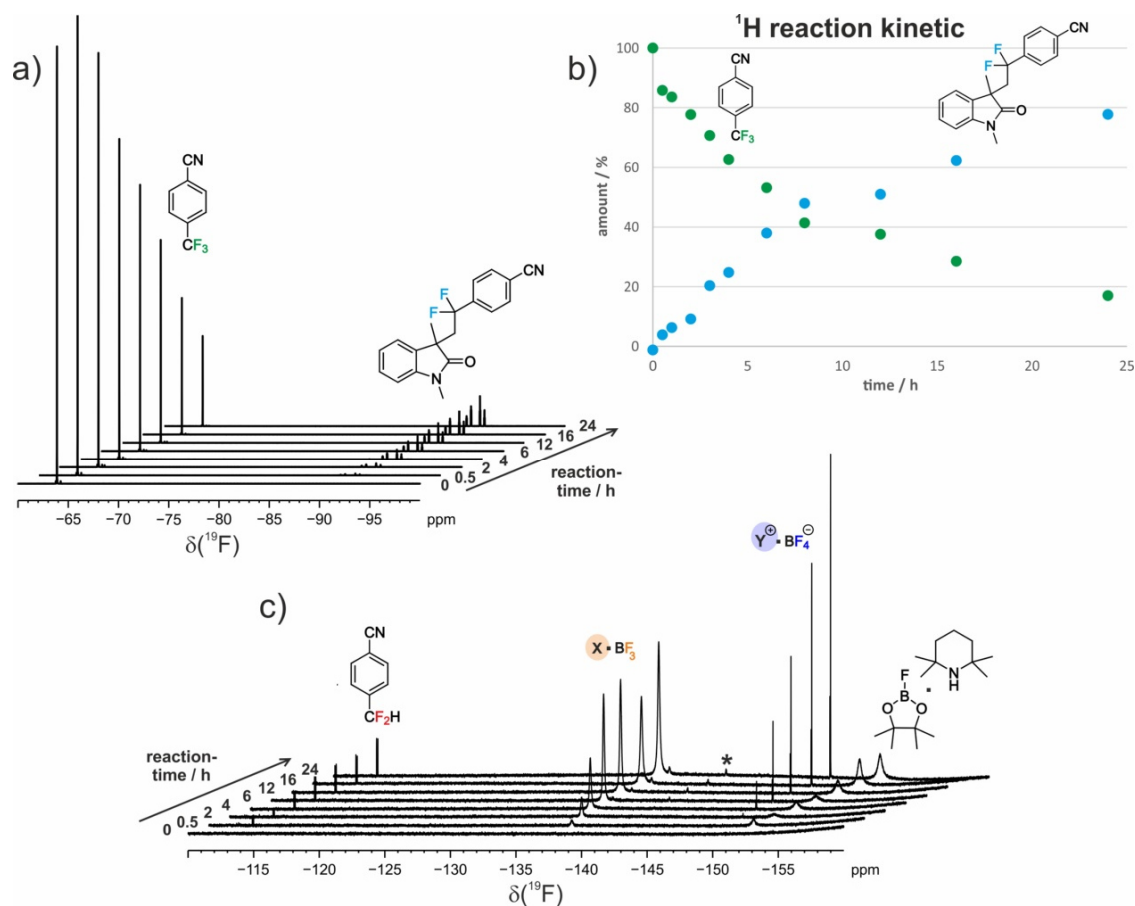


**Figure 4.36:** a) Excerpt of the $^{19}F$ NMR spectra of the photocatalytic *ex-situ* illuminated batch reaction in dry and degassed $CD_2Cl_2$ at 300 K representing the substrate consumption and product evolution over time (0 – 24 hours); b) reaction kinetic based on $^1H$ integration of the corresponding signals; c) excerpt of the $^{19}F$ spectra showing the relevant region of the by-products formed; * species not identified.
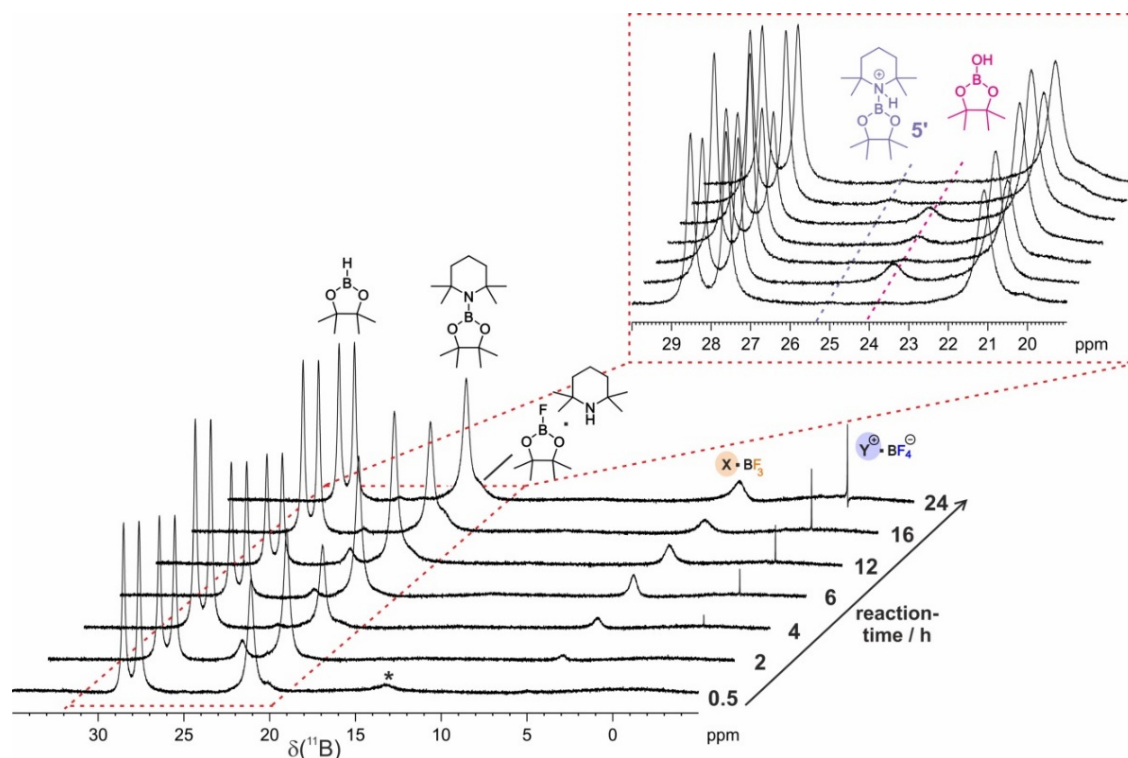
**Figure 4.37:** $^{11}$B NMR spectra of the photocatalytic *ex-situ* illuminated batch reaction in dry and degassed CD$_2$Cl$_2$ at 300 K from 0.5 – 24 hours; * species not identified.

The inhomogeneity of the samples can be seen more drastically regarding the $^{11}$B spectra (Figure 4.37). HBpin and TMP-Bpin, which stay in an equilibrium with each other, show different signal intensities for every sample. However, the generation of BF$_3$, F-Bpin and BF$_4^-$ could be verified, starting from 0.5 hours for BF$_3$ and F-Bpin and from 2 hours for BF$_4^-$ which is in line with the results obtained from $^{19}$F spectra. Moreover, the oxidation product HO-Bpin is randomly generated in a few mixtures. Its formation can potentially be explained by traces of O$_2$ which were potentially introduced into the NMR tube during sample preparation. In addition, the proposed reactive species **5'** could only be identified for the last two samples in low amounts.

### 4.7.5  Conclusion

Via ^{1}H, ^{19}F and ^{11}B and 2D NMR spectroscopic investigations of the photocatalytic monodefluorination in trifluoromethylbenzonitrile merged with Lewis-acid activation, the substrates, Lewis acid/base species, the reactive borenium cation intermediate and several by-products could be detected and assigned. Additional chemical shift analysis of TMP and HBpin in comparison with the resulting TMP-Bpin gives general insight into the electronic environment of boron compounds. Surprisingly, upon generation of neutral TMP-Bpin the tetramethyl-piperidine signals remain unchanged while a new methyl signal was generated for Bpin. Moreover, the reaction was followed by *in-situ* and *ex-situ* illumination, which revealed complementing results. Via irradiation directly inside the NMR device, the reaction rate was very slow, which enabled the detection of the build-up of the crucial TMP-Bpin[+] intermediate. The formation of F-Bpin as by-product could be confirmed as well. The immense reaction acceleration by performing the photocatalysis outside of the spectrometer allowed to follow the conversion of $CF_3$-benzonitrile and the generation of the $CNPhCF_2H$, $BF_3$ and $BF_4^-$ by-products.

### 4.7.6  References

[1]    Harris, R. K., Becker, E. D., Cabral de Menezes, S. M., Goodfellow, R., Granger, P. *Pure Appl. Chem.* **2001**, *73*, 1795–1818.

[2]    Knauber, R., Arikan, F., Röschthaler, G.-V., Gooßen, L. J. *Chem. Eur. J.* **2011**, *17*, 2689-2697.

[3]    H. Motohashi, M. Kato, K. Mikami *J. Org. Chem.* **2019**, *84*, 6483−6490.

[4]    M. Howell, K. Feng, J. R. Clark, L. J. Trzepkowski, M. C. White *JACS* **2015**, *137*, 14590-14593.

[5]    G. Iakobson, J. Du, A. M. Z. Slawin, P. Beier *Beilstein J. Org. Chem.* **2015**, *11*, 1494–1502.

[6]    K. L. Bamford, S. S. Chitnis, Z. Qu, D. W. Stephan *Chem. Eur. J.* **2018**, *24*, 16014-16018.

[7]    S. Bagherzadeh, N. P. Mankad *J. Am. Chem. Soc.* **2015**, *137*, 34, 10898-10901.

# 5   Conclusion

The development and advance of sustainable and efficient chemical reactions are the main goal in various fields of organic and biochemical synthesis. Imitating nature's concept of using light as energy source to accelerate molecular interactions paved the way for the design of visible light mediated photochemical transformations. The concept of photoredox catalysis is one of the most important and forward-looking synthetic strategies, which provides an environmentally friendly and simple procedure for the generation of organic building blocks. Besides the ecological aspect, access to highly energy-demanding and challenging conversions could be achieved. One example is the direct cleavage of strong bonds without prior activation. In order to optimize and advance photocatalytic reactions mechanistic understanding is pivotal. Besides proper photon absorption and redox properties of the reagents and catalytic species, concrete molecular interactions are the basis for successful energy conversion and product formation. In this regard, higher order preaggregates responsible for specific molecular interactions at synthetic conditions are often neglected. Moreover, analytical methods are still limited to get access to such non-covalent preassemblies. As such, the combination of low temperature NMR based H-bond analysis and diffusion measurements is an elegant approach to extract the distinctive reactive aggregate even if hidden by a bulk overall complexation of the reaction mixture. As such, this thesis focused on the NMR spectroscopic analysis of three photocatalytic reactions. Besides reaction monitoring, elucidation of reactive pathways and identification of intermediates, products and by-products, the main emphasis was the investigation of the impact of concrete intermolecular interaction as key to effective molecular transformations.

One prominent concept in the field of photoredox catalysis is the PCET for the activation of strong bonds, such as N-H and O-H. The concerted transfer of a proton and an electron in an oxidative PCET is known in literature to be forced by the formation of a strong H-bond between the substrate and a base. In chapter 2, the hydroamidation reaction of *N*-phenylpent-4-enamides developed by Knowles and co-workers was analyzed in detail. The optimized conditions involve an Iridium photocatalyst, a di-butyl phosphate base and blue light. Moreover, their screening of hydrogen atom donors revealed thiophenol as best performing reagent whereas common HAT donors such as phenol were inefficient. Under irradiation the amide N-H bond (BDFE: 99 kcal/mol) is cleaved in the course of PCET and an amidyl radical is formed, which subsequently adds intramolecularly to the olefin furnishing a carbon-centered radical. To complete the photoredox cycle the catalytic species are regenerated in a HAT process and the lactam product is formed in excellent yields. Besides its function as hydrogen atom donor, thiophenol was found to enhance the

reaction immensely without self-conversion although containing a weaker S-H bond (BDFE: 79 kcal/mol). An extended kinetic analysis of this reaction by Nocera *et al.* showed that the overall reaction efficiency can be enhanced by reducing the BET and thus promoting the PCET although the rate limiting step was determined to be the subsequent intramolecular ring closure. Introducing disulfides as radical trap lead to the accumulation of the reactive amidyl radical in an off-cycle equilibrium. Moreover, the group of Knowles revealed that the chemoselectivity can be modulated by combining H-bond assemblies and kinetic properties. However, both studies include highly diluted UV-based investigations preventing reliable conclusions about concrete H-bond mediated aggregation at synthetic conditions, which is indispensable for ion pairs in apolar solution. In addition, the initial rate kinetics performed in this thesis revealed a supportive effect of a combination of thiophenol and diphenyldisulfide, which drastically enhanced the overall efficiency of the hydroamidation. This cooperativity indicates an underestimated and rather neglected effect of thiophenol on the crucial reaction aggregates beyond radical aspects. Thus, the influence of thiophenol on the effective H-bond networks was elucidated and opposed to the ineffective phenol.

A combination of low temperature $^1$H, $^{15}$N, $^{31}$P chemical shift and $^1J_{NH}$ scalar coupling analysis and molecular dynamics (MD) simulations of the reaction system including *$^{15}$N*-labeled *N*-phenylpent-4-enamide, tetrabutylammonium di-*tert*-butylphosphate, thiophenol and phenol, respectively, unveilled the entire H-bond situation of the photocatalytic system for the first time. Activation modes within a complex ensemble of H-bond assisted ion pairs were identified. As a result of an acid-base reaction between thiophenol and the phosphate base the partial formation of the crucial phosphate-H$^+$-phosphate dimer could be revealed. This extended H-bond network was directly detected as key element in photocatalysis allowing for a productive shortcut for the regeneration of the reduced Iridium photocatalyst. Moreover, the broadly used PhSH additive in photocatalysis was shown to be replaceable by disulfide and acid. This allowed for the first time an individual tuning of radical and ionic channel and and accelerations of the reaction up to a factor of ~10 under synthetic conditions. Light intensity dependent reaction profiles indirectly allowed to trace the accumulation of a photo-generated radical species and to correlate the overall reaction rate to individual mechanistic steps.

On the other hand, the less acidic phenol prevents the generation of the pivotal phosphate dimer and is additionally incorporated into the substrate-activating complex. This was stated as one factor to inhibit a successful PCET driven amide conversion.

Our findings highlight that beyond mere radical effects extended H-bonded preassemblies are crucial for the efficiency of ion pair involved photoredox catalytic reactions and

encourage to investigate the complex aggregation situation of the key reaction system for the development of future photocatalytic transformations.

Future investigations of this concrete photocatalytic reaction system using different aromatic thiol derivatives with variable acidic properties could further elucidate the complex aggregation situation. However, the impact of other thiols on the delicate equilibria between aggregation, BET and rate determining steps have to be considered and analysed for the respective entire system. Furthermore, the knowledge gained in this study should be transferred to investigate further PCET mediated N-H bond activating reactions, which are similar from a synthetic point of view.

In the second chapter, the significance of non-covalent preaggregates was demonstrated for the PCET driven photocatalytic alcohol O-H activation. Moreover, the interplay between reaction design and mechanistic understanding as fundament for the development of optimized photocatalytic conditions was highlighted. A new synthetic protocol for the PCET mediated O-H bond cleavage of cycloalkanols and late-stage remote functionalization was developed. Simple and mild reaction conditions including a mesityl-acridinium organic photocatalyst, a pyridine co-catalyst and blue light enabled the conversion of phenyl-cyclobutanols. Based on an alcohol-pyridine H-bond an alkoxy radical is formed as a result of the PCET step. Subsequent ring opening furnishes a carbon-centered radical, which is trapped by an electron deficient species, such as a Michael acceptor for a Giese type C-C bond coupling. Since oxidative PCET is known to proceed via H-bond formation between substrate and a catalytic base, various pyridines were screened for the activation of aryl-alcohols. In contrast to the literature-based basicity trends, 2-methoxpyridine was found to be most effective for the conversion of phenyl-cycloalcohols followed by the 2-Cl-substitued base, which outperformed 2,6-di-OMe-pyridine. These findings hint at a multifaceted role of the base besides the formation of mere substrate-base H-bonding. This was further corroborated by the fact the optimized reaction system was unproductive for aliphatic alcohols.

Low temperature NMR spectroscopic ^{1}H chemical shift and DOSY analysis revealed a combination of aromatic, C-H-$\pi$, and H-bond interactions between alcohol and base to be key for the formation of the effective preassemblies for our photocatalysis. Hence, the substrate scope could be expanded to alkyl-alcohols by modulating the structure of the base. Applying halogenated quinolines opened the door for drastically accelerated yields. This study demonstrates the crucial interplay between synthesis and mechanistic investigations, which should be interwoven in general to obtain the best performing conversion. Hence, not only a new metal-free ring-opening remote functionalzation of cycloalkanols was presented but the impact of substrate specific preaggregates and dispersion interactions in photoredox catalysis was highlighted as well.

In prospective investigations, the concrete intermolecular interactions between different alcohol substrates and substituted bases including the proposed aromatic, C-H-$\pi$, and halogen assisted H-bond interactions should elucidate the key contributions for successful PCET. This would open the door for improved general understanding of the effect of substituents on the required preassemblies and for the conversion of further substrates.

In chapter 4, the crucial non-covalent preaggregation of trifluoromethylarene substrates and a Lewis acid/base couple was studied, which is key to novel selective mono-defluorination producing valuable aryldifluoromethyl compounds. Using a combination of visible photocatalysis and Lewis acid activation the single C-F bond cleavage, which is challenging due to the inertness of the C-F chemical bond and problems with over-defluorination, was achieved with good chemoselectivity and functional group tolerance. The optimized conditions involve HBpin as Lewis acid fluoride scavenger, TMP as Lewis base, and an Iridium photocatalyst. Under irradiation with blue light the $ArCF_3$ substrate is reduced to the radical anion and subsequently activated by the Lewis acid/base pair. In this regard, NMR spectroscopic analysis revealed the borenium cationic species TMP-Bpin$^+$ as the key activating compound abstracting F$^-$ to furnish the $ArCF_2 \cdot$ radical. After trapping with methacrylamides the aryldifluoromethyl species are generated.

For this challenging transformation the nature of the concrete preaggregation of substrate and the borenium cationic species initiating successful single C-F bond cleavage was unclear. Thus, $^1$H, $^{11}$B, $^{19}$F and 2D NMR spectroscopic investigations were performed. Besides the identification of TMP-Bpin$^+$, its H-bond mediated interaction towards the neutral 4-trifluoromethylbenzonitrile substrate could be demonstrated. However, against our expectations of an interaction between the $CF_3$ group and the proton of the borenium cationic species for efficient fluoride transfer, the TMP-Bpin$^+$ was found to be primary attached via the nitrile group of the substrate due to its higher H-bond acceptor ability. However, the reduced substrate, which is inaccessible via NMR, is assumed to exhibit immensely higher H-bond acceptor abilities and thus, the F$^-$ abstraction is assumed to be forced. Additional reaction profiles of *in-situ* and *ex-situ* illuminated reactions demonstrated the evolution of the essential borenium cationic species. Furthermore, F-Bpin and by-products such as $CNPhCF_2H$, $BF_3$ and $BF_4^-$ could be identified.

In summary, the three studies show that preaggregation is a key factor in photocatalysis and that NMR spectroscopy is ideally suited to detect these complex preassemblies. As such, this work highlights the importance of detailed mechanistic insight, which will be crucial for the development of future photoredox catalytic transformations.

# 6   Abbreviation Register

| | |
|---|---|
| 1D/2D | one/two dimensional |
| Å | Ångström |
| BDFE | bond dissociation free energy |
| BET | back-electron transfer |
| BPT | back-proton transfer |
| br | broad |
| CEST | chemical exchange saturation transfer |
| CIDNP | chemical induced dynamic nuclear polarization |
| CSA | chemical shift anisotropy |
| CV | cyclic voltammetry |
| d | doublet |
| DCE | dichloroethane |
| DOSY | diffusion-ordered spectroscopy |
| δ | chemical shift |
| DCM | dichloromethane |
| EE | ethylacetate |
| ES-MS | electrospray ionization – mass spectrometry |
| EV | electron volt |
| *fac* | facial |
| FID | free induction decay |
| GC-MS | gas chromatography – mass spectrometry |
| HAT | hydrogen atom transfer |
| HMBC | heteronuclear multiple bond correlation |
| HMQC | heteronuclear multiple quantum correlation |
| HOESY | heteronuclear Overhauser enhancement spectroscopy |
| HOMO | highest occupied molecular orbital |
| $^i$Pr | *iso*-propyl |
| J | coupling constant |
| K | Kelvin |
| LED | light-emitting diode |

| LFP | laser flash photolysis |
|-----|------------------------|
| LUMO | lowest occupied molecular orbital |
| m | multiplet |
| MD | molecular dynamics (simulation) |
| MHz | megahertz |
| MLCT | metal-to-ligand-charge-transfer |
| mmol | millimole |
| mM | millimolar |
| NMR | nuclear magnetic resonance |
| NOE | Nuclear Overhauser effect |
| NOESY | Nuclear Overhauser enhancement spectroscopy |
| NS | number of scans |
| PCET | proton-coupled electron transfer |
| PE | petroleum ether |
| PIRAT | photo-induced reversible acceleration of $T_1$-relaxation |
| ppm | part per million |
| q | quartet |
| rt | room temperature |
| SCE | saturated calomel electrode |
| SET | single electron transfer |
| t | triplet |
| $^t$Bu | *tert*-butyl |
| TEMPO | 2,2,6,6-Tetramethylpiperidinyloxyl |
| TLC | thin layer chromatography |
| TOCSY | total correlation spectroscopy |
| TROSY | transverse relaxation-optimized spectroscopy |
| µmol | micromole |
| TMS | tetramethylsilane |
| UV/Vis | ultraviolet/visible light |
| ν | frequency |

# Eidesstattliche Erklärung

(1) Ich erkläre hiermit an Eides statt, dass ich die vorliegende Arbeit ohne unzulässige Hilfe Dritter und ohne Benutzung anderer als der angegebenen Hilfsmittel angefertigt habe; die aus anderen Quellen direkt oder indirekt übernommenen Daten und Konzepte sind unter Angabe des Literaturzitats gekennzeichnet.

(2) Bei der Auswahl und Auswertung folgenden Materials haben mir die zu Beginn des jeweiligen Kapitels aufgeführten Personen in der jeweils beschriebenen Weise unentgeltlich geholfen.

(3) Weitere Personen waren an der inhaltlich-materiellen Herstellung der vorliegenden Arbeit nicht beteiligt. Insbesondere habe ich hierfür nicht die entgeltliche Hilfe eines Promotionsberaters oder anderer Personen in Anspruch genommen. Niemand hat von mir weder unmittelbar noch mittelbar geldwerte Leistungen für Arbeiten erhalten, die im Zusammenhang mit dem Inhalt der vorgelegten Dissertation stehen.

(4) Die Arbeit wurde bisher weder im In- noch im Ausland in gleicher oder ähnlicher Form einer anderen Prüfungsbehörde vorgelegt.

Regensburg, den _____          _____

                                                            Nele Berg